Bioinspired Nanoarchitectonics of Arylenediimides for Optical, Electronic and Biological Applications

A Thesis Submitted for the Degree of

Doctor of Philosophy

By

M. Pandeeswar

Chemistry and Physics of Materials Unit

Jawaharlal Nehru Centre for Advanced Scientific Research

(A Deemed University)

Bengaluru-560064, India

September 2015

Dedicated to my Parents and Brother

DECLARATION

I hereby declare that the matter embodied in the thesis entitled "**Bioinspired Nanoarchitectonics of Arylenediimides for Optical, Electronic and Biological Applications**" is the resultant of the investigations carried out by me at the Bioorganic Chemistry Laboratory, New Chemistry Unit, Chemistry and Physics of Materials Unit, Jawaharlal Nehru Centre for Advanced Scientific Research, Bangaluru, India under the supervision of **Prof. T. Govindaraju** and that it has not been submitted elsewhere for the award of any degree or diploma.

In keeping with the general practice in reporting the scientific observations, due acknowledgement has been made whenever the work described is based on the findings of other investigators. Any omission that might have occurred due to oversight or error in judgement is regretted.

M. Pandeeswar

CERTIFICATE

I hereby certify that the work described in this thesis entitled "**Bioinspired Nanoarchitectonics of Arylenediimides for Optical, Electronic and Biological Applications**" has been carried out by **Mr. M. Pandeeswar** under my supervision at the Bioorganic Chemistry Laboratory, New Chemistry Unit, Chemistry and Physics of Materials Unit, Jawaharlal Nehru Centre for Advanced Scientific Research, Bangaluru, India and that it has not been submitted elsewhere for the award of any degree or diploma.

Prof. T. Govindaraju

(Research Supervisor)

ACKNOWLEDGEMENTS

First and foremost, I wish to express my sincere gratitude to my research supervisor Prof. T. Govindaraju for his kind support, guidance, suggestions and invaluable encouragement he has given to me all through the course of this investigation. I shall remain ever thankful to him for giving me enough freedom to work on my area of interests.

I thank Prof. C. N. R. Rao FRS, who has been a constant source of inspiration for me. I would also like to thank him as the Chairman, NCU for allowing me to use the facilities of the centre.

I would like to thank Prof. Balasubramanian Sundaram, Chairman, CPMU, for his generous support and encouragement throughout my stay in JNCASR. I also thank him for providing the infrastructure and facilities to carry out my research work.

I am thankful to Prof. K.S. Narayan, Prof. G.U. Kulkarni, Prof. Balasubramanian Sundaram, Prof. Chandrabhas Narayana, Prof. M. Eswaramoorthy, Prof. A. Sundaresan, Prof. S. M. Shivaprasad, Prof. Ranganathan, Prof. Ranjan Datta, Prof. T. Govindaraju, Prof. Subi J. George , Prof. Tapas Kumar Maji, Prof. Swapan Pati, Prof. Umesh V. Waghmare , Prof. Shobhana Narasimhan, Prof. P. Balaram and Prof. S. P. Sarma for their excellent courses that has been extremely helpful to this study.

I would like to thank Prof. K. S. Narayan, Dr. Satyaprasad P. Senanayak, Prof. S. Ramakumar, and Mr. H. Khare for their valuable discussions and fruitful collaborations.

I am grateful to all my lab mates Dr. Debabrata Maity, Dr. Avinash, Mr. Nagarjun, Mr. Shivaprasad, Mr. Rajasekhar, Ms. Suseela, Mr. Sourav Samanta, Mr. Asim Samanta, Dr. Atul, Dr. Madhu, Dr. Chandra Shekar, Dr. Sangita, Ms. Shilpa, Mr. Vardhaman, Mr. Sulendar, Ms. Malabika, Mrs. Manju, Dr. M. Sasikumar, Mr. Anand, Mr. Sandeepa, Mr. Manjunath with whom I have had some of the most memorable moments of my life. I am also thankful to SRF students Ms. Kanchan agarwal, Ms. Vinothavarthini, Ms. Paramita sarkar, Mr. Amit Bhattacharya, Mr. Ajesh Vijayan, Dr. Subha Mukhergee for working with me on different research projects.

Thanks to all my Int. Ph.D mates namely Mr. Sharma, Mr. Dileep, Dr. Gayatri, Mr. Rana, Ms. Sudeshna, Mr. Varun, Mr. Arpan, Mr. Chidambar with whom I started my life at this centre and whose cheerful company made these stay in JNC so cherishable.

I thank the timely help of technical staffs namely Mrs. Selvi (FESEM), Mrs. Usha (TEM), Mr. Basavaraj (AFM), Mr. Mahesh (NMR), Mr. Vasu (UV/PL/IR), Mr. Anil (PXRD), Shivakumar (HRMS), Naveen, Mune Gowda for their help with the various characterization techniques.

It is a pleasure to thank all my JNC friends Dr. Sandeep, Dr. Bhadram, Mr. Dasari, Dr. Matte, Dr. Narendra, Dr. Malli, Mr. Sharma, Mr. Satyanarayana and many more for their support and encouragement have been an indispensable in my Ph.D. life. I thank all my well-wishers and those who have helped me directly or indirectly.

I thank Administrative Staff, Hostel Staff, Mess Workers, House Keeping Staff and Security for providing and maintaining the various facilities that have been helped me immensely.

Special thanks to my parents and family members for their love, blessings and affection on me. I am also indebted to my elder brother (Dr. Parameshwar Makam) who has always been there like a guardian and friend to me. This thesis is a minor recognition to my parents and brother for their love and support.

PREFACE

The work outlined in this thesis has been broadly categorized into six chapters as follows,

Chapter 1 gives an overview of bioinspired (nano-)architectonics, design strategies and its advantages in generating functional systems and materials through the integration of biomolecules. In general nanoarchitectonics is a process of organizing nanoscale structural units which are usually a group of atoms or molecules in an intended configuration and paramount importance in chemistry, biology and materials science. Biological systems from biomolecules to cells to complex multi-cellular organisms demonstrate the extraordinary self-assembled nano- and micro-architectures with a range of complex functions. The various self-assembly processes in living organisms viz., programmed or coded, static and dynamic, hierarchical and template assembly inspire the development of new molecular systems and materials which is termed as bioinspired nanoarchitectonics. This process of molecular (nano-)architectonics is widely relied on basic biomolecules i.e., nucleobases, amino acids/peptides, sugars, and lipids. We demonstrate the potential of implementing the bioinspired nanoarchitectonics by conjugating electrically active arylenediimide molecules with biomolecules to generate biomimetic and bioelectronics nanomaterials, and therapeutic candidates.

Chapter 2 comprises of three subchapters. We describe the thoughtfully designed amino acid conjugated n-type organic semiconductor naphthalenediimides (NDIs) and their nanoarchitectonics. The first subchapter describes the amino acids as supramolecular auxiliaries for the crystal engineering of NDI organization. For the first time, we achieved all four possible crystal packing modes namely co-facial, brickwork, herringbone and slipped stacks of the NDI. The minute structural mutations in the form of α–substituents in amino acid offer tunable chiroptical, viscoelastic and nanoscale properties. In the second subchapter, the π–electron deficient nature of central NDI core has been utilized to construct stimuli-responsive ferroelectric charge transfer complexes in the presence of designed complementary π–electron rich pyrene tweezer.

Furthermore, we present the exploitation of excimer to exciplex transformation to develop a filter paper-based reversible fluorometric test kit for the detection of carcinogenic benzene. The third subchapter describes the amino acid appended NDIs as a novel class of modulators of Aβ aggregation which is highly useful in the development of disease-modifying therapeutics for Alzheimer's disease.

Chapter 3 is divided into four subchapters, deals with the conjugation of perylenediimides (PDI) with amino acids to impart water solubility and metal chelation ability among other properties. The host-guest interactions driven dynamic assembly and disassembly modulated fluorescence switching on-off property has been demonstrated to be a promising approach for rapid, highly sensitive and selective detection of metal ions such as Cu^{2+}, Fe^{3+} (first subchapter) and Hg^{2+} (in third subchapter) in aqueous medium. The second subchapter describes the novel PDI based peroxidise-mimicking fluorogenic substrate for the detection of H_2O_2. In the fourth subchapter, we present pH-responsive probe and its reversible chiroptical switching property.

Chapter 4 describes the nanoarchitectonics of peptide functionalized NDI under two subchapters. The first subchapter presents plausible clues for nature’s mysterious selection of homochirality. The second subchapter demonstrates the crystallographic insight-guided nanoarchitectonics and conductivity modulation of NDI through peptide conjugation.

In Chapter 5 glucosamine conjugated NDI and its hierarchical nanoarchitectonics is presented. The detailed spectroscopic studies in water indicated the formation of right handed supramolecular helical organization via transcription of chiral information from sugar backbone to central NDI core. Surprisingly, these conjugates further self-organized into helical nanotapes with opposite helicity (compare to the solution) signifying the formation of hierarchical superstructures similar to that of collagen. In addition, the concentration drives the transformation of the helical tapes to nanotubes and these nanotubes can be uniformly coated with silver through silver mirror test.

The final Chapter 6 deals with the mutual templating of the nucleobase (adenine) conjugated NDI and its complementary single strand DNA (dT_n) for the ultrasensitive detection of hazardous Hg^{2+} in water. Herein, we investigated the template guided assembly (templated DNA nanotechnology) and its unusual template lengths dependent properties such as modulation of 2D morphology and charge transport properties. Furthermore, we exploited the well-known phenomenon of thymine-Hg^{2+} binding interactions for sensitive and selective detection of toxic Hg^{2+} ions in water using chiroptical switching and electronic characteristics.

In summary, this thesis demonstrate the integration of basic biomolecules viz., amino acids (Chapter 2 and 3), peptide (Chapter 4), sugar (Chapter 5) and nucleobase (Chapter 6) with aryelenediimides (NDI and PDI) and their (nano-)architectonics for optical, electronic and biological applications.

List of Figures

Figure 1.1 Schematic illustration of concepts and applications of nanoarchitectonics. 2

Figure 1.2 Schematic illustration of concepts and applications of bioinspired nanoarchitectonics. 3

Figure 1.3 The molecular building blocks of life. Adapted with permission of NPG from reference 53. 5

Figure 1.4 Molecular structures of amino acids, nucleobases, carbohydrates and lipids along with their commonly used abbreviations. Adapted with permission of RSC from reference 22. 6

Figure 1.5 a) Schematic representation of nucleic acids b) nucleobase structures are shown with their common name with one letter abbreviations and their complementary base pairing via hydrogen bonding interactions. 10

Figure 1.6 Schematic representation of sequence specific protein secondary structure. 14

Figure 1.7 Schematic representation of chaperonin-assisted protein folding. 14

Figure 1.8 Hierarchical structure of bone. Adapted with permission of NPG from reference76......... 15

Figure 1.9 Schematic representation of a) static self-assembly of protein folding from native to stable folded form.and b) dynamic assembly in the form of enzyme (E), substrate (S) interactions. 15

Figure 1.10 Chirality at various scales including neutrinos, enantiomeric molecules, nanosized biomacromolecules with chiral structures (DNA and proteins), self-assembled micrometer-sized helical ribbons, microorganisms (helix-shaped bacteria), macroscopic living systems (seashells and plants), and galaxies. Adapted with permission of ACS from reference 107. 17

Figure 1.11 Molecular structures of arylenediimides. 1,2,4,5-benzenetetracarboxydiimide (pyromellitic diimide, PyDI), 1,4,5,8-naphthalenetetracarboxylic diimide (NDI) and 3,4,9,10-perylenetetracarboxic diimide (PDI). 18

Figure 1.12 a) Principal z- and y- polarized π–$\pi*$ transitions in NDI chromophore. b) Schematic representation of the transition of the angles and distance between the z-polarized transition moments of stacked NDI chromophores.[78] 20

Figure 1.13 Overview of bioinspired nanoarchitectonics of arylenediimides presented in this thesis. (S-, static, D-, dynamic, P-, programmed, T-, templated, H-, hierarchical). Where n= 0 for NDI and n= 1 for PDI. 21

Figure 2.1.1 Molecular structures of NDI derivatives of chiral amino acids (L-**ANA**, L-**FNF**, L-**WNW**, D-**ANA**, D-**FNF** and D-**WNW**) and achiral ethylamine (**eNe**) synthesized by conjugating with 1,2,5,8-napthathalenetetracarboxylic dianhydride (NDA). 38

Figure 2.1.2 Single crystal X-ray structures of alanine (L-**ANA** and D-**ANA**), phenylalanine (L-**FNF** and D-**FNF**), tryptophan (L-**WNW** and D-**WNW**) and ethylamine (**eNe**) functionalized NDIs and their molecular organization into all possible crystal packing modes (cofacial, brickwork, herringbone and slipped stack). The prefix L and D correspond to NDIs functionalized with L-amino acid and D-amino acid respectively. Solvent molecules and hydrogen atoms have been omitted from the crystal packing representation for the clarity 40

Figure 2.1.3 a) Transformed UV-vis absorption and b) fluorescence emission spectra of NDI-conjugates in their solid state. i: L-**ANA** , ii: L-**FNF**, iii: **eNe** and iv: L-**WNW**. CT: Charge transfer band. c) TCSPC decay profile of L-**ANA** ($\lambda_{emission}$ 552 nm), L-**FNF** ($\lambda_{emission}$ 490 nm) and **eNe** ($\lambda_{emission}$ 565 nm) with a 405 nm exitation. d) Temperature versus normalized fluorescence emission intesity of L-**FNF (**at 490 nm**)** and **eNe** (at 563 nm). Absorption spectra (a) were recorded in reflection (R) mode 44

Figure 2.1.4 Rheological studies of organogels of amino acid-NDI conjugates. a-c) Stress sweep experiments and d-f) frequency sweep experiments of **ANA** (a and d), **FNF** (b and e) and **WNW** (c and f) respectively. G': storage modulus (■) and G": loss modulus (●). 47

Figure 2.1.5 CD spectra of L- and D-isomers of a) **ANA**, b) **FNF**, c) **WNW** and d) **eNe** in gelling solvents (I: MCH/THF and III: MCH/$CHCl_3$) and crystal forming solvent (II: DMSO). 49

Figure 2.1.6 Solid state helical organization of a) L-**ANA** , b) D-**ANA** , c) L-**FNF**, d) D-**FNF** and e) L-**WNW** in their respective crystal lattice. (a and b) cofacial helical columnar stacks and (c-e) supramolecular tilt helical organization. 50

Figure 2.1.7 The 2_1 helicity inherent in the **eNe** $P2_1/c$ crystal system. Four helices embedded within the crystal lattice: side-to-side enantiomeric pairs AB (left handed) and AC (right handed) along the crystallographic *c* axis and splipped herringbone enantiomeric pairs AD (left handed) and AE (right handed) along crystallographic *a* axis 51

Figure 2.1.8 FESEM micrographs of a) drop casted **eNe** solution (MCH/$CHCl_3$: 80/20 V/V) and xerogels of b) **ANA**, c) **FNF**, and d) **WNW**. *inset:* The respective solution morphology. 53

Figure 2.1.9 Summery of biomimetic molecular organization of NDI in solid state. 55

Figure 2.1.10 a) Molecular structures of glycine and its derivatives conjugated NDIs **1**, **2** and **3**. b) Schematic representation of 2D sheets and their dimensions. c) Proposed noncovalent intermolecular interactions, hydrogen bonding (red dash line) and NDI-NDI aromatic interactions (black dash line) present in 2D sheets. 60

Figure 2.1.11 FESEM image of 2D sheets of **1**(a), **2**(b) and **3**(c). AFM image of **1**(d), **2**(e) and **3**(f) and corresponding AFM height profiles. 61

Figure 2.1.12 Photophysical studies of NDIs **1**, **2** and **3**. a-c) UV-vis absorption spectra and d-f) fluorescence emission spectra. *inset*: the photographs of corresponding films on quartz substrate under UV light (365 nm). 62

Figure 2.1.13 Temperature dependent fluorescence emission spectra of a) **1** 2D sheet, b) **2** 2D sheet and c) **3** 2D sheet. d) Plot of fluorescence emission intensity as a function of temperature (from 20 ^{o}C to 100 °C) of **1** (at 553 nm), **2** (472 nm) and **3** (at 537 nm). e) TCSPC decay profile of **1** (b_{max} 553 nm), **2** (b_{max} 472 nm) and **3** (b_{max} 537 nm) with a 405 nm excitation...64

Figure 2.1.14 a) Comparison of ^{1}H-NMR spectra of **1**, **2** and **3** in full spectral range. b) ^{1}H NMR spectra of **1**, **2** and **3** at NDI region (8.8-8.7 ppm) the dotted box region in a. 65

Figure 2.1. 15 Concentration dependent ^{1}H-NMR spectra of **1** (where (i) 3 mM, (ii) 9 mM, (iii) 18 mM, (iv) 27 mM, (v) 36 mM.; a) full spectral region. b) NDI aromatic region (8.73-8.77 ppm). c) Carboxylic acid OH region (12.7-13.5 ppm). d) Plot of concentration versus NDI (■) and carboxylic acid (▲) proton chemical shifts of **1**. 66

Figure 2.1.16 Concentration dependent ^{1}H-NMR spectra of **2** (where (i) 6 mM, (ii) 1.6 mM, (iii) 3 mM, (iv) 5 mM, (v) 9 mM); a) full spectral region. b) NDI aromatic region (8.71-8.72 ppm). c) amide-1 region (7.70-7.76 ppm). d) Plot of concentration versus NDI (■) and amide (▲) proton proton chemical shifts of **2**. 67

Figure 2.1.17 Concentration dependent ^{1}H-NMR spectra of **3** (where (i) 3 mM, (ii) 9 mM, (iii) 18 mM, (iv) 27 mM, (v) 36 mM); a) Full spectral region. b) NDI aromatic region (8.74-8.77 ppm). c) ester O-CH_3 region (3.70-3.75 ppm). d) Plot of concentration versus NDI (■) and ester proton(▲) proton proton chemical shifts of **3**. 68

Figure 2.1.18 Temperature dependent ^{1}H-NMR spectra of **1**; a) Full spectral region. b) NDI aromatic region (8.39-8.65 ppm). c) Plot of NDI proton chemical shift as a function of temperature. 69

Figure 2.1.19 Temperature dependent ^{1}H-NMR spectra of **2**; a) Full spectral region. b) NDI aromatic region (8.10-8.73 ppm). c) Amide region (6.8-7.8 ppm). d) Plot of NDI proton chemical shift as a function of temperature. 70

Figure 2.1.20 Temperature dependent ^{1}HNMR spectra of **3**; a) Full spectral region. b) NDI aromatic region (8.74-8.78 ppm). c) Plot of NDI proton chemical shift as a function of temperature. 71

Figure 2.1.21 a) IR spectra of 2D sheets of **1-3** in the region 4000-3000 cm^{-1}. b) PXRD diffraction patterns of **1-3** 2D sheets at 25 °C. 71

Figure 2.2.1 a) Molecular structures and schematic representation of acceptors (**A1**-**A2**) and donor (**DPT**). Photographs of **DPT** aqueous solutions (DMSO/water: 20/80,v/v) and solid powder under UV (365 nm) and visible light. b) Schematic representation of stimuli responsive tweezer-inclusion-sandwich (TIS) CT coassembly of **DPT** and **A1**. P-type (right handed) helical self-assembly of **A1**, mechanical stimuli (ultrasonication for solution and grinding for solid powders) induced P-type (right handed) helical tweezer- sandwich mixed-stack CT coassembly, UV-light responsive transformation to achiral CT complex and temperature responsive CT chiral inversion from P-type (right handed) to M-type (left handed). Photographs of corresponding aqueous solution/solids under UV- and visible-light, **A1** aqueous solution and solid powders, Inverted vials of CT (**DPT**:**A1** (1:2)) hydrogel. Mechanically co-ground (**DPT**:**A1** (1:2)) solid powders. 76

Figure 2.2.2 a) UV-vis absorption spectra of **DPT**. b) Fluorescence emission ($\lambda_{excitation}$ = 340 nm) spectra of **DPT.** c) Concentration dependent fluorescence spectra of **DPT (**λ_{ex}= 340 nm). d) Excitation spectra of **DPT**.e) Concentration dependent fluorescence spectra of **A1 (**λ_{ex}= 380 nm). f) the plot of excimer intensity versus concentration of **DPT** and **A1** respectively...78

Figure 2.2.3 a) UV-vis spectra in an aqueous solution ([**A1**]= 0.2 mM, [**DPT**]= 0.1 mM). b) Fluorescence emission spectra in aqueous solution with excitation wavelength= 340 nm, inset corresponding photographs of aqueous solution under UV and visible light. c) and d) UV-vis and fluorescence emission spectra of **DPT**, **A1** and **DPT**:**A1** (after co-grinding) in their solid state respectively. 80

Figure 2.2.4 a) UV-vis absorption titration spectra of **DPT**:**A1**. b) Fluorescence emission titration spectra of **DPT:A1**. c) Plot of CT absorption at 536 nm (blue line) and fluorescence excimer (FE) emission intensity at 475 nm (red line) as a function of fractional **A1** addition to **DPT** (**A1**/**DPT**=0.5, 1, 2 and 3). d) Photographs of corresponding aqueous solutions under visible and UV light show increase in CT color (brick-red) and gradual fluorescence quenching. 81

Figure 2.2.5 a) CD spectra of individual **A1**, **DPT** and **A2** in aqueous solutions. b) CD spectra of CT complexes at 1:2 (**DPT**:**A1**/**A2**) ratio. c) Light responsive CD spectra of **DPT**:**A1** CT complexes. d) CD spectra of **DPT**:**A1**/**A2** CT complexes at 358K. e) Stimuli responsive CD spectral changes of **DPT**:**A1** (1:2) CT complexes in aqueous solution at 400 nm. f) LD spectra. 83

Figure 2.2.6 a) Variable-temperature (VT) UV-visible absorption spectra of **DPT**:**A1.** b) VT-Fluorescence emission (FE) spectra of **DPT**:**A1**. c) and d) are VT-CD spectra of **DPT**:**A1** and **DPT**:**A2** respectively**.** e) The plot of FE intensity at 475 nm (Blue line) and ICD intensity at 400 nm studies of **DPT**:**A1**CT assembly in aqueous solution as a function of temperature, schematic representation of heating induced assembly transformation from P-type helical CT co-assembly to mixture of self-segregated M-type CT co-assembly and **DPT** tweezer. Dotted arrows indicating the respective spectral changes upon heating. 85

Figure 2.2.7 Solvent dependent ^{1}H-NMR (full) spectra of **DPT**:**A1** (1:2) in DMSO-d_6 as a function of addition of water; i) 4 µL, ii) 8 µL, iii) 16 µL, iv) 20 µL and v) 24 µL. b) Photographs of corresponding NMR sample solutions. c) The enlarged ^{1}H-NMR spectra of DPT amide region (8.76-8.66 ppm, red), A1 NDI aromatic ring region (8.75-8.55 ppm, blue) and DPT pyrene aromatic region (8.30-7.90 ppm); doted arrows indicate the chemical shifts upon addition of water. d) IR spectra of **DPT**, **A2** and **DPT**:**A1** (1:2) CT complex at Amide (NH) stretching frequency region (3200 to 3500 cm-1) and Carbonyl (CO) stretching frequency region (1600 to 1800 cm-1). e) Proposed model for the formation of extended mixed-stack tweezer- sandwich CT co-assembly between **DPT** and **A1/A2** via complementary π–surface stacking and hydrogen bonding interactions..87

Figure 2.2.8 a) FESEM images of **A1.** b) FESEM images of **DPT**:**A1** (1:2) CT xerogel. c) AFM Section analysis of individual fibers and corresponding height profile along the blue and red line. d) PXRD pattern of **A1, DPT** and **DPT**:**A1**(1:2) xerogel film. 89

Figure 2.2.9 Demonstration of selected area CT (SACT) formation on flexible substrate; Photographs showing use of donor (**DPT**) as invisible UV-ink (visible under UV light) to write (e.g., NCU) on a filter paper and acceptor (**A1**/**A2**) spray aids the visible (naked eye) readout as the brick-red CT complex forms in the written area. 90

Figure 2.2.10 a) schematic of the device. B) P-E loop of **DPT**:**A1** CT xerogels in dark and under UV (365 nm) illumination. 91

Figure 2.2.11 a) Molecular structure of **eNA** (*D-**eNA** and L-**eNA** corresponds to NDI with D- and L- alanine methylester functionality respectively). b) Tunable multicolour fluorescence of **eNA** in I: DMSO, II: benzene, III: toluene, IV: xylene and V: aqueous solution (H_2O/DMSO: 80/20) under UV light (365 nm). 95

Figure 2.2.12 a) UV-vis absorption and b) Fluorescence emission spectra of D-**eNA**. c) Filter paper based reversible fluorometric test kit for the detection of benzene and the schematic representation of excimer (NDI dimer interaction) and exciplex (NDI-benzene interaction) emission. 96

Figure 2.2.13 a) CD spectra of D-**eNA** and L-**eNA** in DMSO (i) and aqueous solution (ii, H_2O/DMSO: 80/20), arrows indicate the spectral changes. b) Variable temperature UV-vis and CD spectra of D-**eNA** in aqueous solution. 97

Figure 2.2.14 a) FESEM image of D-**eNA** (inset: fluorescence confocal images) nanosheets from aqueous solution. b) HRTEM image of D-**eNA** nanosheet (inset: SAED pattern). c) AFM image of D-**eNA** nanosheet (insets: section analysis of AFM images with height profile, stepwise height ~ 9.6 – 58 nm). d) AFM height profile (topographical thickness ~ 89 nm along the black line in (c). 99

Figure 2.2.15 a) Thin film CD spectra of L-**eNA** and D-**eNA**. b) Linear dicroism (LD) spectra of L-**eNA** and D-**eNA**. 100

Figure 2.2.16 a) DLS plot of D-**eNA** in aqueous solution. b) PXRD pattern of D-**eNA** nanosheets. c) Schematic representation of chiral molecular self-assembly of **eNA** into green fluorescent layered hierarchical 2D nanosheet, height (h) ~ 9.6 - 89 nm, length (l) = 10 to 40 µm and width (w) = 5 to 20 µm. 101

Figure 2.2.17 a) Schematic of the STM measurements on a 2D nanosheet of eNA. b) STM current-voltage (I-V) plot. 102

Figure 2.3.1 Chemical structures of few small phenolic amyloidogenic polypeptide modulators and their natural sources. 104

Figure 2.3.2 Chemical structures of biomolecule conjugated naphthalenediimides (NDIs). 105

Figure 2.3.3 a) Fluorescence study on the inhibition of $A\beta_{11-25}$ aggregates with NDI conjugates by ThT assay. The data shows the effects of different NDI conjugates on the aggregation inhibition of 200uM $A\beta_{11-25}$ (after 48 h incubation at 1:1 molar ratios of $A\beta_{11-25}$:NDI compound). Values are the normalized maximal fluorescence intensity at 485 nm compared to that of the control (A$\beta_{11\text{-}25}$ without NDI conjugates). b) The plot of fluorescence intensity at 485 nm as a function of different NDI conjugates, i) A$\beta_{11\text{-}25}$, ii) **ANA**, iii) **GNA**, iv) **FNF**, v) **YNY**, vi) **Dp**, vii) **WNW** and viii) **LD**......... 107

Figure 2.3.4 a) Fluorescence study on the dissolution of A$\beta_{11\text{-}25}$ aggregates with NDI conjugates by ThT assay. The data shows the effects of different NDI conjugates on the disaggregation of 200uM Aβ11-25 pre-formed aggregates (after 48 h incubation) and further incubated for 24 h at 1:1 molar ratios of A$\beta_{11\text{-}25}$:NDI compound. Values are the normalized maximal fluorescence intensity at 450 nm compared to that of the control (A$\beta_{11\text{-}25}$ without NDI conjugates). b) The plot of fluorescence intensity at 485 nm as a function of different NDI conjugates. i) A$\beta_{11\text{-}25}$, ii) **ANA**, iii) **GNA**, iv) **YNY**, v) **FNF**, vi) **WNW**, vii) **Dp** and viii) **LD.**... 108

Figure 2.3.5 Fluorescence study on the time dependent dissolution of A$\beta_{11\text{-}25}$ aggregates with NDI conjugates; a) **YNY**. b) **FNF**. c) **WNW**. d) **LD**. e) **Dp**. The data shows the effect of NDI compound at different time points (1-6 days) on the disaggregation of 200 uM A$\beta_{11\text{-}25}$ pre-formed aggregates (after 48 h incubation) and further incubation for 24 h at 1:1 molar ratios of A$\beta_{11\text{-}25}$:NDI compound. Values are the normalized maximal fluorescence intensity at 485 nm compared to that of the control (A$\beta_{11\text{-}25}$ without NDI conjugates).. 109

Figure 2.3.6 Fluorescence study on the aggregation inhibition (a) and dissolution (b) of A$\beta_{1\text{-}42}$ aggregates with NDI conjugates by ThT assay. The data shows the effects of different NDI conjugates on the inhibition of 20 μM A$\beta_{1\text{-}42}$ with 20 μM NDI conjugates (A) and disaggregation of 20uM A$\beta_{1\text{-}42}$ pre-formed aggregates (after 24 h incubation) and further incubated for 48 h at 1:1 molar ratios of A$\beta_{1\text{-}42}$:NDI compound. Values are the normalized maximal fluorescence intensity at 450 nm compared to that of the control (A$\beta_{1\text{-}42}$ without NDI conjugates).. 110

Figure 2.3.7 Fluorescence study on the concentration dependent aggregation inhibition of A$\beta_{1\text{-}42}$ with a) **LD** and b) **Dp** by ThT assay. The data shows the effects of **LD**, **Dp** on the inhibition of 20 μM A$\beta_{1\text{-}42}$ with 20 μM NDI conjugates at 1:1 molar ratio. Values are the normalized maximal fluorescence intensity at 450 nm compared to that of the control (A$\beta_{1\text{-}42}$ without NDI conjugates).. 111

Figure 2.3.8 Effect of treatment of concentration dependent prefabricated A$\beta_{1\text{-}42}$ aggregates on cell viability of PC12 cells. PC12 cells were treated with 10-1 μM prefabricated A$\beta_{1\text{-}42}$ aggregates obtained after incubating 100 μM A$\beta_{1\text{-}42}$ in 1X PBS for 24 h. Values shown are means ± SEM of four independent experiments performed in four to six replicates. One-way ANOVA analysis followed by Tukey's multiple comparison post hoc test was performed (**$p < 0.001$ compared to control)........ 112

Figure 2.3.9 Effect of NDI conjugates **LD** (a) and **Dp** (b) on the cell viabilities of PC12 cells. PC12 cells were incubated with 20, 10, 5, 1 μM concentrations of either LD or Dp for 24 h. Control cells received DMEM complete media with 0.01% DMSO. Values shown are means ± SEM of three independent experiments performed in six to eight replicates. One-way ANOVA analysis followed by Tukey's multiple comparison post hoc test was performed (#$p < 0.05$, *$p < 0.01$, **$p < 0.001$ compared to control)... 113

Figure 2.3.10 Effect of treatment of NDI conjugates **LD**, **Dp** against Aβ_{1-42} aggregates on the cell viabilities of PC12 cells. Aβ_{1-42} either alone or with **LD**, **Dp** are incubated for 24 h at 100 μM concentration at 1:1 ratio in 1X PBS. PC12 cells were treated with 1 μM (final concentration per well w.r.t either Aβ or drug) above samples for 24 h and assayed by MTT. Values shown are means ± SEM of four independent experiments performed in four to six replicates. One-way ANOVA analysis followed by Tukey's multiple comparison post hoc test was performed (**$p < 0.001$ compared to control). 114

Figure 2.3.11 Effect of treatment of NDI conjugates **LD**, **Dp** in disaggregation of pre-formed Aβ_{1-42} aggregates on the cell viabilities of PC12 cells. 200 μM of Aβ_{1-42} alone in 1X PBS was incubated for 24 h followed by co-incubation with **LD**, **Dp** for another 48 h at 100 μM concentration at 1:1 ratio in 1X PBS. PC12 cells were treated with 1 μM (final concentration per well w.r.t either Aβ or drug) above samples for 24 h and assayed by MTT. Values shown are means ± SEM of four independent experiments performed in four to six replicates. One-way ANOVA analysis followed by Tukey's multiple comparison post hoc test was performed (**$p < 0.001$ compared to control). 115

Figure 2.3.12 DPPH free-radical scavenging (antioxidant) assay for **LD**, **Dp**, **WNW** and **ANA** conjugates using Ascorbic acid as standard at 0 h (a) and after 2 h (b). **LD**, **Dp** showed high antioxidant activity when compared to standard antioxidant Ascorbic acid. Values shown are means ± SEM of three independent experiments performed in three to four replicates. Radical scavenging activity was expressed as inhibition percentage and was calculated using the formula: % scavenging activity = (absorbance of control − absorbance of sample)/ (absorbance of control)] × 100. 116

Figure 2.3.13 Residue-wise C-alpha RMSD for chains A to F of NMR structure 2LMN.......... 117

Figure 2.3.14 Induced fit docking (IFD) scores for two binding regions. a) Total induced fit score, b) Coulombic score, c) van der Waals' score, d) Hydrogen bond score.......... 120

Figure 3.1.1 Synthesis of L-DOPA conjugated PDI derivative **PDI 1**. 168

Figure 3.1.2 UV-vis absorption (a) and fluorescence emission spectra (b) of **PDI 1** (3.5 μM) in DMSO and water. Inset: solutions of **PDI 1** in DMSO (a) and water (b) under green laser light. c) Schematic representation of molecular organization of **PDI 1** in DMSO (molecularly dissolved State-I) and in aqueous solution (aggregated State-II). 169

Figure 3.1.3 UV-vis absorption (a) and fluorescence emission spectra (b) of **PDI 1** (3.5 μM) in water with increase in concentration of CTAB. Inset: solutions of **PDI 1** in water (a) and in CTAB miceller media (b) under green laser light. c) and d) Fluorescence emission spectra of **PDI 1** in water with increase in concentration of SDS and triton X-100 respectively. e) Schematic representation of transformation of aggregated State -II of **PDI 1** to molecularly dissolved State-III in presence of CTAB micelles.......... 171

Figure 3.1.4 Fluorescence response of **PDI 1** (3.5 μM) in the miceller media of CTAB (9.90 mM) solution. a) Bar diagram depicting the effect of various metal ions on the fluorescence intensity of

PDI 1 (3.5 μM). b) Fluorescence emission spectra of **PDI 1** (3.5 μM) with increasing concentration of Fe^{3+} shows 3.5 fold quenching in aqueous solution. Inset: solutions of **PDI 1** in absence (i) and presence (ii) of Fe^{3+} in the CTAB miceller media under green laser light. c) Fluorescence emission spectra of **PDI 1** (3.5 μM) in the presence of increasing concentration of Cu^{2+} in aqueous media. Inset: solutions of **PDI 1** under green laser light in the absence and presence of Cu^{2+}. 173

Figure 3.1.5 a) and b) Plots of fluorescence response (I_0/I) of **PDI 1** versus concentration of added Fe^{3+} and Cu^{2+} respectively. c) and d) The linear fluorescence response (I_0/I) of **PDI 1** versus concentration of added Fe^{3+} and Cu^{2+} respectively. 174

Figure 3.1.6 pH dependent fluorescence response study. a) Fluorescence emission spectra of [**PDI 1**+CTAB+Fe^{3+}]. b) Fluorescence emission spectra of [**PDI 1**+CTAB+Cu^{2+}]. c) and d) Plot of fluorescence intensity monitored at 540 nm as a function of pH of the media, corresponding to fluorescence spectra in (a) and (b), respectively. 175

Figure 3.1.7 a) and b) UV-vis absorption spectra of **PDI 1** (3.5 μM) with increasing concentration of Fe^{3+} and Cu^{2+} respectively. c) Schematic representation of transformation of State-III to State-IV via metal ion induced reorganization of **PDI 1** in presence of CTAB micelles. 177

Figure 3.1.8 ESI-MS spectra of **PDI 1** in presence of metal ions (a) Fe^{3+} and (b) Cu^{2+}. c) FTIR spectra (C-O stretching frequency region 1500 to 1000 cm-1) of **PDI 1** in absence and presence of Fe^{3+} and Cu^{2+}. d) TCSPC decay profile of **PDI 1** (Emax = 545 nm) with a 500 nm excitation. 178

Figure 3.1.9 Fluorescence emission spectra of a) [**PDI 1**+CTAB+Fe^{3+}] and b) [**PDI 1**+CTAB+Cu^{2+}] in presence of various anions, amino acids and metal chelators. 180

Figure 3.1.10 Fluorescence emission spectra (a and b) and UV-vis absorption spectra (c and d) of [**PDI 1**+ CTAB+Fe^{3+}] and [**PDI 1**+ CTAB+Cu^{2+}] solutions with increase in concentrations of DTPA in CTAB micellar aqueous medium. e) Schematic representation of sequestration of metal ion from metallosupramolecular aggregate (State-IV) using DTPA into molecularly dissolved state (State-III). 181

Figure 3.1.11 FESEM micrographs of a) **PDI 1**, b) **PDI 1**+Cu^{2+}, c) **PDI 1**+Fe^{3+} and d) **PDI 1**+Cu^{2+}+DTPA. Insets in (b) and (c) EDAX chemical composition mapping graph on corresponding nanospheres. 183

Figure 3.1.12 a) Dynamic light scattering (DLS) size distribution graph. b) Schematic representation of assembly-disassembly modulation of **PDI 1** observed from DLS studies (a). 184

Figure 3.1.13 Schematic representation of assembly modulation of **PDI 1** as a supramolecular fluorescence switching probe for detection of metal ions in aqueous media. 186

Figure 3.2.1 ESI mass analysis of a) **PDI 1** and b) its oxidized product **PDI 1_{ox}**. c) Proposed H_2O_2 and hematin catalyzed reaction of **PDI 1** to **PDI 1_{ox}**, photographs of gel to sol transition in presence of hematin (Ht) and H_2O_2 190

Figure 3.2.2 a) Fluorescence emission spectra of i) **PDI 1**, ii) **PDI 1**+Hn and iii) **PDI 1**+Ht. b) Fluorescence emission and c) kinetic studies of i) **PDI 1**, ii) **PDI 1**+Hn+H_2O_2 and iii) **PDI 1**+Ht+H_2O_2, *inset* in b photographs of corresponding solutions under UV light (365 nm), the arrow in c indicating the point of H_2O_2 addition . d) Fluorescence kinetic studies of **PDI 1**+Ht upon addition of H_2O_2 i) 65 μM, ii) 130 μM, iii) 195 μM and iv) 325 μM H_2O_2 respectively. 192

Figure 3.2.3 Energy minimized molecular structures of a) **PDI 1** and b) **PDI 1$_{ox}$** 193

Figure 3.2.4 a) Molecular structure of hematin (Ht). b) Proposed reaction mechanism of hematin catalyzed **PDI 1** to **PDI 1$^\bullet$** radicals conversion in presence of H_2O_2. c) Oxidation of **PDI 1$^\bullet$** radicals to **PDI 1$_{ox}$** 194

Figure 3.2.5 a) The fluorescence signals of the **PDI 1** logic gate in the presence of different inputs [A: Hematin (Ht), B: H_2O_2]. b) The symbol of AND logic-gate and its truth table derived from (a)....... 195

Figure 3.3.1 Synthesis of histidine conjugated PDI derivative **PDI 2** 200

Figure 3.3.2 UV-vis absorption spectra (a), fluorescence emission spectra (b) and CD spectra of **PDI 2** in DMSO and water. c) Schematic representation of molecular organization of **PDI 2** in DMSO (molecularly dissolved) and in aqueous solution (left-handed chiral self-assembly) and corresponding photographs of **PDI 2** in DMSO and water under green laser light... 201

Figure 3.3.3 a) UV-vis absorption spectra of **PDI 2** before and after addition of Hg^{2+}. b) Fluorescence emission spectra of **PDI 2** as a function of increasing concentration of Hg^{2+}. c) The Hill plot at the linear regime, inset: Plot of fluorescence response (I_0/I) of **PDI 2** versus concentration of added Hg^{2+}. d) CD spectra of **PDI 2** before and after addition of Hg^{2+}. e) Schematic representation of Hg^{2+} induced assembly transformation of **PDI 2** from emissive left-handed self-assembly to nonemissive, achiral metallosupramolecular polymerization, Photographs of respective solutions under green laser light. 203

Figure 3.3.4 a) Fluorescence emission spectra of **PDI 2** in presence of various metal ions in water. b) Bar diagram depicting the effect of various metal ions on the fluorescence response (I_0/I) of **PDI 2**. c) Photographs of sol to gel transition of **PDI 2** in presence of Hg^{2+}. 204

Figure 3.3.5 a) Hg^{2+} ^{1}H-NMR titration spectra of **PDI 2**. b) imidazole NH chemical shift (14.6 ppm-13.0 ppm) region. c) PDI and imidazole aromatic protons chemical shift (9.0 ppm-8.8 ppm) region. d) ATIR spectra of **PDI 2** (black curve) and **PDI 2**+Hg^{2+} (red curve). e) HRMS spectra of **PDI 2**+Hg^{2+}. f) Schematic representation of proposed Hg^{2+} binding interaction with **PDI 2**. 206

Figure 3.3.6 a) UV-vis absorption spectra. b) Fluorescence emission spectra upon addition of cysteine. c) Hill plot, inset the plot of fluorescence emission intensity as a function of added cysteine. d) CD spectra. e) Schematic representation of proposed sequestration of Hg^{2+} by cysteine to restore left-handed J-type fluorescent **PDI 2** self-assembly from achiral H-type non emissive metallosupramolecular aggregates. 208

Figure 3.3.7 a) fluorescence emission spectra of **PDI 2**+Hg^{2+} in presence of various amino acids. b) The plot of fluorescence emission intensity at 549 nm as a function of added amino acid analytes. . 209

Figure 3.3.8 FESEM micrographs of a) **PDI 2**, b) **PDI 2**+Hg^{2+} xerogels and c) PDI 2+Hg^{2+}+cysteine. d) DLS spctra. e) Schematic representation of proposed revisable assembly switching of **PDI 2** in presence of Hg^{2+} and cysteine respectively, photographs of respective aqueous solutions and hydrogels. 211

Figure 3.4.1 a) Structure of histidine, at different pH values. b) Molecular structure of **PDI 2** 215

Figure 3.4.2 pH dependent photophysical studies. a) UV-vis absorption spectra of **PDI 2**. b) Fluorescence emission spectra of **PDI 2**. c) CD spectra of **PDI 2**. 217

Figure 3.4.3 Reversible pH responsive switching studies of **PDI 2**. a) UV-vis absorbtion spectra. b) Fluorescence emission spectra. c) The plot of Absorbance at 540 nm versus each cycle of pH. d) The plot of fluorescence intensity at 550 nm versus each cycle of pH. 218

Figure 3.4.4 Reversible pH responsive chiroptical switching studies of **PDI 2**. a) CD spectra at different pH values. b) The plot of CD intensity at 570 nm versus each cycle of pH. c) Schematic representation of the molecular packing model for pH responsive chiroptical swithing self-assembly of **PDI 2.** 219

Figure 3.4.5 FESEM micrographs of **PDI 2** from different pH solutions. a) at pH 10. b) at pH 7. c) at pH 2. d) Schematic representation pH responsive morphologies of **PDI 2**. 220

Figure 4.1.1 Molecular structures of homochiral (**LL** and **DD**), heterochiral (**LD** and **DL**) and achiral (**AA**) peptide conjugates of NDI. 243

Figure 4.1.2 UV-vis spectra of NDI-peptide conjugates a) **LL**. b) **DD**. c) **LD** and d) **DL** in DMSO (blue curve) and in aqueous DMSO (water/DMSO: 85/15) solution at 300 μM. 244

Figure 4.1.3 Fluorescence emission spectra of NDI-peptide conjugates a) **LL**. b) **DD**. c) **LD** and d) **DL** in DMSO (blue curve) and in aqueous DMSO (water/DMSO: 85/15, red curve) solution at 300 μM. Inset: photographs of respective solutions in DMSO (i) and in water/DMSO (85:15) (ii) under UV light. 245

Figure 4.1.4 a) and b) Circular dichrosim (CD) spectra of NDI-peptide conjugates in DMSO (I) and in water/DMSO (85:15) (II). c) and d) Concentration dependent CD spectra in DMSO. e) Schematic representation of the transition of the angles and distance between the z polarized transition moments of stacked NDI chromophores. 246

Figure 4.1.5 CD spectroscopy. a) CD spectra of conventional sergeants-and-soldiers (**LL** and **AA**) experiment at 25 °C in 44% aqueous DMSO (The chiral **LL** was mixed with achiral **AA** in different proportions by keeping the overall concentration constant (500 mM). b) The plot (line+symbol) of fraction chiral with net helicity in a for (a). c) Achiral **AA** (0, 100, 200 and 300 mm) was added to a fixed concentration of chiral **LL** or **DD** (100 mm) in DMSO followed by the addition of deionized water (44%). d) The plot (line+symbol) of fraction chiral with net helicity for (c). e) Majority-rule experiment. f) Spectra of **LD**, **DL** and monophenylalanine methylester (L or D isomer) conjugated NDI. 248

Figure 4.1.6 Temperature dependent CD spectra (10 °C-100 °C); a) Homochiral NDI-peptide conjugates. b) Heterochiral NDI-peptide conjugates. c) Summary of temperature-dependant studies of **LL**, **DD**, **LD** and **DL**. Arrows indicating the spectral changes upon heating from 10 °C-100 °C. 250

Figure 4.1.7 Field emission scanning electron microscopy (FESEM) images of self-assembled structures from water/DMSO (85:15); a) and b) **LL**, c) **DD**, d) **LD** and e) **DL**. 251

Figure 4.1.8 Single crystal XRD structures; a) and b) Single molecular geometry of **LL** and **DD** respectively indicating the mirror image *cis* conformation of cα substituents (methyl) with respect to NDI plan. c) 1D left-handed helical columnar stacks of **LL** (NDI chromophores are highlighted in the space-filling model). d) 1D Right-handed helical columnar stacks of **DD** (NDI chromophores are highlighted in the space-filling model). In c and d hydrogen atoms have been omitted for the clarity. 252

Figure 4.1.9 Summary of probing peptide auxiliaries appended naphthalenediimides for chiral amplification, transcription, retentive helical memory via hierarchical 1D helical molecular, organization.. 255

Figure 4.2.1 Synthesis of peptide conjugated NDI derivatives **1, 2** and **3**. 257

Figure 4.2.2 (a) Molecular structures of bis-dipeptide conjugated NDIs **1**: Aib-Aib, **2**: L-Ala-L-Ala, and **3**: D-Ala-D-Ala.The solid state structural insights: b) face-to-face (**1**) and edge-to-edge (**2**) stacked dimmers and c) Subsequent space fill representation of 1D (**1**) and 2D (**2**) molecular ordering along the crystallographic *a*-axis and *c*-face respectively (solvent molecules and hydrogen atoms have been omitted from the crystal packing representation for clarity). d) Schematic representation of self-assembled 1D and 2D nanostructures of **1** and **2**, respectively. 258

Figure 4.2.3 a) FESEM micrographs showing 1D tapes of **1** from xerogel (a) and 2D sheets of **2** from MCH/CHCl$_3$ (90/10, v/v) solution (b). *Insets*: (a) organogel of **1** under UV light (365 nm), a selected area AFM image of 1D nanotapes and corresponding height profiles along the red line (derived from height image); (b) MCH/CHCl$_3$ (90/10, v/v) solution of **2** under UV light (365 nm). c) AFM image of 1D nanotape network from xerogel of **1**. (d) AFM image of 2D nanosheets form solution of **2**. *Insets*: a selected area 3D AFM height image of single 2D nanosheet and corresponding height profiles along the blue line. 261

Figure 4.2.4 a) ATIR spectra of 1D nanotapes of **1** and 2D nanosheets of **2**. b) Amide NH and carbonyl (C=O) stretching frequency region. c) Single crystal XRD structures of **1** indicating the hydrogen bonding interactions with solvent molecule (DMSO) and d) Single crystal XRD structures of **2** indicating the intermolecular hydrogen bonding interactions to for antiparallel β–bridge secondary structure. 263

Figure 4.2.5 UV-vis absorption (a) and fluorescence emission spectra (b) of **1** and **2** in CHCl$_3$ (i) and MCH/CHCl$_3$ (90/10, v/v) (ii), respectively. Arrows indicating the spectral changes going from CHCl$_3$ solution to MCH/CHCl$_3$ (90/10, v/v) solution. c) TCSPC decay profile of **1** ($^{a}{}_{max}$ 460 nm) and **2** ($^{a}{}_{max}$

522 nm) with a 405 nm excitation. d) Variable-temperature (VT) fluorescence emission studies (from 10 °C to 100 °C) of **1** (at 460 nm) and **2** (522 nm). 264

Figure 4.2.6 a) ^{1}H NMR spectral changes of **1** in $CDCl_3$ with gradual addition of MCH (0 μL, 10 μL, 30 μL, 50 μL, 70 μL and 100 μL). b) NDI aromatic region (8.54-8.51 ppm) of (a). Dashed arrow indicating the gradual aromatic stacking induced up field shifting of NDI protons with the addition of MCH (0 μL, 10 μL, 30 μL, 50 μL, 70 μL and 100 μL) to **1** in $CDCl_3$. c) Amide region (6.34-6.28 ppm) of (a). Dashed arrow indicating the gradual hydrogen bonding induced down field shifting of amide protons with the addition of MCH (0 μL, 10 μL, 30 μL, 50 μL, 70 μL and 100 μL) to **1** in $CDCl_3$. d) ^{1}H NMR data of **1** depicting the change in the chemical shift (ppm) values of NDI aromatic protons (blue line) and peptide-amide NH protons (red line) as a function of volume of MCH added into $CDCl_3$ solution. 265

Figure 4.2.7 a) ^{1}H NMR spectral changes of **2** in $CDCl_3$ with the addition of MCH (0 μL, 10 μL, 30 μL, 50 μL, 70 μL and 100 μL). b) NDI aromatic region (8.69-8.67 ppm) of (a). Dashed arrow indicating the gradual aromatic stacking induced up field shifting of NDI protons with the addition of MCH (0 μL, 10 μL, 30 μL, 50 μL, 70 μL and 100 μL) to **2** in $CDCl_3$. C) Amide region (6.48-6.43 ppm) of (a). Dashed arrows indicating the gradual hydrogen bonding induced down field shifting of amide protons with the addition of MCH (0 μL, 10 μL, 30 μL, 50 μL, 70 μL and 100 μL) to **2** in $CDCl_3$. d) ^{1}H NMR data of **2** depicting the change in the chemical shift (ppm) values of NDI aromatic protons (blue line) and peptide-amide NH protons (red line) as a function of volume fraction of MCH added to $CDCl_3$ solution. 266

Figure 4.2.8 a) CD spectra of **1**, **2** and **3** recorded in $CHCl_3$ solution. The flat CD spectra in $CHCl_3$ solution suggesting the molecularly dissolved state. b) CD spectra of **1**, **2** and **3** recorded in MCH/$CHCl_3$(90/10, v/v) solution. c) Solid-state 1D face-to-face achiral organisation of **1** (i), supramolecular tilt left-handed (ii, in **2**) and right-handed (iii, in **3**) chiral NDI stacks from single crystal XRD studies. 268

Figure 4.2.9 a) Schematic representation of current-voltage (*I-V*) device fabricated using nanotapes network film from xerogel of **1** or 2D nanosheets film from **2** nanostructured materials of NDI. b) *I-V* characteristics of **1** (1D nanotapes network) (i) and **2** (2D nanosheets) (ii) deposited across the aluminium electrodes as shown in a. 269

Figure 4.2.10 Summery of crystallographic insight-guided nanoarchitectonics and conductivity modulation of NDI through peptide conjugation. 271

Figure 5.1 Synthesis of glucosamine conjugated NDI Derivative (**Glc-NDI**) and its schematic representation 308

Figure 5.2 UV−vis absorption spectra of **Glc-NDI**, a) Solvent dependent studies. b) Concentration dependent studies. c) Temperature dependent studies. d) The plot of the change in the absorbance at 400 nm as a function of temperature. 309

Figure 5.3 Circular dichroism (CD) spectra of **Glc-NDI**; a) solvent dependent studies ([**Glc-NDI**] = 100 μM). b) Concentration dependent studies in aqueous solution (H_2O/DMSO (90/10, v/v). c) Schematic representation of molecular organization of **Glc-NDI** from molecularly dissolved state (DMSO) to right hand chiral self-assembly (in aqueous solution). arrows indicating the spectral changes....311

Figure 5.4 Circular dichroism (CD) spectra of **Glc-NDI** (100 μM); a) pH dependent studies. b) Plot of CD intensity at 400 nm as a function of pH. c) Temperature dependent studies in aqueous solution (H_2O/DMSO (90/10, v/v). d) Fraction of aggregates as a function of temperature. e) Schematic representation of stimuli responsive (pH and temperature (Δ)) disassembly of **Glc-NDI.** Arrows indicating the spectral changes. 312

Figure 5.5 FESEM micrographs of **Glc-NDI**; a) From 100 μM aqueous solution (H_2O/DMSO (90/10, v/v) of **Glc-NDI,** show left-handed helical nanotapes; *inset*: Schematic representation of helical nanotapes and corresponding dimensions. b) Conversion of left-handed helical nanotapes to nanotube with schematic representation. c) Dense forest of nanotube morphology from xerogel, *inset:* Photograph of hydrogel, schematic representation of nanotube. d) Schematic representation of the hierarchical self-assembly of **Glc-NDI,** from right-handed chiral molecular stacks to left handed supercoiled helical nanotapes and nanotubes....314

Figure 5.6 a) Schematic representation of formation of uniformly silver coated **Glc-NDI** nanotubes in presence of tollens solution, Photograph **Glc-NDI** hydrogel before, after addition of tollens reagent (a clear visible color change from pale yellow to red was observed) and after complete evaporation of solvent showing deposition of silver metal on the inner surface of the glass vial . b) FESEM micrographs of uniformly silver coated nanotubes; *inset*: magnified image. c) EDAX chemical composition mapping graph on the nanotubes shown in b. 315

Figure 5.7 Schematic representation of overall proposed hierarchical self-assembly of **Glc-NDI** from right-handed chiral molecular stacks to left handed supercoiled helical nanotapes and nanotubes, template for the preparation of uniformly coated silver nanotube, photographs corresponding hydrogels....316

Figure 6.1 a) Molecular structures of BNA, dT_n and their pictorial representation with Hg^{2+}/CH_3Hg^+. b) Proposed molecular packing model for BNA_n-dT_n mutually templated co-assembly via complementary Watson-Crick (WC) A-T hydrogen bonding interactions and mercury mediated disassembly via formation of $[DT\text{-}Hg\text{-}DT]_n$ metallo-DNA duplex; Schematic representation of respective self-assembled structures and thier dimensions (l= length, w= width). 330

Figure 6.2 Syntheis of BNA....332

Figure 6.3 a) UV-vis absorption spectra of BNA_n-dT_n as a function of dT_n sequence length. b) The enlarged band (I) region of BNA_n-dT_n indicted as dotted box in a. 333

Figure 6.4 a) CD spectra of BNA (100 μM), dT_{10} (10 μM) and BNA_{10}-dT_{10} (1:1(BNA:T)) in 10 mM PBS containing 5% DMSO, at pH = 7 and 293 K. b) Linear dichroism (LD) spectra of BNA_{10}-$dT_{10,}$ the flat spectral feature indicates the absence of LD artifacts for the observed CD spectra in a. 334

Figure 6.5 a) CD spectra of BNA in presence of various dB_n ([BNA]= 100 μM, [dB_n]= 10 μM)recorded in PBS containing 5% DMSO, at 293 K, indicating that the dT_{10} selective mutually templated co-assembly of BNA. b) The plot of CD intensity at 405 nm of BNA in presence of different oligonucleotides (dB_{10}) for the observed CD spectra in a. C) CD Job plot experiment after mixing different fractions of BNA to dT_{10}, where the total concentration [BNA]+[dT_{10}]= 110 μM kept constant and varied the fraction of BNA (f= [BNA]/110 μM) in BNA_{10}-dT_{10}. d) CD Job plot monitored at 405 nm as a function of fraction BNA. 335

Figure 6.6 a) The dT_n sequence length dependent CD spectra of BNA_n-dT_n. b) Variable temperature CD (VT-CD) spectra of mutually templated co-assemblies of BNA_n-dT_n (n=6, 10 and 20) in 10 mM, PBS containing 5% DMSO, at pH 7. c) pH dependent CD spectra of BNA_{10}-dT_{10}. d) The plot of CD intensity at 405 nm of BNA as a function of in pH of the solution for the observed CD spectra in c. 337

Figure 6.7 a) ATIR spectra of BNA and BNA_{10}-dT_{10}. b) The BNA adenine amine (NH) symmetric stretching frequency region (3600-3000 cm^{-1}) of BNA before and after addition of dT_{10}. 338

Figure 6.8 FESEM micrographs of BNA (a), BNA_6-dT_6 (b), BNA_{10}-dT_{10} (c) and BNA_{20}-dT_{20} (d); schematic representation of respective structures and their lateral dimensions. 339

Figure 6.9 a) DLS spectra of BNA_n-dT_n. b) PXRD spectra of mutually templated co-assembly of BNA_n-dT_n (n= 6, 10 and 20). c) PXRD diffraction patterns at an aromatic π–stacking region (2θ= 26°-27°) of BNA_n-dT_n for the observed spectra in b. d) Thin film CD spectra of BNA_{10}-dT_{10} recorded on quartz substrate. 340

Figure 6.10 a) Bottom contact top gate FET structures. b) Typical transconductance plots for different self-assembled structures of BNA_n-dT_n. 342

Figure 6.11 a) Thin film CD spectra of BNA_{10}-dT_{10} in the presence of different metal ions ([M^{n+}]=100 μM). (b) Thin film CD spectra of BNA_{10}-dT_{10} upon adding various concentrations of Hg^{2+} (0.1 nM to 100 μM). c) Relative CD intensity of BNA_{10}-dT_{10} thin film at 400 nm in presence of various metal ions (where [M^{n+}]= 100 μM, $\Delta\theta = CD_0 - CD$ where CD_0 and CD are CD intensity at 400 nm before and after addition of metal ions respectively). d) Relative CD intensity of BNA_{10}-dT_{10} thin film at 400 nm as a function of [Hg^{2+}] added. *Inset:* Enhanced selected spectral region (0.1 nM to 10 μM). d) FESEM micrograph of BNA_{10}-dT_{10} +Hg^{2+}. 344

Figure 6.12 a) BNA_{10}-dT_{10} device response before and after addition of KCl. b) Conductometric sensing of CH_3Hg^+ ions. c) Conducting AFM measurements on the self-assembled structure confirming the variation in the assembly with the addition of CH_3Hg^+ ions. d) Probing the mechanism of self-assembly from the conductometric measurements obtained for different concentrations of CH_3Hg^+ ions..346

List of Tables

Table 1.1 Biomolecular nanoarchitectonics and their potential biomedical applications.[56] 11

Table 1.2 Summary of various noncovalent interactions.[56] 13

Table 1.3 Examples of bioinspired self-assembled systems (S, static, D, dynamic, T, templated, B, biological).[86] 16

Table 2.1.1 Summary of various properties of NDI conjugates[a] 39

Table 2.3.1 Qualitative comparison of conjugates 121

Table 4.1.1 Crystallographic information of **LL** and **DD**. 253

Table 4.2.1 Crystallographic information of **1- 3**: Summary. 260

Table 6.1 FET charecteristics................ 343

Chapter 1: Introduction

1.1 Nanoarchitectonics

Design, synthesis and controlled fabrication of functional nanoscale systems are of paramount importance in chemistry, physics, biology, materials Science and nanoscience.[1-12] In this context, over the past two decades considerable efforts have been devoted to develop extensive set of techniques and strategies for the production of nanomaterials and nanostructures based on top-down and bottom-up approaches.[13] The field of nanotechnology is one among the recent developments and it describes the evolution of various microscopy tools and techniques. Nanotechnolgoy enables the advanced microfabrication and nanomanipulation, however suffer from lack of concepts and methods needed for correctly architect these materials into viable applications.[14] Moreover, in contrast to the macroscopic and microscopic regimes, the physical phenomena occurring at the nanoscale operates quite differently which are highly affected by several factors including thermal and statistical fluctuations, as well as mutual interactions among the components.[14-17] Thus, it is not always feasible to simply scale down procedures from microtechnology to the nanoscale fabrication. Consequently, new innovative methodology and concepts are necessary for the harmonization of various nanoscale effects and interactions, to facilitate efficient design and fabrication of functional nanosystems.[14] One such concept is nanoarchitectonics proposed by Masakazu Aono at the 1st International Symposium on Nanoarchitectonics Using Suprainteractions (NASI-1) in 2000 in Tsukuba, Japan.[18-19] Nanoarchitectonics is a methodology for organizing nanoscale structural units which are usually group of atoms or molecules or nanoscale functional components in an intended configuration for the creation of novel functional materials by the synchronization of various processes including controlled supramolecular self-organization, physical manipulation (atom/molecule manipulation), chemical nanomanipulation, field-induced interactions and theoretical modelling

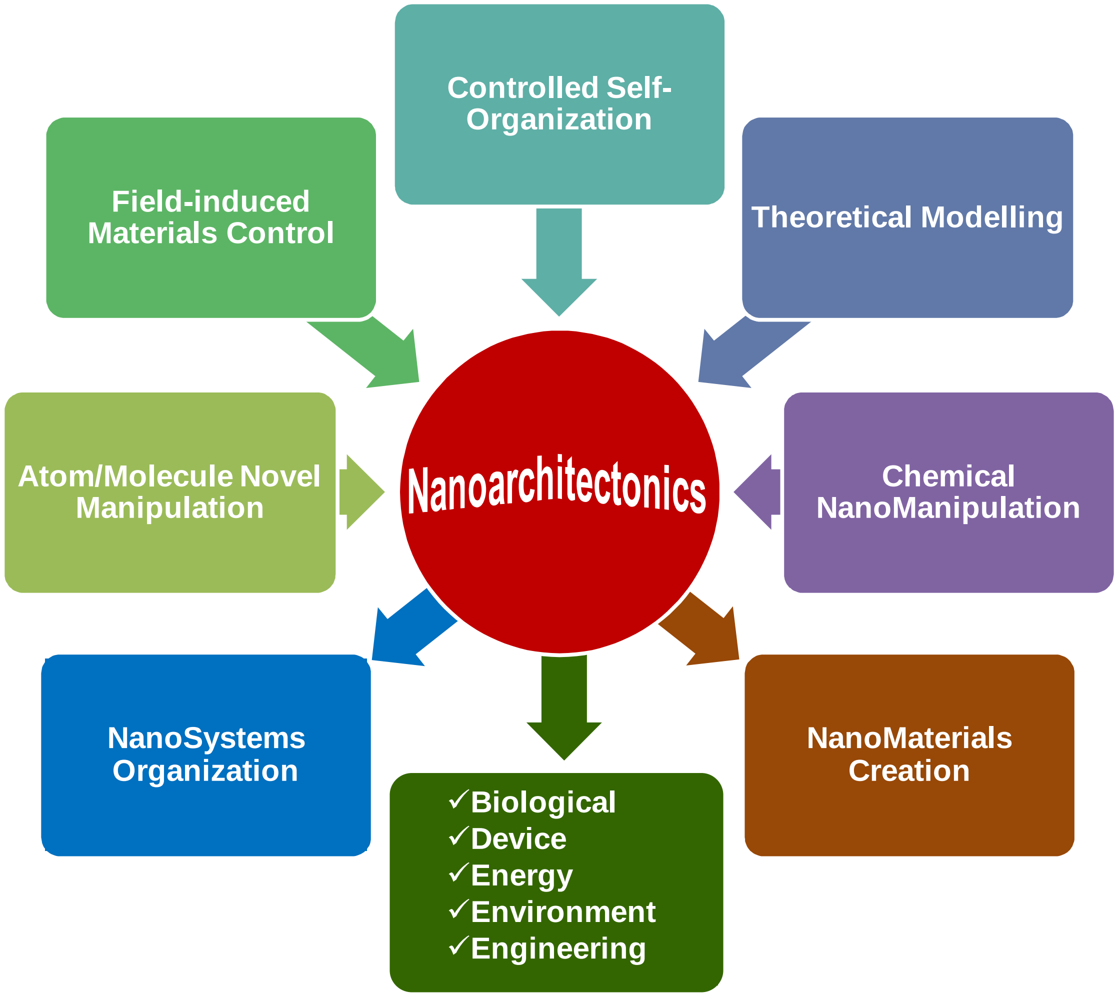
Controlled Self-Organization
Field-induced Materials Control
Theoretical Modelling
Atom/Molecule Novel Manipulation
Nanoarchitectonics
Chemical NanoManipulation
NanoSystems Organization
NanoMaterials Creation
✓Biological
✓Device
✓Energy
✓Environment
✓Engineering

Figure 1.1 Schematic illustration of concepts and applications of nanoarchitectonics.

(Figure 1.1).[14,19-25] Nanoarchitectonics is considered to be a next phase of nanotechnology and aims at two key concepts nanosystem organization and nanomaterials creation. In recent years, nanoarchitectonics has begun to originate as a basic and general subject of pursuit in supramolecular assemblies, energy and environmental sciences, fabrication methodologies, nanostructured materials, hybrid materials, device and physical application, and biomedical applications.[2,20-21,24,26-33]

In particular, construction of complex molecular nanoscale systems with the molecular-level features and control requires the exploration of structure-property correlation and various weak noncovalent interactions among the molecular building blocks. In this regard, the concept of molecular architectonics has been proposed wherein the art of mastering the pre-programmed molecular assemblies is described.[2,34-36] Notably, molecular architectonics is a key concept which contribute immensely in the development of (bioinspired)-nanoarchitectonics. This is because organization of molecules in such systems is directed through meticulous engineering of molecular assemblies. Molecular architectonics allows the construction of challenging tailor-made functional architectures and to build increasingly complex structures for a wide variety of materials that can be used for different purposes, in the area of (bioinspired)-nanoarchitectonics.

1.2 Bioinspired nanoarchitectonics

It is interesting to note that, unlike current nanotechnology, most of the features of nanoarchitectonics are closely related to biochemical systems including self-organization, mutual effects of multiple components and the unavoidable impacts of thermal/statistic

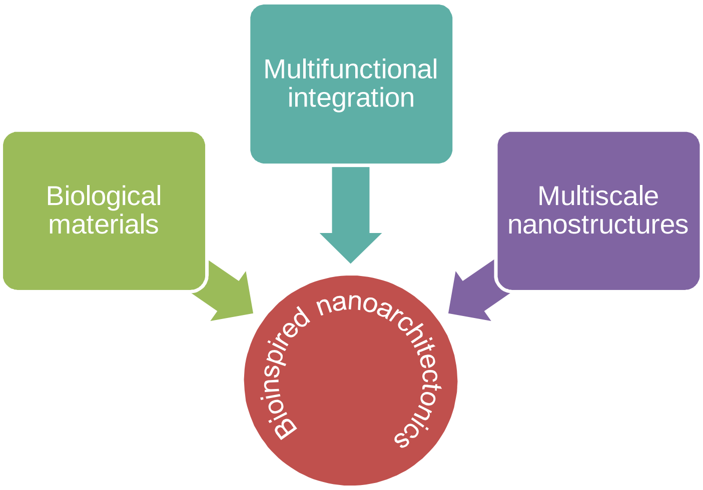
Multifunctional integration
Biological materials
Multiscale nanostructures
Bioinspired nanoarchitectonics

Figure 1.2 Schematic illustration of concepts and applications of bioinspired nanoarchitectonics.

fluctuations. Hence, bioinspired strategies can be considered as the ultimate prototype of nanoarchitectonics.[20,22,33,37-38] The process of the custom-design and engineering of molecular assemblies with functional components of biological origin is conceptualized as bioinspired nanoarchitectonics (Figure 1.2).[22,39] Bioinspiration is a general and one of the largest areas of research that includes biomimetics, biokleptics and biotechnology.[40-49] The phrase biomimetic was derived from the Greek words *bios*, meaning life, and *mimetikos*, meaning to copy or imitate. In this way, it can be expressed that the biomimetics is the mimic (or copying) of biological mechanisms, procedures, functions or structures for studying and creating of artificial systems.[49] The term biomimetics was first used by Otto Schmitt in 1960 for representing usage of fabricated electrical stimuli joined with a squid, as an imitation of biological nerve impulse of the organism.[50] Thereafter biomimetics become a diverse and actively practiced area of research for the understanding and use of mysterious biological processes and principles to create new artificial systmes and materials with exceptional properties.[49] On the other hand, performing biological functions in an artificial environment by utilizing biological components or reagents is known as biokleptics. This concept was first employed in the construction of DNA nanostructures.[51] Biokleptics often overlaps with the biotechnology, which is “any technological application that uses biological systems, living organisms or derivatives thereof, to make or modify products or processes for specific use” (United Nations definition of biotechnology).[52] Biotechnology is a broad area which further overlaps with the biomimetics. Therefore, depending on the tools and applications all the three areas biomimetics, biokleptics and biotechnology have significant overlap among themselves and constituet the broad area of bioinspiration. In general, bioinspiration include design strategies that are inspired by biological principles and encompasses biomimetics, biokleptics and biotechnology.

1.2.1 Basic building blocks of life

All the living organisms composed of four macromolecular building blocks such as nucleic acids, proteins, carbohydrates (glycans), and lipids as shown in Figure 1.3.[53] These macromolecules are responsible for the structure and function majority of living systems . The macromolecules (proteins, carbohydrates, and nucleic acids) intern are

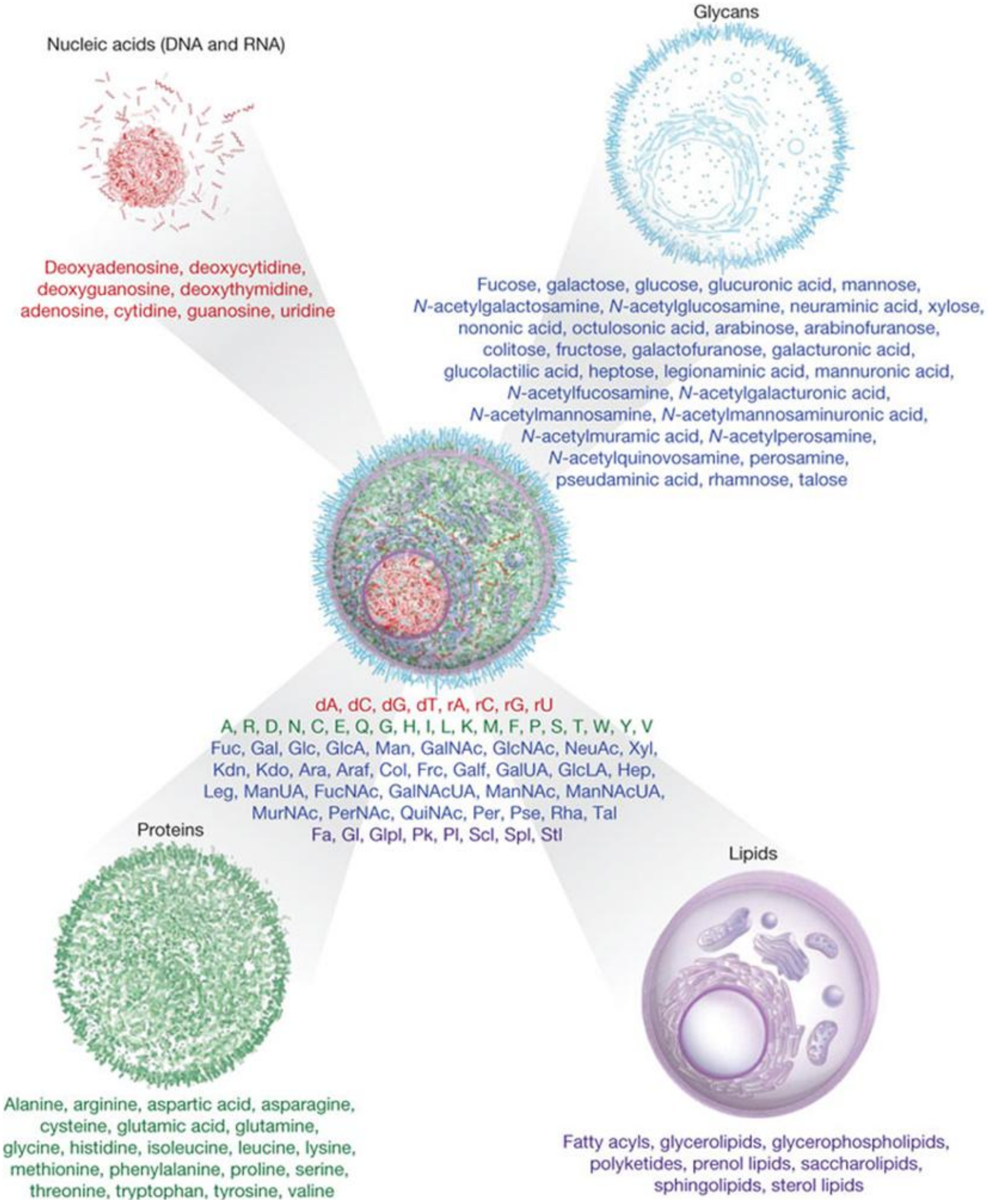
Glycans
Nucleic acids (DNA and RNA)
Deoxyadenosine, deoxycytidine,
deoxyguanosine, deoxythymidine,
adenosine, cytidine, guanosine, uridine
Fucose, galactose, glucose, glucuronic acid, mannose,
N-acetylgalactosamine, N-acetylglucosamine, neuraminic acid, xylose,
nononic acid, octulosonic acid, arabinose, arabinofuranose,
colitose, fructose, galactofuranose, galacturonic acid,
glucolactilic acid, heptose, legionaminic acid, mannuronic acid,
N-acetylfucosamine, N-acetylgalacturonic acid,
N-acetylmannosamine, N-acetylmannosaminuronic acid,
N-acetylmuramic acid, N-acetylperosamine,
N-acetylquinovosamine, perosamine,
pseudaminic acid, rhamnose, talose
dA, dC, dG, dT, rA, rC, rG, rU
A, R, D, N, C, E, Q, G, H, I, L, K, M, F, P, S, T, W, Y, V
Fuc, Gal, Glc, GlcA, Man, GalNAc, GlcNAc, NeuAc, Xyl,
Kdn, Kdo, Ara, Araf, Col, Frc, Galf, GalUA, GlcLA, Hep,
Leg, ManUA, FucNAc, GalNAcUA, ManNAc, ManNAcUA,
MurNAc, PerNAc, QuiNAc, Per, Pse, Rha, Tal
Fa, Gl, Glpl, Pk, Pl, Scl, Spl, Stl
Proteins
Lipids
Alanine, arginine, aspartic acid, asparagine,
cysteine, glutamic acid, glutamine,
glycine, histidine, isoleucine, leucine, lysine,
methionine, phenylalanine, proline, serine,
threonine, tryptophan, tyrosine, valine
Fatty acyls, glycerolipids, glycerophospholipids,
polyketides, prenol lipids, saccharolipids,
sphingolipids, sterol lipids

Figure 1.3 The molecular building blocks of life. Adapted with permission of NPG from reference 53.

polymers of small molecular building blocks (monomers) formed by linking together a large number of monomers.[53] Based on the chemical structures, the small molecular building blocks are further traditionally grouped into four major categories such as nucleobases (as in nucleosides), amino acids, sugars and lipids (Figure 1.3).[53]

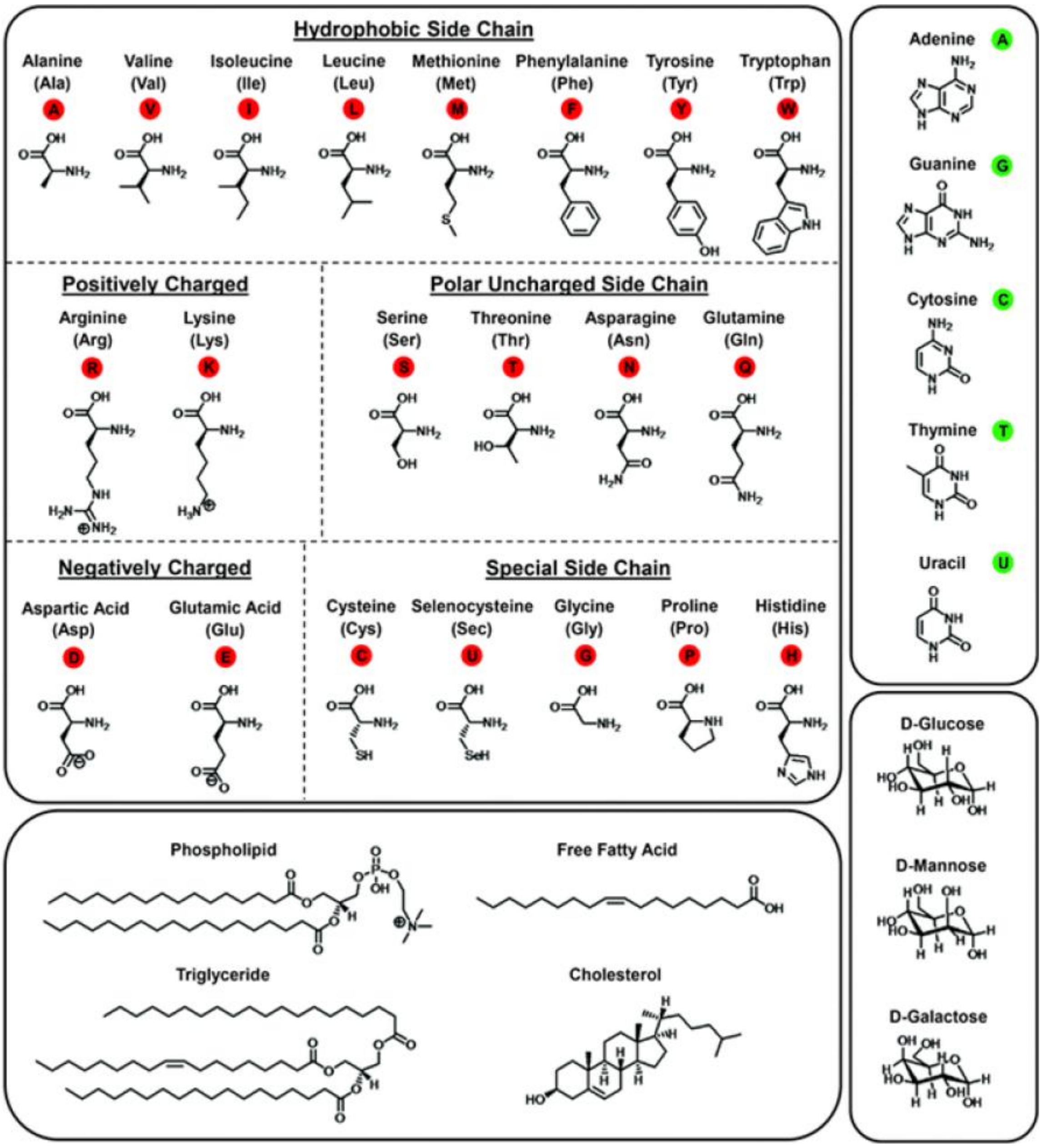
Hydrophobic Side Chain
Alanine (Ala) A
Valine (Val) V
Isoleucine (Ile) I
Leucine (Leu) L
Methionine (Met) M
Phenylalanine (Phe) F
Tyrosine (Tyr) Y
Tryptophan (Trp) W
Positively Charged
Arginine (Arg) R
Lysine (Lys) K
Polar Uncharged Side Chain
Serine (Ser) S
Threonine (Thr) T
Asparagine (Asn) N
Glutamine (Gln) Q
Negatively Charged
Aspartic Acid (Asp) D
Glutamic Acid (Glu) E
Special Side Chain
Cysteine (Cys) C
Selenocysteine (Sec) U
Glycine (Gly) G
Proline (Pro) P
Histidine (His) H
Adenine A
Guanine G
Cytosine C
Thymine T
Uracil U
D-Glucose
D-Mannose
D-Galactose
Phospholipid
Free Fatty Acid
Triglyceride
Cholesterol

Figure 1.4 Molecular structures of amino acids, nucleobases, carbohydrates and lipids along with their commonly used abbreviations. Adapted with permission of RSC from reference 22.

1.2.1.1 Amino acids, peptides, and proteins

Proteins are polymers of amino acids linked together by amide bonds. The structures of the 20 most common naturally occurring amino acids are shown in Figure 1.4. The term 'Amino *acid*' is generally understood to refer to the *aminoalkanoic acids*. They are chemical compounds containing an amino group (-NH_2) and a carboxylic acid group (-COOH) with general formula $H_3N^+–(CR_1R_2)_n– COO^−$ [n = 1 for the series of α– amino acids, n = 2 for β–amino acids series and n = 3 for γ– amino acids series, etc.]. More than 700 amino acids have been discovered in nature and most of them are α–amino acids. Bacteria, fungi, algae, and plants are sourced for all these amino acids and these exist either in the free form or bound to larger molecules (as constituents of peptides, proteins, other types of amide, alkylated and esterified structures). Among 700 amino acids, 20 amino acids (actually, nineteen α–amino acids and one α–imino acid) that are commonly utilized in living systems for protein synthesis under the control of genes are in a special category since they are fundamental to all life forms, as building blocks of peptides and proteins (Figure 1.4). All the amino acids except proline contain a primary amino group. Proline, and α–imino acid contains a secondary amino group incorporated into a five-membered ring. The α–amino acids differ only in the substituent (R_1 in the general formula, R_2=H) attached to the α–carbon. The wide variations in these substituent is responsible to give peptide and proteins with great structural diversity and responsible for their functional multiplicity. Depending on the properties of side chains (R_1), amino acids are categorised as hydrophobic (aliphatic and aromatic), hydrophilic (polar uncharged), charged (negatively charged and positively charged) and others as shown in Figure 1.4 The α–carbon of all the naturally occurring amino acids (except glycine) is chiral. Therefore, 19 of the 20 amino acids are existing as enantiomers and mostly with *L*-configuration. Generally, amino acids are crystalline solids with high melting points (200-

300 ºC) and soluble in water. The extent of solubility in water depends on the nature of the side chain (R_1). At physiological pH (pH = 7.3) amino acid exists as a bipolar ion called a zwitterion. The zwitterion is a compound that has a negative charge on one atom and a positive charge on a non-adjacent atom. Therefore, an amino acid can exist in an acidic form or a basic form depending on the pH of the solution in which the amino acid is dissolved. The carboxyl groups of the amino acids have pK_a values of approximately 2 and the protonated amino groups have pK_a values near 9. Therefore, both groups will be in their acidic forms in a strongly acidic solution ($pH < 7$). At pH = 7, the pH of the solution is greater than the pK_a of the carboxyl group but less than the pK_a of protonated amino group. The carboxyl group therefore will be in its basic form and the amino group will be in its acidic form. Whereas in basic solution ($pH > 7$) both carboxylic acid and amino groups will be in their basic form. Thus, in acidic solution an amino acid exists as a positive ion and migrates towards the cathode in an applied? electric field, while in alkaline solution it exists as a negative ion and migrates towards the anode. At certain hydrogen ion concentration (pH), the bipolar ion exists as a neutral ion and does not migrate to either electrodes and this pH is known as the isoelectric point of the amino acid. In addition, the physicochemical properties of amino acids also depend on the presence of functional groups on the side chain (R_1= hydrophobic, hydrophilic, charged and others) that can be titrated in the pH range of 0–14.

The properties of peptides (usually ≤ 100 amino acids linked together) and proteins (> 100 amino acids) also depend on the similar factors discribe above, but amine and carboxyl acid groups (except N-terminal α–amino group and C-terminal α– carboxy group) of all the amino acid residues are incorporated into peptide *via* amide bonds. The peptide/amide bond exhibit partial double-bond character because of electron delocalization over carbonyl oxygen and lone pair on amide nitrogen. Free rotation about the peptide bond is restricted because of its partial double-bond character. Steric hindrance causes peptide bond to adopt more stable *trans* configuration compared to *cis* configuration, *i.e.* the α–carbons of adjacent amino acids are trans to each other.

1.2.1.2 Sugars

Sugars also called as carbohydrates are the most abundant class of biomolecules in nature, making up more than 50% of the dry weight of the earth's biomass. These are polyhydroxy compounds generally contains 1:2 oxygen: hydrogen ratio with empirical formula $C_m(H_2O)_n$. Sugars are important constituents of all living organisms serves complex cellular functions including major source of metabolic energy, structural components of cells, biological transport, immunological response, blood clotting, cell-cell communication among many others.[54-55] Based on the number of monomeric sugar subunits carbohydrates are classified into monosaccharides (single sugar), disaccharides (two sugar units), oligosaccharides (three to ten sugar subunits) and polysaccharides (more than ten sugar subunits). Monosaccharides are simple polyhydroxy aldehydes (aldoses) or polyhydroxy ketone (ketoses). Monosaccharides are further classified according to the number of carbons they contain into trioses, tetroses, pentoses, hexoses, heptoses etc. The most common and simple monosaccharides are glucose, fructose and galactose which are made in the body and commonly found in food (Figure 1.4).

1.2.1.3 Nucleobases and Nucleic acids

Nucleic acids (DNA: deoxyribonucleic acid and RNA: ribonucleic acid) are long polymers of repeating subunits of nucleotides (Figure 1.5). Each nucleotide consists of a five-membered-ring sugar (ribose in RNA and 2-deoxyribose in DNA), a phosphate (-PO_4^-) group and one of 4 different nitrogenous (nitrogen-containing) nucleobases (Figure 1.5). The nucleobases are further classified into two types such as purines and pyrimidines. Purines are large bicyclic ring molecules found in both DNA and RNA; they

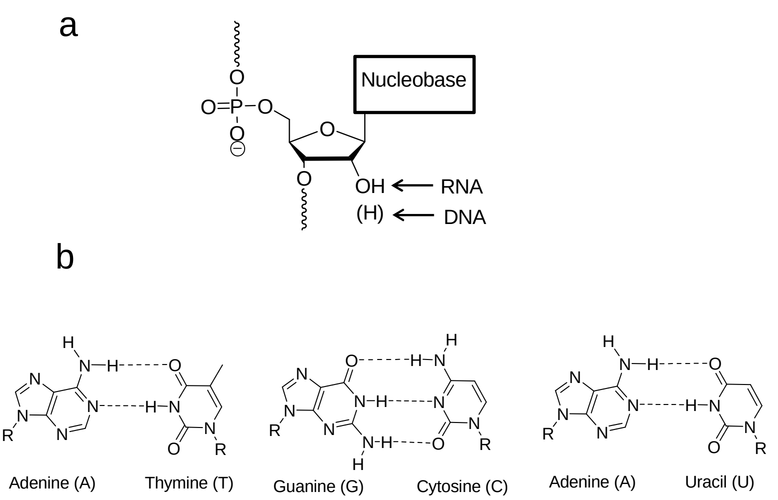

Figure 1.5 a) Schematic representation of nucleic acids b) nucleobase structures are shown with their common name with one letter abbreviations and their complementary base pairing via hydrogen bonding interactions.

are adenine (A) and guanine (G). On the other hand pyrimidines, are smaller, single-ring molecules; they include cytosine (C, in both DNA and RNA), thymine (T, in DNA only), and uracil (U, in RNA only). One of the unique properties of nucleobases is complementary base pairing through hydrogen bonding interactions. The base pairing is conceptualized as Watson-Crick base pairing, wherein adenine can pair only with thymine (in DNA, two hydrogen bonding interactions) or with uracil (in RNA), and cytosine can pair only with guanine (three hydrogen bonding interactions). The nucleobases that participate in base pairing are said to be complementary to each other. These selective base pairing interactions (A=T and G≡C) throguh complementary hydrogen bonding along with $\pi-\pi$ stacking interactions are responsible for the DNA double helix conformation and its functions.

1.2.1.4 Lipids

Lipids are among the most important molecules of the cell, as they are constituents of all biological membranes. Individual phospholipids are a composite molecules made up of three kinds of subunits, glycerol, fatty acid and a phosphate group (Figure 1.4). Glycerol is a trialcohol with each carbon bearing a hydroxyl group and it forms the backbone of the phospholipid molecule. Fatty acids are long hydrocarbon chains ending in a carboxyl (-COOH) group. Two fatty acids are attached to the glycerol backbone in a phospholipid molecule while the phosphate group is bound to one terminal of the glycerol and acts as a polar head group. The charged phosphate group usually possess a charged organic molecule linked to it, such as choline, ethanolamine, or the amino acid serine. Due to amphiphilic character lipid molecules undergo spontaneous cluster formation (polar head groups exposed to water while sequestering the nonpolar tails together within the cluster) in the presence of water. This spontaneous assembly of lipids is of paramount importance to cells, as it underlies the structure of cellular membranes. On account of remarkable structure, properties and functions of biomolecules in living systems, over the past few decades, researchers in the area of materials science have aspired to exploit thier assembly principles to create artificial materials with hierarchical structures and tailored

Table 1.1 Biomolecular nanoarchitectonics and their potential biomedical applications.[56]

Biomolecular building block	**Assembly**	**Applications**
Peptides	Random coil, β-sheet, α-helix and helix protein	Hydrogel biomaterials; drug delivery; tissue engineering; 3D cell culture[57-64]
Nucleic acids DNA; RNA	DNA origami	Therapeutics (vehicles for drug delivery); diagnostics (biosensing)[65-67]
Sugars Amylose (helical) and Cyclodextrin (cyclic)	Double helix; nanotubes; spherical micelle	Drug delivery; biosensors[68-69]
Lipids (Fatty acids; Phospholipid; Cholesterol)	Lipid bilayers; vesicles; films	Nanoreactors; artificial organells; controlled drug delivery[70-72]

properties for potential biomedical applications (Table 1.1)

1.2.2 Biological assembly

In biological systems, from a cell to complex multicellular organisms demonstrates an enormous number of successful functional designs. Ramarkably, self-assembly is one of the central phenomenon responsible for biologically complex structures and functions including molecular recognition, ligand binding, signal transduction, information storage, processing, energy conversion, extraordinary nano- and micro-architectures with self-heal, self-repair, and self-replicate properties.

The phenonmenon of self-assembly is related to molecular systems, it is a procedure in which atoms or parts of molecules spontaneously form ordered aggregates through noncovalent interactions.[13,73] Self-assembly is currently being an active area of interest and extensively studied in chemistry, biology, and materials engineering, in systems ranging from molecular to nano and macroscopic size regime.[73] In particular, process of self-assembly offers novel ways to design and construct ordered structures that are too large to be prepared by chemical synthesis but too small to be manufactured by mechanical or robotic tools.[13] The self-assembly and resultant structures are mainly governed by noncovalent interactions among the constituent molecular units which are much weaker than a covalent bond. Noncovalent interactions can be a repulsive or attractive intermolecular force having interaction energy ranging from 0-250 $KJmol^{-1}$. Various noncovalent interactions and their strength are summarized in Table 1.2. From the Table 1.2 the order of noncovalent interaction strengths is Ion–Ion ≥ Ion–Dipole > Hydrogen bonding > π–π interactions > Dipole–Dipole. Within the definition of self-assembly, Whitesides proposed four main classes of self-assembly in living organisms such as programmed (coded) self-assembly, constrained (templated) self-assembly, hierarchical self-assembly and static and dynamic self-assembly.[74]

Table 1.2 Summary of various noncovalent interactions.[56]

Interaction		**Energy(KJmol^{-1})**	**Example**
Ion-Ion (Repulsive or attractive force)	Non-directional force Long range interactions (1/r) Highly dependent on the dielectric constant of medium	250	Salt bridges in proteins
Ion-Dipole (Repulsive or attractive force)	Non-directional force Medium range interactions ($1/r^2$) Weaker than ion-ion interactions	50-250	Interaction of Mg^{+2} with 2-phosphoglycerate
Hydrogen bonding	Directional force Short range interactions (2.5-3.5Å)	10-50	DNA base pairing
π-π	Weaker electrostatic interactions Between aromatic rings	0-50	Base stacking in DNA
Dipole-Dipole (Repulsive or attractive force)	Somewhat directional force Short range interactions ($1/r^3$) Occurs between polar molecules	5.50	CO_2
Hydrophobic	The tendency of hydrocarbons to form intermolecular aggregates Repulsion of solute by the solvent	Difficult to access the interaction strength	Lipid bilayers, Protein folding

1.2.2.1 Programmed (coded) self-assembly

The self-assembly in living organisms is based on the information that is encoded in the individual segments of themselves.[75] For example, the amino acid sequence (primary structure) and its order in the proteins determine its secondary structures, shape and functions (Figure 1.6).

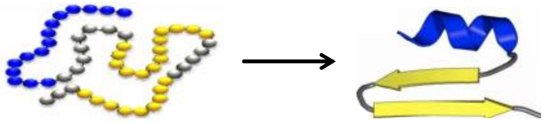

Figure 1.6 Schematic representation of sequence specific protein secondary structure.

1.2.2.2 Constrained (templated) self-assembly

The order, asymmetry and possible 3D structures of self-assembled aggregates of biological molecules are often achieved by imposing constraints or by templating the processes of self-assembly. For example, the chaperonin-assisted protein folding into a particular 3D configuration may be consider as a constrained or templated self-assembly (Figure 1.7).

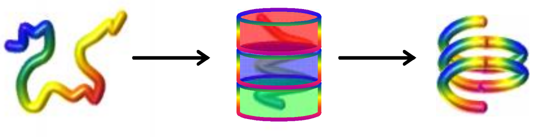

Figure 1.7 Schematic representation of chaperonin-assisted protein folding.

1.2.2.3 Hierarchical self-assembly

The primary building blocks self-organize into larger complex secondary structures which further incorporate into progressively more complex hierarchical structures. Thus, the organization of biological structures is integrated across length scales from molecules to organisms. For example, bone is a macroscale arrangement of Osteons and Haversian canals. Osteons canal consist of lamellar structure made up of hierarchical collagen fibrils which intern comprises the arrays of collagen triple helix, a coiled-coiled structure of collagen molecules (Figure 1.8).[76]

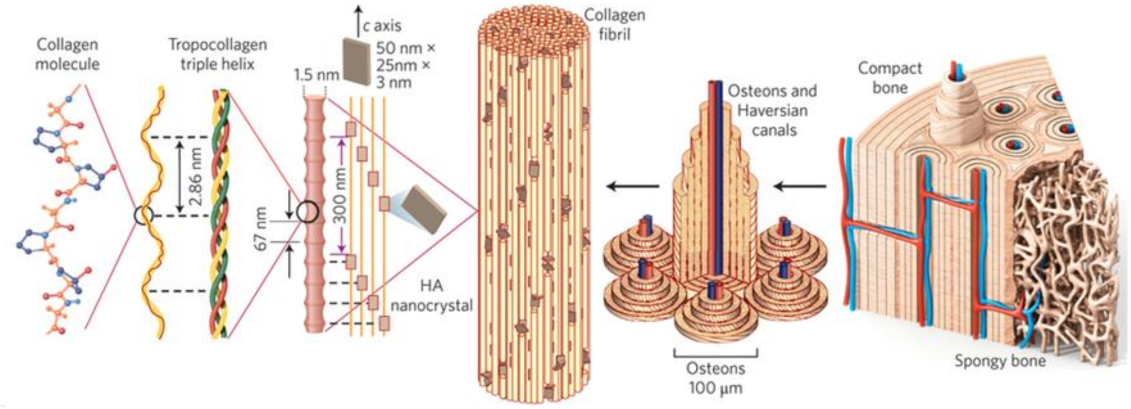
Collagen molecule
Tropocollagen triple helix
2.86 nm
1.5 nm
67 nm
c axis
50 nm × 25nm × 3 nm
300 nm
HA nanocrystal
Collagen fibril
Osteons and Haversian canals
Osteons
100 μm
Compact bone
Spongy bone

Figure 1.8 Hierarchical structure of bone. Adapted with permission of NPG from reference76.

1.2.2.4 Static and dynamic self-assembly

The static and dynamic self-assembly processes are very common in living systems. The static self-assembly generates stable global or local equilibrium structures and does not dissipate energy. For example, most of the folded globular proteins in biological systems are originated from static self-assembly of native polypeptide chains (Figure 1.9a). In contrast, dynamic self-assembly exist in out-of equilibrium and maintain their characteristic order only while dissipating energy. For example, enzyme and substrate interactions are dynamic in nature (Figure 1.9b).

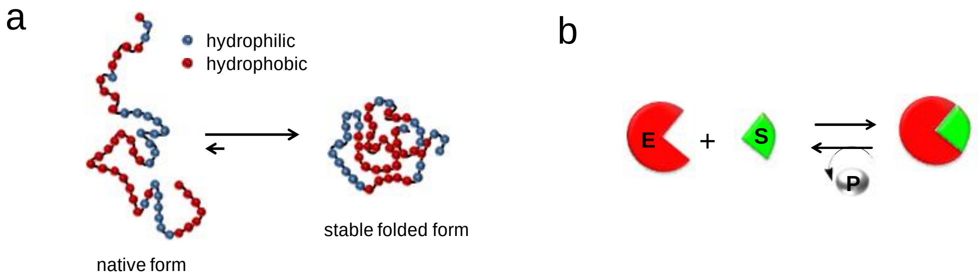
a
hydrophilic
hydrophobic
native form
stable folded form
b
E
+
S
P

Figure 1.9 Schematic representation of a) static self-assembly of protein folding from native to stable folded form.and b) dynamic assembly in the form of enzyme (E), substrate (S) interactions.

Over the past few years, bioinspired self-assembly process has been effectively used in the preparation of artificial materials for a wide range of applications from materials to biology (a few examples are shown in Table 1.3).[1-2,22,35-36,77-87]

Table 1.3 Examples of bioinspired self-assembled systems (S, static, D, dynamic, T, templated, B, biological).[86]

System	Type	Applications/importance	References
Atomic, ionic, and molecular crystals	S	Materials, optoelectronics	88-89
Phase-separated and ionic layered polymers	S		90
Self-assembled monolayers (SAMs)	S, T	Microfabrication, sensors, nanoelectronics	91
Lipid bilayers and black lipid films	S	Biomembranes, emulsions	92
Liquid crystals	S	Displays	93
Colloidal crystals	S	Band gap materials, molecular sieves	94-95
Bubble rafts	S	Models of crack propagation	96
Macro- and mesoscopic structures (MESA)	S or D, T	Electronic circuits	97-99
Fluidic self-assembly	S, T	Microfabrication	100
“Light matter”	D, T		101
Oscillating and reaction-diffusion reactions	D	Biological oscillations	102-103
Bacterial colonies	D, B		104
Swarms (ants) and schools (fish)	D, B	New models for computation/optimization	105-106
Weather patterns	D		88
Solar systems	D		
Galaxies	D		

1.3 Chirality

Chirality is one of the most ubiquitous property in biomolecules and plays a pivotal role in diverse biological functions including structural stability, signal transduction and genetic information replication, transcription and translation.[107] In addition, chirality is universal and can be observed at various hierarchical levels from subatomic and molecular to supramolecular, nanoscopic, macroscopic, and galactic scales as shown in Figure 1.10.[108] Inspired by the biological chiral evolution and unique functions, the design and development of hierarchical chiral nanoarchitectures have become an emerging and challenging interdisciplinary research area of interest among scientific community.[107-122] Owing to the fascinating chiral structural features, these architectures exhibit wide range of applications, in pharmacology as an enantioselective sensing,[120,123-128] separation[115] and catalysis,[129-131] understanding of nature's mysterious selection of homochirality,[78] designing of biomimetics,[132] chiroptical switches,[118,121] chiral memory,[133-134] optical metamaterials[135] and nanomechanical devices,[114] templates for the helical organization of nanoparticles[116] and chiroptical,[136-138] nonlinear optics,[135,139] liquid crystal[140-141] and tissue engineering.[142-144] In particular, introduction of chirality into the

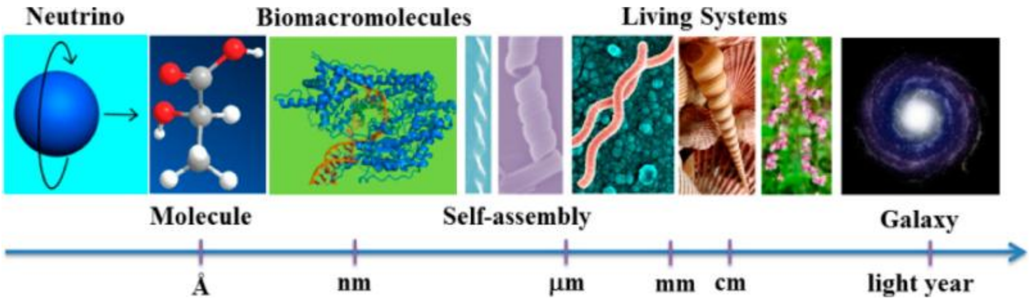

Figure 1.10 Chirality at various scales including neutrinos, enantiomeric molecules, nanosized biomacromolecules with chiral structures (DNA and proteins), self-assembled micrometer-sized helical ribbons, microorganisms (helix-shaped bacteria), macroscopic living systems (seashells and plants), and galaxies. Adapted with permission of ACS from reference 107.

organic conducting molecular systems known to display exceptional charge carrier mobilities, exciton diffusion characteristics and also lead to the observation of new phenomenon refer to electrical magneto-chiral anisotropy effect.[136,139,145-146] Therefore, development of hierarchical, chiral nanoarchitectonics of organic semiconductor is currently receiving great interest in the area of multifunctional materials.[114,132,138,145] In this regard, an intriguing strategy to guide the chiral self-assembly of π-conjugated functional compounds through conjugation of biological moieties (e.g., amino acids, peptides, nucleobases, nucleic acids, or sugars) which provide distinct modes of supramolecular interaction at their disposal.[1,22]

1.4 Arylenediimides

Arylenediimides are polycyclic aromatic molecules consist of two imides attached to the aromatic core (Figure 1.11). The arylenediimides considered herein (except pyromellitic diimide, PyDI) bear two six-membered dicarboxylic imide rings fused to the terminal naphthalene units (Figure 1.11).[1,147-148] The two simplest arylenediimide systems are 1,4,5,8-naphthalenetetracarboxylic diimide (NDI) and 3,4,9,10-perylenetetracarboxic diimide (PDI) (Figure 1.11). Arylenediimides exhibited excellent chemical, thermal, photochemical stabilities, high molecular planarity, high π–acidity, well-defined redox

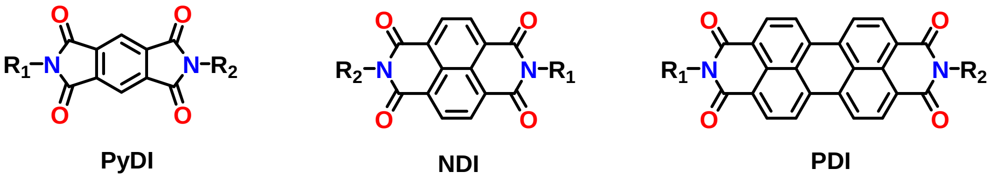

Figure 1.11 Molecular structures of arylenediimides. 1,2,4,5-benzenetetracarboxydiimide (pyromellitic diimide, PyDI), 1,4,5,8-naphthalenetetracarboxylic diimide (NDI) and 3,4,9,10-perylenetetracarboxic diimide (PDI).

behaviours and tuneable optoelectronic properties (both absorbance and fluorescence properties).[147-148] Arylenediimides are the extensively studied class of *n*-type organic semiconducting materials. On account novel characteristics, these molecules and their derivatives received special atttention in organic electronics, and biological as well as in supramolecular chemistry.[1] The high electron affinities and electron mobilities makes them versatile building blocks for electronic and optoelectronic devices namely organic light-emitting diodes,[149] dye lasers,[150] optical switches,[151] photo-detectors,[152] and photoinduced energy and electron-transfer processes.[153] However, the properties and applications of arylenediimides are mainly relied on the $\pi-$electron aromatic core and its solid state molecular packing.[154]

1.4.1 Optical properties of NDIs

NDIs belong to the D_{2h} point group symmetry and consequently their electronic transitions are polarized either along a rotation axis or perpendicular to a reflection plane.[155] NDIs exhibit strong and structured absorption bands in the range of 300-400 nm (Band-I) and 220-260 nm (Band-II) attributed to the $\pi-\pi*$ transitions of NDI chromophores polarized along the z (long axis) and y-axis (short axis) respectively (Figure 1.12a). In general, NDIs are weakly fluorescent exhibit red shifted mirror-image emission bands with small 7 nm stokes-shift. However, the optical properties of NDIs strongly depend on the imide substituents, aromatic core substituents, solvent system, concentration and molecular packing interactions. Due to the degenerate couplings of the $\pi-\pi*$ transitions, the bi-chromophoric NDIs display strong exciton cotton effects. The sign and magnitude of cotton effects depend on the direction, projection angle and distance, the number of interacting NDI chromophores, respectively as shown in Figure 1.12b.

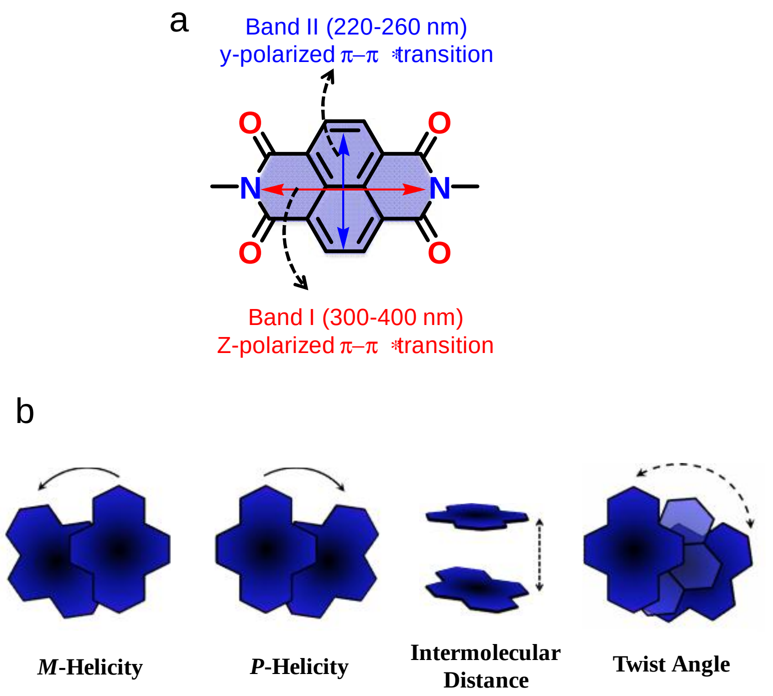
a
Band II (220-260 nm)
y-polarized π–π* transition
O
N
Band I (300-400 nm)
Z-polarized π–π* transition
b
M-Helicity
P-Helicity
Intermolecular Distance
Twist Angle

Figure 1.12 a) Principal z- and y- polarized π–π* transitions in NDI chromophore. b) Schematic representation of the transition of the angles and distance between the z-polarized transition moments of stacked NDI chromophores.[78]

1.4.2 Optical properties of PDIs

Unlike NDIs, PDIs are regarded as a closed chromophoric system with an S_0–S_1 transition (polarized along the extended molecular axis) whose intensity and position remain unaltered by the imide substituents. However, the optical properties of PDIs are minimally affected by the environment i.e. solvatochromism. PDI derivatives have been considered as optimal fluorescent dyes and utilized in a wide variety of applications such as laser dyes, photovoltaic cells, fluorescence switches, molecular wires, molecular transistors and sensors.[156] However, the hydrophobic PDI structure and π-electron deficient aromatic nature is known to promote the formation of aggregates through stacking interactions between the π-conjugated core and this strong aggregation tendency in aqueous media results in fluorescence quenching. In spite of aggregation and resultant low fluorescence, PDI derivatives have been considered to be excellent fluorophores in sensor design because of their excellent electron accepting ability and high fluorescence in the disassembled state.

1.5 Objective (Bioinspired nanoarchitectonics of arylenediimide)

Bioinspired nanoarchitectonics identified with the utilization of ideas and components found in biological systems for design, synthesis and development of functional nanomaterials. In spite of extensive use of arylenediimide from materials to biomedicine, the key overwhelming difficulties in controlling solid state intermolecular packing are remained to be addressed.[1] In this context, we employed the bio-inspired nanoarchitectonics approaches by conjugating biological elements as assembly directing substituents to design ordered assemblies with diverse structural, chemical and chiroptical

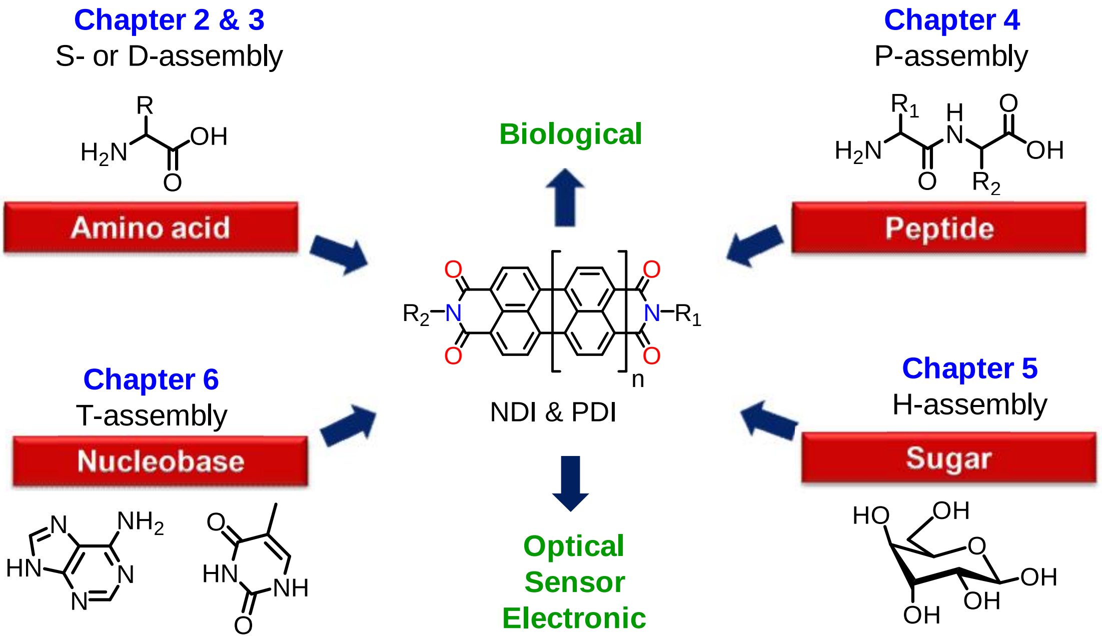
Chapter 2 & 3
S- or D-assembly
R
H2N
OH
O
Amino acid
Chapter 4
P-assembly
R1
H
N
O
H2N
OH
O
R2
Peptide
Biological
R2
N
O
O
O
O
N
R1
n
NDI & PDI
Chapter 6
T-assembly
Nucleobase
N
NH2
HN
N
N
O
HN
NH
O
Optical
Sensor
Electronic
Chapter 5
H-assembly
Sugar
HO
OH
O
OH
OH
OH

Figure 1.13 Overview of bioinspired nanoarchitectonics of arylenediimides presented in this thesis. (S-, static, D-, dynamic, P-, programmed, T-, templated, H-, hierarchical). Where n= 0 for NDI and n= 1 for PDI.

properties.[1,157-175] This novel design based on the marriage between biomolecules and arylenediimide systems (e.g., NDIs and PDIs) not only envision the engineering of solid state molecular ordering through various noncovalent interactions, but also synergistically combine the properties of constituent components. With this in mind, we have chosen basic biological building blocks of life (amino acid, peptide, sugar and nucleobase) as arylenediimide assembly directing groups due to their inherent ability to make complex molecular architectures in biological systems and variable functionality can endow hydrophilic, hydrophobic and aromatic interactions in a single compact moiety and investigated its optical, electronic and in biological applications (Figure 1.13).

The strong reasons for persuing the area of bioinspired nanoarchitectonics are to gain better understanding of living systems and to generate ordered aggregates of components, ranging in size from the molecular to the macroscopic scale in persuit of designing novel drugs, development of biomimetics and nanobiotechnology. The advantages of bioinspired nanoarchitectonics include aqueous processability, biocompatibility, compact, cost effective and these nanosystems and architectures often cannot be generated by any other methods. As one would like to think bioinspired nanoarchitectonics can be adapted in numerous research fields and open up to enormous potential outcomes and applications.

1.5.1 Applications of bioinspired nanoarchitectonics of arylenediimide presented in this thesis

We describe the thoughtfully designed bioinspired nanoarchitectonics of arylenediimide and their versatile applications as follows

i) Supramolecular auxiliaries for the crystal engineering of arylenediimide organization (molecular architectonics) with tunable chiroptical, viscoelastic and nanoscale properties.

ii) Stimuli-responsive ferroelectric charge transfer complexes in the presence of designed complementary π–electron rich pyrene tweezer.

iii) Detection of carcinogenic solvents.

iv) Identification of novel class of modulators of Aβ aggregation which is highly useful in the development of disease-modifying therapeutics for Alzheimer's disease.

v) Rapid, highly sensitive and selective detection of metal ions such as Cu^{2+}, Fe^{3+} and Hg^{2+} in an aqueous medium.

vi) Peroxidase mimicking fluorogenic substrate for the detection of H_2O_2.

vii) pH-responsive probe and its reversible chiroptical switching property.

viii) Plausible clues for nature’s mysterious selection of homochirality.

ix) Conductivity modulation of arylenediimide.

x) Preparation of hierarchical superstructures similar to that of collagen to make uniformly silver coated nanotubes.

xi) Templated DNA nanotechnology: Mutual templated co-assembly of small molecular template and single stranded DNA and its unusual template length dependent properties such as modulation of 2D morphology, charge transport properties for the selective detection of toxic Hg^{2+} ions in water using chiroptical switching and electronic characteristics.

1.6 References

1. Avinash, M. B.; Govindaraju, T., Amino acid derivatized arylenediimides: a versatile modular approach for functional molecular materials. *Adv. Mater.* **2012,** *24*, 3905-3922.

2. Govindaraju, T.; Avinash, M. B., Two-dimensional nanoarchitectonics: organic and hybrid materials. *Nanoscale* **2012,** *4*, 6102-6117.

3. Heeger, A. J., 25th anniversary article: Bulk heterojunction solar cells: understanding the mechanism of operation. *Adv. Mater.* **2014,** *26*, 10-27.

4. Jariwala, D.; Sangwan, V. K.; Lauhon, L. J.; Marks, T. J.; Hersam, M. C., Emerging device applications for semiconducting two-dimensional transition metal dichalcogenides. *ACS Nano* **2014,** *8*, 1102-1120.

5. Lang, X.; Chen, X.; Zhao, J., Heterogeneous visible light photocatalysis for selective organic transformations. *Chem. Soc. Rev.* **2014,** *43*, 473-486.

6. Maiti, U. N.; Lee, W. J.; Lee, J. M.; Oh, Y.; Kim, J. Y.; Kim, J. E.; Shim, J.; Han, T. H.; Kim, S. O., 25th anniversary article: Chemically modified/doped carbon nanotubes & graphene for optimized nanostructures & nanodevices. *Adv. Mater.* **2014,** *26*, 40-66.

7. Li, Y.; Wang, S.; He, G.; Wu, H.; Pan, F.; Jiang, Z., Facilitated transport of small molecules and ions for energy-efficient membranes. *Chem. Soc. Rev.* **2015,** *44*, 103-118.

8. Lim, S. Y.; Shen, W.; Gao, Z., Carbon quantum dots and their applications. *Chem. Soc. Rev.* **2015,** *44*, 362-381.

9. Stephenson, T.; Li, Z.; Olsen, B.; Mitlin, D., Lithium ion battery applications of molybdenum disulfide (MoS2) nanocomposites. *Energy Environ. Sci.* **2014,** *7*, 209-231.

10. Wang, D. W.; Su, D. S., Heterogeneous nanocarbon materials for oxygen reduction reaction. *Energy Environ. Sci.* **2014,** *7*, 576-591.

11. Biju, V., Chemical modifications and bioconjugate reactions of nanomaterials for sensing, imaging, drug delivery and therapy. *Chem. Soc. Rev.* **2014,** *43*, 744-764.

12. Zeng, S.; Baillargeat, D.; Ho, H. P.; Yong, K. T., Nanomaterials enhanced surface plasmon resonance for biological and chemical sensing applications. *Chem. Soc. Rev.* **2014,** *43*, 3426-3452.

13. Boncheva, M.; Whitesides, G. M., Making Things by Self-Assembly. *MRS Bull.* **2011,** *30*, 736-742.

14. Ariga, K., From Nanotechnology to Nanoarchitectonics. *J. Inorg. Organomet. Polym. Mater.* **2015,** *25*, 177-178.

15. Magoga, M.; Joachim, C., Conductance of molecular wires connected or bonded in parallel. *Phys. Rev. B: Condens. Matter Mater. Phys.* **1999,** *59*, 16011-16021.

16. Karagiannis, P.; Ishii, Y.; Yanagida, T., Molecular machines like myosin use randomness to behave predictably. *Chem. Rev.* **2014,** *114*, 3318-3334.

17. Ariga, K.; Ji, Q. M.; Nakanishi, W.; Hill, J. P.; Aono, M., Nanoarchitectonics: a new materials horizon for nanotechnology. *Mater. Horiz.* **2015,** *2*, 406-413.

18. Aono, M., Focus on Materials Nanoarchitectonics. *Sci. Technol. Adv. Mat.* **2011,** *12*, 040301.

19. Aono, M.; Bando, Y.; Ariga, K., Nanoarchitectonics: pioneering a new paradigm for nanotechnology in materials development. *Adv. Mater.* **2012,** *24*, 150-151.

20. Ariga, K.; Ji, Q. M.; Mori, T.; Naito, M.; Yamauchi, Y.; Abe, H.; Hill, J. P., Enzyme nanoarchitectonics: organization and device application. *Chem. Soc. Rev.* **2013,** *42*, 6322-6345.

21. Kujawa, P.; Winnik, F. M., Innovation in nanomedicine through materials nanoarchitectonics. *Langmuir* **2013,** *29*, 7354-7361.

22. Avinash, M. B.; Govindaraju, T., Nanoarchitectonics of biomolecular assemblies for functional applications. *Nanoscale* **2014,** *6*, 13348-13369.

23. Ariga, K.; Li, M.; Richards, G. J.; Hill, J. P., Nanoarchitectonics: a conceptual paradigm for design and synthesis of dimension-controlled functional nanomaterials. *J. Nanosci. Nanotechnol.* **2011,** *11*, 1-13.

24. Hecht, S., Welding, organizing, and planting organic molecules on substrate surfaces--promising approaches towards nanoarchitectonics from the bottom up. *Angew. Chem. Int. Ed.* **2003,** *42*, 24-26.

25. Aono, M.; Ariga, K., The Way to Nanoarchitectonics and the Way of Nanoarchitectonics. *Adv. Mater.* **2015**, doi: 10.1002/adma.201502868.

26. Takada, K., Interfacial nanoarchitectonics for solid-state lithium batteries. *Langmuir* **2013,** *29*, 7538-7541.

27. Ariga, K.; Ishihara, S.; Abe, H.; Li, M.; Hill, J. P., Materials nanoarchitectonics for environmental remediation and sensing. *J. Mater. Chem.* **2012,** *22*, 2369-2377.

28. Ariga, K.; Vinu, A.; Yamauchi, Y.; Ji, Q. M.; Hill, J. P., Nanoarchitectonics for Mesoporous Materials. *Bull. Chem. Soc. Jpn.* **2012,** *85*, 1-32.

29. Ariga, K.; Ji, Q.; Nakanishi, W.; Hill, J., Thin Film Nanoarchitectonics. *Inorg. Organomet. Polym. Mater.* **2015,** *25*, 466-479.

30. Shrestha, L. K.; Strzelczyk, K. M.; Shrestha, R. G.; Ichikawa, K.; Aramaki, K.; Hill, J. P.; Ariga, K., Nonionic amphiphile nanoarchitectonics: self-assembly into micelles and lyotropic liquid crystals. *Nanotechnology* **2015,** *26*, 204002.

31. Rajendran, R.; Shrestha, L. K.; Minami, K.; Subramanian, M.; Jayavel, R.; Ariga, K., Dimensionally integrated nanoarchitectonics for a novel composite from 0D, 1D, and 2D nanomaterials: RGO/CNT/CeO2 ternary nanocomposites with electrochemical performance. *J Mater Chem A* **2014,** *2*, 18480-18487.

32. Ariga, K.; Ji, Q. M.; McShane, M. J.; Lvov, Y. M.; Vinu, A.; Hill, J. P., Inorganic Nanoarchitectonics for Biological Applications. *Chem. Mater.* **2012,** *24*, 728-737.

33. Ariga, K.; Kawakami, K.; Ebara, M.; Kotsuchibashi, Y.; Ji, Q. M.; Hill, J. P., Bioinspired nanoarchitectonics as emerging drug delivery systems. *New J. Chem.* **2014,** *38*, 5149-5163.

34. Barth, J. V., Molecular Architectonic on Metal Surfaces. *Annu. Rev. Phys. Chem.* **2007,** *58*, 375-407.

35. Avinash, M. B.; Samanta, P. K.; Sandeepa, K. V.; Pati, S. K.; Govindaraju, T., Molecular Architectonics of Stereochemically Constrained π-Complementary Functional Modules. *Eur. J. Org. Chem.* **2013,** *2013*, 5838-5847.

36. Pandeeswar, M.; Khare, H.; Ramakumar, S.; Govindaraju, T., Crystallographic insight-guided nanoarchitectonics and conductivity modulation of an n-type organic semiconductor through peptide conjugation. *Chem. Commun.* **2015,** *51*, 8315-8318.

37. Sarikaya, M.; Tamerler, C.; Jen, A. K.; Schulten, K.; Baneyx, F., Molecular biomimetics: nanotechnology through biology. *Nat. Mater.* **2003,** *2*, 577-585.

38. Zhang, S., Fabrication of novel biomaterials through molecular self-assembly. *Nat. Biotechnol.* **2003,** *21*, 1171-1178.

39. Ariga, K.; Kawakami, K.; Ebara, M.; Kotsuchibashi, Y.; Ji, Q.; Hill, J. P., Bioinspired nanoarchitectonics as emerging drug delivery systems. *New J. Chem.* **2014,** *38*, 5149-5163.

40. Rawlings, A. E.; Bramble, J. P.; Staniland, S. S., Innovation through imitation: biomimetic, bioinspired and biokleptic research. *Soft Matter* **2012,** *8*, 6675-6679.

41. Mohammed, J. S.; Murphy, W. L., Bioinspired Design of Dynamic Materials. *Adv. Mater.* **2009,** *21*, 2361-2374.

42. Barron, A. E.; Zuckerman, R. N., Bioinspired polymeric materials: in-between proteins and plastics. *Curr. Opin. Chem. Biol.* **1999,** *3*, 681-687.

43. Sun, T.; Feng, L.; Gao, X.; Jiang, L., Bioinspired surfaces with special wettability. *Acc. Chem. Res.* **2005,** *38*, 644-652.

44. Zhao, Y.; Xie, Z.; Gu, H.; Zhu, C.; Gu, Z., Bio-inspired variable structural color materials. *Chem. Soc. Rev.* **2012,** *41*, 3297-3317.

45. Xia, F.; Jiang, L., Bio-Inspired, Smart, Multiscale Interfacial Materials. *Adv. Mater.* **2008,** *20*, 2842-2858.

46. Ong, J. M.; da Cruz, L., The bionic eye: a review. *Clin. Experiment Ophthalmol.* **2012,** *40*, 6-17.

47. Estroff, L. A.; Hamilton, A. D., At the interface of organic and inorganic chemistry: Bioinspired synthesis of composite materials. *Chem. Mater.* **2001,** *13*, 3227-3235.

48. Chen, P.-Y.; McKittrick, J.; Meyers, M. A., Biological materials: Functional adaptations and bioinspired designs. *Prog. Mat. Sci.* **2012,** *57*, 1492-1704.

49. Bhushan, B., Biomimetics: lessons from nature–an overview. *Philos. Trans. A Math. Phys. Eng. Sci.* **2009,** *367*, 1445-1486.

50. Vincent, J. F.; Bogatyreva, O. A.; Bogatyrev, N. R.; Bowyer, A.; Pahl, A. K., Biomimetics: its practice and theory. *J. R. Soc. Interface* **2006,** *3*, 471-482.

51. Seeman, N. C., DNA enables nanoscale control of the structure of matter. *Q. Rev. Biophys.* **2005,** *38*, 363-371.

52. United Nations Convention on Biological Diversity. *J. Ethnopharmacol.* **1996,** *51*, 287-305.

53. Marth, J. D., A unified vision of the building blocks of life. *Nat. Cell Biol.* **2008,** *10*, 1015-1016.

54. Bertozzi, C. R.; Kiessling, L. L., Chemical glycobiology. *Science* **2001,** *291*, 2357-2364.

55. Werz, D. B.; Seeberger, P. H., Carbohydrates as the Next Frontier in Pharmaceutical Research. *Chem. - Eur. J.* **2005,** *11*, 3194-3206.

56. Mendes, A. C.; Baran, E. T.; Reis, R. L.; Azevedo, H. S., Self-assembly in nature: using the principles of nature to create complex nanobiomaterials. *WIREs Nanomed. Nanobiotechnol.* **2013,** *5*, 582-612.

57. Cui, H.; Webber, M. J.; Stupp, S. I., Self-assembly of peptide amphiphiles: from molecules to nanostructures to biomaterials. *Biopolymers* **2010,** *94*, 1-18.

58. Fairman, R.; Akerfeldt, K. S., Peptides as novel smart materials. *Curr. Opin. Struct. Biol.* **2005,** *15*, 453-463.

59. Jayawarna, V.; Smith, A.; Gough, J. E.; Ulijn, R. V., Three-dimensional cell culture of chondrocytes on modified di-phenylalanine scaffolds. *Biochem. Soc. Trans.* **2007,** *35*, 535-537.

60. Luo, Z. L.; Zhang, S. G., Designer nanomaterials using chiral self-assembling peptide systems and their emerging benefit for society. *Chem. Soc. Rev.* **2012,** *41*, 4736-4754.

61. Matson, J. B.; Stupp, S. I., Self-assembling peptide scaffolds for regenerative medicine. *Chem. Commun.* **2012,** *48*, 26-33.

62. Ryan, D. M.; Nilsson, B. L., Self-assembled amino acids and dipeptides as noncovalent hydrogels for tissue engineering. *Polym. Chem.* **2012,** *3*, 18-33.

63. Webber, M. J.; Kessler, J. A.; Stupp, S. I., Emerging peptide nanomedicine to regenerate tissues and organs. *Journal of internal medicine* **2010,** *267*, 71-88.

64. Yang, Y. L.; Khoe, U.; Wang, X. M.; Horii, A.; Yokoi, H.; Zhang, S. G., Designer self-assembling peptide nanomaterials. *Nano Today* **2009,** *4*, 193-210.

65. Li, H.; Labean, T. H.; Leong, K. W., Nucleic acid-based nanoengineering: novel structures for biomedical applications. *Interface focus* **2011,** *1*, 702-724.

66. Pinheiro, A. V.; Han, D.; Shih, W. M.; Yan, H., Challenges and opportunities for structural DNA nanotechnology. *Nat. Nanotechnol.* **2011,** *6*, 763-772.

67. Krishnan, Y.; Simmel, F. C., Nucleic acid based molecular devices. *Angew. Chem. Int. Ed.* **2011,** *50*, 3124-3156.

68. Gattuso, G.; Menzer, S.; Nepogodiev, S. A.; Stoddart, J. F.; Williams, D. J., Carbohydrate nanotubes. *Angew. Chem. Int. Ed.* **1997,** *36*, 1451-1454.
69. Numata M, S. S., *Self-assembled polysaccharide nanotubes generated from β-1,3-glucan polysaccharides. Self-Assembled Nanomaterials II: Nanotubes*. Springer,Verlag,: Berlin Heidelberg, 2008; Vol. 220.
70. Schnur, J. M., Lipid tubules: a paradigm for molecularly engineered structures. *Science* **1993,** *262*, 1669-1676.
71. Yu, X. F.; Liu, Z. H.; Janzen, J.; Chafeeva, I.; Horte, S.; Chen, W.; Kainthan, R. K.; Kizhakkedathu, J. N.; Brooks, D. E., Polyvalent choline phosphate as a universal biomembrane adhesive. *Nat. Mater.* **2012,** *11*, 468-476.
72. Urata, K.; Takaishi, N., Cholesterol as synthetic building blocks for artificial lipids with characteristic physical, chemical and biological properties. *Eur. J. Lipid Sci. Technol.* **2001,** *103*, 29-39.
73. Siegel, J. S., Supramolecular chemistry. Concepts and perspectives - Lehn,JM. *Science* **1996,** *271*, 949-949.
74. Boncheva, M. W., G. M., In Dekker Encyclopedia of Nanoscience and Nanotechnology. 2nd ed. ed.; Dekker, M., Ed. New York, 2004; p 287− 294.
75. Cademartiri, L.; Bishop, K. J., Programmable self-assembly. *Nat. Mater.* **2015,** *14*, 2-9.
76. Wegst, U. G.; Bai, H.; Saiz, E.; Tomsia, A. P.; Ritchie, R. O., Bioinspired structural materials. *Nat. Mater.* **2015,** *14*, 23-36.
77. Avinash, M. B.; Govindaraju, T., Engineering Molecular Organization of Naphthalenediimides: Large Nanosheets with Metallic Conductivity and Attoliter Containers. *Adv. Funct. Mater.* **2011,** *21*, 3875-3882.
78. Pandeeswar, M.; Avinash, M. B.; Govindaraju, T., Chiral transcription and retentive helical memory: probing peptide auxiliaries appended with naphthalenediimides for their one-dimensional molecular organization. *Chem. - Eur. J.* **2012,** *18*, 4818-4822.
79. Avinash, M. B.; Govindaraju, T., A bio-inspired design strategy: Organization of tryptophan-appended naphthalenediimide into well-defined architectures induced by molecular interactions. *Nanoscale* **2011,** *3*, 2536-2543.
80. Narayanaswamy, N.; Avinash, M. B.; Govindaraju, T., Exploring hydrogen bonding and weak aromatic interactions induced assembly of adenine and thymine functionalised naphthalenediimides. *New J. Chem.* **2013,** *37*, 1302-1306.
81. Dwivedi, A. K.; Pandeeswar, M.; Govindaraju, T., Assembly modulation of PDI derivative as a supramolecular fluorescence switching probe for detection of cationic surfactant and metal ions in aqueous media. *ACS Appl. Mater. Interfaces* **2014,** *6*, 21369-21379.

82. Pandeeswar, M.; Govindaraju, T., Bioinspired Nanoarchitectonics of Naphthalene Diimide to Access 2D Sheets of Tunable Size, Shape, and Optoelectronic Properties. *J. Inorg. Organomet. Polym. Mater.* **2015,** *25*, 293-300.

83. Pandeeswar, M.; Govindaraju, T., Green-fluorescent naphthalene diimide: conducting layered hierarchical 2D nanosheets and reversible probe for detection of aromatic solvents. *RSC Adv.* **2013,** *3*, 11459-11462.

84. Pandeeswar, M.; Khare, H.; Ramakumar, S.; Govindaraju, T., Biomimetic molecular organization of naphthalene diimide in the solid state: tunable (chiro-) optical, viscoelastic and nanoscale properties. *RSC Adv.* **2014,** *4*, 20154-20163.

85. Govindaraju, T.; Pandeeswar, M.; Jayaramulu, K.; Jaipuria, G.; Atreya, H. S., Spontaneous self-assembly of designed cyclic dipeptide (Phg-Phg) into two-dimensional nano- and mesosheets. *Supramol. Chem.* **2011,** *23*, 487-492.

86. Whitesides, G. M.; Grzybowski, B., Self-assembly at all scales. *Science* **2002,** *295*, 2418-2421.

87. Manchineella, S.; Prathyusha, V.; Priyakumar, U. D.; Govindaraju, T., Solvent-induced helical assembly and reversible chiroptical switching of chiral cyclic-dipeptide-functionalized naphthalenediimides. *Chem.--Eur. J.* **2013,** *19*, 16615-16624.

88. Philp, D.; Stoddart, J. F., Self-assembly in natural and unnatural systems. *Angew. Chem. Int. Ed.* **1996,** *35*, 1155-1196.

89. Desiraju, G. R., *Crystal engineering: the design of organic solids*. Elsevier: 1989.

90. De Rosa, C.; Park, C.; Thomas, E. L.; Lotz, B., Microdomain patterns from directional eutectic solidification and epitaxy. *Nature* **2000,** *405*, 433-437.

91. Aizenberg, J.; Black, A. J.; Whitesides, G. M., Control of crystal nucleation by patterned self-assembled monolayers. *Nature* **1999,** *398*, 495-498.

92. M. N. Jones, D. C., Micelles, Monolayers and Biomembranes *(Wiley-Liss, New York, 1995).*

93. Loudet, J. C.; Barois, P.; Poulin, P., Colloidal ordering from phase separation in a liquid-crystalline continuous phase. *Nature* **2000,** *407*, 611-613.

94. vanBlaaderen, A.; Ruel, R.; Wiltzius, P., Template-directed colloidal crystallization. *Nature* **1997,** *385*, 321-324.

95. Xia, Y. N.; Gates, B.; Yin, Y. D.; Lu, Y., Monodispersed colloidal spheres: Old materials with new applications. *Adv. Mater.* **2000,** *12*, 693-713.

96. Simpson, A. W. H., Pauline H., Bubble Raft Model for an Amorphous Alloy. *Nature* **1972,** *237*, 320-322.

97. Bowden, N.; Choi, I. S.; Grzybowski, B. A.; Whitesides, G. M., Mesoscale Self-Assembly of Hexagonal Plates Using Lateral Capillary Forces: Synthesis Using the “Capillary Bond”. *J. Am. Chem. Soc.* **1999,** *121*, 5373-5391.

98. Grzybowski, B. A.; Bowden, N.; Arias, F.; Yang, H.; Whitesides, G. M., Modeling of menisci and capillary forces from the millimeter to the micrometer size range. *J. Phys. Chem. B* **2001,** *105*, 404-412.

99. Gracias, D. H.; Tien, J.; Breen, T. L.; Hsu, C.; Whitesides, G. M., Forming electrical networks in three dimensions by self-assembly. *Science* **2000,** *289*, 1170-1172.

100. Srinivasan, U.; Liepmann, D.; Howe, R. T., Microstructure to substrate self-assembly using capillary forces. *J. Microelectromech. S.* **2001,** *10*, 17-24.

101. Burns, M. M.; Fournier, J. M.; Golovchenko, J. A., Optical Crystallization Work - Response. *Science* **1991,** *252*, 1049-1049.

102. Hess, B., Periodic patterns in biology. *Naturwissenschaften* **2000,** *87*, 199-211.

103. Jakubith, S.; Rotermund, H. H.; Engel, W.; von Oertzen, A.; Ertl, G., Spatiotemporal concentration patterns in a surface reaction: Propagating and standing waves, rotating spirals, and turbulence. *Phys. Rev. Lett.* **1990,** *65*, 3013-3016.

104. Shapiro, J. A., Thinking about bacterial populations as multicellular organisms. *Annu. Rev. Microbiol.* **1998,** *52*, 81-104.

105. Shimoyama, N.; Sugawara, K.; Mizuguchi, T.; Hayakawa, Y.; Sano, M., Collective motion in a system of motile elements. *Phys. Rev. Lett.* **1996,** *76*, 3870-3873.

106. Bonabeau, E.; Dorigo, M.; Theraulaz, G., Inspiration for optimization from social insect behaviour. *Nature* **2000,** *406*, 39-42.

107. Mateos-Timoneda, M. A.; Crego-Calama, M.; Reinhoudt, D. N., Supramolecular chirality of self-assembled systems in solution. *Chem. Soc. Rev.* **2004,** *33*, 363-372.

108. Liu, M.; Zhang, L.; Wang, T., Supramolecular Chirality in Self-Assembled Systems. *Chem. Rev.* **2015,** *115*, 7304-7397.

109. Wang, A. D.; Huang, J. B.; Yan, Y., Hierarchical molecular self-assemblies: construction and advantages. *Soft Matter* **2014,** *10*, 3362-3373.

110. Duan, P. F.; Cao, H.; Zhang, L.; Liu, M. H., Gelation induced supramolecular chirality: chirality transfer, amplification and application. *Soft Matter* **2014,** *10*, 5428-5448.

111. Jin, W.; Fukushima, T.; Niki, M.; Kosaka, A.; Ishii, N.; Aida, T., Self-assembled graphitic nanotubes with one-handed helical arrays of a chiral amphiphilic molecular graphene. *Proc. Natl. Acad. Sci. U. S. A.* **2005,** *102*, 10801-10806.

112. Torsi, L.; Farinola, G. M.; Marinelli, F.; Tanese, M. C.; Omar, O. H.; Valli, L.; Babudri, F.; Palmisano, F.; Zambonin, P. G.; Naso, F., A sensitivity-enhanced field-effect chiral sensor. *Nat. Mater.* **2008,** *7*, 412-417.

113. O'Leary, L. E.; Fallas, J. A.; Bakota, E. L.; Kang, M. K.; Hartgerink, J. D., Multi-hierarchical self-assembly of a collagen mimetic peptide from triple helix to nanofibre and hydrogel. *Nat. Chem.* **2011,** *3*, 821-828.

114. Wang, Y.; Xu, J.; Wang, Y.; Chen, H., Emerging chirality in nanoscience. *Chem. Soc. Rev.* **2013,** *42*, 2930-2962.

115. Perez-Garcia, L.; Amabilino, D. B., Spontaneous resolution under supramolecular control. *Chem. Soc. Rev.* **2002,** *31*, 342-356.

116. Noguez, C.; Garzon, I. L., Optically active metal nanoparticles. *Chem. Soc. Rev.* **2009,** *38*, 757-771.

117. Lee, C. C.; Grenier, C.; Meijer, E. W.; Schenning, A. P., Preparation and characterization of helical self-assembled nanofibers. *Chem. Soc. Rev.* **2009,** *38*, 671-683.

118. Canary, J. W., Redox-triggered chiroptical molecular switches. *Chem. Soc. Rev.* **2009,** *38*, 747-756.

119. Amabilino, D. B., Chiral nanoscale systems: preparation, structure, properties and function. *Chem. Soc. Rev.* **2009,** *38*, 669-670.

120. Hembury, G. A.; Borovkov, V. V.; Inoue, Y., Chirality-sensing supramolecular systems. *Chem. Rev.* **2008,** *108*, 1-73.

121. Feringa, B. L.; van Delden, R. A.; Koumura, N.; Geertsema, E. M., Chiroptical Molecular Switches. *Chem. Rev.* **2000,** *100*, 1789-1816.

122. Cornelissen, J. J.; Rowan, A. E.; Nolte, R. J.; Sommerdijk, N. A., Chiral architectures from macromolecular building blocks. *Chem. Rev.* **2001,** *101*, 4039-4070.

123. Jo, H. H.; Lin, C. Y.; Anslyn, E. V., Rapid optical methods for enantiomeric excess analysis: from enantioselective indicator displacement assays to exciton-coupled circular dichroism. *Acc. Chem. Res.* **2014,** *47*, 2212-2221.

124. Rekharsky, M. V.; Yamamura, H.; Inoue, C.; Kawai, M.; Osaka, I.; Arakawa, R.; Shiba, K.; Sato, A.; Ko, Y. H.; Selvapalam, N.; Kim, K.; Inoue, Y., Chiral recognition in cucurbituril cavities. *J. Am. Chem. Soc.* **2006,** *128*, 14871-14880.

125. Miao, W.; Zhang, L.; Wang, X.; Qin, L.; Liu, M., Gelation-induced visible supramolecular chiral recognition by fluorescent metal complexes of quinolinol-glutamide. *Langmuir* **2013,** *29*, 5435-5442.

126. Li, X.; Tanasova, M.; Vasileiou, C.; Borhan, B., Fluorinated porphyrin tweezer: a powerful reporter of absolute configuration for erythro and threo diols, amino alcohols, and diamines. *J. Am. Chem. Soc.* **2008,** *130*, 1885-1893.

127. Biedermann, F.; Nau, W. M., Noncovalent chirality sensing ensembles for the detection and reaction monitoring of amino acids, peptides, proteins, and aromatic drugs. *Angew. Chem. Int. Ed.* **2014,** *53*, 5694-5699.

128. Pu, L., Enantioselective fluorescent sensors: a tale of BINOL. *Acc. Chem. Res.* **2012,** *45*, 150-163.

129. Shi, L.; Wang, X.; Sandoval, C. A.; Li, M.; Qi, Q.; Li, Z.; Ding, K., Engineering a polymeric chiral catalyst by using hydrogen bonding and coordination interactions. *Angew. Chem. Int. Ed.* **2006,** *45*, 4108-4112.

130. Hatano, M.; Mizuno, T.; Izumiseki, A.; Usami, R.; Asai, T.; Akakura, M.; Ishihara, K., Enantioselective Diels-Alder reactions with anomalous endo/exo selectivities using conformationally flexible chiral supramolecular catalysts. *Angew. Chem. Int. Ed.* **2011,** *50*, 12189-12192.

131. Jin, Q.; Zhang, L.; Cao, H.; Wang, T.; Zhu, X.; Jiang, J.; Liu, M., Self-assembly of copper(II) ion-mediated nanotube and its supramolecular chiral catalytic behavior. *Langmuir* **2011,** *27*, 13847-13853.

132. Zou, W.; Yan, Y.; Fang, J.; Yang, Y.; Liang, J.; Deng, K.; Yao, J.; Wei, Z., Biomimetic superhelical conducting microfibers with homochirality for enantioselective sensing. *J. Am. Chem. Soc.* **2014,** *136*, 578-581.

133. Yashima, E.; Maeda, K.; Iida, H.; Furusho, Y.; Nagai, K., Helical polymers: synthesis, structures, and functions. *Chem. Rev.* **2009,** *109*, 6102-6211.

134. Zhang, W.; Jin, W.; Fukushima, T.; Ishii, N.; Aida, T., Dynamic or nondynamic? Helical trajectory in hexabenzocoronene nanotubes biased by a detachable chiral auxiliary. *J. Am. Chem. Soc.* **2013,** *135*, 114-117.

135. Verbiest, T.; Van Elshocht, S.; Kauranen, M.; Hellemans, L.; Snauwaert, J.; Nuckolls, C.; Katz, T. J.; Persoons, A., Strong enhancement of nonlinear optical properties through supramolecular chirality. *Science* **1998,** *282*, 913-915.

136. Zhang, Y.; Chen, P.; Jiang, L.; Hu, W.; Liu, M., Controllable fabrication of supramolecular nanocoils and nanoribbons and their morphology-dependent photoswitching. *J. Am. Chem. Soc.* **2009,** *131*, 2756-2757.

137. Peeters, E.; Christiaans, M. P. T.; Janssen, R. A. J.; Schoo, H. F. M.; Dekkers, H. P. J. M.; Meijer, E. W., Circularly polarized electroluminescence from a polymer light-emitting diode. *J. Am. Chem. Soc.* **1997,** *119*, 9909-9910.

138. Watanabe, K.; Osaka, I.; Yorozuya, S.; Akagi, K., Helically π-Stacked Thiophene-Based Copolymers with Circularly Polarized Fluorescence: High Dissymmetry Factors Enhanced by Self-Ordering in Chiral Nematic Liquid Crystal Phase. *Chem. Mater*. **2012,** *24*, 1011-1024.

139. Yang, Y.; da Costa, R. C.; Fuchter, M. J.; Campbell, A. J., Circularly polarized light detection by a chiral organic semiconductor transistor. *Nat. Photonics* **2013,** *7*, 634-638.

140. Keith, C.; Reddy, R. A.; Hauser, A.; Baumeister, U.; Tschierske, C., Silicon-containing polyphilic bent-core molecules: The importance of nanosegregation for the development of chirality and polar order in liquid crystalline phases formed by achiral molecules. *J. Am. Chem. Soc.* **2006,** *128*, 3051-3066.

141. Zhang, C.; Diorio, N.; Lavrentovich, O. D.; Jakli, A., Helical nanofilaments of bent-core liquid crystals with a second twist. *Nat. Commun.* **2014,** *5*, 3302.

142. Liu, G. F.; Zhang, D.; Feng, C. L., Control of three-dimensional cell adhesion by the chirality of nanofibers in hydrogels. *Angew. Chem. Int. Ed.* **2014,** *53*, 7789-7793.

143. Das, R. K.; Zouani, O. F.; Labrugere, C.; Oda, R.; Durrieu, M. C., Influence of nanohelical shape and periodicity on stem cell fate. *ACS Nano* **2013,** *7*, 3351-3361.

144. Lv, K.; Zhang, L.; Lu, W.; Liu, M., Control of supramolecular chirality of nanofibers and its effect on protein adhesion. *ACS Appl. Mater. Interfaces* **2014,** *6*, 18878-18884.

145. Feng, X. L.; Marcon, V.; Pisula, W.; Hansen, M. R.; Kirkpatrick, J.; Grozema, F.; Andrienko, D.; Kremer, K.; Mullen, K., Towards high charge-carrier mobilities by rational design of the shape and periphery of discotics. *Nat. Mater.* **2009,** *8*, 421-426.

146. Autschbach, J.; Nitsch-Velasquez, L.; Rudolph, M., Time-dependent density functional response theory for electronic chiroptical properties of chiral molecules. *Top. Curr. Chem.* **2011,** *298*, 1-98.

147. Zhan, X.; Facchetti, A.; Barlow, S.; Marks, T. J.; Ratner, M. A.; Wasielewski, M. R.; Marder, S. R., Rylene and Related Diimides for Organic Electronics. *Adv. Mater.* **2011,** *23*, 268-284.

148. Bhosale, S. V.; Jani, C. H.; Langford, S. J., Chemistry of naphthalene diimides. *Chem. Soc. Rev.* **2008,** *37*, 331-342.

149. Ego, C.; Marsitzky, D.; Becker, S.; Zhang, J.; Grimsdale, A. C.; Mullen, K.; MacKenzie, J. D.; Silva, C.; Friend, R. H., Attaching perylene dyes to polyfluorene: three simple, efficient methods for facile color tuning of light-emitting polymers. *J. Am. Chem. Soc.* **2003,** *125*, 437-443.

150. Sadrai, M.; Hadel, L.; Sauers, R. R.; Husain, S.; Kroghjespersen, K.; Westbrook, J. D.; Bird, G. R., Lasing Action in a Family of Perylene Derivatives - Singlet Absorption and Emission-Spectra, Triplet Absorption and Oxygen Quenching Constants, and Molecular Mechanics and Semiempirical Molecular-Orbital Calculations. *J. Phys. Chem.* **1992,** *96*, 7988-7996.

151. O'Neil M, P.; Niemczyk, M. P.; Svec, W. A.; Gosztola, D.; Gaines, G. L., 3rd; Wasielewski, M. R., Picosecond optical switching based on biphotonic excitation of an electron donor-acceptor-donor molecule. *Science* **1992,** *257*, 63-65.

152. Law, K. Y., Organic Photoconductive Materials - Recent Trends and Developments. *Chem. Rev.* **1993,** *93*, 449-486.

153. Schenning, A. P. H. J.; von Herrikhuyzen, J.; Jonkheijm, P.; Chen, Z.; Wurthner, F.; Meijer, E. W., Photoinduced electron transfer in hydrogen-bonded oligo(p-phenylene vinylene)-perylene bisimide chiral assemblies. *J. Am. Chem. Soc.* **2002,** *124*, 10252-10253.

154. Moulin, E.; Cid, J.-J.; Giuseppone, N., Advances in Supramolecular Electronics – From Randomly Self-assembled Nanostructures to Addressable Self-Organized Interconnects. *Adv. Mater.* **2013,** *25*, 477-487.

155. Gawronski, J.; Brzostowska, M.; Kacprzak, K.; Kolbon, H.; Skowronek, P., Chirality of aromatic bis-imides from their circular dichroism spectra. *Chirality* **2000,** *12*, 263-268.

156. Wurthner, F., Perylene bisimide dyes as versatile building blocks for functional supramolecular architectures. *Chem. Commun.* **2004**, 1564-1579.

157. Shao, H.; Seifert, J.; Romano, N. C.; Gao, M.; Helmus, J. J.; Jaroniec, C. P.; Modarelli, D. A.; Parquette, J. R., Amphiphilic Self-Assembly of an n-Type Nanotube. *Angew. Chem. Int. Ed.* **2010,** *49*, 7688-7691.

158. Shao, H.; Gao, M.; Kim, S. H.; Jaroniec, C. P.; Parquette, J. R., Aqueous Self-Assembly of L-Lysine-Based Amphiphiles into 1D n-Type Nanotubes. *Chem. Eur. J.* **2011,** *17*, 12882-12885.

159. Kim, S. H.; Parquette, J. R., A model for the controlled assembly of semiconductor peptides. *Nanoscale* **2012,** *4*, 6940-6947.

160. Shao, H.; Nguyen, T.; Romano, N. C.; Modarelli, D. A.; Parquette, J. R., Self-Assembly of 1-D n-Type Nanostructures Based on Naphthalene Diimide-Appended Dipeptides. *J. Am. Chem. Soc.* **2009,** *131*, 16374-16376.

161. Shao, H.; Parquette, J. R., A [small pi]-conjugated hydrogel based on an Fmoc-dipeptide naphthalene diimide semiconductor. *Chem. Commun.* **2010,** *46*, 4285-4287.

162. Ponnuswamy, N.; Cougnon, F. B. L.; Clough, J. M.; PantoÅŸ, G. D.; Sanders, J. K. M., Discovery of an Organic Trefoil Knot. *Science* **2012,** *338*, 783-785.

163. Bulheller, B. M.; Pantos, G. D.; Sanders, J. K. M.; Hirst, J. D., Electronic structure and circular dichroism spectroscopy of naphthalenediimide nanotubes. *Phys. Chem. Chem. Phys.* **2009,** *11*, 6060-6065.

164. Pantoş, G. D.; Wietor, J.-L.; Sanders, J. K. M., Filling Helical Nanotubes with C60. *Angew. Chem. Int. Ed.* **2007,** *119*, 2288-2290.

165. Pantoş, G. D.; Pengo, P.; Sanders, J. K. M., Hydrogen-Bonded Helical Organic Nanotubes. *Angew. Chem. Int. Ed.* **2007,** *46*, 194-197.

166. Hu, Z.; Pantoş, G. D.; Kuganathan, N.; Arrowsmith, R. L.; Jacobs, R. M. J.; Kociok-Köhn, G.; O'Byrne, J.; Jurkschat, K.; Burgos, P.; Tyrrell, R. M.; Botchway, S. W.; Sanders, J. K. M.; Pascu, S. I., Interactions Between Amino Acid-Tagged Naphthalenediimide and Single Walled Carbon Nanotubes for the Design and Construction of New Bioimaging Probes. *Adv. Funct. Mater.* **2012,** *22*, 503-518.

167. Hunter, C. A.; Sanders, J. K. M., The nature of .pi.-.pi. interactions. *J. Am. Chem. Soc.* **1990,** *112*, 5525-5534.

168. Anderson, T. W.; Sanders, J. K. M.; Pantos, G. D., The sergeants-and-soldiers effect: chiral amplification in naphthalenediimide nanotubes. *Org. Biomol. Chem.* **2010,** *8*, 4274-4280.

169. Ponnuswamy, N.; PantoÅŸ, G. D.; Smulders, M. M. J.; Sanders, J. K. M., Thermodynamics of Supramolecular Naphthalenediimide Nanotube Formation: The Influence of Solvents, Side Chains, and Guest Templates. *J. Am. Chem. Soc.* **2012,** *134*, 566-573.

170. Bhosale, S.; Sisson, A. L.; Talukdar, P.; Furstenberg, A.; Banerji, N.; Vauthey, E.; Bollot, G.; Mareda, J.; Roger, C.; Wurthner, F.; Sakai, N.; Matile, S., Photoproduction of proton gradients with pi-stacked fluorophore scaffolds in lipid bilayers. *Science* **2006,** *313*, 84-86.

171. Bhosale, R.; Misek, J.; Sakai, N.; Matile, S., Supramolecular n/p-heterojunction photosystems with oriented multicolored antiparallel redox gradients (OMARG-SHJs). *Chem. Soc. Rev.* **2010,** *39*, 138-149.

172. Bhosale, R.; Kishore, R. S. K.; Ravikumar, V.; Kel, O.; Vauthey, E.; Sakai, N.; Matile, S., Zipper assembly of SHJ photosystems: focus on red naphthalenediimides, optoelectronic finetuning and topological matching. *Chem. Sci.* **2010,** *1*, 357-368.

173. Vargas Jentzsch, A.; Hennig, A.; Mareda, J.; Matile, S., Synthetic ion transporters that work with anion-pi interactions, halogen bonds, and anion-macrodipole interactions. *Acc. Chem. Res.* **2013,** *46*, 2791-2800.

174. Martinez, C. R.; Iverson, B. L., Rethinking the term "pi-stacking". *Chem. Sci.* **2012,** *3*, 2191-2201.

175. Holman, G. G.; Zewail-Foote, M.; Smith, A. R.; Johnson, K. A.; Iverson, B. L., A sequence-specific threading tetra-intercalator with an extremely slow dissociation rate constant. *Nat. Chem.* **2011,** *3*, 875-881.

Chapter 2: Amino Acid Conjugated NDI Nanoarchitectonics and Applications*

*Papers based on part of this work have appeared in *RSC Adv.* **2014**, *4*, 20154-20163, *RSC Adv.* **2013**, *3*, 11459-11462 and *J. Inorg. Organomet. Polym.* **2015**, *25*, 293-300. Reproduced with the permission of Royal Society of Chemistry (RSC) and Springer.

Subchapter 2.1 Biomimetic Molecular Organization of Naphthalene diimide in the Solid State: Tunable (Chiro-) Optical, Viscoelastic and Nanoscale Properties

2.1.1 Introduction

The nature and geometry of noncovalent aromatic interactions play an important role in chemistry, biology, and materials science.[1-12] They are responsible for structure and function of DNA, several peptides and proteins, and are believed to be one of the main driving forces in aggregation of amyloid β to form toxic plaques of Alzheimer's disease.[1-5] Similarly, aromatic interactions are fundamental to design and development of optoelectronic systems in the area of organic electronics and biomaterials.[6-12] The experimental and theoretical investigations have provided clear evidence for the role of van der Waals, hydrophobic and electrostatic forces in the existence and stability of aromatic interactions.[13-17] Nature-inspired chiral alignment of aromatic molecules has been attracting great interest owing to their fascinating structural features and relationship to biological structures.[18-21]This concept has been effectively employed in various potential applications like understanding of Nature's mysterious selection of homochirality, designing of biomimetics, chiroptical switching, chiral sensing, separation and catalysis.[22-31] During the past few years, considerable attention has been focused on the design and induction of helical bias in rigid aromatic molecules, polymers and small molecules by utilizing steric effects and noncovalent interactions.[32-44] Interestingly, helical columnar stacks have emerged as promising molecular organizations for optoelectronic applications by displaying exceptional charge carrier mobilities and exciton diffusion along the stacking columnar axis.[45-46] Furthermore, the rational design of high performance organic electronic devices also needs in-depth knowledge of structure and mode of molecular organization which remains to be understood. In this context, there has been a great interest in the low-molecular-weight (LMW) gels and single crystals. Their ordered and frozen molecular orientations lead to general understanding of fundamental chemical aspects behind the structural design to achieve desired molecular interactions and their impact on the properties.[47-52] Consequently, substantial efforts have been devoted to the investigation of various types of packing modes of the p-type (HT: holes transport) organic semiconductor molecules for analyzing intermolecular charge transport property. [49-52] However, the progress of n-type (ET: electrons transport) organic semiconductor molecules are still lagging behind p-type organic semiconductors.[53-56] This necessitates the immediate need for studying n-type organic semiconductor molecular organization to improve their properties, in both academic and industrial research.

Rylene diimides are one of the extensively studied class of n-type organic semiconductor materials.[53-56] Among them naphthalenediimide (NDI) has attracted special attention due to its molecular planarity, high π-acidity, well defined redox behavior, optical properties and wide range of applications from materials to biomedicine.[57-64] However, the key daunting challenges in controlling solid state molecular ordering with helical intermolecular organization remain to be addressed to further the advancement in NDI based materials for technological applications. Very recently, bio-inspired approaches has been reported, employing biological elements as chiral assembly directing substituents to design supramolecular systems and nanomaterials with diverse structural, chemical and chiroptical properties.[30,65-79] This novel design based on the marriage between biomolecules and π-conjugated organic systems (e.g., NDIs) not only envision the engineering of helical molecular ordering through various noncovalent interactions but also synergistically combines the properties of constituent components.[80-84] With this objective, we have chosen amino acids as self-

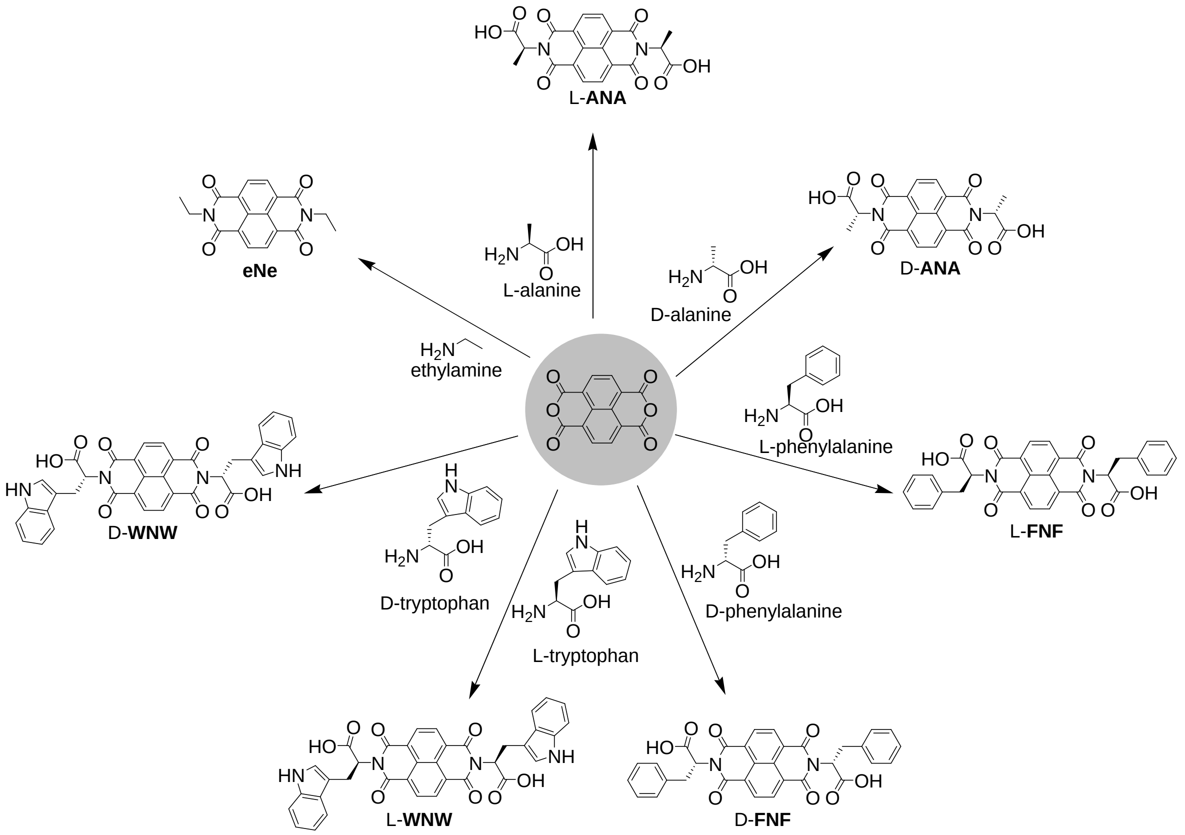

Figure 2.1.1 Molecular structures of NDI derivatives of chiral amino acids (L-**ANA**, L-**FNF**, L-**WNW**, D-**ANA**, D-**FNF** and D-**WNW**) and achiral ethylamine (**eNe**) synthesized by conjugating with 1,2,5,8-napthathalenetetracarboxylic dianhydride (NDA).

assembly directing groups due to their inherent ability to make complex molecular architectures in biological systems and variable α-functionality can endow hydrophilic, hydrophobic and aromatic interactions in a single compact moiety. We methodically designed NDI bolaamphiphiles using enantiomeric amino acids with α-functionalities as aliphatic (alanine, **ANA**), aromatic (phenylalanine, **FNF**), heterocyclic/hetroaromatic (tryptophan, **WNW**) and NDI with flexible achiral ethylamine (**eNe**) (Figure 2.1.1). Herein, we show the biomimetic molecular engineering of NDIs ordering in the solid state by introducing minute structural mutations in the form of amino acids with variable α-functionality.[85] For the first time we demonstrate all the four possible crystal packing modes *viz*. cofacial, brickwork, herringbone and slipped stacks with helical ordering of

Table 2.1.1 Summary of various properties of NDI conjugates[a]

Property	ANA	FNF	WNW	eNe
Solid powder	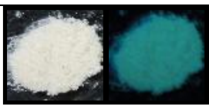	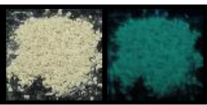	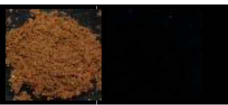	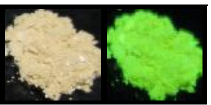
Gelation	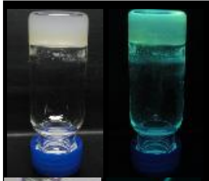	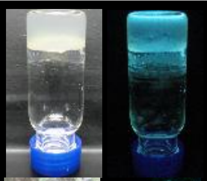	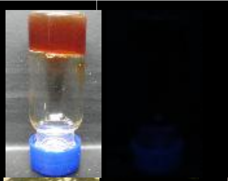	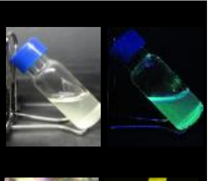
Crystal	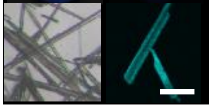	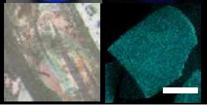	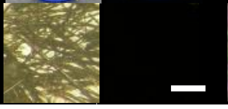	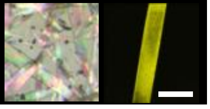
Supramolecular-ar chirality	enantiopure cofacial columnar stacks	enantiopure supramolecular tilt stacks	enantiopure supramolecular tilt stacks	racemic supramolecular tilt stacks
Optoelec-tronic	Blue-green emission	Cyan emission	Charge transfer interactions	Green emission
Viscoelas-ticity	$G'=2.22 \times 10^4$ Pa; $\eta_o=2.06 \times 10^7$ Pas	$G'=2.66 \times 10^3$ Pa; $\eta_o=2.45 \times 10^6$ Pas	$G'=1.83 \times 10^4$ Pa; $\eta_o=6.72 \times 10^6$ Pas	-
Nanoscale ordering	0D (nano sphere)	1D (nanofiber)	0D (nano sphere)	2D (nano sheet)

[a]Sacle bar: 200 μM

NDI and their implication on (chiro)optoelectronic, visco-elastic and mechanical properties.

2.1.2 Results and Discussion

All the functionalized NDIs with L-amino acids (L-**ANA**, L-**FNF** and L-**WNW**), D-amino acids (D-**ANA**, D-**FNF** and D-**WNW**) and ethylamine (**eNe**) were synthesized in single-step reactions (Figure 2.1.1) and characterized by various standard spectroscopic techniques. Interestingly, we observed that amino acid functionalized NDIs (**ANA**, **FNF** and **WNW**) exhibited ultrasonication assisted room temperature low molecular weight (LMW) gelation property in mixed organic solvent system. The mode of intermolecular interactions and its consequence on properties has been investigated by various spectroscopic and microscopic techniques. Circular dichroism (CD) and X-ray diffraction (XRD) studies revealed the existence of helical ordering of NDIs in both solution and solid state respectively. Photophysical, rheological and microscopy studies revealed unique optoelectronic, visco-elastic and nanoscale ordering properties.

2.1.2.1 Single crystal XRD studies

We have sought to analyze the solid state packing of NDIs where amino acids and ethyl substituents are used as imide substituents. In particular, the role of structural mutations in the form of amino acid side-chain functionalities and corresponding stereochemistry on

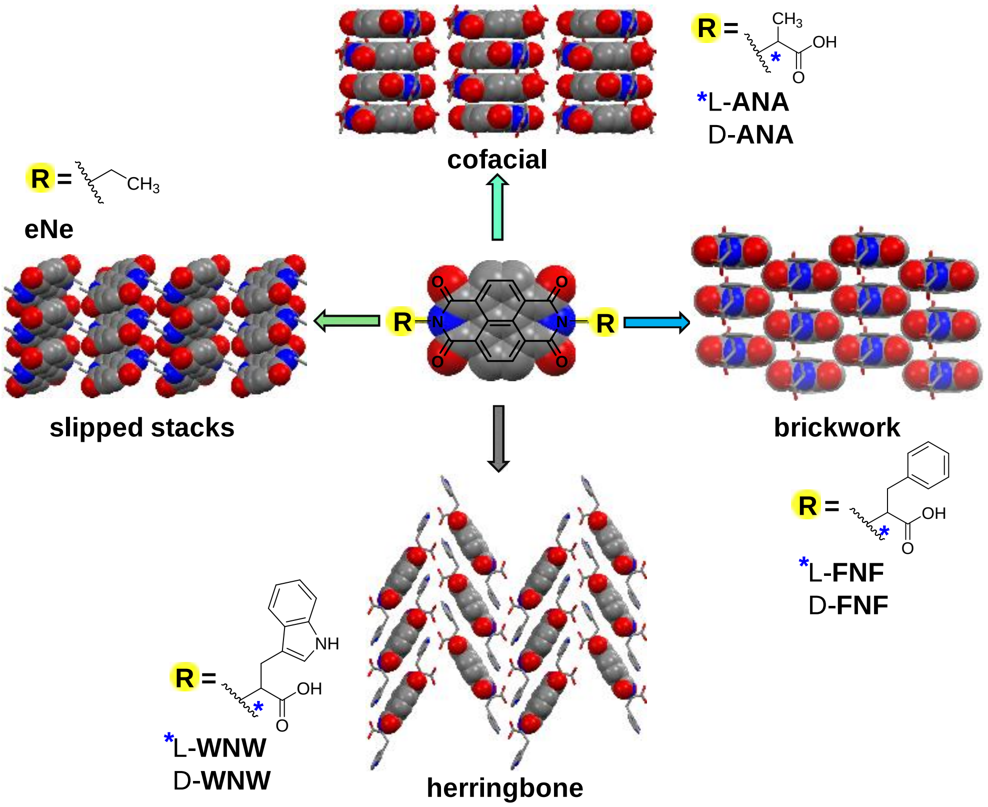

Figure 2.1.2 Single crystal X-ray structures of alanine (L-**ANA** and D-**ANA**), phenylalanine (L-**FNF** and D-**FNF**), tryptophan (L-**WNW** and D-**WNW**) and ethylamine (**eNe**) functionalized NDIs and their molecular organization into all possible crystal packing modes (cofacial, brickwork, herringbone and slipped stack). The prefix L and D correspond to NDIs functionalized with L-amino acid and D-amino acid respectively. Solvent molecules and hydrogen atoms have been omitted from the crystal packing representation for the clarity.

the mode of NDI core organization was investigated by single crystal XRD studies. Previous reports have shown slipped stack and brickwork organization of acyclic and cyclic aliphatic imide substituted NDIs respectively.[86-87] Raymo *et al.* have reported slipped stack packing of glycine functionalized NDI stabilized by solvent induced hydrogen bonding.[77] Later, Sanders *et al*. have shown the hydrogen bonded helical nanotube crystal packing using cysteine functionalized NDI with very week NDI-NDI aromatic interaction.[70] Here we describe the systematic molecular programming of NDI by tuning the NDI–NDI aromatic interactions using enantiomeric amino acids with variable α-functionalities. Single crystals of all the compounds (**ANA**, **FNF**, **WNW** and **eNe**) suitable for X-ray diffraction analysis were grown in a common solvent, dimethyl sulfoxide (DMSO). Alanine (**ANA**) and ethyl (**eNe**) functionalized NDIs were found to crystallize in monoclinic crystal system with C_2 and $P2_1/c$ space groups respectively. Aromatic amino acids phenylalanine (**FNF**) and tryptophan (**WNW**) conjugated NDIs were crystallized in orthorhombic crystal system with space groups $C222_1$ and $P2_12_12_1$ respectively. All NDIs exhibited discrete crystal packing from cofacial (**ANA**), brickwork (**FNF**), herringbone (**WNW**) to slipped stacks (**eNe**) depending the nature of imide substituents as shown in the Figure 2.1.2. The center of symmetry seemed to play a crucial role in solid state packing of our NDI molecules, especially with respect to aromatic $\pi\cdots\pi$ stacking. There are a few reports documented on this effect in the literature, for example, pyrene crystal structure showed discontinuous $\pi\cdots\pi$ stacks in the form of sandwich herringbone packing, while 2-7-di-tert-butylpyrene-4,5,9,10-tetraone exhibited slipped stacks, both of them putting limits on the extent of $\pi\cdots\pi$ interactions.[88-90] Among our NDI molecular systems, **eNe** is centrosymmetric and it was observed that the $\pi\cdots\pi$ interactions did not extend in different layers, rather they were found in slipped stack arrangement with limited π-cloud overlap between the adjacent molecules (Figure 2.1.2).

To further evaluate the role of center of symmetry, we introduced chirality in the *N*-imide substituents of NDI by functionalization with amino acids. First we studied the effect of L and D alanine as *N*-imide substituents in NDI and the resultant molecules L-**ANA** and D-**ANA** respectively exhibited a remarkable cofacial packing with π···π (NDI···NDI) interactions in columnar fashion (Figure 2.1.2).The crystal structure of **ANA** revealed non-centrosymmetric structure with distinct columns of π···π interactions separated by layers of solvent (DMSO) molecules. There exist two kinds of alternating NDI-NDI interactions along the column with distances found to be 3.47 Å and 3.56 Å in L-**ANA**, and 3.48 Å and 3.57 Å in D-**ANA**. The alternate arrangement is also reflected in the alternate van der Waals (H···H distance 2.27 Å in L-**ANA** and 2.28 Å in D-**ANA**) and CH···O (C···O distance 3.07 Å & 3.08 Å in L-ANA and 3.10 Å & 3.08 Å in D-**ANA**) interactions. However, **FNF** and **WNW** with phenylalanine and tryptophan substitutions respectively did not show NDI-NDI cofacial packing. In case of **FNF**, the NDI core showed layers of brickwork arrangement with effective intermolecular π···π stacking of phenyl ring and NDI core with the distance of 3.38 Å in L-**FNF** and 3.46 Å in D-**FNF** (Figure 2.1.2). The 3D network of **FNF** lattice was found to be consisted of alternate layers of solvent (DMSO) stabilized by hydrogen bonding between carboxylic acid OH groups and the oxygen atoms of DMSO molecules. The brickwork layers appeared discontinuous due to alternate solvent layers. This discontinuity is clearly observed along *a* and *b* crystallographic axes. In case of L-**WNW**, a relatively small difference in the side-chain of amino acid from phenyl (in **FNF**) to indole led to the herringbone packing arrangement (Figure 2.1.2). The larger π-electron rich surface of indole (in **WNW**) as compared to that of phenyl (in **FNF**) was found to be more effective in inducing strong intermolecular π-electron donor-acceptor (indole-NDI) interactions with reduced interaction distance of 3.20 Å. Furthermore, additional intermolecular hydrogen bonding interaction of indole-NH with carboxyl oxygen and solvent (DMSO) molecules resulted in confinement of solvent in distinct columns forming solvent channels along the crystallographic *a* axis in the lattice.

It is clear from the above XRD data that only **ANA** showed twisted cofacial packing with maximum π··π overlap between NDI cores. The main difference between the molecular arrangement of **ANA** and other structures lies in the conformation of Cα substituent with respect to central NDI core. **ANA** adopted *cis* conformation in which both the side-chain methyl groups of alanine substituents were oriented towards the same side of NDI core. On the other hand, **FNF** and **WNW** were stabilized by *trans* conformation where the phenyl and indole groups respectively, were oriented in opposite directions with respect to NDI core.

2.1.2.2 Photophysical studies

The visible appearance and fluorescence properties of solid powder, organogels and single crystals of NDI conjugates (**ANA**, **FNF**, **WNW** and **eNe**) under day-light and UV light (365 nm) are shown in Table 2.1.1. The intrinsic fluorescence properties of crystals were demonstrated by fluorescence microscopy images. The effect of molecular ordering on the optoelectronic properties of NDI was investigated by UV-vis diffused reflectance and fluorescence emission spectroscopy techniques. The diffused reflectance data was transformed into pseudo-absorbance spectra using Kubelka-Munk function (Figure 2.1.3a). The broad NDI absorption bands in the wavelength region of 300-410 nm and 450-550 nm suggesting the presence of strong intermolecular π···π stacking between the NDI chromophores (Figure 2.1.3a).[91-95] Notably, the tryptophan appended NDI (**WNW**) exhibited broad absorption band in the visible region (400-600 nm) attributed to intermolecular through-space, face-centred donor-acceptor charge transfer (CT)

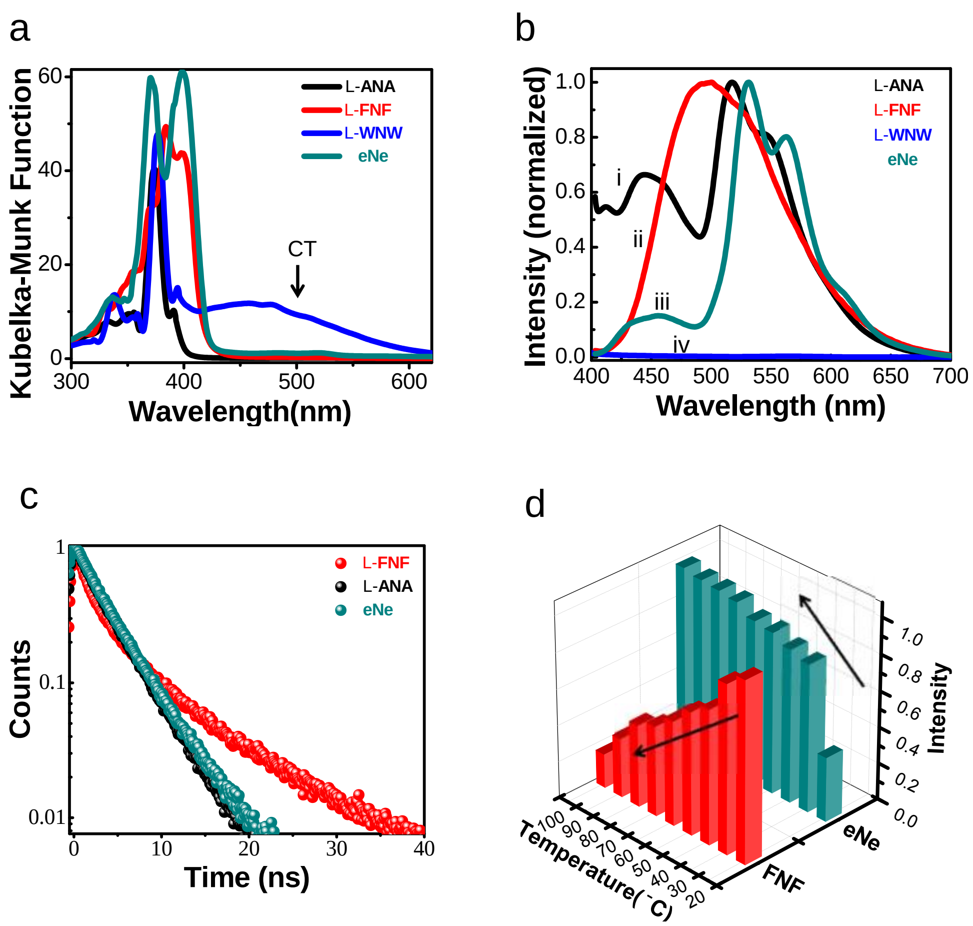

Figure 2.1.3 a) Transformed UV-vis absorption and b) fluorescence emission spectra of NDI-conjugates in their solid state. i: L-**ANA** , ii: L-**FNF**, iii: **eNe** and iv: L-**WNW**. CT: Charge transfer band. c) TCSPC decay profile of L-**ANA** ($\lambda_{emission}$ 552 nm), L-**FNF** ($\lambda_{emission}$ 490 nm) and **eNe** ($\lambda_{emission}$ 565 nm) with a 405 nm exitation. d) Temperature versus normalized fluorescence emission intesity of L-**FNF** **(**at 490 nm**)** and **eNe** (at 563 nm). Absorption spectra (a) were recorded in reflection (R) mode.

interactions between the tryptophan (indole moiety) and NDI chromophore.[91-95] Fluorescence emission spectra of NDI conjugates displayed structureless broad emission bands in the visible spectrum ranging from violet to orange (425 to 650 nm, except **WNW**) with distinct emission maxima as a consequence of charge delocalization among the different relative orientations of the closely stacked NDI chromophore (Figure 2.1.3b).[78] On account of mixture of strong and weak offset π-stacks of NDI-NDI interactions along the inter and intra-layers **ANA** and **eNe** exhibited broad (λ_{max} at 450 nm) and longer wavelength emission bands (λ_{max} at 552 and 563 nm respectively).[69,96] **FNF** displayed a broad excimer-like emission band with λ_{max} at 490 nm.[15,97-98] This is quite remarkable, since most of the unsubstituted and aggregated (solid state) NDIs do not emit in the visible region of the spectrum which makes them unsuitable for fluorescent applications. In the case of **WNW**, fluorescence emission was quenched completely due to CT interaction, in agreement with the intense CT band observed in the UV-vis absorption spectrum and effective intermolecular indole-NDI interactions in crystal structure (Figure 2.1.3b and Figure 2.1.2). To understand the emission behaviour of NDI-conjugates, we performed time-correlated single photon counting (TCSPC) experiments with a nanosecond excitation on the solid samples of L-**ANA**, L-**FNF** and **eNe** (Figure 2.1.3c). TCSPC data displayed distinct biexponential decay profiles, which suggest that the observed longer wavelength emission of NDI conjugates is the resultant of two different excitation paths along intra- and inter- layered NDI-NDI interactions as shown in Figure 2.1.2 **FNF** exhibited significantly longer life-times values (7.23 ns. 36% and 1.63 ns, 64%) as compared to **ANA** (3.74 ns, 96% and 0.94 ns, 13%) and **eNe** (1.21 ns, 14% and 3.88 ns, 96%). In addition, the excitation spectra of **FNF** (monitored at $\lambda_{emission}$ 490 nm) red-shifted by 15 nm from the absorption band (λ_{max}398 nm) indicating the existence of preorganized excimer-like aggregates.[65,96] Interestingly, the xerogel of **FNF** and drop-casted film of **eNe** exhibited temperature responsive emission behaviour as shown in the Figure 2.1.3d. **FNF** showed gradual quenching of broad emission band at λ_{max} 490 nm with increase in temperature from 20 to 100 °C. In contrast, **eNe** exhibited enhancement in the 565 nm emission with the rise in temperature. These contrasting temperature responsive emission behaviours are attributed to thermal disruption of intermolecular aromatic complexation between phenyl and NDI core in **FNF** and formation of emissive dimeric form of **eNe**.[15,97-98] Therefore, the xerogel of **FNF** and drop-casted film of **eNe** can be used as solid state temperature sensor systems.

2.1.2.3 Rheological studies

All amino acid-NDI conjugates showed ultrasonication induced gelation property in mixed organic solvent systems. Here we have selected $CHCl_3$ (for **FNF**) and tetrahydrofuran (THF) (for **ANA** and **WNW**) as good solvents and nonpolar methylcyclohexane (MCH) was slowly added to induce gelation through effective π···π stacking and hydrogen bonding between the molecules (concentration used for gelation was 6 mM and MCH/good solvent: 80/20 v/v). Surprisingly, racemic mixtures of amino acid-NDI conjugates (1:1 mixtures of L and D isomers of **ANA**/**FNF**/**WNW**) and achiral **eNe** did not undergo gelation under similar conditions. We further investigated the influence of Cα-functionalities on mechanical properties of organogels by dynamic rheology studies. The amplitude sweep and frequency sweep experiments at 20 ºC displayed greater storage modulus (G') than loss modulus (G") within the linear visco-elastic region (Figure 2.1.4). These results revealed the presence of a typical soft solid-like gel-phase in organogels of all the amino acid-NDI conjugates. The storage modulus G' and loss modulus G" associated with the energy storage and loss of energy respectively were measured at 20 °C as functions of shear stress (stress sweep) at a constant frequency of 1.6 Hz (Figure 2.1.4a-c). The recorded G' was found to be maximum in case of **ANA** (2.22×10^4 Pa, Figure 2.1.4a) and minimum for **FNF** (2.66×10^3 Pa, Figure 2.1.4b) gels respectively, whereas that of **WNW** gel was found to be 1.83×10^4 Pa (Figure 2.1.4c). Amusingly, **WNW** gel did not show crossover of G' and G" under the given stress sweep, indicating excellent energy storage property. **ANA** and **FNF** displayed crossover of G' and G" at 15.9% and 99.9% strain values respectively. The observed good storage property of **WNW** compared to **ANA** and **FNF** may be attributed to the presence of

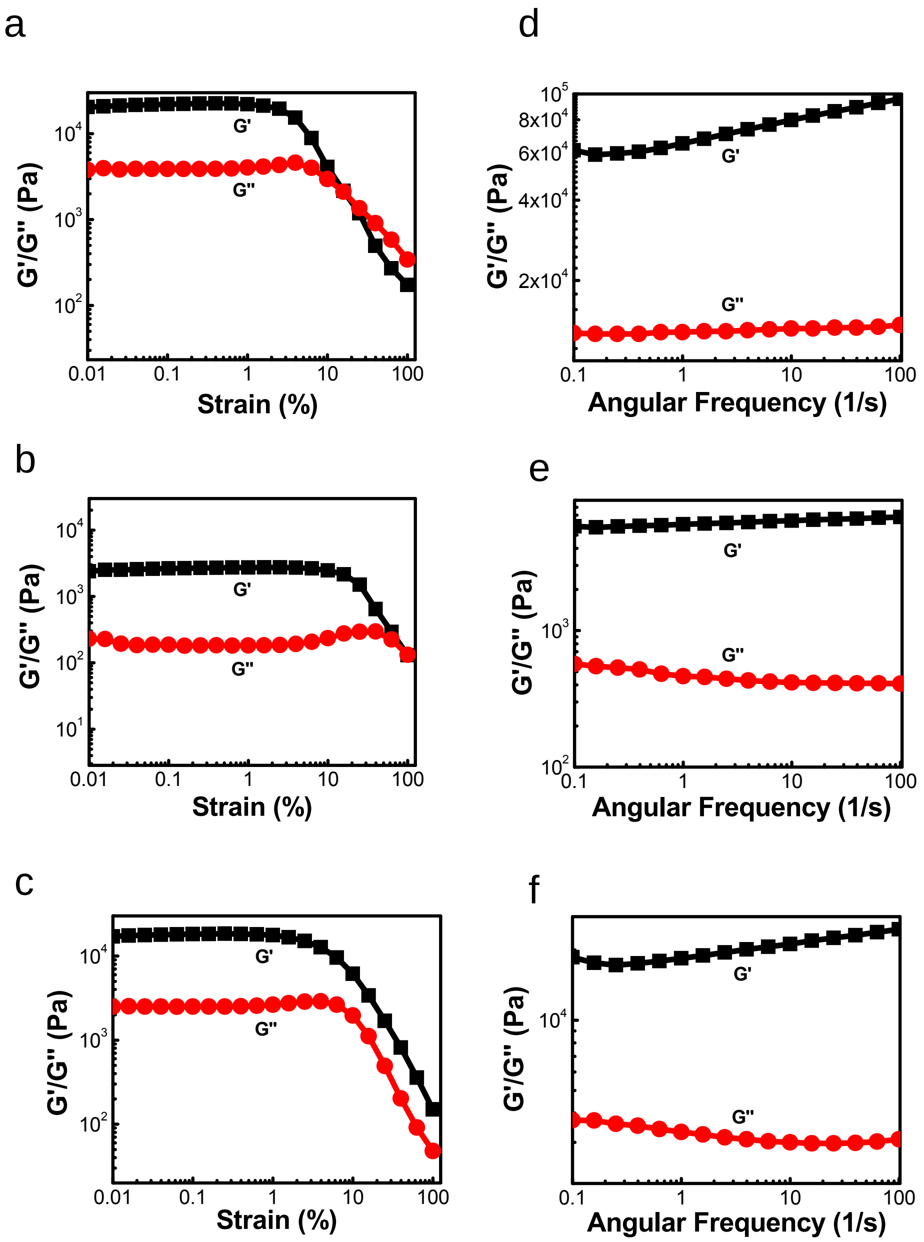

Figure 2.1.4 Rheological studies of organogels of amino acid-NDI conjugates. a-c) Stress sweep experiments and d-f) frequency sweep experiments of **ANA** (a and d), **FNF** (b and e) and **WNW** (c and f) respectively. G': storage modulus (■) and G": loss modulus (●).

strong donor-acceptor CT π··π interactions and additional indole-NH hydrogen bonding among its molecules and with the solvent. To understand the consequence of various noncovalent interactions on the tolerance of the gel upon exposure to external forces, an angle frequency sweep experiment was conducted within the gels linear visco-elastic region (Figure 2.1.4d-f). The results showed higher storage modulus (G') than the loss modulus (G") due to the absence of phase separation or phase transition during the sweep process. Furthermore, both G' and G" remained relatively stable within the whole frequency range indicating that the gel possessed an excellent tolerance to external forces. The property of material to avoid sedimentation upon storage was determined by calculating the zero shear viscosity (η_o) and the values were found to be 2.06×10^7 Pa.s (**ANA**) > 6.72×10^6 Pa.s (**WNW**) > 2.45×10^6 Pa.s (**FNF**). Rheological studies (both stress sweep and frequency sweep) revealed the ability of tuning the mechanical strength and elasticity of NDI organogels by ingeningenious noncovalent interactions drive molecular organization induced through amino acid side-chain functionality.

2.1.2.4 CD studies

In order to probe the effect of enantiomeric amino acids on the chiroptical properties of achiral NDI chromophore organization, we have performed CD studies in both crystal and gel forming solvent systems I) MCH/THF:80:20, v/v, II) DMSO and III) MCH/$CHCl_3$:80/20, v/v (Figure 2.1.5). All the enantiomeric amino acid conjugates, L-**ANA** and D-**ANA** (Figure 2.1.5a), L-**FNF** and D-**FNF** (Figure 2.1.5b) and L-**WNW** and D-**WNW** (Figure 2.1.5c) exhibited mirror image Cotton effects in the NDI absorption region (250-400 nm) ascribed to the presence of chiral intermolecular assembly of NDI molecules.[65-69,77-79] The positive (*D-isomer) and negative (*L-isomer) Cotton effects are attributed to differential absorption of circularly polarized light by right handed (P-type) and left handed (M-type) supramolecular helical organization of NDI chromophores respectively. Whereas, in case of **eNe**, a flat CD signal was observed due its symmetrical (centrosymmetric) structure and the absence of chiral center in the imide-substituents (Figure 2.1.5d). This confirmed the formation of supramolecular chiral aggregates via transcription of chiral information from the α–stereocentre of N-imide amino acid

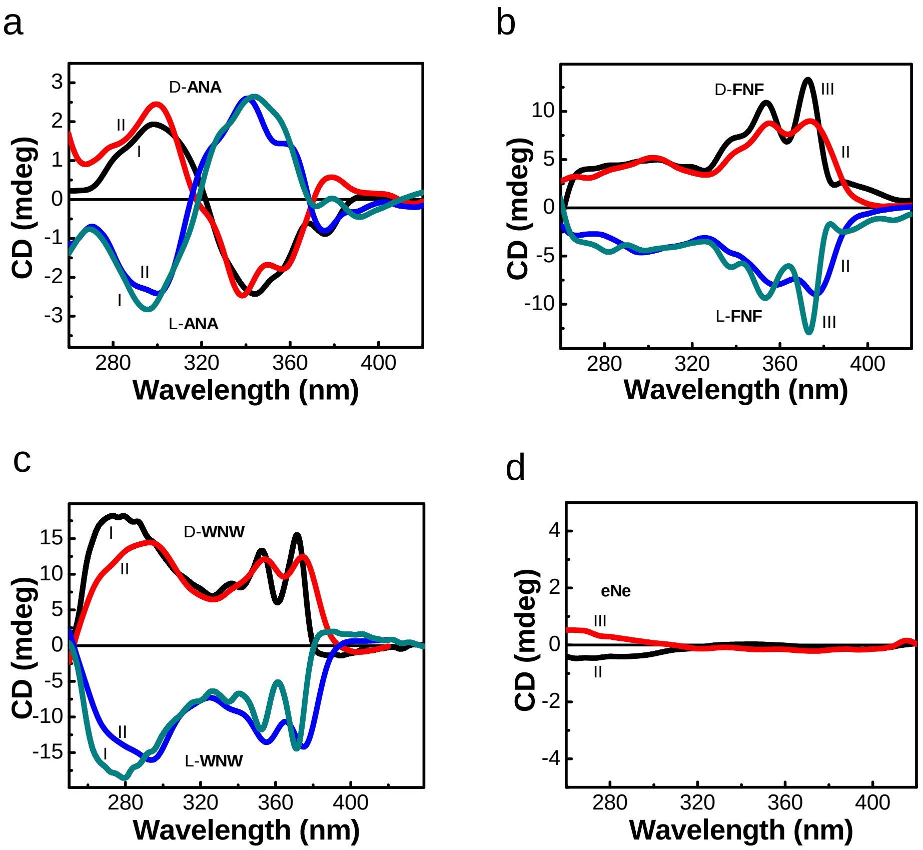

Figure 2.1.5 CD spectra of L- and D-isomers of a) **ANA**, b) **FNF**, c) **WNW** and d) **eNe** in gelling solvents (I: MCH/THF and III: MCH/$CHCl_3$) and crystal forming solvent (II: DMSO).

substituents to central achiral NDI chromophoric unit.[30,65-74] The difference in the shape and amplitude of CD signals for NDI- conjugates with variable amino acid substituents suggested distinct inter-chromophoric distances, projection angles and number of interacting NDI-chromophores.[71]

2.1.2.5 Solid state molecular helical organization studies

To corroborate the CD results discussed above, we further investigated the solid state chirality in crystal packing. Several organic molecules exhibit 2 fold helices in solid state packing by the virtue of presence of 2_1 screw axes in the crystal lattice.[19,22] L-**ANA** and

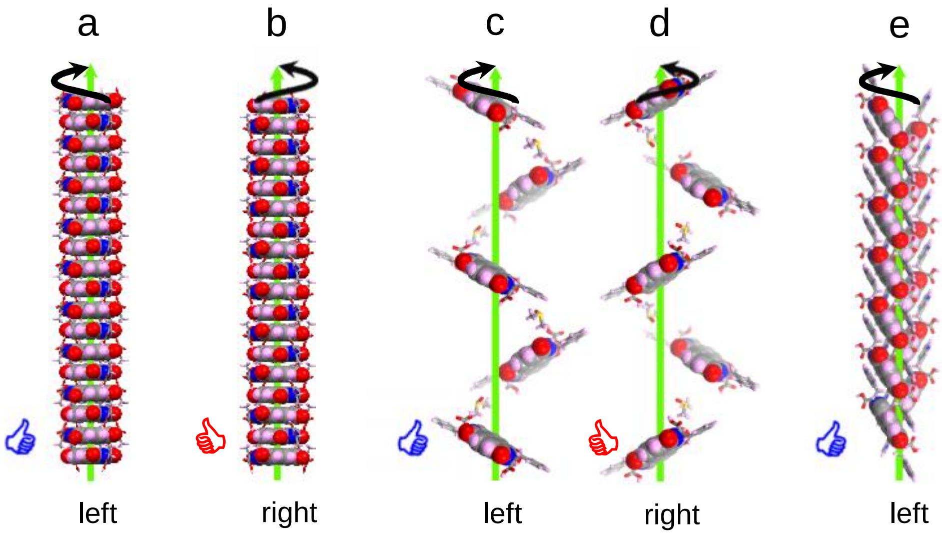

Figure 2.1.6 Solid state helical organization of a) L-**ANA** , b) D-**ANA** , c) L-**FNF**, d) D-**FNF** and e) L-**WNW** in their respective crystal lattice. (a and b) cofacial helical columnar stacks and (c-e) supramolecular tilt helical organization.

D-**ANA** exhibited cofacial helical columnar stacks with a twist of 69.17° (anticlockwise) and 69.27° (clockwise) respectively between successive molecules (Figure 2.1.6a and b). This twist is due to the steric hindrance as well as hydrogen bond potential of alanine residues (-COOH group) on both sides of the NDI core with solvent (DMSO). In contrast, **FNF** and **WNW** displayed supramolecular tilt helical organization of molecules with respect to 2_1 screw axis. Hisaki *et al.*[99-100] have reported a method to distinguish between right and left handed supramolecular tilt chirality of such twofold helical assemblies. Based on this method, we correlated the organization of aromatic amino acid-NDI conjugate with the supramolecular tilt chirality. L-**FNF** and L-**WNW** showed left handed supramolecular tilt chirality whereas D-**FNF** showed right handed helical assemblies (Figure 2.1.6c-e). Our effort in crystallizing D-**WNW** was not fruitful, nevertheless CD data in Figure 2.1.5 strongly suggests right handed helical arrangement in solid state. The centrosymmetric **eNe** showed coexisting left and right handed helical assemblies in the crystal lattice (Figure 2.1.7) as expected from its racemic nature revealed by the flat CD

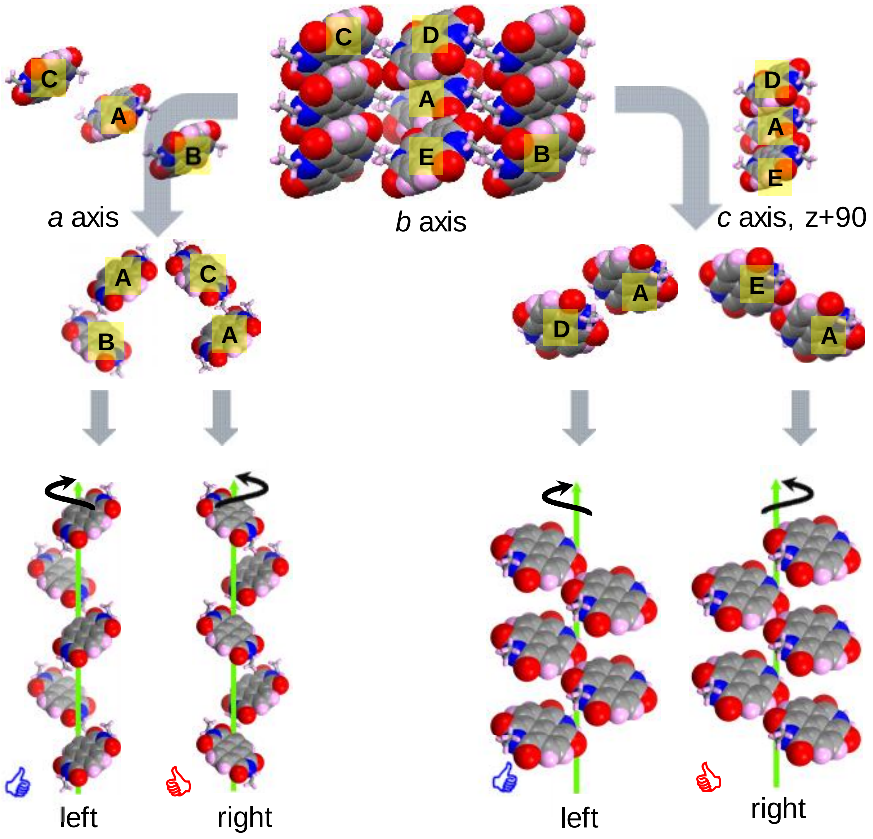

Figure 2.1.7 The 2_1 helicity inherent in the **eNe** $P2_1/c$ crystal system. Four helices embedded within the crystal lattice: side-to-side enantiomeric pairs AB (left handed) and AC (right handed) along the crystallographic *c* axis and splipped herringbone enantiomeric pairs AD (left handed) and AE (right handed) along crystallographic *a* axis.

signals as shown in Figure 2.1.5d.

The three parameters, viz. pitch, tilt and the distance of centroid of the molecule from the helix axis were calculated to define the 2_1 helices. In various conjugates, the helices were considered along different directions based on the arrangement of molecules in their respective crystal lattices. **FNF** showed prominent 2_1 helix along the crystallographic *c* axis with tilt angle of 66.09° for L-**FNF** and 66.15° for D-**FNF**, and the centroid of each molecule is 3.14 Å from the center of the helix. The pitch of the helix was found to be 27.66 Å and 28.20 Å in L-**FNF** and D-**FNF** respectively. These helices were found to be stabilized by interactions of DMSO (solvent) methyl groups with Cα atom of the amino acid (van der Waals interaction) and phenyl ring through CH···π interaction. **WNW** crystallized in $P2_12_12_1$ space group with three mutually perpendicular 2_1 screw axes. However, only two of them, *viz.* *a* and *b* crystallographic axis displayed supramolecular helices with tilt chirality. The 2_1 helix along *a*-axis was considered for determination of various parameters of **WNW**. Here the tilt angle was 115.64°, the centroid to helix axis distance was 3.93 Å and the pitch of the helix was 8.67 Å. As shown by Hisaki *et al*. [99-100] the adjacent 2_1 helices of **WNW** were antiparallel. Two types of CH···O interactions and CT π···π stacking were found to stabilize these antiparallel helices. One of them was observed between indole CH group and imide carbonyl oxygen of NDI core, while the other was found between carboxylic acid oxygen and aromatic CH of NDI core. The 2_1 helicity inherent in the **eNe** $P2_1/c$ crystal system was analyzed using a reported method.[99] On the basis of this method, we have observed four helices embedded within the crystal lattice (Figure 2.1.7). Two of them *viz.* AB (left handed) and AC (right handed), were found to be arranged as side-to-side enantiomeric pairs along the crystallographic *c* axis and the other two *viz.* AD (left handed) and AE (right handed) as slipped herringbone packing along *a* axis. The tilt angle of helices was about 44.63° and centroid to helix axis distance was found to be 3.11 Å. Therefore the observed CD inactiveness of **eNe** (Figure 2.1.5d) was attributed to equal propensity for supramolecular organization of centrosymmetric molecules into left and right handed helices.

2.1.1.1 Morphological studies

The effect of structural mutations on the morphologies of self-assembled structures of NDI from the solution upon drop casting or in the organogels was examined by field emission scanning electron microscopy (FESEM). FESEM samples were prepared by drop casting the solution of **eNe** onto the silicon wafer and dried at room temperature and vacuum. The xerogel samples were prepared by transferring the organogels onto the

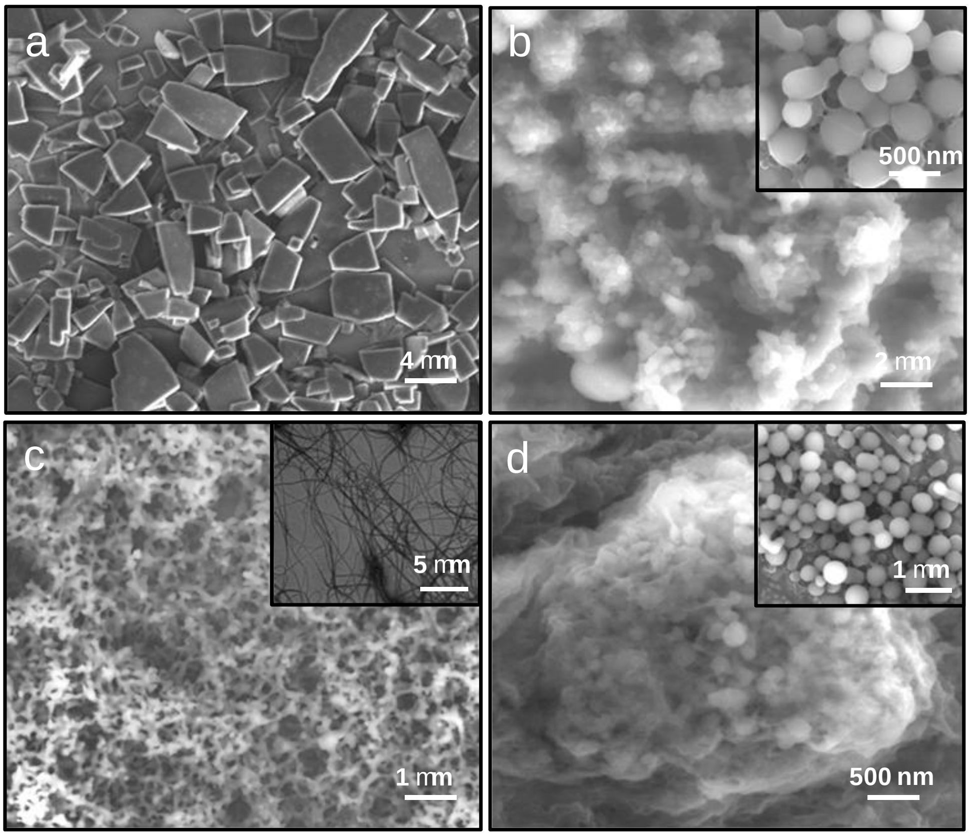

Figure 2.1.8 FESEM micrographs of a) drop casted **eNe** solution (MCH/CHCl$_3$: 80/20 V/V) and xerogels of b) **ANA**, c) **FNF**, and d) **WNW**. *inset:* The respective solution morphology.

silicon wafer fallowed by vacuum drying. Remarkably, FESEM micrographs revealed interesting 0D, 1D and 2D morphological structures (Figure 2.1.8). The eNe self-assembled from its solution (MCH/CHCl$_3$: 80/20, v/v) into large surface area 2D nano and mesosheets with several micrometer lateral dimensions (Figure 2.1.8a). In contrast, the xerogels of amino acid-NDI conjugates revealed the presence of distinct 0D and 1D nanostructures. **ANA** (Figure 2.1.8b) and **WNW** (Figure 2.1.8d) xerogels' matrix displayed embedded nanospheres with diameter of 100 to 300 nm (**ANA**) and 50 to 500 nm (**WNW**) respectively. **FNF** showed remarkable 3D network of interconnected high aspect ratio 1D nanofibers responsible for the observed gelation (Figure 2.1.8c). The fibers were several micrometers in length and 20 to 100 nm in diameter. The observed 2D, 1D and 0D nanostructures of NDI are ascribed to various intermolecular noncovalent interactions (hydrogen bonding, π···π, van der Waals, CH··· π, and CH···O) induced by side chain functionalities. These results clearly supported the potential of minute structural mutations in the imide substitution in fine tuning the nanoscale molecular ordering of NDIs.

2.1.3 Conclusion

In conclusion, for the first time we have demonstrated engineering of most promising NDI-NDI aromatic molecular ordering into all possible packing modes namely cofacial, brickwork, herringbone and slipped stacks using biomimetic approach in solid state (Figure 2.1.9). The center of symmetry, the structural mutations (Cα substituents on amino acids), corresponding chirality and their conformations with respect to planar NDI core were found to have major influence on the solid state molecular organization. Photophysical studies showed remarkable influence of molecular ordering on the absorption and emission properties of NDIs. Interestingly, NDI conjugates showed solid state emission in visible region from violet to orange, promising as potential materials for fluorescence applications. **WNW** exhibited strong absorption in entire visible region with the quenching of fluorescence due to effective charge transfer between indole (tryptophan) ring and NDI core making it a potential candidate for photovoltaic applications. All amino acid-NDI conjugates formed ultrasonication induced organogels and their rheological data revealed tunable visco-elastic ability with promising storage property. Furthermore, xerogel of **FNF** and drop-casted film of **eNe** exhibited contrasting temperature responsive emission behaviors and they can be used as solid state temperature sensor systems. The transcription of chiral information from amino acids to achiral NDI core was demonstrated by the preferential chiral helical arrangement of molecules. Whereas achiral ethyl substituents in NDI led to coexistence of both left and right handed helical (racemic mixture) arrangement of molecules. **ANA** with aliphatic

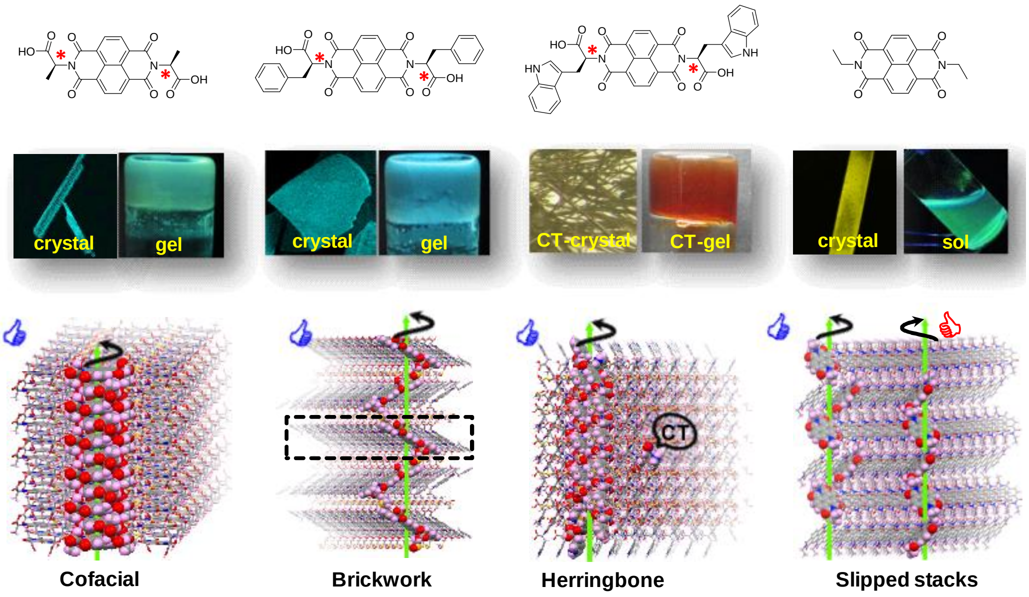

Figure 2.1.9 Summery of biomimetic molecular organization of NDI in solid state.

amino acid (alanine) resulted in cofacial helical columnar stack, whereas **FNF** and **WNW** with aromatic amino acids (phenylalanine and tryptophan respectively) exhibited supramolecular tilt chirality. We were also successful in tuning the nanoscale supramolecular assembly of NDIs into 0D nanospheres (**ANA** and **WNW**), 1D nanofibers (**FNF**) and 2D sheets (**eNe**). Overall, the structural mutations (amino acids) are capable of inducing preferential helical bias and tunable molecular ordering which in turn give rise to interesting optical (for example solid state emission, charge transfer) and viscoelastic (for example gelation and mechanical properties) and distinct nanoscale ordering properties to NDI system. We believe that our novel biomimetic design strategy is highly useful in understanding and mimicking the Nature’s complex molecular interactions and fine-tuning of aromatic functional properties for future electronics, chiroptical and biomedical applications.

2.1.4 Crystal structure determination

eNe. $C_{18}H_{14}N_2O_4$, M = 322.31, monoclinic, a = 4.8667(3), b = 7.7561(4), c = 18.3813(12) Å, β = 90.214(4)°, U = 693.83(7) Å^3, T = 100 K, space group $P2_1$/c (no.14), Z = 2, 7958 reflections measured, 1863 unique (R_{int} = 0.0361) which were used in all calculations. The final $wR(F_2)$ was 0.1257 (all data). CCDC 937648.

L-**FNF**. $C_{36}H_{34}N_2O_{10}S_2$, M = 718.77, orthorhombic, a = 8.953(3), b = 13.508(6), c = 27.663(11) Å, U = 3345(2) Å^3, T = 100 K, space group $C222_1$ (no.20), Z = 4, 8522 reflections measured, 1223 unique (R_{int} = 0.1165) which were used in all calculations. The final $wR(F_2)$ was 0.2233 (all data). CCDC 937649.

D-**FNF**. $C_{36}H_{34}N_2O_{10}S_2$, M = 718.77, orthorhombic, a = 9.104(7), b = 13.550(10), c = 28.20(2) Å, U = 3479(4) Å^3, T = 100 K, space group $C222_1$ (no.20), Z = 4, 5069 reflections measured, 1123 unique (R_{int} = 0.1052) which were used in all calculations. The final $wR(F_2)$ was 0.2050 (all data). CCDC 937650.

L-**WNW**. $C_{42}H_{42}N_4O_{13}S_3$, M = 909.41, orthorhombic, a = 8.670(2), b = 19.624(5), c = 25.099(7) Å, U = 4270.4(19) Å^3, T = 100 K, space group $P2_12_12_1$ (no.19), Z = 4, 12276 reflections measured, 4916 unique (R_{int} = 0.1372) which were used in all calculations. The final $wR(F_2)$ was 0.1685 (all data). CCDC 937651.

L-**ANA**: $C_{24}H_{26}N_2O_{10}S_2$, M = 566.59, monoclinic, a = 24.2349(5), b = 7.02890(10), c = 14.7664(3) Å, β = 90.8260(10)°, U = 2515.12(8) Å^3, T = 100 K, space group $C2$ (no.5), Z = 4, 47595 reflections measured, 4150 unique (R_{int} = 0.0506) which were used in all calculations. The final $wR(F_2)$ was 0.0887 (all data). CCDC 937652.

D-**ANA**. $C_{24}H_{26}N_2O_{10}S_2$, M = 566.59, monoclinic, a = 24.302(2), b = 7.0441(6), c = 14.8026(11) Å, β = 90.782(5)°, U = 2533.7(4) Å^3, T = 100 K, space group $C2$ (no.5), Z = 4, 9893 reflections measured, 4100 unique (R_{int} = 0.0482) which were used in all calculations. The final $wR(F_2)$ was 0.0966 (all data). CCDC 937653.

2.1.5 Bio-inspired Nanoarchitectonics of Naphthalenediimide to Access 2D Sheets of Tunable Size, Shape, and Optoelectronic Properties

2.1.5.1 Introduction

Nanoarchitectonics an emerging area of interdisciplinary nature attracting great deal of interest owing to fascinating structural and functional features, in both scientific and technological research.[10,101-105] In particular, 2D nanoarchitectonics deals with 2D nanostructures with large specific surface area and facets.[101-107] They exhibit exceptional electrical, mechanical, thermal and optical properties desirable for nano(bio)technology, storage, optical, dielectric and electronics, catalysis, sensing, separation, optoelectronics, biomaterials, membranes, and energy storage and conversion related applications.[63,85,98,101-129] Graphene has been one of the most fascinating 2D nanomaterials in the area of 2D nanoarchitectonics.[106-107] In recent times, 2D inorganic nanomaterials namely metal nanosheets, metal oxide/sulfide/selenide nanosheets, perovskite sheets, zeolites and hybrid materials, received remarkable attention owing to their high chemical, thermal stabilities and wide-band-gap semiconducting properties.[123-126,128-129] The soft organic and hybrid materials based 2D nanoarchitectonics is relatively young but exhibit promising multidisciplinary applications and therefore attracting a great deal of attention from the scientific community around the globe.[101-105,118-122] Substantial efforts have been devoted to obtain the 2D nanoarchitectures via both top down and bottom approaches such as exfoliation of layered crystals, templating at the liquid/air, liquid/liquid and liquid/solid interfaces, chemical vapor deposition, self-assembly and chemical synthesis.[1-5,21-25] There are few reports on organic 2D nanoarchitectonics in the literature based on biomacromolecules and synthetic polymers through supramolecular design principles with limited scope and applications owing to their low yields, large molecular size, low stability, lack of long-range order, narrow operating conditions, high cost associated with the processes.[63,85,98,110-122] Interestingly, 2D organic semiconducting nanoarchitectonics have been emerged as promising molecular organizations in organic field effect transistor applications by displaying high field effect mobilities via increased intermolecular interactions with neighboring molecules which preserves the 2D molecular order.[108-109] However direct control of noncovalent interactions in n-type organic semiconductor molecular organization into well-defined 2D nanoarchitectonics remains a key daunting challenge in organic electronics. We have been extensively working in the area of organic nanoarchitectonics which is based on adapting bioinspired approach to understand the design principles as well as to develop 1D and 2D nanomaterials for applications in organic electronics, biomaterials and biomedicine.[30,63,68,85,98,113-114]

Naphthalenediimide (NDI) and its derivatives are extensively studied class of n-type organic semiconducting materials.[53-54,56] On account of the novel characteristics like molecular planarity, high π–acidity, high melting points, high tendency to aggregation through π–π stacking interactions, excellent chemical, thermal, photochemical stabilities, well-defined redox behaviour and tunable optoelectronic properties (absorbance and emission), NDIs received special interest in biological, biomedical, materials science and supramolecular chemistry.[30,57-59,68,77-78,82,96,130-133] NDI derivatives have been used as intercalators of DNA, chemotherapy, conducting materials, optical brighteners, electro-photography, fluorescent labelling systems, metalomacrocycles, models for the photosynthetic reaction centre, sensors and anticancer agents.[30,57-59,68,77-78,82,96,130-133] During the past few years, various bioinspired and abiotic design strategies were employed to realize the nanomaterials of NDIs with diverse structural, chemical and physical properties.[30,57-59,68,77-78,82,96,130-133] Recently, for the first time we reported the amino acid conjugated NDI derivatives and their self-assembly into hierarchical 2D nanosheets with tunable optical properties.[85,98,114] The fabrication of 2D nanostructures of

NDI with precisely tailored size, shape and properties is still in its infancy owing to the difficulty in controlling the intermolecular noncovalent interactions.[101-105]

Nature meticulously employs biomolecules such as amino acids for designing complex biological systems and materials. It should be noted that amino acids exhibit remarkable structure–property correlations, selectivity, specificity and complexity. A bioinspired approach can be envisaged to exploit the extraordinary properties of amino acid in the development of new biomimetic materials with novel functional properties.[10,101-105] In such a design strategy, minute structural mutations in the form of amino acid derivatives play key role in controlling the intermolecular noncovalent interactions and subsequent molecular organization. Herein we report the bioinspired fine tuning of NDI molecular organization into 2D nanostructures with well-defined size, shape and optoelectronic properties by controlling the intermolecular noncovalent interactions such as aromatic and hydrogen bonding interactions.[134] Aromatic and hydrogen bonding interactions play a key role and are critical for various biological processes, for example, DNA helix formation, RNA recognition, stabilization of proteins and peptide secondary structures and enzymatic action among others. With this in mind, we selected a simple amino acid glycine (**1**) and its derivatives glycine methylester (**2**) and glycinamide (**3**) as imide substituents on NDI to induce differential self-assembly properties through variable intermolecular hydrogen bonding (Figure 2.1.10). Remarkably, the designed NDI bolaamphiphiles (**1**, **2** and **3**) were found to self-assembly into 2D nanoarchitectures with distinct size, shape and optoelectronic properties via aromatic interactions induced by central planar, π-electron deficient NDI core and distinct intermolecular hydrogen bonding interactions introduced by the glycine derivatives (**1**: carboxylic acid, **2**: amide and **3**: methyl ester) as shown in Figure 2.1.10.

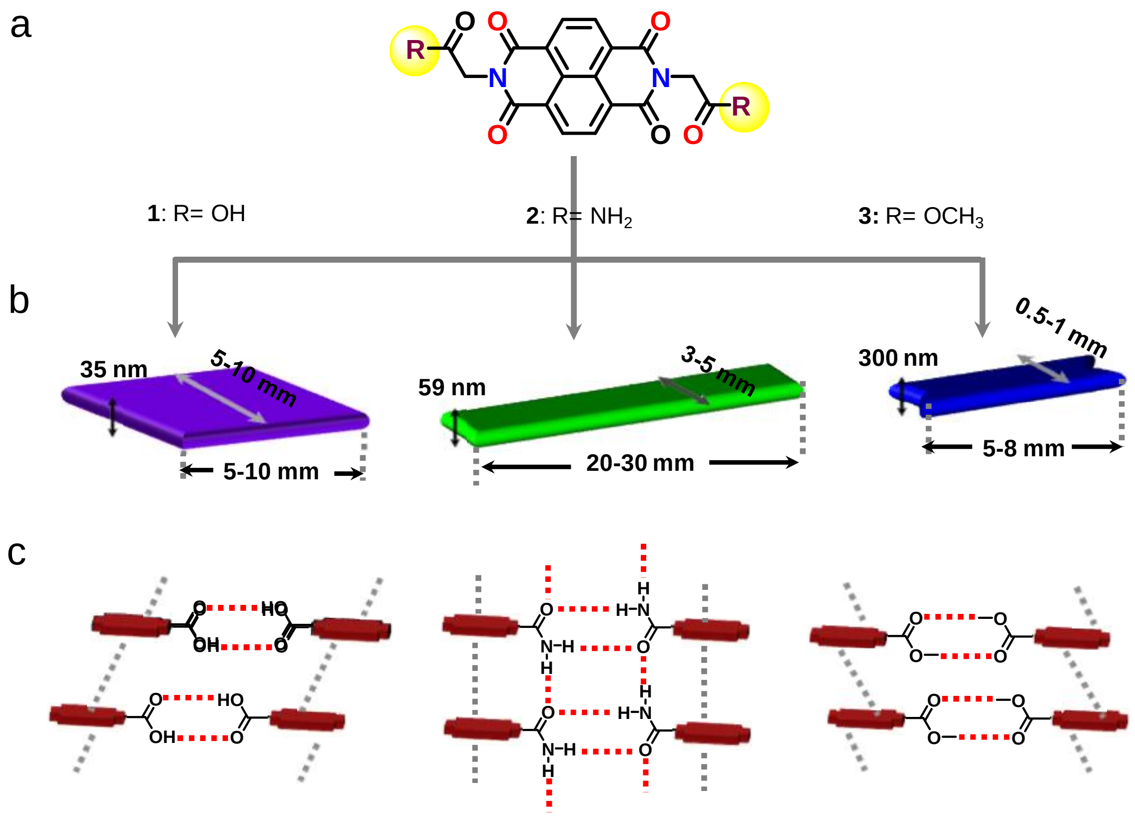
a
R
O
O
O
N
N
O
O
O
O
R
1: R= OH
2: R= NH2
3: R= OCH3
b
35 nm
5-10 mm
5-10 mm
59 nm
3-5 mm
20-30 mm
300 nm
0.5-1 mm
5-8 mm
c
O
HO
OH
O
O
HO
OH
O
O
H-N
H
N-H
H
O
O
H-N
H
N-H
H
O
O
O
O
O
O
O
O
O

Figure 2.1.10 a) Molecular structures of glycine and its derivatives conjugated NDIs **1**, **2** and **3**. b) Schematic representation of 2D sheets and their dimensions. c) Proposed noncovalent intermolecular interactions, hydrogen bonding (red dash line) and NDI-NDI aromatic interactions (black dash line) present in 2D sheets.

2.1.5.2 Results and discursion

NDI bolaamphiphiles **1-3** were synthesized by the condensation of corresponding glycine, glycinamide and glycinemethylester with the 1,4,5,8-naphthalenetetracarboxylic dianhydride (NDA) , in good yields (>80%). All the NDI bolaamphiphiles (**1-3**) were characterized by NMR spectroscopy and elemental analysis. NDI conjugates (**1**, **2** and **3**) were found to be readily soluble in dimethyl sulfoxide (DMSO). To induce the self-assembly of NDIs **1-3** through hydrophobic effect we chose to perform our spectroscopic and microscopy studies in aqueous solution (H_2O/DMSO; 80/20, v/v).

2.1.5.2.1 Morphological studies

Field emission scanning electron microscopy (FESEM) images of **1**, **2** and **3** revealed the presence of well-ordered flat and distinct laterally extended 2D sheets (Figure 2.1.11). **1** displayed the formation of large laterally extended 2D sheets with average length and width is in the range of 5-10 μm (Figure 2.1.11a). Furthermore, self-assembly of **2** and **3** led to the formation of rectangular sheets with differential aspect ratios. 2D sheets with 20-30 μm length and 3-5 μm width were observed in case of **2** (Figure 2.1.11b), whereas **3** formed relatively smaller 2D sheets with 5-8 μm length and 0.5-1 μm width (Figure 2.1.11c). Atomic force microscopy (AFM) studies were employed to measure the height

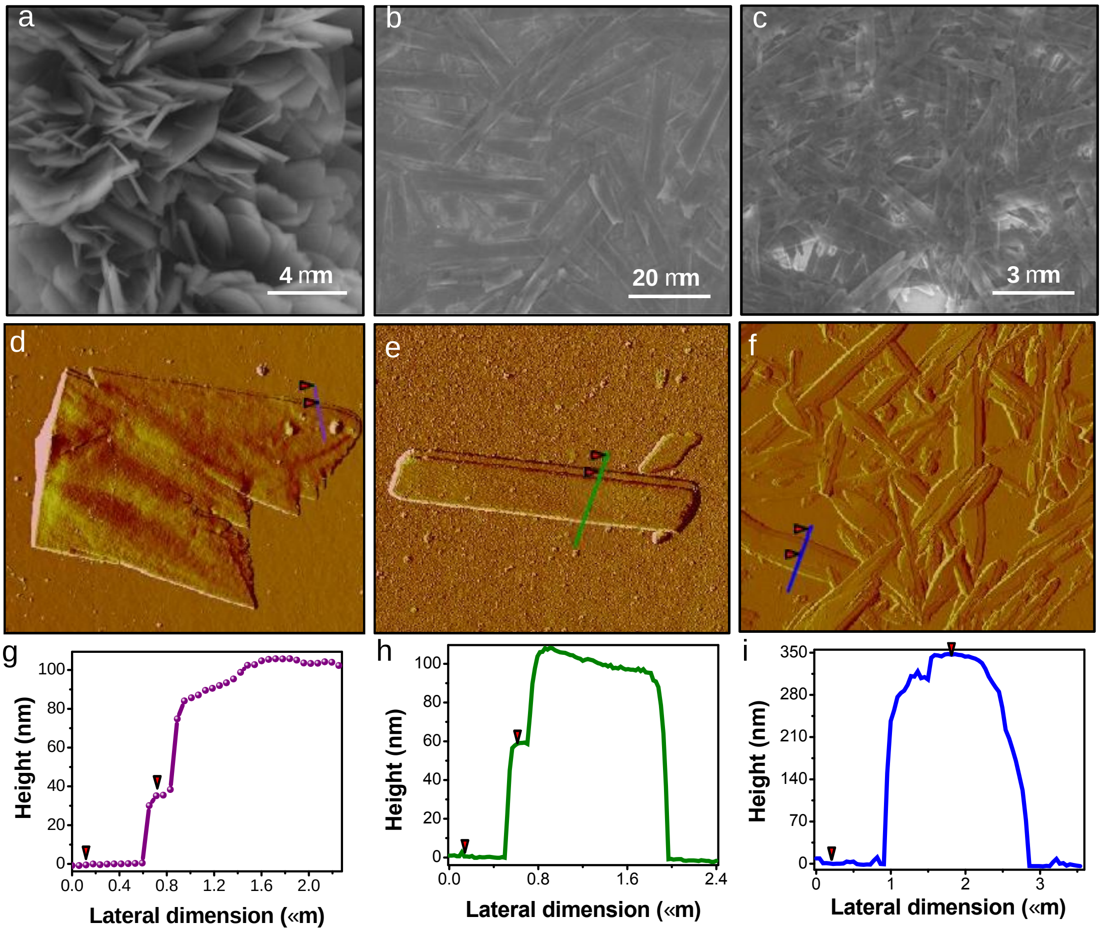

Figure 2.1.11 FESEM image of 2D sheets of **1**(a), **2**(b) and **3**(c). AFM image of **1**(d), **2**(e) and **3**(f) and corresponding AFM height profiles.

profiles of 2D sheets of **1**, **2** and **3** (Figure 2.1.11d-f). AFM micrograph showed relatively smooth and flat 2D nanosheets with average single layer thickness of 35 nm, 59 nm and 300 nm for **1**, **2** and **3** respectively (Figure 2.1.11g-i).

2.1.5.2.2 Photophysical studies

The mode of aromatic interactions with in the 2D nanosheets was explored through UV-vis absorption and fluorescence emission spectroscopic measurements (Figure 2.1.12). UV-vis absorption spectra of **1**, **2** and **3** in DMSO displayed vibronically well-resolved sharp bands in the 300-400 nm region assigned to NDI chromophore π–π* transitions polarized along the long axis (z-axis, band-I).[77-78,82,120-121,135]Interestingly, the 2D sheets formed from the aqueous solution (H_2O/DMSO: 80/20; v/v) of NDIs **1-3** exhibited significant spectral changes with appreciable bathochromic shifts and hypochromicity

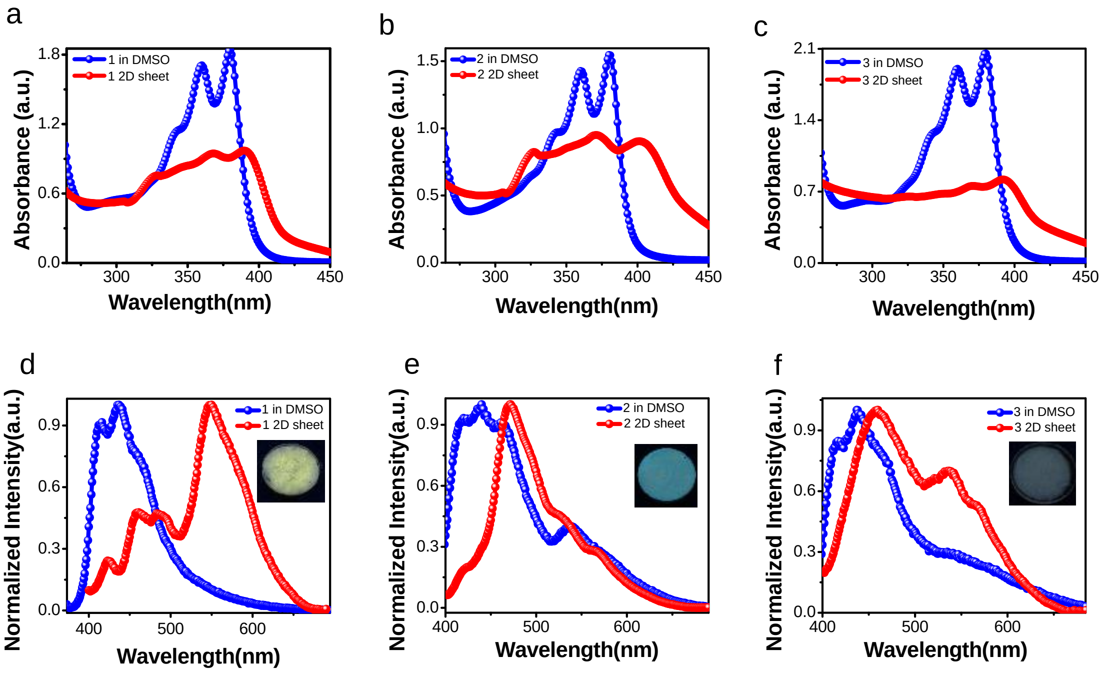

Figure 2.1.12 Photophysical studies of NDIs **1**, **2** and **3**. a-c) UV-vis absorption spectra and d-f) fluorescence emission spectra. *inset*: the photographs of corresponding films on quartz substrate under UV light (365 nm).

along with band broadening at band-I region, suggesting the presence of strong intermolecular NDI-NDI aromatic interactions **(**Figure 2.1.12a, b and c). In agreement with absorption studies, fluorescence emission studies of 2D sheets showed the shift of emission spectral features to higher wavelength region compared to emission bands in DMSO solution and displayed tunable broad fluorescence emission properties in the visible spectrum region (400-650 nm). The emission spectra of 2D sheets showed excimer bands ($E_{\max}$ =553 nm for **1** and $E_{\max}$ = 537 nm for **3**) and excimer-like emission bands at $E_{\max}$ = 472 nm for **2** signifying the effective charge delocalization among the closely packed NDI chromophores (Figure 2.1.12d, e and f).[77-78,82,120-121,135] Therefore, the modulation emission of NDI chromophore from excimer-like (**2**) to excimeric emission (**1** and **3**) was achieved by minute structural mutations in the form of glycine and its derivatives. This is quite remarkable, considering the fact that most of the NDIs and their derivativeness upon aggregation and in solid state exhibit weak or quenched luminescence properties that limited their fluorescence-based applications.

Interestingly, 2D sheets of **1**, **2** and **3** exhibited temperature responsive emission behaviour as shown in the Figure 2.1.13. **1** showed quite stable excimeric emission at 553 nm in the temperature range of 20-100 °C (Figure 2.1.13a and d). A gradual quenching of broad excimer-like emission band of **2** at 472 nm was observed with increase in temperature from 20 to 100 °C (Figure 2.1.13b and d). In contrast, **3** exhibited decrease in the excimer emission at 537 nm from 20 to 50 °C and the recovery of excimer emission with further rise in temperature from 50 to 100 °C was observed (Figure 2.1.13c and d). These contrasting temperature responsive emission behaviours are attributed to thermal disruption of intermolecular NDI-NDI aromatic interactions that led to emissive and nonemissive aggregates.[121] Therefore, 2D sheets of **1**, **2** and **3** are promising materials for solid state temperature sensor systems.

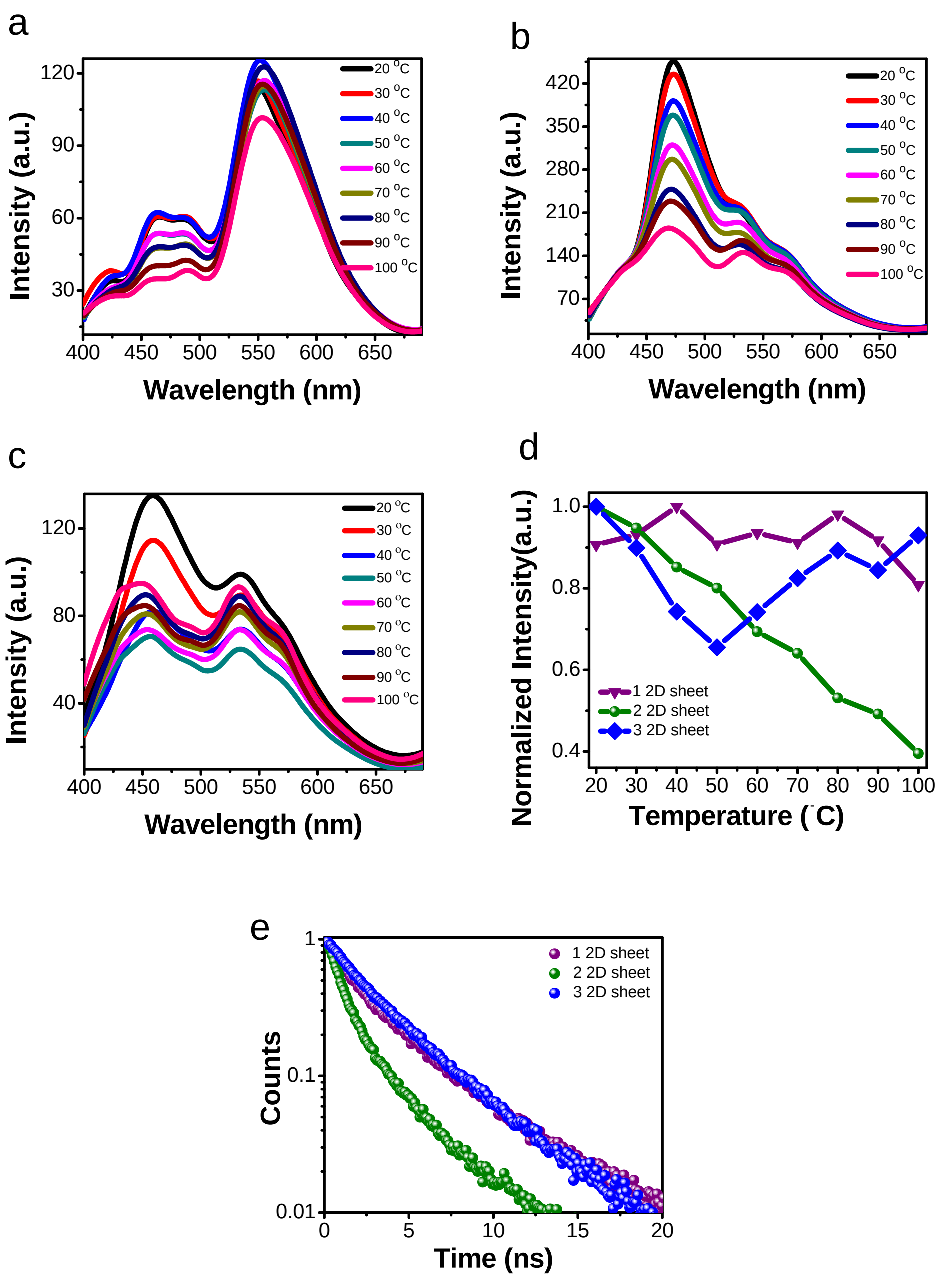

Figure 2.1.13 Temperature dependent fluorescence emission spectra of a) **1** 2D sheet, b) **2** 2D sheet and c) **3** 2D sheet. d) Plot of fluorescence emission intensity as a function of temperature (from 20 ^{o}C to 100 ^{o}C) of **1** (at 553 nm), **2** (472 nm) and **3** (at 537 nm). e) TCSPC decay profile of **1** (b$_{max}$ 553 nm), **2** (b$_{max}$ 472 nm) and **3** (b$_{max}$ 537 nm) with a 405 nm excitation.

Furthermore time- correlated single photon counting (TCSPC) experiments with nanosecond excitation was performed for **1**, **2** and **3** to understand the emission behaviour of 2D sheets (Figure 2.1.13e). TCSPC data displayed distinct biexponential decay profiles excimer-like emission (in case of **2**) and excimer emission (for **1** and **3**). NDI **1** at 553 nm and **3** at 537 nm exhibited significantly longer life-times values (4.17 ns, 56% and 1.11 ns, 44%) and (1.31 ns 26% and 3.83 ns, 74%) respectively. Whereas **2** at 472 nm showed relatively shorter life-times values (0.75 ns, 71% and 2.8 ns, 30%) suggesting the formation of ground state excimeric and excimer-like emissive aggregates.

2.1.5.2.3 NMR studies

In order to probe the hydrogen bonding and aromatic interactions among the NDI molecular units (**1**-**3**) nuclear magnetic resonance (NMR) spectroscopic measurements were performed in DMSO-d_6. The ^{1}H NMR spectra revealed that NDI core aromatic proton chemical shift values were found to be maximum in case of **3** (8.75ppm) and minimum for **2** (8.71ppm) whereas that of **1** was found to be moderate (8.74ppm) (Figure 2.1.14). The observed NDI core chemical shift values clearly suggest the extent of intermolecular NDI-NDI aromatic overlap and are in the order of **2** > **1** > **3**. Interestingly, **2** displayed the two different chemical shift signals for amide protons, indicating the presence of two kinds of hydrogen bonding interactions among molecular units. To understand the influence of hydrogen bonding and aromatic NDI-NDI interactions on

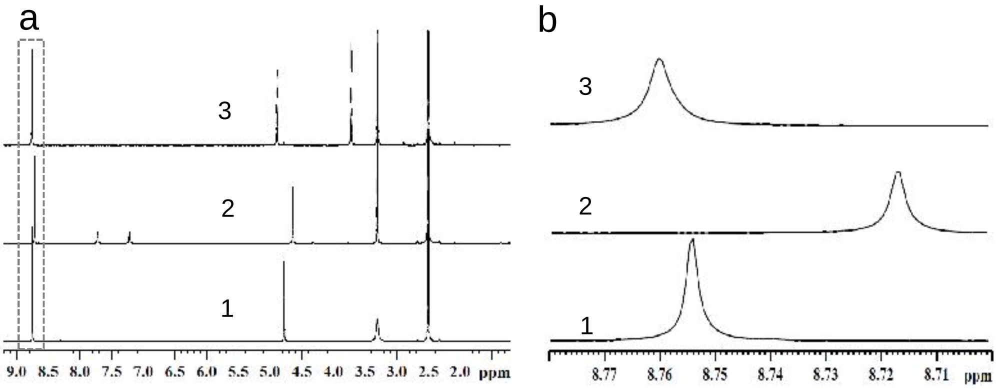

Figure 2.1.14 a) Comparison of ^{1}H-NMR spectra of **1**, **2** and **3** in full spectral range. b) ^{1}H NMR spectra of **1**, **2** and **3** at NDI region (8.8-8.7 ppm) the dotted box region in a.

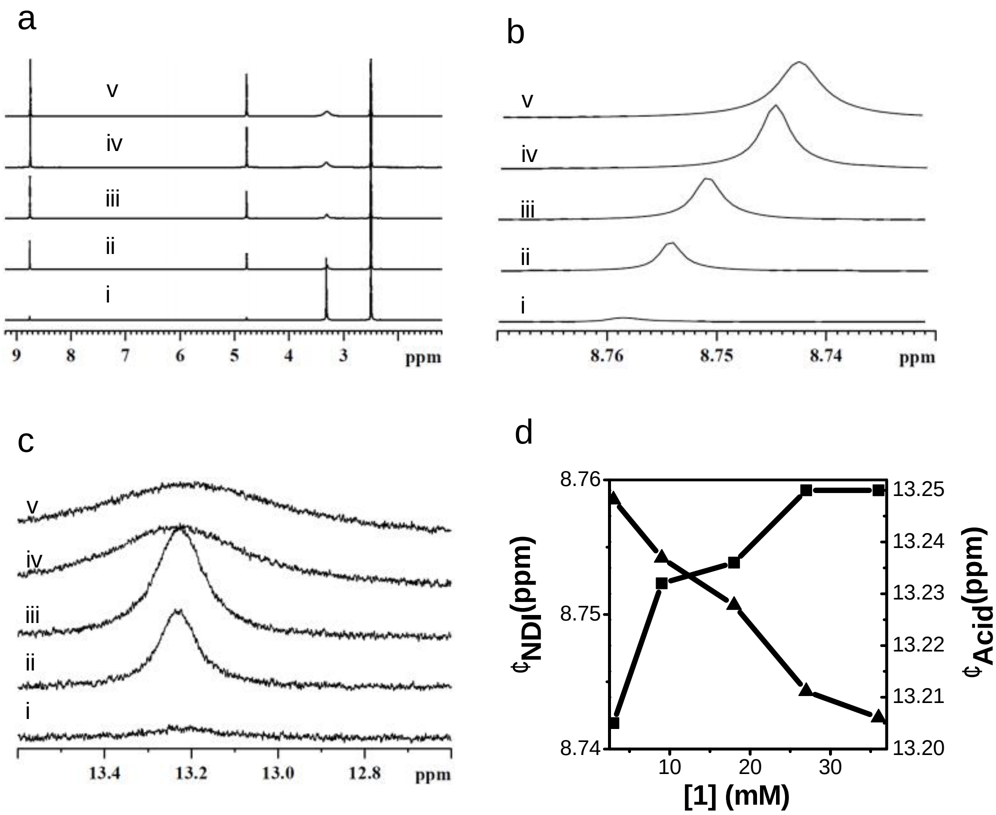

Figure 2.1. 15 Concentration dependent ^{1}H-NMR spectra of **1** (where (i) 3 mM, (ii) 9 mM, (iii) 18 mM, (iv) 27 mM, (v) 36 mM.; a) full spectral region. b) NDI aromatic region (8.73-8.77 ppm). c) Carboxylic acid OH region (12.7-13.5 ppm). d) Plot of concentration versus NDI (■) and carboxylic acid (▲) proton chemical shifts of **1**.

molecular aggregation, we performed concentration dependent ^{1}H NMR studies. All the NDI conjugates (**1**, **2** and **3**) showed upfield shift of NDI aromatic protons to different extent as a function of increasing concentration. **1** showed the upfield shift of NDI aromatic protons ($\Delta\delta_{NDI}$ = 16.2 ppb) along with the downfield shift of carboxylic acid protons with $\Delta\delta_{acid}$ = 45.0 ppb upon increase in the concentration from 3 to 36 mM (Figure 2.1. 15). **2** and **3** also showed upfield shift of NDI core protons ($\Delta\delta_{NDI}$ = 2.1 ppb for **2** (0.6 to 9 mM) and $\Delta\delta_{NDI}$ = 10.0 ppb, **3** (3 to 36 mM)), downfield shift of amide protons in **2** ($\Delta\delta_{amide}$ = 12.0 ppb) and ester protons of **3** ($\Delta\delta_{ester}$ = 3.5 ppb) respectively (Figure 2.1.16 and Figure 2.1.17). Therefore the observed upfield shift of NDI core protons along

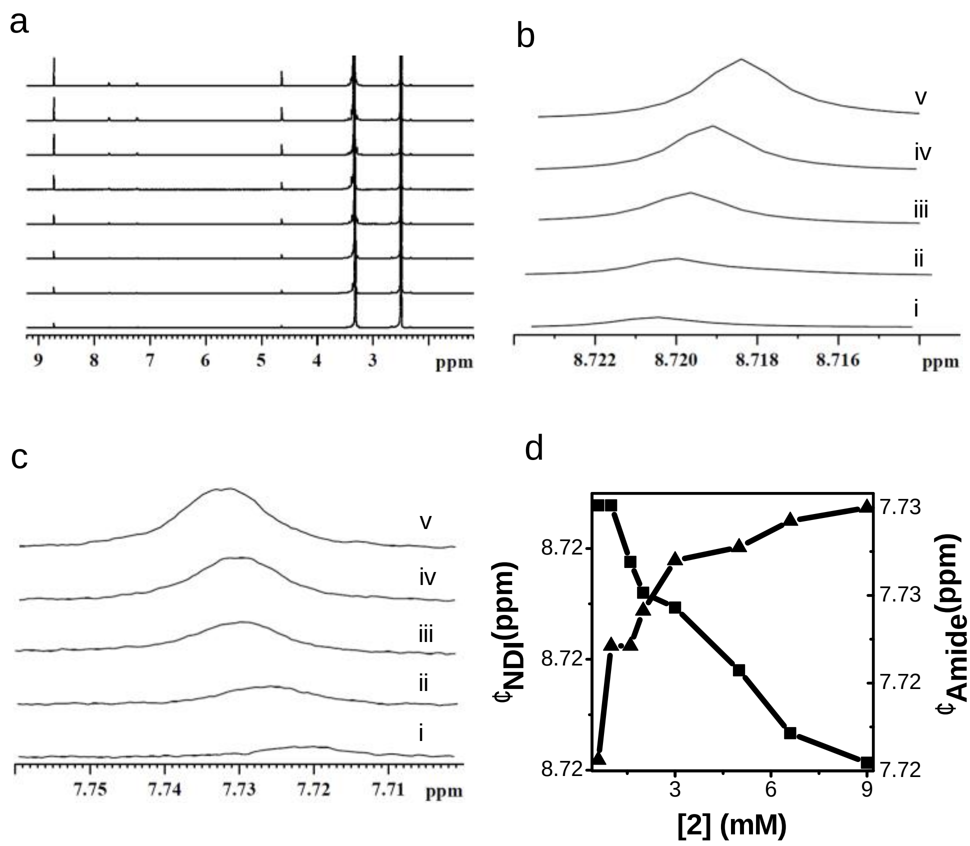

Figure 2.1.16 Concentration dependent ^{1}H-NMR spectra of **2** (where (i) 6 mM, (ii) 1.6 mM, (iii) 3 mM, (iv) 5 mM, (v) 9 mM); a) full spectral region. b) NDI aromatic region (8.71-8.72 ppm). c) amide-1 region (7.70-7.76 ppm). d) Plot of concentration versus NDI (■) and amide (▲) proton proton chemical shifts of **2**.

with downfield shift of corresponding acid, amide and ester protons as a function of increased concentration confirmed the intermolecular associations due to NDI-NDI aromatic *π-π* stacking, hydrogen bonding (carboxylic acid (**1**) and amide (**2**)) and CH---O (ester (**3)**) interactions among the molecular units.

Noncovalent interactions are sensitive towards temperature and therefore we carried out the variable temperature dependent ^{1}H NMR experiments by increase in temperature from20-100 °C. In contrast to concentration dependent NMR studies, variable temperature dependent ^{1}H NMR experiments showed opposite effect (downfield shift) at

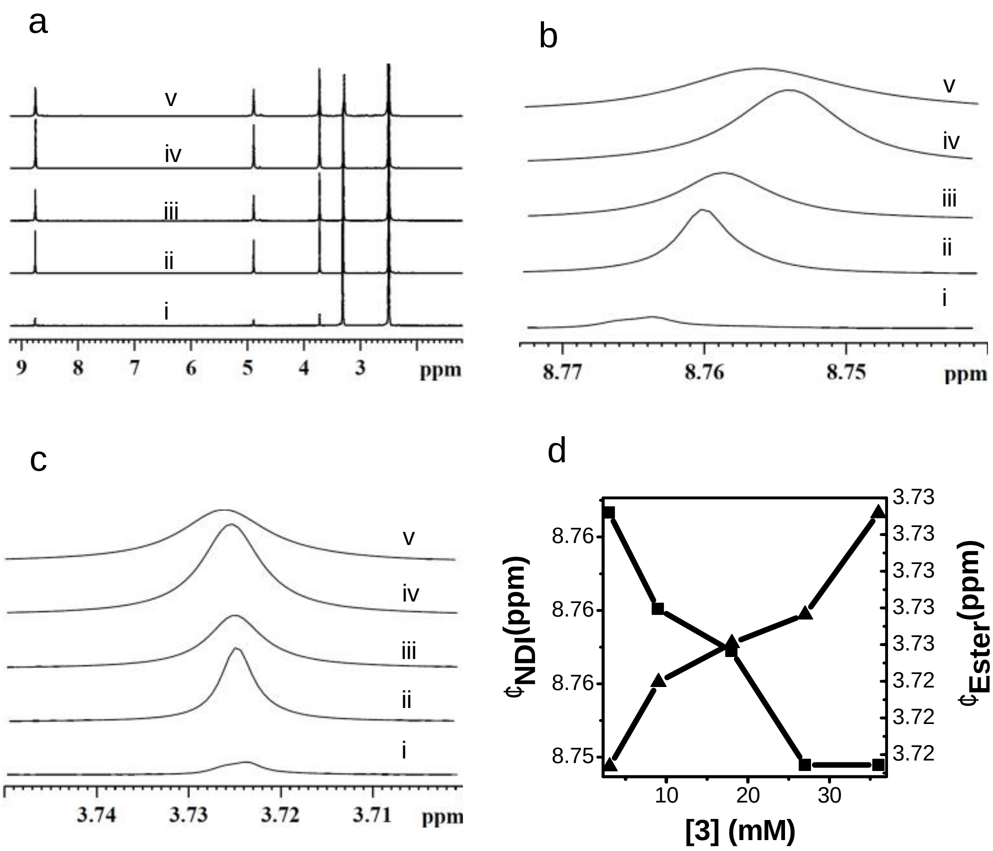

Figure 2.1.17 Concentration dependent ^{1}H-NMR spectra of **3** (where (i) 3 mM, (ii) 9 mM, (iii) 18 mM, (iv) 27 mM, (v) 36 mM); a) Full spectral region. b) NDI aromatic region (8.74-8.77 ppm). c) ester O-CH_3 region (3.70-3.75 ppm). d) Plot of concentration versus NDI (■) and ester proton(▲) proton proton chemical shifts of **3**.

the NDI aromatic proton chemical shift region (Figure 2.1.18, Figure 2.1.19 and Figure 2.1.20). With rise in temperature from 20 to 100 °C the NDI core protons of **1**, **2** and **3** displayed the downfield shift with $\Delta\delta_{NDI}$ values 12.5 ppb, 6.6 ppb and 9.2 ppb respectively. The downfield shift of NDI core protons is evidently due to the effect of temperature on the NDI-NDI aromatic *π*-*π* stacking interactions. Remarkably going from 20 to 100 °C the two amide proton chemical shift signals of **2** (7.75 ppm and 7.25 ppm) are converted into single broad signal centered at 7.15 ppm, revealing the breaking of hydrogen bonding present among the molecules at higher temperature (Figure 2.1.19c).

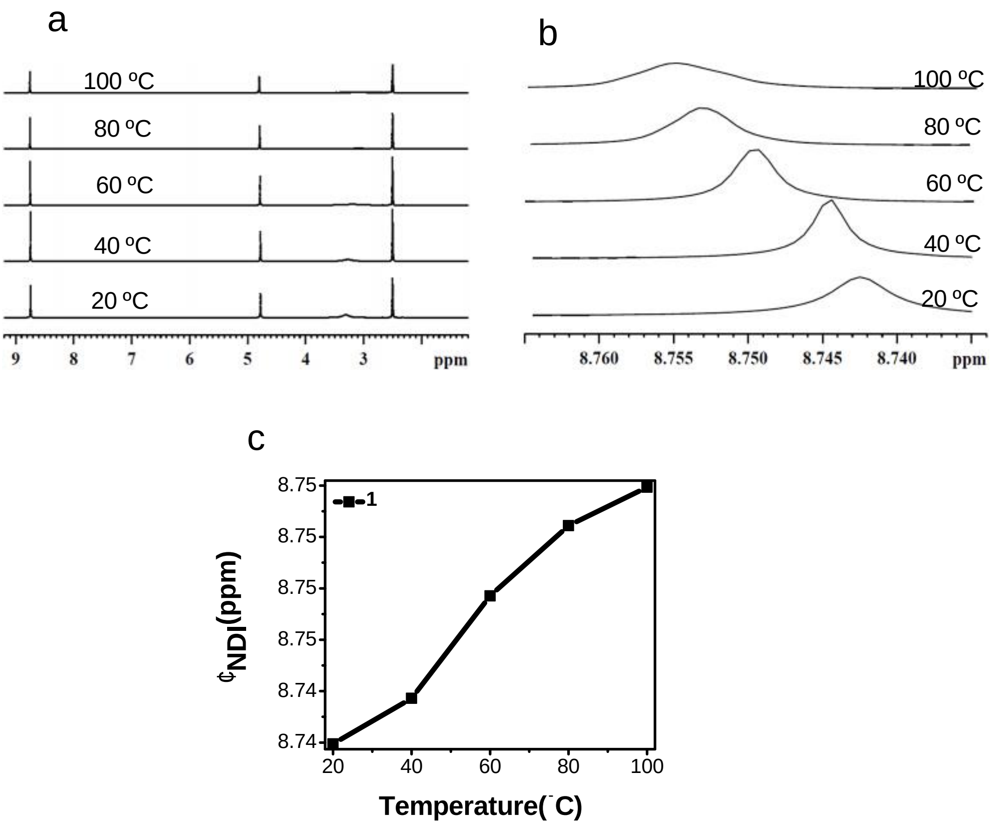

Figure 2.1.18 Temperature dependent ^{1}H-NMR spectra of **1**; a) Full spectral region. b) NDI aromatic region (8.39-8.65 ppm). c) Plot of NDI proton chemical shift as a function of temperature.

Overall, concentration and temperature dependent NMR studies revealed the distinct contribution of strong hydrogen bonding and NDI-NDI aromatic interactions in their self-assembly to form 2D sheets with variable shape and size.

2.1.5.2.4 FTIR and PXRD studies

Fourier transform infrared spectroscopic (FTIR) measurements further confirmed the presence of hydrogen bonding interactions between molecular units in their respective 2D sheets. **1** displayed broad carboxylic acid stretching frequency at 3600-3800 cm^{-1} and amide stretching frequency at 3100-3400 cm^{-1}. Whereas NDI **3** did not show any characteristic band in the 3000-4000 cm^{-1} region (Figure 2.1.21a). Furthermore, the

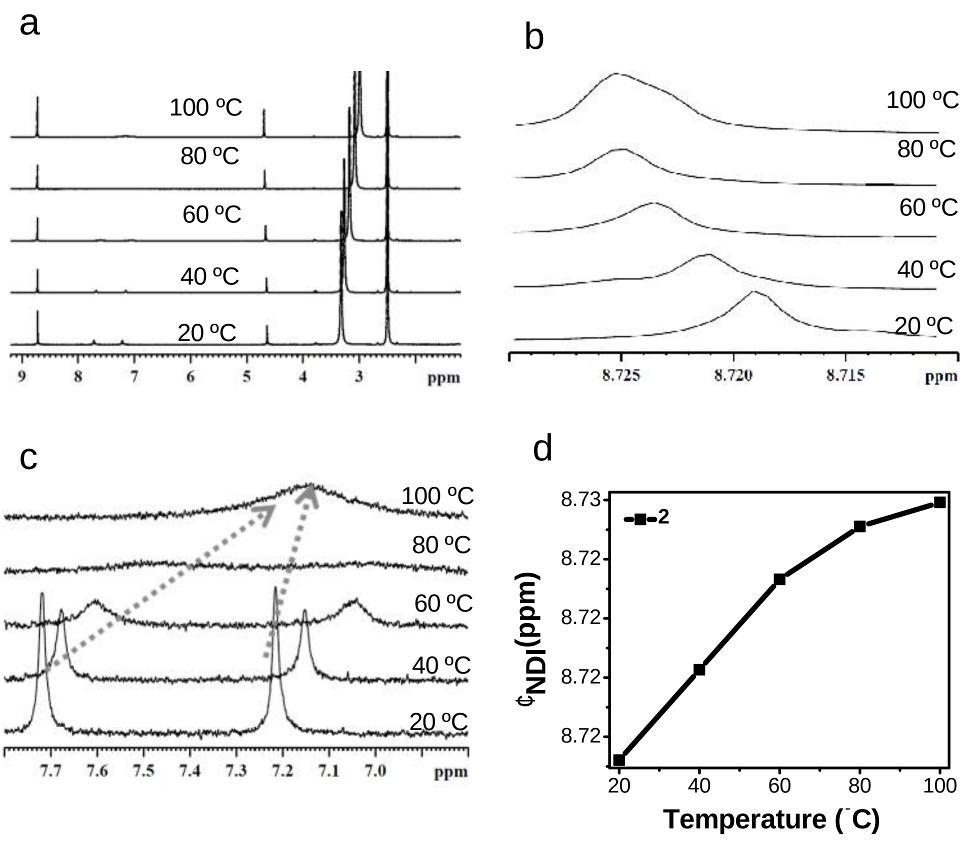

Figure 2.1.19 Temperature dependent ^{1}H-NMR spectra of **2**; a) Full spectral region. b) NDI aromatic region (8.10-8.73 ppm). c) Amide region (6.8-7.8 ppm). d) Plot of NDI proton chemical shift as a function of temperature.

powder X-ray diffraction (PXRD) data showed sharp and intense reflections in the low-angle as well as higher-angle regions for all the 2D sheets of **1**, **2** and **3**. This data suggest crystalline arrangement of molecules and the preferred orientation of molecular planes within the 2D sheets (Figure 2.1.21b). The reflections at low-angle (2θ = 20°-35°) corresponded to intermolecular π-stacking distances and hydrogen bonding distances between the molecules within the 2D sheets of **1**, **2** and **3** respectively.

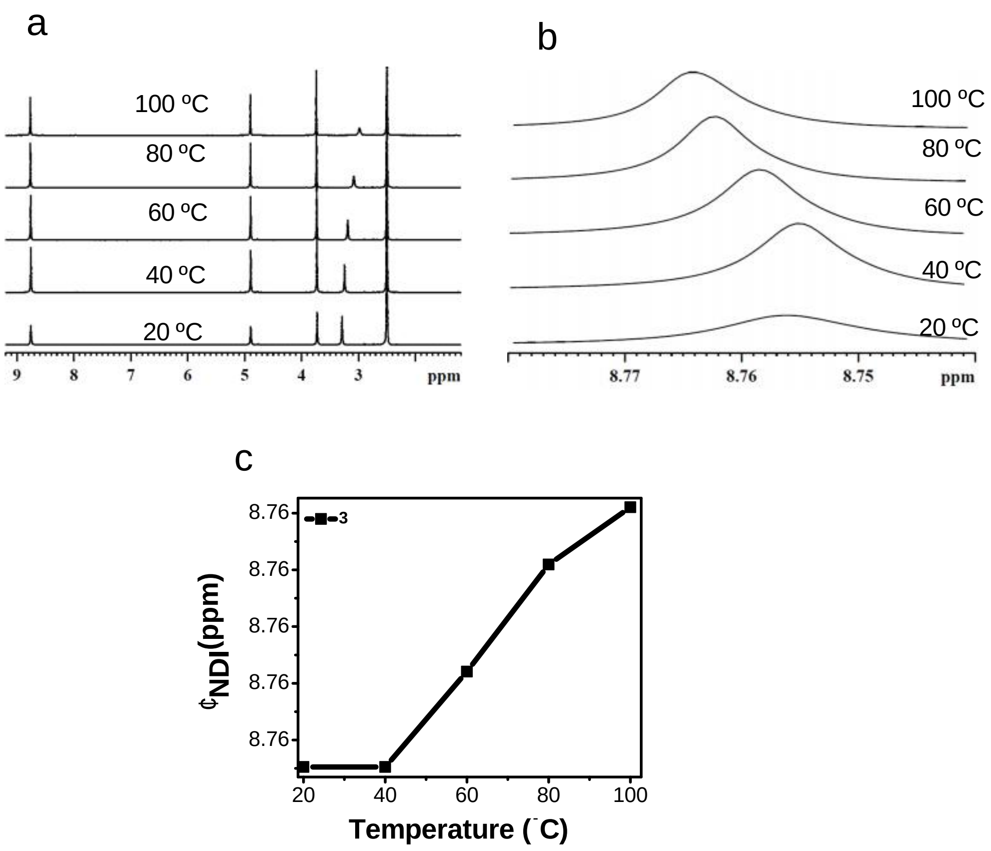

Figure 2.1.20 Temperature dependent ^{1}HNMR spectra of **3**; a) Full spectral region. b) NDI aromatic region (8.74-8.78 ppm). c) Plot of NDI proton chemical shift as a function of temperature.

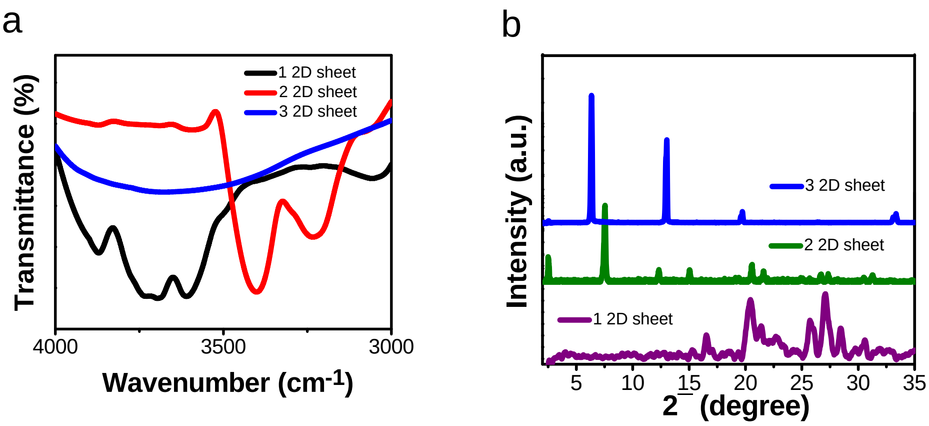

Figure 2.1.21 a) IR spectra of 2D sheets of **1-3** in the region 4000-3000 cm^{-1}. b) PXRD diffraction patterns of **1-3** 2D sheets at 25 °C.

2.1.5.3 Conclusions

We demonstrated a bioinspired nanoarchitectonics design strategy to construct 2D sheets of NDIs by controlling their self-assembly propensity. Subtle changes in the form of structural mutations of glycine derivatives (carboxylic acid, amide and ester respectively) in NDIs **1-3** led to 2D nanosheets with distinct but well-defined shapes in terms of length, width and thickness. The spectroscopic (photophysical, concentration and temperature dependent NMR and IR), microscopy (AFM and FESEM) and powder XRD analysis suggested that the variable strength and directionality of intermolecular hydrogen bonding interactions among the structural units of glycine functionalized NDI are responsible for the observed variable shape and size of 2D sheets of **1-3**. In addition, the variable shape and size of 2D sheets of NDis **1-3** is also attributed to intermolecular hydrogen bonding interactions controlled NDI-NDI aromatic interactions. Remarkably, 2D sheets of NDIs **1-3** exhibited emission in the longer wavelength (visible) region with high Stoke shift signifying the potential of these materials for fluorescence-based applications. Interestingly, 2D sheets showed temperature responsive emission properties and are promising materials for solid state temperature sensor systems. NMR and IR studies confirmed the presence of strong and distinct hydrogen bonding and NDI-NDI aromatic interactions with in the self-assembled 2D sheets. PXRD diffraction patterns revealed highly crystalline molecular organization and preferred molecular planes orientations within the 2D sheets. Overall, our nanoarchitectonics approach based on the bioinspired strategy in the form of minute structural mutations of glycine is capable of controlling the self-assembly of promising n-type organic semiconductor NDI into 2D sheets with tunable shape, size and interesting solid state optical properties. We believe that our bioinspired nanoarchitectonics design strategy is highly useful in controlling the noncovalent interactions of functional aromatic molecules, which in turn give rise to desirable crystalline molecular packing and interesting optical properties important for wide range of applications from materials to biomedicine.

Subchapter 2.2 Stimuli Responsive Donor-Acceptor Co-Assembly

2.2.1 Room Temperature Volatile Organic Ferroelectrics of Stimuli Responsive Chiral Charge-Transfer Co-Assembly Networks

2.2.1.1 Introduction

Development of multifunctional optical and electro-active organic materials is of special interest owing to the advantage of solution processability, for new generation opto-electronic applications.[136-138] One of the interesting and rarely observed properties in organic materials is the phenomenon of ferroelectricity. Ferroelectric materials find applications in sensors, actuators and energy efficient memory units and photonics.[139-140] Unlike inorganic counterparts, organic ferroelectricity has been limited to few polymeric materials[141-142] and very few low molecular mass single crystalline solids.[143-144] The polymer ferroelectrics exhibit high coercive field for the polarization switching. Alternative methods to develop low coercive field organic ferroelectrics seems strongly depend on noncovalent assembly of appropriately designed organic molecules.[139-140] A general guideline to induce the ferroelectric property in organic and hybrid materials is by introducing ordered dipoles through weak noncovalent interactions like hydrogen bonding, and charge-transfer (CT) interactions or by encapsulation of dipoles in three dimensional (3D) lattice and metal organic framework (MOF).[139,145,146] The pioneering work of Tokura and co-workers led to the phenomena of displacive and order-disorder phase transition induced noncovalent organic ferroelectric materials.[139,147] The recent studies indicate that noncovalent materials with ordered π–electron donor-acceptor mixed-stack CT network are good candidates for organic ferroelectrics due to long range unidirectional orientation of CT dipoles.[145] However, most of the known organic CT solids showed ferroelectric switching property at low temperatures (below 71 K) which limits their applications at ambient conditions.[148-149] In a recent work, Stupp and co-workers showed room temperature ferroelectricity in single crystals of supramolecular CT organic mixed-stack attributed to combination of orthogonal noncovalent hydrogen bonding and CT interactions.[145] Notably, all the reported low molecular weight organic solids (hydrogen bonded, mixed-stack CT complexes and combination of both) exhibit the ferroelectric behavior only in their single crystalline state which limit their broad device applications due to high coercive field and limited solution processability.[139-140,145] There is a pressing need for developing novel strategies to design noncovalent organic systems suitable for solution processing to prepare thin films that helps minimizing the coercive field while facilitating the device applications involving ferroelectric junctions.[140] In this context, we demonstrate solution processable noncovalent organic materials based on hydrogen bonding and mixed-stack CT interactions driven co-assembly to facilitate strong network of ordered dipoles which show ferroelectricity near room temperature. Furthermore, we process these organic materials into the thin film ferroelectric junction to fabricate optically switchable energy efficient memory device under ambient conditions. The design strategy adapted in this work is expected to open up new avenues for generating a novel class of thin film ferroelectric materials near room temperature.

In recent years, the concept of low molecular weight (LMW) gels with nano- and micro-scale noncovalent polymeric architectures has been recognized as a convenient strategy to realize technological applications ranging from regenerative medicine to electronic devices.[150-151] Moreover, the inherent solid-like behavior of three-dimensionally cross-linked noncovalent polymeric network within the fluid makes gels easy to fabricate on flexible substrates for variety of applications. Additionally, the studies on nematic and smectic liquid crystals revealed that induction of macroscopic chirality exhibit ferroelectric property due to spontaneous polarization through conformational preference of transverse molecular dipoles to orient in one net direction.[152-157] These remarkable facts inspired us to design mixed two-component CT hydrogels with built-in supramolecular chirality (or noncentrosymmetric) to harvest ferroelectric property (Figure 2.2.1). Two-component mixed-stack CT hydrogels are a special class of gel-systems, remain challenging to achieve because of commonly encountered problems such as self-sorting or phase separation.[158] A careful designing of π-electron donor (D) and acceptor (A) molecular systems is crucial to achieve CT

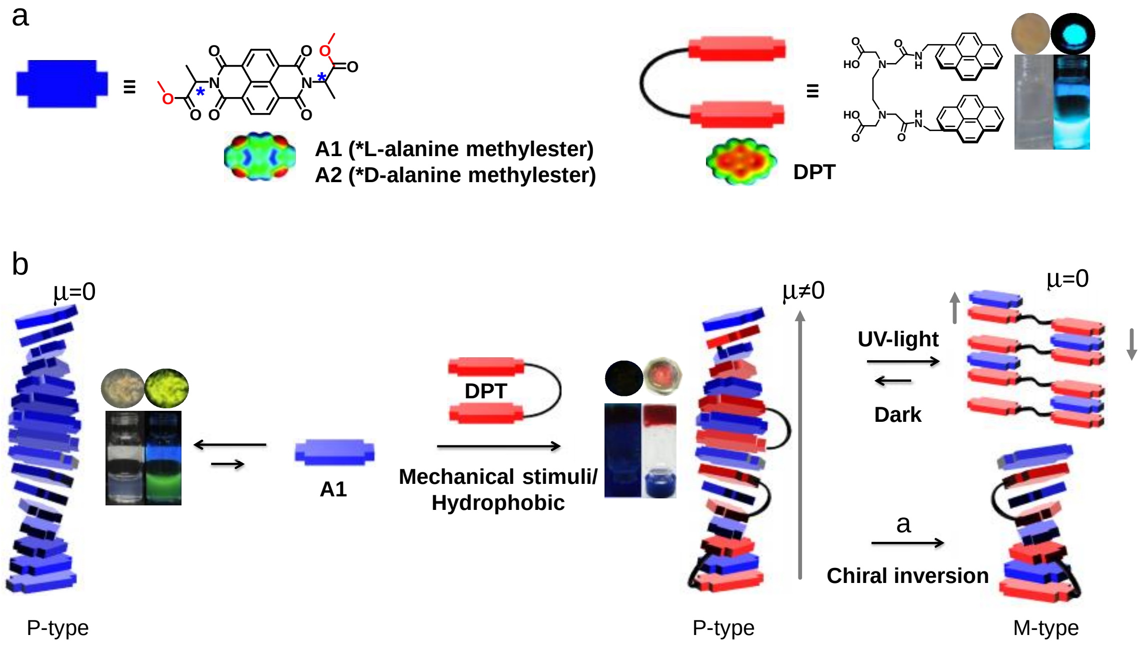

Figure 2.2.1 a) Molecular structures and schematic representation of acceptors (**A1-A2**) and donor (**DPT**). Photographs of **DPT** aqueous solutions (DMSO/water: 20/80,v/v) and solid powder under UV (365 nm) and visible light. b) Schematic representation of stimuli responsive tweezer-inclusion-sandwich (TIS) CT coassembly of **DPT** and **A1**. P-type (right handed) helical self-assembly of **A1**, mechanical stimuli (ultrasonication for solution and grinding for solid powders) induced P-type (right handed) helical tweezer- sandwich mixed-stack CT coassembly, UV-light responsive transformation to achiral CT complex and temperature responsive CT chiral inversion from P-type (right handed) to M-type (left handed). Photographs of corresponding aqueous solution/solids under UV- and visible-light, **A1** aqueous solution and solid powders, Inverted vials of CT (**DPT**:**A1** (1:2)) hydrogel. Mechanically co-ground (**DPT**:**A1** (1:2)) solid powders.

hydrogels with high-level molecular ordering in the form of extended D-A mixed-stacks.

2.2.1.2 Results and discussion

In the present study, we designed an amphiphilic and flexible π-electron-rich di-pyrene tweezer-like (**DPT**) molecular system (pyrene is π-basic with molecular quadrupole moment Q_{zz} = -13.8 B) suitable for complexing electron-deficient aromatic guest molecules such as naphthalenediimides (NDIs) (NDI is π-acidic with Q_{zz} = + 18.6 B) by encapsulating them in the tweezer-cavity (tweezer-inclusion complexation) as well as through intermolecular sandwiching of the tweezer-inclusion complexes (TIS = tweezer-inclusion-sandwich) (Figure 2.2.1a).[159] The two carboxylate functionalities on the backbone of **DPT** are expected to impart enhanced solubility in aqueous solution. The alanine methylester functionalized NDIs (**A1** and **A2**) have been designed as aromatic acceptor molecules to achieve chiral (noncentrosymmetric) supramolecular CT co-assemblies through TIS (Figure 2.2.1a).[130,160-162] Detailed procedure for the synthesis and characterization of donor and acceptors is provided in the experimental section. Interestingly, mixture of highly fluorescent **DPT** and **A1**/**A2** in aqueous solution (DMSO/water: 20/80, v/v) and in solid-state turned into non-fluorescent but visibly dark brick red gel and powder under external mechanical stimuli such as ultrasound and mechanical co-grinding, respectively. The formation of visibly colored, non-fluorescence co-assembly in the gel and solid-state is a naked eye evidence for D-A interaction through CT complexation (Figure 2.2.1b).

2.2.1.3 UV-vis absorption and Fluorescence emission studies

In order to gain more insights into the **DPT**:**A1**/**A2** mixed-stack CT co-assembly, we carried out extensive UV-vis absorption and fluorescence emission studies. DPT in dimethyl sulfoxide (DMSO) displayed as well resolved absorption bands at 250-380 nm

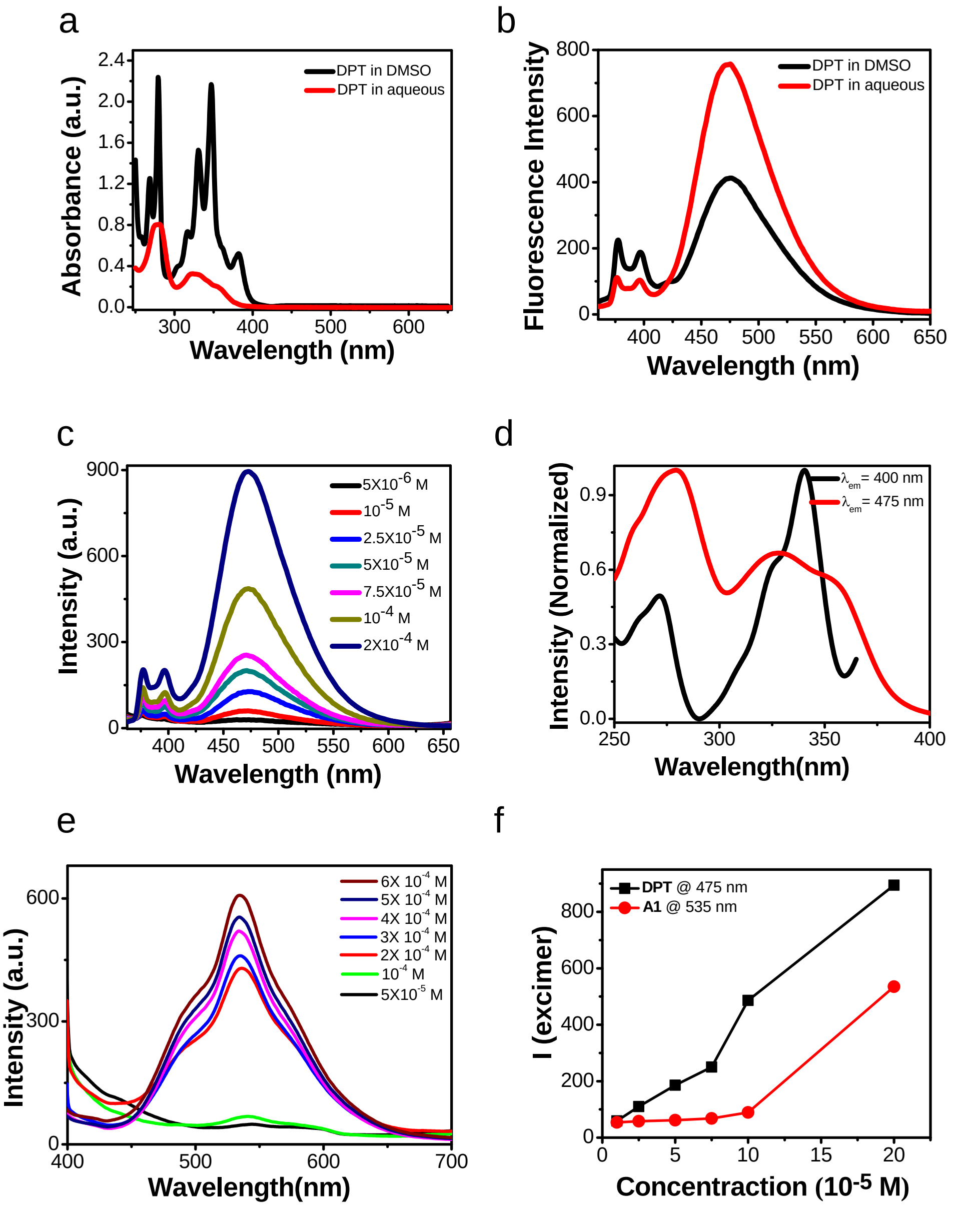

Figure 2.2.2 a) UV-vis absorption spectra of **DPT**. b) Fluorescence emission ($\lambda_{excitation}$ = 340 nm) spectra of **DPT.** c) Concentration dependent fluorescence spectra of **DPT** (λ_{ex}= 340 nm). d) Excitation spectra of **DPT**.e) Concentration dependent fluorescence spectra of **A1** (λ_{ex}= 380 nm). f) the plot of excimer intensity versus concentration of **DPT** and **A1** respectively

attributed $\pi\text{–}\pi*$ transitions of pyrene chromophore (Figure 2.2.2a). However, in aqueous solution (DMSO/water: 20/80, v/v) a drastic decrease in absorption bands accompanied by broadening of bands indicating the presence of self-assembled aggregates. In addition **DPT** exhibited weak monomeric emission with two bands at 376 and 400 nm, and a structureless intense broad emission band centered at 475 nm attributed to excimer emission of the pre-associated pyrene chromophores (Figure 2.2.2b). This was further confirmed by excitation spectra monitored at the excimer emission (at $\lambda_{emission}$ = 475 nm) is red-shifted and the bands are broadened compared to that of spectra monitored at monomer emission ($\lambda_{emission}$ = 400 nm) (Figure 2.2.2d).[163] The concentration-dependent fluorescence study showed intramolecular excimer emission at low concentrations (1×10^{-5} M - 7.5×10^{-5} M) which suggest tweezer-like conformation for the **DPT** molecule (Figure 2.2.2b). Further increase in the concentration of **DPT** (1×10^{-4} M to 2×10^{-4} M) resulted in the coexistence of both intra- and inter-molecular excimers, this was confirmed by the plot of $I_{excimer}$ (at 462 nm) as a function of concentration (Figure 2.2.2b and f). On the other hand, individual acceptor molecules (**A1**/**A2**) showed monomeric emission at low concentrations while intermolecular excimer emissions at higher concentrations ($\geq 2\times 10^{-4}$ M) (Figure 2.2.2e and f).

To know the **DPT-A1** interaction through CT complexation, we recorded the absorption spectrum of thoroughly mixed aqueous solution (DMSO/water: 20/80, v/v) of **DPT** (2×10^{-4} M) and A**1** (4×10^{-4} M). The red shifted (~14 nm) broad absorption band (λ_{max}= 400 nm, aggregation band) and appearance of the new broad absorption band in the visible region centered at 536 nm (λ_{max}) that was absent in the individual spectra of **DPT** and **A1** are clear evidence for the CT interaction between donor (DPT) and acceptor **(A1)** molecules (Figure 2.2.3a). In particular, the new absorption band at 536 nm is a characteristic of mixed-stack CT interaction between **DPT** and **A1**.[164] In accord with the absorption data, mixing of **DPT** and **A1** resulted in quenching of excimer emissions of individual donor (**DPT**) and acceptor (**A1**) molecules due to the CT interaction between them (Figure 2.2.3b). Furthermore, we were succeeded in inducing a high degree of D-A-D-A CT co-assembly in the solid-state by means of simple mechanical co-grinding. The

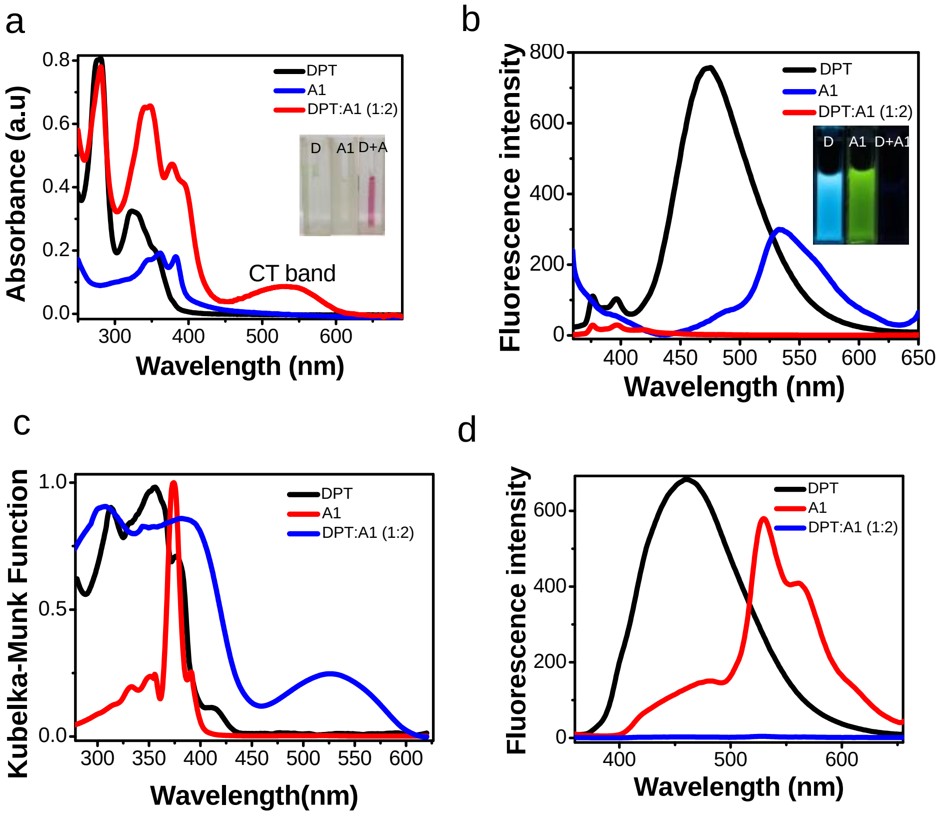

Figure 2.2.3 a) UV-vis spectra in an aqueous solution ([**A1**]= 0.2 mM, [**DPT**]= 0.1 mM). b) Fluorescence emission spectra in aqueous solution with excitation wavelength= 340 nm, inset corresponding photographs of aqueous solution under UV and visible light. c) and d) UV-vis and fluorescence emission spectra of **DPT**, **A1** and **DPT**:**A1** (after co-grinding) in their solid state respectively.

co-grinding of a 1:2 (**DPT**:**A1/A2)** mixture of the highly fluorescent donor (**DPT**, white powder) and acceptor (**A1**/**A2,** pale yellow powder) using a mortar-pestle resulted in a non-fluorescent but visibly intense brick-red colour solid powder (Figure 2.2.1b). The brick-red CT co-assembly of **DPT**:**A1/A2** was further validated by the broad CT absorption band at λ_{max}=536 nm and complete fluorescence quenching of constituent **DPT** and **A1**/**A2** of the co-ground mixture (solid-state) (Figure 2.2.3d). This is an example of stimulus (mechanical force) induced formation of highly ordered CT (D-A-D-A) co-assembly.[165]

To determine the stoichiometry of mixed-stack co-assembly of **DPT** and **A1** to

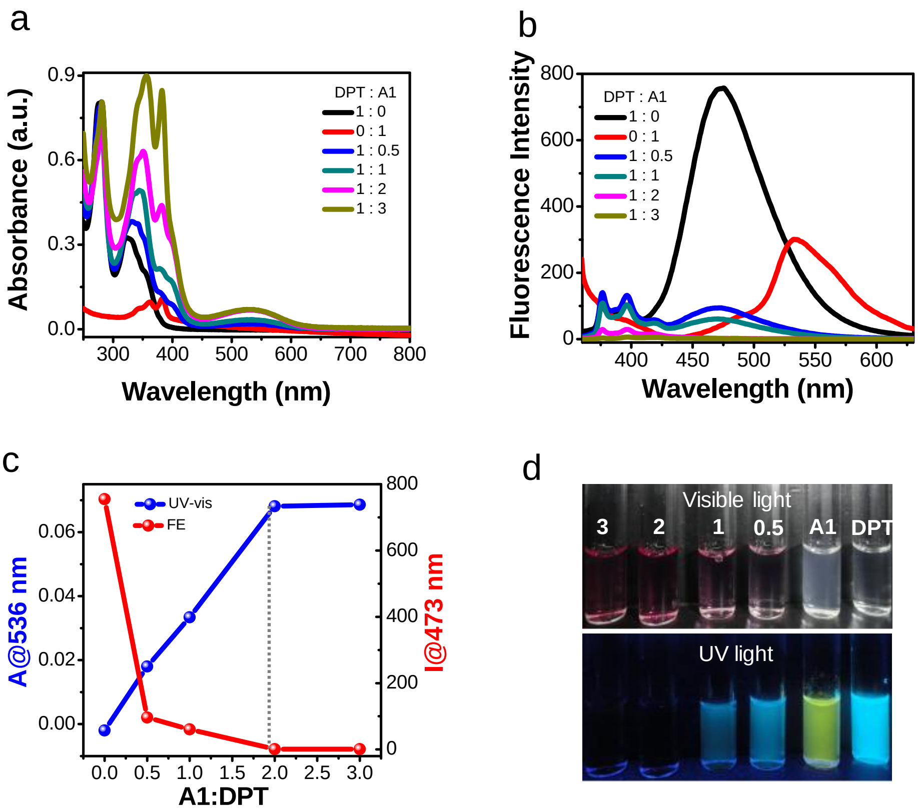

Figure 2.2.4 a) UV-vis absorption titration spectra of **DPT**:**A1**. b) Fluorescence emission titration spectra of **DPT:A1**. c) Plot of CT absorption at 536 nm (blue line) and fluorescence excimer (FE) emission intensity at 475 nm (red line) as a function of fractional **A1** addition to **DPT** (**A1**/**DPT**=0.5, 1, 2 and 3). d) Photographs of corresponding aqueous solutions under visible and UV light show increase in CT color (brick-red) and gradual fluorescence quenching.

form efficient CT complexes, we recorded the absorption and fluorescence emission spectra upon adding different concentration of **A1** (1 × 10^{-4} M to 4 × 10^{-4} M) to the fixed concentration of **DPT** **(**2× 10^{-4} M) (Figure 2.2.4a and b). The plot of absorbance at CT band (λ_{max}=536 nm) and **DPT** excimer emission band (473 nm) versus fraction of **A1** added to **DPT** (**DPT**:**A1**) provided conclusive evidence for the 1:2 (**DPT**:**A1**) complexation (Figure 2.2.4c). At this concentration ratio maximum absorbance of the CT absorption band ((λ_{max}=536 nm) was observed, which also corresponds to complete fluorescence quenching of both **DPT** and **A1** as shown in Figure 2.2.4. Notably, the stoichiometric ratio of 1:2 (**DPT**:**A1**) co-assembly also inferred the formation of **DPT-**

A1-DPT-A1 (D-A-D-A) stacks where **A1** molecules arranged inside the tweezer-cavity of **DPT** as well as outside it as tweezer-sandwich to form extended donor-acceptor tweezer-inclusion-sandwich (TIS) mixed co-assembly (Figure 2.2.1b). Figure 2.2.4d show the photographs of corresponding solutions under visible as well as UV light. The visible colour change from colourless to intense brick red and corresponding gradual quenching of the bright fluorescence are naked eye evidence for the formation of CT co-assembly of **DPT** and **A1**.

2.2.1.4 CD studies

To investigate the long rage intermolecular orientations of the acceptor (**A1**/**A2**), donor (**DPT**) and within their CT co-assembly materials circular dichroism (CD) spectra was recorded in aqueous solution (Figure 2.2.5). The individual enantiomeric acceptors **A1** and **A2** exhibited mirror image cotton effects with λ_{max} at 406 nm (positive signal for **A1** and negative for **A2**) suggesting the formation of right handed (*P*-type) and left handed (*M*-type) helical aggregates of NDI chromophores, respectively (Figure 2.2.5a). While the achiral **DPT** exhibited flat CD signal indicating the absence of any preferential helical organization. Under similar conditions, the mixture of **DPT** (2×10^{-4} M) and **A1**/**A2** (4×10^{-4} M) displayed strong mirror image induced CD (ICD) signals in the absorption regions of tweezer **DPT** (λ_{max}=285 nm) and **A1**/**A2** aggregation band (λ_{max}= 400 nm) suggesting the heterochrophoric exciton coupling between pyrene (**DPT**) and NDI (**A1**/**A2**) (Figure 2.2.5b). Intriguingly, upon irradiation of **DPT**:**A1** with UV light (λ = 365 nm) for 20 min showed drastic decrease in ICD bands at **DPT** (λ_{max}=285 nm) and **A1** aggregation (λ_{max}= 400 nm) regions (Figure 2.2.5c). This reduction in the ICD bands suggests photoinduced transformation of *P*-type CT co-assembly of **DPT**:**A1** into achrial mixed-stacks as the brick red color due to CT interactions retained in the sample. This photoinduced chiral to achiral transformation is found to be reversible, as the achrial

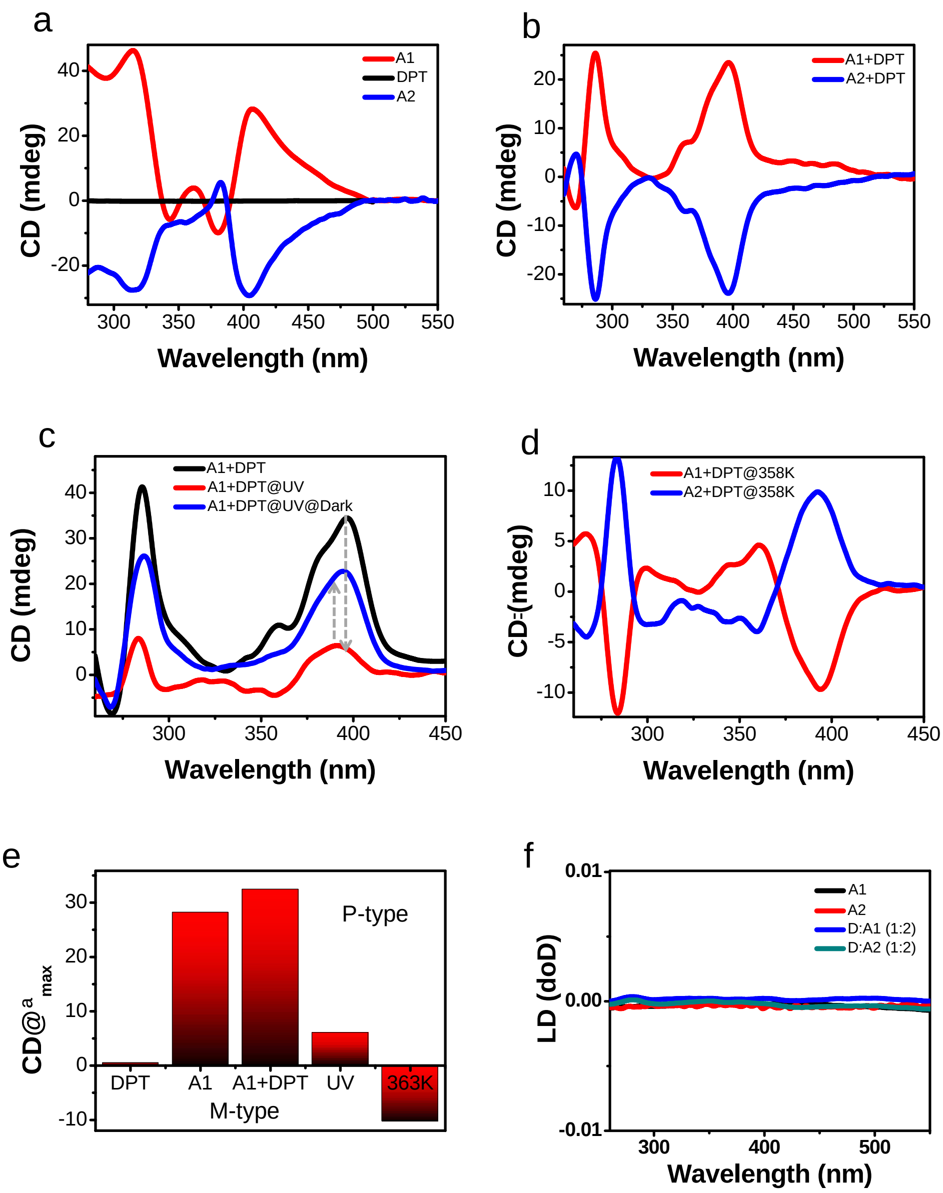

Figure 2.2.5 a) CD spectra of individual **A1**, **DPT** and **A2** in aqueous solutions. b) CD spectra of CT complexes at 1:2 (**DPT**:**A1**/**A2**) ratio. c) Light responsive CD spectra of **DPT**:**A1** CT complexes. d) CD spectra of **DPT**:**A1**/**A2** CT complexes at 358K. e) Stimuli responsive CD spectral changes of **DPT**:**A1** (1:2) CT complexes in aqueous solution at 400 nm. f) LD spectra.

mixed-stacks return to its *P*-type co-assembly form after keeping in the dark for 20 min (Figure 2.2.5c). On the other hand, the rise in temperature (at 358 K) resulted in the inversion of supramolecular chirality of **DPT**:**A1/A2** from *P/M*-type CT co-assembly to

M/P-type assembly, respectively (Figure 2.2.5d). These studies show that the chiral intermolecular orientation of the donor (**DPT**) and acceptor (**A1**/**A2**) in mixed-stack CT co-assembly can be modulated by the external stimuli such as light and temperature. Furthermore, linear dichroism studies suggested the free of any LD artifacts for the observed CD spectra of A1/A2 and DPT:A1/A2 by displaying LD silent spectral feature.

2.2.1.5 Variable temperature spectral studies

To assess the thermal stability of **DPT**:**A1**/**A2** (1:2) CT co-assembly, variable temperature (VT) dependent absorption measurements were carried out (Figure 2.2.6). The increase in temperature from 288 K to 368 K led to significant changes in UV-vis spectra (Figure 2.2.6a). The reduction in the intensity of the CT band at 536 nm and aggregation band at 400 nm was observed with the restoration of vibranically structured monomeric absorption bands of pyrene and NDI at 250 nm and 380 nm, respectively. We further examined the VT-fluorescence emission and VT-CD behavior of **DPT**:**A1**/**A2** (1:2) CT co-assembly. As the temperature increased from 293 K to 363 K, a strong enhancement (~100 fold) in the **DPT** excimer emission (at λ_{max}= 475 nm) was observed (Figure 2.2.6b). In contrast VT-CD experiments (293 K to 343 K) exhibited decrease in ICD intensity at both **DPT** (λ_{max}=285 nm) and **A1**/**A2** aggregation (λ_{max}= 400 nm) bands (Figure 2.2.6c and d). Interestingly, this decrease in ICD band is accompanied by the inversion of the cotton effect (from positive to negative ICD for **DPT**:**A1** and negative to positive ICD in **DPT**:**A2**) at higher temperature ranges of 348 K to 363 K. For thorough comparison, the plot of fluorescence emission intensity at λ_{max}= 475 nm (**DPT** excimer emission) and ICD intensity at 400 nm as a function of temperature (293 K to 363 K) are shown in Figure 2.2.6e. The weak emissive ($I_{473\ nm}$= 0 to 12.5) and intense positive ICD signals ($CD_{400\ nm}$= 35.5) at low temperature region (293 K -324 K) revealed the existence of right handed TIS mixed-stack CT assembly. However, further increase in temperature

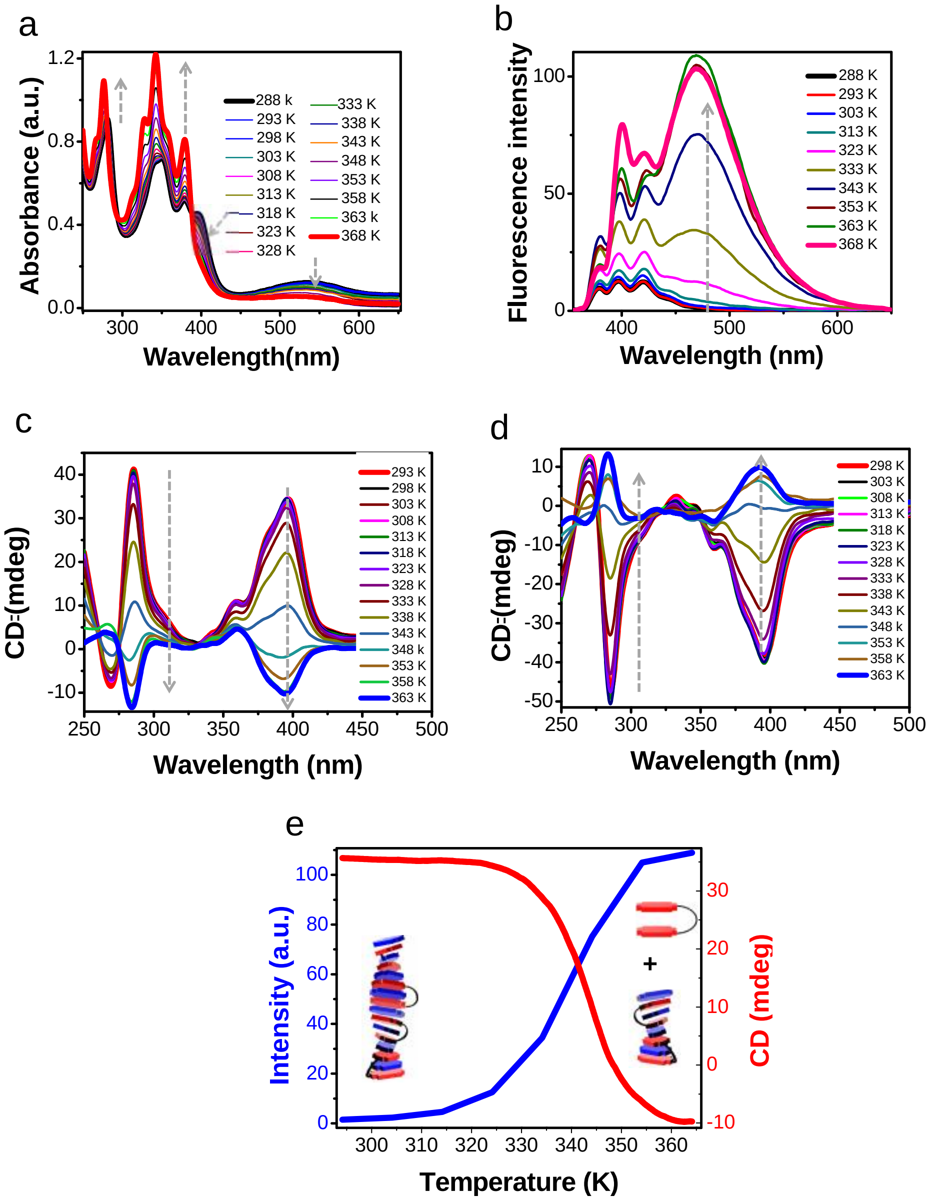

Figure 2.2.6 a) Variable-temperature (VT) UV-visible absorption spectra of **DPT**:**A1.** b) VT-Fluorescence emission (FE) spectra of **DPT**:**A1**. c) and d) are VT-CD spectra of **DPT**:**A1** and **DPT**:**A2** respectively**.** e) The plot of FE intensity at 475 nm (Blue line) and ICD intensity at 400 nm studies of **DPT**:**A1**CT assembly in aqueous solution as a function of temperature, schematic representation of heating induced assembly transformation from P-type helical CT co-assembly to mixture of self-segregated M-type CT co-assembly and **DPT** tweezer. Dotted arrows indicating the respective spectral changes upon heating.

(324-368 K) resulted in strong fluorescence enhancement (I = 12.5 to 109) followed by decrease and reversal of ICD signals from positive (*P*-type, $\theta_{400\ \text{nm}}$=35.5) band to negative

(*M*-type, $\theta_{400\ nm}$= -10) band. These observations clearly suggest the thermally induced release of acceptor molecules (**A1**) from TIS CT mixed-stack co-assembly leading to the mixture of stable M-type CT co-assembly and achiral emissive **DPA** aggregates as shown in the Figure 2.2.6e inset.

Furthermore, the aqueous solutions of **DPT**:**A1** and **DPT**:**A2** transformed into intense brick-red colored non-fluorescent hydrogel upon ultrasonication for 15 min (Figure 2.2.1b). On the other hand, control experiments revealed that neither **DPT** nor **A1/A2** alone could form hydrogels under similar ultrasonification conditions. This is an example of stimulus responsive CT complexation-induced hydrogelation of **DPT**:**A1** and **DPT**:**A2** in aqueous solution.

2.2.1.6 ^{1}H-NMR studies

To understand the changes in the molecular interactions upon mixing **DPT** and **A1** to form CT hydrogel, we performed ^{1}H NMR studies in DMSO-d_6 with the sequential addition of water (Figure 2.2.7). At different volumes of added water (5 μL-30 μL), a significant upfield shift and broadening of all aromatic proton signals of **DPT** (pyrene: 8.30-7.90 ppm, $\Delta\delta_{DPT}$ = 0.10 ppm) and **A1** (NDI core: 8.72-8.57 ppm, $\Delta\delta_{NDI}$ = 0.15 ppm) accompanied by the downfield shifting of amide NH protons (8.68-8.73 ppm, $\Delta\delta_{amide}$ =0.05 ppm) of **DPT** was observed (Figure 2.2.7c). The observed ^{1}H NMR spectral shifts attributed to hydrophobic force induced intermolecular CT stacking of **DPT** and **A1** stabilized by the intermolecular hydrogen bonding between amide protons of **DPT** and imide carbonyl of **A1**. Similarly, IR spectroscopic study supported hydrogen bonding interactions between **DPT** and **A1** upon mixing, which is evident from the red shift (~112 cm^{-1}) and decrease in the intensity of amide (NH) stretching frequency (3326 cm^{-1}) of **DPT** along with significant red shifted (~$\Delta\nu$=15 cm^{-1}) in imide carbonyl (CO) stretching frequency (1647 cm^{-1}) of **A1** (Figure 2.2.7d). Therefore, the hydrogelation of CT co-

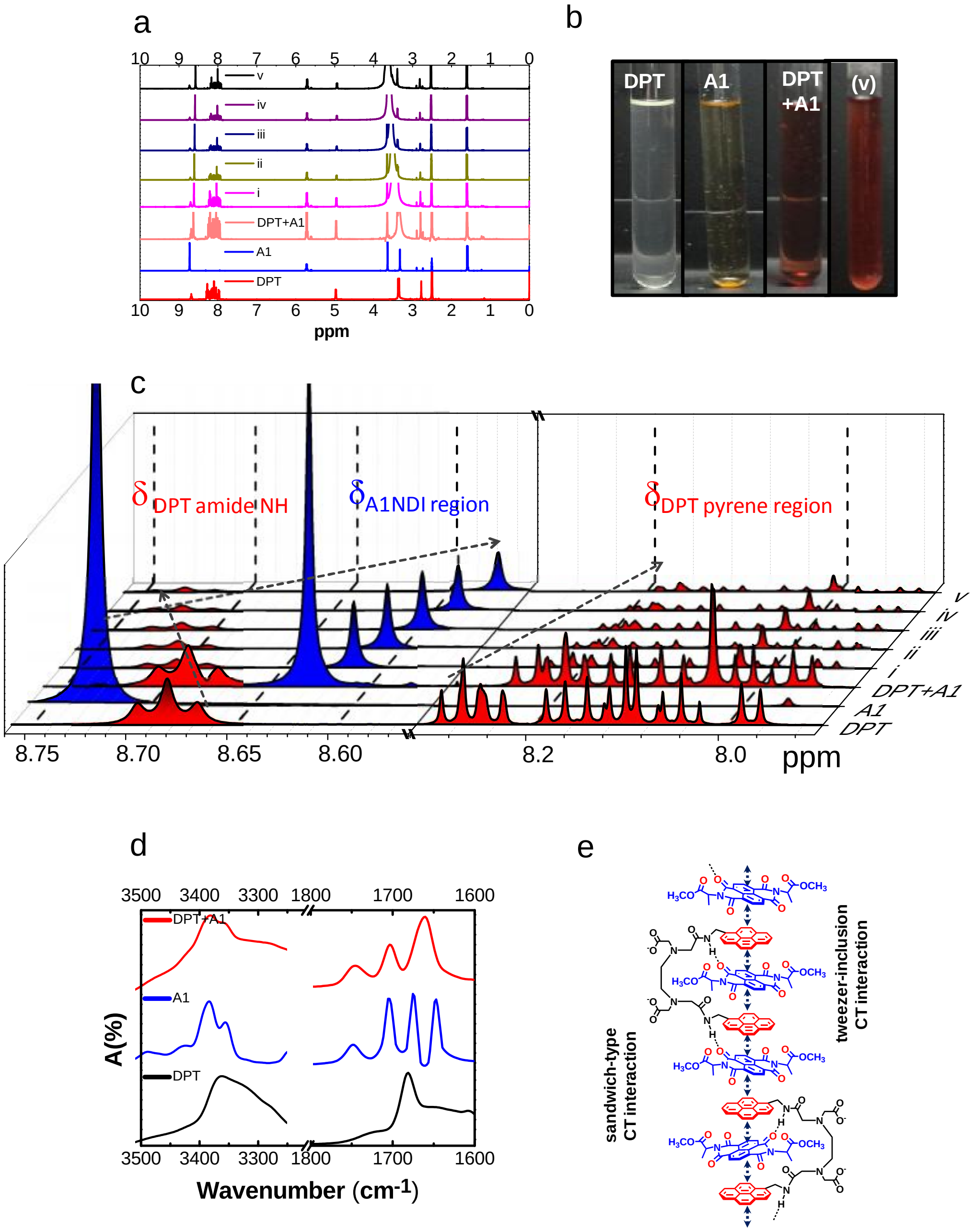

Figure 2.2.7 Solvent dependent ^{1}H-NMR (full) spectra of **DPT**:**A1** (1:2) in DMSO-d_6 as a function of addition of water; i) 4 μL, ii) 8 μL, iii) 16 μL, iv) 20 μL and v) 24 μL. b) Photographs of corresponding NMR sample solutions. c) The enlarged ^{1}H-NMR spectra of DPT amide region (8.76-8.66 ppm, red), A1 NDI aromatic ring region (8.75-8.55 ppm, blue) and DPT pyrene aromatic region (8.30-7.90 ppm); doted arrows indicate the chemical shifts upon addition of water. d) IR spectra of **DPT**, **A2** and **DPT**:**A1** (1:2) CT complex at Amide (NH) stretching frequency region (3200 to 3500 cm-1) and Carbonyl (CO) stretching frequency region (1600 to 1800 cm-1). e) Proposed model for the formation of extended mixed-stack tweezer- sandwich CT co-assembly between **DPT** and **A1**/**A2** via complementary π–surface stacking and hydrogen bonding interactions.

assembly of **DPT**:**A1** is a synergetic effect of complementary aromatic π-surface mixed-stacking interactions among **DPT** (pyrene , π–electron rich) and **A1** (NDI core, π–electron deficient) supported by intermolecular hydrogen bonding between **DPT** amide NH protons and imide CO of **A1** (Figure 2.2.7e).[165-166]

2.2.1.7 Morphological studies

The nanoscale morphology of **DPT**:**A1** CT co-assembly in hydrogel was investigated by field emission scanning electron microscopy (FESEM) and atomic force microscopy (AFM). FESEM micrographs of **A1** alone showed self-assembled 2D sheets with micrometer lateral dimensions (Figure 2.2.8a). However, under similar conditions **DPT** failed to show any ordered self-assembled structures. Interestingly, the xerogels of CT co-assembly of **DPT**:**A1** displayed interconnected network of high aspect ratio 1D fibrils (Figure 2.2.8b). The AFM section analysis on CT xerogel displayed hierarchical nanofiber bundles with an average topographical height of ~4-16 nm and width of ~ 60-150 nm (Figure 2.2.8c).

2.2.1.8 PXRD studies

The nature of molecular arrangement within 1D CT nanofibers of xerogel film was probed by using powder X-ray diffraction (PXRD) measurements and compared with that of individual **DPT** and **A1** films (Figure 2.2.8d). The film of **A1** (2D sheets) displayed a sharp diffraction peaks at 5.7° and 11.4° corresponding to molecular lateral dimensions suggesting crystalline molecular packing within the 2D sheets. On the other hand, **DPT** failed to show any significant diffraction signals indicating the amorphous nature. Remarkably, the 1D CT nanofibrous (xerogel film) displayed an intense sharp diffraction peaks at 5.7° and 11.4° along with the appearance of new diffraction peaks at 30.8° and 31° correspond to hydrogen bonding distances of 2.9 Å and 2.8 Å and revealed that

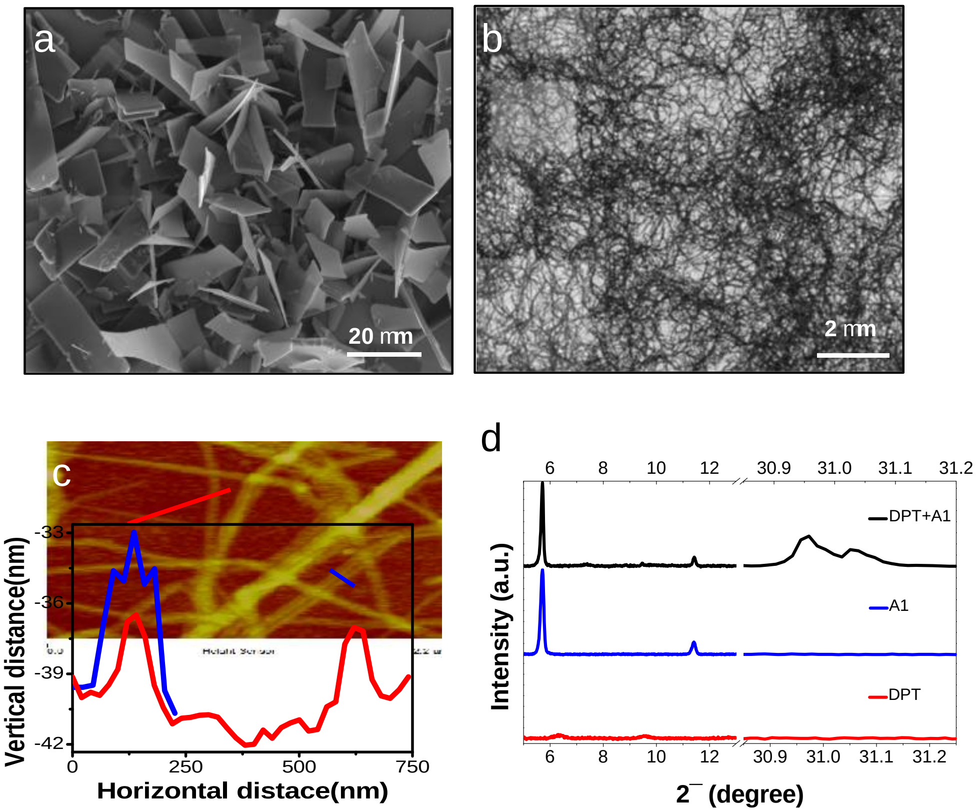

Figure 2.2.8 a) FESEM images of **A1.** b) FESEM images of **DPT**:**A1** (1:2) CT xerogel. c) AFM Section analysis of individual fibers and corresponding height profile along the blue and red line. d) PXRD pattern of **A1, DPT** and **DPT**:**A1**(1:2) xerogel film.

crystalline CT mixed-stacks are connected by hydrogen bonding interactions. The two diffraction signals for hydrogen bonding interactions further support the tweezer-inclusion and sandwiching type (TIS) CT co-assembly held together by two distinct hydrogen bonding interactions i.e., intra-tweezer and inter-tweezers interaction as shown in the Figure 2.2.7e. Overall, it is clear that the formation of 1D crystalline nanofibers of **DPT**:**A1** is the result of efficient synergy between intermolecular CT and hydrogen bonding interactions to form extended (D-A-D-A) co-assembly structures. Furthermore, the simplicity of fabrication on flexible substrate was demonstrated through the selected area CT (SACT) wherein we use the invisible **DPT** solution (UV-ink, blue under UV light) as ink to write (NCU) on a flexible filter paper and **A1** solution as a spray for visible (naked eye) readout in the form of brick-red CT complex formed in the written area (Figure 2.2.9). Such a simple solution processing method without requiring sophisticated instrumentation is a useful material property of **DPT** and **A1** and their CT co-assembly for creating inexpensive, effective, and scalable selected area CT complex microstructures on flexible substrates for large-scale device applications.

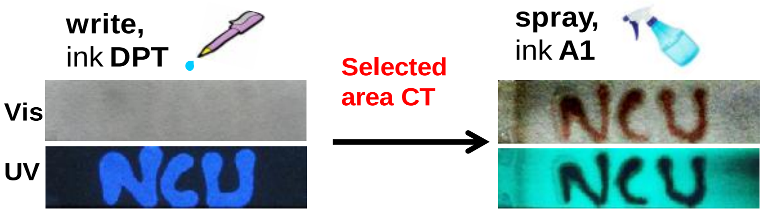

Figure 2.2.9 Demonstration of selected area CT (SACT) formation on flexible substrate; Photographs showing use of donor (**DPT**) as invisible UV-ink (visible under UV light) to write (e.g., NCU) on a filter paper and acceptor (**A1**/**A2**) spray aids the visible (naked eye) readout as the brick-red CT complex forms in the written area.

2.2.1.9 Ferroelectric measurements

To examine the existence of a finite polarization in **DPT**:**A1**(1:2) xerogel film, P-E loop were measured by fabricating sandwich structure devices (Figure 2.2.10). For the device fabrication, C-T mixture was introduced onto the bottom electrodes and the films were dried under a vacuum of 10^{-3} mbar. The top Au electrode is then coated on top of the supramolecular active layer (Figure 2.2.10a). A clean P-E loop was obtained at low frequency in the range of 100 Hz – 10 kHz with a clear saturation behaviour (Figure 2.2.10b). However, at higher frequencies leaky behaviour was obtained with an open loop. A combination of H-bonding and the propensity to form C-T complexes contribute to stronger aggregates in this material which gets reflected in the development of a finite polarization. It should be noted that the magnitude of polarization obtained with these thin

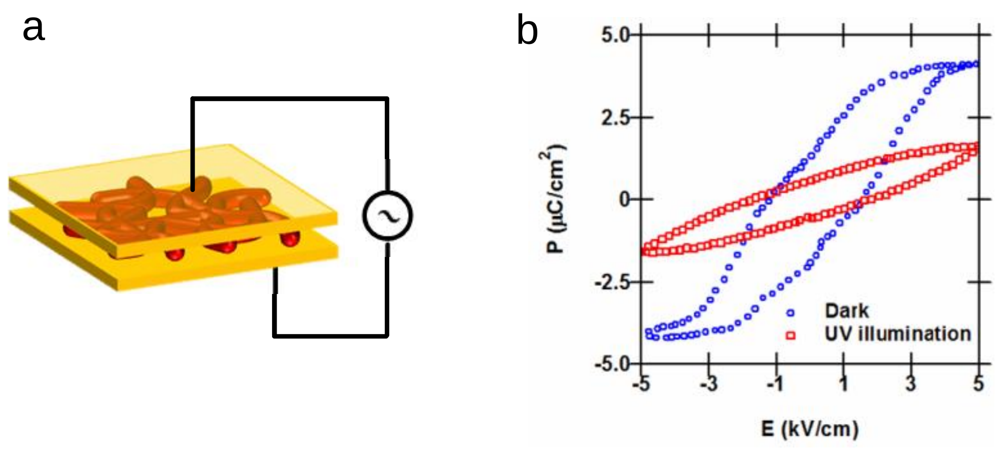

Figure 2.2.10 a) schematic of the device. B) P-E loop of **DPT**:**A1** CT xerogels in dark and under UV (365 nm) illumination.

films is relatively lower than ferroelectrics fabricated with crystals. This could be attributed to surface effects which affects the crystallinity in thin films. Furthermore, upon exposure of the thin films to UV illumination the ferroelectric saturation type behaviour is removed and a typical dielectric type behaviour is obtained (Figure 2.2.10b). This can be attributed to the dissociation of the D-A resulting in decreased CT interaction and hence deduction of FE nature.

2.2.2 Conclusion

In conclusion, we designed and demonstrated a new class of extended noncovalent mixed-stack charge-transfer (CT) co-assembly of tweezer di-pyrene **DPT** (pi-electron electron rich) and napthalenediimede **A1/A2** (pi-electron electron deficient), known n-type organic semiconductor through tweezer-inclusion-sandwich (TIS)-type organization supported by aromatic electron donor-acceptor CT and hydrogen bonding interactions in aqueous solution and in solid-state. The CT co-assembly (TIS) of **DPT**:**A1/A2** was achieved by external stimuli such as solvophobic and mechanical forces (ultrasonification and mechanical co-grinding). The CT co-assembly was confirmed by the mere transformation of colorless (fluorescent under UV light) solution or powder of **DPT** and **A1** to brick-red colour upon mixing and co-grinding, respectively. Interestingly, **DPT**:**A1/A2** CT co-assembly formed high aspect ratio 1D nanofibers that further transformed into hydrogel under external stimulus (ultrasonification). The mixed-stack CT co-assembly of **DPT**:**A1/A2** exhibited interesting stimuli responsive (UV light and temperature) supramolecular chiral organization. The 1D nanofibrous CT xerogel film exhibit volatile ferroelectric polarisation switching behavior in thin film-state near room temperature. Furthermore, we demonstrated the optically switchable energy efficient memory device under ambient conditions.

2.2.3 Green Fluorescent Naphthalenediimide: Conducting Layered Hierarchical 2D Nanosheets and Reversible Probe for Detection of Aromatic Solvents

2.2.3.1 Introduction

Two dimensional (2D) layered nanomaterials have attracted a great deal of attention from the scientific community in the past few years.[63,107-111,113,115,118-119,123,125,167-177] 2D nanostructures exhibit high specific surface area, interesting electronic, chemical, physical and biological properties that are important for sensing, catalysis, biomaterials, nano(bio)technology, storage, optical, dielectric and electronics related applications.[63,107-111,113,115,118-119,123,125,167-177] The well-known 2D nanomaterial graphene comprises of single to stacks of few one-atom-thick carbon layers and is the subject of intense research today. [107,176] Inspired by graphene, there is a growing interest in the development of new organic, inorganic and hybrid 2D nanomaterials.[63,110-111,113,115,118-119,123,125,167-175] Significant progress has been made in the development of inorganic 2D nanostructures.[123,125,173-175] There are few examples of organic 2D nanostructures based on biomolecules and synthetic polymers with limited scope and applications due to their large molecular size, low stability, difficulty in controlling the size and shape, and high cost associated with the processes.[63,110-111,113,115,118-119,167-172] In this context, small molecule-based supramolecular 2D nanostructures are of great interest in the area of organic electronics due to increased intermolecular interactions with neighbouring molecules which preserves the 2D molecular order inducing high field effect mobility.[108-109,177] In particular developing novel method of producing 2D nanostructures of n–type organic semiconductors is an highly promising area.[169] Among all n-type organic semiconductors naphthalenediimide attract considerable attention due to its intriguing applications ranging from biomedicine to electronics.[16,48,55,57,75-76,132-133,178-181]

In recent times bio-inspired approach has been employed by several research groups to design supramolecular systems and nanomaterials of NDIs with diverse structural, chemical and physical properties.[30,65,67,70,73,78,130,182] However, the fabrication of 2D nanostructures of NDI is still in its infancy owing to non-availability of novel and easy to adopt approaches for their preparation. We have recently reported the molecular engineering of symmetrically functionalized NDI with phenylalanine methylester to form conducting 2D nanosheets for the first time.[114] However, the supramolecular chirality was lost during the process of molecular self-assembly of symmetrical amino acid modified NDI to form 2D nanosheets.[114] Therefore 2D nanostructures with retention of supramolecular chirality remain to be achieved. This inspired us to develop 2D nanostructures of asymmetrically functionalized NDIs having well-defined size and shape with retention of chirality in the supramolecular aggregated state. Herein, we report a simple design strategy to produce conducting 2D nanosheets with high-level molecular ordering from a most promising asymmetrically functionalized NDI by self-assembly approach.[183]

Asymmetrically functionalized **eNA** was designed with simple ethyl and amino acid (D-**eNA** and L-**eNA** correspond to NDI with D- and L-alanine methylester functionality respectively) groups as imide substituent's as shown in Figure 2.2.11a. The planar, electron deficient π-conjugated NDI core facilitates π–electron delocalization and favours the strong intermolecular π–π stacking, α–alanine transfer chiral information to central achiral NDI core and enforce the chiral self-assembly,[41,184-185] and ethyl group enhances the solubility and intermolecular hydrophobic interactions. This design was envisioned to have a compact molecular system and thereby induce efficient molecular packing as desirable for its optical performance. Optical and microscopy studies revealed that **eNA** form chiral supramolecular assemblies which undergo further self-organization to form highly crystalline green fluorescent, and thin layered hierarchical 2D nanosheets spanning

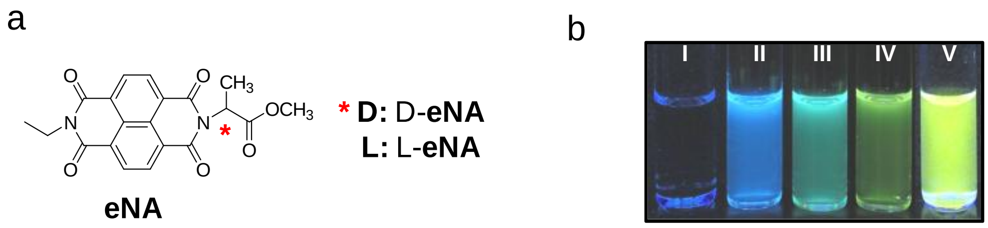

Figure 2.2.11 a) Molecular structure of **eNA** (*D-**eNA** and L-**eNA** corresponds to NDI with D- and L- alanine methylester functionality respectively). b) Tunable multicolour fluorescence of **eNA** in I: DMSO, II: benzene, III: toluene, IV: xylene and V: aqueous solution (H_2O/DMSO: 80/20) under UV light (365 nm).

several micrometers in lateral dimensions. Furthermore, **eNA** in various solvents exhibited multicolour emission (408-540 nm) Figure 2.2.11b).

2.2.3.2 Photophysical studies

The optical properties of **eNA** in dimethyl sulfoxide (DMSO), aqueous (H_2O/ DMSO: 80/20, v/v) and aromatic solvents (benzene, toluene and xylene) were investigated by UV-vis absorption and fluorescence emission (FE) studies (Figure 2.2.12). Absorption studies in DMSO and aromatic solvents displayed well-resolved sharp absorption bands in the range of 300-400 nm (band I), which is attributed to the characteristic $\pi-\pi*$ transitions polarized along the long axis (Z-axis) of NDI chromophore. In aqueous solution significant spectral changes were observed with appreciable hypochromicity, band broadening along with the appearance of a new absorption band at 405 nm suggesting the presence of strong intermolecular $\pi-\pi$ stacking between the NDI chromophores (Figure 2.2.12a).[186-187] In FE studies a very weak fluorescence band with emission maximum at 408 nm corresponding to monomeric emission of NDI was observed in DMSO. Remarkably **eNA** in aqueous solution exhibited a new emission band (broad) in the lower energy region (470-600 nm) with maximum at 540 nm (Figure 2.2.12b) attributed to excimer emission as a consequence of charge delocalization among

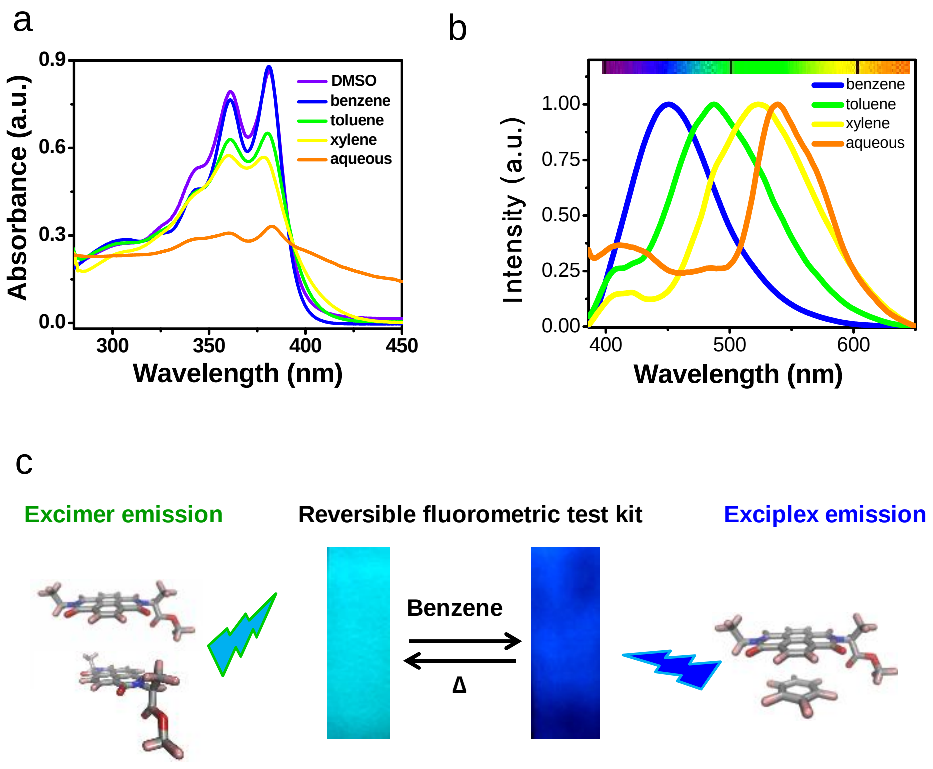

Figure 2.2.12 a) UV-vis absorption and b) Fluorescence emission spectra of D-**eNA**. c) Filter paper based reversible fluorometric test kit for the detection of benzene and the schematic representation of excimer (NDI dimer interaction) and exciplex (NDI-benzene interaction) emission.

the closely packed NDI chromophore induced by the hydrophobic effect.[65,67,78] Interestingly, aromatic solvents displayed tunable fluorescence emission properties in the visible spectrum going from blue to greenish yellow (λ_{max}= 450, 487 and 523 nm for benzene, toluene and xylene respectively) with large Stokes shifts (Figure 2.2.12b). The absence of vibronic spectral changes in the UV-vis absorption spectra together with the corresponding gradual red shifting of FE spectra in the aromatic solvents suggest the excited state specific solvent-fluorophore interactions (or excited state exciplex formation).[97,188] Next we have also developed a filter paper based reversible fluorometric test kit for the detection of benzene which is a classified carcinogen (Figure 2.2.12c). The filter paper strip was coated with D-**eNA** in chloroform and the solvent was evaporated.

This filter paper exhibit cyan fluorescence and turns into bright blue fluorescence on exposure to benzene under UV light. Upon warming the filter paper the blue fluorescence changes to its original cyan fluorescence due to evaporation of benzene rendering reversibility to our filter paper based detection.

2.2.3.3 CD studies

In order to understand the effect of α-alanine methylester (imide substituent) chirality on the molecular assembly of achiral NDI chromophore, we performed circular dichroism (CD) measurements of **eNA** in DMSO and aqueous solution (Figure 2.2.13). The flat CD signals were observed for L-**eNA** and D-**eNA** in DMSO due to absence of molecular assembly which is in agreement with UV-vis absorption and FE studies (Figure 2.2.12). Remarkably, in aqueous solution L-**eNA** and D-**eNA** showed strong mirror image electronic CD spectra at molecular aggregation band (405 nm) and band I (300-400 nm) regions. These CD signals are ascribed to the chiral intermolecular assembly of molecules along the long axis of NDI chromophore.[41,184-185] Accordingly the negative and positive CD signals of D-**eNA** and L-**eNA** at 405 nm indicates M-type and P-type helical stacking

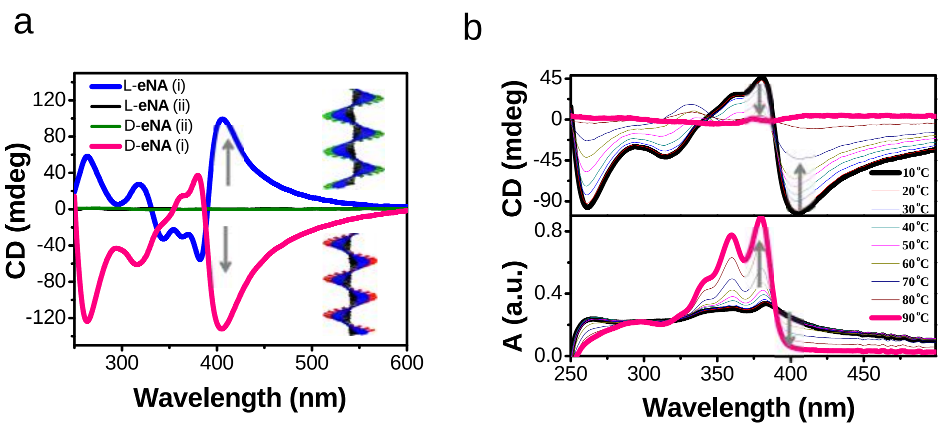

Figure 2.2.13 a) CD spectra of D-**eNA** and L-**eNA** in DMSO (i) and aqueous solution (ii, H_2O/DMSO: 80/20), arrows indicate the spectral changes. b) Variable temperature UV-vis and CD spectra of D-**eNA** in aqueous solution.

of NDI chromophores governed by the stereochemistry of α-amino acid unit (Figure 2.2.13a). This confirms the induction of supramolecular chirality by the α-alanine through central achiral NDI chromophoric unit.[30] Chiral supramolecular assemblies are strongly dependant on temperature and variable-temperature (VT) UV-vis and CD studies in aqueous solution (20 °C to 90 °C) indicated the presence of thermally stable chiral supramolecular assemblies in the range of 20 °C to 80 °C and convert into molecularly dissolved state ≥ 90 °C. (Figure 2.2.13b).

2.2.3.4 Morphological studies

The morphology corresponding to chiral supramolecular self-assembly structures of **eNA** were investigated by drop casting the aqueous solution on silicon (111) surface. FESEM (field emission scanning electron microscopy) images revealed the presence of flat and laterally extended rectangular nanosheets with 10 to 40 µm lateral dimensions (Figure 2.2.14a) while confocal images showed the intrinsic green fluorescence from 2D sheets (Figure 2.2.14a, inset). HRTEM (high-resolution transmission electron microscopy) measurements revealed the presence of layered hierarchy in 2D nanosheets (Figure 2.2.14b), where each sheet is a stack of few layers of much thinner nanosheets. The selected area electron diffraction (SAED) pattern recorded on these nanosheets exhibited well-resolved diffraction patterns (Figure 2.2.14b, inset), revealing the crystalline ordering of molecules within the nanosheets. AFM (atomic force microscopy) data revealed topographical thickness of ~ 9.6 - 89 nm (red and black lines) for D-**eNA** nanosheets with smooth lateral surface (Figure 2.2.14c and d). AFM image also confirm the layered hierarchy of sheets in agreement with the HRTEM data (Figure 2.2.14b). Section analysis of AFM image of an isolated 2D sheet showed that the thickness of single layer in a hierarchical sheet is about 9.6 nm (Figure 2.2.14c, inset) and roughly around five-six such thin layers stacks together to form the observed hierarchical 2D

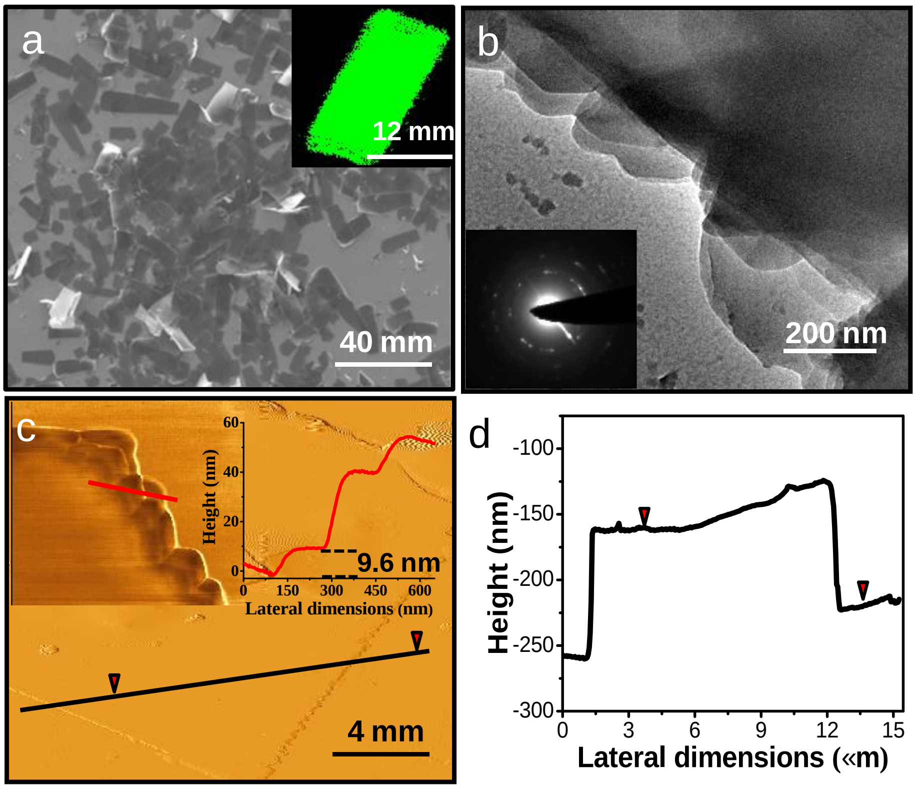

Figure 2.2.14 a) FESEM image of D-**eNA** (inset: fluorescence confocal images) nanosheets from aqueous solution. b) HRTEM image of D-**eNA** nanosheet (inset: SAED pattern). c) AFM image of D-**eNA** nanosheet (insets: section analysis of AFM images with height profile, stepwise height ~ 9.6 – 58 nm). d) AFM height profile (topographical thickness ~ 89 nm along the black line in (c).

nanosheet of ~ 58 nm. On the other hand, L-**eNe** showed similar nanostructures under similar conditions.

2.2.3.5 Thin film CD

To validate retention of supramolecular chirality in 2D nanosheets formed from aqueous solution of **1**, thin film CD studies were performed. The observed mirror image CD cotton effects (D-**eNe** and L-**eNe**) confirmed the retention of molecular chiral assembly within the nanosheets (Figure 2.2.15a). furthermore LD studies displayed a flat spectral features suggesting the lack of any LD artefacts for the observed mirror image CD spectra of D-**eNe** and L-**eNe** respectively (Figure 2.2.15b).

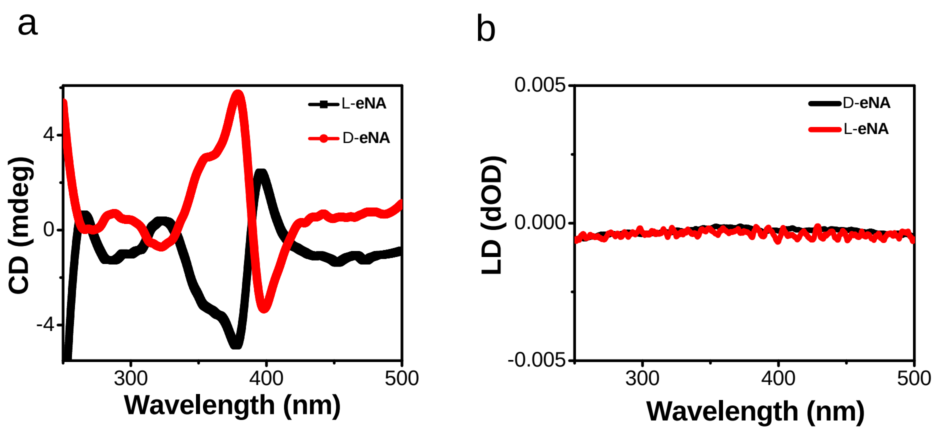

Figure 2.2.15 a) Thin film CD spectra of L-**eNA** and D-**eNA**. b) Linear dicroism (LD) spectra of L-**eNA** and D-**eNA**.

2.2.3.6 DLS and PXRD studies

We also performed DLS (dynamic light scattering) study to confirm the presence of pre preformed self-assembled structures in aqueous solution. DLS study revealed the presence of self-assembled free-standing nanostructures with mean size 956 nm in aqueous solution (Figure 2.2.16a).

PXRD (powder X- ray diffraction) studies indicated the crystalline arrangement of molecules and preferred orientation of molecular planes with in the 2D nanosheets (Figure 2.2.16b). The obtained diffraction peaks of D-**eNA** were indexed with the TREOR 90 program with lattice parameters *a* = 20.0759 Å, b = 6.4481 Å and c =18.8193 Å in a monoclinic crystal system (Experimental section). A sharp and intense reflection in the low-angle region at 15.3 Å correlates well with the calculated energy minimized full length of **eNA** (15.4 Å) (Figure 2.2.16b inset). Reflections at 5.4 Å and 3.4-3.5 Å correspond to intermolecular and interplanar distances between stacked NDI chromophores respectively.[109] The detailed spectroscopic studies suggest the presence of π–stacking and π–extending along the long and short axis of NDI chromophore

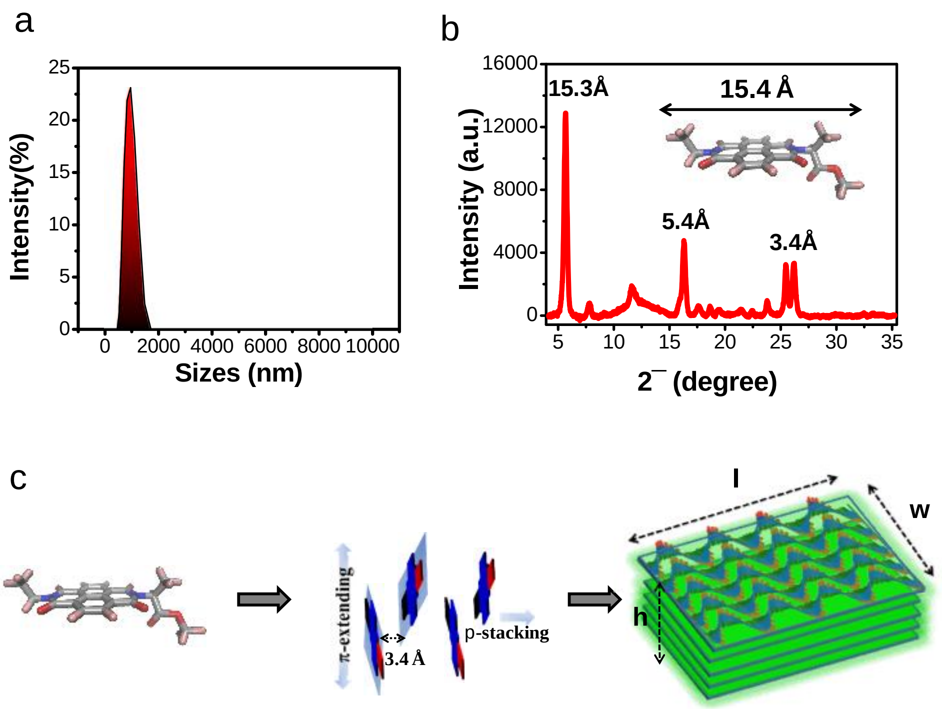

Figure 2.2.16 a) DLS plot of D-**eNA** in aqueous solution. b) PXRD pattern of D-**eNA** nanosheets. c) Schematic representation of chiral molecular self-assembly of **eNA** into green fluorescent layered hierarchical 2D nanosheet, height (h) ~ 9.6 - 89 nm, length (l) = 10 to 40 µm and width (w) = 5 to 20 µm.

respectively, in the self-assembled 2D nanosheets. The schematic representation of proposed molecular arrangement is shown in Figure 2.2.16c, which is in close agreement with the experimental results. This clearly explains the mechanism of molecular self-assembly of **1** to form chiral supramolecular helices and subsequent self-organization of helices to hierarchical 2D nanosheets.

2.2.3.7 I-V measurements

STM was employed to measure the conducting nature of nanosheets. Interestingly the I-V (current-voltage) response (Figure 2.2.17) showed non-linear behaviour with linear conductance 2.22 nS (slope of linear Ohmic region between -0.3 and 0.3 V) signifying semiconducting nature of 2D nanosheets.

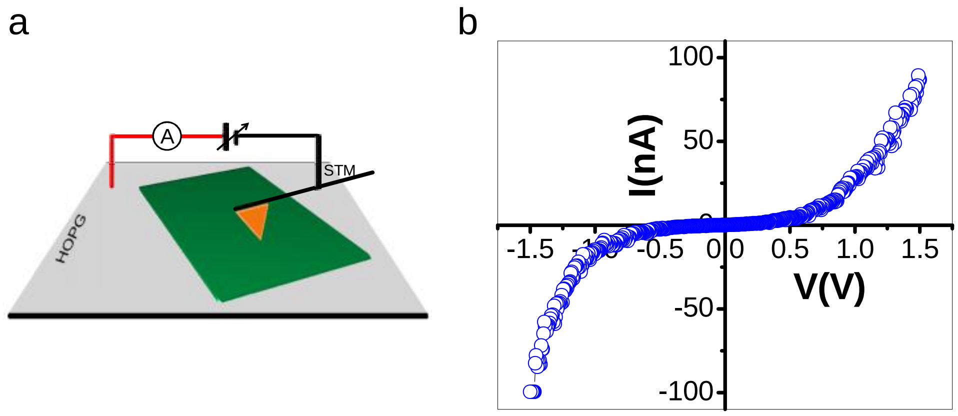

Figure 2.2.17 a) Schematic of the STM measurements on a 2D nanosheet of eNA. b) STM current-voltage (I-V) plot.

2.2.3.8 Conclusions

In summary, we demonstrated the molecular engineering of asymmetrically functionalized NDI with a simple amino acid into robust green fluorescent conducting 2D nanosheets. The 2D nanostructures with optimized crystalline molecular packing have implications in organic electronics and biomaterials applications. Furthermore this NDI molecular system is optically highly sensitive to aromatic solvents and therefore can be used for organic multicolour displays and fluorescent probe for aromatic solvents. We developed a filter paper based reversible fluorometric test kit for the detection of carcinogenic benzene. In general this work offers a novel way of producing organic 2D nanostructures with chiral molecular ordering and has the potential to influence future development of 2D nanoarchitectonics and chiroptical applications.

Subchapter 2.3 Biomolecule Appended Naphthalenediimides as Novel Class of Aβ Aggregation Modulators: Implications for Disease-Modifying Therapeutics of Alzheimer's Disease

2.3.1 Introduction

Alzheimer's disease (AD) has been identified as one of the most common neurodegenerative disorder worldwide with progressive impairment of cognitive abilities leading to dementia and death in elderly population.[189] The prevalence of AD increases with age and affecting large population over the age of 60 years. Neurodegeneration in the cerebral cortex and hippocampus due to formation of extracellular amyloid/senile plaques (SP) and intracellular neurofibrillary tangles (NFT) is the cardinal features of this disease process.[190-191] Aggregation of $A\beta_{1-42}$ peptide and hyperphosphorylated tau protein (in the form of amyloid plaques and neurofibrillary tangles) are strongly implicated in the neurodegeneration of AD.[192] Thus, protein misfolding, aggregation and depositions of the aggregates, which trigger an array of events ultimately leading to neurotoxicity is central to the AD progression.[193-194] Due to multifactorial nature of AD, precise etiology of the disease process is poorly understood. Several hypotheses have been proposed on the pathophysiology of AD and most of them indicating increased production/accumulation of cerebral amyloid plaques.[195-198] The major component of these plaques is amyloid-beta ($A\beta_{1-42}$) peptide, a cleavage product of the amyloid precursor protein (APP). The degree of cognitive impairment in AD patients was found to co-relate with the Aβ accumulation in the brain.[199-200] Although significant efforts from the past few decades yielded several drugs, most of these drugs are symptomatic in nature and offer limited treatment options. Therefore, there is dire unmet need for the development of disease-modifying AD therapeutics. Research on modulation of $A\beta_{1-42}$

aggregation pathways is an emerging approach towards developing disease-modifying AD therapeutics. Towards this end, several groups have reported inhibitors of A$\beta_{1\text{-}42}$ aggregation or disaggregation compounds [200-203] but still there is no common approach for modulating the A$\beta_{1\text{-}42}$ aggregation pathway and dissolution of pre-formed aggregates. In this regard, few natural polyphenolic compounds (Figure 2.3.1) demonstrated promising disrupting effect on amyloidogenic polypeptide self-assembly by perturbing the hydrophobic forces within the aggregated polypeptides via several non-covalent interactions including aromatic, electrostatic, van der Waals and solvophobic forces.[204-206] In addition phenolic compounds also exhibited excellent antioxidant properties.

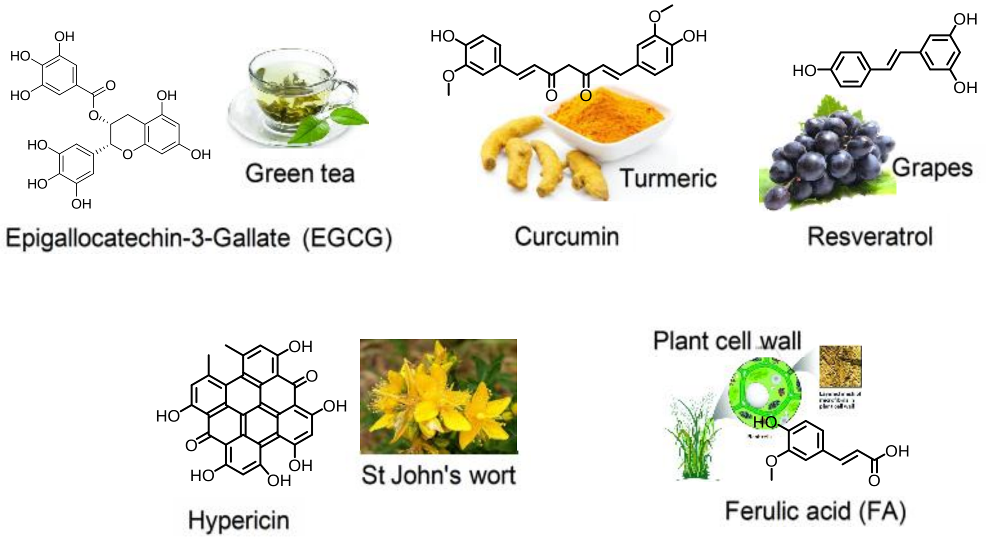

Figure 2.3.1 Chemical structures of few small phenolic amyloidogenic polypeptide modulators and their natural sources.

These observations inspired us to investigate the biomolecule appended naphthalenediimide (NDI) based on the fact that it possess compact planar aromatic skeleton which can fit in to the hydrophobic pocket of A$\beta_{1\text{-}42}$ aggregates. Further, we hypothesized that the functionalization of NDI with polyphenolic biomolecules of natural origin can potentially modulate the A$\beta_{1\text{-}42}$ aggregation process via hydrophobic interaction and hydrogen bonding. In this regard, we used various amino acids (Glycine in **GNG**, Alanine in **ANA**, Tryptophan in **WNW**, Phenyl alanine in **FNF**), well known polyphenolic neurotransmitter dopamine in **Dp** and its precursor L-DOPA in **LD** as potential hydrogen bonding and/or hydrophobic interacting moieties with the hydrophobic pockets of Aβ_{1-42}. The biomolecule conjugated NDIs were prepared by condensing them in 1,4,5,8-naphthalene-tetracarboxylic dianhydride to make symmetrical NDI conjugates (Figure 2.3.2). NDI also known as naphthalene carbodiimides are well-known π–electron deficient planar aromatic compounds and widely used for organic semiconducting materials and supra-molecular science.[57,207]

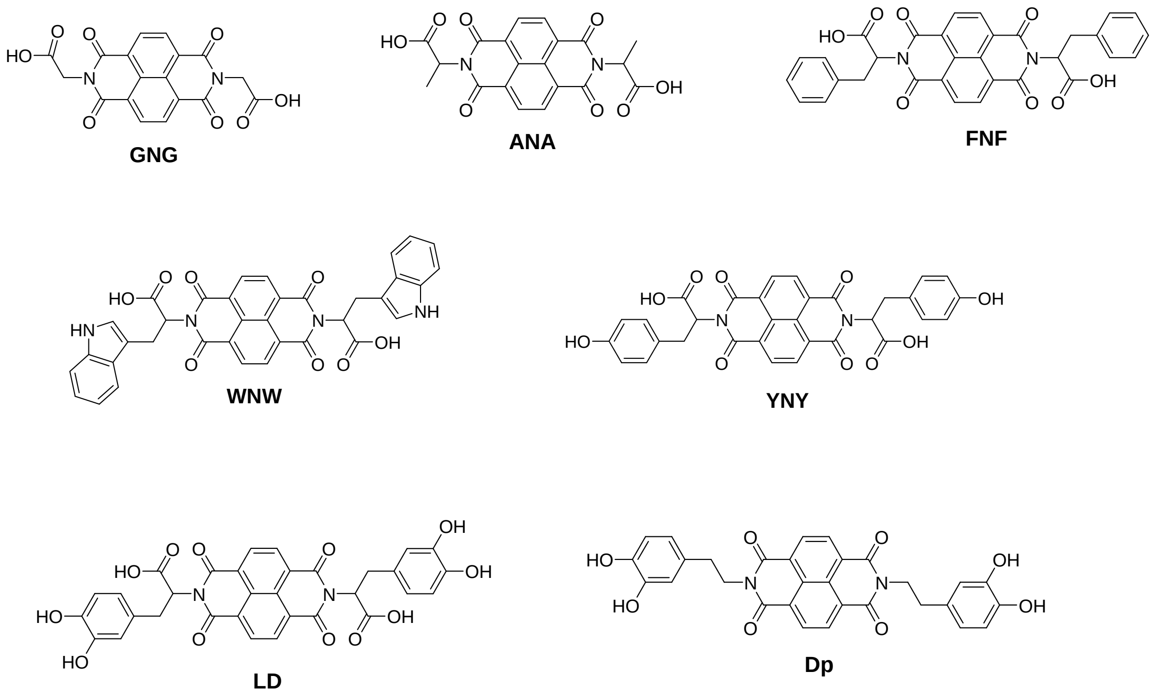

Figure 2.3.2 Chemical structures of biomolecule conjugated naphthalenediimides (NDIs).

For the past few decades, NDI have emerged as versatile molecular template for designing various compounds. NDI based compounds have variety of applications such as DNA intercalators and photodynamic therapy (PDT). NDIs are thermally stable molecules with potential choice of covalent modifications at naphthalene core and the nitrogen of imide groups.

2.3.2 Results and discussion

2.3.2.1 Synthesis

We designed and synthesized a novel series of naphthalenediimide (NDI) based compounds using various bioactive molecules such as amino acids (Gly, L-Ala, L-Phe, D-Phe, L-Phg, L-Tyr, D-Trp, L-Trp), dopamine and L-DOPA. Under mild reaction conditions 1,4,5,8-naphthalene-tetracarboxylic dianhydride was condensed with primary amines of above said bioactive molecules to yield symmetrical biomolecule conjugated NDIs in excellent yields. A simple recrystallization was employed to obtain pure compounds, without requiring to need for any column chromatographic purification. The structural integrity of synthesized NDIs were confirmed by ^{1}H-NMR and ESI-Mass spectral analysis.

2.3.2.2 Fluorescence studies on the modulation effect of NDI compounds against Aβ$_{11\text{-}25}$ pathway

Initially, NDI compounds were screened for their Aβ aggregation inhibition and dissolution efficacies using Aβ fragment (11-25) sequence with key amino acids which are strongly implicated in aggregation process.

2.3.2.2.1 Aggregation inhibition studies

In this experiment, 200uM of Aβ fragment (11-25) was either incubated alone or with NDIs at 1:1 ratio for 48 h. Fluorescence studies with ThT showed high fluorescence for 200uM Aβ alone indicating the formation of fibrils (Figure 2.3.3). Aβ fragment incubated with compounds **GNG**, **ANA** showed fluorescence slightly lesser than Aβ fragment alone while compounds **FNF**, **YNY** showed moderate fluorescence. Further,

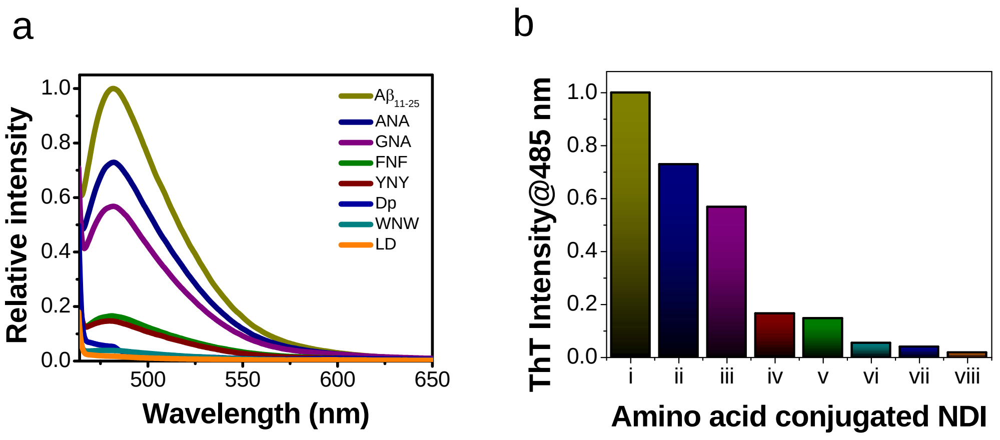

Figure 2.3.3 a) Fluorescence study on the inhibition of Aβ$_{11-25}$ aggregates with NDI conjugates by ThT assay. The data shows the effects of different NDI conjugates on the aggregation inhibition of 200uM Aβ$_{11-25}$ (after 48 h incubation at 1:1 molar ratios of Aβ$_{11-25}$:NDI compound). Values are the normalized maximal fluorescence intensity at 485 nm compared to that of the control (Aβ$_{11-25}$ without NDI conjugates). b) The plot of fluorescence intensity at 485 nm as a function of different NDI conjugates, i) Aβ$_{11-25}$, ii) **ANA**, iii) **GNA**, iv) **FNF**, v) **YNY**, vi) **Dp**, vii) **WNW** and viii) **LD**

compounds **WNW**, **Dp**, and **LD** showed minimal fluorescence (Figure 2.3.3a). This data suggests that possible aggregation inhibition property of compounds **WNW**, **Dp**, **LD** **(**igure 2.3.3b).

2.3.2.2.2 Disaggregation/Dissolution studies

Next, we performed disaggregation/dissolution of pre-formed Aβ fragment (11-25) fibrils using NDIs. Pre-formed fibrils incubated with conjugates **LD**, **Dp**, **WNW** showed minimal fluorescence indicating efficient disaggregation of fibrils. Conjugates **FNF** and

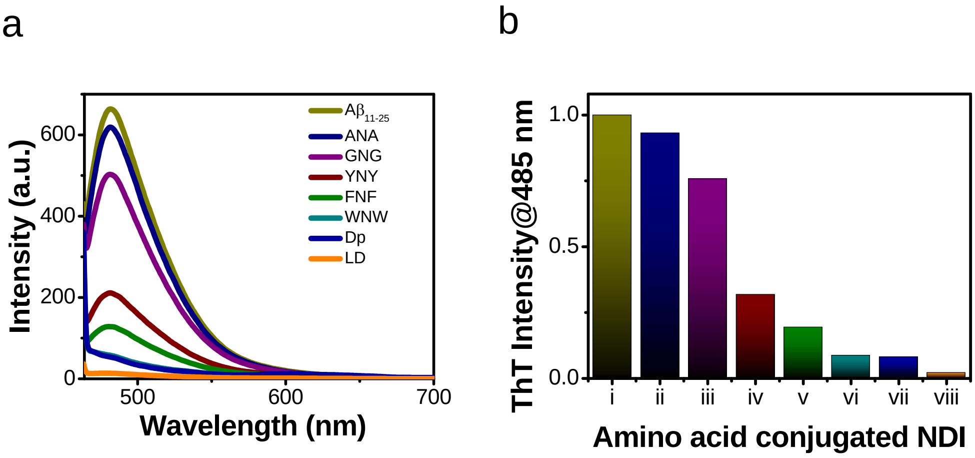

Figure 2.3.4 a) Fluorescence study on the dissolution of Aβ_{11-25} aggregates with NDI conjugates by ThT assay. The data shows the effects of different NDI conjugates on the disaggregation of 200uM Aβ11-25 pre-formed aggregates (after 48 h incubation) and further incubated for 24 h at 1:1 molar ratios of Aβ_{11-25}:NDI compound. Values are the normalized maximal fluorescence intensity at 450 nm compared to that of the control (Aβ_{11-25} without NDI conjugates). b) The plot of fluorescence intensity at 485 nm as a function of different NDI conjugates. i) Aβ_{11-25}, ii) **ANA**, iii) **GNA**, iv) **YNY**, v) **FNF**, vi) **WNW**, vii) **Dp** and viii) **LD.**

YNY showed moderate efficiency as depicted in Figure 2.3.4 while conjugates **GNG** and **ANA** did not show any dissolution activity of fibrils. Based on this preliminary screening for dissolution of pre-formed Aβ_{11-25} aggregates with different NDI conjugates, we further tested the efficacies of these conjugates in time and concentration dependent manner. In these studies, each compound in selected concentrations (10, 25, 50 µM) was incubated with Aβ_{11-25} fragment fibrils for 0, 1, 2, 3 and 6 days. Results showed that there is an increasing trend in disaggregation of fibrils by conjugates as shown in Figure 2.3.5.

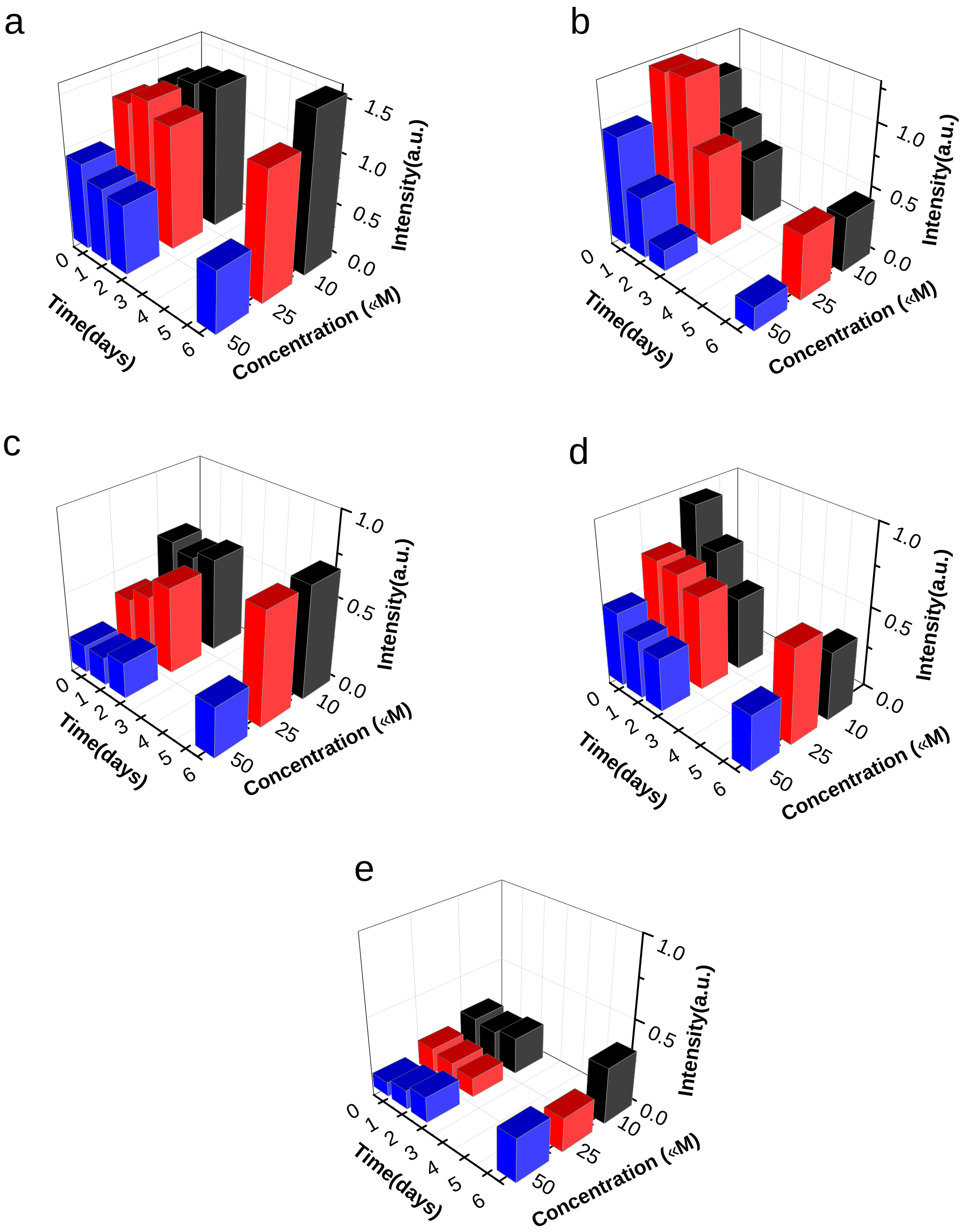

Figure 2.3.5 Fluorescence study on the time dependent dissolution of Aβ_{11-25} aggregates with NDI conjugates; a) **YNY**. b) **FNF**. c) **WNW**. d) **LD**. e) **Dp**. The data shows the effect of NDI compound at different time points (1-6 days) on the disaggregation of 200 uM Aβ_{11-25} pre-formed aggregates (after 48 h incubation) and further incubation for 24 h at 1:1 molar ratios of Aβ_{11-25}:NDI compound. Values are the normalized maximal fluorescence intensity at 485 nm compared to that of the control (Aβ_{11-25} without NDI conjugates)

2.3.2.3 Aggregation inhibition and dissolution of A $_{1-42}$ with NDI conjugates

Results from initial screening of NDI conjugates with Aβ_{11-25} fragment prompted us to evaluate the potential of these conjugates against Aβ_{1-42} peptide aggregation and dissolution. We performed a systematic study with selective NDI conjugates from preliminary screening i.e. **LD**, **Dp**, **WNW**, **FNF** along with inactive compound **ANA** and Aβ_{1-42} peptide. In this aggregation inhibition study, 20 μM of Aβ_{1-42} in 1X PBS either was incubated alone or with 20 μM of NDI conjugates for 24 h at room temperature and fluorescence spectra were recorded in presence of 10 μM ThT. After 24 h, we found that conjugates **LD, Dp** showed highest inhibition activities followed by **WNW** and **FNF** **(**Figure 2.3.6**)** while **ANA** was did not show any inhibition. These findings are consistent with the previous results using Aβ_{11-25} **(**Figure 2.3.3). For dissolution experiment, 50 μM of Aβ_{1-42} in 1X PBS was incubated for 24 h followed by co-incubation with 20 μM of each NDI conjugates with 20 μM of Aβ_{1-42} for another 48 h. Results showed maximum

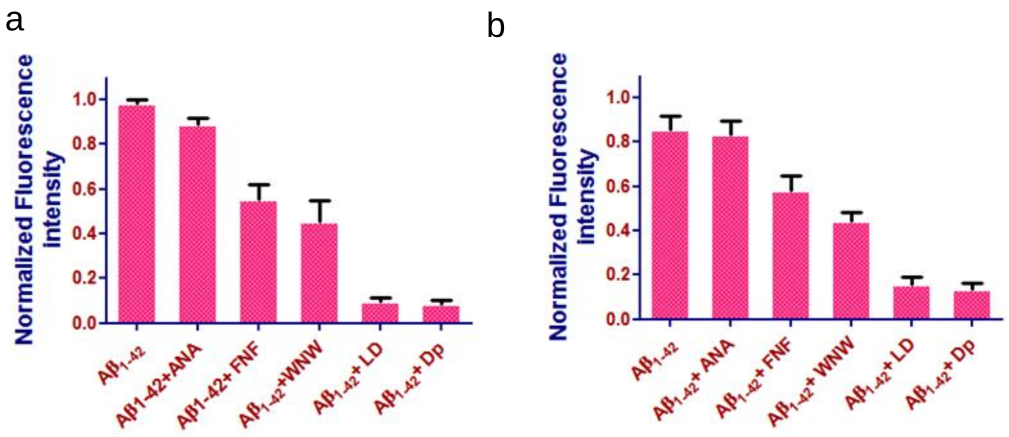

Figure 2.3.6 Fluorescence study on the aggregation inhibition (a) and dissolution (b) of Aβ_{1-42} aggregates with NDI conjugates by ThT assay. The data shows the effects of different NDI conjugates on the inhibition of 20 μM Aβ_{1-42} with 20 μM NDI conjugates (A) and disaggregation of 20uM Aβ_{1-42} pre-formed aggregates (after 24 h incubation) and further incubated for 48 h at 1:1 molar ratios of Aβ_{1-42}:NDI compound. Values are the normalized maximal fluorescence intensity at 450 nm compared to that of the control (Aβ_{1-42} without NDI conjugates).

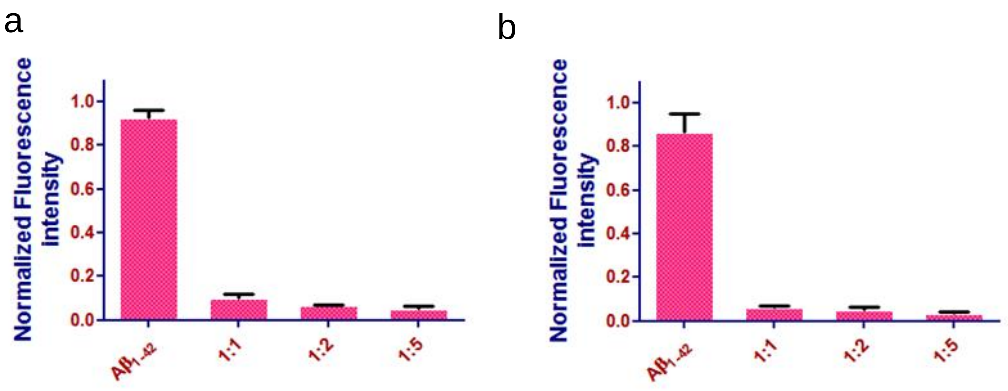

Figure 2.3.7 Fluorescence study on the concentration dependent aggregation inhibition of Aβ$_{1-42}$ with a) **LD** and b) **Dp** by ThT assay. The data shows the effects of **LD**, **Dp** on the inhibition of 20 µM Aβ$_{1-42}$ with 20 µM NDI conjugates at 1:1 molar ratio. Values are the normalized maximal fluorescence intensity at 450 nm compared to that of the control (Aβ$_{1-42}$ without NDI conjugates).

dissolution efficiency for **Dp** and **LD** followed by **WNW** and **FNF.** However, ANA didn't show any dissaggregation activity (Figure 2.3.6b**).** With the results from Aβ$_{1-42}$ aggregation inhibition in hand, we further evaluated the lead conjugates **LD**, **Dp** for concentration dependent activity in inhibiting the Aβ$_{1-42}$ aggregation. Results showed that **LD** and **Dp** inhibited the Aβ$_{1-42}$ aggregation in concentration dependent manner with highest inhibition at 1:5 ratio of Aβ$_{1-42}$ and **LD/Dp** (Figure 2.3.7).

2.3.2.4 Toxicity profile of extracellular Aβ$_{1-42}$ aggregates (preformed) in PC12 Cells

After successful establishment of modulating effects of NDI conjugates with both Aβ$_{11-25}$ and Aβ$_{1-42}$ aggregation from ThT fluorescence studies, we next sought to check the toxicities of pre-formed Aβ$_{1-42}$ aggregates in Pheochromocytoma cells (PC12) of the rat adrenal medulla. For this experiment, we have incubated 100 µM of Aβ$_{1-42}$ in 1X PBS for 24 h at 37 ^{o}C to generate Aβ$_{1-42}$ aggregates and to evaluate the toxicities of extra-cellular generated aggregates in PC12 cells. In this experiment, PC12 cells were treated with Aβ$_{1-42}$ aggregates at different concentrations (10, 7.5, 5, 2.5, 1 µM) for 24 h. The

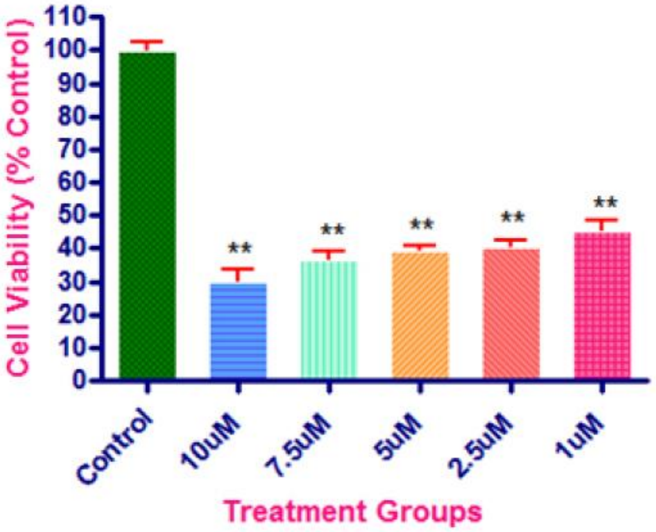

Figure 2.3.8 Effect of treatment of concentration dependent prefabricated Aβ_{1-42} aggregates on cell viability of PC12 cells. PC12 cells were treated with 10-1 µM prefabricated Aβ_{1-42} aggregates obtained after incubating 100 µM Aβ_{1-42} in 1X PBS for 24 h. Values shown are means ± SEM of four independent experiments performed in four to six replicates. One-way ANOVA analysis followed by Tukey's multiple comparison post hoc test was performed (**$p < 0.001$ compared to control).

main objective of this experiment was to decide optimal concentration (~50%) of Aβ_{1-42} aggregates causing cell death. Thus, we found a concentration dependent toxicity profile (~30% for 10 µM to ~45% for 1 µM) upon Aβ_{1-42} aggregates treatment for 24 h at different concentrations (Figure 2.3.8).From the above data, we opted for 1 µM final concentration for the aggregation inhibition and dissolution experiments in presence of **LD** and **Dp**.

2.3.3 Assessment of LD, Dp to alter cytotoxicity in PC12 cells induced by extracellular Aβ_{1-42} aggregates

Initially, we assessed the PC12 cell viabilities in presence of **LD** and **Dp** at varying concentrations (20, 10, 5, 1 µM) for 24 h with MTT assay. Results showed that **LD** was not toxic to PC12 cells even at 20 µM concentration while **Dp** had significant toxicities

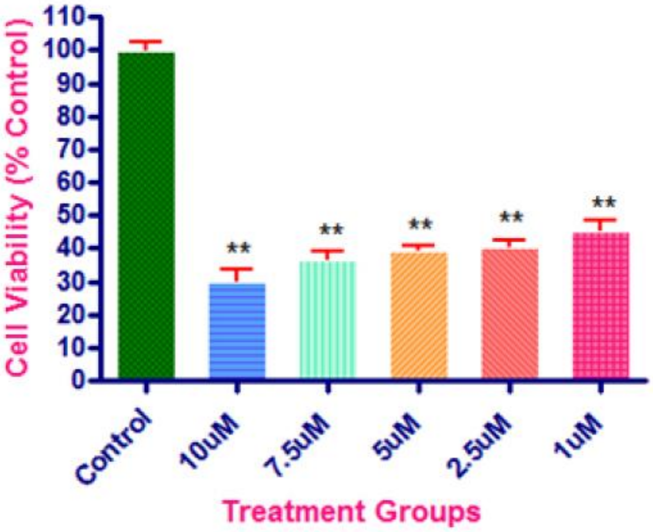

Figure 2.3.8 Effect of treatment of concentration dependent prefabricated Aβ_{1-42} aggregates on cell viability of PC12 cells. PC12 cells were treated with 10-1 μM prefabricated Aβ_{1-42} aggregates obtained after incubating 100 μM Aβ_{1-42} in 1X PBS for 24 h. Values shown are means ± SEM of four independent experiments performed in four to six replicates. One-way ANOVA analysis followed by Tukey's multiple comparison post hoc test was performed (**p < 0.001 compared to control).

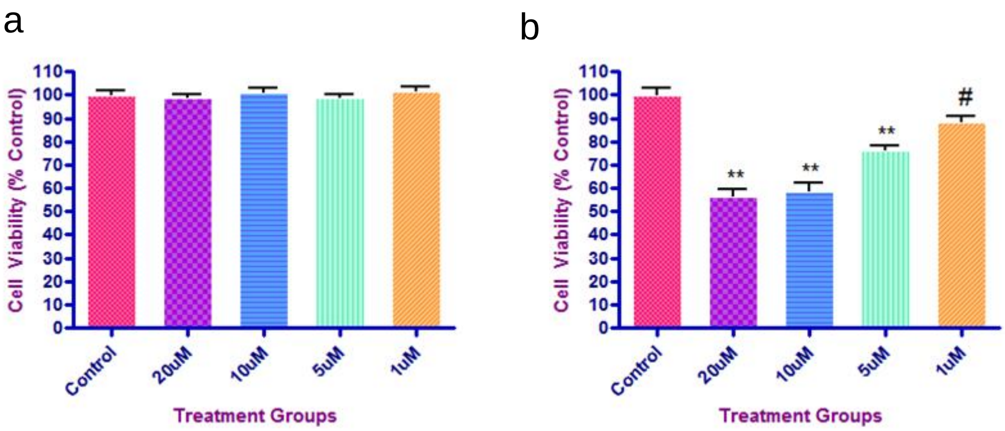

Figure 2.3.9 Effect of NDI conjugates **LD** (a) and **Dp** (b) on the cell viabilities of PC12 cells. PC12 cells were incubated with 20, 10, 5, 1 μM concentrations of either LD or Dp for 24 h. Control cells received DMEM complete media with 0.01% DMSO. Values shown are means ± SEM of three independent experiments performed in six to eight replicates. One-way ANOVA analysis followed by Tukey's multiple comparison post hoc test was performed (#p < 0.05, *p < 0.01, **p < 0.001 compared to control).

ranging from 45% at 20 μM, 40% at 10 μM and 20% at 5 μM. **Dp** at 1μM also showed 10% toxicity (Figure 2.3.9).

Next, we wanted to assess the ability of **LD**, **Dp** conjugates in altering the toxicities induced by Aβ$_{1-42}$ aggregates after co-incubation of NDI conjugates with Aβ$_{1-42}$ (at 1:1 ratio) for 24 h followed by cell viability assay in PC12 cells with these samples. Treatment with Aβ$_{1-42}$ aggregates at 1 μM final concentration showed ~45% toxicity (Figure 2.3.10). Aβ$_{1-42}$ co-incubated with **LD** showed significant reduction in cell death by 15% compared to Aβ$_{1-42}$ alone while with **Dp** showed 5% reduction in cell death (Figure 2.3.10). Although percentage of rescuing cell death is low with **LD**, **Dp** cell death can be further rescued upon increasing Aβ$_{1-42}$ to compound ratio. **LD** alone after 24 h incubation at 1 μM did not show any toxicity on PC12 cells which was consistent with

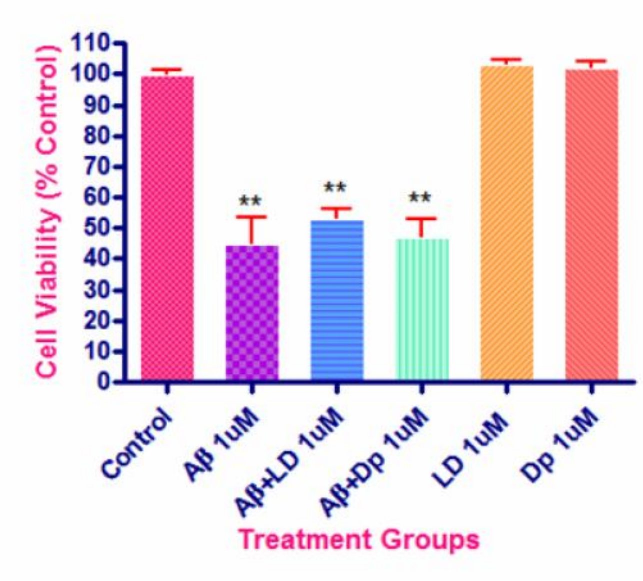

Figure 2.3.10 Effect of treatment of NDI conjugates **LD**, **Dp** against Aβ$_{1-42}$ aggregates on the cell viabilities of PC12 cells. Aβ$_{1-42}$ either alone or with **LD**, **Dp** are incubated for 24 h at 100 μM concentration at 1:1 ratio in 1X PBS. PC12 cells were treated with 1 μM (final concentration per well w.r.t either Aβ or drug) above samples for 24 h and assayed by MTT. Values shown are means ± SEM of four independent experiments performed in four to six replicates. One-way

ANOVA analysis followed by Tukey's multiple comparison post hoc test was performed (**p < 0.001 compared to control).

toxicity studies of **LD** (Figure 2.3.10). Interestingly, **Dp** after 24 h incubation also did not show any toxicity at 1 μM on PC12 cells while the same compound showed ~10% toxicity (Figure 2.3.10). The reduction in the cellular toxicity of **Dp** after 24 h incubation could be due to the formation of quinone derivative (due to aerial oxidation) of the corresponding di-hydroxy groups of dopamine in the **Dp**. [208]

2.3.4 Assessment of LD, Dp in disaggregation of pre-formed Aβ_{1-42} aggregates and evaluation of cytotoxicity in PC12 cells

To evaluate whether these **LD**, **Dp** conjugates can disaggregate the pre-formed Aβ_{1-42} aggregates, we have carried dissolution experiments. In this experiment, Aβ_{1-42} alone was initially aggregated at 200 μM for 24 h followed by co-incubation with **LD**, **Dp** at 100 μM concentration each (at 1:1 ratio) for 48 h. Samples from this experiments were treated with PC12 cells for 24 h at 1 μM final concentration. Results from dissolution experiments are similar to aggregation inhibition data. Aβ_{1-42} alone at 1 μM final concentration showed ~50% cell death while Aβ_{1-42} aggregates co-incubated with **LD** showed only 35% cell death, significantly rescuing by ~15% compared to Aβ_{1-42} alone. **Dp** also showed significant reduction in cell death by ~10% compared to Aβ_{1-42} alone (Figure 2.3.11). The possible reason for reduction in cell death with Aβ_{1-42} aggregates from 72h when compared to 24 h (from aggregation inhibition experiment, Figure 2.3.10) could be due to the presence of higher percentage of oligomers at 24 h aggregates. It is interesting to note that **LD** is potent in both aggregation inhibition and dissolution of pre-formed aggregates while **Dp** also showed significant effect in dissolution. PC12 cells

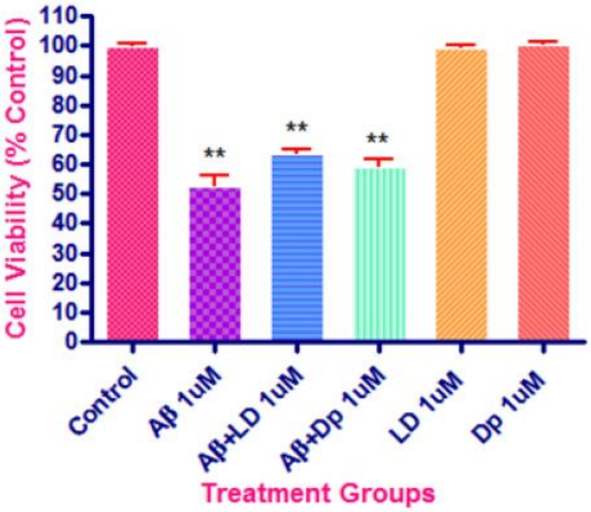

Figure 2.3.11 Effect of treatment of NDI conjugates **LD**, **Dp** in disaggregation of pre-formed Aβ_{1-42} aggregates on the cell viabilities of PC12 cells. 200 μM of Aβ_{1-42} alone in 1X PBS was incubated for 24 h followed by co-incubation with **LD**, **Dp** for another 48 h at 100 μM concentration at 1:1 ratio in 1X PBS. PC12 cells were treated with 1 μM (final concentration per well w.r.t either Aβ or drug) above samples for 24 h and assayed by MTT. Values shown are means ± SEM of four independent experiments performed in four to six replicates. One-way ANOVA analysis followed by Tukey's multiple comparison post hoc test was performed (**p < 0.001 compared to control).

treated with **LD** or **Dp** alone at 1 μM did not cause any cell death (Figure 2.3.9). Thus, it can argued that **LD** possess the property of both aggregation inhibition and disaggregation of pre-formed aggregates and hence could be a potent modulator of Aβ_{1-42} aggregation pathway.

2.3.5 Anti-oxidant property of NDI conjugates

LD and **Dp** are closely related to polyphenol compounds in terms of their structure (having multiple hydroxyl groups on aromatic ring) and function (aggregation modulators and anti-oxidant property). We assesed the anti-oxidant property of these conjugates using DPPH free radical scavenging assay. For this experiment, **LD**, **Dp**, and **ANA** at varying concentrations (20-200 μM) were studied in quenching/scavenging the DPPH free radical for 2 h. Results showed potent activity for **LD**, **Dp** (more than 80% for LD and ~70% for Dp) while **WNW** and **ANA** are completely inactive (Figure 2.3.12).

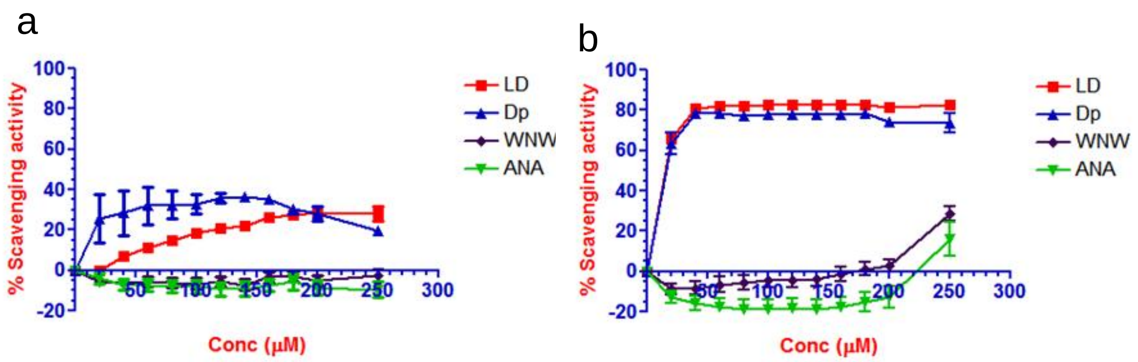

Figure 2.3.12 DPPH free-radical scavenging (antioxidant) assay for **LD**, **Dp**, **WNW** and **ANA** conjugates using Ascorbic acid as standard at 0 h (a) and after 2 h (b). **LD**, **Dp** showed high antioxidant activity when compared to standard antioxidant Ascorbic acid. Values shown are means ± SEM of three independent experiments performed in three to four replicates. Radical scavenging activity was expressed as inhibition percentage and was calculated using the formula: % scavenging activity = (absorbance of control − absorbance of sample)/ (absorbance of control)] × 100.

2.3.6 Docking Studies

To determine the possible binding site in A$\beta_{1\text{-}42}$ aggregates and to further evaluate the binding modes of in *vitro* screened conjugates against aggregation modulation, we performed *in-silico* docking studies using Glide program in Schrodinger Software Suite. Generally, *in-silico* molecular docking is performed for known binding sites of the biological entities such as proteins, enzymes and receptors to obtain the possible conformers of various conjugates under study. However, we wanted to determine the most probable binding site/s or peptide sequence on the amyloid beta protein aggregate model. Towards this end, initially we performed blind docking for all our conjugates

(Figure 2.3.2). In blind docking method, search space near the surface of the receptor is docked uniformly without any bias in the surrounding regions. However, this method needs large sampling space and due to the large space under study, we have opted for low precision blind docking method. Based on the results from low precision blind docking studies, we have selected binding hot spots. Further, we performed extra precision (XP) docking and induced fit docking for the selected hot spots to understand the details of possible binding sites.

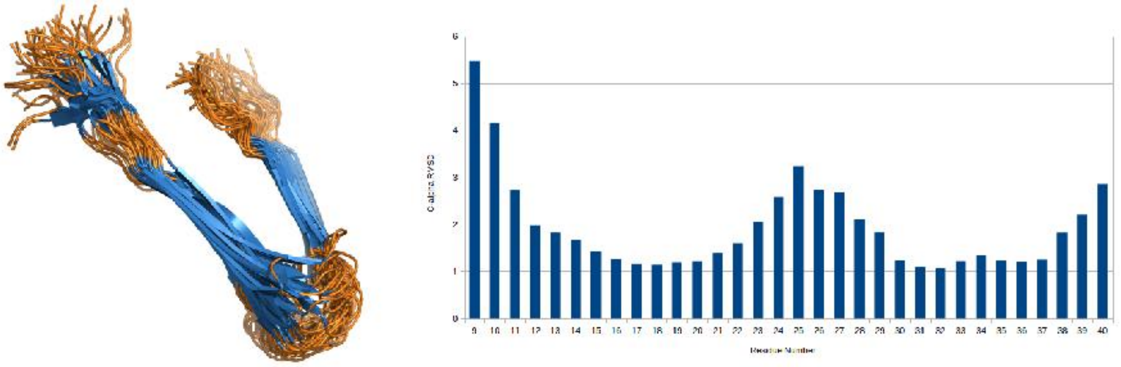

Figure 2.3.13 Residue-wise C-alpha RMSD for chains A to F of NMR structure 2LMN

Currently, several structures were proposed for A$\beta_{1\text{-}42}$ aggregates based on solid state NMR studies. We selected 2LMO, 2LMN, 2LMP and 2LMQ to explore the possible binding sites for blind docking. The selection criteria for the above mentioned structures was based on their comparable relation/activity with actual protein aggregate of interest. Docking studies of residue-wise C-alpha RMSD analysis for these NMR structures showed two regions (residues 13-22 and residues 29-38, Figure 2.3.13) with significantly low RMSD values as compared to other regions in the A$\beta_{1\text{-}42}$ peptide sequence. We considered the docked poses of the regions with low RMSD for further analysis (Figure 2.3.13b shows a representative pictorial demonstration and residue-wise RMSD plot) as the regions with high RMSD values give inconsistent docking results and hence are excluded from analysis. The analysis of docked poses obtained through low precision blind docking suggested two main regions of the Aβ_{1-42} fibril model surface that showed preferential binding for our conjugates with varying degrees of affinities. These two regions are the beta-strand forming regions in the Aβ_{1-42} sequence and have been consistently shown to form beta-sheets by many researchers. These are the sequences, viz. Aβ_{16-20} (KLVFFA) and Aβ_{31-35} (IIGLM) that mainly occur as beta-strands leading to the formation of beta-sheets in amyloid fibrils. Hence we concentrated our attention on the docked conjugates in these two regions of Aβ_{1-42} fibril models. Initial results of docking studies showed a co-relation between the docked poses of our conjugates and two key regions of Aβ_{1-42} fibril model, namely KLVFFA and IIGLM. In this, all conjugates except **GNG** and **ANA** docked to KLVFFA and IIGLM regions. We performed in-depth docking studies using XP and Induced Fit docking (IFD) to investigate the effect/docking of conjugates at KLVFFA and IIGLM regions. For XP docking, we used rigid receptor and flexible ligand which showed highest IFD score for **LD** and **Dp** followed by **WNW** and **FNF** for IIGLM site while there was difference in the scores for KLVFFA site where **LD** showed highest score followed by **FNF**, **WNW**, **ANA** and **GNG**. Interestingly, **Dp** showed least preference towards KLVFFA. Overall, XP docking results showed highest docking for **Dp** followed by **LD** with a G-score of -8.37 kcal/mol and -6.95 kcal/mol respectively for IIGLM site. **WNW** and **FNF** had G-scores of -5.29 kcal/mol and -5.09 kcal/mol at the same region, while **GNG** and **ANA** did not show any docked poses. For KLVFFA region, **LD** showed highest G-score of -6.67 kcal/mol followed by **WNW** (-5.56 kcal/mol). **FNF**, **ANA** and **GNG** showed -5.17, -4.81, -4.21 kcal/mol G-scores respectively. Surprisingly, **Dp** had the lowest G-score of 3.18 kcal/mol. With the above results in hand, we further performed similar induced fit docking analysis where receptor was also made flexible. Preference of various conjugates (as obtained from IFD) towards two binding sites is compared in Figure 2.3.14.

The idea behind performing analysis of interactions of docked conjugates is to understand the possible binding mechanism of the conjugates and to identify the commonalities and differences in their binding mechanism. Results show that hydroxyl groups on the phenyl ring (aromatic group at imide) have strong influence on hydrogen bonding with amyloid beta sequence. These hydroxyl groups make hydrogen bonds with the side chains (in case of KLVFFA) and main chains (in case of IIGLM) of the amyloid beta sequence. This can be clearly observed upon comparing docked poses and docking scores of **LD**, **Dp** and **FNF**, where **FNF** lacks the hydrogen bonding potential on the phenyl rings. Docking data is consistent with our experimental results where **LD**, **Dp** are found to be lead molecules in $A\beta_{1\text{-}42}$ aggregation inhibition and dissolution compared to **FNF**. These results provide an evidence on the role of hydroxyl groups of aromatic phenyl ring in binding to the selected regions (KLVFFA, IIGLM) of the amyloid beta sequence. Also, presence of phenyl ring at imide position seems to have influence on

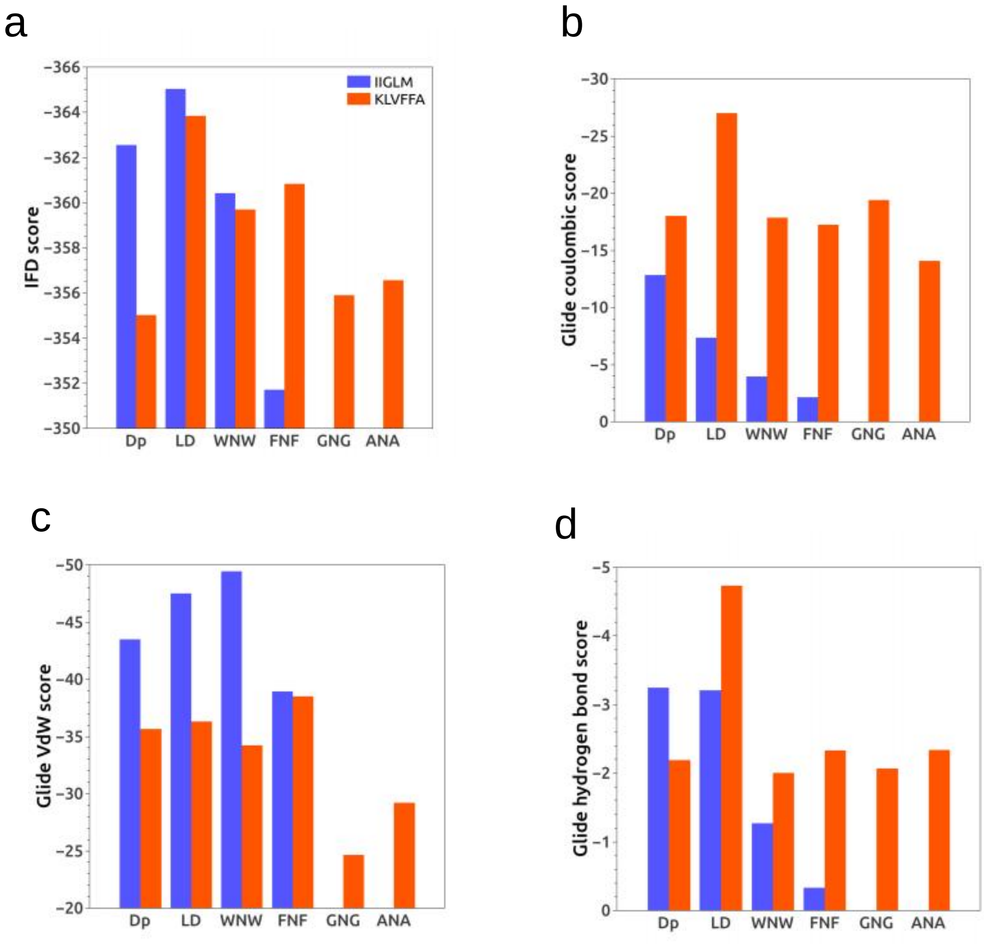

Figure 2.3.14 Induced fit docking (IFD) scores for two binding regions. a) Total induced fit score, b) Coulombic score, c) van der Waals' score, d) Hydrogen bond score.

binding potential. This is supported by poor docking scores of both **ANA** and **GNG** in KLVFFA region and no docked poses at IIGLM region. It was observed that Dp shows lowest IFD scores at KLVFFA region which lacks carboxylic functionality among all the NDI conjugates. It might be possible that carboxylic group has some role in binding to KLVFFA region (Figure 2.3.14).

These results are qualitatively summarized in showing Table 2.3.1 the correlation of docking preferences of individual conjugates with the attached functional groups in them. A close look at the Table 2.3.1 shows that conjugates with aromatic ring and hydroxyl groups attached the aromatic ring gave best docking scores (**LD**, **WNW**, **Dp**) with maximum non-covalent interactions with KLVFFA and IIGLM sequences of Aβ_{1-42}. Interestingly, these *in-silico* observations are in agreement with experimental results which showed high activity for **LD**, **WNW**, **Dp** although **Dp** has less preference to KLVFFA. With the docking observations and *in vitro* results, it can be generalized that conjugates obeying three main characteristics (preference to IIGLM and KLVFFA, aromatic ring and hydrogen bond potential) found to show the best Aβ_{1-42} aggregation modulation properties. Those conjugates which show poor binding preferences towards IIGLM, KLVFFA were found to be experimentally inactive in inhibiting as well as disaggregating the Aβ_{1-42} aggregates. Overall, it is evident from the above results that various functional groups attached to the NDI core show different preferences based on their interaction potentials with the selected regions/sequences of Aβ_{1-42} aggregates. Although *in-silico* docking has certain limitations in accurately predicting the binding sites/regions of Aβ_{1-42}, results from both docking and *in vitro* experiments have similar findings. Taken together, current investigation with a series of conjugates with varying

Table 2.3.1 Qualitative comparison of conjugates

Observation	**Dp**	**LD/ WNW**	**FNF**	**ANA/ GNG**
Preference to IIGLM	High	High	Low	Avoid
Preference to KLVFFA	Low	High	High	High
R group has carboxylic group	No	Yes	Yes	Yes
R group has aromatic ring	Yes	Yes	Yes	No
R group has H-bond potential on aromatic ring	Yes	Yes	No	No
R group size (No. of non-Hydrogen atoms)	10	13	11	4,5
Number of rotatable bonds in R group	3	4	4	2

functionalities sheds a significant insight and paves a new path for designing highly effective ligands for Aβ_{1-42} aggregation modulators.

2.3.7 Conclusion

In conclusion, we designed and synthesized biomolecule appended naphthalenediimide (NDI) conjugates as Aβ_{1-42} aggregation modulators for Alzheimer's disease. Fluorescence spectroscopic data with ThT assays revealed an interesting trend of inhibitory activities for **LD**, **Dp** and **WNW** conjugates in modulating Aβ_{1-42} aggregation. PC12 cell culture based studies revealed highest efficacies for **LD** and **Dp** conjugates in both aggregation inhibition and dissolution experiments. Molecular docking studies are consistent with *in vitro* findings and indicated possible hydrogen bonding, hydrophobic interactions between hydrophobic pockets of Aβ_{1-42} aggregates and NDI conjugates. In general, we reported **LD**, **Dp** appended NDIs as novel Aβ_{1-42} aggregation modulators. However, further studies are needed to establish potential of these conjugates as Aβ_{1-42} aggregation modulating agents.

2.3.8 Experimental section

Materials. 1,4,5,8-Naphthalenetetracarboxylic dianhydride (NDA), triethylamine and amino acids were obtained from Sigma-Aldrich. All other reagents and solvents were of reagent grade and used without further purification.

Absorption spectroscopy. UV–vis spectra were recorded on a Perkin Elmer Model Lambda 900 spectrophotometer by using quartz cuvette of 1 mm path length. Solvent systems I=MCH:THF = 80:20 (V/V)), II=DMSO, III= MCH:$CHCl_3$ = 80:20 (V/V)). Diffused reflectance measurements were performed on the solid powder sample with $BaSO_4$ as a reference and converted in to *pseudo-absorbance spectra using Kubelka-Munk function* as follows

$$f^{km} = \frac{(1-R(hv))^2}{2R(hv)} = \frac{\alpha(hv)}{S}$$

where *R*(*hv*) is the reflectance of the sample measured *vs.* 100% reflectivity standard, *α*(*hv*) is the absorption coefficient and *S* stands for the scattering factor of the mixture, which practically is equal to scattering factor.

Fluorescence spectroscopy. Fluorescence spectra were recorded on a Perkin Elmer Model LS 55 spectrophotometer. All fluorescence spectra with excitation wavelength λ_{ex} = 380 nm.

Circular dichroism (CD). CD measurements were carried out on a Jasco J-815 spectropolarimeter under nitrogen atmosphere by using quartz cuvette of 1 mm path length. Solvent systems I=MCH:THF = 80:20 (V/V)), II=DMSO, III= MCH:$CHCl_3$ = 80:20 (V/V)).

NMR spectroscopy. ^{1}H and ^{13}C NMR spectra were recorded on a Bruker AV-400 spectrometer with chemical shifts reported as ppm (in $CDCl_3$/DMSO-d_6 with tetramethylsilane as internal standard).

Mass spectrometry (MS*)*. High resolution mass spectra (HRMS) were obtained from on Agilent Technologies 6538 UHD Accurate-Mass Q-TOF LC/MS spectrometer.

Field emission scanning electron microscopy (FESEM). FESEM images were acquired with a FEI Nova nanoSEM-600 equipped with a field-emission gun operating at 15 kV. The xerogels were prepared by transfer of organogels onto a Si (111) substrate and dried in air followed by vacuum drying at room temperature.

Fluorescence confocal microscopy. Fluorescence confocal microscopy images were obtained from LSM 510 META-Carl Zeiss. A 365 nm laser was employed to excite the crystals.

Gelation experiments. Methylcyclohexene (MCH) was added to the solution of amino acid –naphthalenediimide (NDI) conjugate in tetrahydrofuran (THF)/chloroform to make 6 mM under ultrasonication (MCH:(THF/$CHCl_3$) = 80:20 (v/v)). After few minutes the formation of organogels was observed. The gel formation is determined by tilting or inverting the sample vial upside down.

Rheology studies. Amplitude and frequency sweeps were performed on a Anton Paar rheomater MCR302 SN000000; ID80963516; FW3.65; Slot(11,-1) series device. All the measurements were performed at room temperature.

Time-correlated single photon counting (TCSPC) studies. Fluorescence decay profiles were performed using FLSP 920 spectrometer, Edinburgh Instrument. EPLED.

Crystallographic data and structure refinement details

Crystal growth: Crystals were grown at room temperature in DMSO as solvent.

Data collection: Data collection was done on Bruker AXS SMART APEX Single Crystal Diffractometer: All the datasets were collected at 100 K.

Structure solution and refinement: SHELXS-2013 and SHELXL-2013 programs were used to solve and refine the X-ray diffraction data. WinGx package (version 1.80.05)[3] was used as front end to SHELX programs.

Gelation experiments. 25μL of **DPT** and 50 μL of **A1**/**A2** (from the stock solutions of **DPT** and **A1**/**A2** i.e., 8 mM in DMSO) was mixed together in 25 μL DMSO. The mixture was sonicated at ambient temperature for 15 min and then 400 μL of deionized water was slowly added under ultrasonication. The resultant aqueous solution was left to stand for 15 minutes. The gel formation is determined by tilting/inverting the sample vial upside down.

Scanning tunnelling microscopy (STM). STM measurements were performed on a Brucker diInnova scaning probe microscope. The samples were prepared by drop casting the aqueous solution of **1a** onto a HOPG and allowed to dry in air followed by vacuum drying at room temperature. Measurements were performed under ambient conditions using mechanically cut Pt/Ir wire from several points on the nanosheets of different topographical thickness with set point of 1 nA and a bias voltage of 500 mV was used.

Biological studies

Materials. PC12 Adh cells, a rat adrenal pheochromocytoma cell line were kind gift from Dr. Praveen Vemula lab, inSTEM, NCBS, Bengaluru. Roswell Park Memorial Institute

(RPMI) 1640 media, heat-inactivated horse serum, fetal bovine serum, penicillin-streptomycin and trypsin were purchased from Gibco (Grand Island, NY, USA). A$\beta_{1\text{-}42}$ peptide was purchased from Calbiochem, Merck. Rink amide resin, Fmoc-amino acids were purchased from Novabiochem, USA. Dimethyl sulfoxide, methyl thiazolyl blue tetrazolium bromide (MTT), Dulbecco's phosphate-buffered saline (PBS) were purchased from Sigma-Aldrich. Dimethyl formamide and Isopropanol were purchased from Acros Organics. DIPEA, HBTU, Piperidine were puchased from Spectrochem, India. All the other chemicals are purchased from local vendors unless otherwise stated.

Cell culture and treatments. PC12 Cells were cultured in T-75 flasks (Nest, India) and maintained in RPMI 1640 medium supplemented with 10% heat-inactivated horse serum, 5% fetal bovine serum, 100 U/mL penicillin, and 100 μg/mL streptomycin at 37 °C in 95% air/ 5%CO2. Stock solutions of 142 and 143 were prepared in dimethylsulfoxide (DMSO) and aliquots were stored at -20 °C. 10 mM stock solution of DCF-DA was prepared in methanol and stored at -20 °C. For all experiments assessing protective effects of **LD** and **Dp**, PC12 cells were pre-treated with indicated concentrations of conjugates for 24 h and then assayed for MTT unless stated otherwise. Controls were treated with media containing 0.01% DMSO.

ThT assay (fluorescence spectroscopy). Fluorescence spectral measurements were carried out using Perkin Elmer Model LS 55 fluorescence spectrophotometer. Maximum fluorescence of ThT was observed with the excitation and emission wavelengths set to 450 and 483 nm, respectively. A ThT concentration of 5-10 μM was used for amyloid fibrillization and dissolution assay based on the Aβ1-42 fibrillar concentration.

DPPH radical scavenging assay (antioxidant activity) To a 96-well plate, an amount of 100 μL of NDI compound solutions (dissolved in methanol) ranging from 250 to 20 μM was added. Next 100 µL of 200 µM methanolic solution of 1,1-DPPH was added, and the plate was shaken at 30 °C for 30 min. Control wells received 100 µL of methanol and 100 µL of 200 µM methanolic DPPH solution. Wells containing only 200 µL of methanol served as a background correction. The change in absorbance of all samples was measured at 517 nm. Absorbance was measured at every 30 min. For 0 min, absorbance was measured immediately after addition of DPPH solution. Radical scavenging activity was expressed as inhibition percentage and was calculated using the following formula:

% scavenging activity = (absorbance of control −absorbance of sample)/ (absorbance of control)] × 100.

Generation of Aβ_{1-42} aggregates to assess extracellular toxicity in PC 12 Cells. Aβ_{1-42} peptide (0.25 mg) (Calbiochem, Merck) was dissolved in hexafluoro-2-propanol (HFIP, 0.2 mL) and incubated at room temperature for 1 h. HFIP was then removed by the thin flow of nitrogen and further dried under vacuum. HFIP-treated Aβ_{1-42} was then dissolved in 1X PBS buffer to a concentration of 100 µM at pH 7.4 and vortexed for approximately 30 s. The solution was incubated at 37 ^{o}C for 24 h. The formation of Aβ_{1-42} aggregates was confirmed by ThT fluorescence and electron microscopy.

Assessment of NDI conjugates to alter cytotoxicity induced by extracellular Aβ_{1-42} aggregates. Aβ_{1-42} alone (10 µM) was able to induce around ~60% cell death after incubating for 24 h. Therefore, we assessed the ability of active NDI conjugates, **LD** and **Dp** to alter cytotoxicity induced by Aβ_{1-42} (10 µM) after incubating for 24 h. All solutions were prepared in 1× PBS. Aβ_{1-42} peptide (0.25 mg) (Calbiochem, Merck) was dissolved in hexafluoro-2-propanol (HFIP, 0.2 mL) and incubated at room temperature for 1 h. HFIP was then removed by the thin flow of nitrogen and further dried under vacuum. HFIP-treated Aβ_{1-42} was then dissolved in 1X PBS buffer to a concentration of 200 uM at pH 7.4 and vortexed for approximately 30 s. For Aβ_{1-42} aggregates alone or Compound alone, 50 uL of 100 µM solution was incubated at 37 ^{o}C for 24 h. For aggregation inhibition experiment, 50 µL of Aβ$_{1-42}$ (200 µM) was mixed with 50 µL of NDI conjugates (200 µM) to yield 100 µM Aβ$_{1-42,}$ vortexed for approximately 30s and incubated for 24 h at 37 oC. For aggregates dissolution experiment, preformed Aβ$_{1-42}$ aggregates were incubated either alone or with 10 µM of NDI conjugates for 24 and 48 h.

Evaluation of cytotoxicity of extracellular Aβ$_{1-42}$ aggregates (preformed) in PC12 Cells. Samples obtained from experiments mentioned above were used to evaluate the effect of (preformed) various species generated from Aβ$_{1-42}$ aggregation experiments on PC12 cell viability (extracellular toxicity). PC12 cells were seeded at 17, 000 cells/well density in 100 µL of medium in a 96-well plate. Cells were allowed to adhere to the plate for 24 h. 24 µL (100 µM Aβ$_{1-42}$) sample was diluted with PC12 cell medium to make the varying concentrations of Aβ$_{1-42}$ 10, 7.5, 5, 2.5, 1 µM for cell culture experiments. Media was removed, and the adhered PC12 cells were treated with 60 µL of Aβ$_{1-42}$ (10-1 µM) containing medium. For Aβ$_{1-42}$ + Compound screening, samples were diluted with PC12 medium to get the final concentration of Aβ$_{1-42}$ and Compound to 10 µM in PC12 medium. Control cells were treated with appropriately diluted PC12 medium with 1X PBS. Treatment with extracellular Aβ1-42 was conducted for 24 h. After incubation, 6 µL of 5 mg/mL MTT was added to the cells and the plate was incubated for another 4 h at 37 °C under 5% CO2 atmosphere. Next, the plate was centrifuged at 1500 rpm for 10 min and the supernatants were removed carefully. The formazan crystals were dissolved in 100 µL of a 1:1 mixture of DMSO/methanol solution by shaking gently at 400 rpm for 30 min at room temperature. Then the absorbance was measured at 570 and 690 nm using an microplate reader (make:). Background-corrected values (570−690 nm) were used to plot the graph. Data from at least three experiments were analyzed using GraphPad software (version 4, San Diego, CA).

General procedure for the synthesis of amino acid conjugated NDIs (ANA, FNF, WNW and eNe).

1,4,5,8- Naphthalenetetracarboxylic dianhydride (NDA) (0.5 g, 1.8 mmol) and corresponding amino acid (0.6 g, 3.7 mmol) were suspended in 10 mL of dimethylformamide (DMF). To this suspension, triethylamine (TEA) (0.2 mL) was added and allowed to reflux for 12 h. After cooling to room temperature the reaction mixture was added into 500 mL of 2N HCl and was stirred for 1 h. The precipitate was collected through suction funnel, washed with excess of distilled water (to remove excess HCl) and dried under vacuo to obtain amino acid-naphthalenediimide (NDI) conjugates (L-**ANA**, D-**ANA**, L-**FNF**, D-**FNF**, L-**WNW**, and D-**WNW**) in quantitative yield.

To prepare **eNe** and **A1,** 1,4,5,8- naphthalenetetracarboxylicdianhydride (0.5 g, 1.8 mmol) and ethylamine (0.2 mL, 3.7 mmol) were suspended in 10 mL of dimethylformamide (DMF). To this suspension, triethylamine (TEA) (0.2 mL) was added and allowed to reflux for 12 h. After cooling to room temperature the precipitate was collected through suction funnel, washed with excess of distilled water (to remove TEA), and dried under vacuo to obtain the product in quantitative yield.

Synthesis of di-pyrene tweezer (DPT).

Ethylenediaminetetraacetic dianhydride (**EDTA dianhydride**) (0.5 mg, 1.9 mmol) and pyrenemethylamine hydrochloride (1g, 4 mmol) taken in 20 mL of *N*,*N*-dimethylformamide. After 15 min., triethylamine (0.5 mL, 4.2 mmol) was added dropwise and allowed to stir over night. The resulting precipitate was filtered and washed with ice cold water to afford white solid in quantitative yield.

Synthesis of aminoacid methylester

Anhydrous methanol (50 mL) was placed into a 100 mL two necked round-bottom flask, fitted with a reflux condenser and an additional dropping funnel and cooled to ice temperature. Acetyl chloride (3 mL) was added dropwise through the dropping funnel. After 15 min., alanine (6.9 g, 18.16 mmol) was added and the reaction mixture was refluxed overnight at 70 °C. The reaction mixture was dried in vacuo to obtain alanine methylester hydrochloride in quantitative yield and used for further reaction without purification.

Synthesis of A1 and A2.

1,4,5,8- naphthalenetetracarboxylicdianhydride (0.5 g, 1.8 mmol) and α-(L/D) Alanine methylester (0.52 g, 3.72 mmol) were suspended in 10 mL of dimethylformamide (DMF). To this suspension, triethylamine (TEA) (0.2 mL) was added and allowed to reflux for 12 h. After cooling to room temperature the solvent was removeded and added into 250 mL of distilled water. The precipitate was collected through suction funnel, washed with excess of distilled water. The organic layer was separated, dried under vacuo and the residue was purified by column chromatography (CH_2Cl_2/ MeOH: 10/1).

Synthesis of eNA.

1,4,5,8-Naphthalenetetracarboxylic dianhydride (NDA) (0.5 g, 1.86 mmol) was suspended in 450 mL of isopropanol. α−Alanine methylester (0.26 g, 1.86 mmol) and ethylamine (0.1 mL, 1.86 mmol) were added to the mixture, followed by *N*, *N*-diisopropylethylamine (6.4 mL, 37 mmol). The mixture was allowed to reflux for 24 h. After cooling to room temperature, the resulting precipitate was filtered and washed with water. The organic layer was separated, dried under vacuo and the residue was purified by column chromatography (CH_2Cl_2/ MeOH: 10/1).

Characterization data for amino acid-NDI conjugates

L-**ANA.** Yield 73.2%; mp 345-348 °C; ^{1}H NMR (*DMSO*-d_6, 400 MHz) δ_H 12.85 (2H, s), 8.71 (4H, s), 5.6 (2H, dd), 1.57 (6H, d); ^{13}C NMR (*DMSO*-d_6, 100 MHz) δ_C 171.0, 162.0, 130.9, 126.1, 49.0, 14.3; HRMS: found 411.0853 $[M+H]^+$, calcd 411.0828 for $[C_{20}H_{14}N_2O_8+H]$.

D-**ANA.** Yield 73.2%; mp 345-348 °C; ^1H NMR (*DMSO-d*$_6$, 400 MHz) δ_H 12.84 (2H, s), 8.71 (4H, s), 5.6 (2H, dd), 1.57 (6H, d); ^{13}C NMR (*DMSO-d*$_6$, 100 MHz) δ_C 171.0, 162.0, 130.9, 126.1, 49.0, 14.3; HRMS: found 411.0816 $[M+H]^+$, calcd 411.0828 for $[C_{20}H_{14}N_2O_8+H]$.

L-**FNF.** Yield: 70%; mp 170-173 °C; ^1H NMR (*DMSO-d*$_6$, 400 MHz) δ_H 12.88 (2H, s), 8.64 (4H, s), 7.18-7.02 (10H, m), 5.85 (2H, dd), 3.61 (2H, dd), 3.50 (2H, dd); ^{13}C NMR (*DMSO-d*$_6$, 100 MHz) δ_C 170.1, 161.9, 137.8, 131.2, 128.9, 128.1, 126.3, 126.0, 125.6, 54.5, 34.2; HRMS: found 563.1477 $[M+H]^+$, calcd 563.1454 for $[C_{32}H_{22}N_2O_8+H]$.

D-**FNF.** Yield: 70%; mp 170-173 °C; ^1H NMR (*DMSO-d*$_6$, 400 MHz) δ_H 13.04 (2H, s), 8.64 (4H, s), 7.17-7.03 (10H, m), 5.85 (2H, dd), 3.60 (2H, dd), 3.35 (2H, dd); ^{13}C NMR (*DMSO-d*$_6$, 100 MHz) δ_C 170.1, 161.9, 137.7, 131.2, 128.9, 128.1, 126.3, 126.0, 125.6, 54.5, 34.2; HRMS: found 563.1421 $[M+H]^+$, calcd 563.1454 for $[C_{32}H_{22}N_2O_8+H]$.

L-**WNW.** Yield: 88.6%; mp 220-223 °C; ^1H NMR (*DMSO-d*$_6$, 400 MHz) δ_H 12.99 (2H, s), 10.64 (2H, d), 8.60 (4H, s), 7.48-6.78 (10H, m), 5.85 (2H, dd), 3.70 (2H, dd), 3.52 (2H, dd); ^{13}C NMR (*DMSO-d*$_6$, 100 MHz) δ_C 170.4, 162.0, 135.8, 131.1, 127.0, 125.9, 125.6, 123.6, 120.7, 118.1, 117.8, 111.2, 110.0, 54.2, 24.0; HRMS: found 641.1653 $[M+H]^+$, calcd 641.1672 for $[C_{36}H_{24}N_4O_8+H]$.

D-**WNW.** Yield: 88.6%; mp 220-223 °C; ^1H NMR (*DMSO-d*$_6$, 400 MHz) δ_H 13.0 (2H, s), 10.64 (2H, d), 8.60 (4H, s), 7.47-6.78 (10H, m), 5.85 (2H, dd), 3.69 (2H, dd), 3.50 (2H, dd); ^{13}C NMR (*DMSO-d*$_6$, 100 MHz) δ_C 170.4, 162.0, 135.8, 131.1, 127.0, 125.9, 125.6, 123.6, 120.7, 118.1, 117.8, 111.2, 110.0, 54.2, 24.0; HRMS: found 641.1623 $[M+H]^+$, calcd 641.1672 for $[C_{36}H_{24}N_4O_8+H]$.

eNe. Yield: 85%; mp 320-322 °C; ^1H NMR (*CDCl$_3$*+Trifluoroacetic acid(TFA, 3μL), 400 MHz) δ_H 8.81 (4H, s), 4.29 (4H, q), 1.37 (6H, t); ^{13}C NMR (*CDCl$_3$+TFA*(3μL),100 MHz) δ_C 163.2, 131.4, 126.6, 126.5, 36.5, 13.1; HRMS: found 323.1027 $[M+H]^+$, calcd for 323.1032 $[C_{18}H_{14}N_2O_4+H]$.

Characterization data for 1. Yield 88%; ^1H NMR (*DMSO-d$_6$*, 400 MHz) δ_H 13.22 (2H, b), 8.74 (4H, s), 4.77 (4H, s), Elemental analysis: Found: C, 56.50; H, 2.70; N, 7.30; calcd: C, 56.55; H, 2.64; N, 7.33 for $C_{18}H_{10}N_2O_8$

Characterization data for 2. Yield 80 %; ^1H NMR (*DMSO-d$_6$*, 400 MHz) δ_H 8.71 (4H, s), 7.72 (2H, s), 7.22 (2H, s), 4.63 (4H, s), Elemental analysis: Found: C, 56.80; H, 3.20; N, 14.69; calcd: C, 56.85; H, 3.18; N, 14.73 for $C_{18}H_{12}N_4O_6$

Characterization data for 3. Yield 85 %; ^1H NMR (*DMSO-d$_6$*, 400 MHz) δ_H 8.75 (4H, s), 4.89 (4H, s), 3.72 (6H, s), Elemental analysis: Found: C, 58.45; H, 3.48; N, 6.76; calcd: C, 58.54; H, 3.44; N, 6.83 for $C_{20}H_{14}N_2O_8$

Characterization data for DPT. Yield 82 %. ^1H NMR (DMSO-*d*$_6$, 400 MHz) δ_H 12.28 (2H, s), 8.70 (2H, t), 8.29-7.96 (18H, m), 4.97 (4H, d), 3.36 (8H, d), 2.78 (4H, s); ^{13}C NMR (DMSO-*d*$_6$, 400 MHz) δ_C 172.5, 170.5, 132.3, 130.7, 130.2, 129.9, 127.8, 127.4, 127.3, 126.8, 126.1, 125.1, 124.6, 123.9, 123.8, 122.9, 57.4, 55.1, 52.3, 40.1. HRMS: found 719.2821 $[M+H]^+$, calcd. 718.2791 for $C_{44}H_{38}N_4O_6$.

Characterization data for A1. Yield 82 %. ^1H NMR (DMSO-*d6*, 400 MHz) δ_H 8.72 (4H, s), 5.72 (2H, q), 3.64 (6H, s), 1.58 (6H, d); ^{13}C NMR (DMSO-*d6*, 100 MHz) δ_C 170.0, 162.0, 131.0, 126.3, 126.1, 52.2, 48.9, 14.2. HRMS: found 439.1130 $[M+H]^+$, calcd. 438.1063 for $C_{22}H_{18}N_2O_8$.

Characterization data for A2. Yield 78 %. ^{1}H NMR (DMSO-*d6*, 400 MHz) δ_H 8.72 (4H, s), 5.72 (2H, q), 3.64 (6H, s), 1.58 (6H, d); ^{13}C NMR (DMSO-*d6*, 100 MHz) δ_C 170.0, 162.0, 131.0, 126.3, 126.1, 52.2, 48.9, 14.2. . HRMS: found 439.1130 [M+H]$^+$, calcd. 438.1063 for $C_{22}H_{18}N_2O_8$.

Characterization data for D-eNA. Yield 58 %. ^{1}H NMR (*CDCl$_3$*, 400 MHz) δ_H 8.77 (4H, d), 5.76 (1H, q), 4.27 (2H, q), 3.75 (3H, s), 1.72 (3H, dd), 1.36 (3H, t); ^{13}C NMR (*CDCl$_3$*, 400 MHz) δ_C 170.3, 162.5, 162.3, 131.3, 130.9, 126.9, 126.7, 126.6, 126.3, 52.6, 49.6, 36.1, 14.8, 13.3. HRMS: found 381.1063 [M+H]$^+$, calcd. 381.1087 for $C_{20}H_{17}N_2O_6$. GCMS: 380 [M]$^+$, calcd. 380.3 for $C_{20}H_{16}N_2O_6$.

Characterization data for L-eNA. Yield 58 %. ^{1}H NMR (*CDCl$_3$*, 400 MHz) δ_H 8.76 (4H, d), 5.76 (1H, q), 4.27 (2H, q), 3.75 (3H, s), 1.72 (3H, dd), 1.36 (3H, dt); ^{13}C NMR (*CDCl$_3$*, 400 MHz) δ_C 170.4, 162.8, 162.6, 131.4, 130.9, 126.8, 126.7, 126.4, 126.3, 52.7, 49.7, 36.2, 14.9, 13.4. HRMS: found 381.1058 [M+H]$^+$, calcd. 381.1087 for $C_{20}H_{17}N_2O_6$. GCMS: 380 [M]$^+$, calcd. 380.3 for $C_{20}H_{16}N_2O_6$.

LD: Yield: 75%; ^{1}H NMR (*DMSO-d$_6$*, 400 MHz) δ_H 12.98 (2H, s), 8.66 (4H, s), 8.61 (2H, br), 8.52 (2H, br), 6.53-6.35 (8H, m), 5.74 (2H, q), 3.38 (2H, dd), 3.16 (2H, dd); ^{13}C NMR (*DMSO-d$_6$*, 100 MHz) δ_C 170.3, 161.9, 144.7, 143.5, 131.2, 128.4, 126.0, 125.6, 119.6, 116.2, 115.3, 54.8, 33.5; HRMS: found 627.1248 [M+H]$^+$, calcd. 627.1246 for [$C_{32}H_{22}N_2O_{12}$+H].

Dp: Yield: 75%; ^{1}H NMR (*DMSO-d$_6$*, 400 MHz) δ_H 8.81 (2H, s), 8.67 (2H, s), 8.65 (4H, s), 6.68-6.62 (4H, m), 6.50 (2H, q), 4.17 (2H, dd), 2.75 (2H, dd); ^{13}C NMR (*DMSO-d$_6$*, 100 MHz) δ_C 162.3, 145.1, 143.7, 130.3, 129.2, 126.1, 125.9, 119.2, 115.9, 115.6, 41.7, 32.7; HRMS: found 539.1451 [M+H]$^+$, calcd. 539.1449 for [$C_{30}H_{22}N_2O_8$+H].

2.3.9 Appendix

- ^{1}H NMR and ^{13}C NMR spctra of L-**ANA**
- ^{1}H NMR and ^{13}C NMR spctra of D-**ANA**
- ^{1}H NMR and ^{13}C NMR spctra of L-**FNF**
- ^{1}H NMR and ^{13}C NMR spctra of D- **FNF**
- ^{1}H NMR and ^{13}C NMR spctra of L-**WNW**
- ^{1}H NMR and ^{13}C NMR spctra of D-**WNW**
- ^{1}H NMR and ^{13}C NMR spctra of **eNe**
- ^{1}H NMR spctra of **1**
- ^{1}H NMR spctra of **2**
- ^{1}H NMR spctra of **3**
- ^{1}H NMR and ^{13}C NMR spctra of **DPT**
- ^{1}H NMR and ^{13}C NMR spctra of **A1**
- ^{1}H NMR and ^{13}C NMR spctra of L-**eNA**
- ^{1}H NMR and ^{13}C NMR spctra of D-**eNA**
- ^{1}H NMR and ^{13}C NMR spctra of **LD**
- ^{1}H NMR and ^{13}C NMR spctra of **Dp**

^{1}H NMR spectra (*DMSO-d_6*, 400 MHz) of L-**ANA**

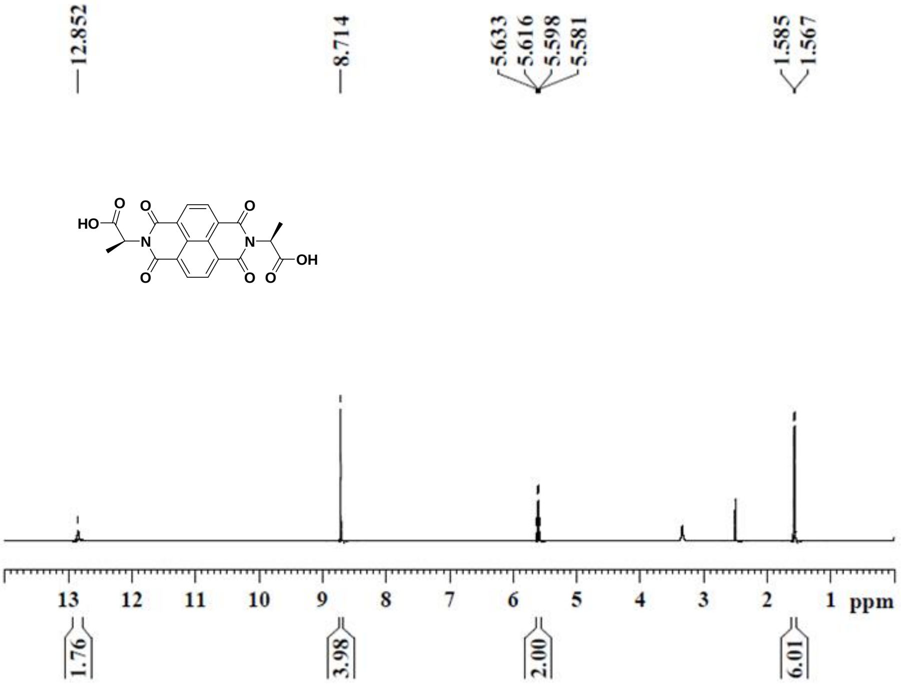

^{13}C NMR spectra (*DMSO-d_6*, 100 MHz) of L-**ANA**

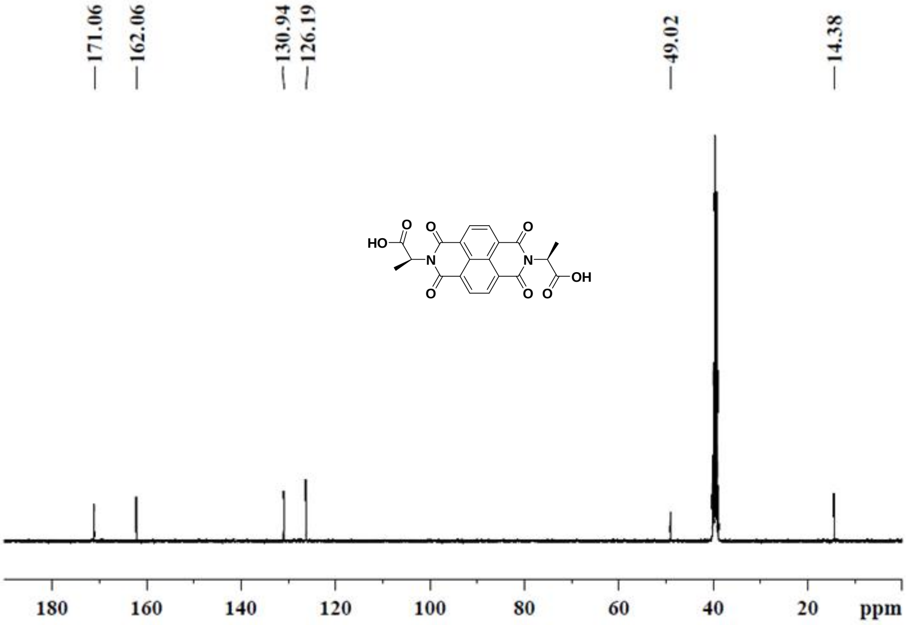

^{1}H NMR spectra (*DMSO-d_6*, 400 MHz) of D-**ANA**

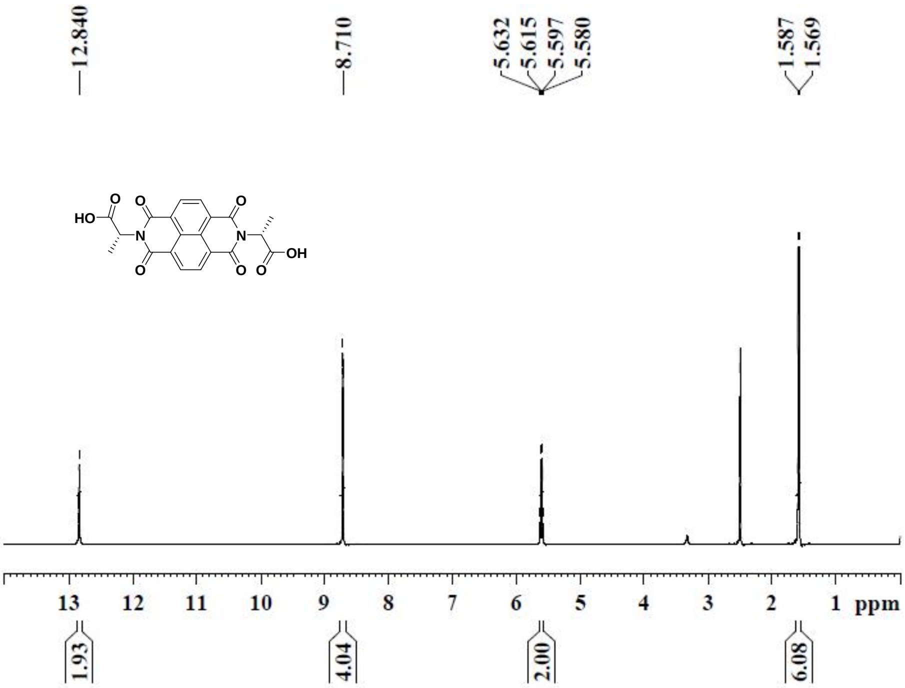

^{13}C NMR spectra (*DMSO-d_6*, 100 MHz) of D-**ANA**

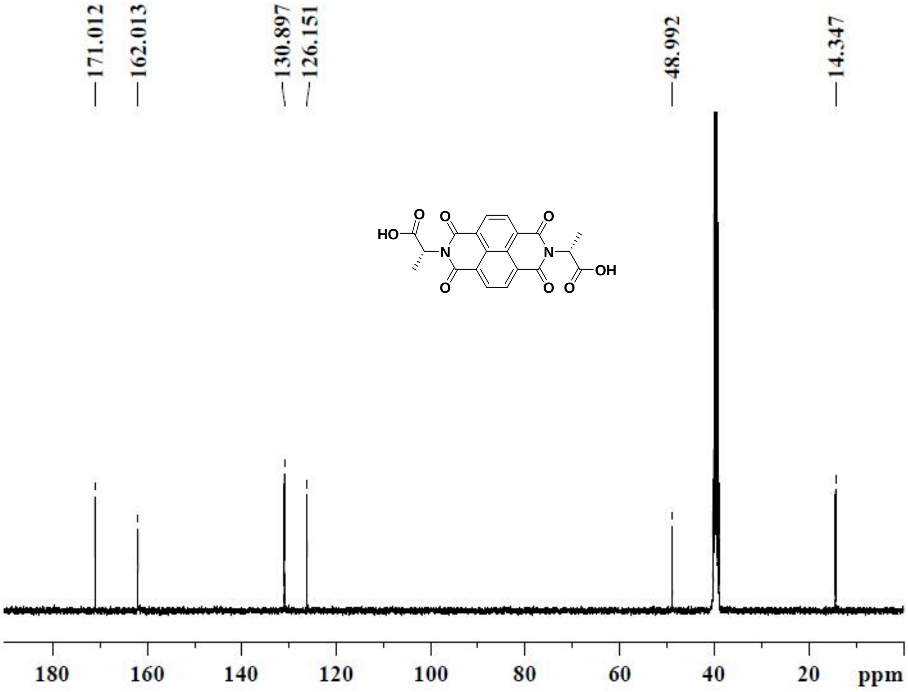

^{1}H NMR spectra (*DMSO-d_6*, 400 MHz) of L-**FNF**

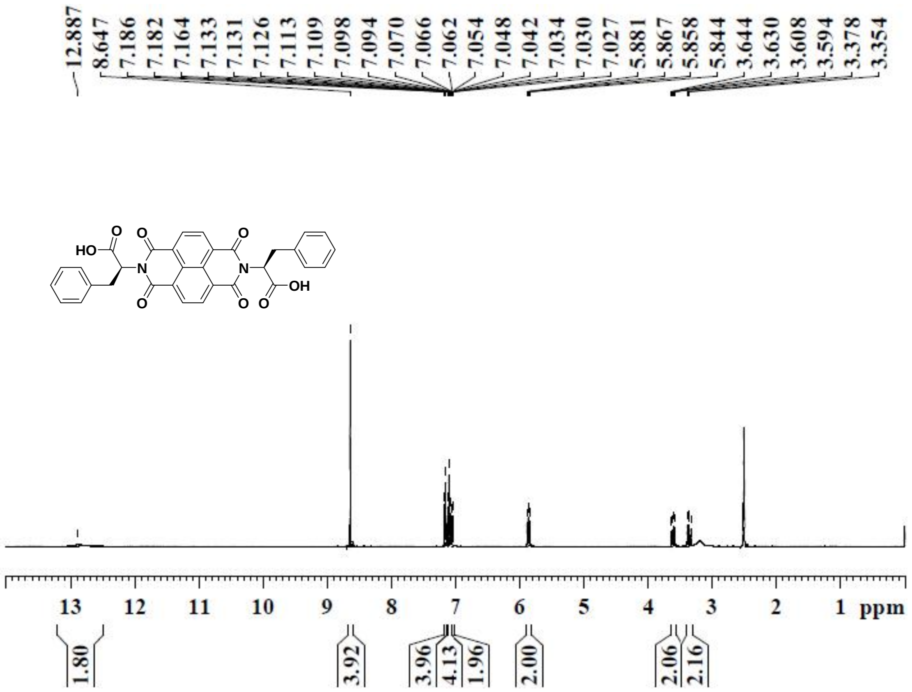

^{13}C NMR spectra (*DMSO-d_6*, 100 MHz) of L-**FNF**

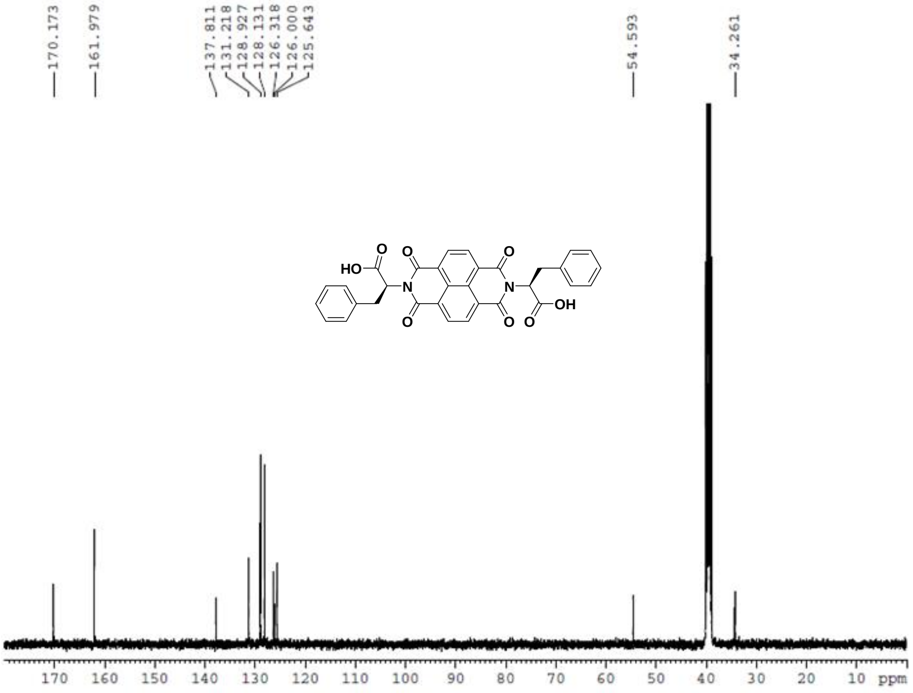

^{1}H NMR spectra (*DMSO-d$_6$*, 400 MHz) of D-**FNF**

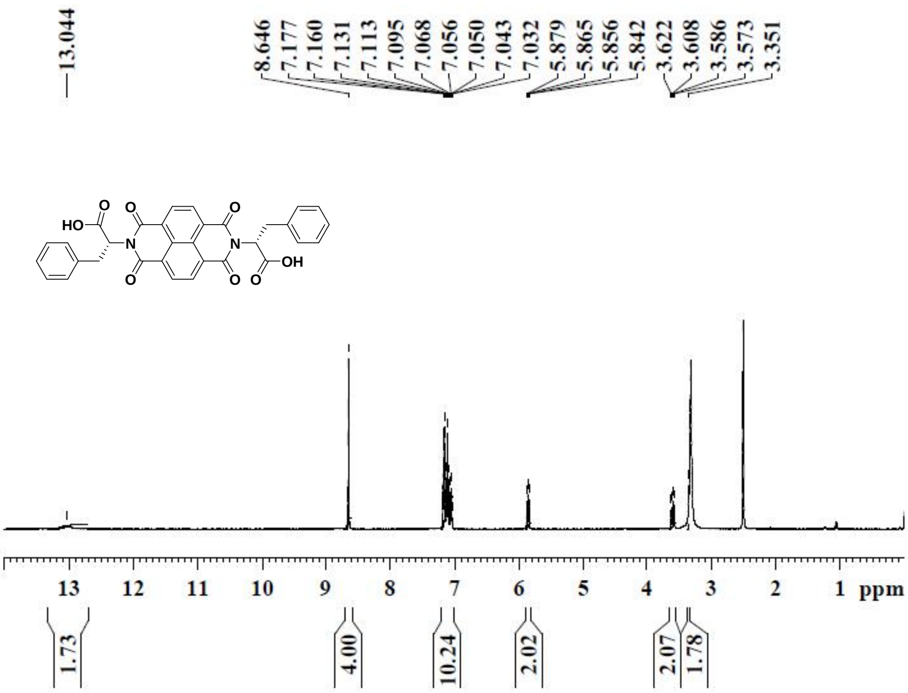

^{13}C NMR spectra (*DMSO-d$_6$*, 100 MHz) of D-**FNF**

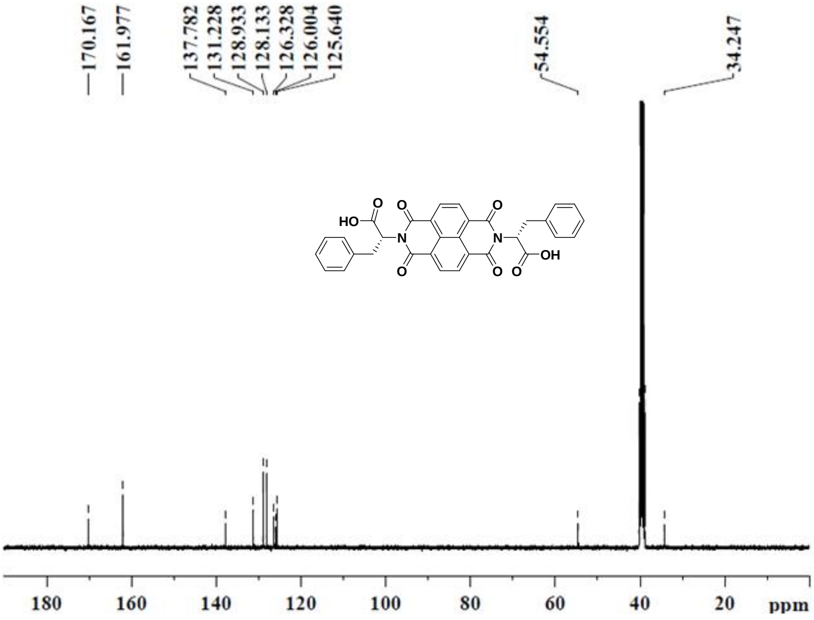

^{1}H NMR spectra (*DMSO-d_6*, 400 MHz) of L-**WNW**

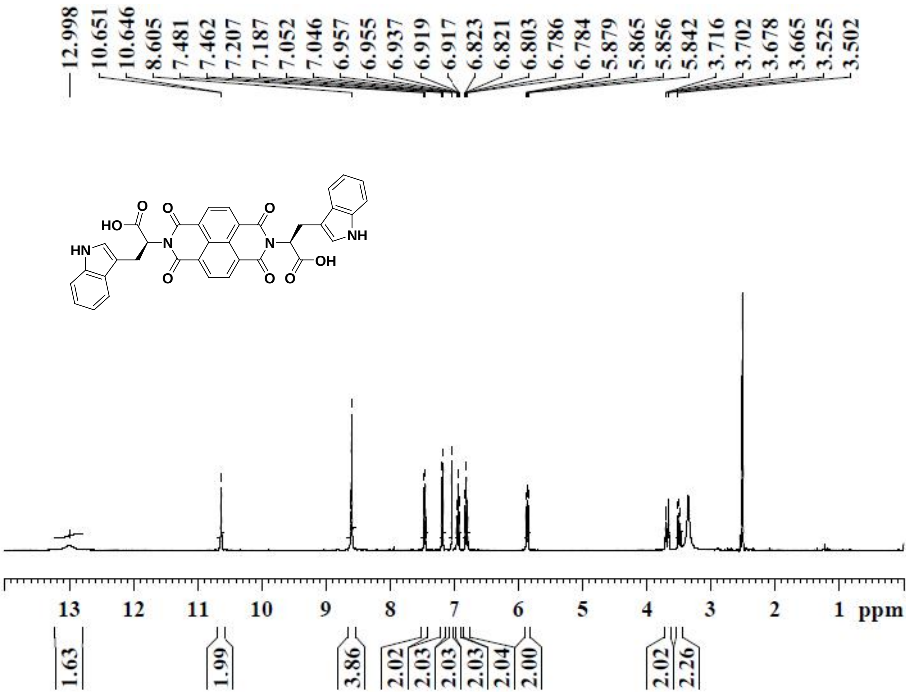

^{13}C NMR spectra (*DMSO-d_6*, 100 MHz) of L-**WNW**

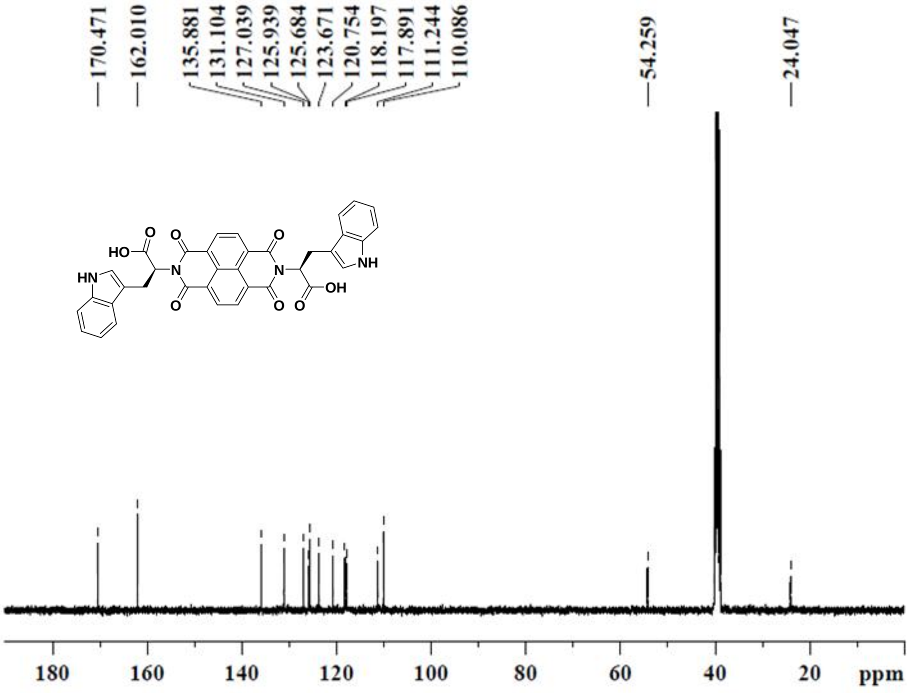

^{1}H NMR spectra (*DMSO-d_6*, 400 MHz) of D-**WNW**

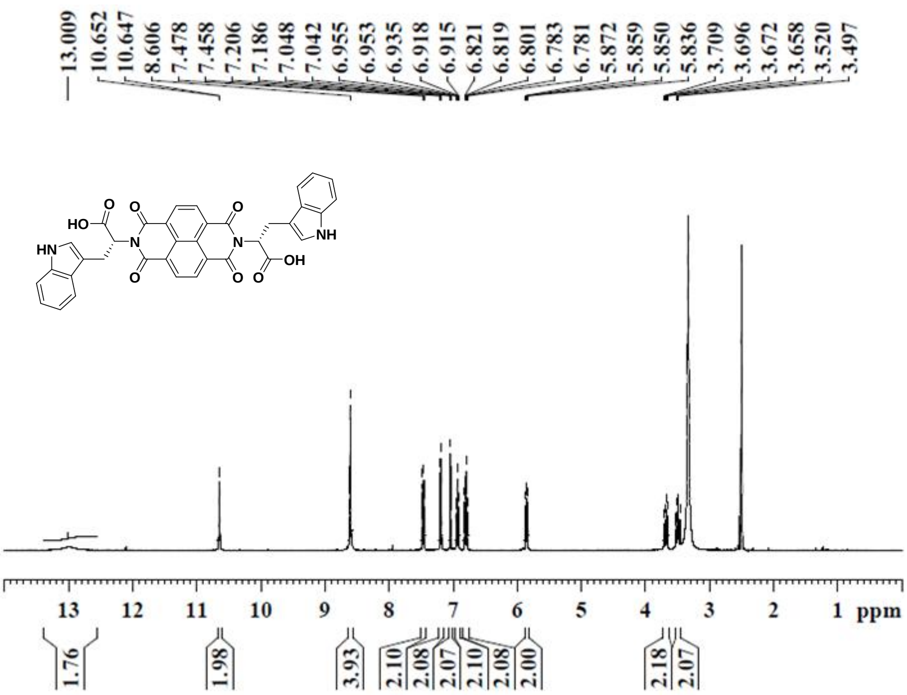

^{13}C NMR spectra (*DMSO-d_6*, 100 MHz) of D-**WNW**

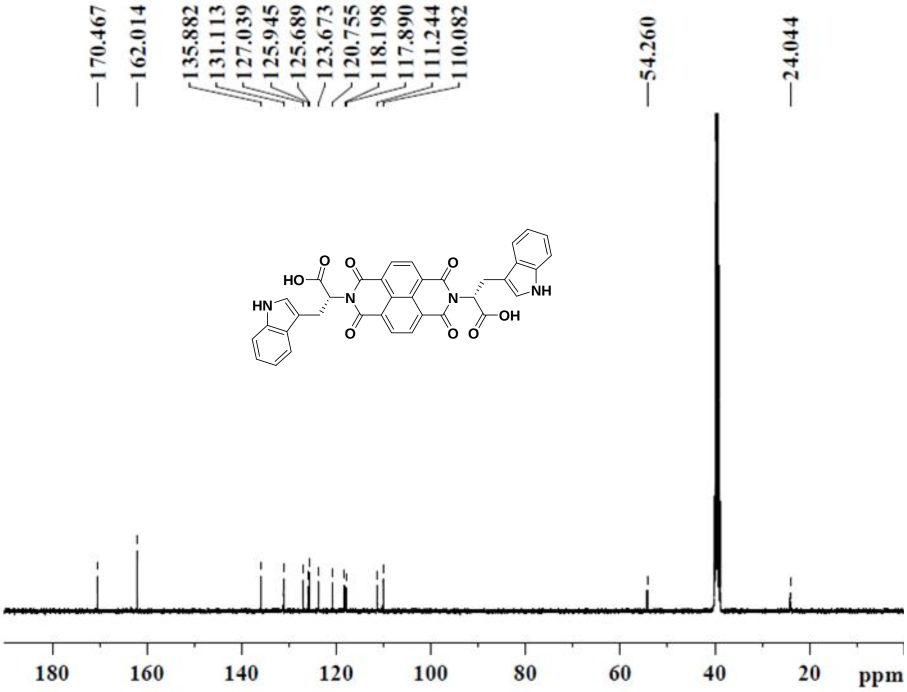

^{1}H NMR spectra ($CDCl_3$+*TFA*(3μL), 400 MHz) of **eNe**

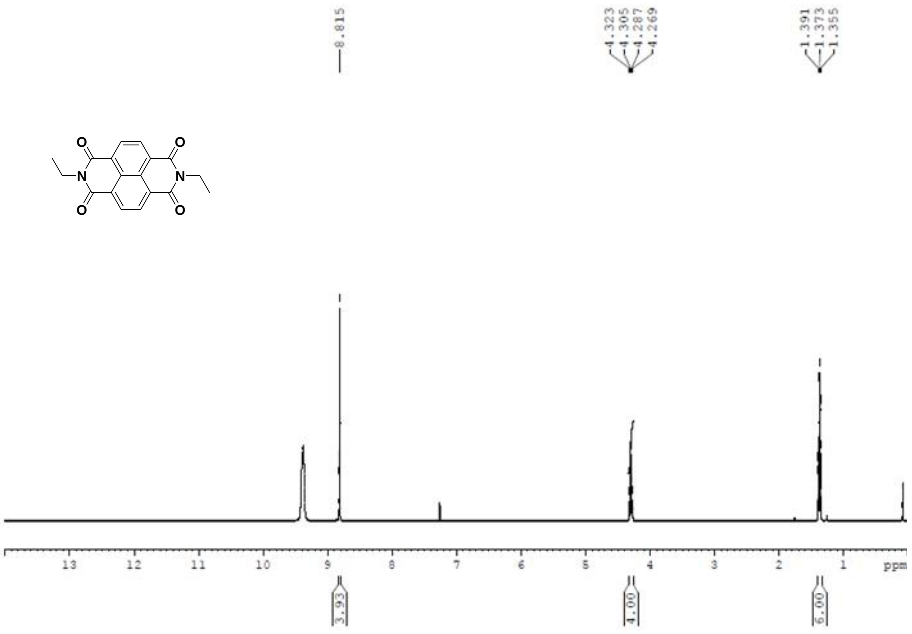

^{13}C NMR spectra ($CDCl_3$+*TFA* (3μL), 100 MHz) of **eNe**

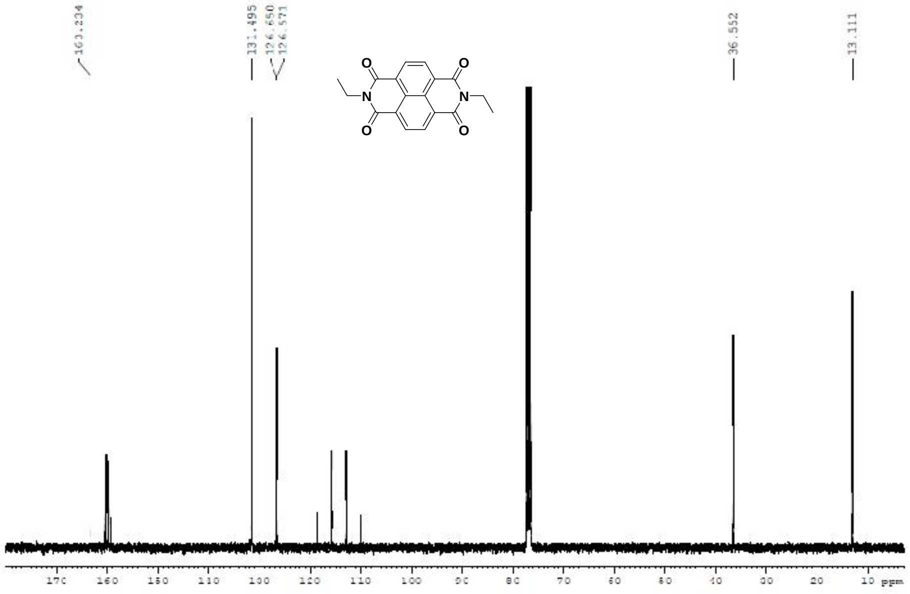

^{1}H NMR spectra (*CDCl$_3$+TFA*(3μL), 400 MHz) of **1**

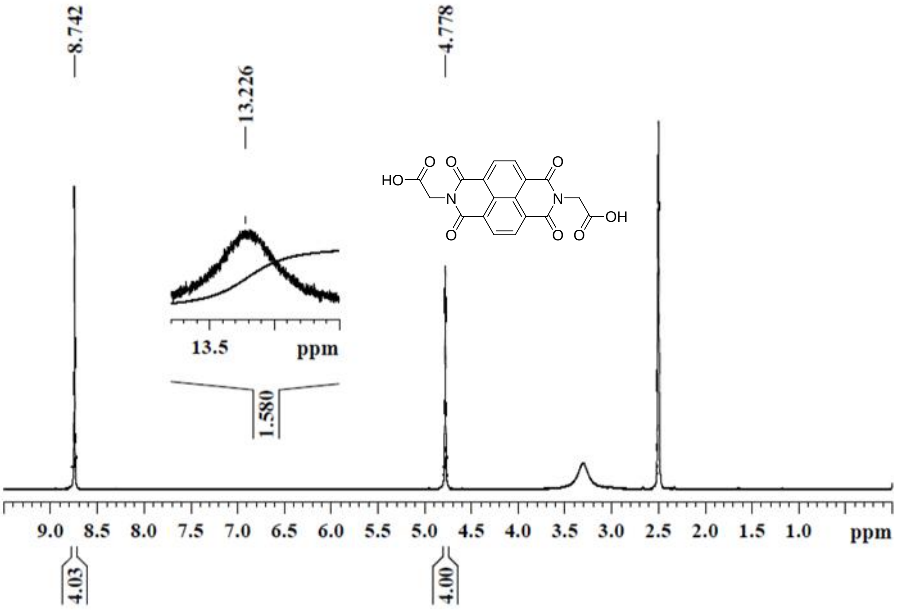

^{1}H NMR spectra (*CDCl$_3$+TFA*(3μL), 400 MHz) of **2**

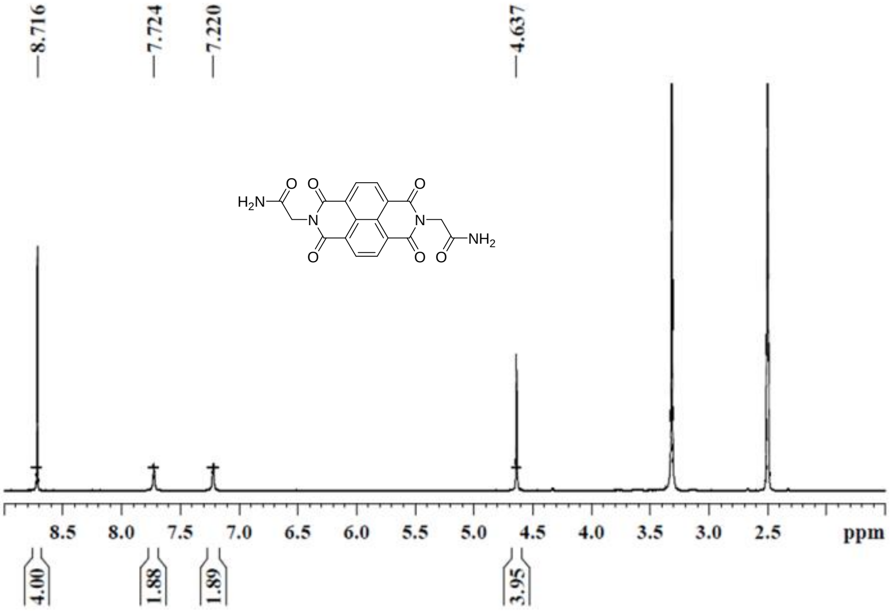

^{1}H NMR spectra ($CDCl_3$+TFA(3μL), 400 MHz) of **3**

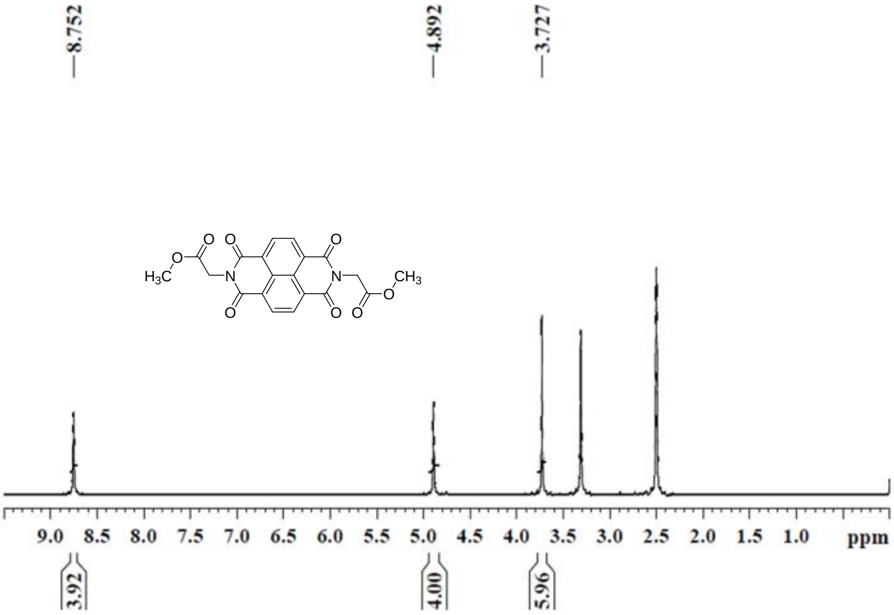

^{1}H NMR spectra ($DMSO$-d_6, 400 MHz) of **DPT**

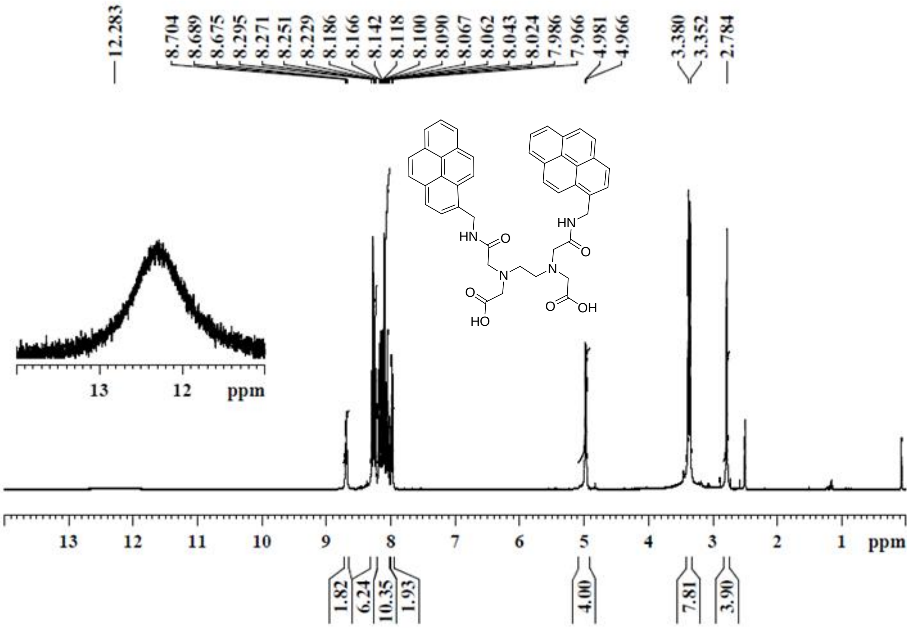

^{13}C NMR spectra (*DMSO-d_6*, 100 MHz) of **DPT**

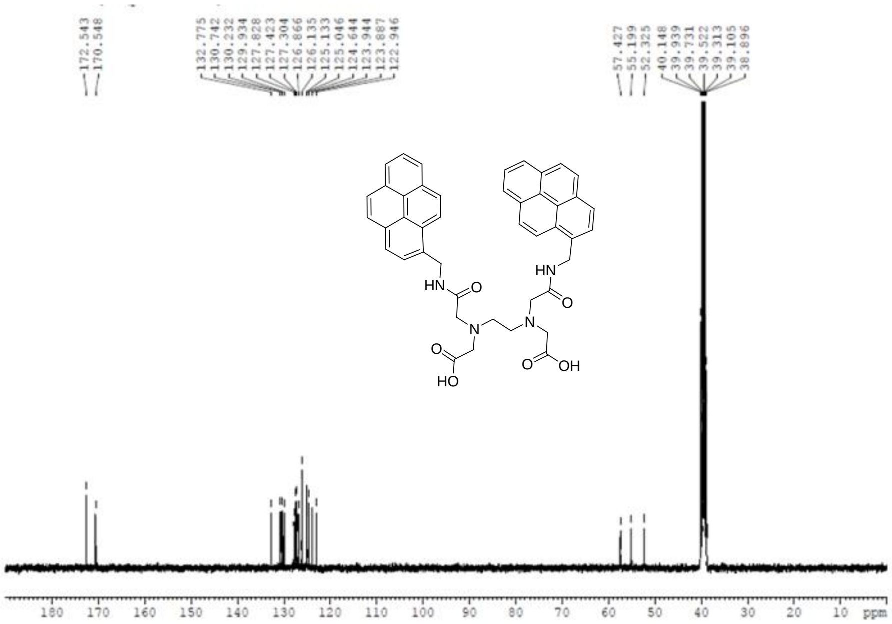

^{1}H NMR spectra (*DMSO-d_6*, 400 MHz) of **A1**

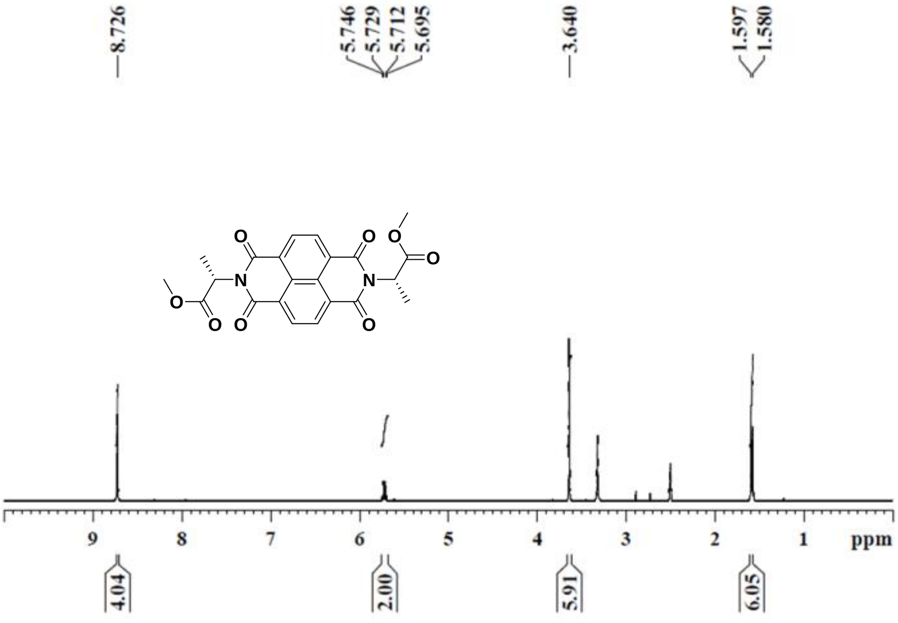

^{13}C NMR spectra (*DMSO-d_6*, 100 MHz) of **A1**

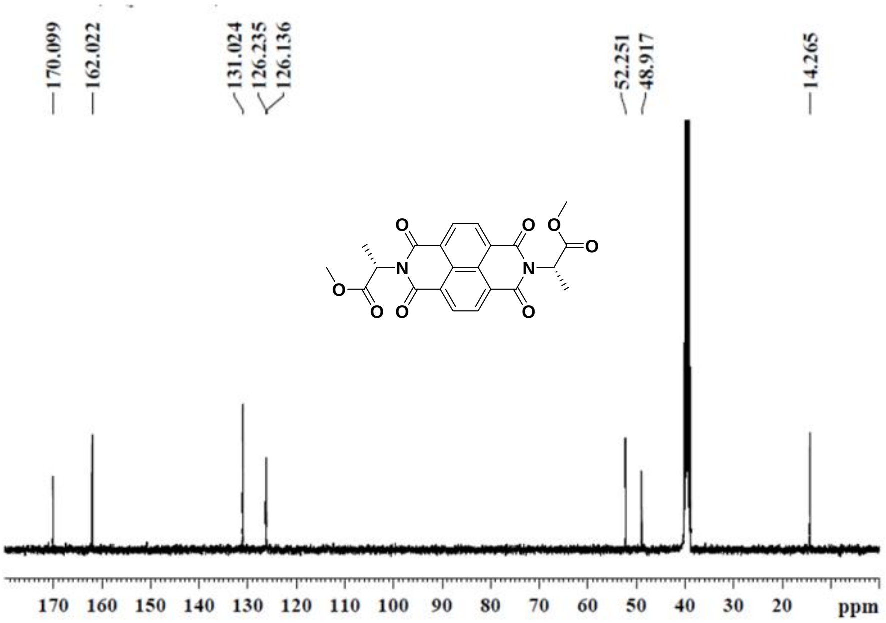

^{1}H NMR spectra (*$CDCl_3$*), 400 MHz) of L-**eNA**

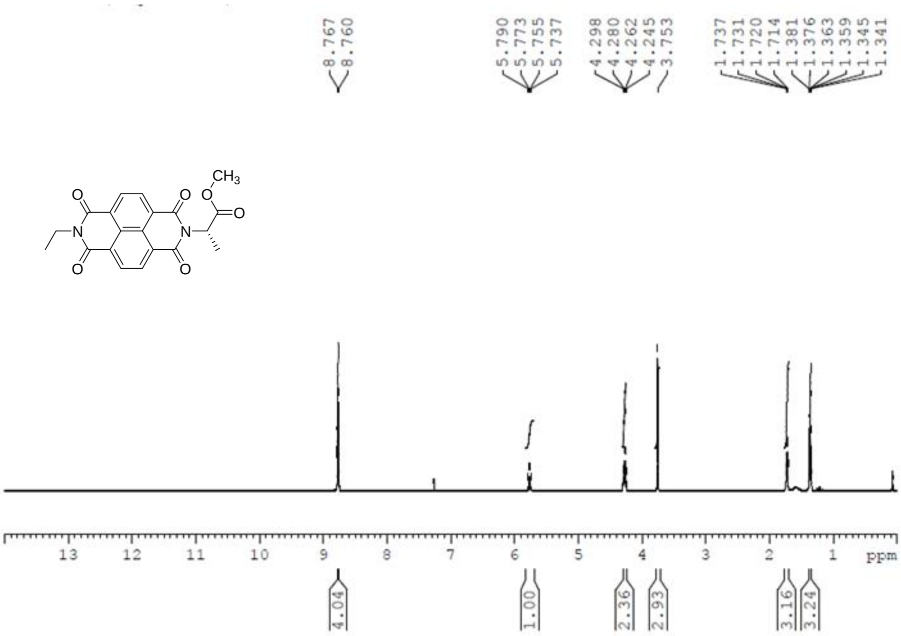

^{13}C NMR spectra (*CDCl$_3$*), 100 MHz) of L-**eNA**

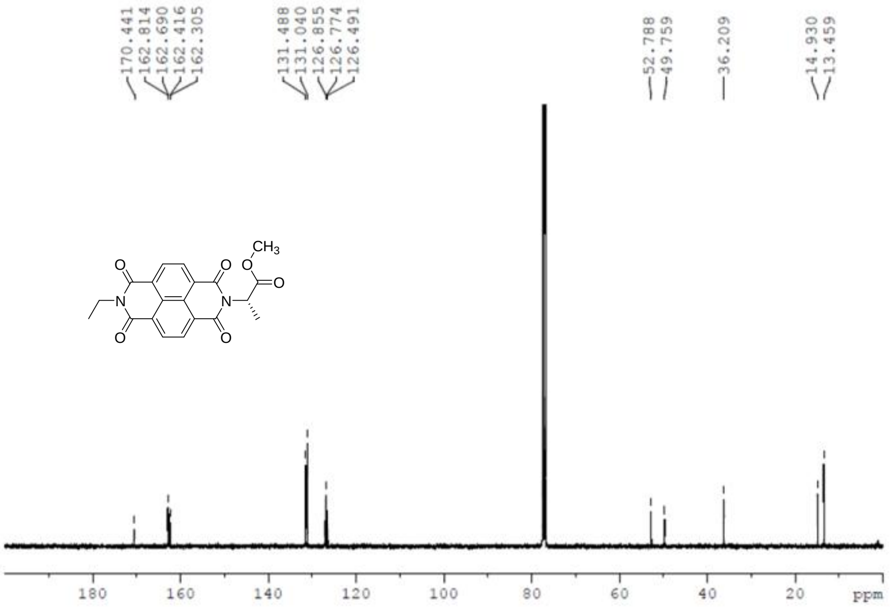

^{1}H NMR spectra (*CDCl$_3$*), 400 MHz) of D-**eNA**

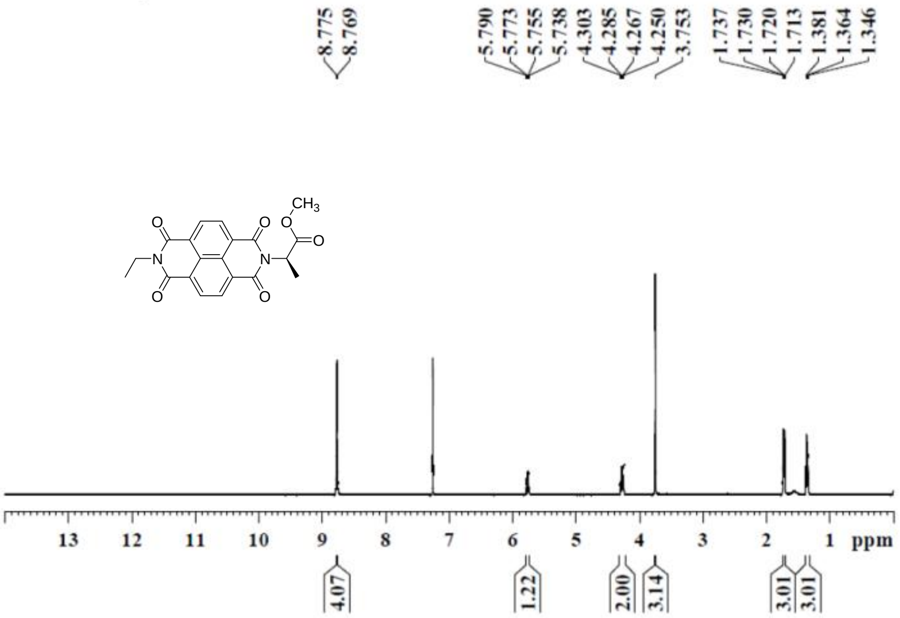

^{13}C NMR spectra (*CDCl$_3$*), 100 MHz) of D-**eNA**

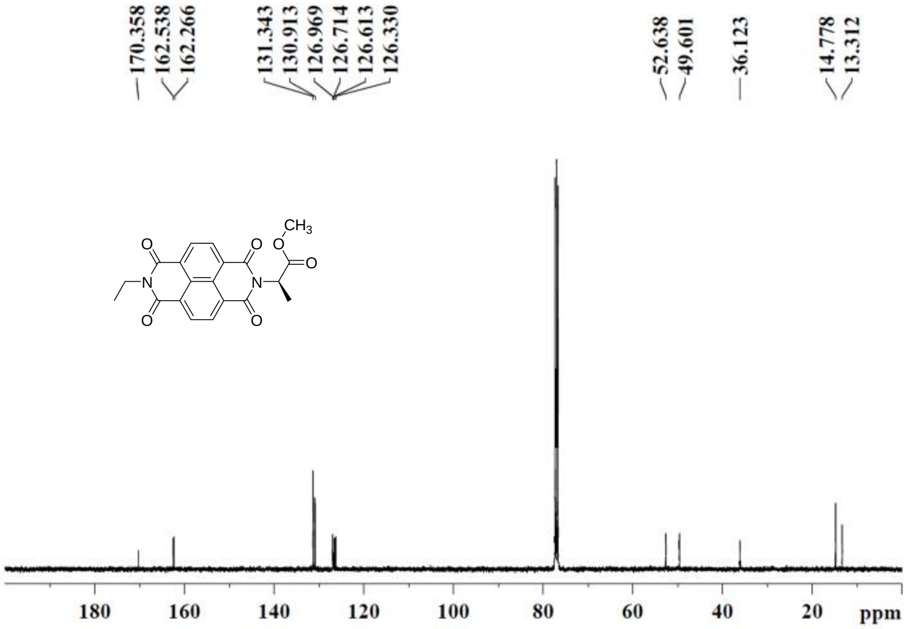

^{1}H NMR spectra (*DMSO-d$_6$*, 400 MHz) of **LD**

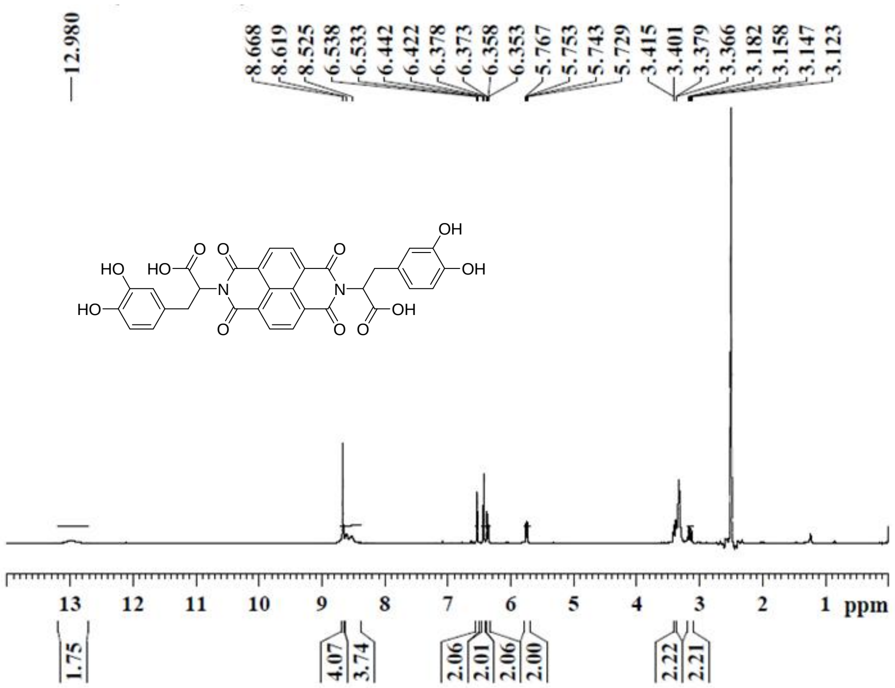

^{13}C NMR spectra (*DMSO-d_6*, 100 MHz) of **LD**

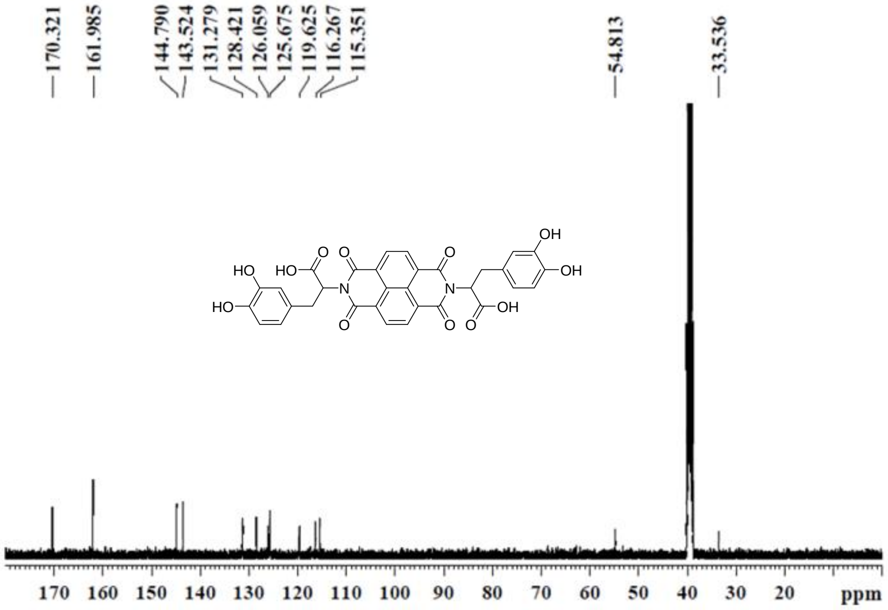

^{1}H NMR spectra (*DMSO-d_6*, 400 MHz) of **Dp**

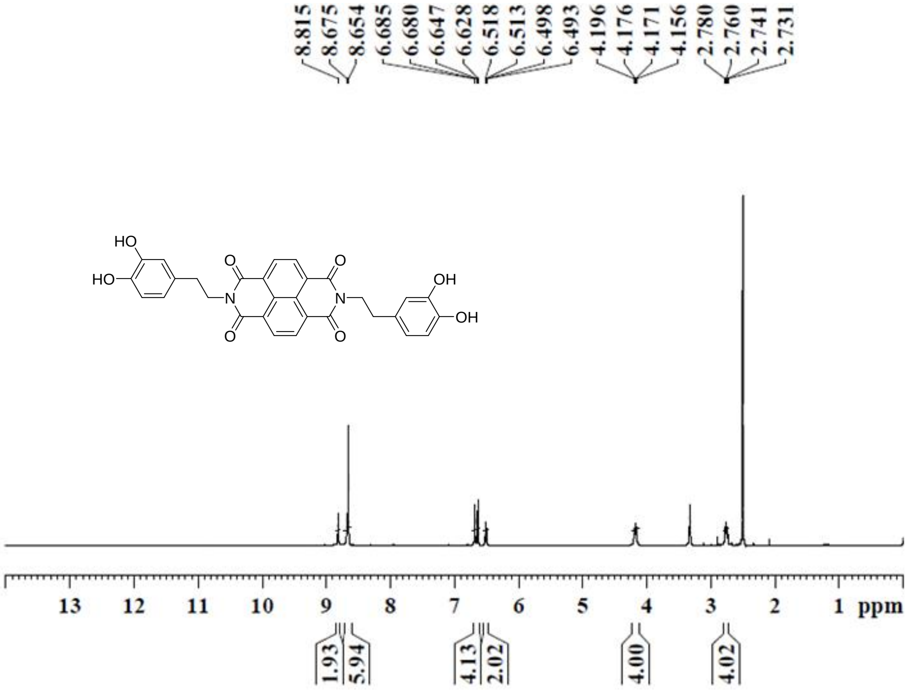

^{13}C NMR spectra (*DMSO-d_6*, 100 MHz) of **Dp**

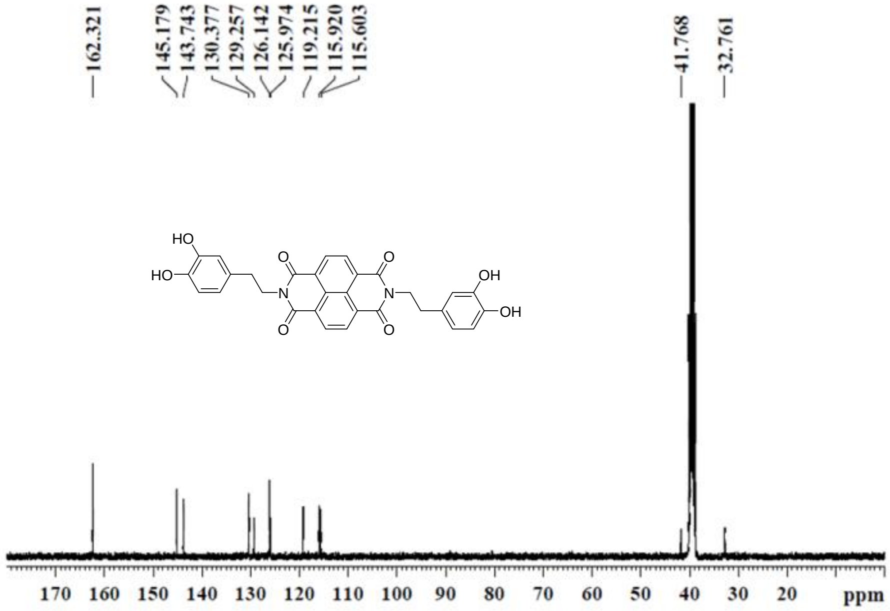

2.3.10 References

1. Burley, S. K.; Petsko, G. A., Aromatic-aromatic interaction: a mechanism of protein structure stabilization. *Science* **1985,** *229*, 23-28.

2. Hunter, C. A., Aromatic interactions in proteins, DNA and synthetic receptors. *Philos. Trans. R. Soc. London, Ser. A* **1993,** *345*, 77-85.

3. Gazit, E., A possible role for π-stacking in the self-assembly of amyloid fibrils. *FASEB J.* **2002,** *16*, 77-83.

4. Salonen, L. M.; Ellermann, M.; Diederich, F., Aromatic rings in chemical and biological recognition: energetics and structures. *Angew. Chem., Int. Ed.* **2011,** *50*, 4808-4842.

5. Riley, K. E.; Hobza, P., On the Importance and Origin of Aromatic Interactions in Chemistry and Biodisciplines. *Acc. Chem. Res.* **2013,** *46*, 927-936.

6. Cejas, M. A.; Kinney, W. A.; Chen, C.; Leo, G. C.; Tounge, B. A.; Vinter, J. G.; Joshi, P. P.; Maryanoff, B. E., Collagen-Related Peptides: Self-Assembly of Short, Single Strands into a Functional Biomaterial of Micrometer Scale. *J. Am. Chem. Soc.* **2007,** *129*, 2202-2203.

7. Zang, L.; Che, Y.; Moore, J. S., One-Dimensional Self-Assembly of Planar π-Conjugated Molecules: Adaptable Building Blocks for Organic Nanodevices. *Acc. Chem. Res.* **2008,** *41*, 1596-1608.

8. Bowerman, C. J.; Liyanage, W.; Federation, A. J.; Nilsson, B. L., Tuning β-Sheet Peptide Self-Assembly and Hydrogelation Behavior by Modification of Sequence Hydrophobicity and Aromaticity. *Biomacromolecules* **2011,** *12*, 2735-2745.

9. Aida, T.; Meijer, E. W.; Stupp, S. I., Functional supramolecular polymers. *Science* **2012,** *335*, 813-817.

10. Avinash, M. B.; Govindaraju, T., Amino acid derivatized arylenediimides: a versatile modular approach for functional molecular materials. *Adv. Mater.* **2012,** *24*, 3905-3922.

11. Meisner, J. S.; Sedbrook, D. F.; Krikorian, M.; Chen, J.; Sattler, A.; Carnes, M. E.; Murray, C. B.; Steigerwald, M.; Nuckolls, C., Functionalizing molecular wires: a tunable class of α,ω-diphenyl-μ,ν-dicyano-oligoenes. *Chem. Sci.* **2012,** *3*, 1007-1014.

12. Fahrenbach, A. C.; Warren, S. C.; Incorvati, J. T.; Avestro, A.-J.; Barnes, J. C.; Stoddart, J. F.; Grzybowski, B. A., Organic Switches for Surfaces and Devices. *Adv. Mater.* **2013,** *25*, 331-348.

13. Hunter, C. A.; Sanders, J. K. M., The nature of π-π interactions. *J. Am. Chem. Soc.* **1990,** *112*, 5525-5534.

14. Wheeler, S. E., Local nature of substituent effects in stacking interactions. *J. Am. Chem. Soc.* **2011,** *133*, 10262-10274.

15. Yan, D.; Delori, A.; Lloyd, G. O.; Friscic, T.; Day, G. M.; Jones, W.; Lu, J.; Wei, M.; Evans, D. G.; Duan, X., A cocrystal strategy to tune the luminescent properties of stilbene-type organic solid-state materials. *Angew. Chem. Int. Ed.* **2011,** *50*, 12483-12486.

16. Martinez, C. R.; Iverson, B. L., Rethinking the term "pi-stacking". *Chem. Sci.* **2012,** *3*, 2191-2201.

17. Stojakovic, J.; Whitis, A. M.; MacGillivray, L. R., Discrete double-to-quadruple aromatic stacks: stepwise integration of face-to-face geometries in cocrystals based on indolocarbazole. *Angew. Chem. Int. Ed.* **2013,** *52*, 12127-12130.

18. Safont-Sempere, M. M.; Osswald, P.; Stolte, M.; Grune, M.; Renz, M.; Kaupp, M.; Radacki, K.; Braunschweig, H.; Wurthner, F., Impact of molecular flexibility on binding strength and self-sorting of chiral pi-surfaces. *J. Am. Chem. Soc.* **2011,** *133*, 9580-9591.

19. Freire, F.; Seco, J. M.; Quinoa, E.; Riguera, R., Chiral Amplification and Helical-Sense Tuning by Mono- and Divalent Metals on Dynamic Helical Polymers. *Angew. Chem. Int. Ed.* **2011,** *50*, 11692-11696.

20. Nagata, Y.; Yamada, T.; Adachi, T.; Akai, Y.; Yamamoto, T.; Suginome, M., Solvent-Dependent Switch of Helical Main-Chain Chirality in Sergeants-and-Soldiers-Type Poly(quinoxaline-2,3-diyl)s: Effect of the Position and Structures of the "Sergeant" Chiral Units on the Screw-Sense Induction. *J. Am. Chem. Soc.* **2013,** *135*, 10104-10113.

21. Schneebeli, S. T.; Frasconi, M.; Liu, Z.; Wu, Y.; Gardner, D. M.; Strutt, N. L.; Cheng, C.; Carmieli, R.; Wasielewski, M. R.; Stoddart, J. F., Electron sharing and anion-pi recognition in molecular triangular prisms. *Angew. Chem. Int. Ed.* **2013,** *52*, 13100-13104.

22. Ogoshi, H.; Mizutani, T., Multifunctional and chiral porphyrins: Model receptors for chiral recognition. *Acc. Chem. Res.* **1998,** *31*, 81-89.

23. Feringa, B. L.; van Delden, R. A.; Koumura, N.; Geertsema, E. M., Chiroptical Molecular Switches. *Chem. Rev.* **2000,** *100*, 1789-1816.

24. Zhang, J.; Albelda, M. T.; Liu, Y.; Canary, J. W., Chiral nanotechnology. *Chirality* **2005,** *17*, 404-420.

25. Hembury, G. A.; Borovkov, V. V.; Inoue, Y., Chirality-sensing supramolecular systems. *Chem. Rev.* **2008,** *108*, 1-73.

26. Yamamoto, T.; Yamada, T.; Nagata, Y.; Suginome, M., High-Molecular-Weight Polyquinoxaline-Based Helically Chiral Phosphine (PQXphos) as Chirality-Switchable, Reusable, and Highly Enantioselective Monodentate Ligand in Catalytic Asymmetric Hydrosilylation of Styrenes. *J. Am. Chem. Soc.* **2010,** *132*, 7899-7901.

27. Rosen, B. M.; Peterca, M.; Morimitsu, K.; Dulcey, A. E.; Leowanawat, P.; Resmerita, A.-M.; Imam, M. R.; Percec, V., Programming the supramolecular helical polymerization of dendritic dipeptides via the stereochemical information of the dipeptide. *J. Am. Chem. Soc.* **2011,** *133*, 5135-5151.

28. Suk, J. M.; Naidu, V. R.; Liu, X.; Lah, M. S.; Jeong, K. S., A foldamer-based chiroptical molecular switch that displays complete inversion of the helical sense upon anion binding. *J. Am. Chem. Soc.* **2011,** *133*, 13938-13941.

29. Dai, Z.; Lee, J.; Zhang, W., Chiroptical switches: applications in sensing and catalysis. *Molecules* **2012,** *17*, 1247-1277.

30. Pandeeswar, M.; Avinash, M. B.; Govindaraju, T., Chiral transcription and retentive helical memory: probing peptide auxiliaries appended with naphthalenediimides for their one-dimensional molecular organization. *Chem. - Eur. J.* **2012,** *18*, 4818-4822.

31. Gopal, A.; Hifsudheen, M.; Furumi, S.; Takeuchi, M.; Ajayaghosh, A., Thermally Assisted Photonic Inversion of Supramolecular Handedness. *Angew. Chem. Int. Ed.* **2012,** *51*, 10505-10509.

32. M. M. Green, M. P. R., R. D. Johnson, G. Darling,; D. J. O'Leary and G. Willson, *J. Am. Chem. Soc.* **1989,** *111*, 6452–6454.

33. Rowan, A. E.; Nolte, R. J. M., Helical molecular programming. *Angew. Chem. Int. Ed.* **1998,** *37*, 63-68.

34. Berl, V.; Huc, I.; Khoury, R. G.; Lehn, J.-M., Helical molecular programming: supramolecular double helices by dimerization of helical oligopyridine-dicarboxamide strands. *Chem. - Eur. J.* **2001,** *7*, 2810-2820.

35. Schmuck, C., Molecules with helical structure: How to build a molecular spiral staircase. *Angew. Chem., Int. Ed.* **2003,** *42*, 2448-2452.

36. Mateos-Timoneda, M. A.; Crego-Calama, M.; Reinhoudt, D. N., Supramolecular chirality of self-assembled systems in solution. *Chem. Soc. Rev.* **2004,** *33*, 363-372.

37. Ohta, E.; Sato, H.; Ando, S.; Kosaka, A.; Fukushima, T.; Hashizume, D.; Yamasaki, M.; Hasegawa, K.; Muraoka, A.; Ushiyama, H.; Yamashita, K.; Aida, T., Redox-responsive molecular helices with highly condensed π-clouds. *Nat. Chem.* **2010,** *3*, 68-73.

38. Watanabe, K.; Suda, K.; Akagi, K., Hierarchically self-assembled helical aromatic conjugated polymers. *J. Mater. Chem. C* **2013,** *1*, 2797-2805.

39. Yang, Y.; Zhang, Y.; Wei, Z., Supramolecular helices: chirality transfer from conjugated molecules to structures. *Adv. Mater.* **2013,** *25*, 6039-6049.

40. Palmans, A. R. A.; Meijer, E. W., Amplification of chirality in dynamic supramolecular aggregates. *Angew. Chem., Int. Ed.* **2007,** *46*, 8948-8968.

41. Praveen, V. K.; Babu, S. S.; Vijayakumar, C.; Varghese, R.; Ajayaghosh, A., Helical Supramolecular Architectures of Self-Assembled Linear π-Systems. *Bull. Chem. Soc. Jpn.* **2008,** *81*, 1196-1211.

42. Rosen, B. M.; Wilson, C. J.; Wilson, D. A.; Peterca, M.; Imam, M. R.; Percec, V., Dendron-Mediated Self-Assembly, Disassembly, and Self-Organization of Complex Systems. *Chem. Rev.* **2009,** *109*, 6275-6540.

43. Chakrabarti, D.; Fejer, S. N.; Wales, D. J., Rational design of helical architectures. *Proc. Natl. Acad. Sci. U. S. A.* **2009,** *106*, 20164-20167.

44. Yashima, E.; Maeda, K.; Iida, H.; Furusho, Y.; Nagai, K., Helical Polymers: Synthesis, Structures, and Functions. *Chem. Rev.* **2009,** *109*, 6102-6211.

45. Adam, D.; Schuhmacher, P.; Simmerer, J.; Haeussling, L.; Siemensmeyer, K.; Etzbach, K. H.; Ringsdorf, H.; Haarer, D., Fast photoconduction in the highly ordered columnar phase of a discotic liquid crystal. *Nature* **1994,** *371*, 141-143.

46. Percec, V.; Glodde, M.; Bera, T. K.; Miura, Y.; Shiyanovskaya, I.; Singer, K. D.; Balagurusamy, V. S. K.; Heiney, P. A.; Schnell, I.; Rapp, A.; Spiess, H. W.; Hudson, S. D.; Duan, H., Self-organization of supramolecular helical dendrimers into complex electronic materials. *Nature* **2002,** *419*, 384-387.

47. Amabilino, D. B.; Puigmarti-Luis, J., Gels as a soft matter route to conducting nanostructured organic and composite materials. *Soft Matter* **2010,** *6*, 1605-1612.

48. Babu, S. S.; Prasanthkumar, S.; Ajayaghosh, A., Self-Assembled Gelators for Organic Electronics. *Angew. Chem., Int. Ed.* **2012,** *51*, 1766-1776.

49. Anthony, J. E., Functionalized acenes and heteroacenes for organic electronics. *Chem. Rev.* **2006,** *106*, 5028-5048.

50. Mas-Torrent, M.; Rovira, C., Role of Molecular Order and Solid-State Structure in Organic Field-Effect Transistors. *Chem. Rev.* **2011,** *111*, 4833-4856.

51. Wang, C.; Dong, H.; Hu, W.; Liu, Y.; Zhu, D., Semiconducting π-Conjugated Systems in Field-Effect Transistors: A Material Odyssey of Organic Electronics. *Chem. Rev.* **2012,** *112*, 2208-2267.

52. Ghosh, S.; Reddy, C. M., Elastic and Bendable Caffeine Cocrystals: Implications for the Design of Flexible Organic Materials. *Angew. Chem. Int. Ed.* **2012,** *51*, 10319-10323.

53. Anthony, J. E.; Facchetti, A.; Heeney, M.; Marder, S. R.; Zhan, X., n-Type Organic Semiconductors in Organic Electronics. *Adv. Mater.* **2010,** *22*, 3876-3892.

54. Weil, T.; Vosch, T.; Hofkens, J.; Peneva, K.; Muellen, K., The Rylene Colorant Family-Tailored Nanoemitters for Photonics Research and Applications. *Angew. Chem., Int. Ed.* **2010,** *49*, 9068-9093.

55. Wurthner, F.; Stolte, M., Naphthalene and perylene diimides for organic transistors. *Chem. Commun.* **2011,** *47*, 5109-5115.

56. Zhan, X.; Facchetti, A.; Barlow, S.; Marks, T. J.; Ratner, M. A.; Wasielewski, M. R.; Marder, S. R., Rylene and Related Diimides for Organic Electronics. *Adv. Mater.* **2011,** *23*, 268-284.

57. Bhosale, S. V.; Jani, C. H.; Langford, S. J., Chemistry of naphthalene diimides. *Chem. Soc. Rev.* **2008,** *37*, 331-342.

58. Tumiatti, V.; Milelli, A.; Minarini, A.; Micco, M.; Gasperi Campani, A.; Roncuzzi, L.; Baiocchi, D.; Marinello, J.; Capranico, G.; Zini, M.; Stefanelli, C.; Melchiorre, C., Design,

Synthesis, and Biological Evaluation of Substituted Naphthalene Imides and Diimides as Anticancer Agent. *J. Med. Chem.* **2009,** *52*, 7873-7877.

59. Takashima, Y.; Martinez, V. M.; Furukawa, S.; Kondo, M.; Shimomura, S.; Uehara, H.; Nakahama, M.; Sugimoto, K.; Kitagawa, S., Molecular decoding using luminescence from an entangled porous framework. *Nat. Commun.* **2011,** *2*, 1-8, 8 pp.
60. Guha, S.; Goodson, F. S.; Corson, L. J.; Saha, S., Boundaries of Anion/Naphthalenediimide Interactions: From Anion-π Interactions to Anion-Induced Charge-Transfer and Electron-Transfer Phenomena. *J. Am. Chem. Soc.* **2012,** *134*, 13679-13691.
61. Molla, M. R.; Ghosh, S., Hydrogen-Bonding-Mediated J-Aggregation and White-Light Emission from a Remarkably Simple, Single-Component, Naphthalenediimide Chromophore. *Chem. - Eur. J.* **2012,** *18*, 1290-1294.
62. Bhosale, S. V.; Bhosale, S. V.; Bhargava, S. K., Recent progress of core-substituted naphthalenediimides: highlights from 2010. *Org. Biomol. Chem.* **2012,** *10*, 6455-6468.
63. Narayanaswamy, N.; Avinash, M. B.; Govindaraju, T., Exploring hydrogen bonding and weak aromatic interactions induced assembly of adenine and thymine functionalized naphthalenediimides. *New J. Chem.* **2013,** *37*, 1302-1306.
64. Takai, A.; Yasuda, T.; Ishizuka, T.; Kojima, T.; Takeuchi, M., A Directly Linked Ferrocene-Naphthalenediimide Conjugate: Precise Control of Stacking Structures of π-Systems by Redox Stimuli. *Angew. Chem. Int. Ed.* **2013,** *52*, 9167-9171.
65. Shao, H.; Nguyen, T.; Romano, N. C.; Modarelli, D. A.; Parquette, J. R., Self-assembly of 1-D n-type nanostructures based on naphthalene diimide-appended dipeptides. *J. Am. Chem. Soc.* **2009,** *131*, 16374-16376.
66. Shao, H.; Seifert, J.; Romano, N. C.; Gao, M.; Helmus, J. J.; Jaroniec, C. P.; Modarelli, D. A.; Parquette, J. R., Amphiphilic self-assembly of an n-type nanotube. *Angew. Chem., Int. Ed.* **2010,** *49*, 7688-7691.
67. Shao, H.; Gao, M.; Kim, S. H.; Jaroniec, C. P.; Parquette, J. R., Aqueous Self-Assembly of L-Lysine-Based Amphiphiles into 1D n-Type Nanotubes. *Chem. - Eur. J.* **2011,** *17*, 12882-12885.
68. Manchineella, S.; Prathyusha, V.; Priyakumar, U. D.; Govindaraju, T., Solvent-Induced Helical Assembly and Reversible Chiroptical Switching of Chiral Cyclic-Dipeptide-Functionalized Naphthalenediimides. *Chem. - Eur. J.* **2013,** *19*, 16615-16624.
69. Molla, M. R.; Gehrig, D.; Roy, L.; Kamm, V.; Paul, A.; Laquai, F.; Ghosh, S., Self-Assembly of Carboxylic Acid-Appended Naphthalene Diimide Derivatives with Tunable Luminescent Color and Electrical Conductivity. *Chem. - Eur. J.* **2014,** *20*, 760-771.
70. Pantos, G. D.; Pengo, P.; Sanders, J. K. M., Hydrogen-bonded helical organic nanotubes. *Angew. Chem., Int. Ed.* **2007,** *46*, 194-197.

71. Bulheller, B. M.; Pantos, G. D.; Sanders, J. K. M.; Hirst, J. D., Electronic structure and circular dichroism spectroscopy of naphthalenediimide nanotubes. *Phys. Chem. Chem. Phys.* **2009,** *11*, 6060-6065.

72. Anderson, T. W.; Sanders, J. K. M.; Pantos, G. D., The sergeants-and-soldiers effect: chiral amplification in naphthalenediimide nanotubes. *Org. Biomol. Chem.* **2010,** *8*, 4274-4280.

73. Ponnuswamy, N.; Pantos, G. D.; Smulders, M. M. J.; Sanders, J. K. M., Thermodynamics of Supramolecular Naphthalenediimide Nanotube Formation: The Influence of Solvents, Side Chains, and Guest Templates. *J. Am. Chem. Soc.* **2012,** *134*, 566-573.

74. Tambara, K.; Olsen, J.-C.; Hansen, D. E.; Pantos, G. D., The thermodynamics of the self-assembly of covalently linked oligomeric naphthalenediimides into helical organic nanotubes. *Org. Biomol. Chem.* **2014,** *12*, 607-614.

75. Bhosale, S.; Sisson, A. L.; Talukdar, P.; Fuerstenberg, A.; Banerji, N.; Vauthey, E.; Bollot, G.; Mareda, J.; Roeger, C.; Wuerthner, F.; Sakai, N.; Matile, S., Photoproduction of proton gradients with π-stacked fluorophore scaffolds in lipid bilayers. *Science* **2006,** *313*, 84-86.

76. Bhosale, R.; Misek, J.; Sakai, N.; Matile, S., Supramolecular n/p-heterojunction photosystems with oriented multicolored antiparallel redox gradients (OMARG-SHJs). *Chem. Soc. Rev.* **2010,** *39*, 138-149.

77. Tomasulo, M.; Naistat, D. M.; White, A. J. P.; Williams, D. J.; Raymo, F. M., Self-assembly of naphthalene diimides into cylindrical microstructures. *Tetrahedron Lett.* **2005,** *46*, 5695-5698.

78. Ashkenasy, N.; Horne, W. S.; Ghadiri, M. R., Design of self-assembling peptide nanotubes with delocalized electronic states. *Small* **2006,** *2*, 99-102.

79. Avinash, M. B.; Govindaraju, T., A bio-inspired design strategy: organization of tryptophan-appended naphthalenediimide into well-defined architectures induced by molecular interactions. *Nanoscale* **2011,** *3*, 2536-2543.

80. Jatsch, A.; Schillinger, E. K.; Schmid, S.; Baeuerle, P., Biomolecule assisted self-assembly of π-conjugated oligomers. *J. Mater. Chem.* **2010,** *20*, 3563-3578.

81. Owens, R. M.; Malliaras, G. G., Organic electronics at the interface with biology. *MRS Bull.* **2010,** *35*, 449-456.

82. Kim, S. H.; Parquette, J. R., A model for the controlled assembly of semiconductor peptides. *Nanoscale* **2012,** *4*, 6940-6947.

83. Sengupta, S.; Wurthner, F., Chlorophyll J-aggregates: from bioinspired dye stacks to nanotubes, liquid crystals, and biosupramolecular electronics. *Acc. Chem. Res.* **2013,** *46*, 2498-2512.

84. Tovar, J. D., Supramolecular Construction of Optoelectronic Biomaterials. *Acc. Chem. Res.* **2013,** *46*, 1527-1537.

85. Pandeeswar, M.; Khare, H.; Ramakumar, S.; Govindaraju, T., Biomimetic molecular organization of naphthalene diimide in the solid state: tunable (chiro-) optical, viscoelastic and nanoscale properties. *RSC Adv.* **2014,** *4*, 20154-20163.

86. Alvey, P. M.; Reczek, J. J.; Lynch, V.; Iverson, B. L., A systematic study of thermochromic aromatic donor-acceptor materials. *J. Org. Chem.* **2010,** *75*, 7682-7690.

87. Kakinuma, T.; Kojima, H.; Ashizawa, M.; Matsumoto, H.; Mori, T., Correlation of mobility and molecular packing in organic transistors based on cycloalkyl naphthalene diimides. *J. Mater. Chem. C* **2013,** *1*, 5395-5401.

88. Frampton, C. S.; Knight, K. S.; Shankland, N.; Shankland, K., Single-crystal X-ray diffraction analysis of pyrene II at 93 K. *J. Mol. Struct.* **2000,** *520*, 29-32.

89. Wang, Z.; Enkelmann, V.; Negri, F.; Muellen, K., Rational design of helical columnar packing in single crystals. *Angew. Chem. Int. Ed.* **2004,** *43*, 1972-1975.

90. Kobayashi, K.; Shimaoka, R.; Kawahata, M.; Yamanaka, M.; Yamaguchi, K., Synthesis and cofacial pi-stacked packing arrangement of 6,13-bis(alkylthio)pentacene. *Org. Lett.* **2006,** *8*, 2385-2388.

91. Mukhopadhyay, P.; Iwashita, Y.; Shirakawa, M.; Kawano, S.-i.; Fujita, N.; Shinkai, S., Spontaneous colorimetric sensing of the positional isomers of dihydroxynaphthalene in a 1D organogel matrix. *Angew. Chem. Int. Ed.* **2006,** *45*, 1592-1595.

92. Ofir, Y.; Zelichenok, A.; Yitzchaik, S., 1,4;5,8-Naphthalene-tetracarboxylic diimide derivatives as model compounds for molecular layer epitaxy. *J. Mater. Chem.* **2006,** *16*, 2142-2149.

93. Ganesan, P.; van Lagen, B.; Marcelis, A. T.; Sudholter, E. J.; Zuilhof, H., Siloxanes with pendent naphthalene diimides: synthesis and fluorescence quenching. *Org. Lett.* **2007,** *9*, 2297-2300.

94. Liu, K.; Yao, Y.; Liu, Y.; Wang, C.; Li, Z.; Zhang, X., Self-assembly of supra-amphiphiles based on dual charge-transfer interactions: from nanosheets to nanofibers. *Langmuir* **2012,** *28*, 10697-10702.

95. McCarthy, B. D.; Hontz, E. R.; Yost, S. R.; Van Voorhis, T.; Dinca, M., Charge Transfer or J-Coupling? Assignment of an Unexpected Red-Shifted Absorption Band in a Naphthalenediimide-Based Metal-Organic Framework. *J Phys Chem Lett* **2013,** *4*, 453-458.

96. Bodapati, J. B.; Icil, H., A new tunable light-emitting and π-stacked hexa-ethyleneglycol naphthalene-bisimide oligomer: synthesis, photophysics and electrochemical properties. *Photochem. Photobiol. Sci.* **2011,** *10*, 1283-1293.

97. Bell, T. D. M.; Bhosale, S. V.; Forsyth, C. M.; Hayne, D.; Ghiggino, K. P.; Hutchison, J. A.; Jani, C. H.; Langford, S. J.; Lee, M. A. P.; Woodward, C. P., Melt-induced fluorescent signature in a simple naphthalenediimide. *Chem. Commun.* **2010,** *46*, 4881-4883.

98. Pandeeswar, M.; Govindaraju, T., Green-fluorescent naphthalene diimide: conducting layered hierarchical 2D nanosheets and reversible probe for detection of aromatic solvents. *RSC Adv.* **2013,** *3*, 11459-11462.

99. Hisaki, I.; Sasaki, T.; Sakaguchi, K.; Liu, W.-T.; Tohnai, N.; Miyata, M., Right- and left-handedness of 21 symmetrical herringbone assemblies of benzene. *Chem. Commun.* **2012,** *48*, 2219-2221.

100. Hisaki, I.; Sasaki, T.; Tohnai, N.; Miyata, M., Supramolecular-tilt-chirality on twofold helical assemblies. *Chem. - Eur. J.* **2012,** *18*, 10066-10073.

101. Avinash, M. B.; Govindaraju, T., Nanoarchitectonics of biomolecular assemblies for functional applications. *Nanoscale* **2014,** *6*, 13348-13369.

102. Ariga, K.; Kawakami, K.; Ebara, M.; Kotsuchibashi, Y.; Ji, Q.; Hill, J. P., Bioinspired nanoarchitectonics as emerging drug delivery systems. *New J. Chem.* **2014,** *38*, 5149-5163.

103. Ariga, K.; Vinu, A.; Yamauchi, Y.; Ji, Q. M.; Hill, J. P., Nanoarchitectonics for Mesoporous Materials. *Bull. Chem. Soc. Jpn.* **2012,** *85*, 1-32.

104. Aono, M.; Bando, Y.; Ariga, K., Nanoarchitectonics: pioneering a new paradigm for nanotechnology in materials development. *Adv. Mater.* **2012,** *24*, 150-151.

105. Govindaraju, T.; Avinash, M. B., Two-dimensional nanoarchitectonics: organic and hybrid materials. *Nanoscale* **2012,** *4*, 6102-6117.

106. Geim, A. K.; Novoselov, K. S., The rise of graphene. *Nat. Mater.* **2007,** *6*, 183-191.

107. Rao, C. N. R.; Sood, A. K.; Subrahmanyam, K. S.; Govindaraj, A., Graphene: the new two-dimensional nanomaterial. *Angew. Chem. Int. Ed.* **2009,** *48*, 7752-7777.

108. Osterbacka, R.; An, C. P.; Jiang, X. M.; Vardeny, Z. V., Two-dimensional electronic excitations in self-assembled conjugated polymer nanocrystals. *Science* **2000,** *287*, 839-842.

109. Shukla, D.; Nelson, S. F.; Freeman, D. C.; Rajeswaran, M.; Ahearn, W. G.; Meyer, D. M.; Carey, J. T., Thin-Film Morphology Control in Naphthalene-Diimide-Based Semiconductors: High Mobility n-Type Semiconductor for Organic Thin-Film Transistors. *Chem. Mater.* **2008,** *20*, 7486-7491.

110. Davis, R.; Berger, R.; Zentel, R., Two-dimensional aggregation of organogelators induced by biaxial hydrogen-bonding gives supramolecular nanosheets. *Adv. Mater.* **2007,** *19*, 3878-3881.

111. Wang, Z.; Li, Z.; Medforth, C. J.; Shelnutt, J. A., Self-Assembly and Self-Metallization of Porphyrin Nanosheets. *J. Am. Chem. Soc.* **2007,** *129*, 2440-2441.

112. Ariga, K.; Hill, J. P.; Wakayama, Y., Supramolecular chemistry in two dimensions: self-assembly and dynamic function. *Phys. Status Solidi A* **2008,** *205*, 1249-1257.

113. Govindaraju, T.; Pandeeswar, M.; Jayaramulu, K.; Jaipuria, G.; Atreya, H. S., Spontaneous self-assembly of designed cyclic dipeptide (Phg-Phg) into two-dimensional nano- and mesosheets. *Supramol. Chem.* **2011,** *23*, 487-492.

114. Avinash, M. B.; Govindaraju, T., Engineering Molecular Organization of Naphthalenediimides: Large Nanosheets with Metallic Conductivity and Attoliter Containers. *Adv. Funct. Mater.* **2011,** *21*, 3875-3882.

115. Xu, J.; Wu, G.; Wang, Z.; Zhang, X., Generation of 2D organic microsheets from protonated melamine derivatives: suppression of the self assembly of a particular dimension by introduction of alkyl chains. *Chem. Sci.* **2012,** *3*, 3227-3230.

116. Zhuang, X.; Mai, Y.; Wu, D.; Zhang, F.; Feng, X., Two-dimensional soft nanomaterials: a fascinating world of materials. *Adv. Mater.* **2015,** *27*, 403-427.

117. Sleytr, U. B.; Messner, P.; Pum, D.; Sara, M., Crystalline bacterial cell surface layers (S layers): from supramolecular cell structure to biomimetics and nanotechnology. *Angew. Chem., Int. Ed.* **1999,** *38*, 1034-1054.

118. Sakamoto, J.; van Heijst, J.; Lukin, O.; Schluter, A. D., Two-dimensional polymers: just a dream of synthetic chemists? *Angew. Chem., Int. Ed.* **2009,** *48*, 1030-1069.

119. Nam, K. T.; Shelby, S. A.; Choi, P. H.; Marciel, A. B.; Chen, R.; Tan, L.; Chu, T. K.; Mesch, R. A.; Lee, B.-C.; Connolly, M. D.; Kisielowski, C.; Zuckermann, R. N., Free-floating ultrathin two-dimensional crystals from sequence-specific peptoid polymers. *Nat. Mater.* **2010,** *9*, 454-460.

120. Ariga, K.; Yamauchi, Y.; Mori, T.; Hill, J. P., 25th anniversary article: what can be done with the Langmuir-Blodgett method? Recent developments and its critical role in materials science. *Adv. Mater.* **2013,** *25*, 6477-6512.

121. Ariga, K.; Yamauchi, Y.; Rydzek, G.; Ji, Q.; Yonamine, Y.; Wu, K. C. W.; Hill, J. P., Layer-by-layer nanoarchitectonics: invention, innovation, and evolution. *Chem. Lett.* **2014,** *43*, 36-68.

122. Jiang, T.; Xu, C.; Liu, Y.; Liu, Z.; Wall, J. S.; Zuo, X.; Lian, T.; Salaita, K.; Ni, C.; Pochan, D.; Conticello, V. P., Structurally defined nanoscale sheets from self-assembly of collagen-mimetic peptides. *J. Am. Chem. Soc.* **2014,** *136*, 4300-4308.

123. Mas-Balleste, R.; Gomez-Navarro, C.; Gomez-Herrero, J.; Zamora, F., 2D materials: to graphene and beyond. *Nanoscale* **2011,** *3*, 20-30.

124. Liu, J.; Liu, X. W., Two-dimensional nanoarchitectures for lithium storage. *Adv. Mater.* **2012,** *24*, 4097-4111.

125. Osada, M.; Sasaki, T., Two-dimensional dielectric nanosheets. Novel nanoelectronics from nanocrystal building blocks. *Adv. Mater.* **2012,** *24*, 210-228.

126. Geng, F.; Ma, R.; Nakamura, A.; Akatsuka, K.; Ebina, Y.; Yamauchi, Y.; Miyamoto, N.; Tateyama, Y.; Sasaki, T., Unusually stable ~100-fold reversible and instantaneous swelling of inorganic layered materials. *Nat. Commun.* **2013,** *4*, 2641- 2647.

127. Rao, C. N. R.; Matte, H. S. S. R.; Maitra, U., Graphene analogues of inorganic layered materials. *Angew. Chem. Int. Ed.* **2013,** *52*, 13162-13185.

128. Rao, C. N. R.; Maitra, U.; Waghmare, U. V., Extraordinary attributes of 2-dimensional MoS2 nanosheets. *Chem. Phys. Lett.* **2014,** *609*, 172-183.

129. Peng, X.; Peng, L.; Wu, C.; Xie, Y., Two dimensional nanomaterials for flexible supercapacitors. *Chem. Soc. Rev.* **2014,** *43*, 3303-3323.

130. Avinash, M. B.; Govindaraju, T., Amino acid derivatized arylenediimides: a versatile modular approach for functional molecular materials. *Adv. Mater.* **2012,** *24*, 3905-3922.

131. Nalluri, S. K. M.; Berdugo, C.; Javid, N.; Frederix, P. W. J. M.; Ulijn, R. V., Biocatalytic Self-Assembly of Supramolecular Charge-Transfer Nanostructures Based on n-Type Semiconductor-Appended Peptides. *Angew. Chem., Int. Ed.* **2014,** *53*, 5882-5887.

132. Holman, G. G.; Zewail-Foote, M.; Smith, A. R.; Johnson, K. A.; Iverson, B. L., A sequence-specific threading tetra-intercalator with an extremely slow dissociation rate constant. *Nat. Chem.* **2011,** *3*, 875-881.

133. Trivedi, D. R.; Fujiki, Y.; Fujita, N.; Shinkai, S.; Sada, K., Crystal engineering approach to design colorimetric indicator array to discriminate positional isomers of aromatic organic molecules. *Chem. - Asian J.* **2009,** *4*, 254-261.

134. Pandeeswar, M.; Govindaraju, T., Bioinspired Nanoarchitectonics of Naphthalene Diimide to Access 2D Sheets of Tunable Size, Shape, and Optoelectronic Properties. *J. Inorg. Organomet. Polym. Mater.* **2015,** *25*, 293-300.

135. Pantos, G. D.; Pengo, P.; Sanders, J. K., Hydrogen-bonded helical organic nanotubes. *Angew. Chem. Int. Ed.* **2007,** *46*, 194-197.

136. Aida, T.; Meijer, E. W.; Stupp, S. I., Functional supramolecular polymers. *Science* **2012,** *335*, 813-817.

137. Haedler, A. T.; Kreger, K.; Issac, A.; Wittmann, B.; Kivala, M.; Hammer, N.; Kohler, J.; Schmidt, H. W.; Hildner, R., Long-range energy transport in single supramolecular nanofibres at room temperature. *Nature* **2015,** *523*, 196-199.

138. Moulin, E.; Cid, J. J.; Giuseppone, N., Advances in supramolecular electronics - from randomly self-assembled nanostructures to addressable self-organized interconnects. *Adv. Mater.* **2013,** *25*, 477-487.

139. Horiuchi, S.; Tokura, Y., Organic ferroelectrics. *Nat. Mater.* **2008,** *7*, 357-366.

140. Tayi, A. S.; Kaeser, A.; Matsumoto, M.; Aida, T.; Stupp, S. I., Supramolecular ferroelectrics. *Nat. Chem.* **2015,** *7*, 281-294.

141. Furukawa, T.; Date, M.; Fukada, E., Hysteresis phenomena in polyvinylidene fluoride under high electric field. *J. Appl. Phys.* **1980,** *51*, 1135-1141.

142. Noda, K.; Ishida, K.; Kubono, A.; Horiuchi, T.; Yamada, H.; Matsushige, K., Remanent polarization of evaporated films of vinylidene fluoride oligomers. *J. Appl. Phys.* **2003,** *93*, 2866-2870.

143. Solomon, A. L., Thiourea, a New Ferroelectric. *Phy. Rev.* **1956,** *104*, 1191-1191.

144. Bordeaux, D.; Bornarel, J.; Capiomont, A.; Lajzerowicz-Bonneteau, J.; Lajzerowicz, J.; Legrand, J. F., New Ferroelastic-Ferroelectric Compound: Tanane. *Phys. Rev. Lett.* **1973,** *31*, 314-317.

145. Tayi, A. S.; Shveyd, A. K.; Sue, A. C.; Szarko, J. M.; Rolczynski, B. S.; Cao, D.; Kennedy, T. J.; Sarjeant, A. A.; Stern, C. L.; Paxton, W. F.; Wu, W.; Dey, S. K.; Fahrenbach, A. C.; Guest, J. R.; Mohseni, H.; Chen, L. X.; Wang, K. L.; Stoddart, J. F.; Stupp, S. I., Room-temperature ferroelectricity in supramolecular networks of charge-transfer complexes. *Nature* **2012,** *488*, 485-489.

146. Pan, L.; Liu, G.; Li, H.; Meng, S.; Han, L.; Shang, J.; Chen, B.; Platero-Prats, A. E.; Lu, W.; Zou, X.; Li, R. W., A resistance-switchable and ferroelectric metal-organic framework. *J. Am. Chem. Soc.* **2014,** *136*, 17477-17483.

147. Horiuchi, S.; Kumai, R.; Tokura, Y., Hydrogen-bonded donor--acceptor compounds for organic ferroelectric materials. *Chem. Commun.* **2007**, 2321-2329.

148. Kagawa, F.; Horiuchi, S.; Matsui, H.; Kumai, R.; Onose, Y.; Hasegawa, T.; Tokura, Y., Electric-field control of solitons in a ferroelectric organic charge-transfer salt. *Phys. Rev. Lett.* **2010,** *104*, 227602.

149. Kobayashi, K.; Horiuchi, S.; Kumai, R.; Kagawa, F.; Murakami, Y.; Tokura, Y., Electronic ferroelectricity in a molecular crystal with large polarization directing antiparallel to ionic displacement. *Phys. Rev. Lett.* **2012,** *108*, 237601.

150. Hirst, A. R.; Escuder, B.; Miravet, J. F.; Smith, D. K., High-tech applications of self-assembling supramolecular nanostructured gel-phase materials: from regenerative medicine to electronic devices. *Angew. Chem. Int. Ed.* **2008,** *47*, 8002-8018.

151. Babu, S. S.; Praveen, V. K.; Ajayaghosh, A., Functional π-Gelators and Their Applications. *Chem. Rev.* **2014,** *114*, 1973-2129.

152. Lemieux, R. P., Chirality transfer in ferroelectric liquid crystals. *Acc. Chem. Res.* **2001,** *34*, 845-853.

153. Popova, E. V.; Fedoryako, A. P.; Drushlyak, T. G.; Vashchenko, V. V.; Kutulya, L. A., Influence of chiral dopant molecular structure on ferroelectric liquid crystal parameters. *Ferroelectrics* **2006,** *343*, 33-40.

154. Boulton, C. J.; Finden, J. G.; Yuh, E.; Sutherland, J. J.; Wand, M. D.; Wu, G.; Lemieux, R. P., Ferroelectric liquid crystals induced by dopants with axially chiral 2,2 '-spirobiindan-1,1 '-dione cores. *J. Am. Chem. Soc.* **2005,** *127*, 13656-13665.

155. McCubbin, J. A.; Tong, X.; Wang, R. Y.; Zhao, Y.; Snieckus, V.; Lemieux, R. P., Directed metalation route to ferroelectric liquid crystals with a chiral fluorenol core: The effect of restricted rotation on polar order. *J. Am. Chem. Soc.* **2004,** *126*, 1161-1167.

156. Finden, J. G.; Yuh, E.; Huntley, C.; Lemieux, R. P., Ferroelectric liquid crystals induced by dopants with axially chiral 2,2 '-spirobiindan-1,1 '-dione cores: diether vs. diester side-chains. *Liq. Cryst.* **2007,** *34*, 1095-1106.

157. McCubbin, J. A.; Tong, X.; Zhao, Y.; Snieckus, V.; Lemieux, R. P., Directed metalation-cross coupling route to ferroelectric liquid crystals with a chiral fluorenol core: The effect of intermolecular hydrogen bonding on polar order. *Chem. Mater.* **2005,** *17*, 2574-2581.

158. Safont-Sempere, M. M.; Fernandez, G.; Wurthner, F., Self-sorting phenomena in complex supramolecular systems. *Chem. Rev.* **2011,** *111*, 5784-5814.

159. Hardouin-Lerouge, M.; Hudhomme, P.; Salle, M., Molecular clips and tweezers hosting neutral guests. *Chem. Soc. Rev.* **2011,** *40*, 30-43.

160. Pandeeswar, M.; Khare, H.; Ramakumar, S.; Govindaraju, T., Crystallographic insight-guided nanoarchitectonics and conductivity modulation of an n-type organic semiconductor through peptide conjugation. *Chem. Commun.* **2015,** *51*, 8315-8318.

161. Pandeeswar, M.; Avinash, M. B.; Govindaraju, T., Chiral transcription and retentive helical memory: probing peptide auxiliaries appended with naphthalenediimides for their one-dimensional molecular organization. *Chem. - Eur. J.* **2012,** *18*, 4818-4822.

162. Bhosale, S.; Sisson, A. L.; Talukdar, P.; Fürstenberg, A.; Banerji, N.; Vauthey, E.; Bollot, G.; Mareda, J.; Röger, C.; Würthner, F.; Sakai, N.; Matile, S., Photoproduction of Proton Gradients with π-Stacked Fluorophore Scaffolds in Lipid Bilayers. *Science* **2006,** *313*, 84-86.

163. Winnik, F. M., Photophysics of preassociated pyrenes in aqueous polymer solutions and in other organized media. *Chem. Rev.* **1993,** *93*, 587-614.

164. Scott Lokey, R.; Iverson, B. L., Synthetic molecules that fold into a pleated secondary structure in solution. *Nature* **1995,** *375*, 303-305.

165. Koshkakaryan, G.; Klivansky, L. M.; Cao, D.; Snauko, M.; Teat, S. J.; Struppe, J. O.; Liu, Y., Alternative donor-acceptor stacks from crown ethers and naphthalene diimide derivatives: rapid, selective formation from solution and solid state grinding. *J. Am. Chem. Soc.* **2009,** *131*, 2078-2079.

166. Martinez, C. R.; Iverson, B. L., Rethinking the term "pi-stacking". *Chem. Sci.* **2012,** *3*, 2191-2201.

167. Sleytr, U. B.; Messner, P.; Pum, D.; Sara, M., Crystalline bacterial cell surface layers (s layers): from supramolecular cell structure to biomimetics and nanotechnology. *Angew. Chem. Int. Ed.* **1999,** *38*, 1034-1054.

168. Sotiropoulou, S.; Sierra-Sastre, Y.; Mark, S. S.; Batt, C. A., Biotemplated nanostructured materials. *Chem. Mater.* **2008,** *20*, 821-834.

169. Govindaraju, T.; Avinash, M. B., Two-dimensional nanoarchitectonics: organic and hybrid materials. *Nanoscale* **2012,** *4*, 6102-6117.

170. Lei, Y. L.; Liao, Q.; Fu, H. B.; Yao, J. N., Phase- and Shape-Controlled Synthesis of Single Crystalline Perylene Nanosheets and Its Optical Properties. *J. Phys. Chem. C* **2009,** *113*, 10038-10043.

171. Sathish, M.; Miyazawa, K.; Hill, J. P.; Ariga, K., Solvent engineering for shape-shifter pure fullerene (C60). *J. Am. Chem. Soc.* **2009,** *131*, 6372-6373.

172. Yu, Z.; Yan, H.; Lu, K.; Zhang, Y.; Wei, Z., Self-assembly of two-dimensional nanostructures of linear regioregular poly(3-hexylthiophene). *RSC Adv.* **2012,** *2*, 338-343.

173. Saines, P. J.; Steinmann, M.; Tan, J.-C.; Yeung, H. H. M.; Li, W.; Barton, P. T.; Cheetham, A. K., Isomer-Directed Structural Diversity and Its Effect on the Nanosheet Exfoliation and Magnetic Properties of 2,3-Dimethylsuccinate Hybrid Frameworks. *Inorg. Chem.* **2012,** *51*, 11198-11209.

174. Tan, J.-C.; Saines, P. J.; Bithell, E. G.; Cheetham, A. K., Hybrid Nanosheets of an Inorganic-Organic Framework Material: Facile Synthesis, Structure, and Elastic Properties. *ACS Nano* **2012,** *6*, 615-621.

175. Saines, P. J.; Tan, J.-C.; Yeung, H. H. M.; Barton, P. T.; Cheetham, A. K., Layered inorganic-organic frameworks based on the 2,2-dimethylsuccinate ligand: structural diversity and its effect on nanosheet exfoliation and magnetic properties. *Dalton Trans.* **2012,** *41*, 8585-8593.

176. Geim, A. K.; Novoselov, K. S., The rise of graphene. *Nat. Mater.* **2007,** *6*, 183-191.

177. Sirringhaus, H.; Brown, P. J.; Friend, R. H.; Nielsen, M. M.; Bechgaard, K.; Langeveld-Voss, B. M. W.; Spiering, A. J. H.; Janssen, R. A. J.; Meijer, E. W.; Herwig, P.; De Leeuw, D. M., Two-dimensional charge transport in self-organized, high-mobility conjugated polymers. *Nature* **1999,** *401*, 685-688.

178. Nandre, K. P.; Bhosale, S. V.; Rama Krishna, K. V. S.; Gupta, A.; Bhosale, S. V., A phosphonic acid appended naphthalene diimide motif for self-assembly into tunable nanostructures through molecular recognition with arginine in water. *Chem. Commun.* **2013,** *49*, 5444-5446.

179. Bhosale, S. V.; Jani, C. H.; Lalander, C. H.; Langford, S. J.; Nerush, I.; Shapter, J. G.; Villamaina, D.; Vauthey, E., Supramolecular construction of vesicles based on core-substituted naphthalene diimide appended with triethyleneglycol motifs. *Chem. Commun.* **2011,** *47*, 8226-8228.

180. Bhosale, R.; Kishore, R. S. K.; Ravikumar, V.; Kel, O.; Vauthey, E.; Sakai, N.; Matile, S., Zipper assembly of SHJ photosystems: focus on red naphthalenediimides, optoelectronic finetuning and topological matching. *Chem. Sci.* **2010,** *1*, 357-368.

181. Scott Lokey, R.; Iverson, B. L., Synthetic molecules that fold into a pleated secondary structure in solution. *Nature* **1995,** *375*, 303-305.

182. Avinash, M. B.; Govindaraju, T., A bio-inspired design strategy: Organization of tryptophan-appended naphthalenediimide into well-defined architectures induced by molecular interactions. *Nanoscale* **2011,** *3*, 2536-2543.

183. Pandeeswar, M.; Govindaraju, T., Green-fluorescent naphthalene diimide: conducting layered hierarchical 2D nanosheets and reversible probe for detection of aromatic solvents. *RSC Adv.* **2013,** *3*, 11459-11462.

184. Gottarelli, G.; Lena, S.; Masiero, S.; Pieraccini, S.; Spada, G. P., The use of circular dichroism spectroscopy for studying the chiral molecular self-assembly: an overview. *Chirality* **2008,** *20*, 471-485.

185. Anderson, T. W.; Pantos, G. D.; Sanders, J. K. M., Supramolecular chemistry of monochiral naphthalenediimides. *Org. Biomol. Chem.* **2011,** *9*, 7547-7553.

186. Molla, M. R.; Ghosh, S., Structural Variations on Self-Assembly and Macroscopic Properties of 1,4,5,8-Naphthalene-diimide Chromophores. *Chem. Mater.* **2011,** *23*, 95-105.

187. Molla, M. R.; Ghosh, S., Hydrogen-Bonding-Mediated J-Aggregation and White-Light Emission from a Remarkably Simple, Single-Component, Naphthalenediimide Chromophore. *Chem. - Eur. J.* **2012,** *18*, 1290-1294, S1290/1291-S1290/1299.

188. Lakowicz, J. R., *Principles of fluorescence spectroscopy*. 3rd ed.; springer 2006.

189. Braak, H.; Del Tredici, K., Where, when, and in what form does sporadic Alzheimer's disease begin? *Curr. Opin. Neurobiol.* **2012,** *25*, 708-714.

190. Huang, Y.; Mucke, L., Alzheimer mechanisms and therapeutic strategies. *Cell* **2012,** *148*, 1204-1222.

191. Bossy-Wetzel, E.; Schwarzenbacher, R.; Lipton, S. A., Molecular pathways to neurodegeneration. *Nat. Med.* **2004,** *10*, S2-9.

192. Selkoe, D. J., Alzheimer's disease: genes, proteins, and therapy. *Physiol. Rev.* **2001,** *81*, 741-766.

193. Selkoe, D. J., Cell biology of protein misfolding: the examples of Alzheimer's and Parkinson's diseases. *Nat. Cell Biol.* **2004,** *6*, 1054-1061.

194. Selkoe, D. J., Folding proteins in fatal ways. *Nature* **2003,** *426*, 900-904.

195. Karran, E.; Mercken, M.; De Strooper, B., The amyloid cascade hypothesis for Alzheimer's disease: an appraisal for the development of therapeutics. *Nat. Rev. Drug Discov.* **2011,** *10*, 698-712.

196. Swerdlow, R. H., Pathogenesis of Alzheimer's disease. *Clin. Interv. Aging* **2007,** *2*, 347-359.

197. Hardy, J. A.; Higgins, G. A., Alzheimer's disease: the amyloid cascade hypothesis. *Science* **1992,** *256*, 184-185.

198. Shen, J.; Kelleher, R. J., 3rd, The presenilin hypothesis of Alzheimer's disease: evidence for a loss-of-function pathogenic mechanism. *Proc. Natl. Acad. Sci. U. S. A.* **2007,** *104*, 403-409.

199. Naslund, J.; Haroutunian, V.; Mohs, R.; Davis, K. L.; Davies, P.; Greengard, P.; Buxbaum, J. D., Correlation between elevated levels of amyloid beta-peptide in the brain and cognitive decline. *Jama-J Am Med Assoc* **2000,** *283*, 1571-1577.

200. Nie, Q.; Du, X. G.; Geng, M. Y., Small molecule inhibitors of amyloid beta peptide aggregation as a potential therapeutic strategy for Alzheimer's disease. *Acta Pharmacol. Sin.* **2011,** *32*, 545-551.

201. Hawkes, C. A.; Deng, L. H.; Shaw, J. E.; Nitz, M.; McLaurin, J., Small molecule beta-amyloid inhibitors that stabilize protofibrillar structures in vitro improve cognition and pathology in a mouse model of Alzheimer's disease. *Eur. J. Neurosci.* **2010,** *31*, 203-213.

202. Re, F.; Airoldi, C.; Zona, C.; Masserini, M.; La Ferla, B.; Quattrocchi, N.; Nicotra, F., Beta amyloid aggregation inhibitors: small molecules as candidate drugs for therapy of Alzheimer's disease. *Curr. Med. Chem.* **2010,** *17*, 2990-3006.

203. Rajasekhar, K.; Chakrabarti, M.; Govindaraju, T., Function and toxicity of amyloid beta and recent therapeutic interventions targeting amyloid beta in Alzheimer's disease. *Chem. Commun.* **2015,** *51*, 13434-13450.

204. Sgarbossa, A., Natural biomolecules and protein aggregation: emerging strategies against amyloidogenesis. *Int. J. Mol. Sci.* **2012,** *13*, 17121-17137.

205. Bemporad, F.; Taddei, N.; Stefani, M.; Chiti, F., Assessing the role of aromatic residues in the amyloid aggregation of human muscle acylphosphatase. *Protein Sci.* **2006,** *15*, 862-870.

206. Porat, Y.; Abramowitz, A.; Gazit, E., Inhibition of amyloid fibril formation by polyphenols: Structural similarity and aromatic interactions as a common inhibition mechanism. *Chem. Biol. Drug Des.* **2006,** *67*, 27-37.

207. Suraru, S. L.; Wurthner, F., Strategies for the synthesis of functional naphthalene diimides. *Angew. Chem. Int. Ed.* **2014,** *53*, 7428-7448.

208. Modi, G.; Voshavar, C.; Gogoi, S.; Shah, M.; Antonio, T.; Reith, M. E.; Dutta, A. K., Multifunctional D2/D3 agonist D-520 with high in vivo efficacy: modulator of toxicity of alpha-synuclein aggregates. *ACS Chem. Neurosci.* **2014,** *5*, 700-717.

Chapter 3: Amino Acid Conjugated PDI: Molecular Probe for Biologically Important Metal ions, H_2O_2 and pH*

---

*Papers based on part of this work have appeared in *ACS Appl. Mater. Interfaces* **2014**, *6, 21369-21379*. Reproduced with permission of the American Chemical Society (ACS).

Subchapter 3.1 Assembly Modulation of PDI Derivative as a Supramolecular Fluorescence Switching Probe for Detection of Cationic Surfactant and Metal Ions in Aqueous Media

3.1.1 Introduction

Over the past few years molecular and supramolecular probes based on perylene diimide (PDI) derivatives in aqueous medium have attracted much attention because of their several advantageous properties such as thermal stability, chemical inertness and high tinctorial strength with a wide range of colors, photochemical stability and high fluorescence.[1-7] With such advantageous properties, PDI derivatives have been considered as optimal fluorescent dyes and utilized in a wide variety of applications such as laser dyes, photovoltaic cells, fluorescence switches, molecular wires, molecular transistors and sensors.[8-17] However, PDI structure and planar π-electron deficient aromatic nature are known to promote strongly the formation of aggregates through stacking interactions between the π-conjugated core and this strong aggregation tendency in aqueous media results in fluorescence quenching.[18-19] In spite of aggregation and resultant low fluorescence, PDI derivatives have been considered to be excellent fluorophore in sensor design because of excellent electron accepting ability and high fluorescence in the disassembled state.[20-21] Thus, recent years witnessed some efforts towards developing PDI derivatives based fluorescence sensors. In these reports, organic solvent along with some composition of aqueous solutions were used to obtain PDI derivatives in disassembled state. Moreover, limited reports are known to use PDI derivatives in only aqueous solution. To overcome disadvantage owing to aggregation, aqueous solubility of PDI derivatives was improved by incorporating hydrophilic substituents at the diimide positions.[3,22-26] However, PDI derivatives with hydrophilic substituents such as carboxylic, sulphonic and other ionic functionalities generally show low fluorescence emission due to predominant π-π stacking and especially in case of ionic functionalities π-π stacking was supposed to be removed by the complexation with oppositely charged moieties.[27] In all these reports fluorescence sensing was supposed to be based on either photo-induced electron transfer (PET) mechanism or assembly and disassembly of PDI derivative.[5,21-23] However, the key daunting challenge of making PDI fluoresce under aqueous media remain to be addressed to further the advancement in PDI based molecular systems and materials for biological and environmental applications.

Detection of biologically important metal ions such as Fe^{3+} and Cu^{2+} has gained significant interest. Although these metal ions are essential for the proper functioning of all living cells, their excessive concentrations are detrimental and leads to various biological disorders.[28-32] In this context, biomolecules such as amino acids and their derivatives are particularly appealing due to their remarkable metal chelating nature, aqueous solubility, specific molecular recognition, and ability to self-assemble into functional, complex and highly ordered molecular systems and nanomaterials through various noncovalent interactions.[33-38] Herein we report an easy and one step synthesis of PDI derivative **PDI 1** with L-DOPA functionality as a well-known receptor at the N-imide positions, and assembly-disassembly modulated detection of Fe^{3+} and Cu^{2+} metal ions.[39] It was presumed that incorporation of L-DOPA would render the aqueous solubility to PDI derivative **PDI 1** and consequently a fluorescence probe in aqueous medium could be established. However, synthesized PDI derivative **PDI 1** was found to be predominantly assembled in aqueous medium, as confirmed by weak fluorescence and characteristic absorption spectral features. We hypothesized that disassembly of **PDI 1** can be achieved in the micellar media of cationic surfactant. Consequently, our investigations in the present study revealed a disassembly and a bright yellow fluorescence of **PDI 1** under laser light, in presence of miceller aqueous media of cationic surfactant cetyltrimethylammonium bromide (CTAB) over other neutral (Triton X 100) and anionic (sodium dodecyl sulfate (SDS)) surfactants. Moreover, such a bright yellow fluorescence of disassembled PDI could be quenched (aggregated state) by the selective interaction with metal ions (Fe^{3+} and Cu^{2+}) leading to formation of a complex between L-DOPA in **PDI 1** and metal ions. Furthermore, metal ions induced aggregated fluorescence switch off state of **PDI 1** could be reversed back into switch on yellow fluorescence (molecularly dissolved state) by sequestrating the metal ions (Fe^{3+} and Cu^{2+}) using a well known metal ions chelator DTPA. Thus, fluorescence switching off-on probe was established through modulation of assembly and disassembly of PDI derivative **PDI 1**. To the best of our knowledge, present study represent the first example of the assembly–disassembly driven ‘‘switching off–on’’ fluorescence for the detection and sensing cationic surfactant and metal ions in aqueous medium respectively. We believe our investigations could provide valuable insights to elucidate the role of host species towards assembly and disassembly of PDI derivatives.

3.1.2 Results and discussion

3.1.2.1 Assembly in aqueous medium

We report the use of synthesized amphiphilic PDI derivative **PDI 1** with L-DOPA functionality at the N-imide positions as fluorescence switch off on probe for cationic surfactant and metal ions (Figure 3.1.1). In a series of investigations to explore the photophysical properties of **PDI 1**, we recorded absorption and fluorescence spectra in dimethyl sulphoxide (DMSO) and water (Figure 3.1.2). Absorption spectrum in DMSO solution showed well-resolved vibronic absorption bands centered at 522 nm (0–0 transition) along with four higher electronic excitation states at 485 nm (0–1 transition),

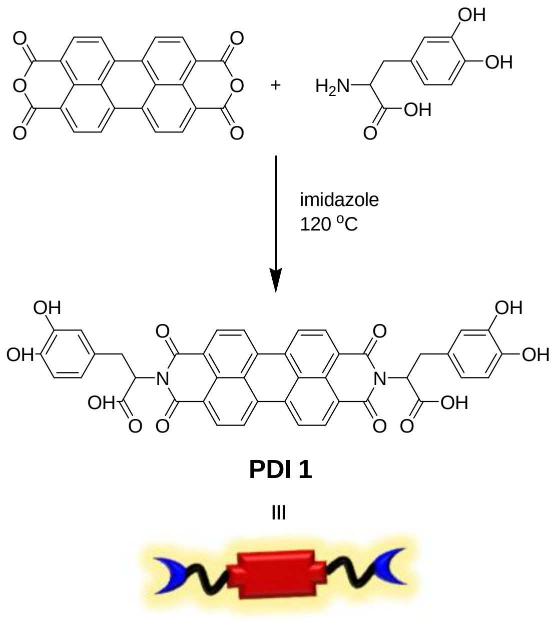

Figure 3.1.1 Synthesis of L-DOPA conjugated PDI derivative **PDI 1**.

454 nm (0–2 transition) and 425 nm (0–3 transition), which are assigned to the typical absorption spectrum of the molecularly dissolved state of **PDI 1** (Figure 3.1.2a).[27] The corresponding fluorescence emission studies further confirmed the absence of any assembled state by displaying mirror image emission spectrum with b_{max} at 545 nm (Figure 3.1.2b). The yellow fluorescence as a consequence of molecularly dissolved state of **PDI 1** can be visualized under green laser light (Figure 3.1.2b, state-I in Figure 3.1.2c). It has been established in previous reports that the absorption intensity ratio of 0–0 and 0–1 transitions (A_{0-0}/A_{0-1}) can be utilized as an indicator of the degree of aggregation of the PDI derivatives.[1,3,5-6,9,12,15-27] The calculated ratio was reported to be 1.59 for the disassembled PDI. Absorption spectrum of **PDI 1** (3.5 μM) in pure water was found to be broad structured, attributed to predominantly assembled state (Figure 3.1.2a). This led to a significant fluorescence quenching of **PDI 1** in pure water as visualized under green laser light (Figure 3.1.2b, inset). While the absorption intensity observed for the 0–0 band

was found to be still higher than 0–1 band (A_{0-0}/A_{0-1}, Frank-Condon value = 1.1) indicating a favorable Franck–Condon factor for (0–0) excited state and thus suggesting the formation of J-type π−π stacking assembly in aqueous solution (State-II, Figure 3.1.2c). Assembled state of **PDI 1** in water was further confirmed by concentration dependant emission spectra from 0 to 3.5 μM. The fluorescence intensity decreased as a function of increased concentration of **PDI 1** and the trend reached saturation at 3.5 μM. Moreover, the decrease in fluorescence may be attributed to intermolecular π−π stacking which is believed to play a significant role in controlling the emissive properties of PDI fluorophore. Therefore, intermolecular interactions at higher concentrations were solely

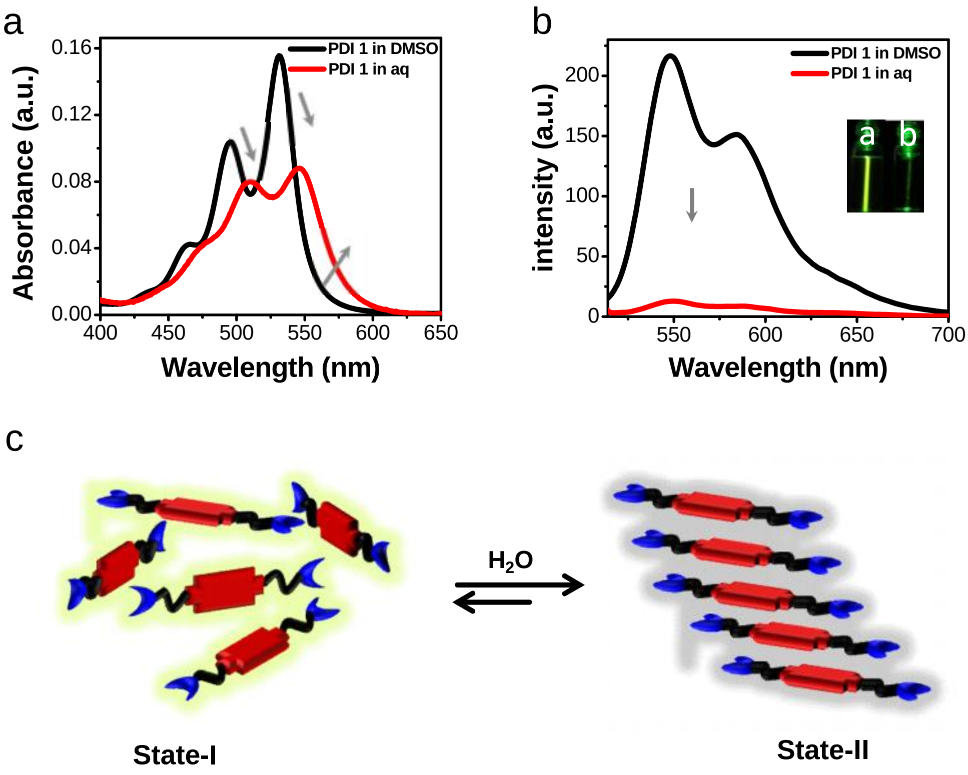

Figure 3.1.2 UV-vis absorption (a) and fluorescence emission spectra (b) of **PDI 1** (3.5 μM) in DMSO and water. Inset: solutions of **PDI 1** in DMSO (a) and water (b) under green laser light. c) Schematic representation of molecular organization of **PDI 1** in DMSO (molecularly dissolved State-I) and in aqueous solution (aggregated State-II).

responsible for self-quenching of **PDI 1**. Furthermore, changes in fluorescence response of **PDI 1** at concentrations > 3.5 μM was found to be insignificant in the presence of various cationic, anionic and neutral species.

3.1.2.2 Disassembly in miceller medium: Detection of Cationic Surfactant

In order to examine whether or not self-assembled **PDI 1** could be used as a probe to detect targeted analytes, initially spectroscopic behavior was investigated in the miceller media of cationic, neutral and anionic surfactants such as CTAB, Triton X 100 and SDS (Figure 3.1.3). It is evident from previous reports that surfactants above their critical micelle concentration (CMC) can solubilize even hydrophobic species in water, and could break up aggregates formed by the intermolecular hydrophobic interactions.[18] With this concept in mind, changes in photophysical properties of **PDI 1** were monitored by performing the controlled experiments in the absence and presence of cationic (CTAB), neutral (triton X 100) and anionic (SDS) surfactants in aqueous media (Figure 3.1.3). Eleven samples, with increasing concentrations of surfactants (0, 1, 2, 3, 4, 5, 6, 7, 8, 9 and 10 mM) were added to fixed concentration of **PDI 1** (3.5 μM) and the changes in the photophysical properties were recorded. **PDI 1** in the presence of lower concentration of aqueous CTAB (0 to 1.98 mM) did not exhibit significant change in the fluorescence as well as absorption intensities due to aggregates as shown in Figure Figure 3.1.3a and b. This is presumably due to the formation of non-fluorescent premicellar aggregates as a result of electrostatic interactions between aggregates of **PDI 1** and CTAB. Whereas further addition of CTAB from 2 to 10 mM, induced dramatic changes in absorption as well as fluorescence intensities of **PDI 1**. Absorption spectrum of **PDI 1** at higher CTAB concentration (10 mM) displayed 15 nm blue shift along with the well-resolved vibronic absorption bands at 530 nm, 492 nm, 460 nm and 430 nm corresponding to 0–0, 0–1, 0–2

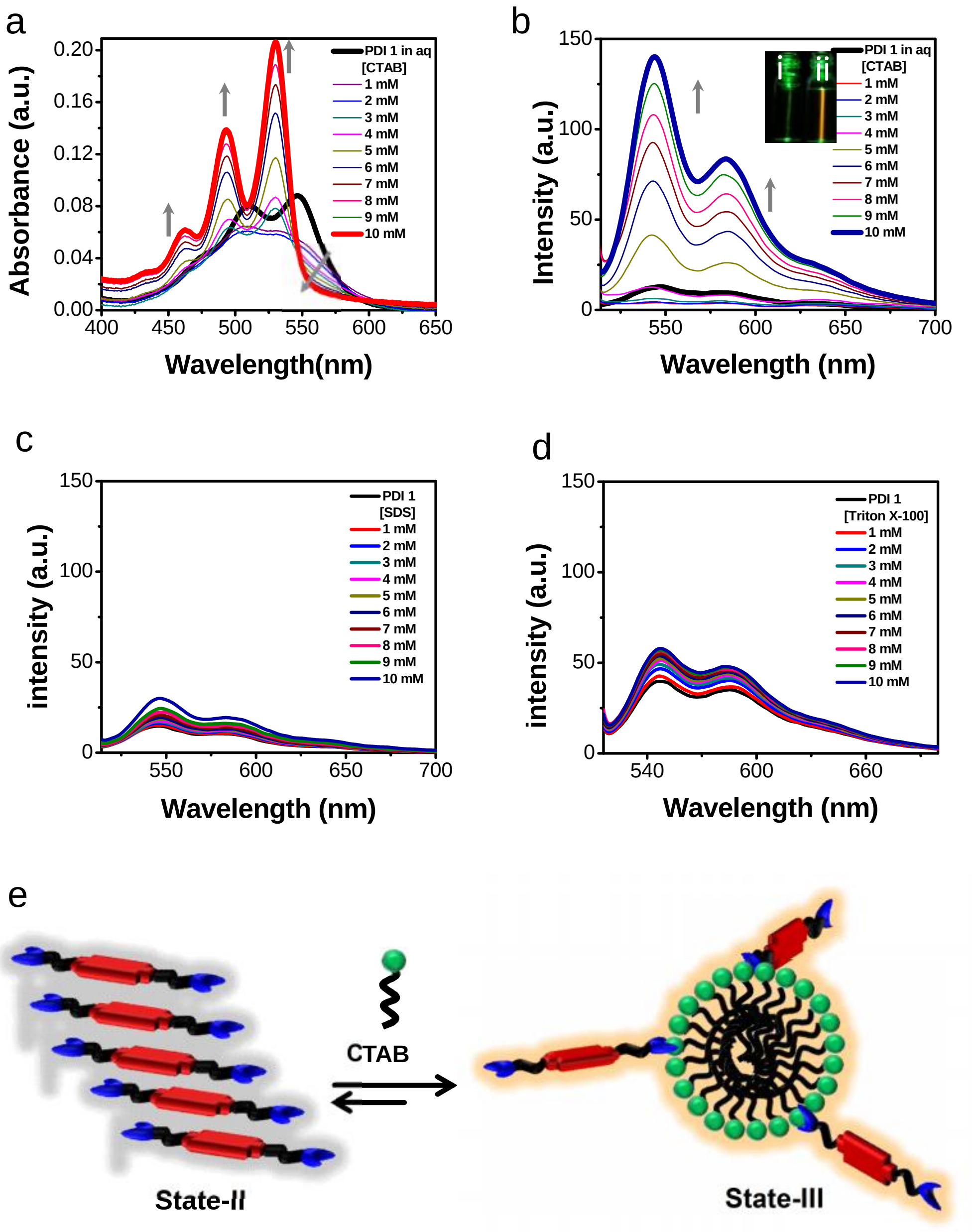

Figure 3.1.3 UV-vis absorption (a) and fluorescence emission spectra (b) of **PDI 1** (3.5 μM) in water with increase in concentration of CTAB. Inset: solutions of **PDI 1** in water (a) and in CTAB miceller media (b) under green laser light. c) and d) Fluorescence emission spectra of **PDI 1** in water with increase in concentration of SDS and triton X-100 respectively. e) Schematic representation of transformation of aggregated State -II of **PDI 1** to molecularly dissolved State-III in presence of CTAB micelles.

and 0–3 transitions, respectively.[40] Employing the reported method, we calculated the ratio of absorption intensities of 0−0 to 0−1 transitions and found to be around 1.51 which is almost equals to the normal Frank-Condon progressions ($A_{0-0}/A_{0-1} \approx 1.6$) for the free PDI molecules.[41] Corresponding fluorescence emission spectra exhibited steady increase of almost 12 fold in the fluorescence intensity of **PDI 1** and reached a plateau at 10 mM concentration of CTAB as shown in Figure 3.1.3b. A rapid fluorescence response (within 1 min) was observed after each consecutive addition of CTAB and the emission intensity was saturated at above 10 mM CTAB. The fluorescence switching off and on (assembly and disassembly respectively) process of **PDI 1** could be visualized by the naked eye under green laser light as shown in Figure 3.1.3b inset. To ascertain the selectivity of cationic surfactant CTAB towards disassembly of **PDI 1** we further carried out similar experiments with neutral (Triton X100) and anionic (SDS) surfactants (Figure 3.1.3c and d). The photophysical studies of **PDI 1** revealed limited absorption and fluorescence emission changes over the investigated concentration range in presence of Triton X100 and SDS. These studies confirmed that only cationic surfactant CTAB micellar medium could able to disassemble the intermolecular $\pi-\pi$ stacking interactions of **PDI 1** into molecularly dissolved State-III through complementary electrostatic interactions between L-DOPA of **PDI 1** and CTAB which subsequently led to fluorescence emission with b_{max} at 545 nm (Figure 3.1.3e). This study also emphasized the utility of assembled state of **PDI 1** as a selective supramolecular fluorescent probe for the cationic surfactant (CTAB).

3.1.2.3 Metallosupramolecular assemblies: Detection of metal ion

The pendant L-DOPA functional group is a known receptor and assumed to facilitate the binding events with metal ions. We hypothesized that the metal ions may disrupt the electrostatic interactions present in CTAB micellar bound **PDI 1** via strong metal

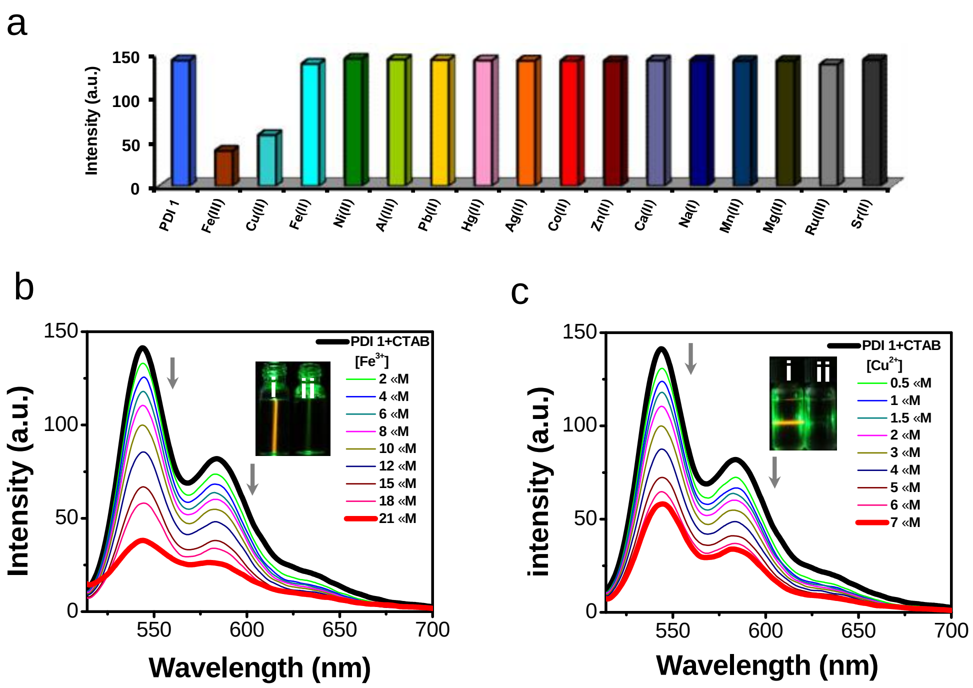

Figure 3.1.4 Fluorescence response of **PDI 1** (3.5 μM) in the miceller media of CTAB (9.90 mM) solution. a) Bar diagram depicting the effect of various metal ions on the fluorescence intensity of **PDI 1** (3.5 μM). b) Fluorescence emission spectra of **PDI 1** (3.5 μM) with increasing concentration of Fe^{3+} shows 3.5 fold quenching in aqueous solution. Inset: solutions of **PDI 1** in absence (i) and presence (ii) of Fe^{3+} in the CTAB miceller media under green laser light. c) Fluorescence emission spectra of **PDI 1** (3.5 μM) in the presence of increasing concentration of Cu^{2+} in aqueous media. Inset: solutions of **PDI 1** under green laser light in the absence and presence of Cu^{2+}.

chelating interaction which results in metallosupramolecular aggregates.[41] Various alkali as well as transition metal perchlorate ions were chosen to study the selectivity, change in optical properties, and probable metal chelation driven reorganization of **PDI 1** in the miceller media of CTAB solution. Our preliminary investigations based on the changes in fluorescence emission of **PDI 1** in presence of various metal ions are shown in Figure 3.1.4. The fluorescence emission of **PDI 1** in the miceller media of CTAB was almost unaffected upon excitation at 490 nm in the presence of most of the alkali and transition metal ions (Fe^{2+}, Ni^{2+}, Al^{3+}, Pb^{2+}, Hg^{2+}, Ag^{+}, Co^{2+}, Zn^{2+}, Ca^{2+}, Na^{+}, Mn^{2+}, Mg^{2+}, Ru^{3+} and Sr^{2+}) even at their 25 μM concentrations (Figure 3.1.4a). However, addition of Fe^{3+} and

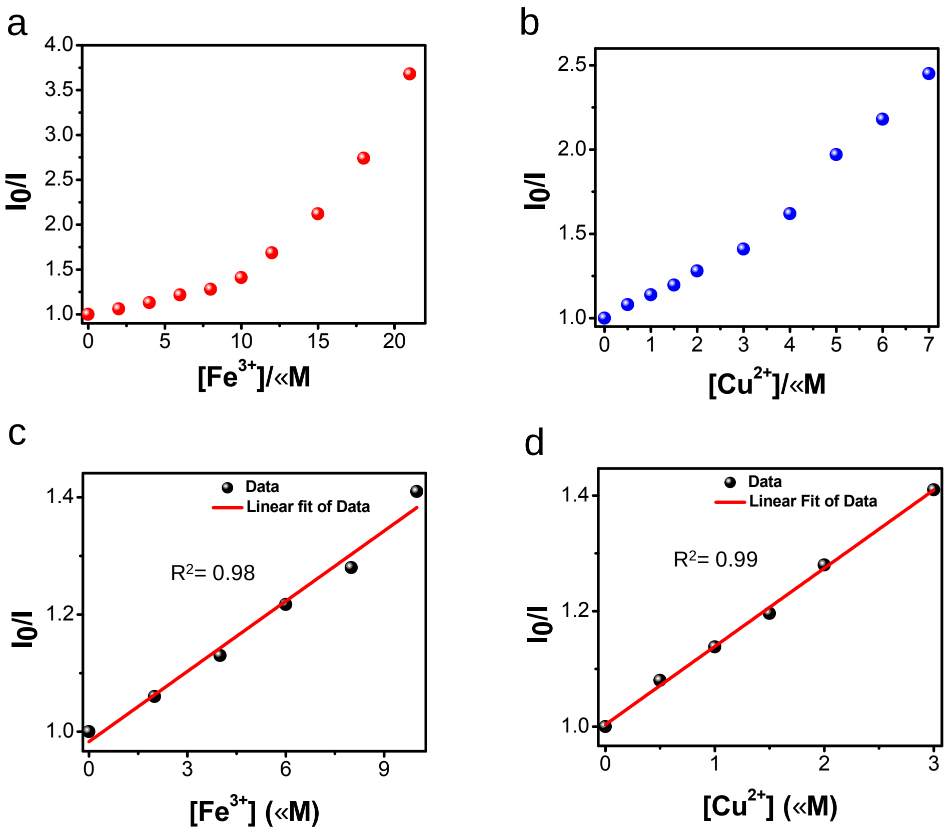

Figure 3.1.5 a) and b) Plots of fluorescence response (I_0/I) of **PDI 1** versus concentration of added Fe^{3+} and Cu^{2+} respectively. c) and d) The linear fluorescence response (I_0/I) of **PDI 1** versus concentration of added Fe^{3+} and Cu^{2+} respectively.

Cu^{2+} quenched the fluorescence of **PDI 1** in the micellar media of CTAB in aqueous solution. With increasing concentration of metal ions ranging from 0 to 21 μM (Fe^{3+}) and 0 to 7 μM (Cu^{2+}) respectively, significant fluorescence quenching was observed and leveled off due to the formation of larger non-emitting aggregates of metal bound **PDI 1** (Figure 3.1.4b and c). Moreover, the fluorescence quenching of **PDI 1** with Fe^{3+} and Cu^{2+} was found to be 3.5 fold and 2.5 fold respectively within the investigated concentration range. This change in fluorescence emission was also visualized by the diminished yellow emission quenching corresponds to metallosupramolecular aggregates (State IV) formed by the association of metal coordinated **PDI 1**. Figure 3.1.5 depicts

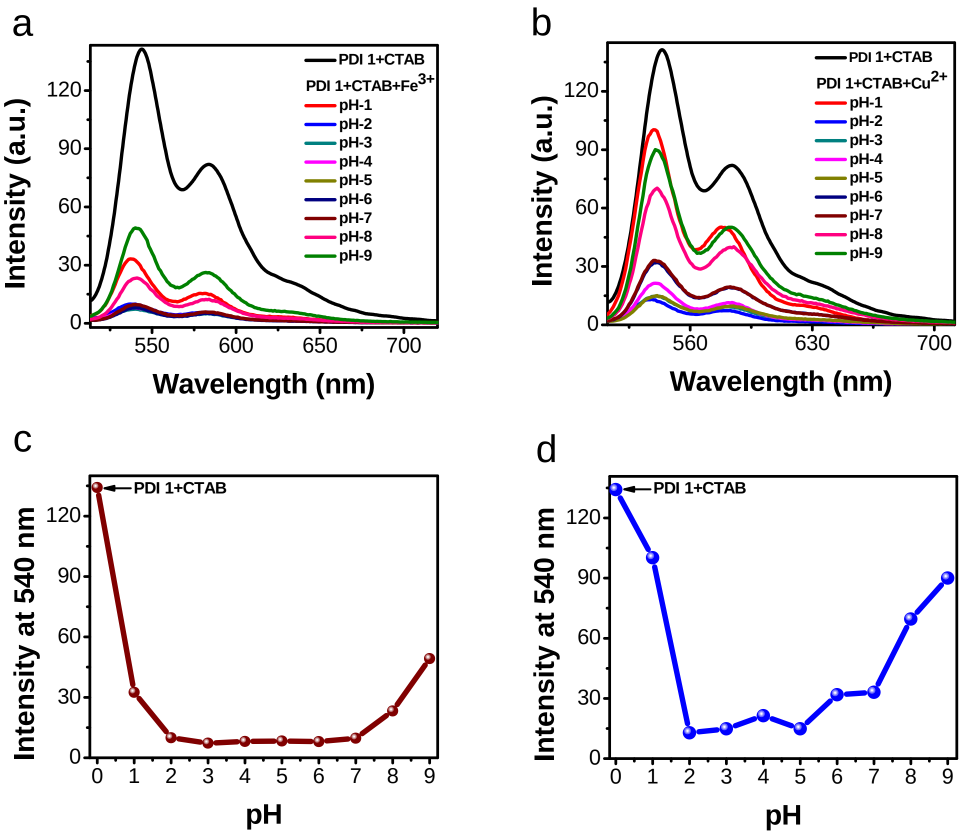

Figure 3.1.6 pH dependent fluorescence response study. a) Fluorescence emission spectra of [**PDI 1**+CTAB+Fe^{3+}]. b) Fluorescence emission spectra of [**PDI 1**+CTAB+Cu^{2+}]. c) and d) Plot of fluorescence intensity monitored at 540 nm as a function of pH of the media, corresponding to fluorescence spectra in (a) and (b), respectively.

decreasing fluorescence intensity pattern of **PDI 1** in presence of Fe^{3+} and Cu^{2+}, respectively. At lower concentrations of metal ions, the fluorescence quenching behavior of **PDI 1** was found to be linear. However, at higher concentrations linearity was lost and plot became nonlinear indicating static type of quenching. Furthermore, efficiencies of fluorescence quenching of **PDI 1** in the presence of metal ions were determined over the linear region of plot by generating a Stern–Volmer plot and compared.

$$I_o/I = 1 + K_{sv}\,[Q]$$

Where I_o and I are fluorescence intensities in the absence and presence of the quencher, respectively, K_{sv} is the Stern–Volmer constant and the value of K_{sv} of an artificial assay indicates the sensitivity of the probe towards the analyte, and [Q] is the quencher concentration. K_{sv} values for **PDI 1** in presence of Fe^{3+} and Cu^{2+} metal ions were found to be 4×10^4 and 1.35×10^5 M^{-1} respectively, as shown in Figure 3.1.5c and d. The high K_{sv} values of **PDI 1** towards Cu^{2+} and Fe^{3+} further confirmed that **PDI 1** is a selective and sensitive supramolecular probe for sensing of Cu^{2+} and Fe^{3+} in aqueous medium. Further, we explored the pH dependence on the sensing propensity of **PDI 1** towards Cu^{2+} and Fe^{3+} in CTAB aqueous media (Figure 3.1.6). The sensing behavior of **PDI 1** in CTAB aqueous media towards Cu^{2+} and Fe^{3+} was found to be sensitive at lower (< 2) and higher (>8) pH values. However, sensing of these metal ions (Cu^{2+} and Fe^{3+}) by **PDI 1** was unaffected in the normal pH range of 2-8. After investigating the significant fluorescence quenching of **PDI 1**, we further examined changes in the absorption intensity of **PDI 1** in presence of Fe^{3+} and Cu^{2+} in aqueous CTAB miceller conditions. Our observations revealed a broadened absorption spectrum of **PDI 1** (3.5 μM) with decrease in absorption intensity at 530 nm (0-0 transition), whereas 492 nm (0-1 transition) band was significantly increased and thus changing the ratio of 0−0 and 0−1 transition bands effectively as shown in Figure 3.1.7. However, higher concentrations of metal ions (> 21 μM of Fe^{3+} and > 7 μM of Cu^{2+}) were found to be not effective in further decreasing or increasing the intensity of 0−0 or 0-1 transition bands respectively. Thus, UV-vis absorption and fluorescence emission studies showed that **PDI 1** was in predominantly assembled state at the stoichiometric ratio (**PDI 1**: metal ion) of 1:6 with Fe^{3+} and 1:2 with Cu^{2+} in aqueous CTAB miceller conditions. Moreover, the observed absorption spectral features upon addition of Fe^{3+}/Cu^{2+} reflect a different kind of assembly behavior of **PDI 1**, as compared to assembly of **PDI 1** in water (State-II, Figure 3.1.2c). It is reported in the literature that 0−0 as well as 0−1 bands in absorption spectra of PDI decrease simultaneously while stacking.[42] However, absorption spectrum of **PDI 1** revealed decreased 0−0 band intensity and increased 0−1 band intensity simultaneously in presence of Fe^{3+} and Cu^{2+} in aqueous miceller media (Figure 3.1.7a and b). We reason that metal ions play important role towards coordination with L-DOPA in **PDI 1** and thus facilitating the reorganization of **PDI 1** via metallosupramolecular aggregate formation(transformation of State-III to State-IV, Figure 3.1.7c).

3.1.2.4 Characterization of metallosupramolecular assemblies

Furthermore, complexation and stoichiometry between **PDI 1** and Fe^{3+}/Cu^{2+} was

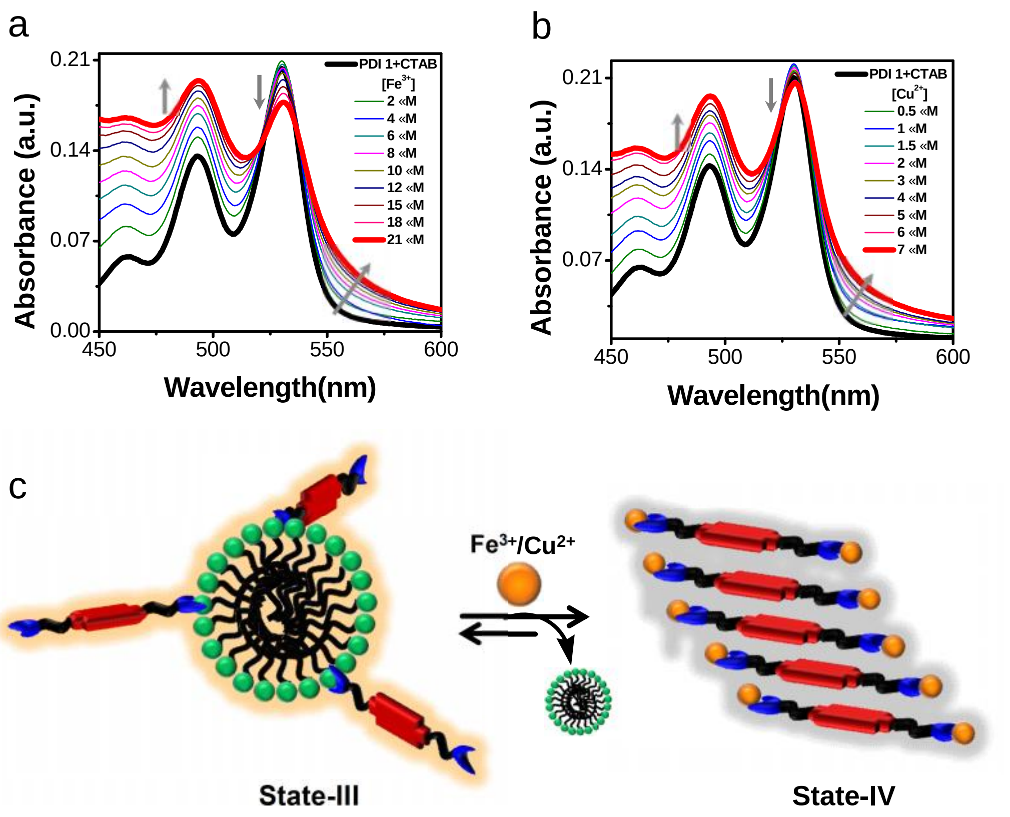

Figure 3.1.7 a) and b) UV-vis absorption spectra of **PDI 1** (3.5 μM) with increasing concentration of Fe^{3+} and Cu^{2+} respectively. c) Schematic representation of transformation of State-III to State-IV via metal ion induced reorganization of **PDI 1** in presence of CTAB micelles.

confirmed by electrospray ionisation mass spectrometry (ESI-MS) studies in aqueous media (Figure 3.1.8). Due to high concentration of surfactant (CTAB) used in our experiments discussed above as compared to **PDI 1** and metal ion, mass spectrometry studies were performed without CTAB in pure water. The molecular-ion peak showed the formation of [(**PDI 1**-4H$^+$**)**+6(Fe^{3+})] [MW: found.1081.80; calcd. 1081.73 for $C_{42}H_{22}Fe_6N_2O_{12}$)] and [(**PDI 1**+H$^+$)+2(Cu^{2+})] [MW: found 878.80; calcd, 878.75 for $C_{42}H_{27}Cu_2N_2O_{12}$)] respectively (Figure 3.1.8a and b). Therefore, in agreement with photophysical studies mass analysis revealed the formation of matallosupramolecular aggregates with the stoichiometric compositions (**PDI 1**: metal ion) of 1: 6 and 1: 2 for

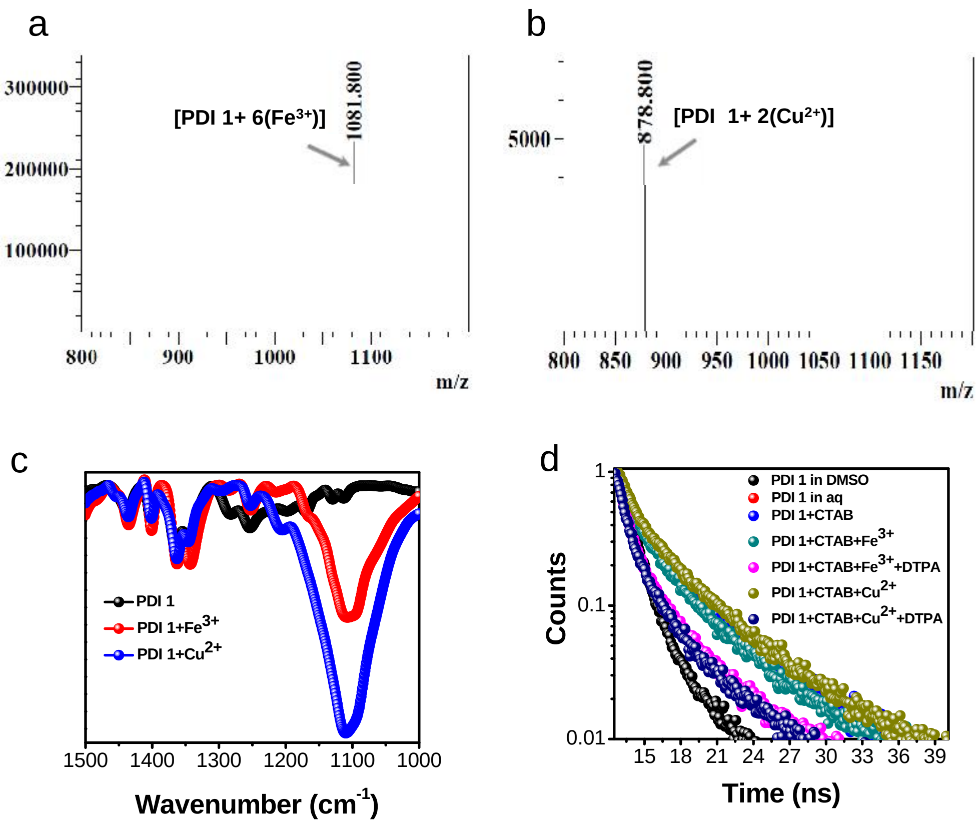

Figure 3.1.8 ESI-MS spectra of **PDI 1** in presence of metal ions (a) Fe^{3+} and (b) Cu^{2+}. c) FTIR spectra (C-O stretching frequency region 1500 to 1000 cm-1) of **PDI 1** in absence and presence of Fe^{3+} and Cu^{2+}. d) TCSPC decay profile of **PDI 1** (Emax = 545 nm) with a 500 nm excitation.

Fe^{3+} and Cu^{2+} respectively.

To determine the mode of metal chelation in **PDI 1**, we performed FTIR spectroscopy measurements of **PDI 1** with and without metal ions. Upon metal complexation the intense band at 1109 cm^{-1} was observed which was absent in **PDI 1** alone (Figure 3.1.8c). The appearance of the new band at 1109 cm^{-1} corresponds to C-O stretching (νCO) with the metal ion (Fe^{3+}/Cu^{2+}) bonded to the L-DOPA catechol oxygen.[43-44] Overall, photophysical studies, mass and IR analyses further confirmed the formation of metallosupramolecular aggregates via strong M-O chelation.

To investigate the fluorescence quenching mechanism of **PDI 1** in presence of Fe^{3+} and Cu^{2+} we further carried out the time-correlated single photon counting (TCSPC) experiments with a nanosecond excitation (Figure 3.1.8d). TCSPC data displayed quite similar biexponential decay patterns of **PDI 1** in the absence and presence of metal ions in aqueous CTAB media. The life time values for **PDI 1** in CTAB solutions (1.27 ns 63% and 5.44 ns 41%), were almost unaffected upon interaction with Fe^{3+} (1.31 ns 69% and 5.1 ns 35%) and Cu^{2+} (1.38 ns 55% and 5.4 ns 42%) metal ions. The unaffected life times and decay patterns clearly indicating the occurrence of static type quenching via displacement of **PDI 1** from CTAB-micelle to non-fluorescent ground state with stable [**PDI 1**+ Fe^{3+}/Cu^{2+}] metallosupramolecular aggregates (State-IV in Figure 3.1.7c). It is reasonable to assume a type of complexation between **PDI 1** and metal ion (Fe^{3+}/Cu^{2+}) in the ground state and such a complexation efficiently facilitated the reassembly of **PDI 1** in CTAB micellar aqueous solution.

3.1.2.5 Metal ion sequestration

Next, we explored disassembly of metallosuparamolecular aggregate (State-IV) of **PDI 1** in a reversible manner by engaging a metal chelator. In literature, it has been established that anions, amino acids and other related compounds are capable of taking out or make a ternary complex from/with ligand-metal system.[43,45] To test this concept, various kinds of anions and neutral, metal ion receptors such as amino acids, ethylenediaminetetraacetic acid (EDTA) and diethylenetriamine pentaacetic acid (DTPA) were employed in our investigations (Figure 3.1.9). Fluorometric study of **PDI 1** in State-IV indicated no change in the quenched fluorescence in presence of various anions and amino acids even at six times higher concentrations indicating these ligands are unable to disassemble perylene core of **PDI 1** in State-IV. Further, our study was continued with well- known metal ion chelators such as EDTA and DTPA. We found that EDTA, even at 100 μMconcentrations could hardly alter the metal ions (Fe^{3+} and Cu^{2+}) mediated quenched fluorescence of **PDI 1** (State-IV). Interestingly, significant fluorescence enhancement was observed upon treating State-IV (**PDI 1** + Fe^{3+}/ Cu^{2+}) with DTPA as shown in Figure 3.1.10. Addition of DTPA (0-50 μM) into the solution of [**PDI 1** + Fe^{3+}/ Cu^{2+}] in the miceller media of CTAB significantly altered the quenched fluorescence of **PDI 1**. A turn-on fluorescence signal with a yellow emission color under green laser was detected

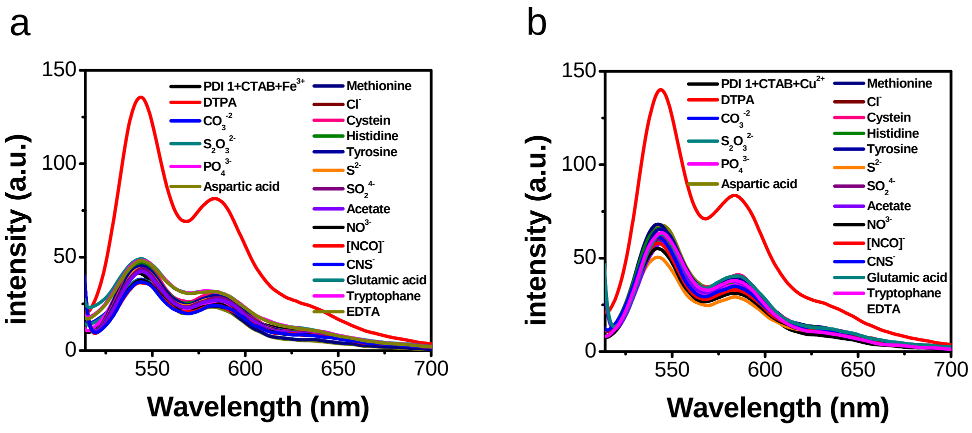

Figure 3.1.9 Fluorescence emission spectra of a) [**PDI 1**+CTAB+Fe^{3+}] and b) [**PDI 1**+CTAB+Cu^{2+}] in presence of various anions, amino acids and metal chelators.

(Figure 3.1.10a and b inset). This fluorescence recovery was found to be almost 98 % for DTPA concentration of 50 μM. The quantitative fluorescence recovery is attributed to efficient metal ion (Fe^{3+}/Cu^{2+}) sequestration by DTPA in the miceller media. This was further confirmed by the changes in absorption spectra of [**PDI 1** + Fe^{3+}/ Cu^{2+}] in the

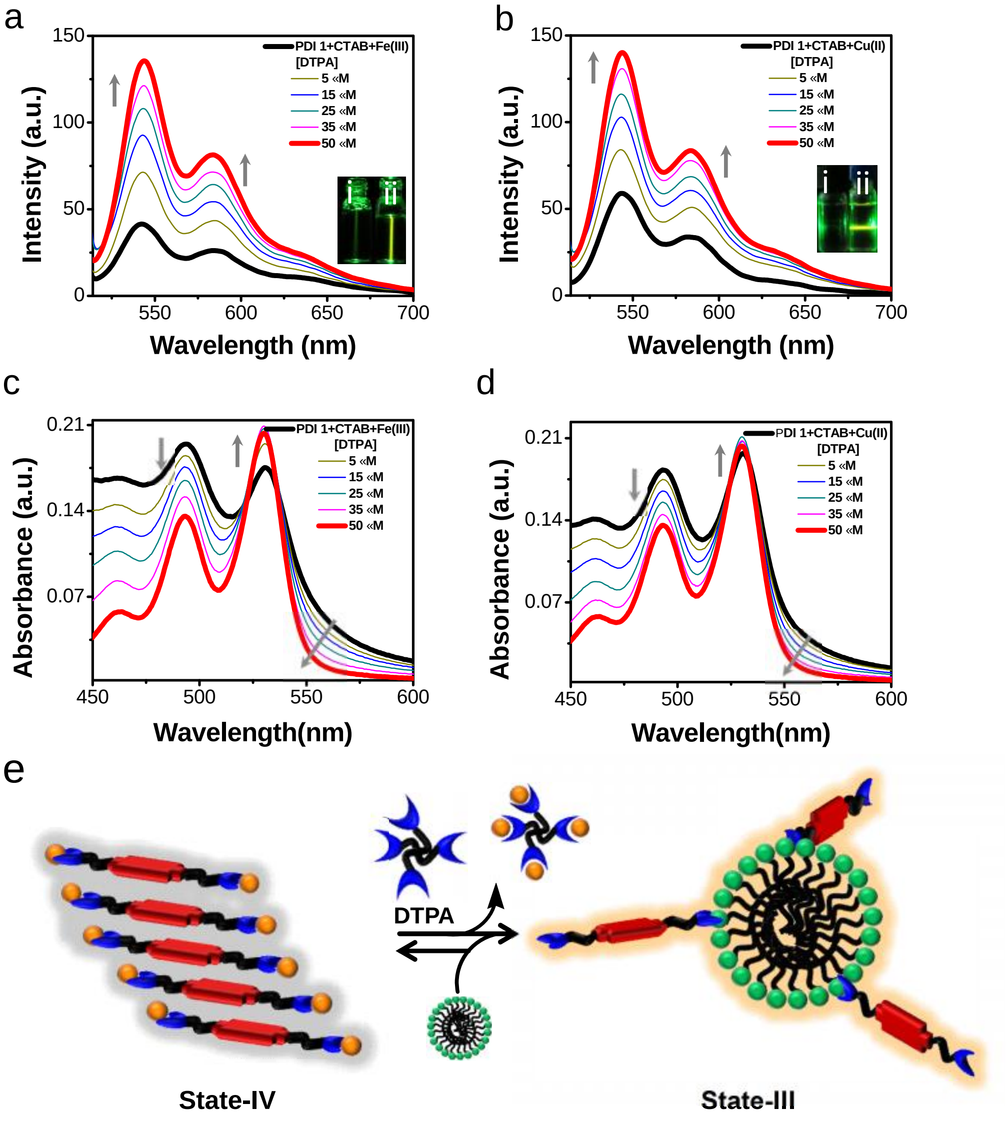

Figure 3.1.10 Fluorescence emission spectra (a and b) and UV-vis absorption spectra (c and d) of [**PDI 1**+ CTAB+Fe^{3+}] and [**PDI 1**+ CTAB+Cu^{2+}] solutions with increase in concentrations of DTPA in CTAB micellar aqueous medium. e) Schematic representation of sequestration of metal ion from metallosupramolecular aggregate (State-IV) using DTPA into molecularly dissolved state (State-III).

presence of DTPA (0-50 µM), in the miceller media as shown in Figure 3.1.10c and d. Absorption spectra of [**PDI 1** + Fe^{3+}] and [**PDI 1** + Cu^{2+}] displayed an increase in 0-0 and decrease in 0-1 transition bands upon addition of DTPA. The increase or decrease in transition bands continued until the ratio of 0-0 and 0-1 bands reached closed to 1.6, which is almost similar to the normal Frank-Condon progressions for disassembled **PDI 1** in CTAB solution. Therefore, absorption spectra with 530, 492, 460 and 430 nm bands be considered as characteristic of the well-resolved vibronic structures corresponding to 0–0, 0–1, 0–2 and 0–3 transitions, respectively. Interestingly, DTPA treated metallosupramolecular aggregates (State-IV), showed absorption spectral changes similar to absorption patterns observed for **PDI 1** in CTAB micellar aqueous medium (State-III) and just reverse as compared to [**PDI 1** + Fe^{3+}] and [**PDI 1** + Cu^{2+}] (Figure 1A). Overall, the strong metal chelator DTPA was able to sequestrate the metal ion (Fe^{3+}/Cu^{2+}) in a competitive environment of metal ion bound **PDI 1** in CTAB miceller media. This resulted in the recovery of disassembled or molecularly dissolved State-III of **PDI 1** from State-IV which clearly reflected in the change of spectral features in both absorption and emission studies (Figure 3.1.10e).

3.1.2.6 Morphological studies

To visualize the effect of assembly modulation of **PDI 1**, we performed field emission scanning electron microscopy (FESEM) studies by drop casting the aqueous solutions onto Si wafer fallowed by vacuum drying under room temperature. PDI **PDI 1** alone formed a uniform film with porous nature (Figure 3.1.11a). Interestingly, complexation of metal ions (Cu^{2+} or Fe^{3+}), transformed the morphology into nanospheres with 50-300 nm diameter (Figure 3.1.11b and c). The observed nanospheres as a consequence of metallosupramolecular aggregates were further validated by energy dispersive X-ray

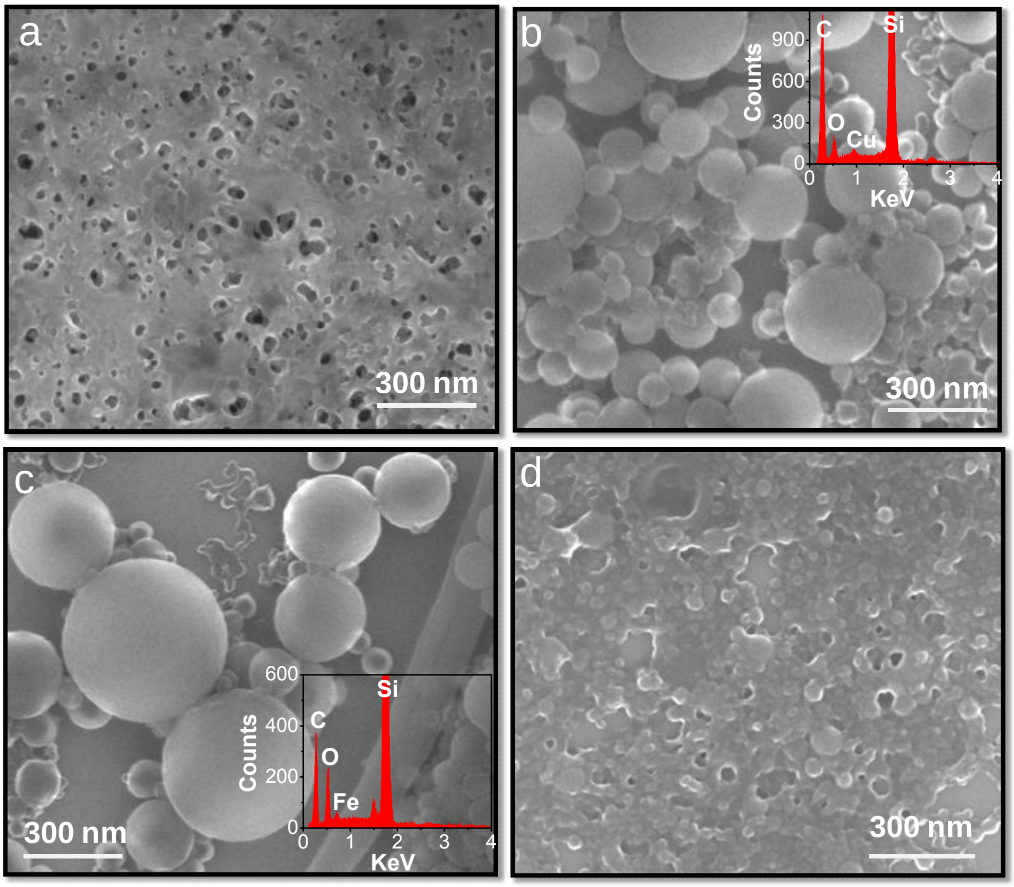
a
300 nm
b
Counts
900
600
300
0
C
Si
O
Cu
0
1
2
3
4
KeV
300 nm
c
600
400
200
0
Counts
Si
C
O
Fe
0
1
2
3
4
KeV
300 nm
d
300 nm

Figure 3.1.11 FESEM micrographs of a) **PDI 1**, b) **PDI 1**+Cu^{2+}, c) **PDI 1**+Fe^{3+} and d) **PDI 1**+Cu^{2+}+DTPA. Insets in (b) and (c) EDAX chemical composition mapping graph on corresponding nanospheres.

analysis (EDAX). EDAX chemical composition mapping graph, on corresponding nanospheres indicated the presence of metals (Cu and Fe) along with carbon (C) and oxygen (O) as shown in Figure 3.1.11b and c (insets). Further, the metal mediated metallosupramolecular nanospheres could be reverted back to film state by the addition of metal scavenger DTPA as shown in the Figure 3.1.11d. Therefore, in addition to photophysical studies the reversible assembly-disassembly of **PDI 1** was clearly established by the microscopy studies.

3.1.2.7 DLS studies

Dynamic light scattering (DLS) experiments further supported the assembly modulation of **PDI 1** (Figure 3.1.12a). **PDI 1** alone (State-II) showed the presence of smaller aggregates with mean size of 44 nm. Whereas the addition of CTAB transformed the smaller aggregates of **PDI 1** into two distinct aggregates with mean sizes of 90 nm and 4000 nm, suggested the formation of state-III. Further, addition of metal ions (Cu^{2+} or Fe^{3+}) into **PDI 1** under miceller condition of CTAB led to appearance of aggregates in the region of 50-300 nm along with the a small fraction centered around 4000 nm and thus corresponding to state IV. However, upon addition of metal chelator/scavenger DTPA, a significant decrease in the number of aggregates in the region 50-300 nm was observed

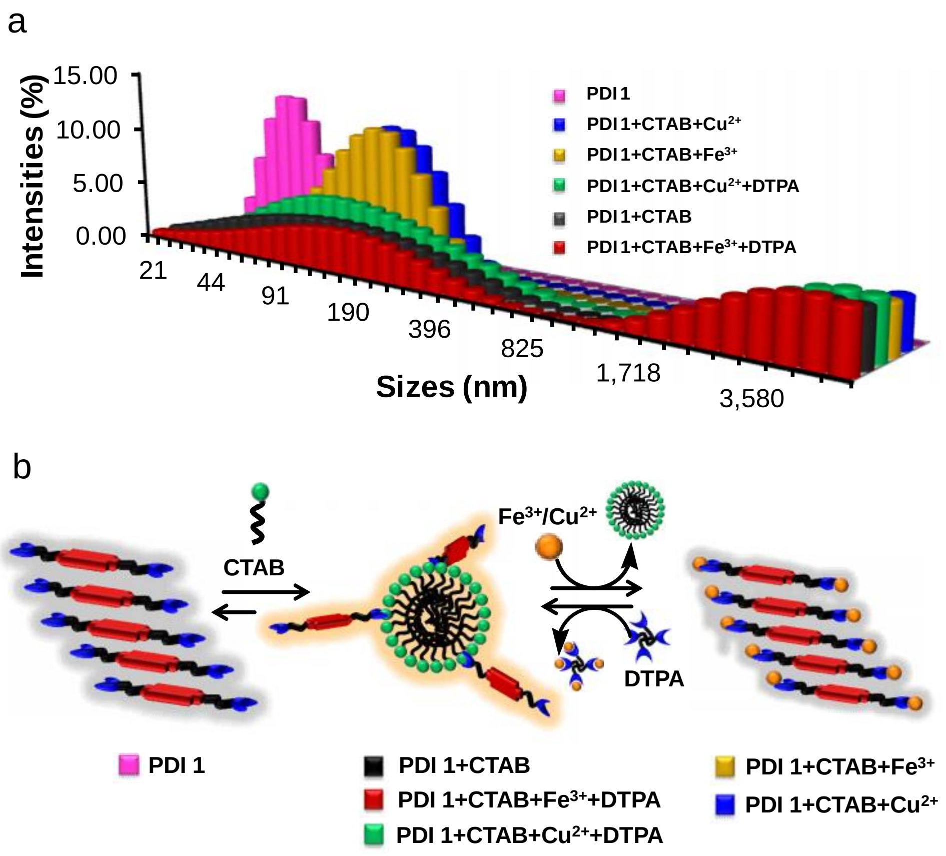

Figure 3.1.12 a) Dynamic light scattering (DLS) size distribution graph. b) Schematic representation of assembly-disassembly modulation of **PDI 1** observed from DLS studies (a).

and the size distribution was found to be similar to state III (**PDI 1**+CTAB). Overall, in agreement with photophysical and microscopy studies DLS data confirmed predominant assembled state of **PDI 1** in water which could be disrupted into disassembled form in miceller conditions of CTAB. Addition of metal ions ($Cu^{2+/}Fe^{3+}$) ions led to the assembled state as consequence of formation of metallosupramolecular aggregates of **PDI 1.** **A**gain, addition of DTPA into metallosupramolecular aggregates of [**PDI 1**/CTAB/Fe^{3+}] and [**PDI 1**/CTAB/Cu^{2+}] restored the disassembled state of **PDI 1** as shown in the Figure 3.1.12b.

In solution molecular self-assemblies are considered to be more sensitive towards its environment, nature of solvents, pH of solution, guest molecules among other factors. Guest molecules may either stimulate or suppress the molecular self-assemblies. Conversely, sometimes guest molecules may not influence the molecular assemblies and disassemblies due to lack of specific interaction. However, in the present study we were able to modulate the molecular self-assembly of PDI derivative **PDI 1** in aqueous media (assembled state, State-II) by means of host-guest interactions provided by micellar structures of CTAB (disassembled state, State-III), metal ion (Fe^{3+} and Cu^{2+}) interactions (assembled state, State-IV) and metal ion sequestration agent DTPA (disassembled state, State-III).

3.1.3 Conclusion

In conclusion, we developed amphiphilic L-DOPA functionalized PDI derivative **PDI 1** and investigated photophysical properties to achieve its disassembled (molecularly dissolved) state in aqueous media using cationic micellar conditions. Assembly-disassembly modulation of **PDI 1** was established as a supramolecular fluorescent probe (switch off-on probe) for metal ions Fe^{3+} and Cu^{2+} in the miceller media of cationic surfactant solution. Our study demonstrated that the complementary electrostatic

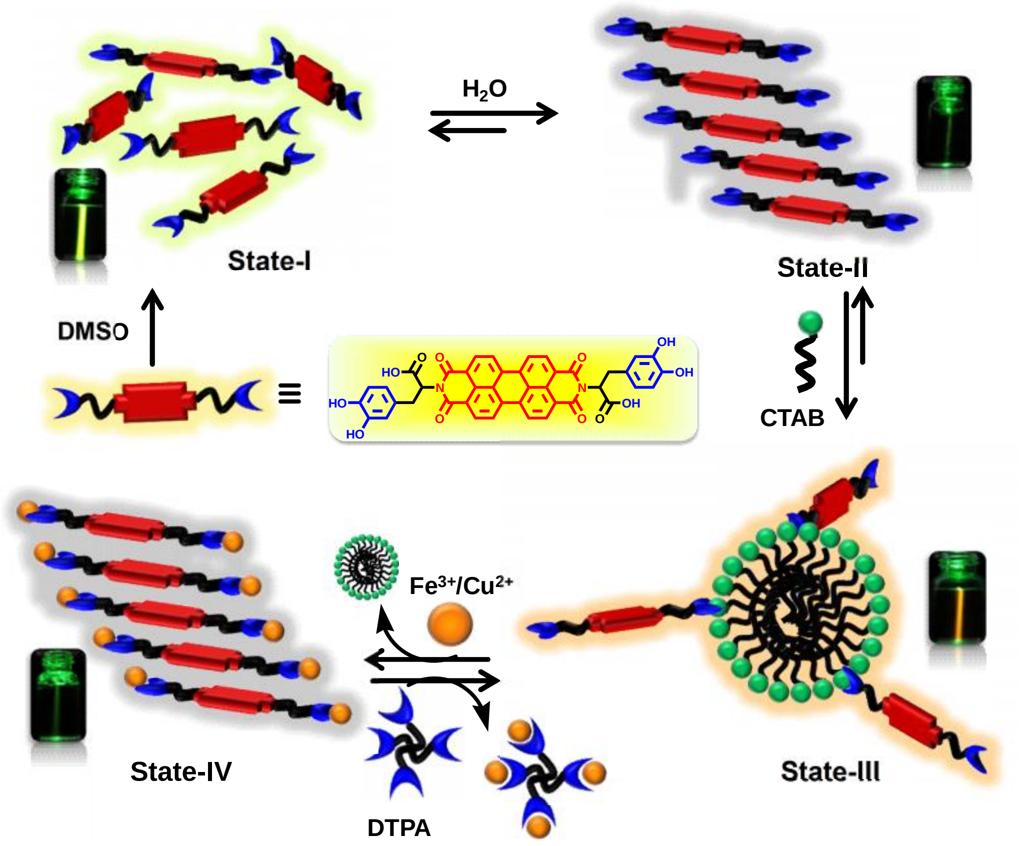

Figure 3.1.13 Schematic representation of assembly modulation of **PDI 1** as a supramolecular fluorescence switching probe for detection of metal ions in aqueous media.

interactions of cationic surfactant (CTAB) and L-DOPA led to a well-structured absorption spectra and a dramatic increase in the yellow fluorescence of **PDI 1** in aqueous medium. These spectral properties were similar to parent disassembled PDI chromophore **PDI 1** in DMSO. Anionic and neutral surfactant could hardly modify the assembled state of **PDI 1** in aqueous media. This emphasizes the utility of assembled state of **PDI 1** as a selective fluorescent probe for the cationic surfactant (CTAB). Furthermore, **PDI 1** serve as a fluorometric probe for Fe^{3+} and Cu^{2+} by means of fluorescence switch off state due to the formation of metallosupramolecular assemblies. Interestingly, DTPA could sequestrate Fe^{3+}/Cu^{2+} from metallosupramolecular assemblies and transform **PDI 1** into disassembly state which corresponds to fluorescence switch on state. The assembly-disassembly modulation of **PDI 1** was extensively studied using IR, ESI-MS analysis, FESEM and DLS techniques. Overall, fluorescence switch off–on probe (**PDI 1**) based on assembly modulation offer practical utility for analytes detection and to understand reversible assembly and disassembly of PDI derivate by means of tunable host-guest interactions in aqueous media (Figure 3.1.13).

Subchapter 3.2 L-DOPA Conjugated PDI as a Fluorescence Light-Up Probe for the Detection of H_2O_2 in Water

3.2.1 Introduction

Reactive oxygen species (ROS) are important class of chemically reactive species, essential for normal cellular functions including cell proliferation and differentiation.[46-49] In general ROS are highly reactive, unstable ions and radicals which contain oxygen and peroxide ions. However, misregulation of ROS recognized as a potential cause of cell damage, which is directly linked to oxidative stress-related disorders, aging and many pathological conditions including cancer, cardiovascular, inflammatory and neurodegenerative diseases.[50-55] ROS mainly comprises of superoxide anion (O^{2-}), the hydroxyl radical ($OH^{\cdot}$), singlet oxygen ($^1O_2$), and hydrogen peroxide (H_2O_2).[56] Among them the H_2O_2 is found to be relatively stable, prominent and essential ROS in biological systems and play roles as messengers and signalling molecule in transducing receptor and marker for oxidative damage in many disease-associated cells.[57] Apart from biology, H_2O_2 has been extensively used in industrial applications as a strong oxidizer and disinfectant. On the other hand, imbalance caused by excess of H_2O_2 in cell leads to cell injury by damaging cellular macromolecules such as DNA and lipids and responsible for various fatal diseases including diabetes, cancer, neurodegeneration (Parkinsonism, Alzheimer disease), thyroid related, atherosclerosis, cardiovascular and aging etc.[50-55] Therefore, it is of crucial to develop ultrasensitive probe for the detection of H_2O_2 in biomedical research including neurobiology, cardiology and cancer.

In recent years, considerable efforts have been focused on the development of fluorometric and colorimetric assays for H_2O_2 detection. The horseradish peroxidases (HRP) assay is a most conventional enzymatic method used for biological systems. It utilises 10-acetyl-3,7-dihydroxyphenoxazine (Amplex Red) as reducing substrate which undergoes N- deacetylation and oxidation to form highly fluorescent resorufin which is measured by fluorometric technique.[58] Although Amplex red- HRP system is 5-20 times more sensitive than colorimetric assays,[59] the oxidised product resorufin gets further oxidised by HRP to form non-fluorescent resazurin which leads to loss of fluorescence intensity.[60-62] In this regard, very recently DNAzyme coupled with reducing substrate has emerged as more reliable and label-free colorimetric and fluorometric method.[63] However issues like lower dynamic range, intrinsic sensitivity, colour fading and high background noise ratio makes it less reliable for practical applications. Hence, the development of ultrasensitive and rapid fluorogenic H_2O_2 biosensor which is more reliable, sensitive, give minimum signal-to-background noise, stable, inexpensive, biocompatible and water soluble, remains a considerable challenge.

Herein, we present L-DOPA conjugated perylenediimide (**PDI 1**), where perylenediimide (PDI) acts a fluorogenic substrates and L-DOPA as H_2O_2 responsive moiety. The choice of L-DOPA is due to the fact that the phenol and its derivative are known to show promising H_2O_2 oxidation propensities in presence of iron-containing oxidative enzymes such as HRP, DNAzyme and PS2.M8 and imparts water solubility.[64-66] Thus, we envision that probe **PDI 2**, in combination with small iron-containing porphyrin molecules (hemin and hematin), will be a promising H_2O_2-responsive fluorescence probe for detection of H_2O_2 in water.

3.2.2 Results and discussion

3.2.2.1 ESI-MS analysis

In a preliminary study, we carried out Electrospray ionization-mass (ESI) spectrometry analysis of **PDI 1** in the absence and presence of hematin along with H_2O_2 to assess the

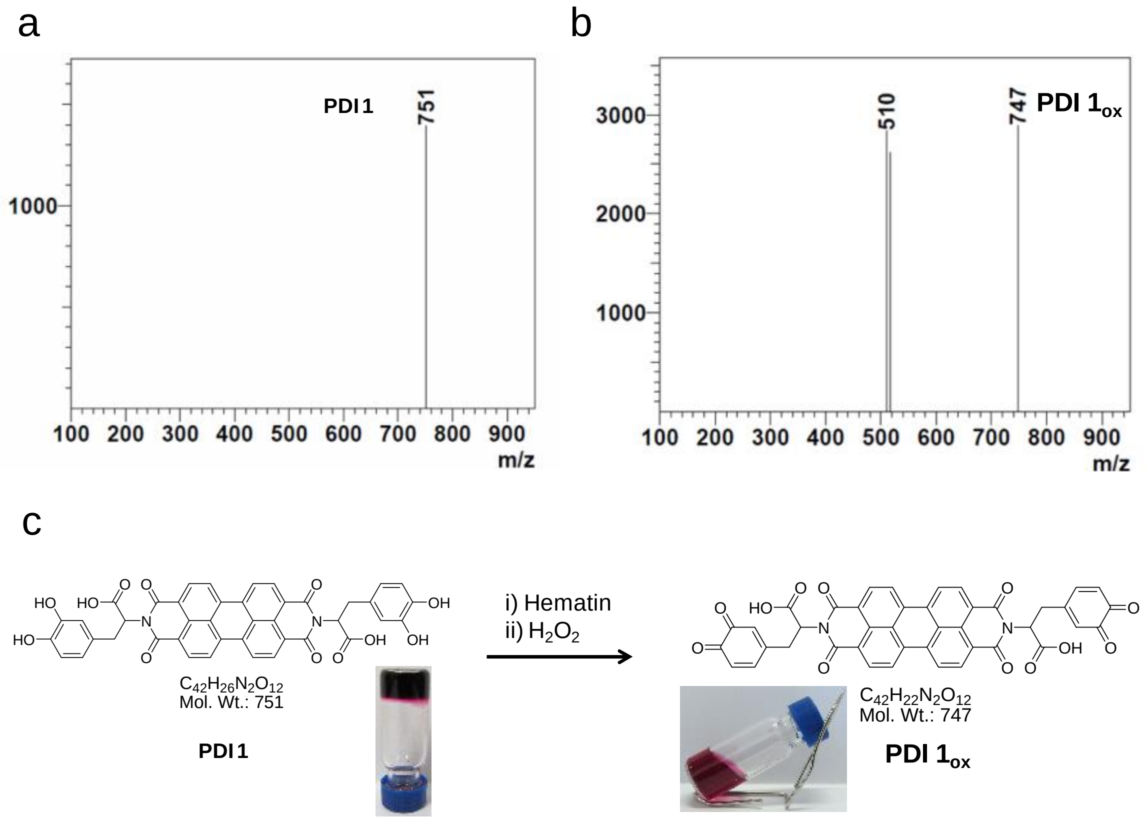

Figure 3.2.1 ESI mass analysis of a) **PDI 1** and b) its oxidized product **PDI 1_{ox}**. c) Proposed H_2O_2 and hematin catalyzed reaction of **PDI 1** to **PDI 1_{ox}**, photographs of gel to sol transition in presence of hematin (Ht) and H_2O_2.

H_2O_2 induced redox reaction (Figure 3.2.1). The ESI-mass spectrum of **PDI 1** alone in water showed a single m/z signal at 751 corresponding to the molecular ion peak of **PDI 1**. Interestingly, in the presence of hematin and H_2O_2 the **PDI 1** molecular ion peak was replaced by a new prominent peak at 747 attributed to the molecular ion peak of oxidized **PDI 1_{ox}** as shown in the Figure 3.2.1. Thus, ESI mass analysis confirmed the hematin and H_2O_2 catalyzed conversion of **PDI 1** to **PDI 1_{ox}** in presence of hematin. Interestingly, a gel to sol transition was observed after the addition of H_2O_2 to **PDI 1+**hematin hydrogel, indicating the naked eye detection of H_2O_2 in water (Figure 3.2.1).

3.2.2.2 H_2O_2 detection studies

The detailed photophysical studies of **PDI 1** in water has been described in subchapter 2.1. Further, we carried out fluorescence emission studies of **PDI 1** in the presence of iron-containing porphyrin small molecules such as hemin and hematin in milli-Q water. **PDI 1** alone displayed a very low emission bands at 545 nm and 586 nm due to the self-assembly of **PDI 1** (Figure 3.2.2a). Whereas, in the presence of hemin (Hn) or hematin (Ht) quenching of **PDI 1** fluorescence was observed, possibly due to the formation of **PDI 1**-Hn/Ht complexation. Interestingly, upon addition of H_2O_2 to the nonfluorescent **PDI 1**-Hn/Ht complex transformed into highly fluorescent **PDI 1$_{ox}$** with emission bands at 545 nm and 586 nm was observed (Figure 3.2.2b). Furthermore, without the aid of any spectroscopic techniques the H_2O_2 induced fluorescence enhancement can be visualized under UV light as shown in Figure 3.2.2b inset. Interestingly, **PDI 1**-Ht complex showed maximum fluorescence enhancement (~40 folds) as compared to that of **PDI 1**-Hn complex (~11 folds) in presence of H_2O_2 suggesting the maximum conversion of **PDI 1** to **PDI 1$_{ox}$** in presence of Ht. Next, the reaction kinetics of **PDI 1$_{ox}$** conversion in the presence of H_2O_2 was investigated using the **PDI 1**-Hn, **PDI 1**-Ht and **PDI 1** by monitoring the emission intensity at 545 nm as a function of time (Figure 3.2.2c). Upon addition of H_2O_2 (1 mM) the **PDI 1**-Hn, **PDI 1**-Ht complex showed continuous increase in fluorescence emission intensity and even after 75 min no saturation was observed. However, under similar conditions the control **PDI 1** alone in the presence of H_2O_2 did not show any significant increase in fluorescence intensity indicating the curial role of Hn/Ht in the conversion of **PDI 1** to **PDI 1$_{ox}$** (Figure 3.2.2c). Next, the fluorescence was monitored by adding increasing concentrations of H_2O_2 (0 to 300 μM) to the **PDI 1**-Ht complex (Figure 3.2.2d). The lowest concentration of H_2O_2 (detection limit) that induce

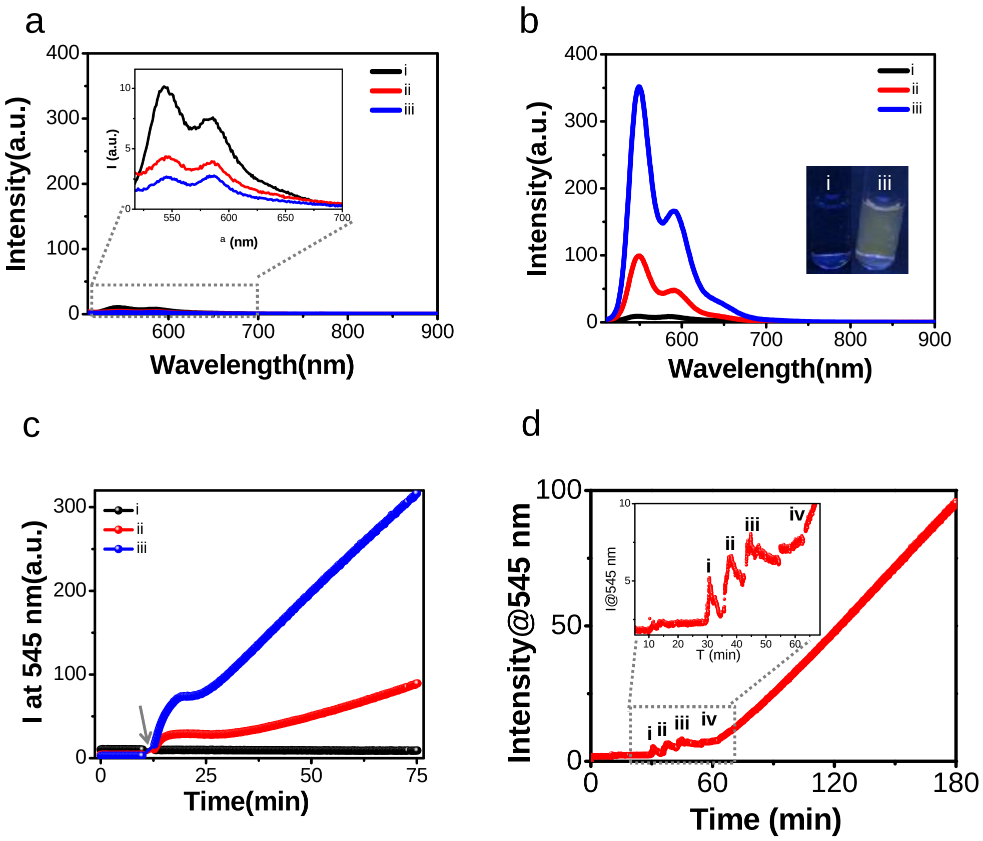

Figure 3.2.2 a) Fluorescence emission spectra of i) **PDI 1**, ii) **PDI 1**+Hn and iii) **PDI 1**+Ht. b) Fluorescence emission and c) kinetic studies of i) **PDI 1**, ii) **PDI 1**+Hn+H_2O_2 and iii) **PDI 1**+Ht+H_2O_2, *inset* in b photographs of corresponding solutions under UV light (365 nm), the arrow in c indicating the point of H_2O_2 addition . d) Fluorescence kinetic studies of **PDI 1**+Ht upon addition of H_2O_2 i) 65 μM, ii) 130 μM, iii) 195 μM and iv) 325 μM H_2O_2 respectively.

significant fluorescence enhancement of **PDI 1**-Ht complex was found to be 65 μM, as depicted in the Figure 3.2.2d.

To obtain more insights into the observed fluorescence enhancement of **PDI 1** in the presence of Ht/Hn and H_2O_2, we further looked into the energy minimized molecular structures of **PDI 1** and **PDI 1$_{ox}$**. The molecular structures of **PDI 1** and **PDI 1$_{ox}$** were optimized in a gas phase using Gaussian 09 within the B3LYP/6-31g(d) level of theory. The optimized structures are stabilized by *trans* conformation where the catechol and quinone groups respectively, were oriented in opposite directions with respect to PDI core (Figure 3.2.3). Interestingly, in case of **PDI 1** the π–electron rich catechol ring exhibited the intramolecular edge to face aromatic interaction with that of π–electron deficient PDI core (Figure 3.2.3a). However, the **PDI 1$_{ox}$** did not show any such interactions. Therefore the intermolecular structural modifications are responsible for the observed enhanced emission of the PDI chromophore in presence of H_2O_2 and hematin (Figure 3.2.3b). Based on our observations and literatures on hemin DNAzymes[67] and HRP[68], the proposed mechanism of H_2O_2 detection using PDI **1** and hematin is summarized in Figure 3.2.4. Initially, the hematin coordinates with H2O in water. Next H_2O_2 replaces H_2O, coordinated with hematin and withdraws two electrons from hematin to form

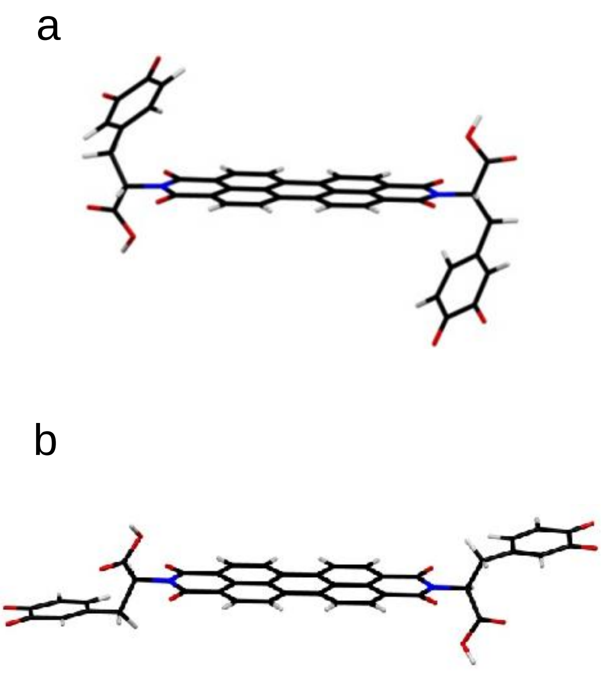

Figure 3.2.3 Energy minimized molecular structures of a) **PDI 1** and b) **PDI 1$_{ox}$**.

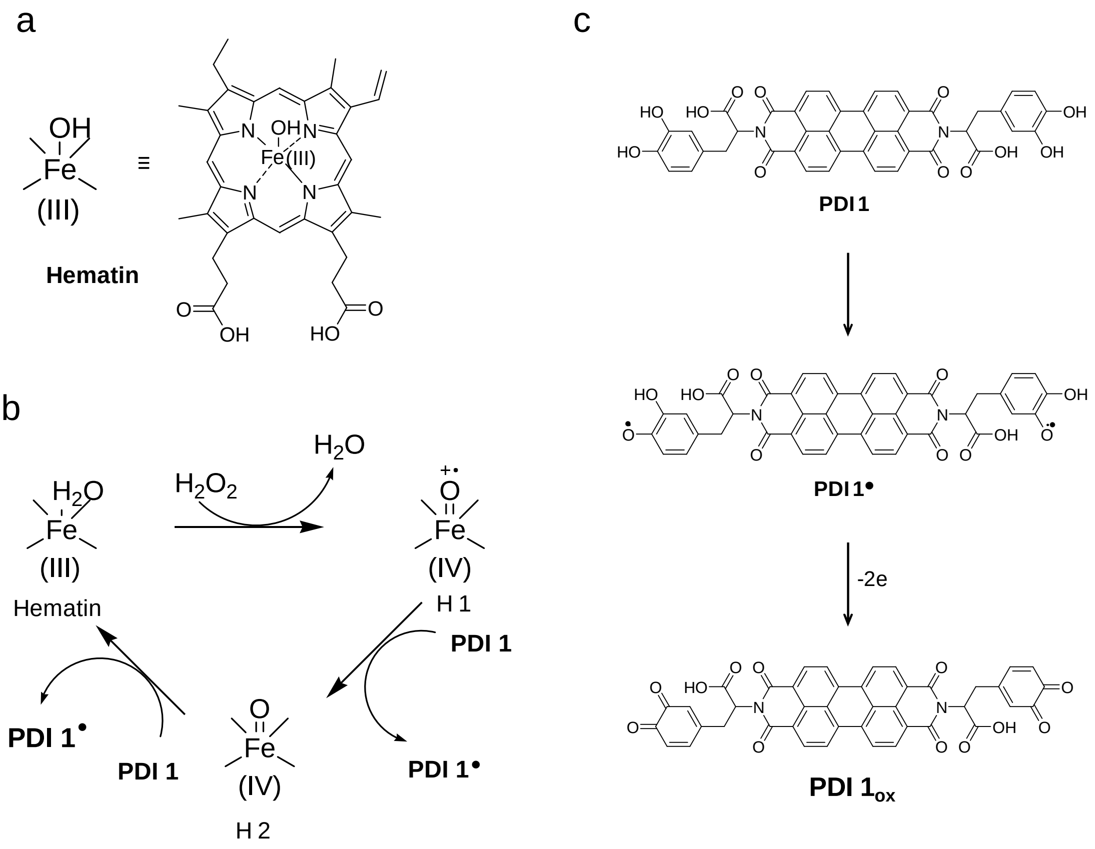

Figure 3.2.4 a) Molecular structure of hematin (Ht). b) Proposed reaction mechanism of hematin catalyzed **PDI 1** to **PDI 1$^\bullet$** radicals conversion in presence of H_2O_2. c) Oxidation of **PDI 1$^\bullet$** radicals to **PDI 1$_{ox}$**.

intermediates H1 and H2. Finally, H1 and H2 withdraw electrons from PDI 1, thus generates initial hematin and **PDI 1** radicals (**PDI 1$^\bullet$**). The PDI 1$^\bullet$ radicals further oxidized into highly fluorescent **PDI 1$_{ox}$** by losing two electrons as shown in the Figure 3.2.4.

Furthermore, based on the fluorescence emission studies, we constructed an AND logic gate of **PDI 1** with Ht and H_2O_2 as inputs A and B respectively. The enhanced fluorescence emission at 545 nm was defined as output “1” whereas the no fluorescence signal as output “0” (Figure 3.2.5a). As in a typical AND gate operation, the output “1"

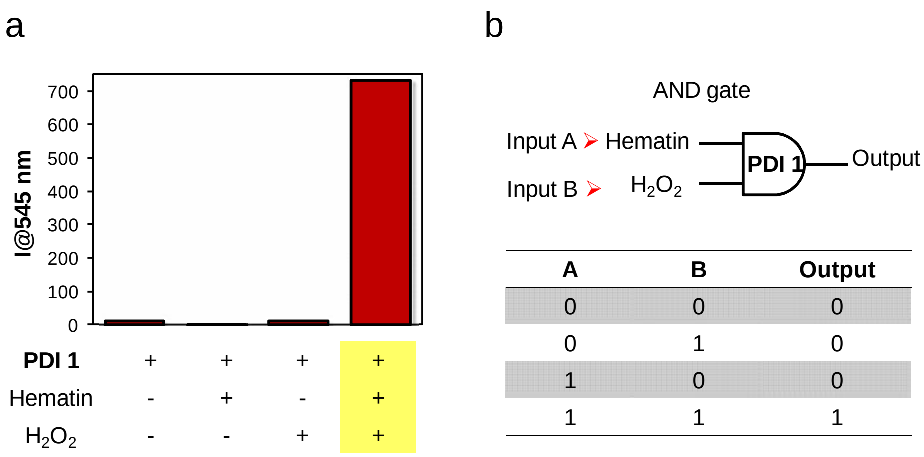

A	B	Output
0	0	0
0	1	0
1	0	0
1	1	1

Figure 3.2.5 a) The fluorescence signals of the **PDI 1** logic gate in the presence of different inputs [A: Hematin (Ht), B: H_2O_2]. b) The symbol of AND logic-gate and its truth table derived from (a).

was observed only in the presence of both inputs A (Ht) and B (H_2O_2) (input A/B: 1/1) (Figure 3.2.5b). In all other cases, when only one of them or neither was added into the system (input A/B: 0/0, 0/1, and 1/0) the output was "0". Therefore, the AND logic gate operations also confirmed the enhanced fluorescence signal of **PDI 1** originates from H_2O_2 catalyzed structural conversion of **PDI 1** to **PDI 1$_{ox}$** in presence of hematin.

3.2.2.3 Conclusion

In summary, we developed an L-DOPA-functionalized **PDI 1** probe in combination with Ht/Hn for turn-on fluorescence detection of H_2O_2 in water. ESI analysis indicated the effective oxidation of catechol functionality on **PDI 1** to quinone (**PDI 1$_{ox}$**) in the presence of H_2O_2. Furthermore, gel to sol and nonfluorescent to fluorescent solution (under UV light) transformations are the useful means to naked eye detection of H_2O_2. Fluorescence emission studies exhibited a huge enhancement of emission intensity only in the presence of hematin (Ht) and H_2O_2. Absence of any one of them fail to show fluorescence enhancement, which further supported the hematin and H_2O_2 catalyzed structural transformation (**PDI 1** to **PDI 1$_{ox}$**) induced switch on fluorescence property. Furthermore, we built Boolean logic gate (AND) into the **PDI 1**, which is able to sense simultaneously H_2O_2, hematin and execute fluorescence enhancement in accordance with the logic operation. Overall, this study gives insights on the development of new switch-on fluorescence biosensor for H_2O_2 and its utilization on installing the flexible logic gates response.

Subchapter 3.3 Histidine Conjugated PDI as a Reversible Off-On Fluorescence Probe for the Detection of Hg^{2+} and Cysteine in Water

3.3.1 Introduction

Mercury is one of the extremely toxic and globally widespread hazardous environmental pollutants.[69-76] Most of the mercury contamination of air, water and soil have resulted from human activities such as combustion of fossil fuels and gold mining just to name a few.[73] Mercury mainly exists in three different forms such as metallic or elemental mercury (Hg^0), inorganic mercury (Hg^{2+}) and organic mercury complex.[73] Among them, the water soluble inorganic mercury ion (Hg^{2+}) is one of the most common and stable forms of mercury and readily taken up by living organisms which further transforms into the most toxic form (organomercury, CH_3Hg^+ and CH_3HgCH_3) via microbial biomethylation processes.[75] Organomercury can accumulate in aquatic life, orders of magnitude higher than the surrounding concentrations before entering the food chain and subsequently affecting the human health. Even at low concentrations of mercury exposure (> 0.2 mg/cm^3 elemental mercury vapor and > 2 mg/Kg body weight per day) can cause fatal diseases related to lungs, skin, brain, immune system, heart and kidneys such as pulmonary edema, cyanosis, Minamata disease, loss of intelligence quotient (IQ) and nephritic syndrome respectively.[74-75] USEPA reports indicate that more than 60,000 babies are born annually with mercury related diseases in the US alone. Unfortunately, mercury has been widely used in industries as a chemical additives and energy source for the development of lamps, arc rectifiers, mercury cells, switches, thermometers, barometers, fungicides, antiseptics, preservatives, pharmaceuticals, electrodes and reagents. Therefore, on account of increasing threat and adverse effects of mercury on human health and the environment, controlling and monitoring of its levels have become a prime interest among the scientific community. During the past few years, significant efforts have been devoted to developing sensitive and selective probes for the detection of mercury which are based upon photoluminescence, surface enhanced Raman spectroscopy (SERS)[77-88] and chemical sensors[89-94] (i.e. conductometric or film resistivity, microcantilever, surface acoustic wave (SAW) transducer, piezoelectric transducers). However, most of these systems have limitations with respect to sensitivity, selectivity, simplicity, time consuming, environmental friendly, cost and biodegradability. Therefore, development of portable, quick method with sensitive, selective, cost effective, and environmentally friendly for aqueous Hg^{2+} detection is great challenge. In this regard, Nature has mastered the way to handle the materials with the extraordinary sensitivity and specificity in binding, transport and storage of metal ions in biological cells. Inspired by the biological processes, non-covalent host-guest interactions driven supramolecular fluorescence sensors have been shown to be a promising approach.[39] On account of its highly specific, sensitive, cooperative, cost-effective, environmental friendly, dynamic, reversibility, self-repairable, stimuli-responsive and well defined optical properties, supramolecular design was applied in various fields from biology to materials science and most importantly fluorescence sensing and diagnostics.[95-101] In general such dynamic self-assembled fluorescence sensors consist of receptor-spacer-reporter where receptor consisting of a binding site that binds the analyte in preference to all competing species and transform to a reporter via the spacer. Subsequently the analyte binding event induced changes in the assembly of reporter will be reflected as a variation in fluorescence readout signal. Herein we selected a well known biological metal-chelating amino acid histidine as a receptor and perylene diimide (PDI) system as a reporter to design fluorescence supramolecular sensor **PDI 2** for mercury. Histidine is a basic $\alpha-$amino acid with imidazole functional group and a common metal chelating ligand in many metalloproteins and known to bind with Hg^{2+}.[102-103] On the other hand PDI, is an $\pi-$electron difficient aromatic compound with high molecular planarity, well defined optoelectronic, redox properties, excellent photochemical and thermal stability.[1] Due to its remarkable properties PDI has been widely used as a versatile supramolecular building block for wide range of functional architecture.[1] Although the high fluorescence properties of PDIs makes them excellent sensing of various metal ions in the literature, the rigid hydrophobic extended π–surface limits the water solubility while the aggregation induced fluorescence quenching limits its practical applications. Therefore, our bio-inspired PDI bolaamphiphile (**PDI 2**) approach imparts water solubility to PDI by the zwitterionic form of histidine on both ends and selectively sense the Hg^{2+} via formation of **PDI 2**-Hg^{2+} metallosupramolecular complex in water.[39] In the literature, it has been established that thiol containing amino acids (cysteine) and related compounds are capable of forming strong ternary complex with Hg^{2+}.[104-105] With this in mind, we further explored the disassembly of the metallosuparamolecular complex of **PDI 2**-Hg^{2+} in a reversible manner by engaging with cysteine. Therefore, **PDI 2** can act as a supramolecular dual fluorescece probe for highly toxic Hg^{2+} ions and biologically important amino acid cysteine.

3.3.2 Results and discussion

PDI 2 was synthesized in one step reaction by the condensation of histidine with 3,4,9,10-perylenetetracarboxylic dianhydride (PDA) in the presence of imidazole at 120 ^{o}C for 1 hour as shown in Figure 3.3.1 (the detailed experimental procedure was given in experimental section)

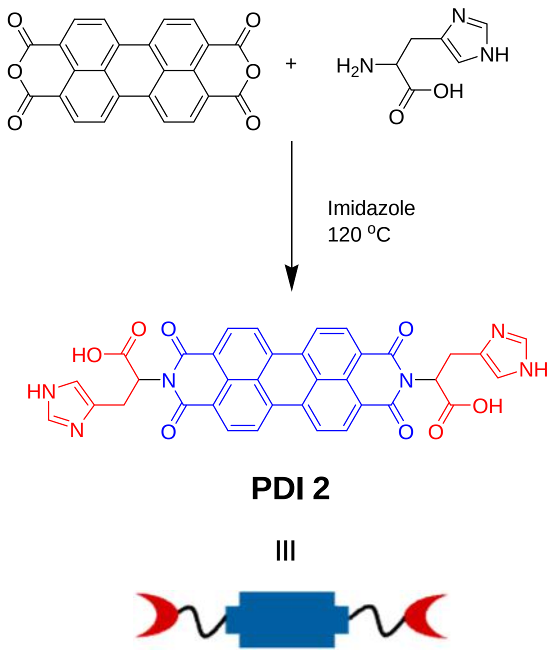

Figure 3.3.1 Synthesis of histidine conjugated PDI derivative **PDI 2**.

3.3.2.1 Self-assembly in aqueous medium

The self-assembly behavior of **PDI 2** in water was monitored by means of the optoelectronic properties of PDI using of UV-vis absorption, fluorescence emission, and Circular dichroism (CD) spectroscopy (Figure 3.3.2). The UV-vis absorption spectrum of **PDI 2** in DMSO solution exhibited the well-resolved vibronic electronic excitation state absorption bands at 525 nm (0−0 transition) 489 nm (0−1 transition), 458 nm (0−2 transition) and 430 nm (0−3 transition) with Franck−Condon progressions (A_{0-0}/A_{0-1}) of 1.59, characteristics of S_0-S_1 transitions polarized along the long axis of molecularly dissolved PDI chromophore (Figure 3.3.2a). The corresponding fluorescence emission spectrum suggested the non-aggregated state of **PDI 2** in DMSO solution by displaying a mirror image emission bands and slightly stoke shifted (~12 nm) sharp emission bands centered at 537 nm, 577 nm and 630 nm respectively (Figure 3.3.2b). In contrast, the UV-vis spectrum of **PDI 2** in pure water exhibited significantly diminished red shifted broad

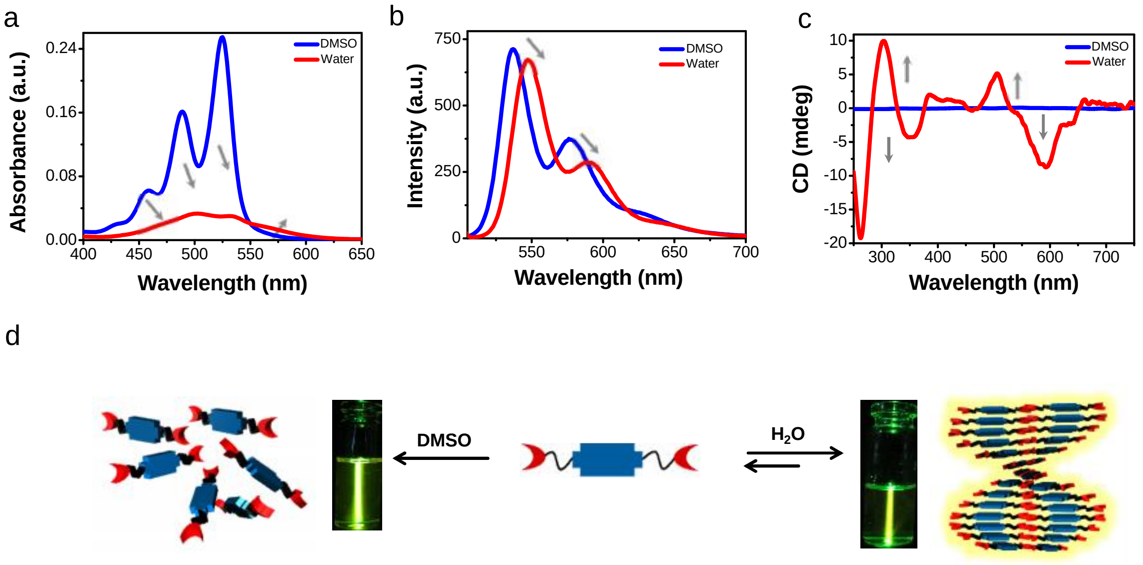

Figure 3.3.2 UV-vis absorption spectra (a), fluorescence emission spectra (b) and CD spectra (c) of **PDI 2** in DMSO and water. d) Schematic representation of molecular organization of **PDI 2** in DMSO (molecularly dissolved) and in aqueous solution (left-handed chiral self-assembly) and corresponding photographs of **PDI 2** in DMSO and water under green laser light.

absorption bands along with a new absorption band at 560 nm (Figure 3.3.2a). The absorption intensity of $A_{0\text{-}0}$ (532 nm) transition was found to be smaller than that of $A_{0\text{-}1}$ (503 nm) electronic transition band with Franck−Condon progressions (A_{0-0}/A_{0-1}) value of 0.90. While the fluorescence emission spectrum displays the large stoke shifted emission bands (~23 nm) with λ_{max} at 548 nm as compared to DMSO solution, signifying the formation of J-type self-assembly of **PDI 2** enforced by the hydrophobic PDI π–surface (Figure 3.3.2b). In order to understand the effect of histidine conjugation on long-range molecular ordering of **PDI 2** in water, we further carried out CD spectroscopy measurements. In agreement with UV-vis and fluorescence emission spectroscopic studies, CD spectra of **PDI 2** in DMSO exhibited flat CD signal due to molecularly dissolved state (Figure 3.3.2c). Remarkably, in pure water **PDI 2** displayed an intense bisignated CD signal in the PDI absorption region with negative cotton effect at 594 nm, 350 nm, followed by the positive signal at 506 nm, 303 nm and zero crossing at 529 nm, 328 nm respectively, characteristic of excitonically coupled left-handed (M-type) helical organization of PDI chromophores (Figure 3.3.2c). Therefore, the supramolecular chiral organization of **PDI 2** in water clearly signifying the transcription of chiral information from histidine to self-assembled PBI chromophores (Figure 3.3.2d).

3.3.2.2 Detection of Hg^{2+} ions in water

In line with the strategy, we sought to investigate the fluorescence property of chiral self-assembled **PDI 2** as a probe for the detection of analytes specifically Hg^{2+}. In the presence of Hg^{2+} in water the UV-vis spectra showed diminished 0-0 (532 nm) transition accompanied by hypsochromically shifted by ~22 nm at 0-0 and 0-1 absorption bands and enhanced shoulder band at 560 nm as compared with that of **PDI 2** alone, which signified extended strongly exciton-coupled H-type PDI chromophore aggregation (Figure 3.3.3a). Simultaneously, fluorescence emission spectra displayed rapid and gradual quenching behavior with the addition of increased Hg^{2+} concentration, indicating the formation of non-emitting **PDI 2**-Hg^{2+} supramolecular aggregates (Figure 3.3.3b). Furthermore, the Hg^{2+} fluorescence titration study exhibited clear sigmoidal shape as a function of Hg^{2+} concentration indicative of cooperative Hg^{2+} binding interactions induced transformation of J-type self-assembly of **PDI 2** to H-type metallosupramolecular **PDI 2**-Hg^{2+}aggregates (Figure 3.3.3c inset). The fluorescence quenching behavior of **PDI 2** in presence of Hg^{2+} was found to be linear at lower concentrations (5 nM to 1 μM) and became nonlinear with further addition (1.5 μM to 5 mM) indicating a static type of quenching. The cooperative Hg^{2+} binding interactions was further supported by Hill plot at the linear region with a Hill coefficient of 1.23 (>1, positive allosterism) and apparent association constant ($\log K_{app}$) value 7.87 (Figure 3.3.3c). The lowest concentration

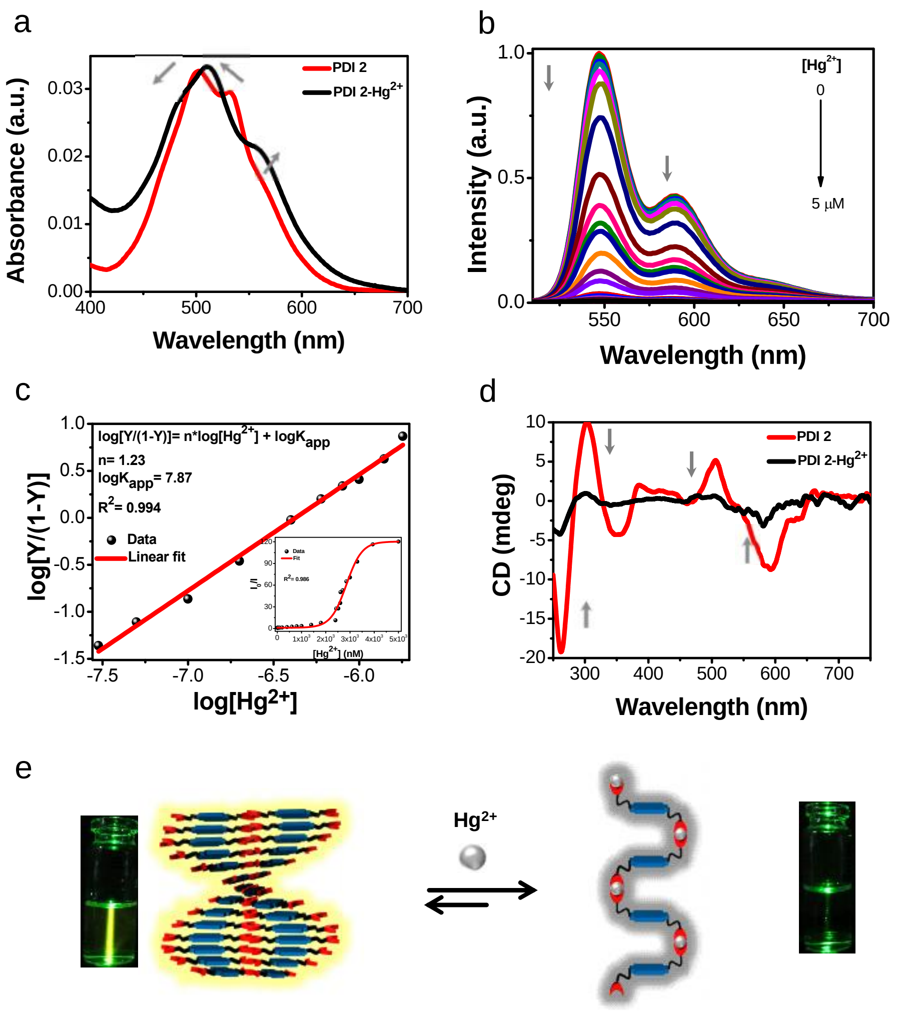

Figure 3.3.3 a) UV-vis absorption spectra of **PDI 2** before and after addition of Hg^{2+}. b) Fluorescence emission spectra of **PDI 2** as a function of increasing concentration of Hg^{2+}. c) The Hill plot at the linear regime, inset: Plot of fluorescence response (I_0/I) of **PDI 2** versus concentration of added Hg^{2+}. d) CD spectra of **PDI 2** before and after addition of Hg^{2+}. e) Schematic representation of Hg^{2+} induced assembly transformation of **PDI 2** from emissive left-handed self-assembly to nonemissive, achiral metallosupramolecular polymerization, Photographs of respective solutions under green laser light.

of Hg^{2+} (detection limit) that can induce significant fluorescence quenching of **PDI 2** was found to be 5 nM, which is 2 folds of magnitude lesser than the EPA allowed standard limit (10 nM, 2 ppb) in drinking water (Figure 3.3.3c). Furthermore, in support with the UV-vis and fluorescence studies, upon addition of Hg^{2+} (1 eq) from pure water, **PDI 2** show diminished CD signals in the PDI absorption bands due to Hg^{2+} coordination induced structural transformation from chiral molecular self-assembly to achiral metallosupramolecular organization (Figure 3.3.3d and e).

In order to accesses metal ion selectivity of the probe **PDI 2**, several alkali and transition metal perchlorate salts were tested. **PDI 2** did not show any significant emission spectral changes in the presence of most of the metal ions (Cu^{2+}, Cd^{2+}, Co^{3+}, Fe^{3+}, Mg^{2+}, Pb^{2+}, Ca^{2+}, Zn^{2+}, K^{+}, Na^{+}, Ni^{2+}) at 1:1 (**1**: M^{n+}) ratio (Figure 3.3.4). Therefore, histidine conjugated PDI bolaamphiphile **PDI 2** exhibited a rapid, highly selective, sensitive and ratiometric fluorescence response towards Hg^{2+} ion by means of reorganization of J- type chiral self-assembly into H-type achiral metallosupramolecular aggregates as shown in Figure 3.3.3e. The Hg^{2+} induced assembly transformation responsible for the fluorescence switching off-on process of **PDI 2** could be visualized by

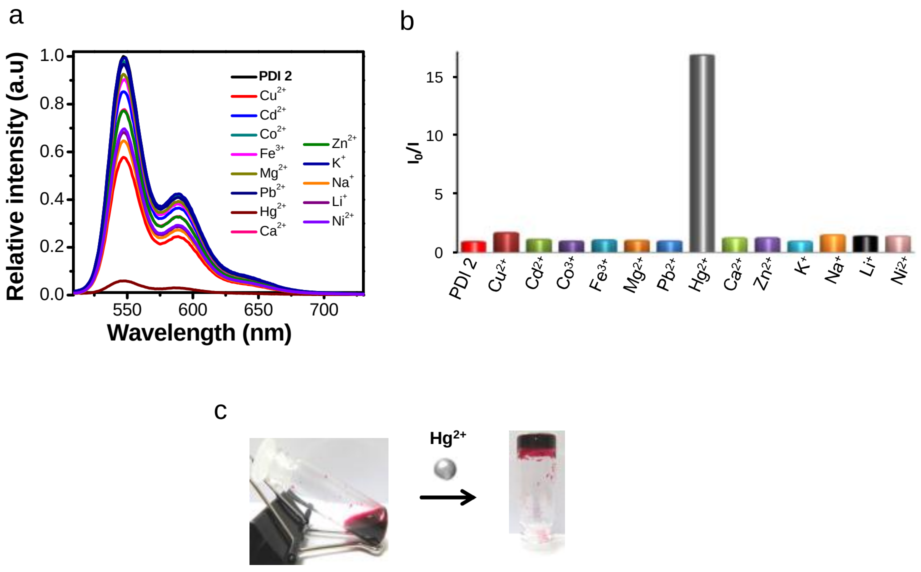

Figure 3.3.4 a) Fluorescence emission spectra of **PDI 2** in presence of various metal ions in water. b) Bar diagram depicting the effect of various metal ions on the fluorescence response (I_0/I) of **PDI 2**. c) Photographs of sol to gel transition of **PDI 2** in presence of Hg^{2+}.

the naked eye under the green laser illumination as shown in the Figure 3.3.3e. Moreover a rapid sol to hydrogel transformation with the addition of 1 equivalent Hg^{2+} into a solution of **PDI 2** in water, is a clear naked eye evidence for the formation of Hg^{2+} coordination induced extended metallosupramolecular aggregates in water (Figure 3.3.4c).

In order to study the interactions responsible for the **PDI 2**-Hg^{2+} metallosupramolecular aggregates in water, we further carried out ^{1}H-NMR, high-resolution Mass spectrometry (HRMS) and attenuated total reflection infrared (ATIR) spectroscopic measurements. ^{1}H-NMR spectra of **PDI 2** were recorded in DMSO-d_6 followed by the sequential addition of Hg^{2+} (1 M D_2O solution). Significant spectral changes were observed upon addition of Hg^{2+} (2 mM-18 mM) to **PDI 2** and are depicted in Figure 3.3.5a. The main peaks considered for assigning the binding mode of **PDI 2-**Hg^{2+} are NH protons (τ) of imidazole moiety, imidazole ring (i) and PDI aromatic protons (P1 and P2). Remarkably, in presence of Hg^{2+}, the broad imidazole NH protons (τ) cantered at 14.25 ppm in DMSO-d_6 was splitted into two different sharp downfield and upfield shifted signals at 14.27 ppm and 13.89 ppm respectively (Figure 3.3.5b). This is a clear indication of the direct involvement of imidazole nitrogen atom in coordinating with Hg^{2+} (Figure 3.3.5f). Similarly, the aromatic protons corresponding to imidazole ring (i) were upfield shifted by ~20 ppb (Figure 3.3.5c). Consequently, the PDI aromatic protons (P_1) are downfield shifted from 8.85 ppm to 9.00 ppm, with $\Delta\delta_{Ha} = 0.15$ ppm (Figure 3.3.5c), indicating the Hg^{2+} coordination induced face centered π–stacked **PDI 2** organization (Figure 3.3.5f). Further, ATIR spectroscopic study supported the interaction of Hg^{2+} with imidazole nitrogen atom which is evident from the large redshift (~206 cm^{-1}) of imidazole NH symmetric stretching frequency (3312.6 cm^{-1}) of **PDI 2** along with

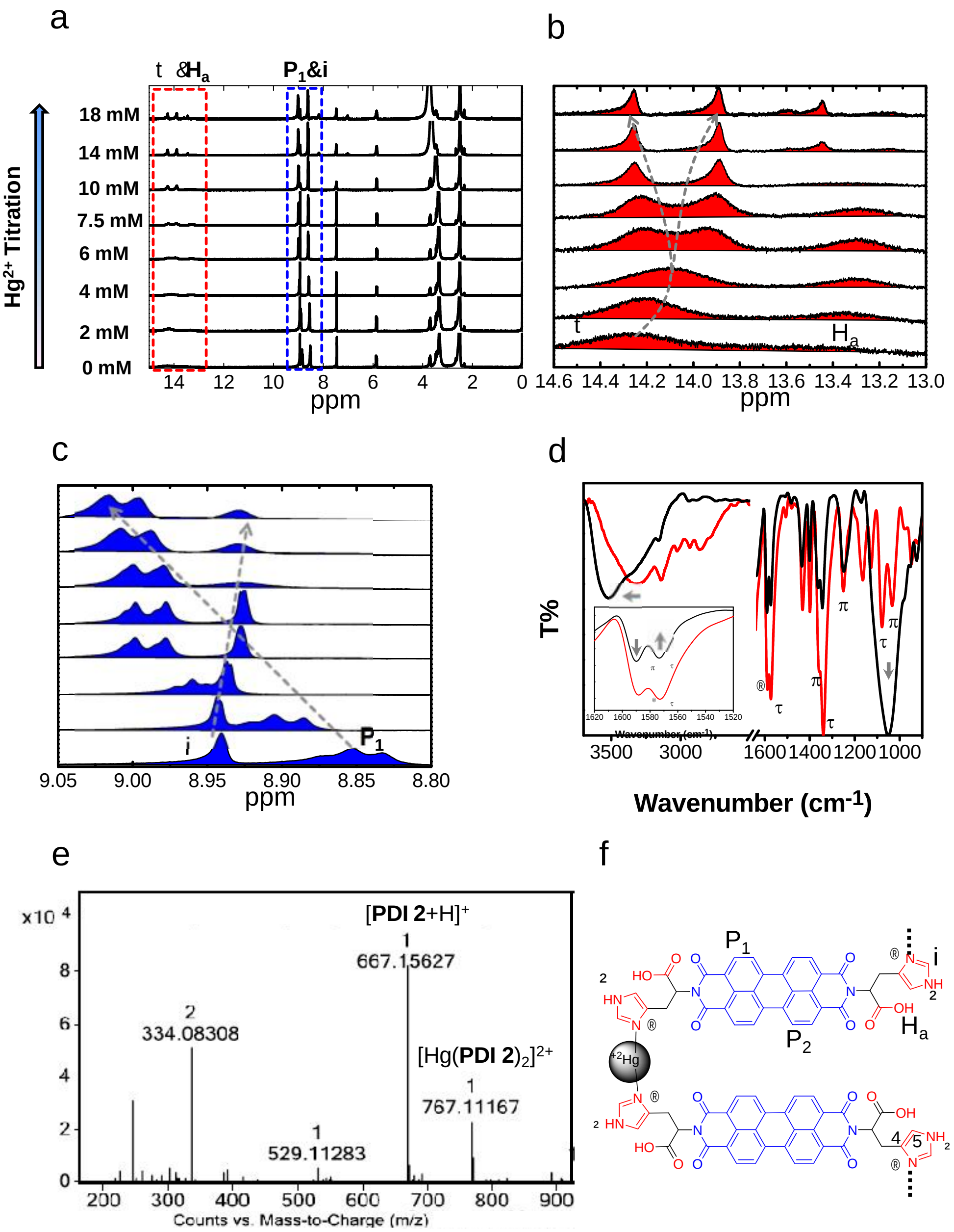

Figure 3.3.5 a) Hg^{2+} ^{1}H-NMR titration spectra of **PDI 2**. b) imidazole NH chemical shift (14.6 ppm-13.0 ppm) region. c) PDI and imidazole aromatic protons chemical shift (9.0 ppm-8.8 ppm) region. d) ATIR spectra of **PDI 2** (black curve) and **PDI 2**+Hg^{2+} (red curve). e) HRMS spectra of **PDI 2**+Hg^{2+}. f) Schematic representation of proposed Hg^{2+} binding interaction with **PDI 2**.

significant changes in respective imidazole τ and π bending frequencies and C^4=C^5 stretch (1590 –1560 cm^{-1}) region (Figure 3.3.5d). Furthermore, in presence of Hg^{2+}, HRMS spectra of **PDI 2** displayed a new m/z peak at 767.1116 attributed to the [Hg (**PDI 2**)$^{2+}$+H] coordination complex as shown in the Figure 3.3.5e. Thus HRMS clearly showed the formation of 1:1 (**PDI 2**: Hg^{2+}) coordination complex via sharing of one Hg^{2+} ion by the two the imidazole moieties on both sides of bolaamphiphile **PDI 2** to form extend 1D metallosupramolecular hydrogel as shown in Figure 3.3.5f.

3.3.2.3 Detection of cysteine

Given the fact that cysteine has a strong affinity toward Hg^{2+} with respect to histidine, next we explored reversibility of non-emissive achiral metallosupramolecular aggregates of **PDI 2**-Hg^{2+} into the fluorescent chiral organization by engaging with cysteine. As expected in the presence of cysteine, emissive behaviour of **PDI 2** was restored (Figure 3.3.6). Upon addition of cysteine absorption bands associated with the **PDI 2**-Hg^{2+} showed a significant red shifted (~22 nm) in the 0-0 absorbance band and the band at 532 nm were reappeared along with the disappearance of the aggregation band at 560 nm, characteristics of J-type self-assembly of **PDI 2** (Figure 3.3.6a). This was further confirmed by quick turn-on fluorescence with emission at 548 nm, 590 nm and 642 nm as similar to that of **PDI 2** in water (Figure 3.3.6b). Interestingly ~ 100% of the initial intensity of **PDI 2** in water was archived upon addition of 2 equivalent of cysteine signifying the sequestration of Hg^{2+} from non-emissive H-type of **PDI 2**-Hg^{2+}aggregates to restore to highly emissive J-type assembly of **PDI 2**. The fluorescence emission intensity monitored at 548 nm as a function of cysteine concentration exhibited a sigmoidal profile revealing the allosteric structural transformation (Figure 3.3.6c inset). Furthermore, an analysis of cysteine sequestration by means of the Hill equation gave the supreme apparent association constant (logK$_{app}$) value 30.06 and Hill coefficient of 5.54, suggesting the Hg^{2+} sequestration induced cooperative reorganization of **PDI 2**

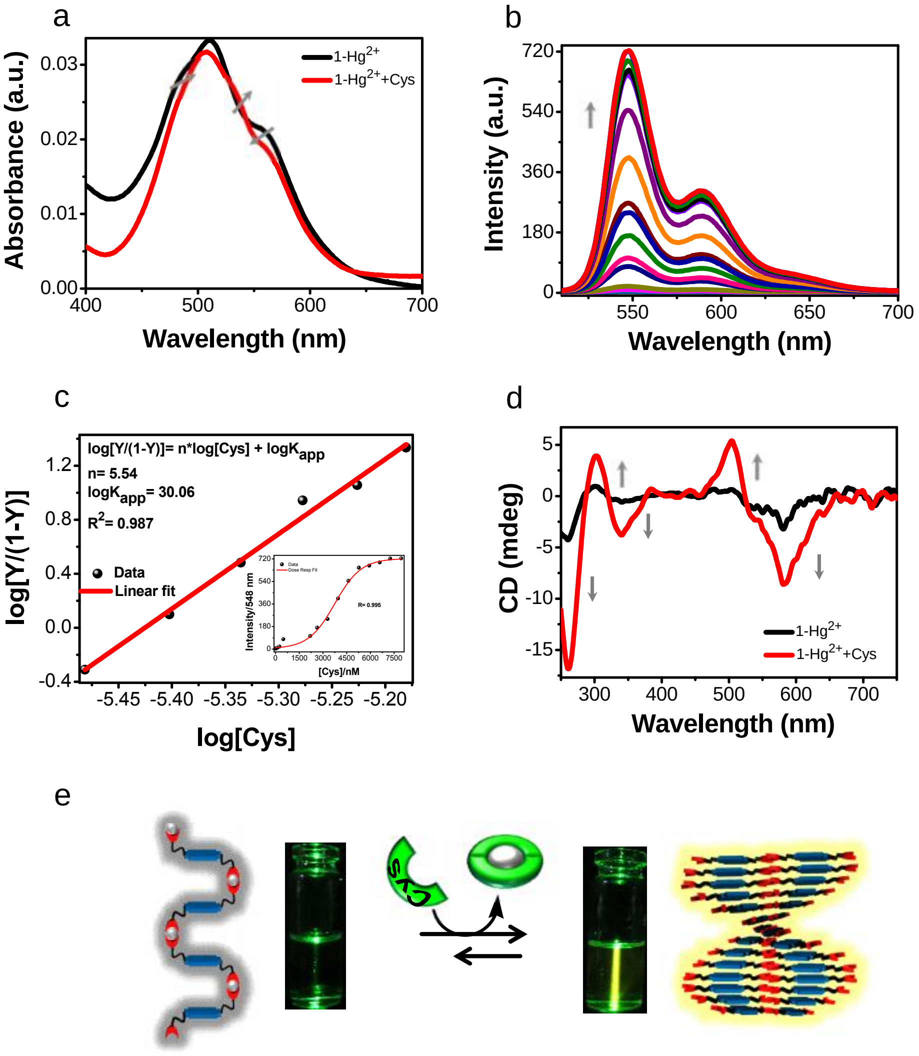

Figure 3.3.6 a) UV-vis absorption spectra. b) Fluorescence emission spectra upon addition of cysteine. c) Hill plot, inset the plot of fluorescence emission intensity as a function of added cysteine. d) CD spectra. e) Schematic representation of proposed sequestration of Hg^{2+} by cysteine to restore left-handed J-type fluorescent **PDI 2** self-assembly from achiral H-type non emissive metallosupramolecular aggregates.

(Figure 3.3.6c). The cysteine titration experiments revealed that the ≤10 nM of cysteine is good enough to achieve considerable fluorescence emission enhancement. Interestingly the CD spectra of **PDI 2**-Hg^{2+} in the presence of cysteine showed supramolecular chiral restoration with the enhanced bisignated CD signals at the PDI absorption bands 581 nm,

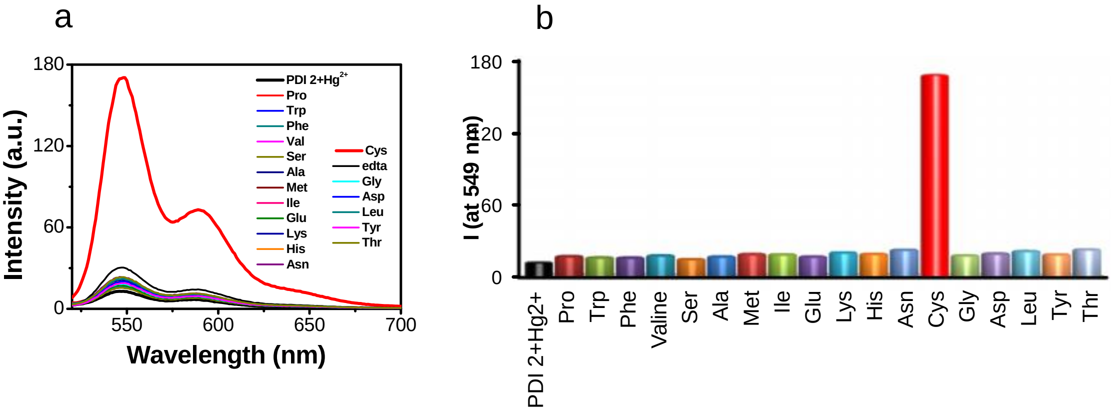

Figure 3.3.7 a) fluorescence emission spectra of **PDI 2**+Hg^{2+} in presence of various amino acids. b) The plot of fluorescence emission intensity at 549 nm as a function of added amino acid analytes.

340 nm (negative band,) 504 nm, 302 nm (positive band) and zero crossing at 523 nm, 320 nm respectively (Figure 3.3.6d).

Furthermore, the selectivity of this system for detection of cysteine over other amino acids was investigated. The naturally occurring amino acids alanine (Ala), arginine (Arg), asparagine (Asn), aspartic acid (Asp), cysteine (Cys), glutamine (Gln), glutamic acid (Glu), glycine (Gly), histidine (His), isoleucine (ile), leucine (leu), lysine (lys), methionine (Met), phenylalanine (Phe), proline (pro), serine (ser), threonine (Thr), tyrosine (Tyr), tryptophan (Trp), valine (Val) were added at higher concentrations (4.2 μM) to **PDI 2**-Hg^{2+} aggregates and change in fluorescence emission spectra was recorded (Figure 3.3.7a). Except cysteine, all other amino acids failed to show any significant fluorescence enhancement, indicating the inability of Hg^{2+} sequestration thereby unaffecting the **PDI 2**-Hg^{2+} H-type non-emissive metallosupramolecular aggregates (Figure 3.3.7a). Overall, the total recovery of optical (UV-vis, Fluorescence emission and CD) features of **PDI 2** in water from **PDI 2**-Hg^{2+} upon addition of cysteine signify the sequestration of Hg^{2+} from the **PDI 2**-Hg^{2+} metallosupramolecular aggregates via strong

Hg–S coordination complex formation and resulting in the reorganization of **PDI 2** into highly emissive J-type chiral self-assembly as illustrated in the Figure 3.3.6e. These changes on the fluorescence behaviour can be visualized under green laser light as shown in the Figure 3.3.6e. Therefore, the nonemissive metallosupramolecular aggregates **PDI 2**-Hg^{2+} can be used as a rapid, highly selective and sensitive turn-on fluorescence probe for the detection of cysteine in water (Figure 3.3.7b).

3.3.2.4 Morphological studies

In order to visualize morphological changes in reversible assembly reorganization process, we performed the field emission scanning electron microscopy (FESEM) studies by drop casting the corresponding sample solution on silicon (111) wafer. **PDI 2** alone in water self-assembled into high aspect ratio and well-separated nanofibers with 20-30 nm width and micrometer long (Figure 3.3.8a). Interestingly, in the presence of Hg^{2+} nanofibers transformed into highly dense interconnected network of nanotapes attributed to the formation of metallosupramolecular hydrogels ((Figure 3.3.8b). Furthermore, EDAX measurements on the nanotape network revealed the presence of Hg along with C, N and O elements conforming the presence of **PDI 2**-Hg^{2+} metallosupramolecular aggregates (Figure 3.3.8b inset). Remarkably, upon addition of cysteine to **PDI 2**-Hg^{2+} hydrogels, the nanotapes 3D network was completely transformed into a less dense nanofibers network with 20-50 nm width and micrometer long lateral dimensions indicating the metal sequestration induced reversible morphology transformation (Figure 3.3.8c). Therefore, the reversible metal and metal sequestration-induced supramolecular structural transformations were not only limited to spectroscopic changes but observed on the morphological changes as well. These observations were further strengthened by dynamic light scattering (DLS) studies in water. A sharp monodispersed aggregate with

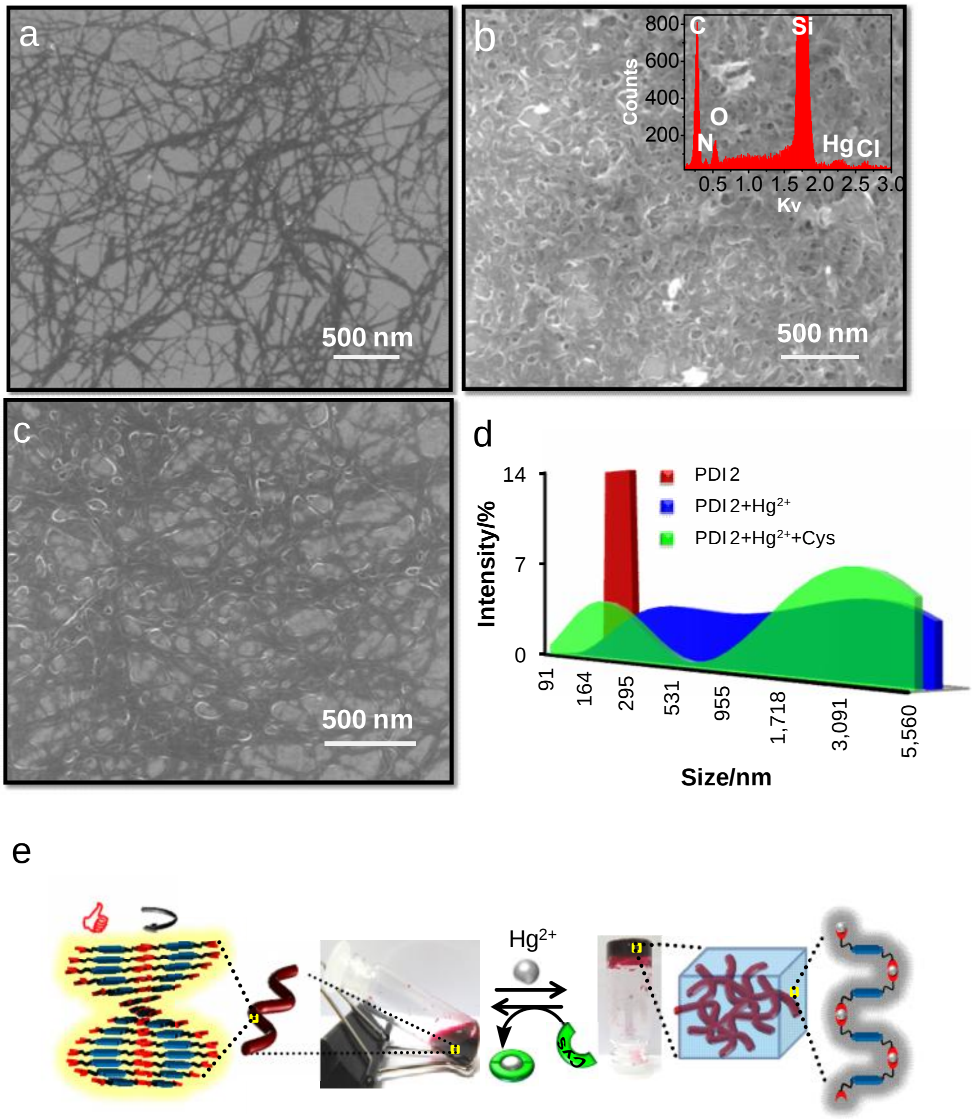

Figure 3.3.8 FESEM micrographs of a) **PDI 2**, b) **PDI 2**+Hg^{2+} xerogels and c) **PDI 2**+Hg^{2+}+cysteine. d) DLS spctra. e) Schematic representation of proposed revisable assembly switching of **PDI 2** in presence of Hg^{2+} and cysteine respectively, photographs of respective aqueous solutions and hydrogels.

a mean size around 150 nm was observed from an aqueous solution of **PDI 2** alone (Figure 3.3.8d). Upon addition of 1 equivalent Hg^{2+} into a solution of **PDI 2** in water resulted into more extended and broad aggregates spanning from 190 nm to 5.5 µm was observed. Subsequently further addition of cysteine in **PDI 2**-Hg^{2+} aqueous solution, the broad aggregates of **PDI 2**-Hg^{2+} transformed into two kinds of aggregates with mean size

3.1 μm and 196 nm (similar to that of **PDI 2** in water) respectively (Figure 3.3.8d). Therefore, DLS studies further provide evidence for assembly transformation of **PDI 2** in the presence of Hg^{2+} and cysteine are indeed also occur in solution state, which is further eliminated the possible substrate artifacts with respect to observed morphology changes.

3.3.3 Conclusion

In summary, water soluble fluorescent **PDI 2** was synthesized and explored its assembly modulation for the reversible and rapid sensing of highly toxic Hg^{2+} and cysteine in water with high sensitivity. **PDI 2** alone in water self-assembled into highly emissive J-type left-handed organization. From the pool of metal ions Hg^{2+} selectively translate the self-assembly of **PDI 2** into nonemissive H-type achiral reorganization via formation of cooperative metallosupramolecular aggregates (Hill coefficient = 1.23 and $\log K_{app} = 7.87$) renders a rapid, highly selective and sensitive (detection limit > 5 nM) fluorescence turn-off probe for the detection of Hg^{2+} in water. The Hg^{2+} induced metallosupramolecular aggregates of **PDI 2** was well characterized by various spectroscopic tools. On account of high binding affinity of Hg^{2+} to words cysteine ($\log K_{app}$=30.06), cysteine cooperatively (Hill coefficient of 5.54) sequestrate the Hg^{2+} from the nonemissive **PDI 2**-Hg^{2+} metallosupramolecular aggregates into highly emissive chiral J-type self-organization with high sensitivity (> 10 nM). The reversible dual sensing ability of probe **PDI 2** can be visualized under green laser light by means of visible fluorescence changes without any prior spectroscopic tools. Furthermore, upon addition of Hg^{2+} to the solution **PDI 2** in water, the sol transformed into the metallosupramolecular hydrogel, which again trasnsformed to the sol in the presence of cysteine. Moreover, the modulation of the nanoscale organization of **PDI 2** from nanofibers to highly denser interconnected nanotapes network was achieved using cysteine and Hg^{2+} respectively in a reversible manner. Overall reversible assembly switching of **PDI 2** in water was achieved and effectively used for the sensing of extremely toxic Hg^{2+} and biologically important amino acid cysteine at very low concentrations. The present study on host-guest interaction mediated assembly modulation of fluorescent organic semiconductor (PDI) may catalyze further understanding of metal induced assembly processes in biological systems for development of efficient sensor systems for extremely toxic, hazardous environmental pollutants as well as biologically important analytes.

Subchapter 3.4 pH Responsive Chiroptical Switching of Histidine Conjugated PDI

3.4.1 Introduction

The development of novel stimuli responsive molecular systems and materials has recently been attracting great interest.[106-110] In particular, the design of chiroptical switches wherein reversible chiral transformation is induced in response to chemical, electrical and optical stimuli is a major endeavour in many advanced applications including chiral analysis, absolute configurational assignment, optical devices, information storage, light modulators, electro-optical displays, catalysis and sensors.[111-140] Many molecular, supramolecular and polymeric chiroptical switches have been proposed that are responsive to light, temperature, solvent, mechanical forces, chiral/achiral guests, redox/electrochemical potential agents, metal ions, anions.[111-140] The most attractive one in this field is the pH-responsive supramolecular chiral optical switch because of its relevance to biological processes.[141-142] In contrast, although many stimuli responsive supramolecular systems are known, the chiral assemblies with pH-switchable negative-positive chiroptical inversion is still a challenging task. In this regard, biomolecules are more appealing due to the fact that most of the structural and functional attributes of biopolymers are determined by the pH-responsive protonation-deprotonation induced conformational switching events.

On the other hand, chiral molecular ordering of organic semiconductors has been known to show remarkable charge carrier mobilities and exciton diffusion along the helical stacking columnar axis and hence perceived as a promising molecular packing geometry for optoelectronic applications.[143-144] Herein, we describe the histidine conjugated perylene diimide (**PDI 2**) and it’s pH-responsive reversible chiroptical self-assembly switching behavior in water. PDIs are one of the extensively studied classes of n-type organic semiconductor materials. On account of molecular planarity, high π-acidity, well-defined redox behavior, photophysical properties, PDI and its derivatives have been known for a wide range of applications from materials to biomedicine.[1-17] On the other hand, histidine is the only proteinogenic amino acid that has an inflection point at pH= 6. It has four different states at pH = 0, 4, 8 and 12 as shown in the Figure 3.4.1a. No other amino acid has an ionizable side chain with a pKa value near enough to pH 7.0 to be an effective physiological buffer. Therefore, **PDI 2** has two different pKa values at 3.6 (carboxylic acid) and 7.3 (imidazole ring) and expected to form distinct pH dependent self-organization (Figure 3.4.1b).

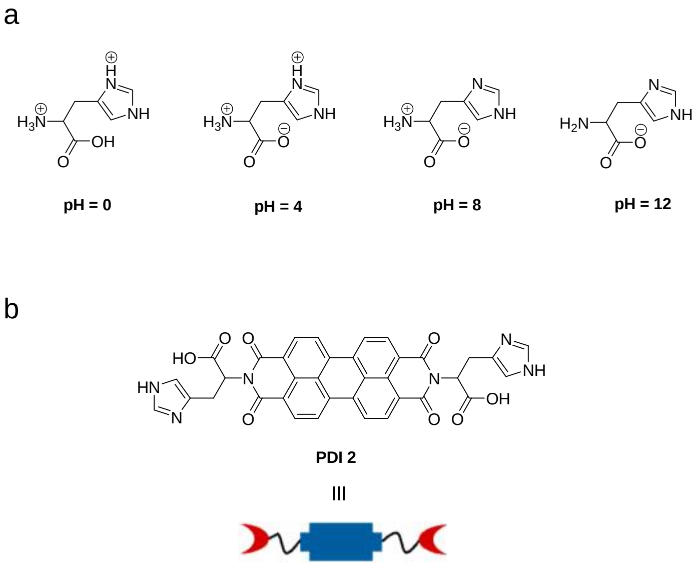

Figure 3.4.1 a) Structure of histidine, at different pH values. b) Molecular structure of **PDI 2**.

3.4.2 Results and discussion

The synthesis and characterization of **PDI 2** is described in subchapter 3.3 and the experimental section.

3.4.2.1 pH dependent photophysical studies

The detailed self-assembly behavior of **PDI 2** in water was explained in subchapter 3.1. Next we studied pH-responsive self-assembly properties of **PDI 2** by UV-vis absorption, fluorescence emission, and circular dichroism (CD) spectroscopy mesurements. As the pH of the solution increased, the UV-vis absorption spectra of **PDI 2** displayed distinct 0–0 (545 nm) and 0–1 (500 nm) vibronic transition intensities. The respective Frank-Condon progressions (A_{0-0}/A_{0-1}) values were found to be 0.99 at low pH (from 1 to 2), 0.67 at neutral pH 7 and 1.05 for basic pH 11 (Figure 3.4.2a). The calculated Frank-Condon progressions values clearly suggesting the formation of pH-tunable **PDI 2** $\pi-$stacked assembly in aqueous solution. In agreement with the absorption studies, pH-dependent fluorescence emission spectra displayed a decrease in fluorescence intensity as a function of increase in pH of the solution (Figure 3.4.2b). To probe the pH-responsive chiral stacking of **PDI 2**, we further carried out CD spectroscopy study. Interestingly, opposite CD signals were observed at extreme acidic and basic conditions (Figure 3.4.2c). The solutions of **PDI 2** at pH 1-2 exhibited intense bisignated CD signal in the PDI absorption region with negative cotton effect at 565 nm, followed by the positive cotton effect at 473 nm and zero crossover at 514 nm respectively, characteristic of excitonically coupled left-handed (M-type) helical organization of PDI chromophores. Further increase in pH from 2 to 9 resulted in red shifted (28 nm) relatively less intense CD signals with similar spectral features as that of pH 1 to 2. However, at strong basic pH (10 and 11) conditions the less intense but inverted bisignated CD spectra was observed with positive cotton effect at 565 nm, followed by the negative cotton effect at 533 nm and zero crossover at 551 nm respectively, indicating the formation of excitonically coupled right-handed (*P*-type) helical organization of PDI chromophores. Consequently, it may state in

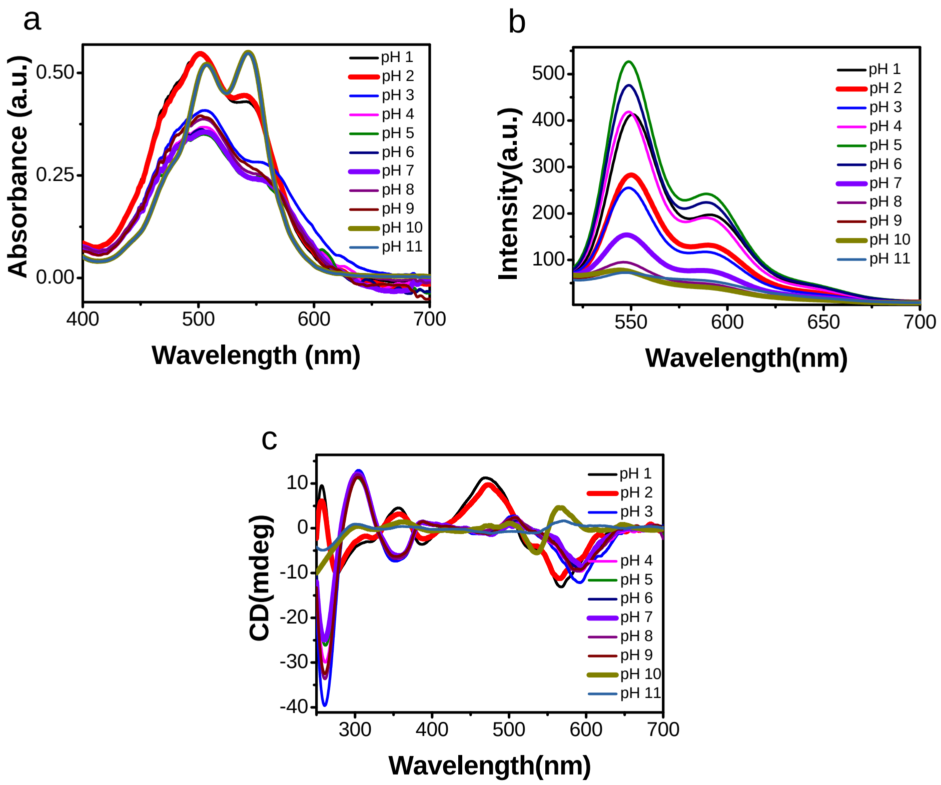

Figure 3.4.2 pH dependent photophysical studies. a) UV-vis absorption spectra of **PDI 2**. b) Fluorescence emission spectra of **PDI 2**. c) CD spectra of **PDI 2**.

that the handedness of self-assembled **PDI 2** is pH-responsive nature, at acid and neutral pH *M*-type (left handed) while at basic pH *P*-type (right handed) helical organization was observed (Figure 3.4.2c).

3.4.2.2 Reversible pH switching

We further investigated the reversible switching property of **PDI 2** self-assembly as a function of pH of the solution. Initially, the spectral studies were recorded at neutral pH 7 followed by an adjusting the pH to 2 and 10 using 1M HCl and NaOH aqueous solutions, respectively. This procedure was repeated over cycles and recorded the UV-vis, fluorescence emission, and CD spectral changes (Figure 3.4.3). UV-vis absorption studies showed reversible switching of 0–0 (545 nm) and 0–1 (500 nm) transitions and

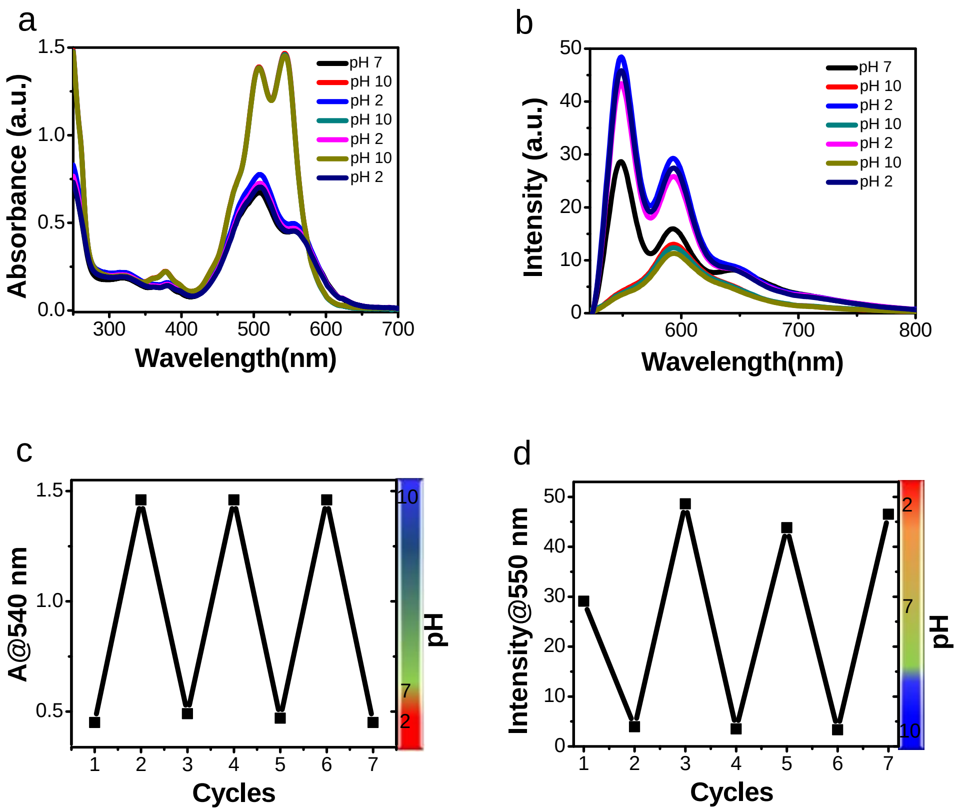

Figure 3.4.3 Reversible pH responsive switching studies of **PDI 2**. a) UV-vis absorbtion spectra. b) Fluorescence emission spectra. c) The plot of Absorbance at 540 nm versus each cycle of pH. d) The plot of fluorescence intensity at 550 nm versus each cycle of pH.

corresponding Frank-Condon progressions values from 0.99 to 1.05 with the change of pH from 2 to 10 respectively (Figure 3.4.3a). The plot of absorbance at 0–0 (545 nm) transition absorbance versus cycles clearly displayed the reversible self-assembly switching property of **PDI 2** and is very effective even after seven cycles, as shown in the Figure 3.4.3c. In agreement with the absorption studies, fluorescence emission studies also showed similar reversible enhancement and diminishing of emission band at 550 nm as the pH of the solution from 2 and 10 respectively (Figure 3.4.3b). The cycles of fluorescence switching as a function of pH are shown in the Figure 3.4.3d. Further, we investigated the reversibility of the chiroptical switching property of **PDI 2** between *M*- and *P*-type helical assemblies by carrying out CD studies at pH 2 and pH 10 in cycles

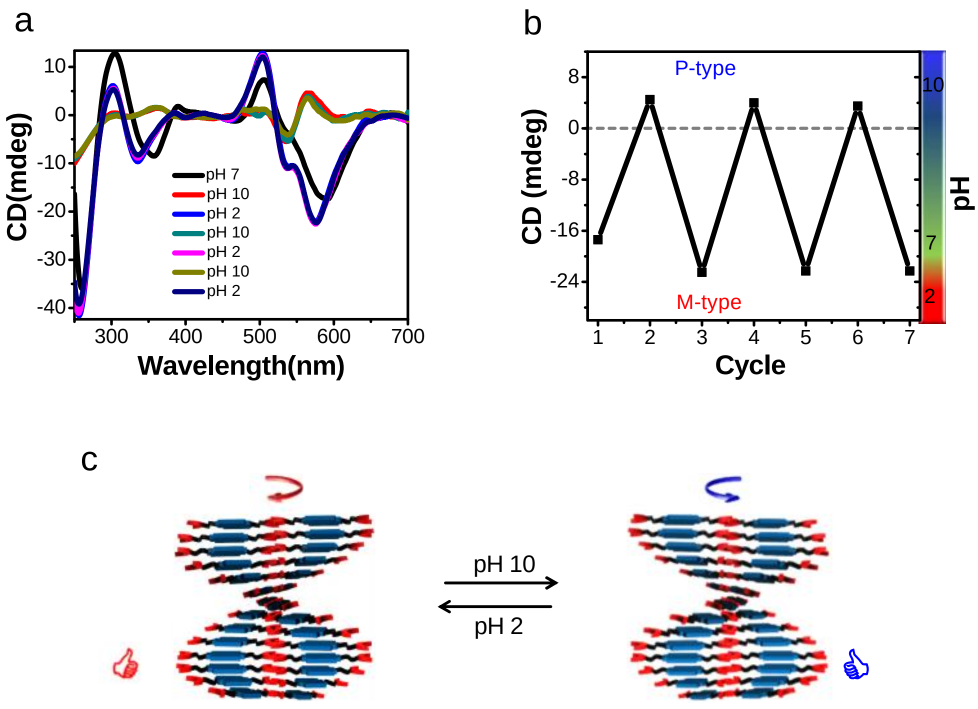

Figure 3.4.4 Reversible pH responsive chiroptical switching studies of **PDI 2**. a) CD spectra at different pH values. b) The plot of CD intensity at 570 nm versus each cycle of pH. c) Schematic representation of the molecular packing model for pH responsive chiroptical swithing self-assembly of **PDI 2.**

(Figure 3.4.4). Remarkably, the CD data clearly demonstrated the reversibility of the pH-induced chiroptical switching, as reflected in changeover of negative and positive CD features at λ_{max} (570 nm) of **PDI 2** between pH 2 (*M*-helicity) and pH 10 (*P*-helicity), which is observed even after seven cycles of pH adjustments. The plot of reversible chiroptical switching property of **PDI 2** as a function of pH was shown in Figure 3.4.4b. These observations clearly suggest the protonation (at pH 2) and deprotonation (at pH 10) of imidazole nitrogen and carboxylic acid induced self-assembly switching of **PDI 2** from *M*-type to *P*-type respectively as shown in the Figure 3.4.4c.

3.4.2.3 Morphological studies

In order to study the effect of pH on the nanoscale self-organization of **PDI 2** we carriedout the field emission scanning electron microscopy (FESEM) studies as a function of pH (at 10, 7 and 2). Interestingly, going from higher pH (10) to lower pH (7, 2) a drastic change in the morphology of assembly structures was observed (Figure 3.4.5). Initially, **PDI 2** in pH 10 self-assembled into a uniform micrometer long, thin nanofibril network with 12±1 nm width (Figure 3.4.5a). At pH 7, relatively thick intertwined fibril bundles with 22±1 nm width was observed (Figure 3.4.5b). Interestingly, at pH 2, the fiber bundles transform into interconnected belt structure with 120±5 nm in width and a few micrometers in length, indicating the interfibrillar interactions (Figure 3.4.5c). The observed pH tuneable morphology of **PDI 2** can be explained based on variation in the charge of imidazole nitrogen and carboxylic acid on either side of **PDI 2** (Figure 3.4.1). Since the fibrils are negatively charged (carboxylate anion) under the basic conditions, the interfibrillar repulsive interactions favor in thin split nanofibrils. As the pH decreases, the imidazole nitrogen and carboxylate groups are progressively protonated, decreasing interfibrillar repulsion, thus allowing greater interfibrillar interaction that contributes to

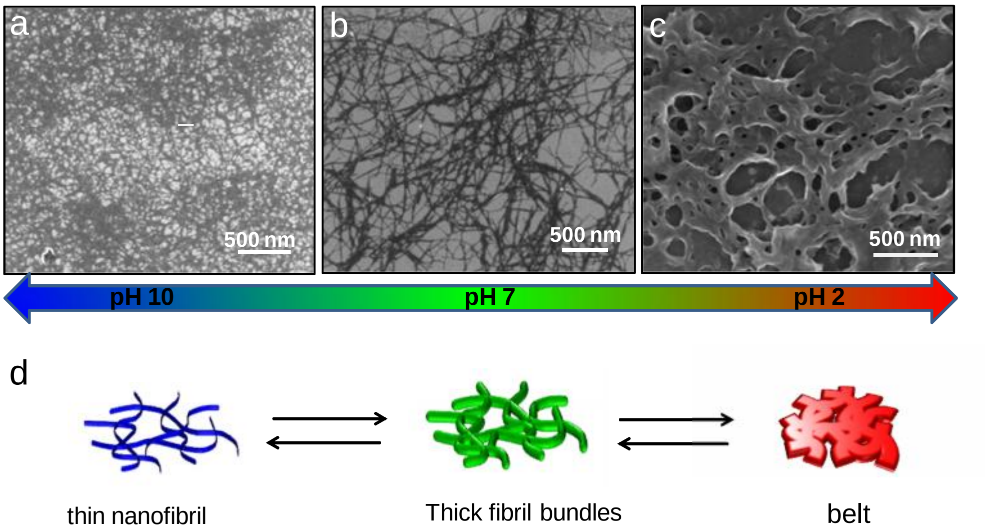

Figure 3.4.5 FESEM micrographs of **PDI 2** from different pH solutions. a) at pH 10. b) at pH 7. c) at pH 2. d) Schematic representation pH responsive morphologies of **PDI 2**.

the increased lateral interfibrillar contact which resulted in fibril bundles to belt structure as revealed in the FESEM images (Figure 3.4.5d).

Therefore, all the spectroscopic and microscopy results showed the reversible pH responsive chiral self-assembly switching of **PDI 2** by perturbing the balance between the electrostatic attractive and repulsive interactions, thus resulting in reversible chiroptical switching and different dominant morphologies at different pH values.

3.4.3 Conclusion

In summary, bioinspired PDI bolaamphiphile with histidine auxiliaries (**PDI 2**) was designed and investigated its pH-responsive self-assembly behavior using various spectroscopy and microscopy techniques. The pH-responsive helical molecular organization and reversible chiroptical switching (*M*- to *P*-type) of **PDI 2** have been validated through UV-visible absorption, fluorescence emission, and CD studies. Interestingly microscopy studies showed 1D nanostructures with pH tuneable lateral dimensions. Overall, we demonstrated the pH-responsive perturbation in the electrostatic interactions among the self-assembled **PDI 2** resulting in reversible supramolecular chiroptical switching in solution and distinct 1D morphologies. This study provides valuable information on designing bio-inspired functional supramolecular chiroptical switch for exploring the future electronics, chiroptical and biomedical applications.

3.4.4 2. Experimental Section

Materials

3,4,9,10-Perylenetetracarboxylic dianhydride (PDA), L-3,4-dihydroxyphenylalanine (L-DOPA), imidazole, amino acids and all the perchlorate salts of metal ions were obtained from Sigma-Aldrich. All other reagents and solvents utilized in the experiments were of reagent and spectroscopic grades and used as received without further purification unless otherwise mentioned. Milli-Q water was used in all the experiments.

Measurements

UV–vis absorption and fluorescence emission spectra were recorded on a Perkin–Elmer Lambda-25 spectrometer. A 10 mm x 10 mm quartz cuvette was used for recording spectra of samples in solution. Fourier transform infrared (FTIR) spectra were recorded on a Perkin–Elmer spectrometer. ^{1}H and ^{13}C NMR spectra were recorded on a Bruker AV-400 spectrometer with chemical shifts reported as ppm (in DMSO-d_6 with tetramethylsilane as internal standard). High resolution mass spectrometry (HRMS) analysis was performed on Agilent Technologies 6538 UHD Accurate-Mass Q-TOF LC/MS spectrometer (HRMS). Electrospray ionisation mass spectrometry (ESI-MS) analysis performed on Shimadzu LCMS-2020 spectrometer. Fluorescence decay profiles were performed using FLSP 920 spectrometer, Edinburgh Instrument, EPLED.

Preparation of working solution of PDI 1 in water. 1 mM stock solution of **PDI 1** in pure DMSO was prepared and 10 µL stock solution was added into 2990 µL of pure water to make 3.5 µM working solution, which was found to be completely soluble with a transparent solution.

Fluorescence and UV-vis absorption titration of PDI 1 with surfactants. To the eleven samples, each containing equal concentration of **PDI 1** (3.5 μM), surfactants (CTAB, Triton X 100, SDS) were added in a increasing concentrations of 0, 1, 2, 3, 4, 5, 6, 7, 8, 9 and 10 mM and the changes in absorption and fluorescence spectra of **1** were recorded after proper mixing.

Fluorescence and UV-vis absorption behaviour of PDI 1/CTAB in presence various metal ions. Changes in fluorescence and UV-vis absorption spectra of **PDI 1** (3.5 μM) in the miceller CTAB (10 mM) were monitored upon excitation at 490 nm, in the presence of perchlorate and chlorides salts of alkali and transition metal ions (Fe^{2+}, Ni^{2+}, Al^{3+}, Pb^{2+}, Hg^{2+}, Ag^{+}, Co^{2+}, Zn^{2+}, Ca^{2+}, Na^{+}, Mn^{2+}, Mg^{2+}, Ru^{3+} and Sr^{2+}) at their 25 μM concentrations.

Fluorescence and UV-vis absorption behavior of PDI 1/CTAB with Fe^{3+} and Cu^{2+} metal ions. Perchlorate and chloride salts of Fe^{3+} and Cu^{2+} from 0 to 21 μM and 0 to 7 μM respectively were added into **PDI 1** (3.5 μM) in CTAB (10 mM) solution, and corresponding spectral changes in fluorescence and absorption of **PDI 1** were monitored and recorded.

Fluorescence and UV-vis absorption behavior of PDI 1/CTAB/Fe^{3+} and PDI 1/CTAB/Cu^{2+} with various anionic, neutral and metal ion chelators. To an aggregated solution of **PDI 1** (3.5 μM) in CTAB (10 mM) in presence of Fe^{3+} (21 μM) and Cu^{2+} (7 μM), various anions and neutral, metal ion receptors (CO_3^{2-}, $S_2O_3^{2-}$, PO_4^{3-}, Cl^-, S^{2-}, SO_4^{2-}, NO^{3-}, NCO^-, CNS^-, CH_3COO^-, ethylenediaminetetraacetic acid (EDTA), aspartic acid (Asp), methionine (Met), cysteine (Cys), histidine (His), tyrosine (Tyr), glutamic acid (Glu), tryptophan (Trp), were added at a higher concentration of 300 μM and spectral changes were monitored and recorded.

Fluorescence and UV-vis absorption behavior of PDI 1/CTAB/Fe^{3+} and PDI 1/CTAB/Cu^{2+} with diethylene triamine pentaacetic acid (DTPA). Increasing concentrations of DTPA (0-50 μM) was added into the solution of **PDI 1** (3.5 μM) in CTAB (10 mM) in presence of Fe^{3+} (21 μM) and Cu^{2+} (7 μM), respectively and corresponding spectral changes in fluorescence and absorption of **PDI 1** were recorded.

Preparation of working solution of PDI 2 in water. 50 mM stock solution of **PDI 2** in milliQ water was prepared and 13.2 µL stock solution was added into 2986 µL of milliQ water to make 2.2 µM working solution, which was visualized to be completely soluble with a transparent solution in water.

Fluorescence and UV-vis absorption behaviour of PDI 2 in presence of various metal ions. Metal ion selectivity studies. Changes in fluorescence emission spectra of **PDI 2** (2.2 μM) in milliQ water were monitored upon excitation at 490 nm (with excitation slit width 10 nm, emission slit width 10 nm and path length 10 mm) in the presence of perchlorate salts of alkali and transition metal ions (Fe^{2+}, Ni^{2+}, Al^{3+}, Pb^{2+}, Hg^{2+}, Ag^{+}, Co^{2+}, Zn^{2+}, Ca^{2+}, Na^{+}, Mn^{2+}, Mg^{2+}, Ru^{3+} and Sr^{2+}) at their 2.2 μM concentrations.

Fluorescence and UV-vis absorption behaviour of Hg (II) and Cu (II) sensitivity studies. Perchlorate salts of Hg^{2+} and Cu^{2+} from 0 to 2.4 μM and 0 to 2.4 μM respectively were added into **PDI 2** (2.2 μM) solution, and corresponding spectral changes in fluorescence emission of **PDI 2** were monitored and recorded.

Fluorescence and UV-vis absorption behavior of PDI 2-Hg^{2+} in presence of various amino acids. To an aggregated solution of **PDI 2** (2.2 μM) in presence of Hg^{2+} (2.2 μM) in water various natural L-amino acids alanine (Ala), arginine (Arg), asparagine (Asn), aspartic acid (Asp), cysteine (Cys), glutamine (Gln), glutamic acid (Glu), glycine (Gly), histidine (His), isoleucine (Ile), leucine (leu), lysine (lys), methionine (Met), phenylalanine (Phe), proline (pro), serine (ser), threonine (Thr), tyrosine (Tyr), tryptophan (Trp), valine (Val) were added at a higher concentration of 4.2 μM and spectral changes were recorded.

Fluorescence and UV-vis absorption behaviour of cysteine sensitivity studies. Increasing concentrations of cysteine (0-13 μM) was added into the solution of **116** (2.2 μM) in presence of Hg^{2+} (2.2 μM) in milliQ water and corresponding spectral changes in fluorescence emission of **PDI 2** were recorded.

Synthesis of PDI 1. 3,4,9,10-Perylenetetracarboxylic dianhydride (PDA) (500 mg, 1.2 mmol), L-3,4-dihydroxyphenylalanine (L-DOPA) (500 mg, 2.5 mmol), and imidazole (2.0 g) were added into a round bottom flask and heated at 120 °C for 1 h with stirring under nitrogen atmosphere. The reaction mixture was allowed to cool to 90 °C, and then poured into Milli-Q water and filtered. The filtrate was acidified with 2.0 N HCl, and the precipitate was filtered, washed with excess of Milli-Q water and dried under vacuum at 80 °C to obtain the product **PDI 1** in high yield (94%). ^{1}H NMR (*DMSO-d_6*, 400 MHz) δ_H 13.01 (2H, s), 8.83 (2H, s), 8.56 (2H, s), 8.18-7.98 (8H, br), 6.71-6.58 (6H, m), 5.96 (2H, t), 3.49-3.37 (4H, m); ^{13}C NMR (*DMSO-d_6*, 100 MHz) δ_C 170.7, 162.1, 144.8, 143.7,133.2, 130.9, 128.3, 127.8, 124.8, 123.0, 121.6, 119.8, 116.4, 115.3, 53.7, 33.5; HR-MS: m/z found 751.1563 $[M+H]^+$; calcd. 750.1486 for $C_{42}H_{26}N_2O_{12}$.

Synthesis of PDI 2. 3,4,9,10-Perylenetetracarboxylic dianhydride (PDA) (500 mg, 1.2 mmol), L-histidine (435 mg, 2.5 mmol), and imidazole (2.0 g) were added into a round bottom flask and heated at 120 °C for 1 h with stirring under nitrogen atmosphere. The reaction mixture was allowed to cool to 90 °C, and then poured into Milli-Q water and filtered. The filtrate was acidified with 2.0 N HCl, and the precipitate was filtered, washed with excess of Milli-Q water and dried under vacuum at 80 °C to obtain the

product **PDI 2** in good yield (76%). ^{1}H NMR (*DMSO-d*$_6$, 400 MHz) δ_H 14.01 (2H, br), 8.92 (2H, d), 8.64 (4H, s), 8.40 (4H, br), 7.43 (2H, s), 5.86 (2H, q), 3.71 (2H, dd), 3.46 (2H, dd); ^{13}C NMR (*DMSO-d*$_6$, 100 MHz) δ_C 169.6, 162.1, 134.0, 133.7, 131.2, 129.7, 128.2, 123.8, 121.7, 119.1, 116.8, 52.6, 23.8; HR-MS: m/z found 667.1567 $[M+H]^+$; calcd. 666.1499 for $C_{36}H_{22}N_6O_8$.

3.4.4.1 Appendix

- ^{1}H NMR and ^{13}C NMR spectra of **PDI 1**
- ^{1}H NMR and ^{13}C NMR spectra of **PDI 2**
- HRMS of **PDI 1**
- HRMS of **PDI 2**

^{1}H NMR spectra (DMSO-*d6*, 400 MHz) of **PDI 1**

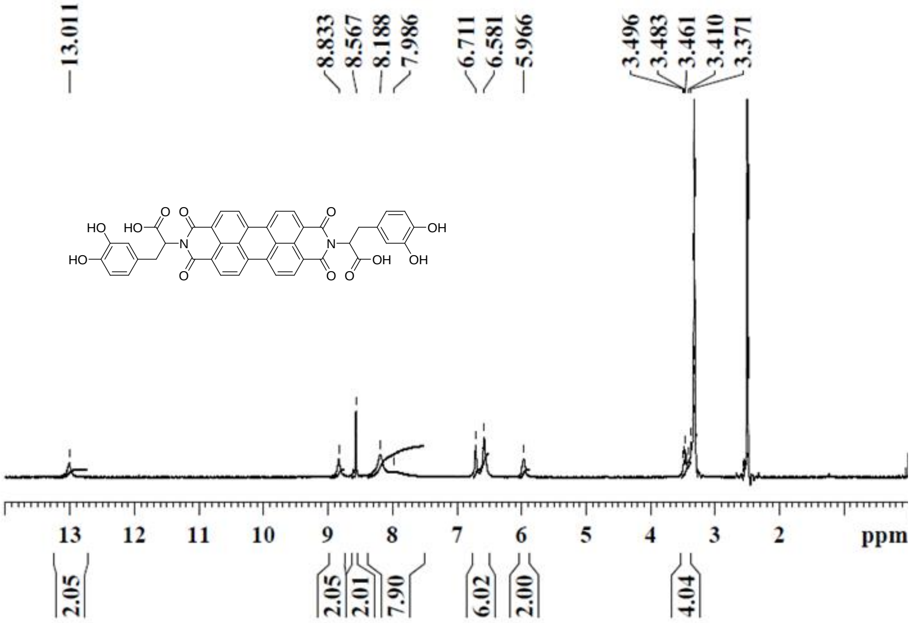

^{13}C NMR spectra (DMSO-*d6*, 100 MHz) of **PDI 1**

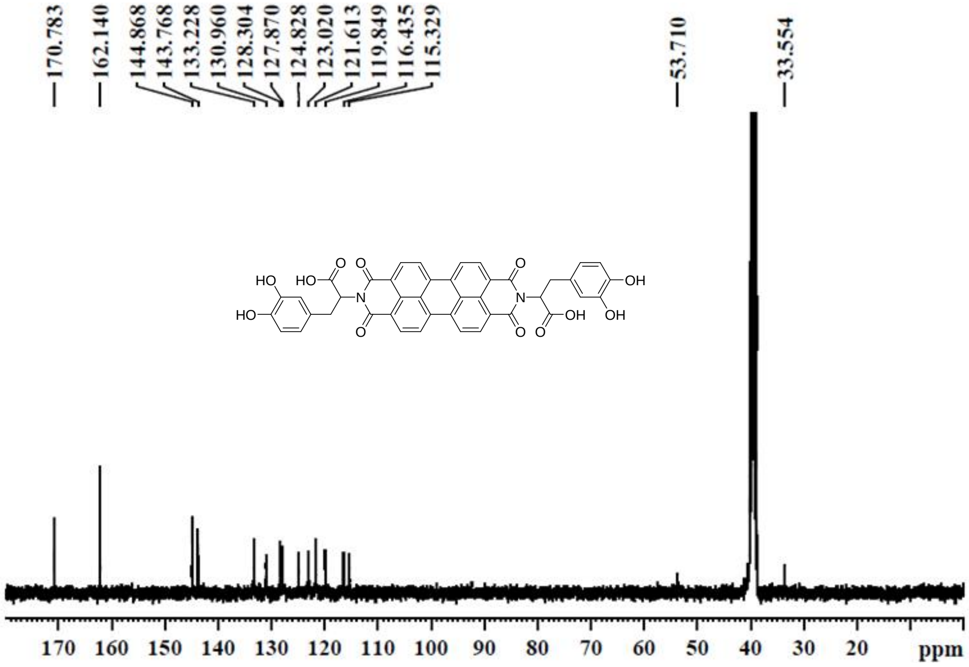

^{1}H NMR spectra (DMSO-*d6*, 400 MHz) of **PDI 2**

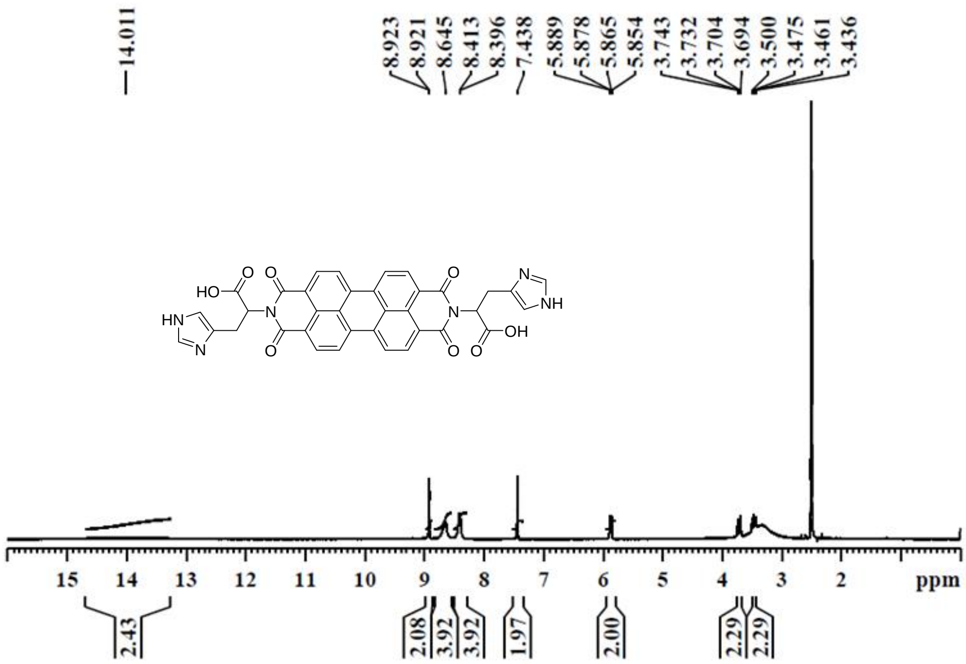

^{13}C NMR spectra (DMSO-*d6*, 100 MHz) of **PDI 2**

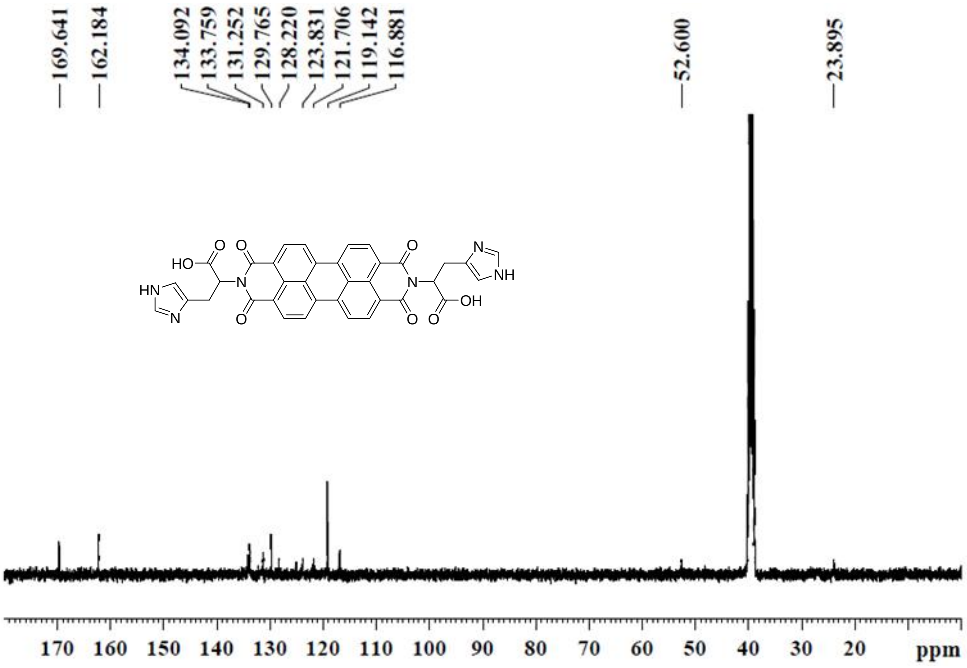

HRMS of **PDI 1**

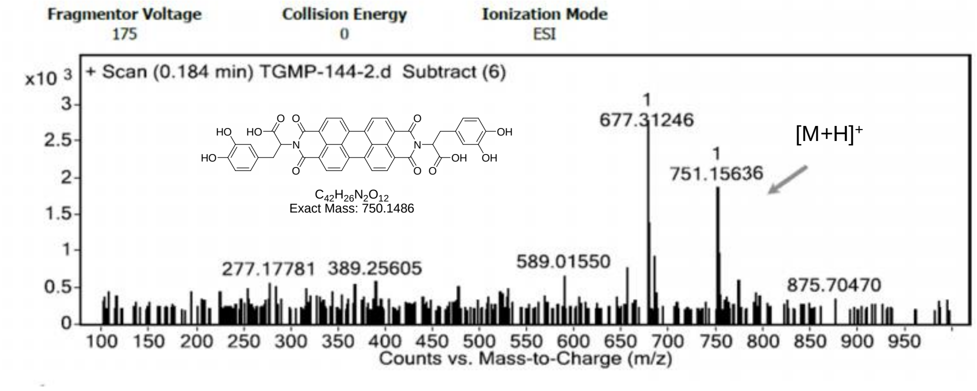

HRMS of **PDI 2**

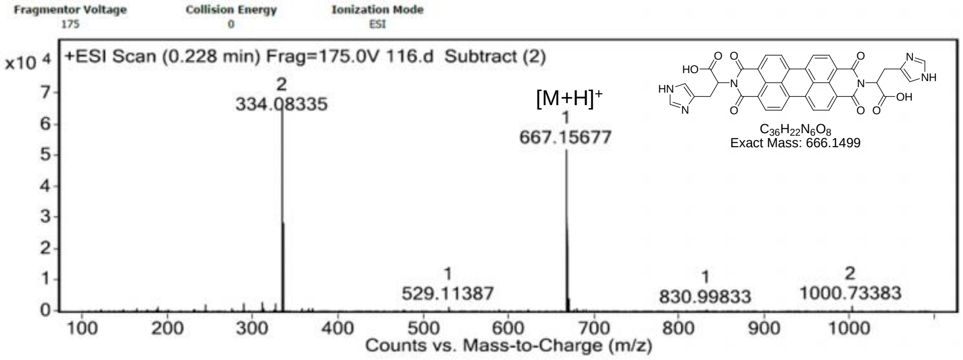

3.4.5 References

1. Wurthner, F., Perylene bisimide dyes as versatile building blocks for functional supramolecular architectures. *Chem. Commun.* **2004**, 1564-1579.
2. Avinash, M. B.; Govindaraju, T., Amino acid derivatized arylenediimides: a versatile modular approach for functional molecular materials. *Adv. Mater.* **2012,** *24*, 3905-3922.
3. Che, Y.; Yang, X.; Zang, L., Ultraselective fluorescent sensing of Hg2+ through metal coordination-induced molecular aggregation. *Chem. Commun.* **2008**, 1413-1415.
4. Peneva, K.; Mihov, G.; Herrmann, A.; Zarrabi, N.; Borsch, M.; Duncan, T. M.; Mullen, K., Exploiting the nitrilotriacetic acid moiety for biolabeling with ultrastable perylene dyes. *J. Am. Chem. Soc.* **2008,** *130*, 5398-5399.
5. Chen, X.; Jou, M. J.; Yoon, J., An "Off-On" type UTP/UDP selective fluorescent probe and its application to monitor glycosylation process. *Org. Lett.* **2009,** *11*, 2181-2184.
6. Wang, B.; Yu, C., Fluorescence turn-on detection of a protein through the reduced aggregation of a perylene probe. *Angew. Chem. Int. Ed.* **2010,** *49*, 1485-1488.
7. Szelke, H.; Schubel, S.; Harenberg, J.; Kramer, R., A fluorescent probe for the quantification of heparin in clinical samples with minimal matrix interference. *Chem. Commun.* **2010,** *46*, 1667-1669.
8. Sadrai, M.; Bird, G. R., A new laser dye with potential for high stability and a broad band of lasing action: perylene-3,4,9,10-tetracarboxylic acid-bis-N,N'-(2',6'-xylidyl)diimide. *Opt. Commun.* **1984,** *51*, 62-64.
9. Ford, W. E.; Kamat, P. V., Photochemistry of 3,4,9,10-perylenetetracarboxylic dianhydride dyes. 3. Singlet and triplet excited-state properties of the bis(2,5-di-tert-butylphenyl)imide derivative. *J. Phys. Chem.* **1987,** *91*, 6373-6380.
10. Schmidt-Mende, L.; Fechtenkotter, A.; Mullen, K.; Moons, E.; Friend, R. H.; MacKenzie, J. D., Self-organized discotic liquid crystals for high-efficiency organic photovoltaics. *Science* **2001,** *293*, 1119-1122.
11. Li, J.; Dierschke, F.; Wu, J.; Grimsdale, A. C.; Muellen, K., Poly(2,7-carbazole) and perylene tetracarboxydiimide: a promising donor/acceptor pair for polymer solar cells. *J. Mater. Chem.* **2006,** *16*, 96-100.
12. Ye, T.; Singh, R.; Butt, H. J.; Floudas, G.; Keivanidis, P. E., Effect of local and global structural order on the performance of perylene diimide excimeric solar cells. *ACS Appl. Mater. Interfaces* **2013,** *5*, 11844-11857.
13. Singh, R. M. z., M. M.; Di Fonzo, F.; Cabanillas-Gonzalez, J.; Marchi, E.; Bergamini, G.; Müllen, K.; Jacob, J.; Keivanidis, P. E., Improving the Layer Morphology of Solution-

Processed Perylene Diimide Organic Solar Cells with the Use of a Polymeric Interlayer. *Org. Photonics Photovoltaics* **2013,** *1*, 24−38.

14. Liu, Y.; Wang, N.; Li, Y.; Liu, H.; Li, Y.; Xiao, J.; Xu, X.; Huang, C.; Cui, S.; Zhu, D., A New Class of Conjugated Polyacetylenes Having Perylene Bisimide Units and Pendant Fullerene or Porphyrin Groups. *Macromolecules* **2005,** *38*, 4880-4887.
15. Feng, X.; An, Y.; Yao, Z.; Li, C.; Shi, G., A turn-on fluorescent sensor for pyrophosphate based on the disassembly of Cu2+-mediated perylene diimide aggregates. *ACS Appl. Mater. Interfaces* **2012,** *4*, 614-618.
16. Liu, X.; Zhang, N.; Zhou, J.; Chang, T.; Fang, C.; Shangguan, D., A turn-on fluorescent sensor for zinc and cadmium ions based on perylene tetracarboxylic diimide. *Analyst* **2013,** *138*, 901-906.
17. Bo, F.; Gao, B.; Duan, W.; Li, H.; Liu, H.; Bai, Q., Assembly-disassembly driven "off-on" fluorescent perylene bisimide probes for detecting and tracking of proteins in living cells. *RSC Adv.* **2013,** *3*, 17007-17010.
18. Tang, T.; Peneva, K.; Mullen, K.; Webber, S. E., Photophysics of water soluble perylene diimides in surfactant solutions. *J. Phys. Chem. A* **2007,** *111*, 10609-10614.
19. Zheng, Y.; Long, H.; Schatz, G. C.; Lewis, F. D., Duplex and hairpin dimer structures for perylene diimide-oligonucleotide conjugates. *Chem. Commun.* **2005**, 4795-4797.
20. Jones, B. A.; Ahrens, M. J.; Yoon, M.-H.; Facchetti, A.; Marks, T. J.; Wasielewski, M. R., Electron transport: High-mobility air-stable n-type semiconductors with processing versatility: dicyanoperylene-3,4:9,10-bis(dicarboximides). *Angew. Chem. Int. Ed.* **2004,** *43*, 6363-6366.
21. Zhao, C.; Zhang, Y.; Li, R.; Li, X.; Jiang, J., Di(alkoxy)- and di(alkylthio)-substituted perylene-3,4;9,10-tetracarboxy diimides with tunable electrochemical and photophysical properties. *J. Org. Chem.* **2007,** *72*, 2402-2410.
22. Wang, H.; Wang, D.; Wang, Q.; Li, X.; Schalley, C. A., Nickel(II) and iron(III) selective off-on-type fluorescence probes based on perylene tetracarboxylic diimide. *Org. Biomol. Chem.* **2010,** *8*, 1017-1026.
23. He, X.; Liu, H.; Li, Y.; Wang, S.; Li, Y.; Wang, N.; Xiao, J.; Xu, X.; Zhu, D., Gold nanoparticle-based fluorometric and colorimetric sensing of copper(II) ions. *Adv. Mater.* **2005,** *17*, 2811-2815.
24. Ehli, C.; Oelsner, C.; Guldi, D. M.; Mateo-Alonso, A.; Prato, M.; Schmidt, C.; Backes, C.; Hauke, F.; Hirsch, A., Manipulating single-wall carbon nanotubes by chemical doping and charge transfer with perylene dyes. *Nat. Chem.* **2009,** *1*, 243-249, s243/241-s243/246.
25. Backes, C.; Schmidt, C. D.; Hauke, F.; Bottcher, C.; Hirsch, A., High population of individualized SWCNTs through the adsorption of water-soluble perylenes. *J. Am. Chem. Soc.* **2009,** *131*, 2172-2184.

26. Zhang, X.; Rehm, S.; Safont-Sempere, M. M.; Wuerthner, F., Vesicular perylene dye nanocapsules as supramolecular fluorescent pH sensor systems. *Nat. Chem.* **2009,** *1*, 623-629.

27. Biedermann, F.; Elmalem, E.; Ghosh, I.; Nau, W. M.; Scherman, O. A., Strongly fluorescent, switchable perylene bis(diimide) host-guest complexes with cucurbit[8]uril in water. *Angew. Chem. Int. Ed.* **2012,** *51*, 7739-7743.

28. Maity, D.; Govindaraju, T., Highly selective visible and near-IR sensing of Cu2+ based on thiourea-salicylaldehyde coordination in aqueous media. *Chem. - Eur. J.* **2011,** *17*, 1410-1414.

29. Maity, D.; Manna, A. K.; Karthigeyan, D.; Kundu, T. K.; Pati, S. K.; Govindaraju, T., Visible-near-infrared and fluorescent copper sensors based on julolidine conjugates: selective detection and fluorescence imaging in living cells. *Chem. - Eur. J.* **2011,** *17*, 11152-11161.

30. Narayanaswamy, N.; Govindaraju, T., Aldazine-based colorimetric sensors for Cu2+ and Fe3+. *Sens. Actuators, B* **2012,** *161*, 304-310.

31. Sahoo, S. K.; Sharma, D.; Bera, R. K.; Crisponi, G.; Callan, J. F., Iron(III) selective molecular and supramolecular fluorescent probes. *Chem. Soc. Rev.* **2012,** *41*, 7195-7227.

32. Barnham, K. J.; Bush, A. I., Biological metals and metal-targeting compounds in major neurodegenerative diseases. *Chem. Soc. Rev.* **2014,** *43*, 6727-6749.

33. Lemouchi, C.; Simonov, S.; Zorina, L.; Gautier, C.; Hudhomme, P.; Batail, P., Amino acid derivatives of perylenediimide and their N-H···O peptide bond dipoles-templated solid state assembly into stacks. *Org. Biomol. Chem.* **2011,** *9*, 8096-8101.

34. Ponnuswamy, N.; Pantos, G. D.; Smulders, M. M.; Sanders, J. K., Thermodynamics of supramolecular naphthalenediimide nanotube formation: the influence of solvents, side chains, and guest templates. *J. Am. Chem. Soc.* **2012,** *134*, 566-573.

35. Pandeeswar, M.; Govindaraju, T., Green-fluorescent naphthalene diimide: conducting layered hierarchical 2D nanosheets and reversible probe for detection of aromatic solvents. *RSC Adv.* **2013,** *3*, 11459-11462.

36. Pandeeswar, M.; Khare, H.; Ramakumar, S.; Govindaraju, T., Biomimetic molecular organization of naphthalene diimide in the solid state: tunable (chiro-) optical, viscoelastic and nanoscale properties. *RSC Adv.* **2014,** *4*, 20154-20163.

37. Bai, S.; Debnath, S.; Javid, N.; Frederix, P. W. J. M.; Fleming, S.; Pappas, C.; Ulijn, R. V., Differential self-assembly and tunable emission of aromatic peptide bola-amphiphiles containing perylene bisimide in polar solvents including water. *Langmuir* **2014,** *30*, 7576-7584.

38. Pandeeswar, M.; Avinash, M. B.; Govindaraju, T., Chiral transcription and retentive helical memory: probing peptide auxiliaries appended with naphthalenediimides for their one-dimensional molecular organization. *Chem. - Eur. J.* **2012,** *18*, 4818-4822.

39. Dwivedi, A. K.; Pandeeswar, M.; Govindaraju, T., Assembly modulation of PDI derivative as a supramolecular fluorescence switching probe for detection of cationic surfactant and metal ions in aqueous media. *ACS Appl. Mater. Interfaces* **2014,** *6*, 21369-21379.

40. Li, A. D. Q.; Wang, W.; Wang, L.-Q., Folding versus self-assembling. *Chem. - Eur. J.* **2003,** *9*, 4594-4601.

41. Wurthner, F.; Chen, Z. J.; Dehm, V.; Stepanenko, V., One-dimensional luminescent nanoaggregates of perylene bisimides. *Chem. Commun.* **2006**, 1188-1190.

42. Garcia, C. R.; Angele-Martinez, C.; Wilkes, J. A.; Wang, H. C.; Battin, E. E.; Brumaghim, J. L., Prevention of iron- and copper-mediated DNA damage by catecholamine and amino acid neurotransmitters, L-DOPA, and curcumin: metal binding as a general antioxidant mechanism. *Dalton Trans.* **2012,** *41*, 6458-6467.

43. Dwivedi, A. K.; Saikia, G.; Iyer, P. K., Aqueous polyfluorene probe for the detection and estimation of Fe3+ and inorganic phosphate in blood serum. *J. Mater. Chem.* **2011,** *21*, 2502-2507.

44. Mialane, P.; Anxolabehere-Mallart, E.; Blondin, G.; Nivorojkine, A.; Guilhem, J.; Tchertanova, L.; Cesario, M.; Ravi, N.; Bominaar, E.; Girerd, J.-J.; Munck, E., Structure and electronic properties of (N,N'-bis(4-methyl-6-tert-butyl-2-methyl-phenolato)-N,N'-bis(methyl-1,2-diaminoethane))FeIII(DBSQ). Spectroelectrochemical study of the redox properties. Relevance to intradiol catechol dioxygenases. *Inorg. Chim. Acta* **1997,** *263*, 367-378.

45. Saikia, G.; Dwivedi, A. K.; Iyer, P. K., Development of solution, film and membrane based fluorescent sensor for the detection of fluoride anions from water. *Anal. Methods* **2012,** *4*, 3180-3186.

46. Abo, M.; Urano, Y.; Hanaoka, K.; Terai, T.; Komatsu, T.; Nagano, T., Development of a highly sensitive fluorescence probe for hydrogen peroxide. *J. Am. Chem. Soc.* **2011,** *133*, 10629-10637.

47. Van de Bittner, G. C.; Dubikovskaya, E. A.; Bertozzi, C. R.; Chang, C. J., In vivo imaging of hydrogen peroxide production in a murine tumor model with a chemoselective bioluminescent reporter. *Proc. Natl. Acad. Sci. U. S. A.* **2010,** *107*, 21316-21321.

48. Dickinson, B. C.; Chang, C. J., Chemistry and biology of reactive oxygen species in signaling or stress responses. *Nat. Chem. Biol.* **2011,** *7*, 504-511.

49. Lippert, A. R.; Van de Bittner, G. C.; Chang, C. J., Boronate oxidation as a bioorthogonal reaction approach for studying the chemistry of hydrogen peroxide in living systems. *Acc. Chem. Res.* **2011,** *44*, 793-804.

50. Lin, M. T.; Beal, M. F., Mitochondrial dysfunction and oxidative stress in neurodegenerative diseases. *Nature* **2006,** *443*, 787-795.

51. Houstis, N.; Rosen, E. D.; Lander, E. S., Reactive oxygen species have a causal role in multiple forms of insulin resistance. *Nature* **2006,** *440*, 944-948.

52. Jay, D.; Hitomi, H.; Griendling, K. K., Oxidative stress and diabetic cardiovascular complications. *Free Radical Bio. Med.* **2006,** *40*, 183-192.

53. Finkel, T.; Serrano, M.; Blasco, M. A., The common biology of cancer and ageing. *Nature* **2007,** *448*, 767-774.

54. Trachootham, D.; Alexandre, J.; Huang, P., Targeting cancer cells by ROS-mediated mechanisms: a radical therapeutic approach? *Nat. Rev. Drug Discov.* **2009,** *8*, 579-591.

55. Nair, R. R.; Bagheri, M.; Saini, D. K., Temporally distinct roles of ATM and ROS in genotoxic-stress-dependent induction and maintenance of cellular senescence. *J. Cell Sci.* **2015,** *128*, 342-353.

56. Andreyev, A. I.; Kushnareva, Y. E.; Starkov, A. A., Mitochondrial metabolism of reactive oxygen species. *Biochem (Mosc)* **2005,** *70*, 200-214.

57. Rhee, S. G., Cell signaling. H2O2, a necessary evil for cell signaling. *Science* **2006,** *312*, 1882-1883.

58. Thurlow, S., Studies on Xanthine Oxidase: Relation of Xanthine Oxidase and similar Oxidising Systems to Bach's Oxygenase. *Biochem. J.* **1925,** *19*, 175-187.

59. Zhou, M.; Diwu, Z.; Panchuk-Voloshina, N.; Haugland, R. P., A stable nonfluorescent derivative of resorufin for the fluorometric determination of trace hydrogen peroxide: applications in detecting the activity of phagocyte NADPH oxidase and other oxidases. *Anal. Biochem.* **1997,** *253*, 162-168.

60. Towne, V.; Will, M.; Oswald, B.; Zhao, Q., Complexities in horseradish peroxidase-catalyzed oxidation of dihydroxyphenoxazine derivatives: appropriate ranges for pH values and hydrogen peroxide concentrations in quantitative analysis. *Anal. Biochem.* **2004,** *334*, 290-296.

61. Brotea, G. P.; Thibert, R. J., Fluorometric-Determination of Hydrogen-Peroxide Using Resorufin and Peroxidase. *Microchem. J.* **1988,** *37*, 368-376.

62. Goodwin, D. C.; Grover, T. A.; Aust, S. D., Roles of efficient substrates in enhancement of peroxidase-catalyzed oxidations. *Biochemistry* **1997,** *36*, 139-147.

63. Travascio, P.; Li, Y.; Sen, D., DNA-enhanced peroxidase activity of a DNA-aptamer-hemin complex. *Chem. Biol.* **1998,** *5*, 505-517.

64. Rojas, A. M.; Gonzalez, P. A.; Antipov, E.; Klibanov, A. M., Specificity of a DNA-based (DNAzyme) peroxidative biocatalyst. *Biotechnol. Lett.* **2007,** *29*, 227-232.

65. Gross, A. J.; Sizer, I. W., The oxidation of tyramine, tyrosine, and related compounds by peroxidase. *J. Biol. Chem.* **1959,** *234*, 1611-1614.

66. Nakayama, S.; Sintim, H. O., Biomolecule detection with peroxidase-mimicking DNAzymes; expanding detection modality with fluorogenic compounds. *Mol. BioSyst.* **2010,** *6*, 95-97.

67. Yang, X.; Fang, C.; Mei, H.; Chang, T.; Cao, Z.; Shangguan, D., Characterization of G-quadruplex/hemin peroxidase: substrate specificity and inactivation kinetics. *Chem. - Eur. J.* **2011,** *17*, 14475-14484.

68. Gorris, H. H.; Walt, D. R., Mechanistic aspects of horseradish peroxidase elucidated through single-molecule studies. *J. Am. Chem. Soc.* **2009,** *131*, 6277-6282.

69. Smith, R. P., Chemistry to die for. *Nature* **2005,** *436*, 779-779.

70. Lamborg, C. H.; Hammerschmidt, C. R.; Bowman, K. L.; Swarr, G. J.; Munson, K. M.; Ohnemus, D. C.; Lam, P. J.; Heimburger, L.-E.; Rijkenberg, M. J. A.; Saito, M. A., A global ocean inventory of anthropogenic mercury based on water column measurements. *Nature* **2014,** *512*, 65-68.

71. Kim, H. N.; Ren, W. X.; Kim, J. S.; Yoon, J., Fluorescent and colorimetric sensors for detection of lead, cadmium, and mercury ions. *Chem. Soc. Rev.* **2012,** *41*, 3210-3244.

72. Nicholson, J. K.; Kendall, M. D.; Osborn, D., Cadmium and mercury nephrotoxicity. *Nature* **1983,** *304*, 633-635.

73. UNEP, Global Mercury Assessment 2013: Sources, Emissions, Releases and Environmental Transport *UNEP Chemicals Branch,Geneva* **2013**, Switzerland.

74. Nolan, E. M.; Lippard, S. J., Tools and tactics for the optical detection of mercuric ion. *Chem. Rev.* **2008,** *108*, 3443-3480.

75. Jensen, S.; Jernelov, A., Biological methylation of mercury in aquatic organisms. *Nature* **1969,** *223*, 753-754.

76. Renzoni, A.; Zino, F.; Franchi, E., Mercury levels along the food chain and risk for exposed populations. *Environ. Res.* **1998,** *77*, 68-72.

77. Ono, A.; Togashi, H., Highly selective oligonucleotide-based sensor for mercury(II) in aqueous solutions. *Angew. Chem., Int. Ed. Engl.* **2004,** *43*, 4300-4302.

78. Kim, I. B.; Bunz, U. H., Modulating the sensory response of a conjugated polymer by proteins: an agglutination assay for mercury ions in water. *J. Am. Chem. Soc.* **2006,** *128*, 2818-2819.

79. Liu, J.; Lu, Y., Rational design of "turn-on" allosteric DNAzyme catalytic beacons for aqueous mercury ions with ultrahigh sensitivity and selectivity. *Angew. Chem., Int. Ed. Engl.* **2007,** *46*, 7587-7590.

80. Wegner, S. V.; Okesli, A.; Chen, P.; He, C., Design of an emission ratiometric biosensor from MerR family proteins: a sensitive and selective sensor for Hg2+. *J. Am. Chem. Soc.* **2007,** *129*, 3474-3475.

81. Dave, N.; Chan, M. Y.; Huang, P. J.; Smith, B. D.; Liu, J., Regenerable DNA-functionalized hydrogels for ultrasensitive, instrument-free mercury(II) detection and removal in water. *J. Am. Chem. Soc.* **2010,** *132*, 12668-12673.

82. Loe-Mie, F.; Marchand, G.; Berthier, J.; Sarrut, N.; Pucheault, M.; Blanchard-Desce, M.; Vinet, F.; Vaultier, M., Towards an efficient microsystem for the real-time detection and quantification of mercury in water based on a specifically designed fluorogenic binary task-specific ionic liquid. *Angew. Chem. Int. Ed.* **2010,** *49*, 424-427.

83. Ye, B. C.; Yin, B. C., Highly sensitive detection of mercury(II) ions by fluorescence polarization enhanced by gold nanoparticles. *Angew. Chem. Int. Ed.* **2008,** *47*, 8386-8389.

84. Han, D.; Lim, S. Y.; Kim, B. J.; Piao, L.; Chung, T. D., Mercury(ii) detection by SERS based on a single gold microshell. *Chem. Commun.* **2010,** *46*, 5587-5589.

85. Wen, S.; Zeng, T.; Liu, L.; Zhao, K.; Zhao, Y.; Liu, X.; Wu, H. C., Highly sensitive and selective DNA-based detection of mercury(II) with alpha-hemolysin nanopore. *J. Am. Chem. Soc.* **2011,** *133*, 18312-18317.

86. Xue, X.; Wang, F.; Liu, X., One-step, room temperature, colorimetric detection of mercury (Hg2+) using DNA/nanoparticle conjugates. *J. Am. Chem. Soc.* **2008,** *130*, 3244-3245.

87. Zheng, P.; Li, M.; Jurevic, R.; Cushing, S. K.; Liu, Y.; Wu, N., A gold nanohole array based surface-enhanced Raman scattering biosensor for detection of silver(i) and mercury(ii) in human saliva. *Nanoscale* **2015,** *7*, 11005-11012.

88. Du, J.; Jiang, L.; Shao, Q.; Liu, X.; Marks, R. S.; Ma, J.; Chen, X., Colorimetric detection of mercury ions based on plasmonic nanoparticles. *Small* **2013,** *9*, 1467-1481.

89. Mor-Piperberg, G.; Tel-Vered, R.; Elbaz, J.; Willner, I., Nanoengineered electrically contacted enzymes on DNA scaffolds: functional assemblies for the selective analysis of Hg2+ ions. *J. Am. Chem. Soc.* **2010,** *132*, 6878-6879.

90. Zeng, T.; Li, T.; Li, Y.; Liu, L.; Wang, X.; Liu, Q.; Zhao, Y.; Wu, H. C., DNA-based detection of mercury(II) ions through characteristic current signals in nanopores with high sensitivity and selectivity. *Nanoscale* **2014,** *6*, 8579-8584.

91. Lin, Z. H.; Zhu, G.; Zhou, Y. S.; Yang, Y.; Bai, P.; Chen, J.; Wang, Z. L., A self-powered triboelectric nanosensor for mercury ion detection. *Angew. Chem. Int. Ed.* **2013,** *52*, 5065-5069.

92. Zhang, T.; Cheng, Z.; Wang, Y.; Li, Z.; Wang, C.; Li, Y.; Fang, Y., Self-assembled 1-octadecanethiol monolayers on graphene for mercury detection. *Nano Lett.* **2010,** *10*, 4738-4741.

93. Cho, E. S.; Kim, J.; Tejerina, B.; Hermans, T. M.; Jiang, H.; Nakanishi, H.; Yu, M.; Patashinski, A. Z.; Glotzer, S. C.; Stellacci, F.; Grzybowski, B. A., Ultrasensitive detection of toxic cations through changes in the tunnelling current across films of striped nanoparticles. *Nat. Mater.* **2012,** *11*, 978-985.

94. Knopfmacher, O.; Hammock, M. L.; Appleton, A. L.; Schwartz, G.; Mei, J.; Lei, T.; Pei, J.; Bao, Z., Highly stable organic polymer field-effect transistor sensor for selective detection in the marine environment. *Nat. Commun.* **2014,** *5*, 2954.

95. Hu, W.; Ding, L.; Cao, J.; Liu, L.; Wei, Y.; Fang, Y., Protein binding-induced surfactant aggregation variation: a new strategy of developing fluorescent aqueous sensor for proteins. *ACS Appl. Mater. Interfaces* **2015,** *7*, 4728-4736.

96. Liu, Y.; Minami, T.; Nishiyabu, R.; Wang, Z.; Anzenbacher, P., Jr., Sensing of carboxylate drugs in urine by a supramolecular sensor array. *J. Am. Chem. Soc.* **2013,** *135*, 7705-7712.

97. Minami, T.; Esipenko, N. A.; Zhang, B.; Kozelkova, M. E.; Isaacs, L.; Nishiyabu, R.; Kubo, Y.; Anzenbacher, P., Jr., Supramolecular sensor for cancer-associated nitrosamines. *J. Am. Chem. Soc.* **2012,** *134*, 20021-20024.

98. Minami, T.; Liu, Y.; Akdeniz, A.; Koutnik, P.; Esipenko, N. A.; Nishiyabu, R.; Kubo, Y.; Anzenbacher, P., Jr., Intramolecular indicator displacement assay for anions: supramolecular sensor for glyphosate. *J. Am. Chem. Soc.* **2014,** *136*, 11396-11401.

99. Villari, V.; Mineo, P.; Micali, N.; Angelini, N.; Vitalini, D.; Scamporrino, E., Uncharged water-soluble porphyrin tweezers as a supramolecular sensor for α-amino acids. *Nanotechnology* **2007,** *18*, 375503-375503.

100. Resendiz, M. J. E.; Noveron, J. C.; Disteldorf, H.; Fischer, S.; Stang, P. J., A self-assembled supramolecular optical sensor for NiII, CdII, and CrIII. *Org. Lett.* **2004,** *6*, 651-653.

101. Liu, K.; Yao, Y.; Kang, Y.; Liu, Y.; Han, Y.; Wang, Y.; Li, Z.; Zhang, X., A supramolecular approach to fabricate highly emissive smart materials. *Sci. Rep.* **2013,** *3*, 2372.

102. Li, H.; Bian, Y., Selective colorimetric sensing of histidine in aqueous solutions using cysteine modified silver nanoparticles in the presence of Hg2+. *Nanotechnology* **2009,** *20*, 145502-145507.

103. Brooks, P.; Davidson, N., Mercury(II) Complexes of Imidazole and Histidine. *J. Am. Chem. Soc.* **1960,** *82*, 2118-2123.

104. Jia, S.-M.; Liu, X.-F.; Li, P.; Kong, D.-M.; Shen, H.-X., G-quadruplex DNAzyme-based Hg2+ and cysteine sensors utilizing Hg2+-mediated oligonucleotide switching. *Biosens. Bioelectron.* **2011,** *27*, 148-152.

105. Li, H.; Bian, Y., Selective colorimetric sensing of histidine in aqueous solutions using cysteine modified silver nanoparticles in the presence of Hg2+. *Nanotechnology* **2009,** *20*, 145502-145502.

106. Wang, Y.; Shim, M. S.; Levinson, N. S.; Sung, H.-W.; Xia, Y., Stimuli-responsive materials for controlled release of theranostic agents. *Adv. Funct. Mater.* **2014,** *24*, 4206-4220.

107. Shigemitsu, H.; Hamachi, I., Supramolecular Assemblies Responsive to Biomolecules toward Biological Applications. *Chem.--Asian J.* **2015**, doi.10.1002/asia.201500563.

108. Yan, X.; Wang, F.; Zheng, B.; Huang, F., Stimuli-responsive supramolecular polymeric materials. *Chem. Soc. Rev.* **2012,** *41*, 6042-6065.

109. Ma, X.; Tian, H., Stimuli-responsive supramolecular polymers in aqueous solution. *Acc. Chem. Res.* **2014,** *47*, 1971-1981.

110. Qi, Z.; Schalley, C. A., Exploring macrocycles in functional supramolecular gels: from stimuli responsiveness to systems chemistry. *Acc. Chem. Res.* **2014,** *47*, 2222-2233.

111. Haberhauer, G., A metal-ion-driven supramolecular chirality pendulum. *Angew. Chem. Int. Ed.* **2010,** *49*, 9286-9289.

112. Jones, I. M.; Hamilton, A. D., Anion-dependent switching: dynamically controlling the conformation of hydrogen-bonded diphenylacetylenes. *Angew. Chem. Int. Ed.* **2011,** *50*, 4597-4600.

113. Takashima, S.; Abe, H.; Inouye, M., Copper(II)-mediated chiral helicity amplification and inversion of meta-ethynylpyridine polymers with metal coordination sites. *Chem. Commun.* **2011,** *47*, 7455-7457.

114. Yamada, T.; Nagata, Y.; Suginome, M., Non-hydrogen-bonding-based, solvent-dependent helix inversion between pure P-helix and pure M-helix in poly(quinoxaline-2,3-diyl)s bearing chiral side chains. *Chem. Commun.* **2010,** *46*, 4914-4916.

115. Feringa, B. L.; van Delden, R. A.; Koumura, N.; Geertsema, E. M., Chiroptical Molecular Switches. *Chem. Rev.* **2000,** *100*, 1789-1816.

116. Irie, M., Diarylethenes for Memories and Switches. *Chem. Rev.* **2000,** *100*, 1685-1716.

117. Canary, J. W., Redox-triggered chiroptical molecular switches. *Chem. Soc. Rev.* **2009,** *38*, 747-756.

118. Tian, H.; Yang, S., Recent progresses on diarylethene based photochromic switches. *Chem. Soc. Rev.* **2004,** *33*, 85-97.

119. Feringa, B. L., The art of building small: from molecular switches to molecular motors. *J. Org. Chem.* **2007,** *72*, 6635-6652.

120. Chang, K. J.; Kang, B. N.; Lee, M. H.; Jeong, K. S., Oligoindole-based foldamers with a helical conformation induced by chloride. *J. Am. Chem. Soc.* **2005,** *127*, 12214-12215.

121. Hua, Y.; Flood, A. H., Flipping the switch on chloride concentrations with a light-active foldamer. *J. Am. Chem. Soc.* **2010,** *132*, 12838-12840.

122. Maeda, H.; Bando, Y.; Shimomura, K.; Yamada, I.; Naito, M.; Nobusawa, K.; Tsumatori, H.; Kawai, T., Chemical-stimuli-controllable circularly polarized luminescence from anion-responsive π-conjugated molecules. *J. Am. Chem. Soc.* **2011,** *133*, 9266-9269.

123. Martinez, A.; Guy, L.; Dutasta, J. P., Reversible, solvent-induced chirality switch in atrane structure: control of the unidirectional motion of the molecular propeller. *J. Am. Chem. Soc.* **2010,** *132*, 16733-16734.

124. Miyake, H.; Yoshida, K.; Sugimoto, H.; Tsukube, H., Dynamic helicity inversion by achiral anion stimulus in synthetic labile cobalt(II) complex. *J. Am. Chem. Soc.* **2004,** *126*, 6524-6525.

125. Suk, J. M.; Naidu, V. R.; Liu, X.; Lah, M. S.; Jeong, K. S., A foldamer-based chiroptical molecular switch that displays complete inversion of the helical sense upon anion binding. *J. Am. Chem. Soc.* **2011,** *133*, 13938-13941.

126. Ogoshi, T.; Akutsu, T.; Yamafuji, D.; Aoki, T.; Yamagishi, T. A., Solvent- and achiral-guest-triggered chiral inversion in a planar chiral pseudo[1]catenane. *Angew. Chem. Int. Ed.* **2013,** *52*, 8111-8115.

127. Liu, M.; Zhang, L.; Wang, T., Supramolecular Chirality in Self-Assembled Systems. *Chem. Rev.* **2015,** *115*, 7304-7397.

128. Knipe, P. C.; Thompson, S.; Hamilton, A. D., Ion-mediated conformational switches. *Chem. Sci.* **2015,** *6*, 1630-1639.

129. Marino, N.; Armentano, D.; Pardo, E.; Vallejo, J.; Neve, F.; Di Donna, L.; De Munno, G., Homochiral self-assembly of biocoordination polymers: anion-triggered helicity and absolute configuration inversion. *Chem. Sci.* **2015,** *6*, 4300-4305.

130. Bak, K. M.; Chmielewski, M. J., Sulfate Anion as a pH-Switchable Template: Three-State Switchable Systems Based on Diamidocarbazoles. *Eur. J. Org. Chem.* **2015**, 4077-4080.

131. Katoono, R.; Tanaka, Y.; Kusaka, K.; Fujiwara, K.; Suzuki, T., Dynamic Figure Eight Chirality: Multifarious Inversions of a Helical Preference Induced by Complexation. *J. Org. Chem.* **2015,** *80*, 7613-7625.

132. Brioche, J.; Pike, S. J.; Tshepelevitsh, S.; Leito, I.; Morris, G. A.; Webb, S. J.; Clayden, J., Conformational Switching of a Foldamer in a Multicomponent System by pH-Filtered Selection between Competing Noncovalent Interactions. *J. Am. Chem. Soc.* **2015,** *137*, 6680-6691.

133. Maeda, H.; Shirai, T.; Bando, Y.; Takaishi, K.; Uchiyama, M.; Muranaka, A.; Kawai, T.; Naito, M., Chiroptical control in helical receptor-anion complexes. *Org. Lett.* **2013,** *15*, 6006-6009.

134. Takaishi, K.; Muranaka, A.; Kawamoto, M.; Uchiyama, M., Photoinversion of cisoid/transoid binaphthyls. *Org. Lett.* **2012,** *14*, 276-279.

135. Zheng, J.; Qiao, W. Q.; Wan, X. H.; Gao, J. P.; Wang, Z. Y., Near-Infrared Electrochromic and Chiroptical Switching Materials: Design, Synthesis, and Characterization of Chiral Organogels Containing Stacked Naphthalene Diimide Chromophores. *Chem. Mater.* **2008,** *20*, 6163-6168.

136. Beer, G.; Niederalt, C.; Grimme, S.; Daub, J., Redox Switches with Chiroptical Signal Expression Based on Binaphthyl Boron Dipyrromethene Conjugates. *Angew. Chem. Int. Ed.* **2000,** *39*, 3252-3255.

137. Wang, Z. Y.; Todd, E. K.; Meng, X. S.; Gao, J. P., Dual modulation of a molecular switch with exceptional chiroptical properties. *J. Am. Chem. Soc.* **2005,** *127,* 11552-11553.

138. Jiang, X.; Lim, Y.-K.; Zhang, B. J.; Opsitnick, E. A.; Baik, M.-H.; Lee, D., Dendritic molecular switch: chiral folding and helicity inversion. *J. Am. Chem. Soc.* **2008,** *130,* 16812-16822.

139. Akine, S.; Sairenji, S.; Taniguchi, T.; Nabeshima, T., Stepwise helicity inversions by multisequential metal exchange. *J. Am. Chem. Soc.* **2013,** *135*, 12948-12951.

140. Dai, Z.; Lee, J.; Zhang, W., Chiroptical switches: applications in sensing and catalysis. *Molecules* **2012,** *17*, 1247-1277.

141. Frisch, H.; Unsleber, J. P.; Luedeker, D.; Peterlechner, M.; Brunklaus, G.; Waller, M.; Besenius, P., pH-switchable ampholytic supramolecular copolymers. *Angew. Chem. Int. Ed.* **2013,** *52*, 10097-10101.

142. Frisch, H.; Besenius, P., pH-switchable self-assembled materials. *Macromol. Rapid Commun.* **2015,** *36*, 346-363.

143. Adam, D.; Schuhmacher, P.; Simmerer, J.; Haeussling, L.; Siemensmeyer, K.; Etzbach, K. H.; Ringsdorf, H.; Haarer, D., Fast photoconduction in the highly ordered columnar phase of a discotic liquid crystal. *Nature* **1994,** *371*, 141-143.

144. Percec, V.; Glodde, M.; Bera, T. K.; Miura, Y.; Shiyanovskaya, I.; Singer, K. D.; Balagurusamy, V. S. K.; Heiney, P. A.; Schnell, I.; Rapp, A.; Spiess, H. W.; Hudson, S. D.; Duan, H., Self-organization of supramolecular helical dendrimers into complex electronic materials. *Nature* **2002,** *419*, 384-387.

Chapter 4: Peptide Conjugated NDI for Understanding Homochirality and Electronic Applications*

*Papers based on this work have appeared in *Chem. - Eur. J.* **2012,** *18*, 4818-4822 and *Chem. Commun.* **2015,** *51*, 8315-8318. Reproduced with the permission of Wiley-VCH and Royal Society of Chemistry (RSC).

Subchapter 4.1 Chiral Transcription and Retentive Helical Memory: Probing Peptide Auxiliaries Appended with Naphthalenediimides for Their One Dimensional Molecular Organization

4.1.1 Introduction

The single handedness of biomolecular building blocks of life as in L-amino acids and D-sugars have been one of the greatest mysteries of the biotic world.[1] The biological macromolecules evolved from these chiral building blocks such as DNA double helix, secondary α-helix of proteins and the macroscopic sea shells are exclusively homochiral. The origin of this homochirality has evoked enormous interest in the scientific community for the past several decades. [2-12] In this regard, pioneering work on synthetic covalent polymers by Green and co-workers led to the phenomenon of amplification of chirality.[13-14] On the contrary, the noncovalent interactions driven supramolecular polymers are of recent interest as they offer modularity, tunability and reversibility. Meijer and Reinhoudt groups independently developed various noncovalent systems to construct elegant chiral supramolecular assemblies.[15-19] Since then, supramolecular chirality has gained unprecedented importance from the fundamental science perspective and due to their practical applications in areas such as asymmetric catalysis, determination of absolute configuration, sensors, optoelectronics, materials science and biomedicine.[7,20-25] Benefits of introducing chirality into synthetic covalent polymeric structures and their effect on function have been well documented.[26-27] However, supramolecular chirality is still in its infancy and will have profound role in the development of fast emerging dynamic supramolecular polymers.

In particular, dedicated efforts towards chirogenesis and chiral amplification significantly influence the structural and functional evolution of nano and macroscale supramolecular polymeric materials through weak noncovalent interactions driven molecular self-assembly approach. Moreover, the use of modular biomolecules as chiral auxiliaries either freely or in conjugation with chromophores is largely unknown and an unexplored area.[28-32] Thus the study of chiral transcription and amplification in the design of chiral supramolecular polymers enable the production of novel hybrid materials with interesting functions as alternative to covalent polymers. These observations inspired us to design homochiral, heterochiral and achiral peptide auxiliaries appended with naphthalenediimides (NDIs) as shown in Figure 4.1.1.[33] Homochiral peptide appended NDIs (**LL** and **DD**) comprises of identical L or D stereochemistry for the two α-phenylalanine units. Heterochiral peptide appended NDIs (**LD** and **DL**) comprises of alternative L and D or D and L stereochemistry for the two α-phenylalanine units. The dipeptide auxiliary with two glycine units formulates the achiral peptide appended NDI (**AA**). The choice of phenylalanine was due to its favorable steric factors which is expected to play a major role in the stereospecific orientation of supramolecular building units to least sterically hindered conformations and partly inspired by the interesting results reported earlier.[34-35] In addition, organic chromophores are employed as an additional optical probe to study the process of chiral supramolecular assemblies. Herein we have employed NDI (n-type semiconductor) due to its versatile properties and potential applications ranging from electronics to biomedicine. [36-50] NDI choromophore not only serve as an optical probe, but also facilitate a planar central aromatic core structure, complimenting self-assembly characteristics of the peptide conjugates. Thus, we report the induction of supramolecular chirality to achiral NDI via phenylalanine peptide auxiliaries. Chiral enhancement is demonstrated via sergeants-and-soldiers and majority-rules experiments. Furthermore, we show that in case of heterochiral peptide

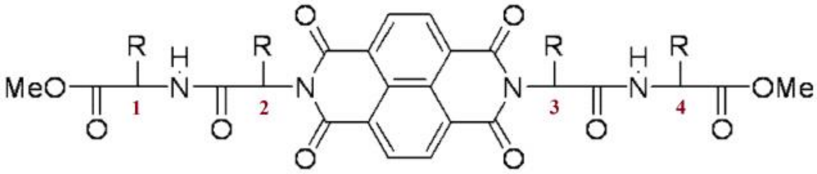

NDI-peptide conjugate	Amino acid configuration				R
	1	2	3	4	
LL	L	L	L	L	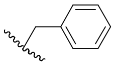
DD	D	D	D	D	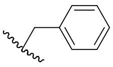
LD	D	L	L	D	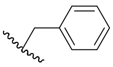
DL	L	D	D	L	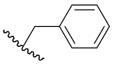
AA	-	-	-	-	H

Figure 4.1.1 Molecular structures of homochiral (**LL** and **DD**), heterochiral (**LD** and **DL**) and achiral (**AA**) peptide conjugates of NDI.

conjugates (**LD** and **DL**), the chirality of the first stereocenter (irrespective of the stereochemistry of second stereo center) adjacent to NDI core determine the memory. Remarkably, morphological studies reveal that the homochiral **LL** and **DD** self-organize into one dimensional (1D) hierarchical supramolecular polymers with opposite helicity. Interestingly, the heterochiral peptide conjugates **LD** and **DL** form microspheres. The chiral enhancement experiments and the propensity of **LL** and **DD** conjugates to form 1D architectures, in principle may support the mechanism of both spontaneous deracemization and chiral enhancement pathways for biological homochirality.[35]

4.1.2 Results and discussion

The molecular aggregation behavior of peptide conjugates **LL**, **DD**, **LD** and **DL** were explored through absorption and fluorescence spectroscopy studies. All the above NDI-

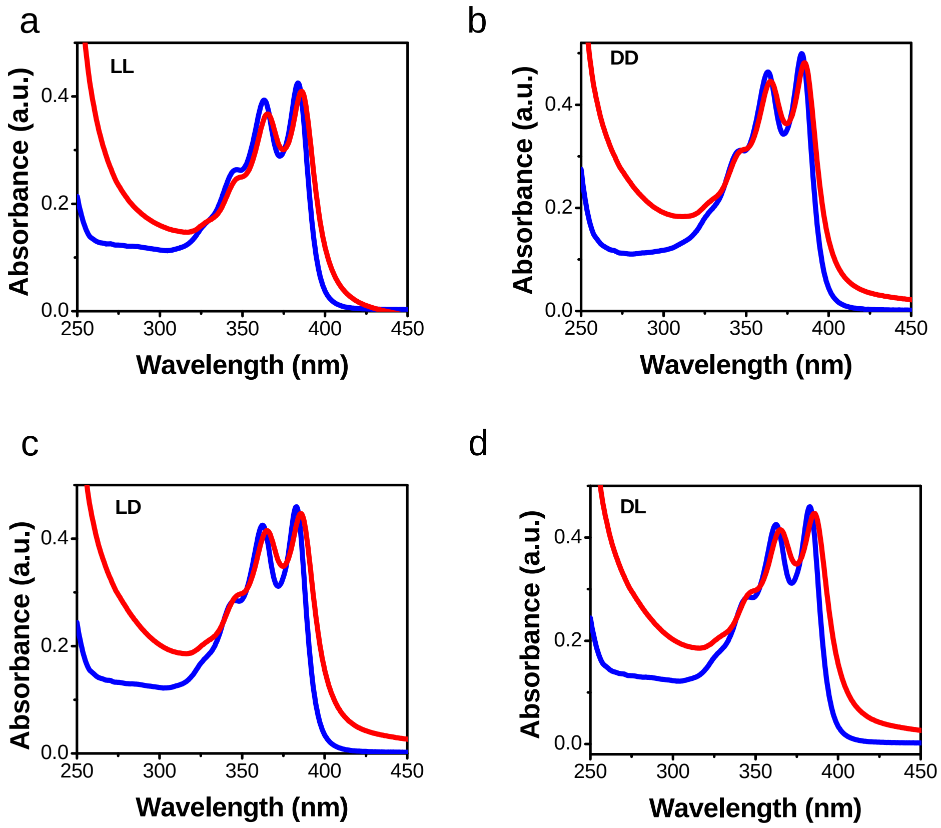

Figure 4.1.2 UV-vis spectra of NDI-peptide conjugates a) **LL**. b) **DD**. c) **LD** and d) **DL** in DMSO (blue curve) and in aqueous DMSO (water/DMSO: 85/15, red curve) solution at 300 μM.

peptide conjugates in dimethylsulfoxide (DMSO) exhibit strong absorption bands in the region of 300-400 nm (band I), which is attributed to the characteristic π−π∗ transitions of NDI chromophore polarized along the Z-axis (Figure 4.1.2). In aqueous DMSO (water/DMSO: 85/15), 3 nm bathochromic shift of band I was observed. However, a weak fluorescent emission was observed for NDI chromophores in DMSO (Figure 4.1.3). Interestingly, in aqueous DMSO (water/DMSO: 85/15), a very broad band centered at 475 nm with a shoulder at 530 nm appeared (Figure 4.1.3). This red-shifted fluorescence is attributed to excimer-like emission due to the formation of ground state aggregates as reported earlier.[51-52] The insets in Figure 4.1.3 show the excimer-like emission of **LL** upon UV irradiation.

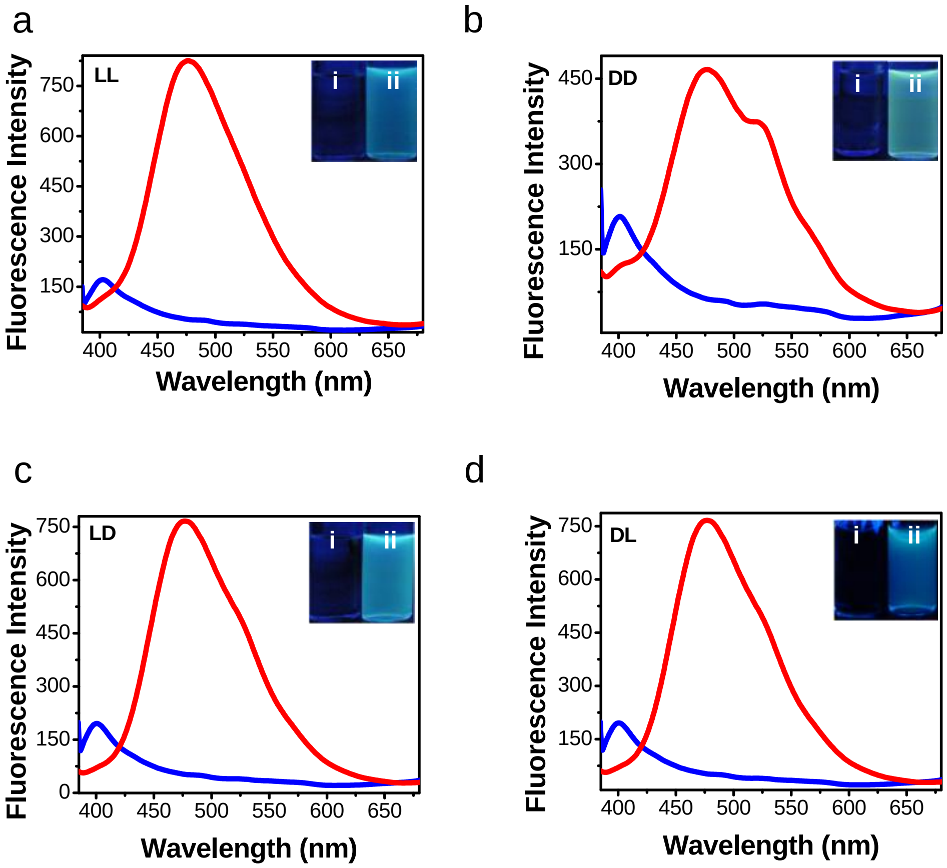

Figure 4.1.3 Fluorescence emission spectra of NDI-peptide conjugates a) **LL**. b) **DD**. c) **LD** and d) **DL** in DMSO (blue curve) and in aqueous DMSO (water/DMSO: 85/15, red curve) solution at 300 μM. Inset: photographs of respective solutions in DMSO (i) and in water/DMSO (85:15) (ii) under UV light.

4.1.2.1 Circular dichroism studies

In order to probe the induction of molecular chirality on achiral NDI chromophores, circular dichrosim (CD) spectroscopic measurements were performed (Figure 4.1.4). The CD spectra of **LL** shows negative excitonic cotton effects between 300-400 nm, corresponding to the $\pi-\pi*$ transitions of NDI chromophore (Figure 4.1.4a). Thus L-phenylalaninyl-L-phenylalanine methyl ester based peptide auxiliaries transcript their stereochemical information to achiral NDI chromophore. The negative cotton effect indicates M-type supramolecular helical assembly of **LL**. On the other hand, **DD** exhibits positive cotton effect, suggesting P-type helicity (Figure 4.1.4a). Surprisingly, in aqueous

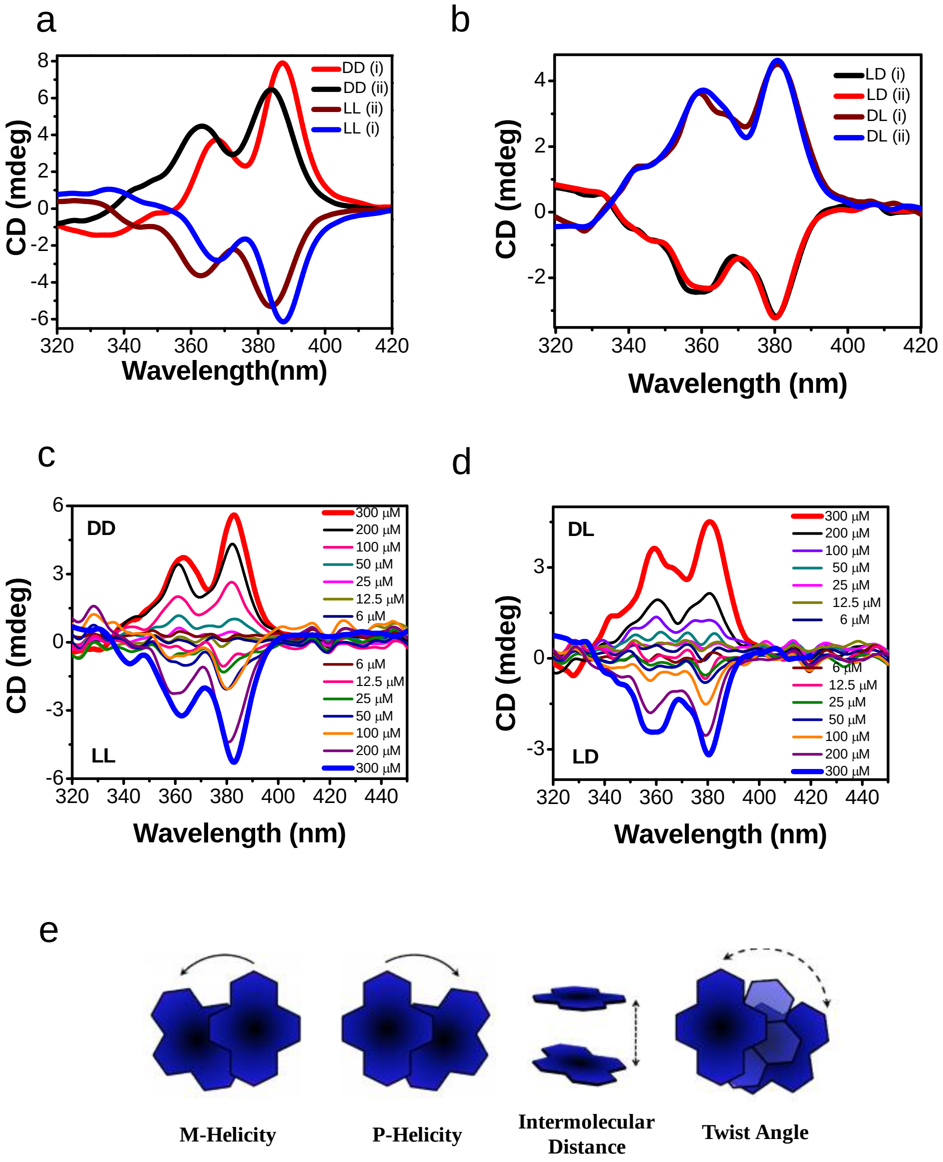

Figure 4.1.4 a) and b) Circular dichrosim (CD) spectra of NDI-peptide conjugates in DMSO (i) and in water/DMSO (85:15) (ii). c) and d) Concentration dependent CD spectra in DMSO. e) Schematic representation of the transition of the angles and distance between the z polarized transition moments of stacked NDI chromophores.

DMSO (water/DMSO: 85/15), both **LL** and **DD** undergo a bathochromic shift of 3 nm with an enhanced cotton effect (Figure 4.1.4a). The observed bathochromic shift in the CD was attributed to the π–π stacking as revealed in absorption studies. Similar CD spectral changes were observed in case of LD (negative CD) and DL (positive CD) with reduced CD intensity (Figure 4.1.4b). Further concentration dependent CD studies of NDI peptide conjugates showed a gradual increase in CD intensity with the increase in concentration revealing the formation of supramolecular chiral organization of the NDI chromophore (Figure 4.1.4c and d). Previous reports have shown that the amplitude of the CD signal depends on the molar extinction coefficient, length of the helical polymer, angle and the intermolecular distance between the chromophores (Figure 4.1.4e). [53-55] Therefore the enhanced CD signal in aqueous DMSO can arguably be attributed, predominantly due to modifications in the angle and intermolecular distance between the NDI chromophores by hydrophobic effect.

4.1.2.2 Sergeants-and-soldiers and majority rule experiment

We further investigated sergeants-and-soldiers effect in the case of homochiral **LL** and **DD** (Figure 4.1.5). In a conventional sergeants-and-soldiers experiment the chiral **LL** was mixed with achiral **AA** in different proportions by keeping the overall concentration (500 µM) constant (Figure 4.1.5a and b). In order to induce self-organization, a mixture of **LL** and **AA** in DMSO was sonicated for 15 min (for homogeneity) followed by the addition of 44% deionized water prior to recording CD spectra. The plot of fraction chiral with net helicity reveals a complex chiral behavior as shown in Figure 4.1.5b. For a clear visualization of chiral enhancement, we performed another experiment wherein increasing amounts of achiral **AA** (0, 100, 200 and 300 µM) were added to a fixed concentration of chiral **LL** or **DD** (100 µM) (Figure 4.1.5c and d). The obtained CD spectra after sonication and addition of water are shown in Figure 4.1.5c. The chiral enhancement clearly shows that the achiral soldier **AA** undergo chiral supramolecular assembly as guided by the helicity of the sergeant, **LL** or **DD**. The plot of fraction

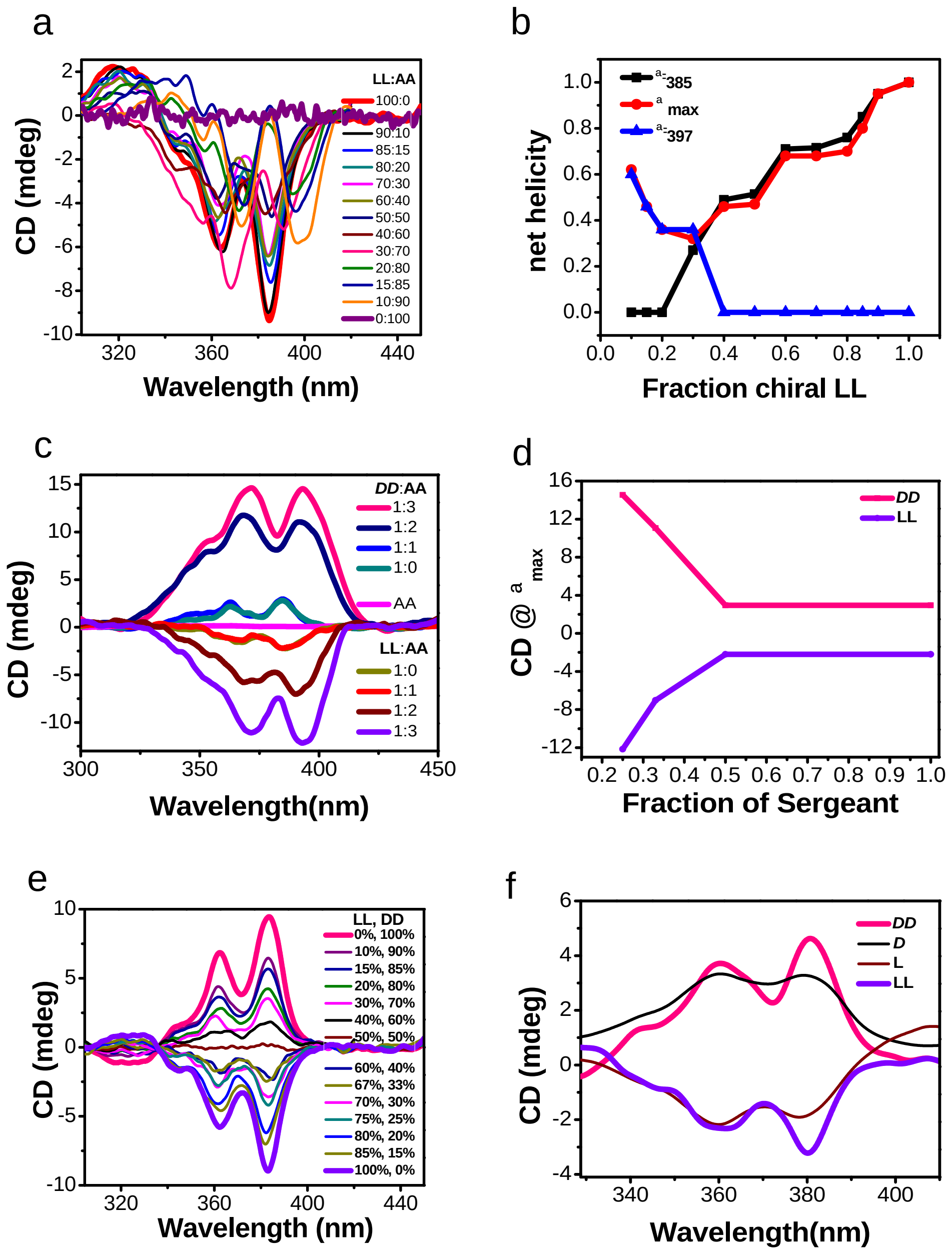

Figure 4.1.5 CD spectroscopy. a) CD spectra of conventional sergeants-and-soldiers (**LL** and **AA**) experiment at 25 °C in 44% aqueous DMSO (The chiral **LL** was mixed with achiral **AA** in different proportions by keeping the overall concentration constant (500 mM). b) The plot (line+symbol) of fraction chiral with net helicity in a for (a). c) Achiral **AA** (0, 100, 200 and 300 mm) was added to a fixed concentration of chiral **LL** or **DD** (100 mm) in DMSO followed by the addition of deionized water (44%). d) The plot (line+symbol) of fraction chiral with net helicity for (c). e) Majority-rule experiment. f) Spectra of **LD**, **DL** and monophenylalanine methylester (L or D isomer) conjugated NDI.

chiral with net helicity confirms the non-linear behavior with a remarkable chiral enhancement (Figure 4.1.5d). To further elucidate the effect of incorporating homochiral NDI-peptide conjugates of mismatched chirality into a single column, a majority-rules experiment was performed (Figure 4.1.5e). Subsequently homochiral NDI-peptide conjugates were mixed in different ratios keeping the overall concentration constant (500 μM). The net helicity was determined as a function of enantiomeric excess (ee) at 387 nm. The marginal non-linear dependence of net helicity on the enantiomeric excess suggests a minimal chiral enhancement under majority-rules experiments.

4.1.2.3 Retentive helical memory

We further investigated the effect of heterochirality of peptide auxiliary on supramolecular chirality. The CD spectra of **LD** showed a negative cotton effect indicating M-helicity similar to that of **LL** (Figure 4.1.5f). On the contrary, **DL** showed P-helicity similar to that of **DD**. **LD** and **DL** exhibited relatively low induced-chirality compared to **LL** and **DD** respectively. Furthermore the amplitude of the CD signal observed in **LD** and **DL** were almost similar to mono-phenylalanine methyl ester appended NDI. These results clarify that the supramolecular helicity is determined by the first stereocenter adjacent to the NDI core while the second regulates chiral enhancement. This ability of the stereocenter to retain the memorized stereochemical information in supramolecular chirogenesis even in the presence of neighbors with opposite chirality is termed as retentive helical memory. The retentive helical memory of the stereocenter is attributed to its direct connection with achiral NDI chromophore. A similar helical retention behavior was observed in case of dendritic dipeptides[35] very recently while a reverse helical retention was observed in case of benzenetricarboxamides.[28] The reverse retentive helical memory observed in the latter was attributed to peripheral mesogen driven aggregation.

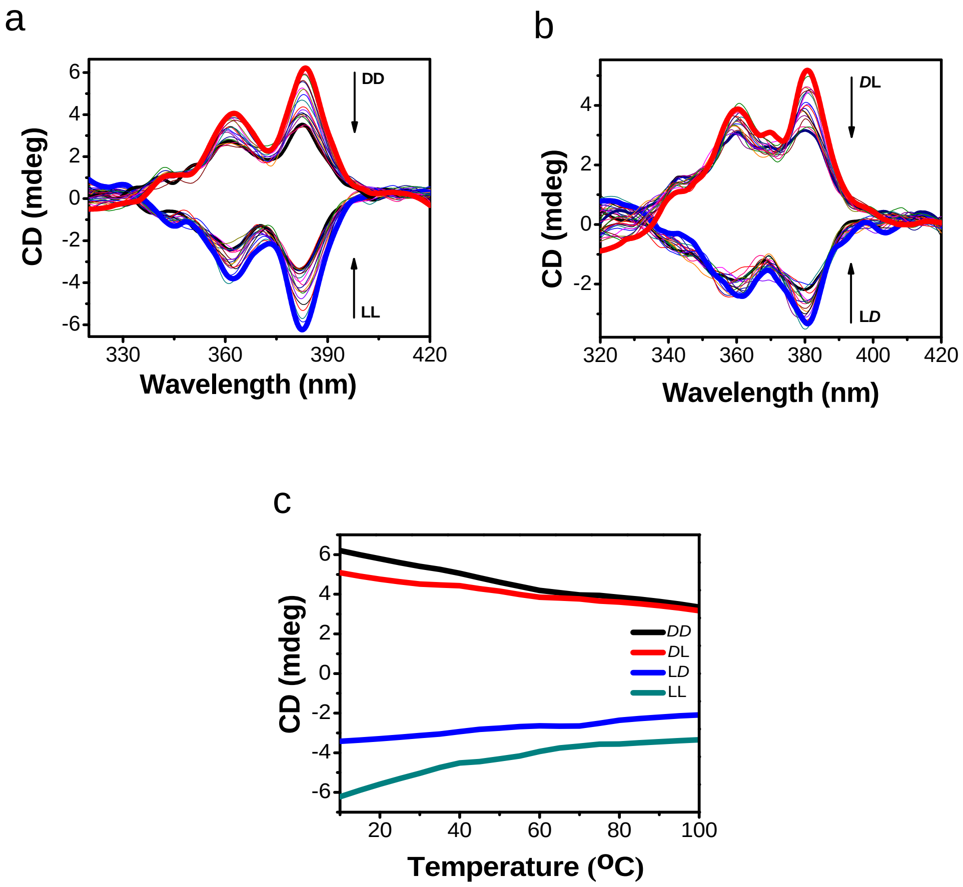

Figure 4.1.6 Temperature dependent CD spectra (10 °C-100 °C); a) Homochiral NDI-peptide conjugates. b) Heterochiral NDI-peptide conjugates. c) Summary of temperature-dependant studies of **LL**, **DD**, **LD** and **DL**. Arrows indicating the spectral changes upon heating from 10 °C-100 °C.

Unlike covalent polymers, the chiral supramolecular assemblies are strongly dependant on temperature, as it determines the strength of intermolecular, noncovalent interactions. Temperature dependent CD spectra for both homochiral and heterochiral NDI-peptide conjugates were carried out in 10 ^{o}C to 100 ^{o}C regime (Figure 4.1.6a and b). The summary of the temperature dependent CD data is shown in (Figure 4.1.6c and d). Even though noncovalent interactions are weak in nature, approximately 55% of the CD intensity was retained at 100 ^{o}C, which strongly emphasize the strength of the peptide auxiliaries driven chiral supramolecular assembly.

4.1.2.4 Morphological studies

The homochiral peptide auxiliaries driven supramolecular helical polymerization leads to 1D assembly of NDI chromophores (Figure 4.1.7a, b and c) in aqueous DMSO (water/DMSO: 85/15). Both peptide conjugates **LL** (Figure 4.1.7a and b) and **DD** (Figure 4.1.7c) forms 1D belt like nanostructures of over 50 µm in length. These 1D belts pile up to form hierarchical structures with helical signatures. Such morphological helicity in a hierarchical structure is rarely observed to the best of our knowledge.[56-60] However, **LD** (Figure 4.1.7d and **DL** (Figure 4.1.7e) forms mesospheres in aqueous DMSO (water/DMSO: 85/15). These morphological studies strongly emphasize that the formation of 1D single handed supramolecular helical polymers are more favorable in

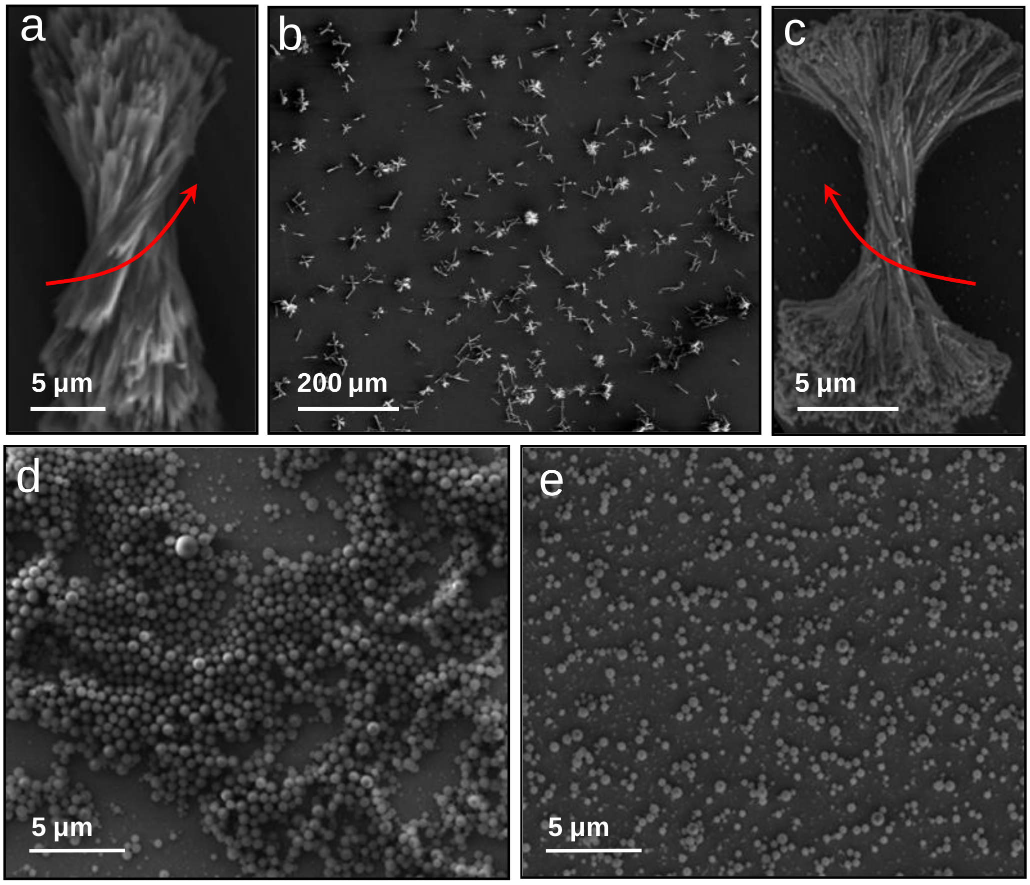

Figure 4.1.7 Field emission scanning electron microscopy (FESEM) images of self-assembled structures from water/DMSO (85:15); a) and b) **LL**, c) **DD**, d) **LD** and e) **DL**.

homochiral NDI-peptide conjugates (**LL** and **DD**) than in heterochiral NDI-peptide conjugates (**LD** and **DL**).

4.1.2.5 Crystallographic insights

Insights into molecular packing of NDI-peptide conjugate **LL** and **DD** were obtained from single crystals grown in DMSO. The single crystals of both **LL** and **DD** were found

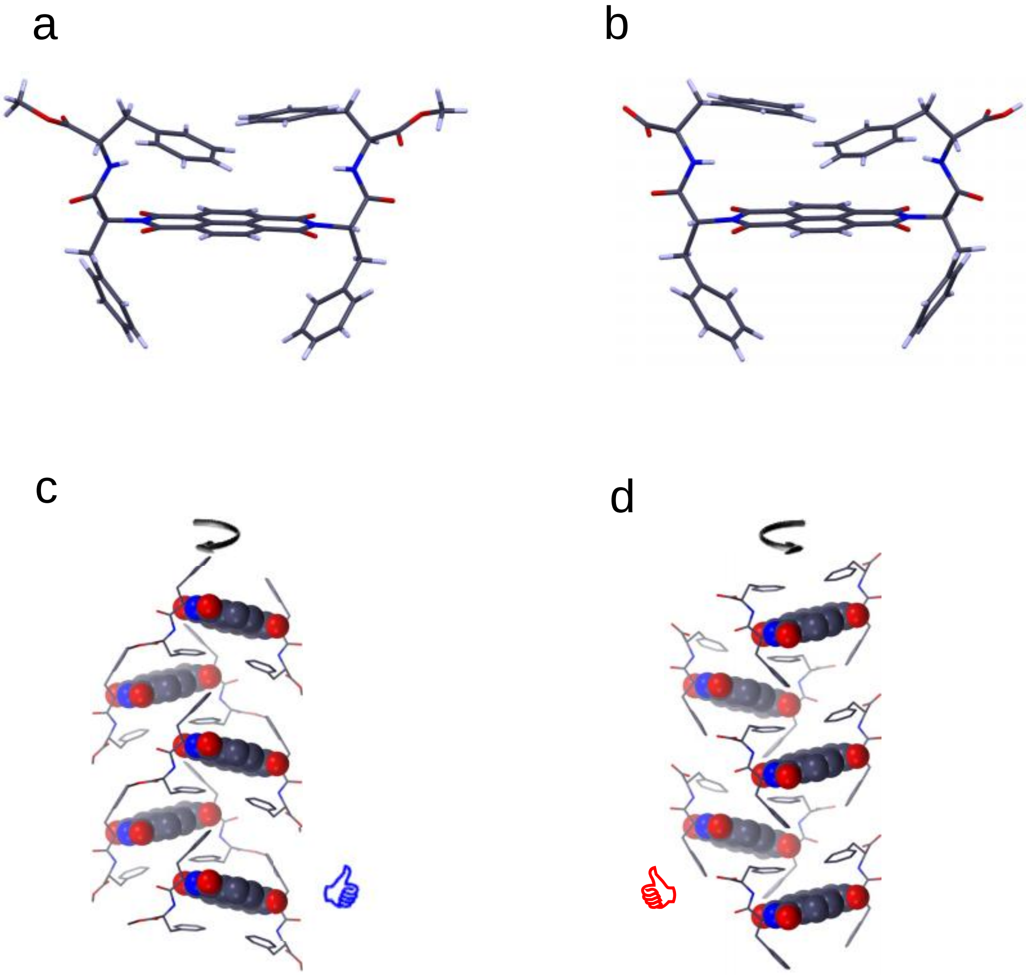

Figure 4.1.8 Single crystal XRD structures; a) and b) Single molecular geometry of **LL** and **DD** respectively indicating the mirror image *cis* conformation of cα substituents (methyl) with respect to NDI plan. c) 1D left-handed helical columnar stacks of **LL** (NDI chromophores are highlighted in the space-filling model). d) 1D Right-handed helical columnar stacks of **DD** (NDI chromophores are highlighted in the space-filling model). In c and d hydrogen atoms have been omitted for the clarity.

to be orthorhombic with $P2_12_12_1$ space group (Table 4.1.1). The crystals comprises complex interplay of π-π interactions and hydrogen bonding (both conventional and unconventional) involving amide group, NDI core hydrogen, NDI imide carbonyl, α-carbon proton, phenyl rings and the cocrystallized DMSO molecule.[61-63] The four phenyl groups of **LL** and **DD** surround the NDI core on either side as a tetrapod and mirror image to each other (Figure 4.1.8a and b). These phenyl groups furnish intramolecular π-π interactions with acidic NDI core. In total each NDI core is engulfed by six phenyl groups, four of which from the same molecule and other two from its neighbors. The crystalline DMSO molecule provides additional intermolecular bridges through

Table 4.1.1 Crystallographic information of **LL** and **DD**.

	LL	**DD**
X-radiation	Mo *Kα* radiation, λ= 0.71073 Å	Mo *Kα* radiation, λ= 0.71073 Å
Crystal system	Orthorhombic	Orthorhombic
Space group	$P2_12_12_1$	$P2_12_12_1$
a, *b*, *c* (Å)	12.2845 (11), 20.8803(16) 21.4074(16)	12.318(2), 20.803(4), 21.489(4)
α, β, γ (°)	90, 90, 90	90, 90, 90
Volume (Å^3)	5491.1(8)	5506.3(18)
# measured reflections	78592	24739
# unique reflections	6654	4320
Mean I/σ(I)	9.62	3.5
R factor (R1) (%)	8.14	6.06
$wR(F_2)$	7.76 and 17.76	14.48
Goodness of fit	0.967	1.035
# molecules in unit cell	4	4
# solvent molecules in unit cell	8	8
CCDC number	856472	1418088

conventional and unconventional hydrogen bonding. A unit cell comprises of four molecules and extended into 3D molecular packing. **LL** and **DD** displayed 1D supramolecular tilt chiral organization of molecules with respect to 2_1 screw axis. The **LL** demonstrated prominent left handed supramolecular tilt stacks, on the other hand DD exhibited mirror image right handed supramolecular tilt chiral stacks (Figure 4.1.8c and d). The helices were found to be stabilized by intermolecular π-π interactions between phenyl groups on peptide backbone and NDI core of the neighboring molecule and extend into helical 1D molecular stacks. Overall, the mirror image helical organization of homochiral peptide conjugates (**LL** and **DD**), within the lattices of their respective crystals is in excellent agreement with the CD data (Figure 4.1.4). These results further corroborated the transcription of chiral information of intrinsically chiral amino acid (phenyl alanine) of the peptide backbones in **LL** and **DD** to their supramolecular homochiral organisation in solution and solid state.

4.1.3 Conclusion

In conclusion, we have successfully demonstrated chirality transcription and amplification by employing the homochiral, heterochiral and achiral peptide conjugates of NDI (Figure 4.1.9). An unprecedented amplification of chirality is presented via sergeants and soldiers experiment. Temperature dependent CD data showed high thermal stability of the peptide auxiliaries driven chiral supramolecular assembly of naphthalenediimide conjugates. Moreover an interesting phenomenon coined as retentive helical memory is reported. Remarkably the homochiral **LL** and **DD** show one dimensional molecular organization unlike zero dimensional organization of heterochiral **LD** and **DL**. These observations in principle, may support the mechanism of both spontaneous deracemization and amplification pathways for biological homochirality. This work finds significance from the fundamental science perspective as well as

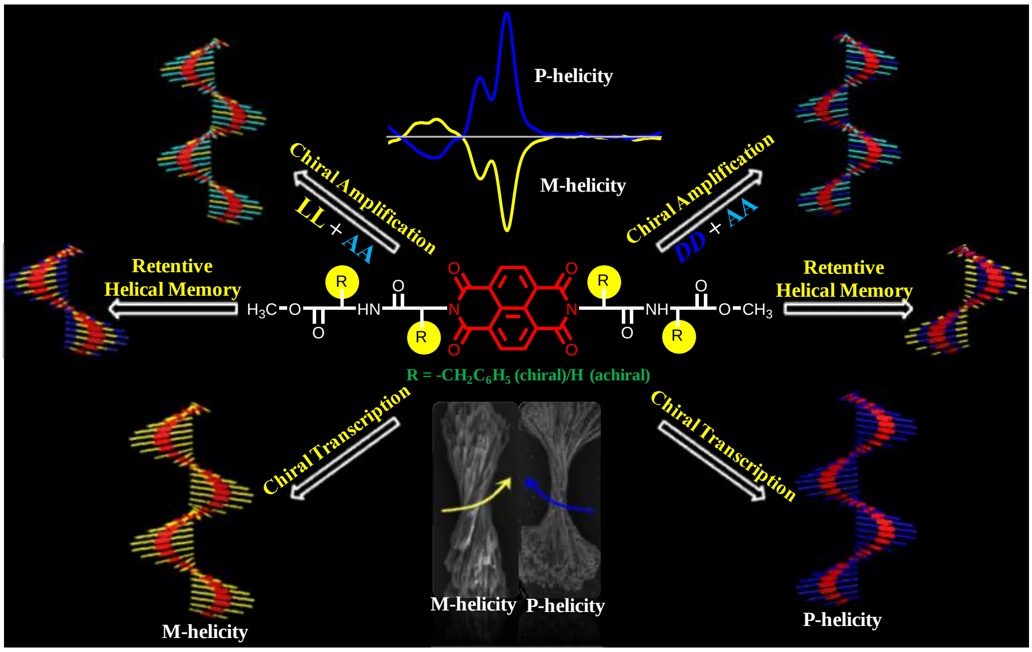
P-helicity
M-helicity
Chiral Amplification
LL + AA
Chiral Amplification
DD + AA
Retentive Helical Memory
Retentive Helical Memory
H3C-O
HN
N
N
NH
O-CH3
R
O
R = -CH2C6H5 (chiral)/H (achiral)
Chiral Transcription
Chiral Transcription
M-helicity
M-helicity
P-helicity
P-helicity

Figure 4.1.9 Summary of probing peptide auxiliaries appended naphthalenediimides for chiral amplification, transcription, retentive helical memory via hierarchical 1D helical molecular, organization.

envisioned potential applications of NDI-peptide conjugates in chiral optoelectronics, biomaterials and chiral technology.

Subchapter 4.2 Crystallographic Insight-Guided Nanoarchitectonics and Conductivity Modulation of NDI through Peptide Conjugation

4.2.1 Introduction

Ingenious organization of functional aromatic molecular systems is one of the key challenges in the fields of chemistry, biology and material science.[64-70] In particular, the performance of solution-processable, flexible, organic thin-film devices is determined by the nature of solid-state molecular ordering and resultant nanoscale morphology on the substrate.[69-76] In this context, several strategies have been attempted to gain control over noncovalent interaction-driven molecular self-assembly of organic semiconductors to achieve the desired nanoscale morphology.[71-76] However, the art of pre-programmed molecular assembly and structure-property correlation in case of self-assembled molecular materials to facilitate development of new organic electronic devices is still in its infancy. The ideal way to investigate the structure-property correlations of molecular materials are essentially through the study of similar molecular structures that differ in their molecular ordering.[69-70] Theoretical calculations have predicted that on account of maximum electronic coupling, face-to-face π-π molecular ordering facilitates a higher charge carrier mobility.[69-70] However, such prerequisite of perfect face-to-face stacked molecular organization of organic semiconductors is seldom met in real solid-state structures.[69]

In nature, biomolecules, specifically (poly) peptides, have built-in information to undergo highly ordered sequence-specific molecular organization by means of synchronized noncovalent interactions to form complex biological materials with predetermined functions.[64-68,77-81] In the past few years, principles of bio-inspired engineering of molecular assemblies (molecular architectonics) has motivated the

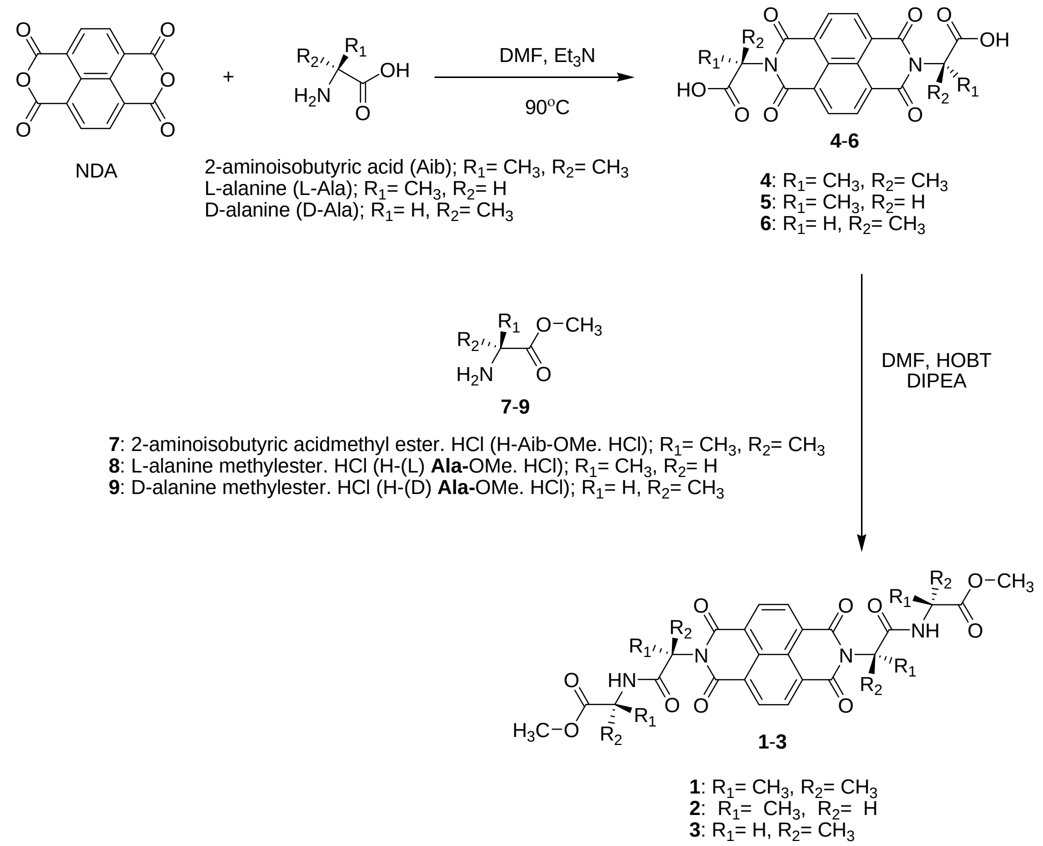
NDA
DMF, Et$_3$N
90°C
2-aminoisobutyric acid (Aib); R$_1$= CH$_3$, R$_2$= CH$_3$
L-alanine (L-Ala); R$_1$= CH$_3$, R$_2$= H
D-alanine (D-Ala); R$_1$= H, R$_2$= CH$_3$
4-6
4: R$_1$= CH$_3$, R$_2$= CH$_3$
5: R$_1$= CH$_3$, R$_2$= H
6: R$_1$= H, R$_2$= CH$_3$
7-9
7: 2-aminoisobutyric acidmethyl ester. HCl (H-Aib-OMe. HCl); R$_1$= CH$_3$, R$_2$= CH$_3$
8: L-alanine methylester. HCl (H-(L) Ala-OMe. HCl); R$_1$= CH$_3$, R$_2$= H
9: D-alanine methylester. HCl (H-(D) Ala-OMe. HCl); R$_1$= H, R$_2$= CH$_3$
DMF, HOBT
DIPEA
1-3
1: R$_1$= CH$_3$, R$_2$= CH$_3$
2: R$_1$= CH$_3$, R$_2$= H
3: R$_1$= H, R$_2$= CH$_3$

Figure 4.2.1 Synthesis of peptide conjugated NDI derivatives **1, 2** and **3**.

scientific community to design the assembly of functional aromatic molecules, producing nanomaterials with tunable molecular ordering for various multidisciplinary applications.[77-89]

Herein, we demonstrate the bio-inspired structure-property correlation *via* the modulation of the molecular organization of the promising n-type organic semiconductor naphthalene diimide (NDI) by conjugating dipeptides.[90] We chose to functionalize NDI with structurally comparable unnatural and natural peptides Aib-Aib (**1**) and Ala-Ala (**2** and **3**), respectively via two step reaction condition as shown in Figure 4.2.1. They differ in just one additional methyl group at C$_\alpha$ position in case of Aib, and are capable of forming unique secondary structures, as shown in Figure 4.2.2a and b. The minute structural mutations (methyl groups) are expected to influence their distinct molecular

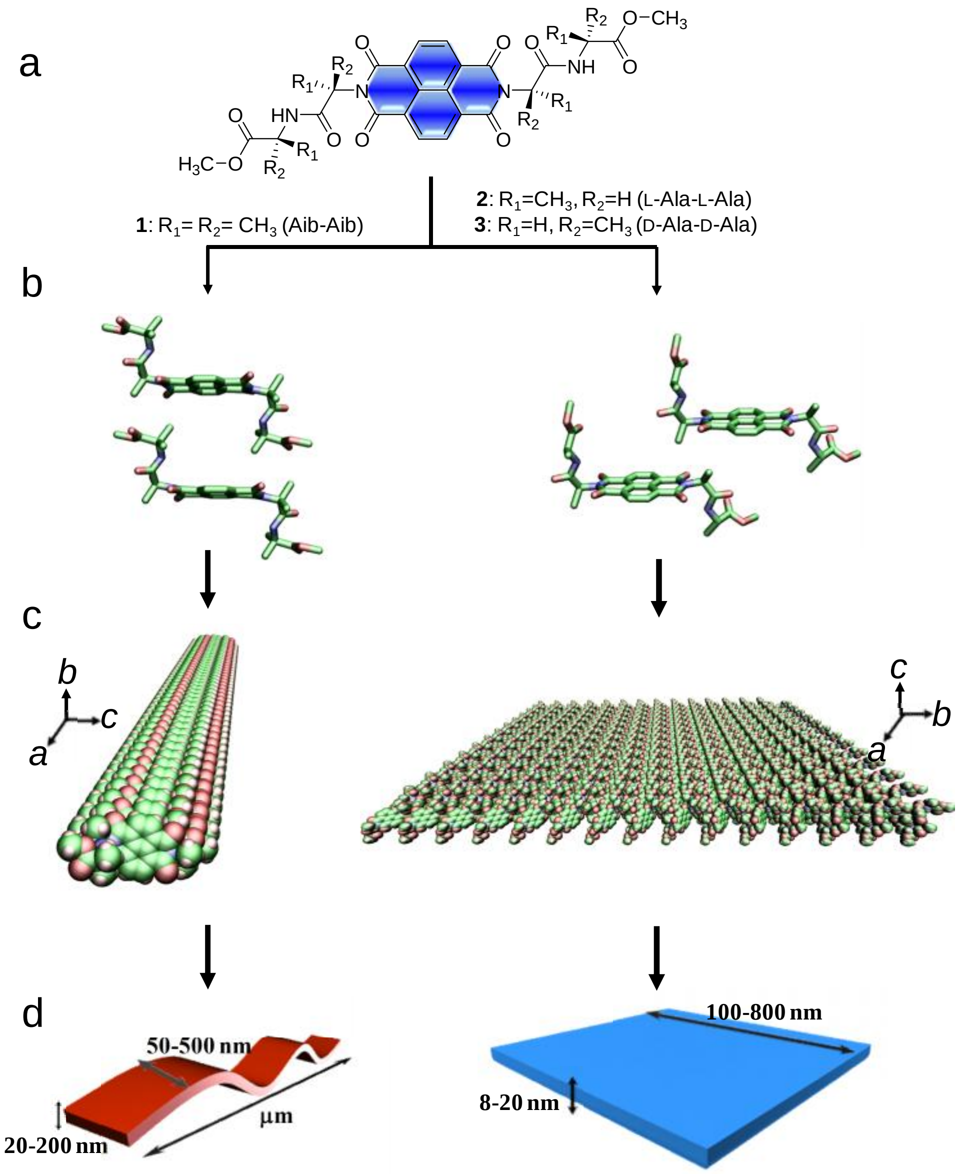
a
1: R1= R2= CH3 (Aib-Aib)
2: R1=CH3, R2=H (L-Ala-L-Ala)
3: R1=H, R2=CH3 (D-Ala-D-Ala)
b
c
b
c
a
c
b
a
d
50-500 nm
µm
20-200 nm
100-800 nm
8-20 nm

Figure 4.2.2 (a) Molecular structures of bis-dipeptide conjugated NDIs **1**: Aib-Aib, **2**: L-Ala-L-Ala, and **3**: D-Ala-D-Ala.The solid state structural insights: b) face-to-face (**1**) and edge-to-edge (**2**) stacked dimmers and c) Subsequent space fill representation of 1D (**1**) and 2D (**2**) molecular ordering along the crystallographic *a*-axis and *c*-face respectively (solvent molecules and hydrogen atoms have been omitted from the crystal packing representation for clarity). d) Schematic representation of self-assembled 1D and 2D nanostructures of **1** and **2**, respectively.

organization. Notably, Aib-rich peptides are known to promote helix conformation while the Ala-rich peptides assist β–sheet formation, as in the case of spider silk proteins.[91-92] The influence of structural mutations in (*bis*-dipeptide)-NDI conjugates (NDIs **1**-**3**) on their solid-state ordering and resultant properties *viz.*, (chiro-)optoelectronic, self-assembled nanoscale morphology and electrical conductivity was studied.

To the best of our knowledge, we present crystallographic insight-guided distinct solid-state molecular ordering to modulate the conducting property of n-type organic semiconductor molecule NDI by peptide conjugation, for the first time. The impact of minute structural mutations in the form of peptides revealed the distinct but well-defined nanostructures (1D nanotapes and 2D nanosheets) with perfect face-to-face (achiral) and edge-to-edge (chiral) NDI-NDI self-assembly, respectively (Figure 4.2.2). The significance of such bio-inspired molecular architectonics[64-68,77-89,93] of NDI and resultant structure-property correlation was thoroughly studied by various spectroscopic and microscopy techniques.

4.2.2 Results and discursion

4.2.2.1 Crystallographic insights

In line with the strategy, we sought to investigate the molecular ordering of *bis*-dipeptide-conjugated NDIs **1**-**3** by single crystal X-ray diffraction (XRD) studies (Figure 4.2.2). The crystals of **1**-**3**, suitable for single crystal XRD, were grown in dimethyl sulfoxide (DMSO) by the slow solvent evaporation method. NDI **1** was found to crystallize in the monoclinic system with $P2_1/n$ space group while NDIs **2** and **3** crystallized in orthorhombic systems with space group $P2_12_12_1$ (Table 4.2.1). Single crystal structures revealed that the imide substituents (dipeptides, **1**: Aib-Aib, **2**: L-Ala-L-Ala, and **3**: D-Ala-D-Ala) in NDIs (**1-3**) adopt *trans*-conformation (i.e., peptide chains on either side of NDI oriented in opposite directions with respect to the central aromatic core) and exhibit distinct sequence-specific molecular packing (Figure 4.2.2b). To our surprise, an unnatural dipeptide (Aib-Aib)-conjugated NDI (**1**) showed 1D molecular ordering with face-to-face NDI-NDI organization along crystallographic *a*-axis. The face-to-face 1D orientation of NDI-core is stabilized by CH---CO (α-methyl on the peptide to

Table 4.2.1 Crystallographic information of **1**- **3**: Summary.

	1	**2**	**3**
X-radiation	Mo *Kα* radiation, λ= 0.71073 Å	Mo *Kα* radiation, λ= 0.71073 Å	Mo *Kα* radiation, λ= 0.71073 Å
Crystal system	Monoclinic	Orthorhombic	Orthorhombic
Space group	$P2_1/n$	$P2_12_12_1$	$P2_12_12_1$
a, *b*, *c* (Å)	8.6053(13), 18.642(3), 12.190(2)	9.942(5), 14.412(5), 18.805(5)	9.9943(15), 14.470(2), 18.796(3)
α, β, γ (°)	90.000, 98.319(5), 90.000	90.000, 90.000, 90.000	90.000, 90.000, 90.000
Volume (Å^3)	1934.9(5)	2694.5(18)	2718.2(7)
# measured reflections	11865	8117	11662
# unique reflections	2759	1864	3194
Mean I/σ(I)	4.22	5.84	6.46
R factor (R1) (%)	6.22	7.68	5.21
$wR(F_2)$	0.1781	0.2021	0.1211
Goodness of fit	1.041	1.041	1.049
# molecules in unit cell	2	4	4
# solvent molecules in unit cell	4	0	0
CCDC number	1015722	1015723	1015724

acyl carbon on NDI), NH---O hydrogen bond (between peptide-NH and Oxygen atom from solvent molecules, DMSO) and CH---O (between α-methyl groups on peptide and solvent molecule, DMSO) (Figure 4.2.2b and c). In contrast, **2** and **3** displayed 2D edge-to-edge NDI-NDI molecular ordering through β–bridge-like interactions (series of CO---NH hydrogen bonds) between the peptide backbones along the crystallographic *a*-axis, giving rise to a hydrogen bond network spreading across the *c*-face of the crystal lattice (Figure 4.2.2b and c). Furthermore, **1** exhibited gelation propensity by forming bright cyan fluorescent organogel in $CHCl_3$/methylcyclohexane (MCH) (90/10 v/v) with a minimum gelation concentration (MGC) of 1 mM (Figure 4.2.3a, inset). On the other hand, **2** and **3** failed to form organogel under similar conditions (Figure 4.2.3b, inset). Thus, the observed distinct solid-state molecular organization and gelation ability of *bis*-(Aib-Aib) (**1**)- and *bis*-(Ala-Ala) (**2** and **3**)-functionalized NDIs validated the importance of bio-inspired molecular architectonics to rationally design molecular systems with desired molecular ordering, by utilizing minute structural mutations in the form of peptide sequence.

4.2.2.2 Morphological studies

The consequence of distinct molecular ordering on nanoscale morphology of **1** and **2** was examined by field emission scanning electron microscopy (FESEM) and atomic force microscopy (AFM) (Figure 4.2.3). The xerogel of **1** revealed the presence of several

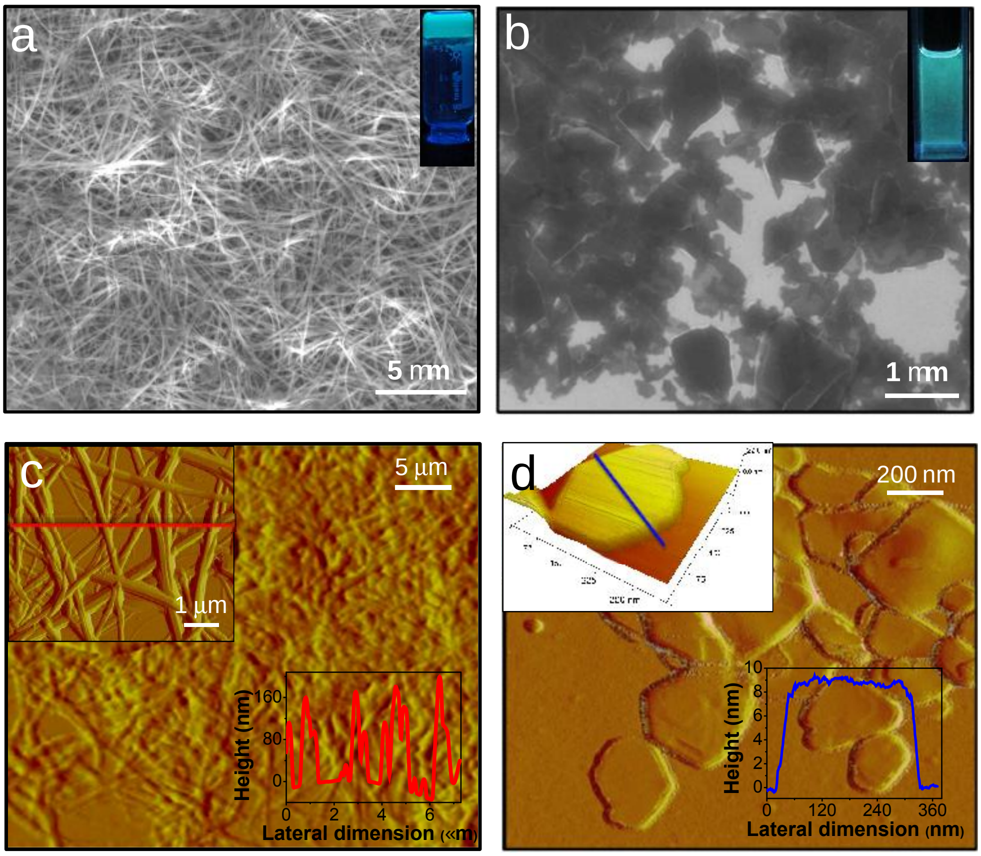
a
5 mm
b
1 mm
c
5 μm
1 μm
Height (nm)
160
80
0
0
2
4
6
Lateral dimension («m)
d
200 nm
Height (nm)
10
8
6
4
2
0
0
120
240
360
Lateral dimension (nm)

Figure 4.2.3 a) FESEM micrographs showing 1D tapes of **1** from xerogel (a) and 2D sheets of **2** from MCH/CHCl$_3$ (90/10, v/v) solution (b). *Insets*: (a) organogel of **1** under UV light (365 nm), a selected area AFM image of 1D nanotapes and corresponding height profiles along the red line (derived from height image); (b) MCH/CHCl$_3$ (90/10, v/v) solution of **2** under UV light (365 nm). c) AFM image of 1D nanotape network from xerogel of **1**. (d) AFM image of 2D nanosheets form solution of **2**. *Insets*: a selected area 3D AFM height image of single 2D nanosheet and corresponding height profiles along the blue line.

micrometer long, high-aspect-ratio 1D tape network (Figure 4.2.3a). AFM height profile analysis revealed 1D nanotapes with 20-200 nm height and 50-500 nm width (Figure 4.2.3c). On the other hand, **2** self-assembled from its solution (MCH/$CHCl_3$: 90/10, v/v) into thin, large surface area 2D sheets with ~ 8-20 nm thickness and 100-800 nm lateral dimensions (Figure 4.2.3b and d). Thus, 1D and 2D molecular packing observed in the single crystals were found to be replicated in the self-assembled nanoscale structures of **1** and **2** (Figure 4.2.2).

4.2.2.3 Spectroscopic studies

4.2.2.3.1 Vibrational spectroscopic studies

Attenuated total reflection infrared (ATIR) spectroscopy further provided the information on secondary structures of peptides and hydrogen bonding interactions among the molecules within the 1D nanotapes (**1**) and 2D nanosheets (**2**) (Figure 4.2.4). 1D nanobelts of **1** exhibited intense amide-I ($\nu_{C=O}$) absorption band at 1675 cm^{-1}, indicating the random structure of Aib-Aib peptide backbone. On the other hand, Ala-Ala (**2** and **3**) displayed a strong amide-I band at 1636 cm^{-1} and a weak signal at 1682 cm^{-1}, suggesting the presence of antiparallel β–sheet like structure within the 2D nanosheets (Figure 4.2.4a and b).[94-95] In agreement with the solid-state crystal structures (Figure 4.2.4c and d), 2D nanosheets (**2**) revealed the existence of strong intermolecular hydrogen bonding network *via* amide N-H and C=O by displaying blue-shifted broad amide N-H symmetric stretching band (3261 cm^{-1}) as compared to that of 1D nanobelts of **1** (3425 cm^{-1}).

4.2.2.3.2 Photophysical studies

UV-vis absorption spectra of **1** in $CHCl_3$ exhibited vibronically well-resolved absorption bands in the 300-400 nm regions, which is a characteristic of $\pi-\pi^*$ transitions along the long-axis of the NDI chromophore (Figure 4.2.5). A mirror image emission

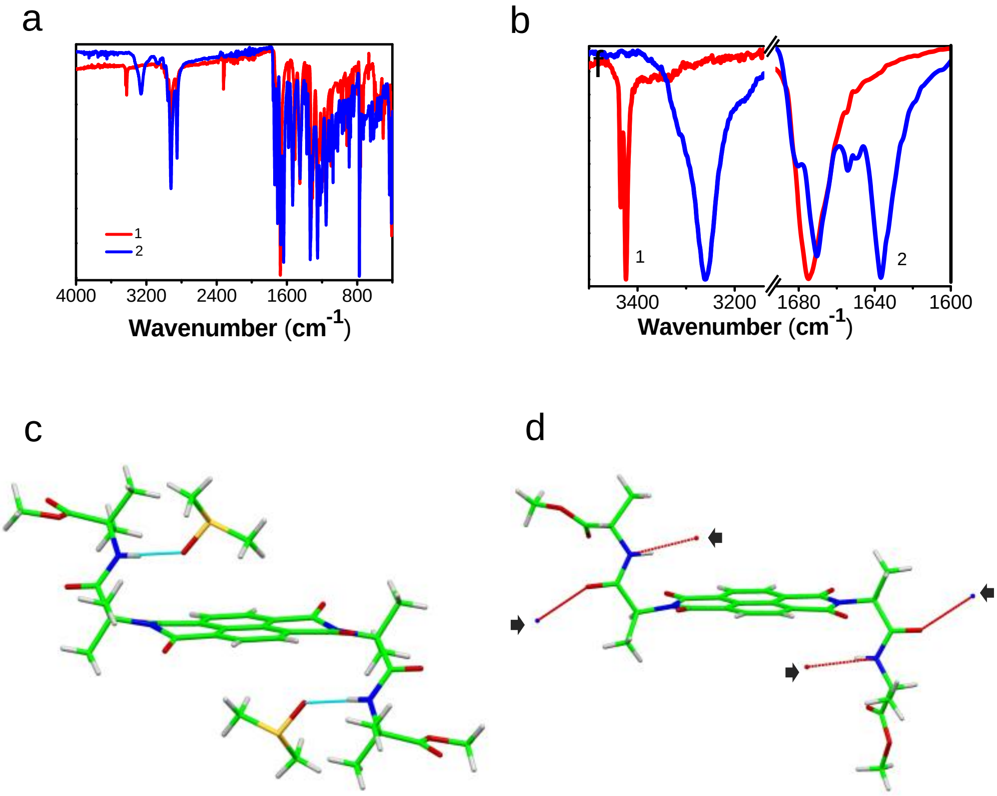

Figure 4.2.4 a) ATIR spectra of 1D nanotapes of **1** and 2D nanosheets of **2**. b) Amide NH and carbonyl (C=O) stretching frequency region. c) Single crystal XRD structures of **1** indicating the hydrogen bonding interactions with solvent molecule (DMSO) and d) Single crystal XRD structures of **2** indicating the intermolecular hydrogen bonding interactions to for antiparallel β–bridge secondary structure.

spectra around 413 nm (λ_{max}) suggested typical monomeric state in $CHCl_3$. Interestingly, absorption spectra of **1** in MCH/$CHCl_3$ (90/10, v/v) displayed significant hypochromicity (~ 42%), blue-shift (~ 5 nm) and band broadening. Furthermore, a new band appeared in the longer wavelength region (415 nm) (Figure 4.2.5a). The fluorescence emission spectra of **1** in MCH/$CHCl_3$ exhibited a significantly enhanced, broad and large Stoke-shifted (~ 93 nm) emission band, centered around 468 nm, with bi-exponential lifetime values of 9 ns (18%) and 1 ns (82%) (Figure 4.2.5b and c). This study suggests the formation of face-to-face (H-type) exciton-coupled NDI-NDI π–π stacked self-assembly among the molecules of **1** (Figure 4.2.2).[93,96]In contrast, **2** showed red-shifted (~ 5 nm) absorption

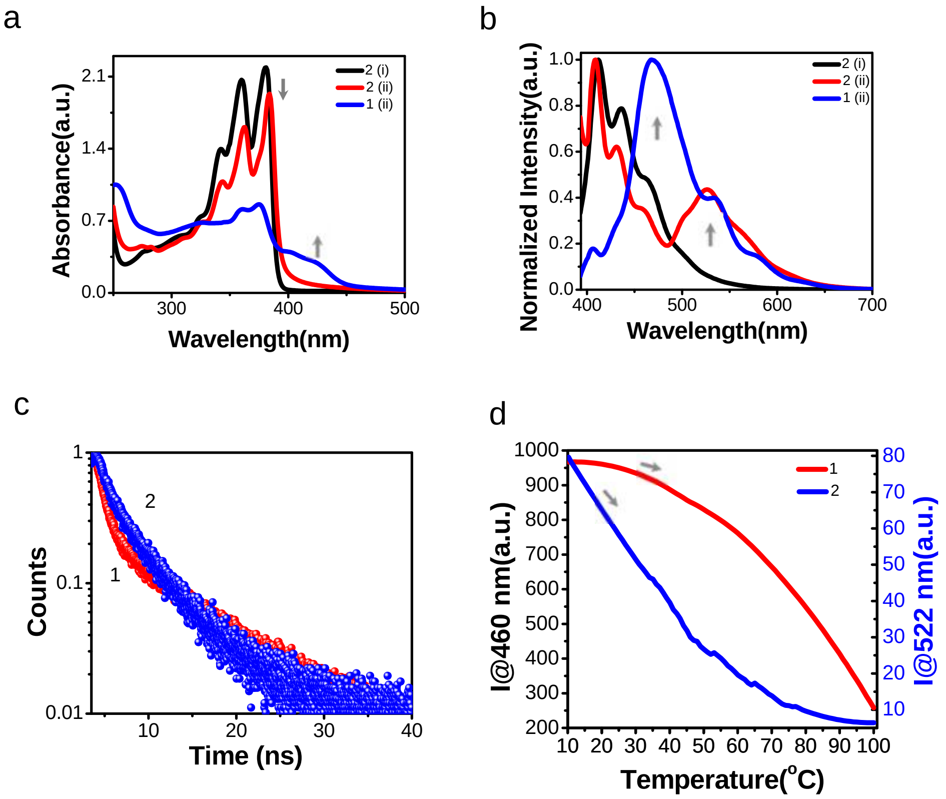

Figure 4.2.5 UV-vis absorption (a) and fluorescence emission spectra (b) of **1** and **2** in $CHCl_3$ (i) and MCH/$CHCl_3$ (90/10, v/v) (ii), respectively. Arrows indicating the spectral changes going from $CHCl_3$ solution to MCH/$CHCl_3$ (90/10, v/v) solution. c) TCSPC decay profile of **1** ($^{a}{}_{max}$ 460 nm) and **2** ($^{a}{}_{max}$ 522 nm) with a 405 nm excitation. d) Variable-temperature (VT) fluorescence emission studies (from 10 °C to 100 °C) of **1** (at 460 nm) and **2** (522 nm).

bands by changing the solvent system from $CHCl_3$ to MCH/$CHCl_3$ (90/10, v/v) (Figure 4.2.5a). Corresponding emission spectra displayed a large Stoke-shifted broad emission band centered at 522 nm with relatively shorter lifetime values of 4.9 ns (48%) and 1.3 ns (52%), thus, signifying the formation of edge-to-edge (J-type) stacked NDI-NDI self-assembly (Figure 4.2.5b and c).[93,96] To know thermal stability of distinct stacked NDIs in **1** and **2**, variable temperature (VT) dependent fluorescence emission studies were carried at the 460 nm and 522 nm respectively (Figure 4.2.5d). The emission intensity versus temperature plot displayed distinct melting behaviour, **1** showed two times higher thermal stability (50% aggregates present at 75 °C than **2** (50% aggregates present at 38 °C).

4.2.2.3.3 Nuclear magnetic resonance (NMR) studies

The above results were further strengthened by ^{1}H NMR data. Due to enhanced ring current shielding in the face-to-face π-stacked arrangement, a significant up-field shift ($\Delta\delta_{NDI}$= 160 ppb) was observed for NDI-core protons of **1** compared to edge-to-edge interacting NDI-core in **2**. The influence of MCH on the NDI-NDI aromatic stacking and

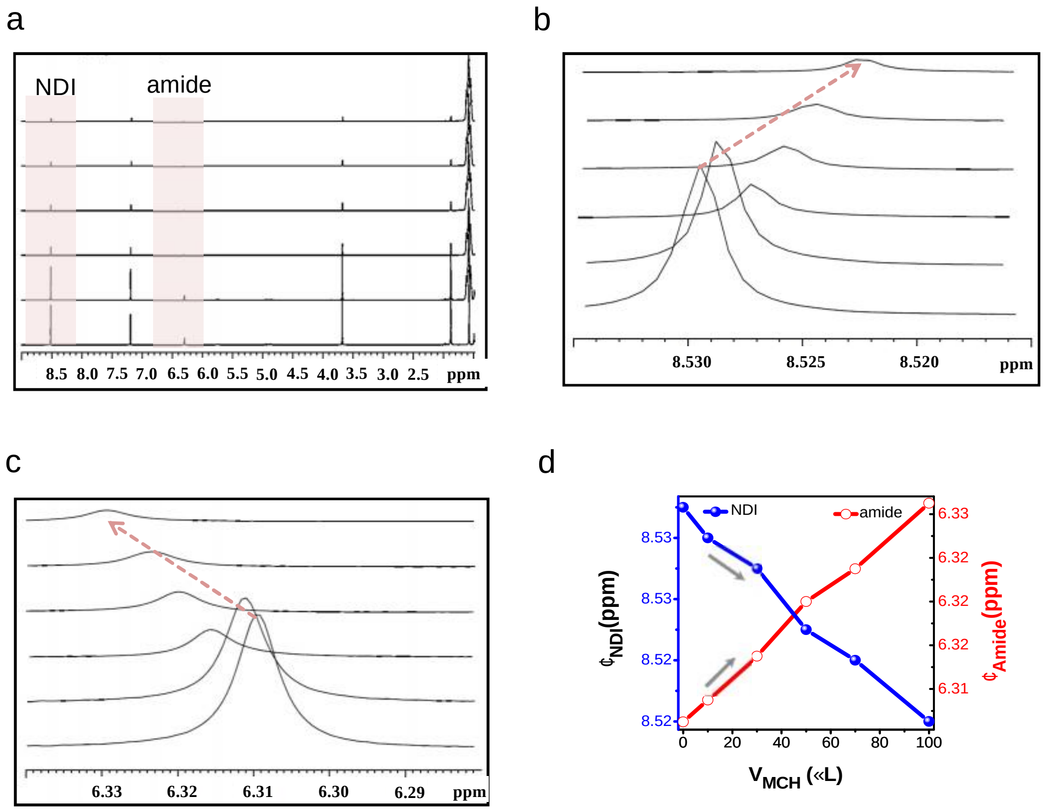

Figure 4.2.6 a) ^{1}H NMR spectral changes of **1** in $CDCl_3$ with gradual addition of MCH (0 μL, 10 μL, 30 μL, 50 μL, 70 μL and 100 μL). b) NDI aromatic region (8.54-8.51 ppm) of (a), Dashed arrow indicating the gradual aromatic stacking induced up field shifting of NDI protons with the addition of MCH (0 μL, 10 μL, 30 μL, 50 μL, 70 μL and 100 μL) to **1** in $CDCl_3$. c) Amide region (6.34-6.28 ppm) of (a). Dashed arrow indicating the gradual hydrogen bonding induced down field shifting of amide protons with the addition of MCH (0 μL, 10 μL, 30 μL, 50 μL, 70 μL and 100 μL) to **1** in $CDCl_3$. d) ^{1}H NMR data of **1** depicting the change in the chemical shift (ppm) values of NDI aromatic protons (blue line) and peptide-amide NH protons (red line) as a function of volume of MCH added into $CDCl_3$ solution.

hydrogen bonding interactions of **1** and **2** were probed by solvent-dependent ^{1}H NMR measurements (Figure 4.2.6 and Figure 4.2.7). Figure 4.2.6 clearly shows the up-field and down-field shifting of NDI-aromatic (7 ppb) (face-to- face NDI self-assembly) and peptide-amide protons (20 ppb) (solvent induced hydrogen bonding), with the increasing volume fraction of MCH in $CDCl_3$ solution of **1**. Under similar conditions, **2** exhibited relatively less down-field shift (6 ppb) (β–bridge interactions) of peptide-amide protons

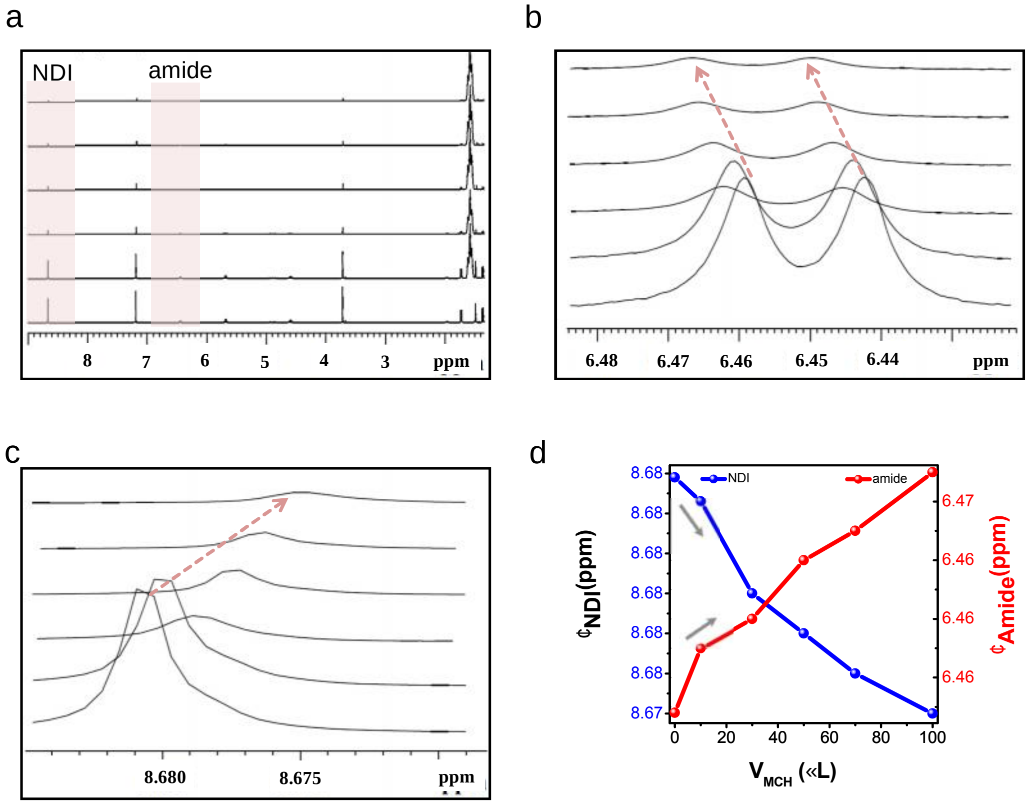

Figure 4.2.7 a) ^{1}H NMR spectral changes of **2** in $CDCl_3$ with the addition of MCH (0 μL, 10 μL, 30 μL, 50 μL, 70 μL and 100 μL). b) NDI aromatic region (8.69-8.67 ppm) of (a). Dashed arrow indicating the gradual aromatic stacking induced up field shifting of NDI protons with the addition of MCH (0 μL, 10 μL, 30 μL, 50 μL, 70 μL and 100 μL) to **2** in $CDCl_3$. c) Amide region (6.48-6.43 ppm) of (a). Dashed arrows indicating the gradual hydrogen bonding induced down field shifting of amide protons with the addition of MCH (0 μL, 10 μL, 30 μL, 50 μL, 70 μL and 100 μL) to **2** in $CDCl_3$. d) ^{1}H NMR data of **2** depicting the change in the chemical shift (ppm) values of NDI aromatic protons (blue line) and peptide-amide NH protons (red line) as a function of volume fraction of MCH added to $CDCl_3$ solution.

and increased up-field shifts (8 ppb) of NDI-aromatic protons (edge-to-edge NDI self-assembly) (Figure 4.2.7). These changes in chemical shifts suggested that the MCH facilitated distinct self-assembly among the molecules of **1** and **2** by reinforcing the noncovalent interactions *via* intermolecular NDI-NDI aromatic and hydrogen bonding among the peptide chains. Furthermore, although solvent systems used for crystal growth and nanostructures of **1** and **2** are different, the detailed spectroscopic and microscopy studies in MCH/$CHCl_3$ (90/10, v/v) support face-to-face (H-type) and edge-to-edge (J-type) molecular arrangements for **1** and **2** respectively (Figure 4.2.2), which is in good agreement with XRD data.

4.2.2.3.4 Circular dichroism studies

The effect of chiral information of peptide backbones in **2** and **3** against achiral backbone in **1** on the long-range intermolecular organization of NDI was investigated by circular dichroism (CD) spectroscopic studies (Figure 4.2.8). In agreement with the UV-vis and fluorescence emission data, NDIs **1-3** displayed flat CD spectra in $CHCl_3$ solution due to their molecularly dissolved state (Figure 4.2.8a) which also confirmed the absence of any Cotton effects originating from achiral conformations of methyl (C_α) group. However, **2** and **3** in $CHCl_3$/MCH (90/10, v/v) displayed mirror image cotton effects in the NDI absorption region (250-400 nm) as shown in Figure 4.2.8b). The negative and positive cotton effects of **2** and **3**, around 400 nm (NDI long axis $\pi-\pi*$ electronic transitions), suggests left (*M*)- and right (*P*)-handed supramolecular helical organization of NDI chromophores.[33,93] NDI **1** with achiral and non-proteinogenic peptide (Aib-Aib) did not show CD signal under similar conditions, indicating the absence of any preferred helical assembly.

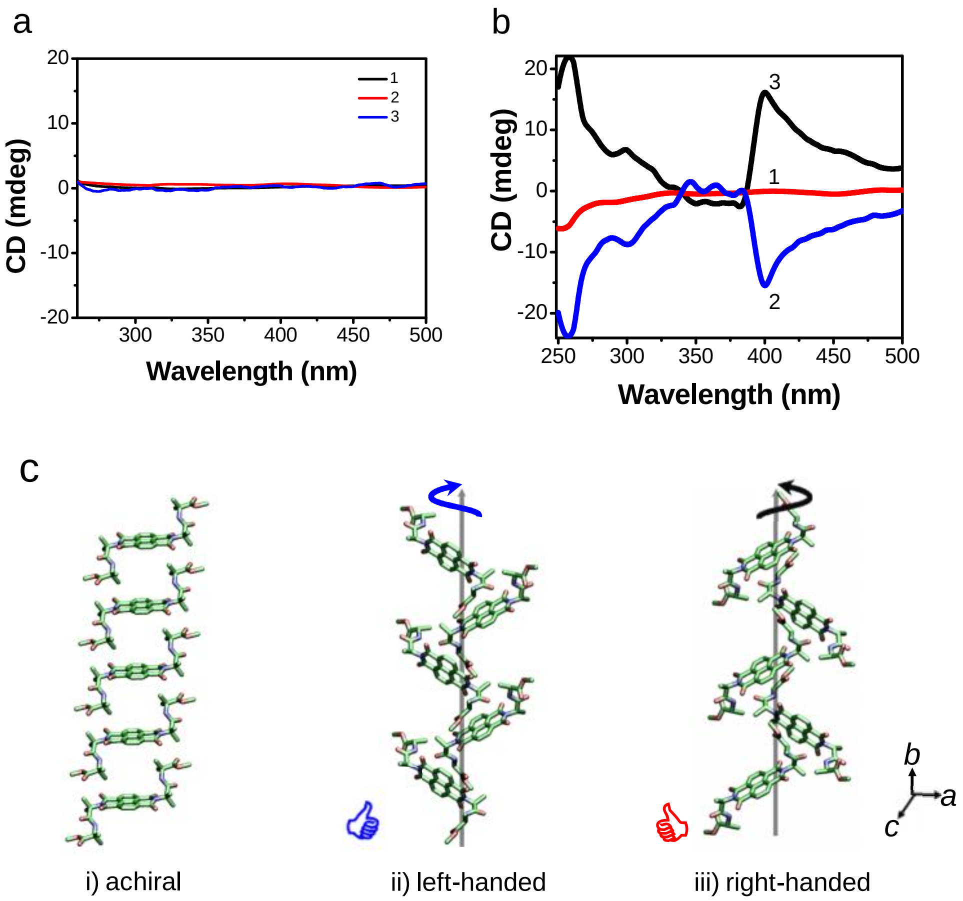

Figure 4.2.8 a) CD spectra of **1**, **2** and **3** recorded in $CHCl_3$ solution. The flat CD spectra in $CHCl_3$ solution suggesting the molecularly dissolved state. b) CD spectra of **1**, **2** and **3** recorded in MCH/$CHCl_3$(90/10, v/v) solution. c) Solid-state 1D face-to-face achiral organisation of **1** (i), supramolecular tilt left-handed (ii, in **2**) and right-handed (iii, in **3**) chiral NDI stacks from single crystal XRD studies.

4.2.2.4 Solid state chiral organization

To validate the CD data, we further analyzed solid- state molecular organization in the single crystal packing of **1-3** (Figure 4.2.8c). The linear 1D face-to-face molecular stacks of **1** in the crystal lattice were found to co-exist as both left- and right-handed 2_1 chiral helices, thus nullifying the chiral signature in the CD spectra. On the other hand, **2** and **3** showed prominent 2_1 supramolecular tilt stacks with opposite helical assembly along the crystallographic *a* and *b*-axis. In the case of **2**, the tilt angles were found to be 30.67° and 59.79° along *a* and *b*-axis, respectively. Similarly, in the case of **3**, the tilt angles were found to be 30.56° and 59.93° along *a* and *b*-axis, respectively.[33,93] The pitch of the helices was found to be 9.94 Å (along *a-axis*) and 14.41 Å (along *b*-axis) for **2**, while for **3** the pitch was 9.99 Å (along *a*-axis) and 14.47 Å (along *b*-axis). The helices were found to be stabilized by β–bridge like intermolecular CO---NH hydrogen bonding between the peptide backbones. Overall, achiral (**1**) and chiral (**2** and **3**) organization of *bis*-dipeptide-conjugated NDIs, within the lattices of their respective crystals (Figure 4.2.8c), is in excellent agreement with the CD data (Figure 4.2.8b). These results further corroborated the transcription of chiral information of intrinsically chiral amino acid (alanine) of the peptide backbones in **2** and **3** to their supramolecular homochiral organization in solution and solid state.[33,74,93]

4.2.2.5 Conductivity studies

Furthermore, we examined the effect of minute structural mutations (dipeptide) guided distinct NDI molecular organization of **1** (1D face-face) and **2** (2D edge-edge) on the charge carrier mobility (Figure 4.2.9). The two-probe method was employed to generate the current-voltage (I-V) response from the films of **1** (1D nanotapes) and **2** (2D sheets) as shown in Figure 4.2.9a. Remarkably, the current-voltage (*I-V*) measurements on NDI **1**

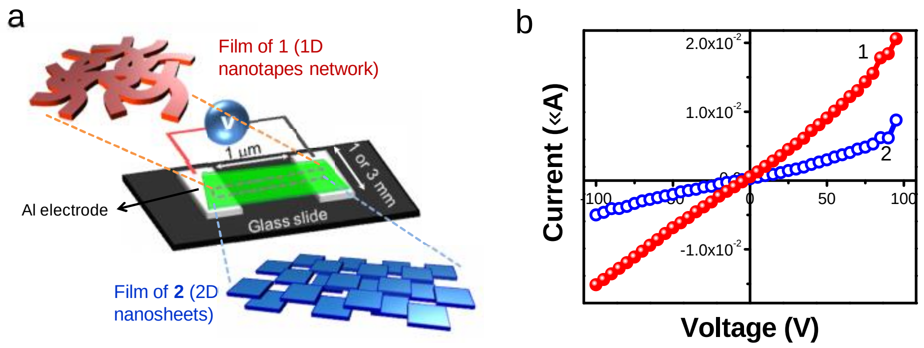

Figure 4.2.9 a) Schematic representation of current-voltage (*I-V*) device fabricated using nanotapes network film from xerogel of **1** or 2D nanosheets film from **2** nanostructured materials of NDI. b) *I-V* characteristics of **1** (1D nanotapes network) (i) and **2** (2D nanosheets) (ii) deposited across the aluminium electrodes as shown in a.

(1D nanotapes) with face-to-face NDI organization showed two-times more conductivity (3.5×10^{-6} S/m) as compared to NDI **2** (2D nanosheets) with edge-to-edge NDI organization (1.6×10^{-6} S/m) (Figure 4.2.9b). Similar *I-V* characteristics was observed for film of **3** (2D nanosheets) which confirmed that chirality has no role in the modulation of conductivity in our peptide conjugated NDIs. The significantly enhanced conductivity of **1** is attributed to perfect face-to-face molecular arrangement, which is known to maximize the electronic coupling among the $\pi-\pi$ overlapped NDI molecules.[69-70] Therefore, difference in the conductivity values of NDI chromophore in 1D nanotapes of **1** and 2D nanosheets of **2** further exemplifies the potential of bio-inspired molecular architectonics guided by the crystallographic insights for the modulation of functional properties (*viz.*, nanoscale morphology, (chiro-)optical and conductivity) of electronically active aromatic systems.

4.2.3 Conclusion

In conclusion, we demonstrated the crystallographic insight-guided structure-property correlation in the form of nanomorphology, optoelectronic and conductivity behavior of *bis*-dipeptide-conjugated naphthalene diimides (NDI) (Figure 4.2.10). In our bio-inspired design strategy, minute structural mutations played a significant role in the modulation of functional properties of n-type organic semiconductor (NDI). The non-proteinogenic (achiral) dipeptide (Aib-Aib) promoted 1D face-to-face arrangement (H-type) while the proteinogenic (chiral) dipeptide (Ala-Ala) led to the formation of 2D edge-to-edge (J-type) supramolecular tilted chiral molecular organisation in solid state. The molecular ordering in both single crystals and self-assembled nanostructures (1D and 2D) showed unusually high correlations, which reflected in their distinct optoelectronic and conductivity properties. Thus, our report on crystallographic insight-guided and bio-inspired molecular architectonics is not only envisioning novel way of engineering

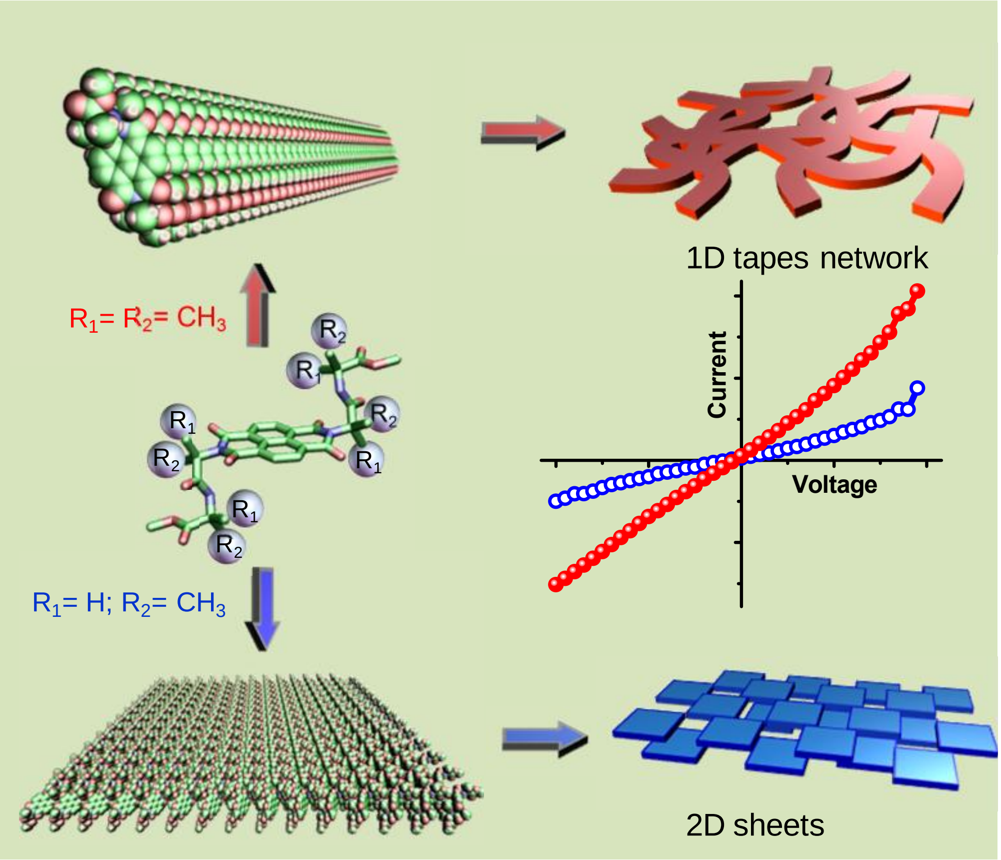
1D tapes network
R_1= R_2= CH_3
Current
Voltage
R_1= H; R_2= CH_3
2D sheets

Figure 4.2.10 Summery of crystallographic insight-guided nanoarchitectonics and conductivity modulation of NDI through peptide conjugation.

molecular assemblies and to undertake structure-property correlations but it may also facilitate the interfacing of the electronic materials with biology to enable many advanced biomaterials (bioelectronics) applications.

4.2.4 Experimental section

4.2.4.1 Materials and methods

Materials 1,4,5,8-Naphthalenetetracarboxylic dianhydride (NDA), triethylamine and all amino acids were obtained from Sigma-Aldrich. All other reagents and solvents were of reagent grade and used without further purification.

Absorption spectroscopy UV–vis spectra were recorded on a Perkin Elmer Model Lambda 900 spectrophotometer by using quartz cuvette of 10 mm path length.

Fluorescence spectroscopy Fluorescence spectra were recorded on a Perkin Elmer Model LS 55 spectrophotometer. All fluorescence spectra were recorded with excitation wavelength λ_{ex} = 380 nm.

Circular dichroism (CD) CD measurements were carried out on a Jasco J-815 spectropolarimeter under nitrogen atmosphere by using quartz cuvette of 10 mm path length.

NMR spectroscopy ^{1}H and ^{13}C NMR spectra were recorded on a Bruker AV-400 spectrometer with chemical shifts reported as ppm (in $CDCl_3$/DMSO-d_6 with tetramethylsilane as internal standard).

Mass spectrometry (MS) High resolution mass spectra (HRMS) were obtained from Agilent Technologies 6538 UHD Accurate-Mass Q-TOF LC/MS spectrometer.

Field emission scanning electron microscopy (FESEM) FESEM images were acquired with a FEI Nova nanoSEM-600 equipped with a field-emission gun operating at 15 kV. The xerogels were prepared by transfer of organogels onto a Si (111) substrate and dried in air followed by vacuum drying at room temperature.

Gelation experiments Methylcyclohexene (MCH) was added to the solution of **1** in chloroform to make 1 mM, under ultrasonication (MCH/$CHCl_3$) = 80:20 (v/v)). After few minutes the formation of organogels was observed. The gel formation is determined by tilting or inverting the sample vial upside down.

Time-correlated single photon counting (TCSPC) studies Fluorescence decay profiles were performed using FLSP 920 spectrometer, Edinburgh Instrument. EPLED.

Crystallographic data and structure refinement details Crystal growth. Crystals were grown at room temperature in DMSO as solvent. Data collection. Data was collected on Bruker AXS SMART APEX Single Crystal Diffractometer. All the datasets were collected at 100 K.

Structure solution and refinement SHELXS-2013 and SHELXL-2013 programs were used to solve and refine the X-ray diffraction data. WinGx package (version 1.80.05)[3] was used as front end to SHELX programs.

Electrical conductivity measurements The silver electrodes were prepared by thermal evaporation of silver through a shadow mask on glass substrate. The 1D nanotapes from organogel **1** or 2D sheets from $CHCl_3$/methylcylohexane (MCH) (90/10 v/v) solution of **2** was drop-casted over the gap between electrodes. The solvent was dried in air followed by vacuum drying at room temperature to form a thin film of nanostructures bridging across the micro-fabricated silver electrodes. Known bias was applied across the electrodes and abtained the current (*I*) versus voltage (*V*) plot. The value of conductance (*I*/*V*) is measured from the inverse slope of *I*-*V* curve. The room temperature conductivity was calculated from $\sigma = 1/\rho$ (where $\rho = A/GL$). Where σ= conductivity, ρ= resistivity, A= cross sectional area (width X thickness of film), G= conductance and L= lengh of film or gap between the electrods

General procedure for the synthesis of amino acid appended naphthalenediimide 1,4,5,8-Naphthalenetetracarboxylic dianhydride (0.5 g, 1.8 mmol) and corresponding amino acid derivative (0.6 g, 3.7 mmol) were suspended in 20 mL of DMF. To this suspension Et_3N (0.2 mL) was added and allowed to reflux for 12 h. After cooling the reaction mixture to room temperature, the precipitate was filtered and recrystallized from ethanol.

Characterization data for L-phenylalanine appended NDI. Yield 70%. ^{1}H NMR (*DMSO-d6*, 400 MHz) δ_H 13.03 (2H, s), 8.64 (4H, s), 7.17-7.03 (10H, m), 5.85 (2H, dd), 3.60 (2H, dd), 3.32 (2H, dd); ^{13}C NMR (*DMSO-d6*, 100 MHz) δ_C 170.1, 161.9, 137.8, 131.2,128.9, 128.1, 126.3, 126.0, 125.6, 54.5, 34.2.

Characterization data for D-phenylalanine appended NDI. Yield 70%. ^{1}H NMR (*DMSO-d6*, 400 MHz) δ_H 13.00 (2H, s), 8.64 (4H, s), 7.17-7.03 (10H, m), 5.86 (2H, dd), 3.60 (2H, dd), 3.32 (2H, dd); ^{13}C NMR (*DMSO-d6*, 100 MHz) δ_C 170.1, 161.9, 137.7, 131.2, 128.9, 128.1, 126.3, 126.0, 125.6, 54.5, 34.2.

Characterization data for glycine appended NDI. Yield 70%. ^{1}H NMR (*DMSO-d6*, 400 MHz) δ_H 13.20 (2H, s), 8.74 (4H, s), 4.7 (4H, s); ^{13}C NMR (*DMSO-d6*, 100 MHz) δ_C 168.9, 162.2, 130.9, 126.2 126.0, 41.5.

General procedure for the synthesis of amino acid methylester. Anhydrous methanol (50 mL) was placed into a 100 mL two necked round-bottom flask, fitted with a reflux condenser and an additional dropping funnel, and cooled to ice temperature. Acetyl chloride (3 mL) was added drop-wise through the dropping funnel. After 15 min., phenylalanine (3.0 g, 18.16 mmol) was added, and the reaction mixture was refluxed overnight at 70°C. The reaction mixture was dried in vacuo to obtain phenylalanine methylester hydrochloride in quantitative yield and used for further reaction without purification.

General procedure for the Synthesis of L and D. Compounds **L** and **D** were synthesized using previously reported methods.

Characterization data for L Yield 74 %.^{1}H NMR (400 MHz, $CDCl_3$) δ_H 8.63 (4H, s), 7.1 (10H, m), 6.02 (2H, dd), 3.77 (6H, s), 3.73 (2H, dd), 3.50 (2H, dd); $^{1\ 3}$ C NMR (100 MHz, $CDCl_3$) δ_C 169.6, 162.4, 136.9, 131.3, 129.2, 128.5, 126.9, 126.8, 126.3, 54.8, 52.8, 34.9.

Characterization data for D. Yield 71%. ^{1}H NMR (400 MHz, $CDCl_3$) δ_H 8.63 (4H, s), 7.1 (10H, m), 6.02 (2H, dd), 3.77 (6H, s), 3.73 (2H, dd), 3.50 (2H, dd); $^{1\ 3}$ C NMR (100 MHz, $CDCl_3$) δ_C 169.6, 162.4, 136.9, 131.3, 129.2, 128.5, 126.9, 126.8, 126.4, 54.9, 52.8, 34.9.

General procedure for the Synthesis of NDI-peptide conjugates (LL, *DD*, L*D*, *D*L and AA). Amino acid-appended naphthalenediimide (300 mg, 0.5 mmol), 1-ethyl-3-(3 dimethyllaminopropyl) carbodiimide hydrochloride (220 mg, 1.1 mmol) and 1-hydroxybenzotriazole (230 mg, 1.1 mmol) were suspended in DMF (10 mL). After 15 min., amino acid methylester (230 mg, 1 mmol) and N, N-diisopropylethylamine (440 mg, 3.4 mmol) were added to the reaction mixture and allowed to stir at room temperature for 12 h. Reaction progress was monitored by TLC. The solvent was removed under reduced pressure and washed with water. The organic layer was separated, dried under vacuo and the residue was purified by column chromatography (CH_2Cl_2/ MeOH: 10/2).

Characterization data for LL. Yield 50 %. ^{1}H NMR (*$CDCl_3$*, 400 MHz) δ_H 8.63 (4H, s), 7.19-6.91 (20H, m), 6.22 (2H, dd), 5.98 (2H, dd), 4.92 (2H, dd), 3.74 (6H, s), 3.65 (2H, dd), 3.51(2H, dd), 3.14 (2H, dd), 3.05 (2H, dd); ^{13}C NMR (*$CDCl_3$*, 100 MHz) δ_C 171.7, 167.9, 162.4, 136.6, 135.6, 131.2, 129.6, 129.0, 128.9, 128.7, 128.3, 127.0, 126.8, 126.5, 126.2, 55.9, 53.4, 52.4, 37.65, 34.6. MALDI-TOF-MS: 906.94 $[M+Na]^+$, calcd 906.93 for $C_{52}H_{44}N_4O_{10}Na$

Characterization data for DD. Yield 50 %. ^{1}H NMR (*$CDCl_3$*, 400 MHz) δ_H 8.63 (4H, s), 7.19-6.91 (20H, m), 6.21 (2H, dd), 5.98 (2H, dd), 4.92 (2H, dd), 3.74 (6H, s), 3.66

(2H, dd), 3.51(2H, dd), 3.14 (2H, dd), 3.03 (2H, dd); ^{13}C NMR (*CDCl$_3$*, 100 MHz) δ_C 171.8, 168.0, 162.5, 136.7, 135.7, 131.3, 129.2, 129.1, 128.8, 128.7, 128.5, 127.2, 127.0, 126.6, 126.3, 56.0, 53.5, 52.5, 37.7, 34.7. MALDI-TOF-MS: 906.94 [M+Na]$^+$, calcd 906.93 for $C_{52}H_{44}N_4O_{10}Na$.

Characterization data for LD. Yield 50 %. ^{1}H NMR (*CDCl$_3$*, 400 MHz) δ_H 8.57 (4H, s), 7.23-7.00 (20H, m), 6.20 (2H, d), 5.94 (2H, dd), 4.88 (2H, dd), 3.58 (6H, s), 3.53 (2H, dd), 3.43(2H, dd), 3.11 (4H, d; ^{13}C NMR (*CDCl$_3$*, 100 MHz) δ_C 170.4, 166.6, 161.5, 135.3, 134.6, 130.1, 128.5, 127.9, 127.7, 127.5, 126.1, 126.0, 125.6, 125.2, 55.0, 52.3, 51.2, 36.8, 33.7. MALDI-TOF-MS: 906.94 [M+Na]$^+$, calcd 906.93 for $C_{52}H_{44}N_4O_{10}Na$.

Characterization data for DL. Yield 50 %. ^{1}H NMR (*CDCl$_3$*, 400 MHz) δ_H 8.57 (4H, s), 4.67(4H, s), 3.85(4H, d), 3.56(6H, s); ^{13}C NMR (*CDCl$_3$*, 100 MHz) δ_C 170.4, 166.6, 161.5, 135.3, 134.6, 130.1, 128.5, 127.9, 127.7, 127.5, 126.1, 126.0, 125.6, 125.2, 55.0, 52.3, 51.2, 36.8, 33.7. MALDI-TOF-MS: 907.619 [M+Na]$^+$ calcd 906.93 for $C_{52}H_{44}N_4O_{10}Na$.

Characterization data for AA. Yield 60 %. ^{1}H NMR (*DMSO-d6*, 400 MHz) δ_H 8.67 (2H, s), 8.64 (4H, s), 6.20 (2H, d), 5.94 (2H, dd), 4.88 (2H, dd), 3.58 (6H, s), 3.53 (2H, dd), 3.43(2H, dd), 3.11 (4H, d; ^{13}C NMR (*DMSO-d6*, 100 MHz) δ_C 170.0, 166.9, 162.3, 130.8, 130.6, 130.1, 126.2, 51.6, 42.5, 40.5. MALDI-TOF-MS: 547.11 [M+Na]$^+$, calcd 547.43 for $C_{24}H_{20}N_4O_{10}Na$.

General procedure for the synthesis of amino acid appended naphthalenediimide (4-6). 1,4,5,8-Naphthalenetetracarboxylic dianhydride (0.5 g, 1.8 mmol) and corresponding amino acid (0.6 g, 3.7 mmol) were suspended in 20 mL of DMF. To this suspension triethylamine (0.2 mL) was added and allowed to reflux for 12 h. After cooling to room temperature the reaction mixture was added into 2N HCl (500 mL) and was stirred for 1 hour. The precipitate was filtered, washed with excess of distilled water and dried in vacuum to obtain amino acid appended naphthalenediimide product in quantitative yield.

Characterization data for 4. Yield 70%; ^{1}H NMR (*DMSO-d*$_6$, 400 MHz) δ_H 12.55 (2H, s), 8.57 (4H, s), 1.79 (12H, s);), Elemental analysis: Found: C, 60.25; H, 4.16; N, 6.37; calcd: C, 60.27; H, 4.14; N, 6.39 for $C_{22}H_{18}N_2O_8$. HRMS found: 438.1070, calcd 438.1063 for $C_{22}H_{19}N_2O_8$ (M+H)$^+$.

Characterization data for 5. Yield 73.2%; ^{1}H NMR (*DMSO-d*$_6$, 400 MHz) δ_H 12.85 (2H, s), 8.71 (4H, s), 5.6 (2H, dd), 1.57 (6H, d); ^{13}C NMR (*DMSO-d*$_6$, 100 MHz) δ_C 171.0, 162.0, 130.9, 126.1, 49.0, 14.3; HRMS found: 411.0853, calcd 411.0828 for $C_{20}H_{15}N_2O_8$ (M+H)$^+$.

Characterization data for 6. Yield 73.2%; ^{1}H NMR (*DMSO-d*$_6$, 400 MHz) δ_H 12.84 (2H, s), 8.71 (4H, s), 5.6 (2H, dd), 1.57 (6H, d); ^{13}C NMR (*DMSO-d*$_6$, 100 MHz) δ_C 171.0, 162.0, 130.9, 126.1, 49.0, 14.3; HRMS found: 411.0816, calcd 411.0828 for $C_{20}H_{15}N_2O_8$ (M+H)$^+$.

General procedure for the synthesis of amino acid methylester (7-9). Anhydrous methanol (50 mL) was placed into a 100 mL two necked round-bottom flask, fitted with a reflux condenser and an additional dropping funnel, and cooled to ice temperature. Acetyl chloride (3 mL) was added dropwise through the dropping funnel. After 15 min., amino acid (3.0 g, 18.16 mmol) was added, and the reaction mixture was refluxed overnight at 70 °C. Solvent was evaporated and dried in vacuum to obtain amino acid methylester in quantitative yield and used for further reaction without purification.

General procedure for the Synthesis of NDI-peptide conjugates (1, 2 and **3).** Amino acid-appended naphthalenediimide (300 mg, 0.5 mmol), 1-ethyl-3-(3 dimethyllaminopropyl) carbodiimide hydrochloride (220 mg, 1.1 mmol) and 1-hydroxybenzotriazole (230 mg, 1.1 mmol) were suspended in DMF (10 mL). After 15 min., curresponding amino acid methylester (230 mg, 1 mmol) and N, N-diisopropylethylamine (440 mg, 3.4 mmol) were added to the reaction mixture and allowed to stir at room temperature for 12 h. Reaction progress was monitored by TLC. The solvent was removed under reduced pressure and washed with water. The organic layer was separated, dried under vacuo and the residue was purified by column chromatography (CH_2Cl_2/ MeOH: 10/2).

Characterization data for 1. Yield 70%; ^{1}H NMR (*CDCl*$_3$, 400 MHz) δ_H 8.59 (4H, s), 6.38 (2H, s), 3.74 (6H, s), 1.94 (12H, s), 1.64 (12H, s); ^{13}C NMR (*DMSO-d*$_6$, 100 MHz) δ_C 175.4, 172.3, 163.8, 130.5, 127.5, 126.1, 64.8, 56.7, 52.6, 24.6, 24.2; HRMS found 659.2322, calcd 659.2324 for $C_{32}H_{36}N_4NaO_{10}$ $(M+Na)^+$.

Characterization data for 2. Yield 65%; ^{1}H NMR (*DMSO-d*$_6$, 400 MHz) δ_H 8.69 (4H, s), 8.34 (2H, d), 5.45 (2H, q), 4.35 (2H, q), 3.61 (6H, s), 1.51 (6H, d), 1.09 (6H, d); ^{13}C NMR (*DMSO-d*$_6$, 100 MHz) δ_C 173.2, 168.7, 162.4, 130.2, 126.8, 126.3, 51.8, 49.5, 47.6, 16.8, 14.0; HRMS found: 581.1867, calcd 581.1878 for $C_{28}H_{29}N_4O_{10}$ $(M+H)^+$.

Characterization data for 3. Yield 65%; ^{1}H NMR (*DMSO-d*$_6$, 400 MHz) δ_H 8.69 (4H, s), 8.34 (2H, d), 5.45 (2H, q), 4.35 (2H, q), 3.61 (6H, s), 1.51 (6H, d), 1.09 (6H, d); ^{13}C NMR (*DMSO-d*$_6$, 100 MHz) δ_C 173.2, 168.7, 162.4, 130.2, 126.8, 126.3, 51.8, 49.5, 47.6, 16.8, 14.0; HRMS found: 581.1867, calcd 581.1878 for $C_{28}H_{29}N_4O_{10}$ $(M+H)^+$.

4.2.5 Appendix

- ^{1}H NMR and ^{13}C NMR spectra of L-phenylalanine appended NDI
- ^{1}H NMR and ^{13}C NMR spectra of D-phenylalanine appended NDI
- ^{1}H NMR and ^{13}C NMR spectra of glycine appended NDI
- ^{1}H NMR and ^{13}C NMR spectra of **LL**
- ^{1}H NMR and ^{13}C NMR spectra of **DD**
- ^{1}H NMR and ^{13}C NMR spectra of **LD**
- ^{1}H NMR and ^{13}C NMR spectra of **DL**
- ^{1}H NMR and ^{13}C NMR spectra of **AA**
- ^{1}H NMR spectra of **4**
- ^{1}H NMR spectra of **5**
- ^{1}H NMR spectra of **6**
- ^{1}H NMR and ^{13}C NMR spectra of **1**
- ^{1}H NMR and ^{13}C NMR spectra of **2**
- ^{1}H NMR and ^{13}C NMR spectra of **3**
- MALDI-TOF-MS of **LL**
- MALDI-TOF-MS of **DD**
- MALDI-TOF-MS of **LD**
- MALDI-TOF-MS of **DL**
- MALDI-TOF-MS of **AA**
- HRMS of **1**, **2** and **3**

^{1}H NMR spectra (DMSO-*d6*, 400MHz) of L-phenylalanine appended NDI

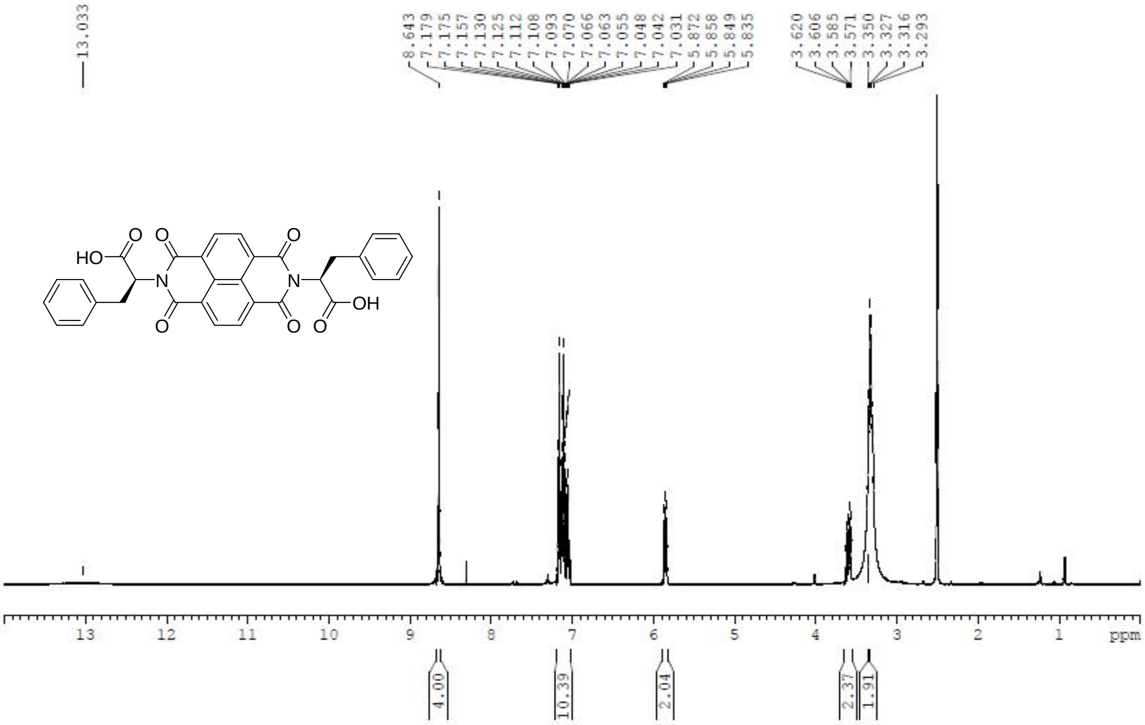

^{13}C NMR spectra (DMSO-*d6*, 100MHz) of L-phenylalanine appended NDI

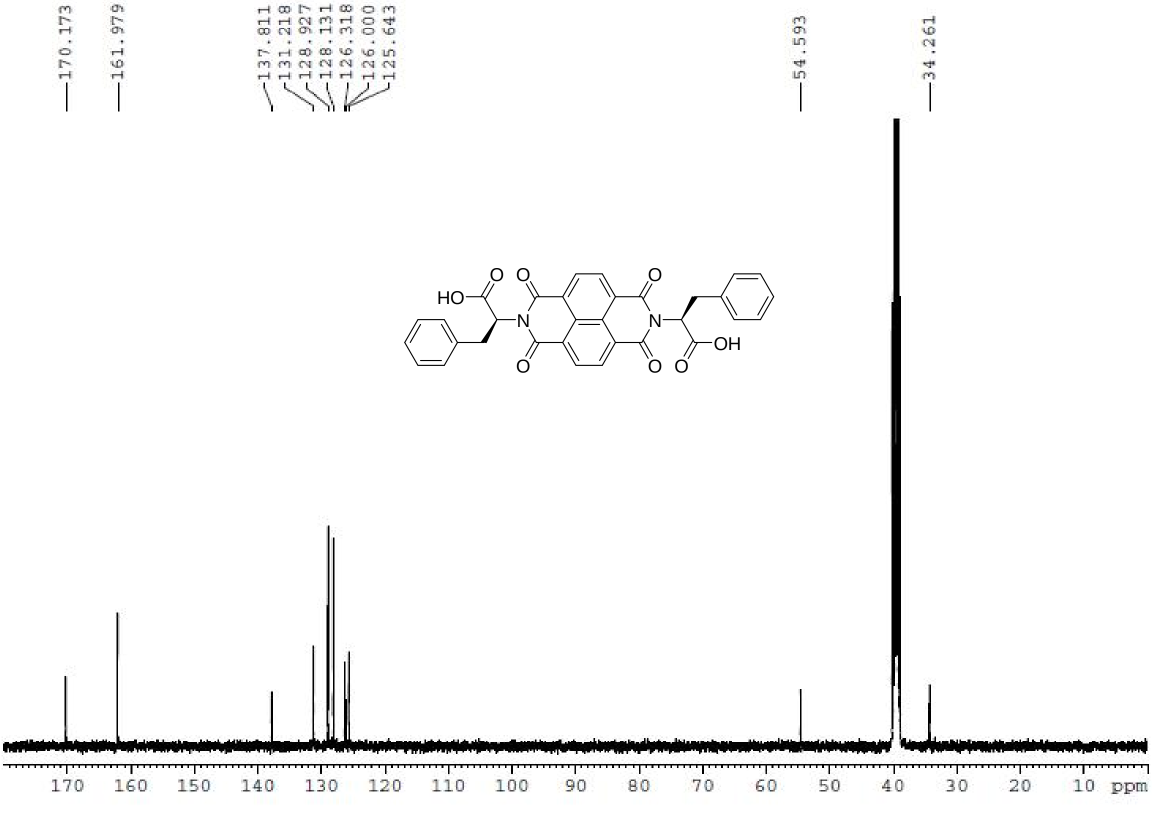

^{1}H NMR spectra (DMSO-*d6*, 400MHz) of D-phenylalanine appended NDI

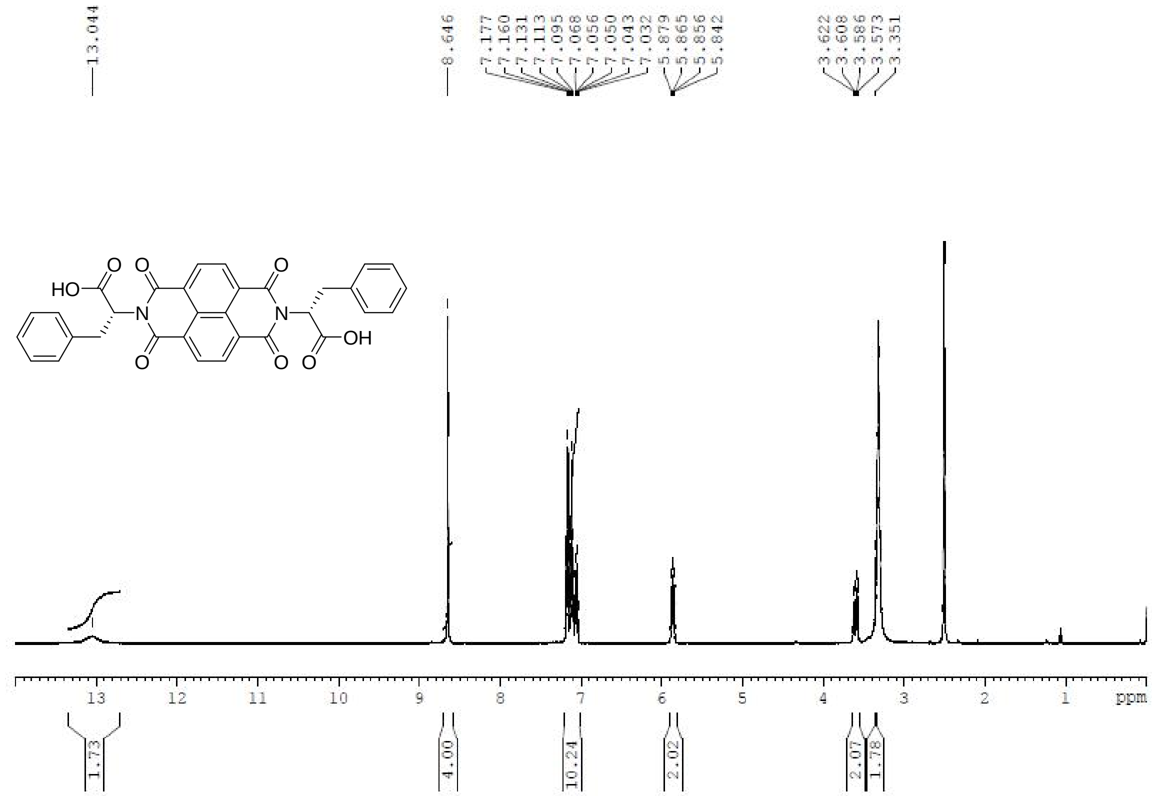

^{13}C NMR spectra (DMSO-*d6*, 100MHz) of D-phenylalanine appended NDI

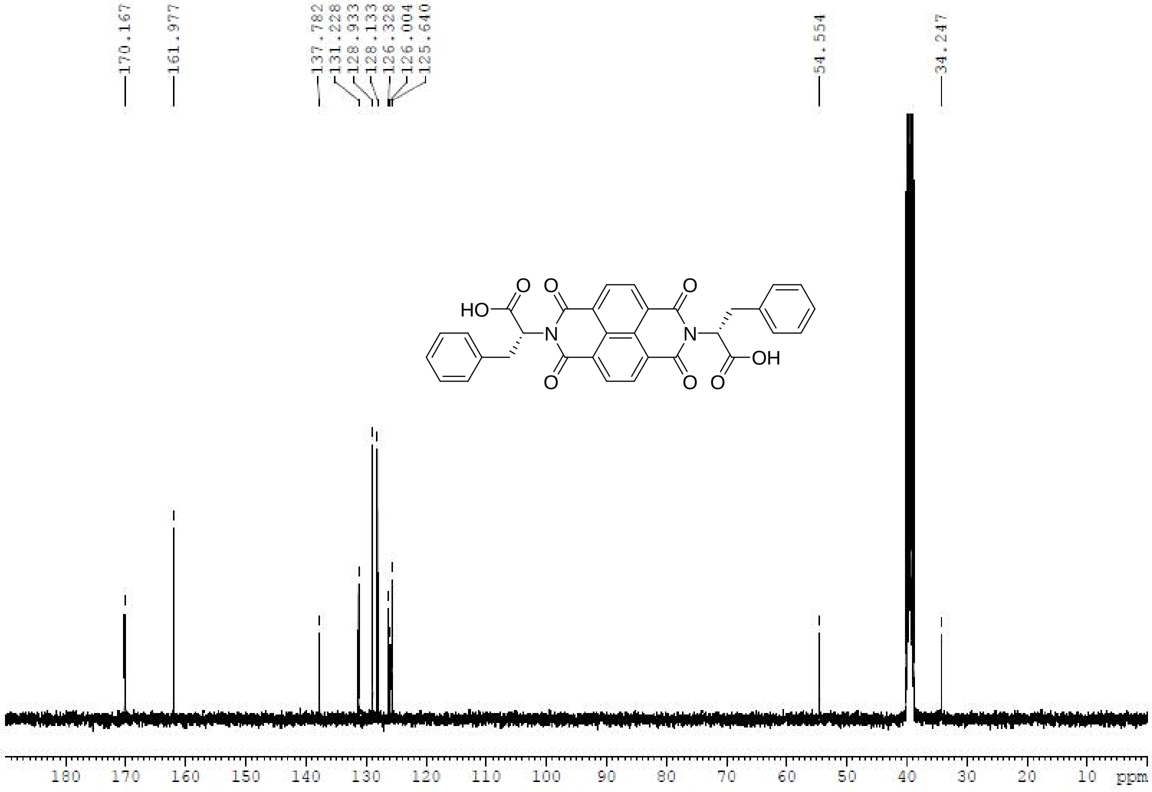

^{1}H NMR spectra (DMSO-*d6*, 400MHz) of glycine appended NDI

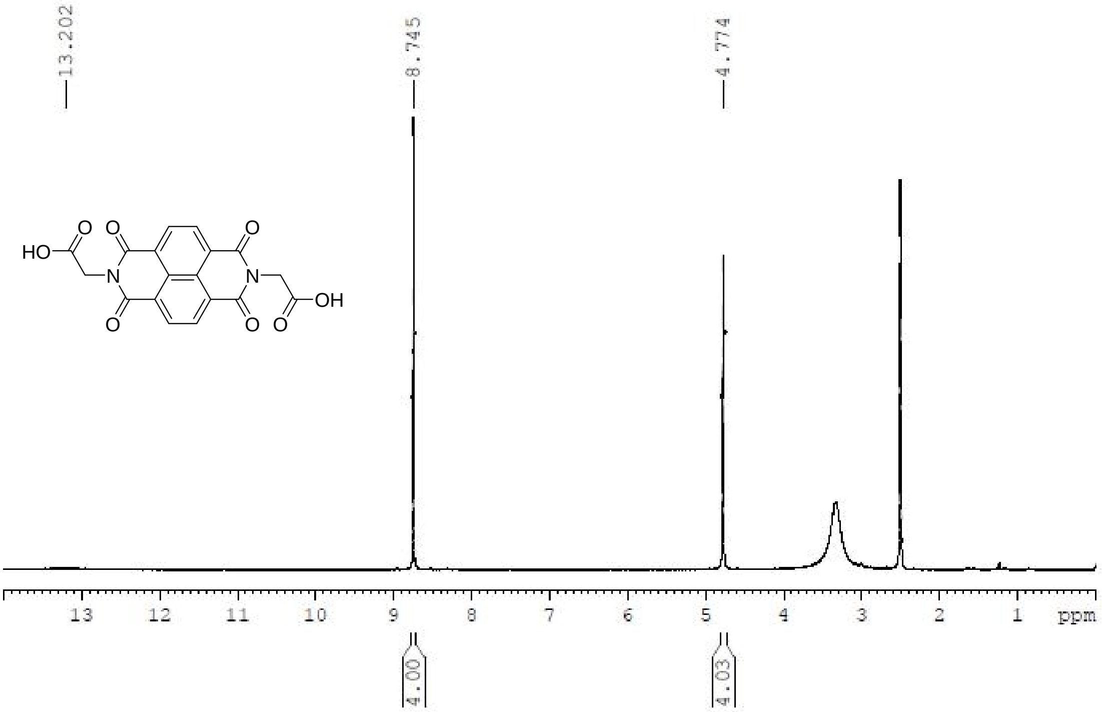

^{13}C NMR spectra (DMSO-*d6*, 100MHz) of glycine appended NDI

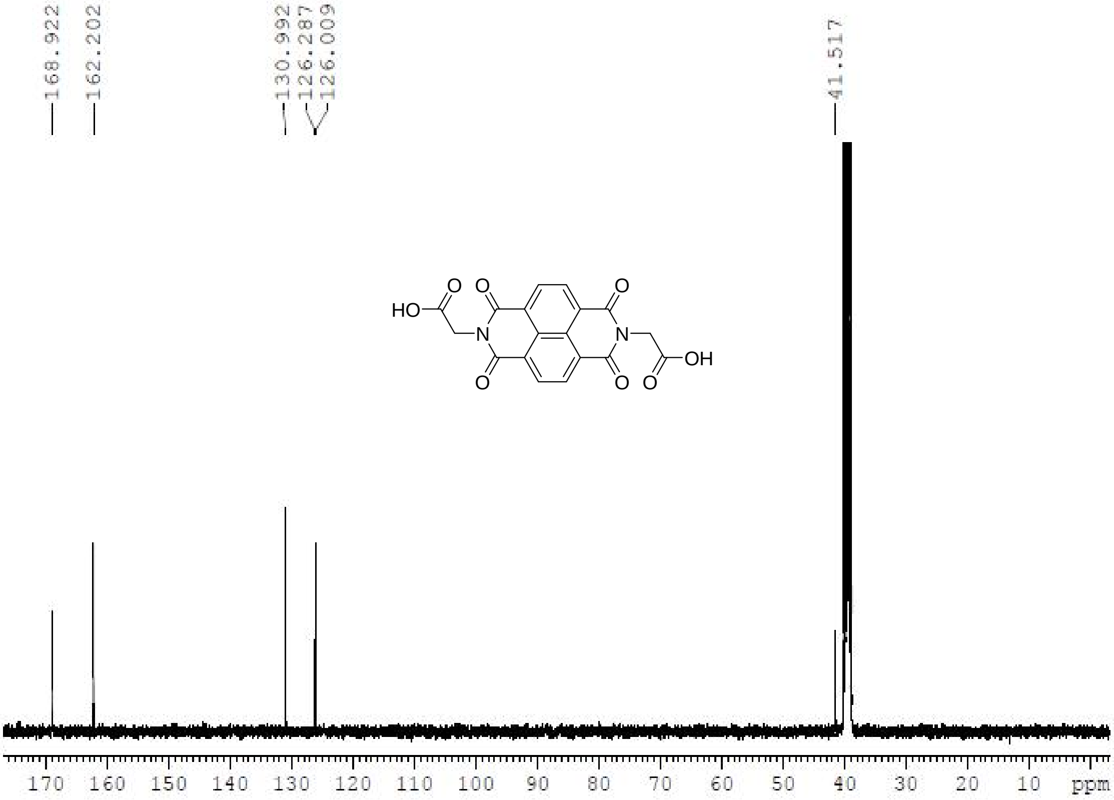

^{1}H NMR spectra ($CDCl_3$, 400MHz) of **LL**

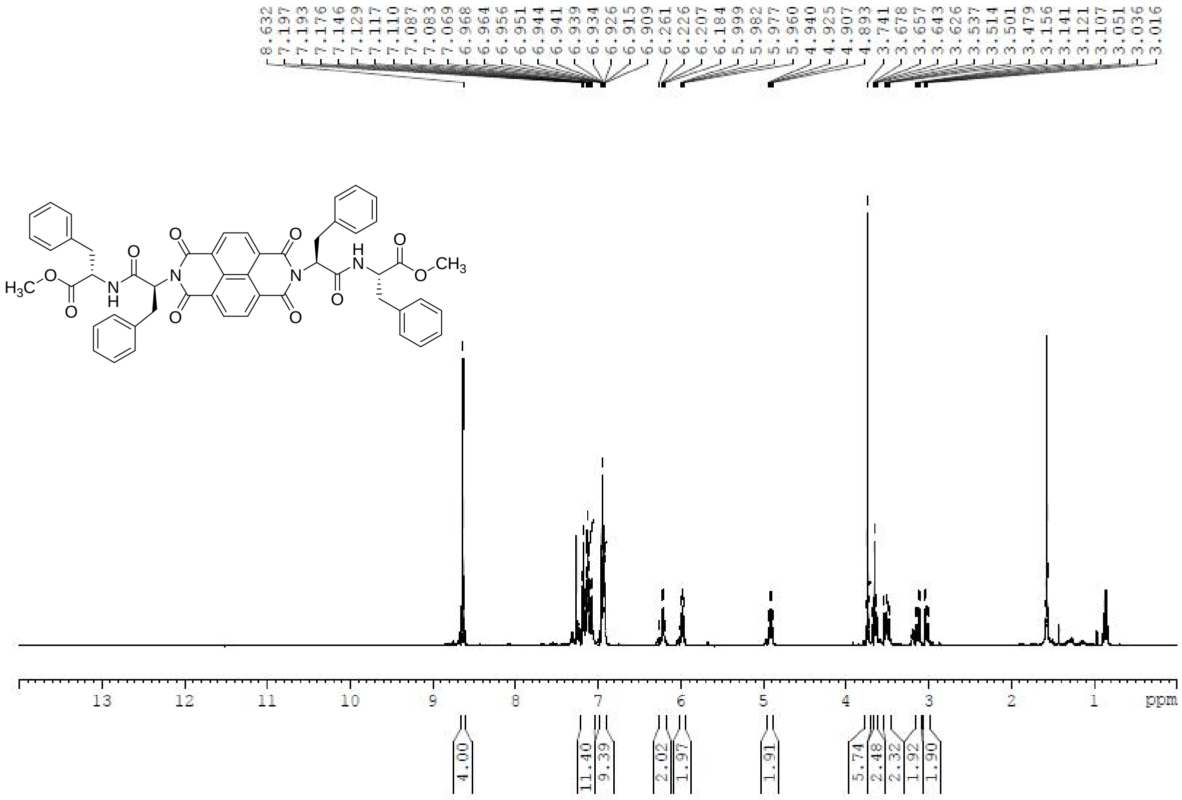

^{13}C NMR spectra ($CDCl_3$, 100MHz) of **LL**

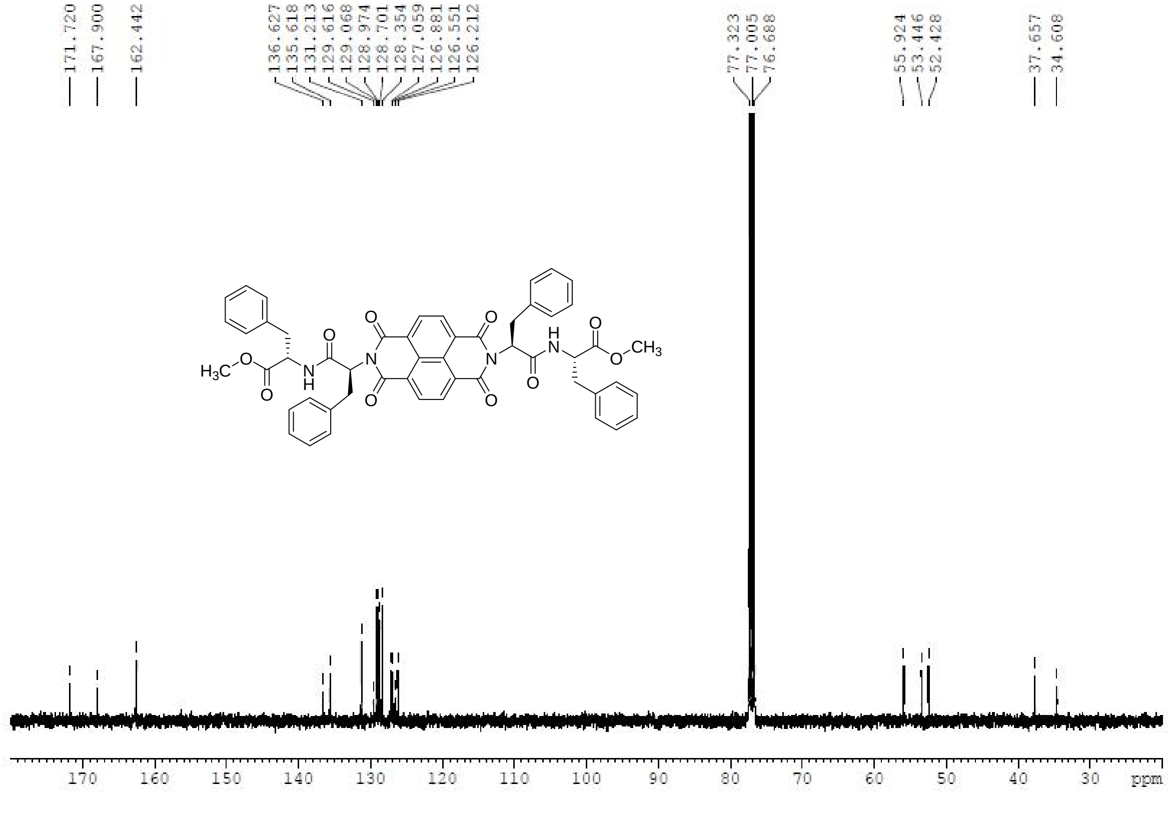

^{1}H NMR spectra ($CDCl_3$, 400MHz) of **DD**

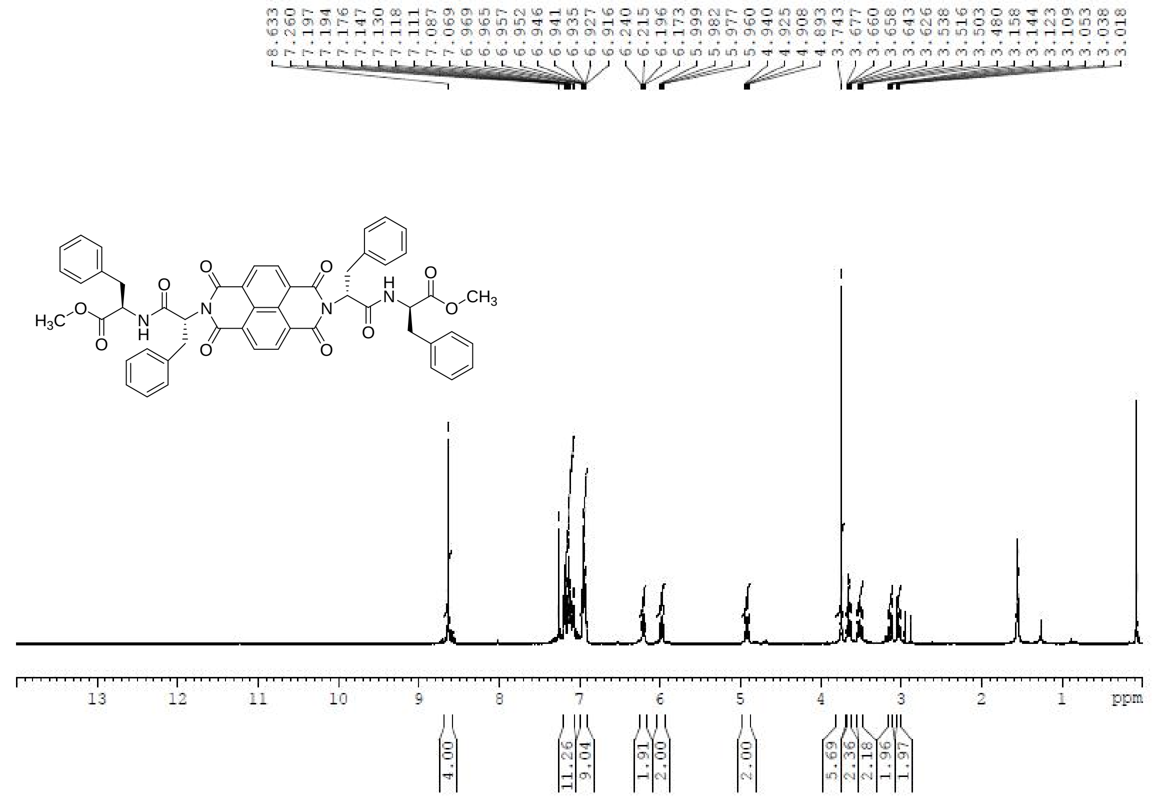

^{13}C NMR spectra ($CDCl_3$, 100MHz) of **DD**

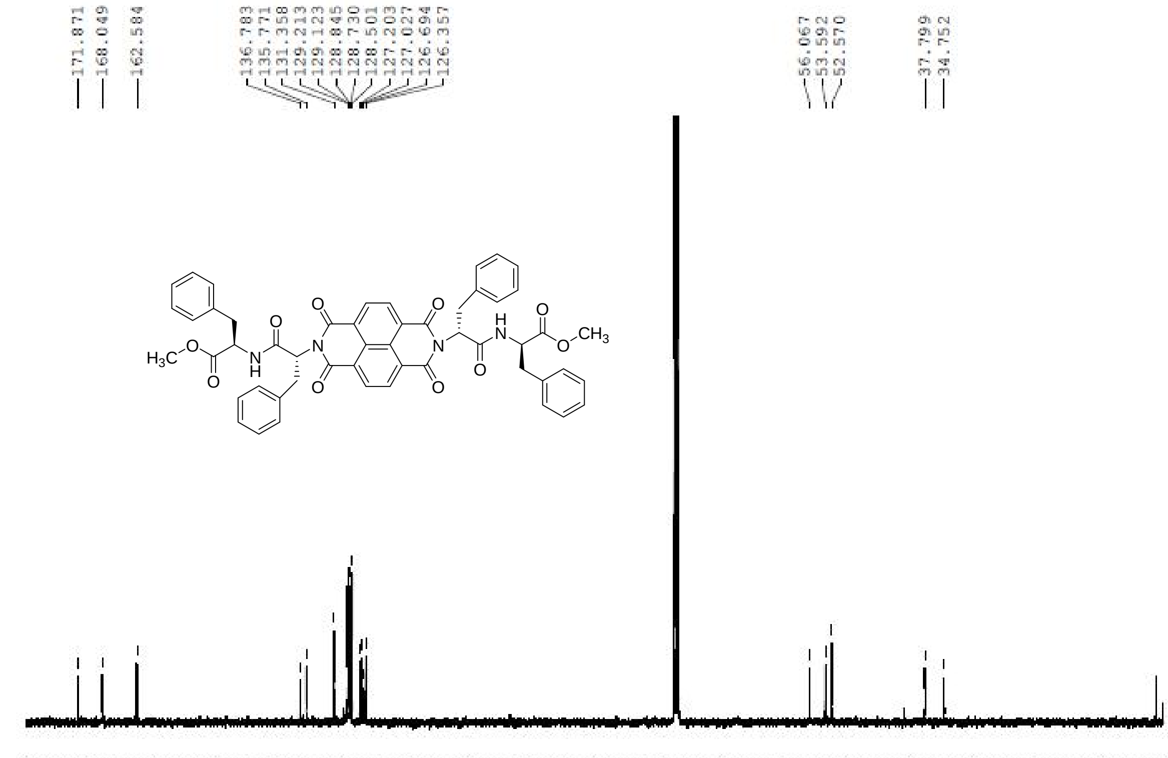

^{1}H NMR spectra (*$CDCl_3$*, 400MHz) of **LD**

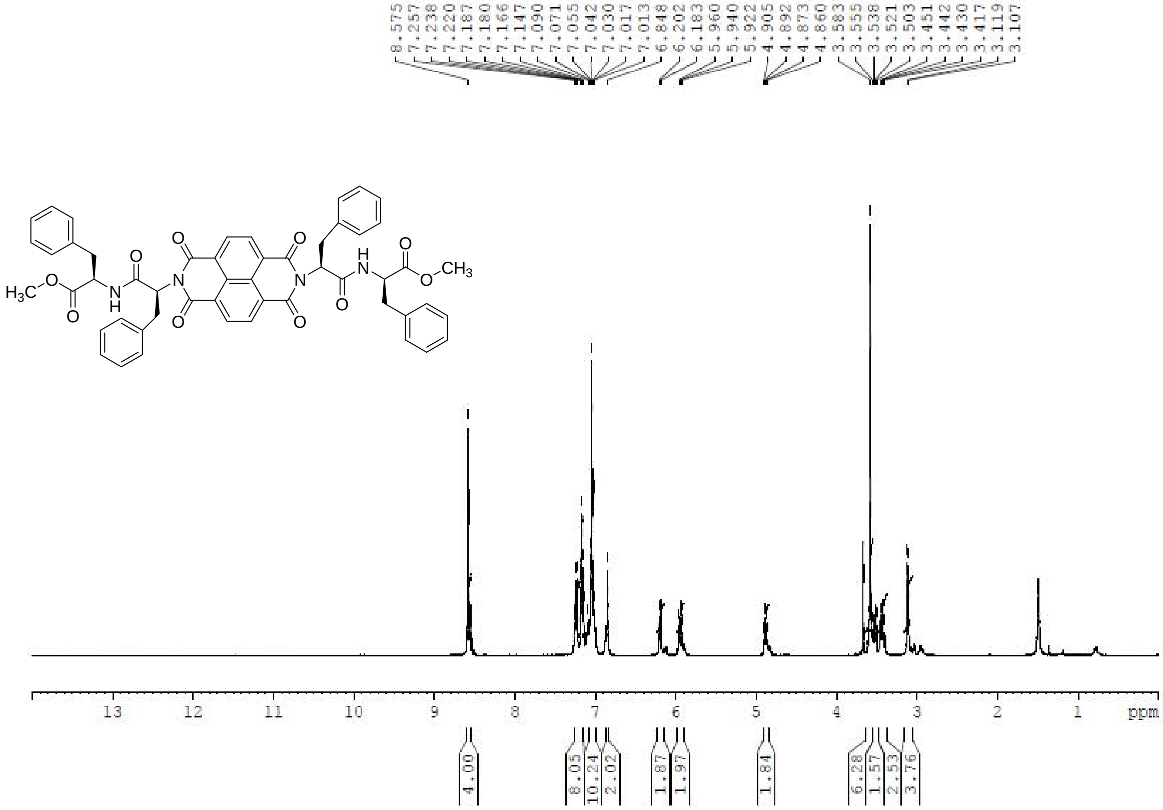

^{13}C NMR spectra (*$CDCl_3$*, 100MHz) of **LD**

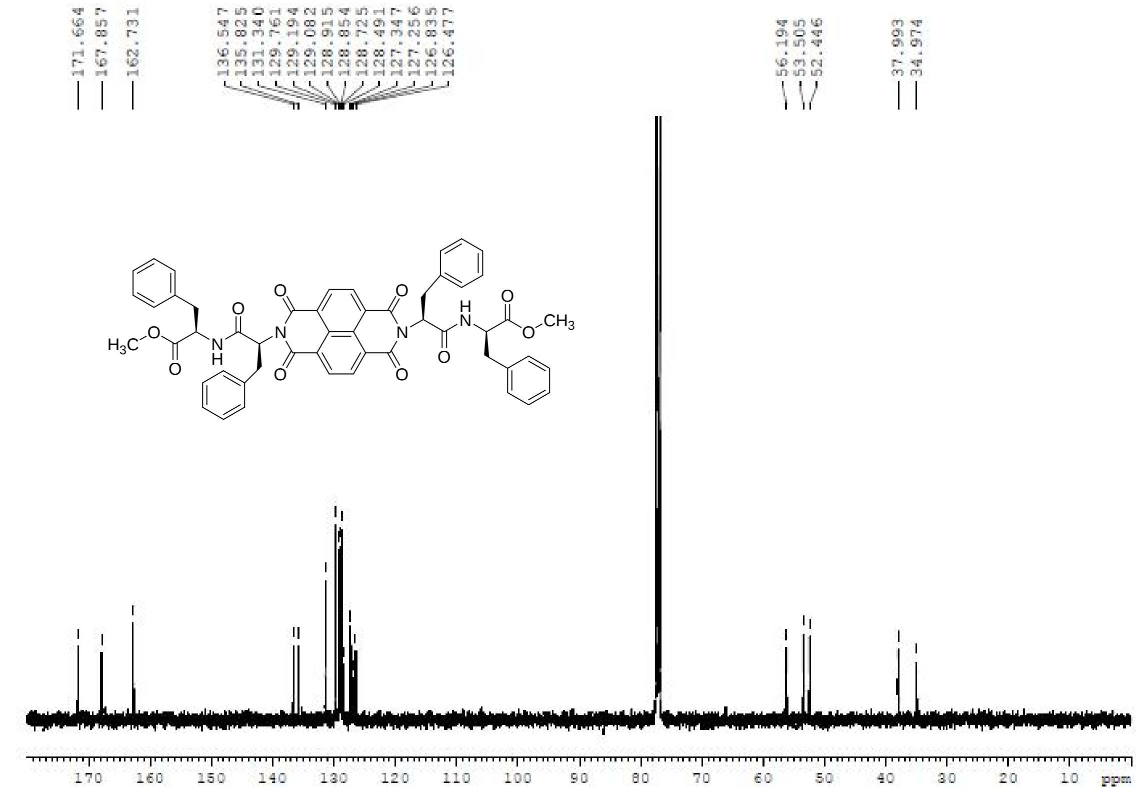

^{1}H NMR spectra (*CDCl$_3$*, 400MHz) of **DL**

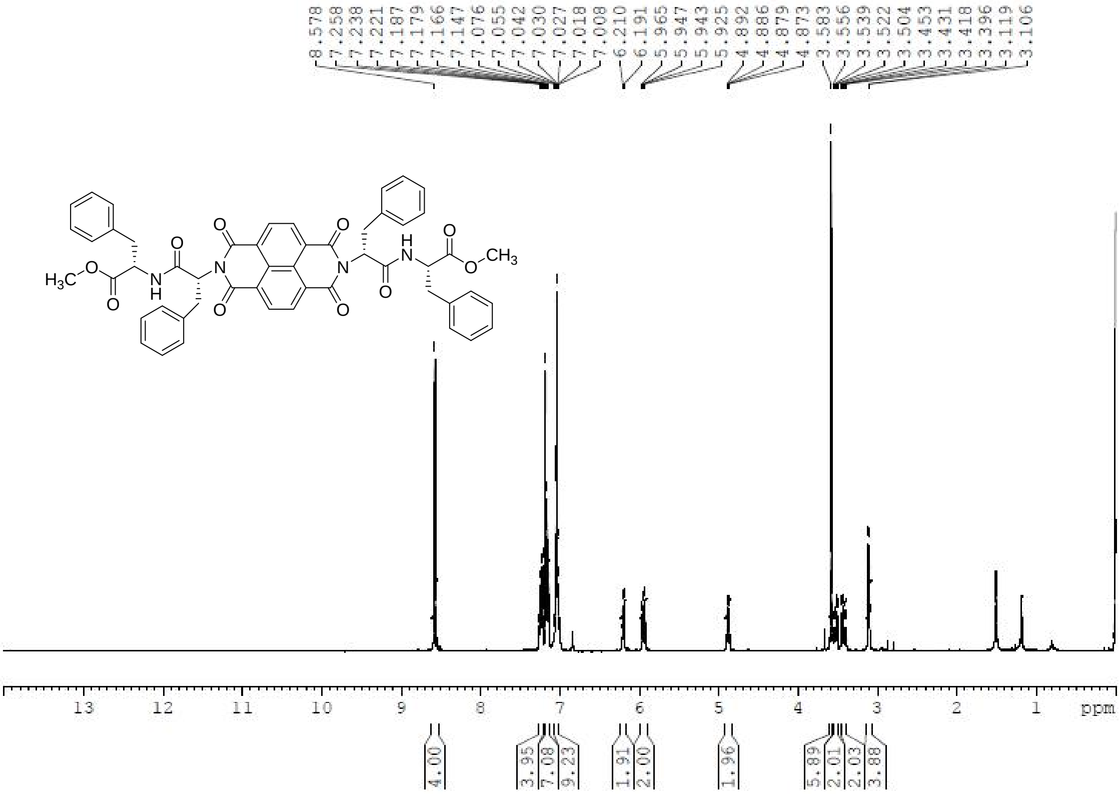

^{13}C NMR spectra (*CDCl$_3$*, 100MHz) of **DL**

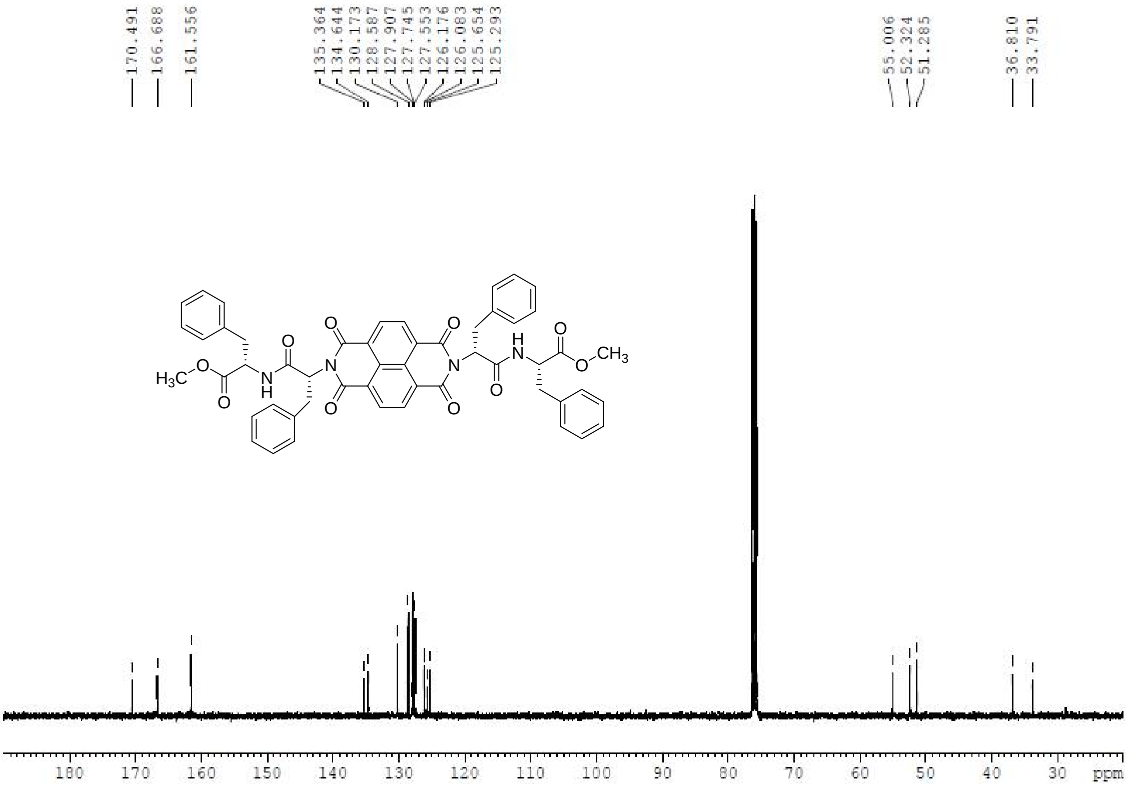

^{1}H NMR spectra (DMSO-*d6*, 400MHz) of **AA**

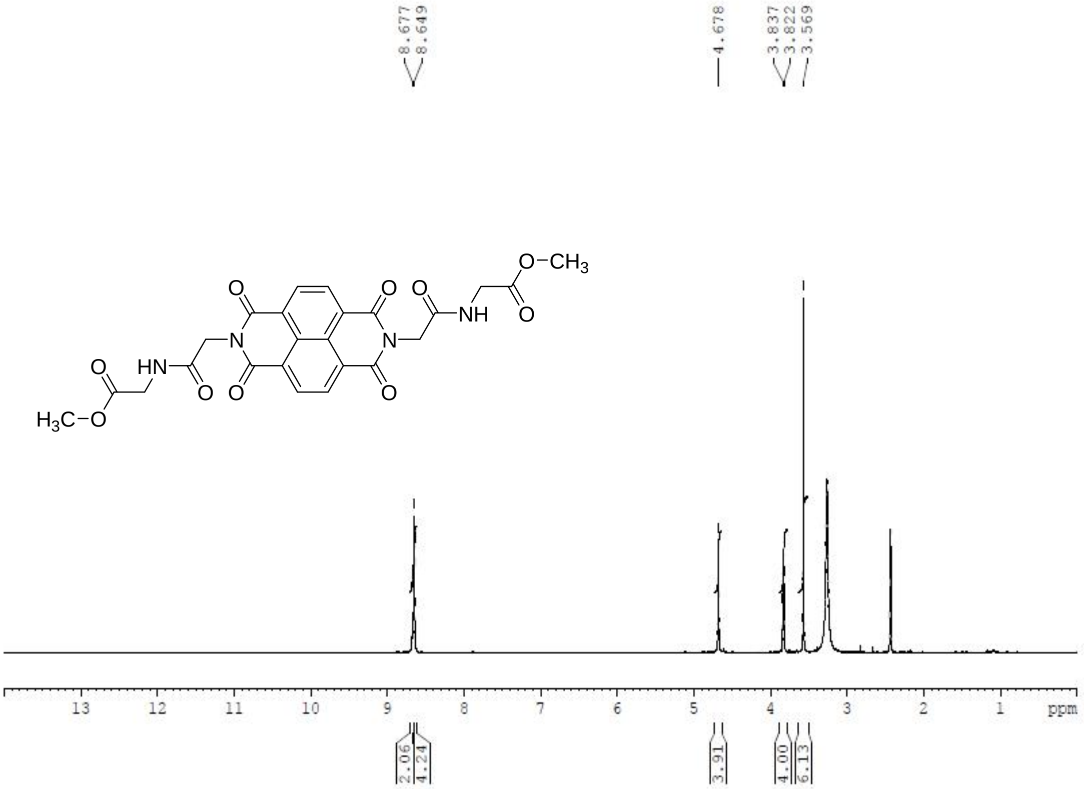

^{13}C NMR spectra (DMSO-*d6*, 100MHz) of **AA**

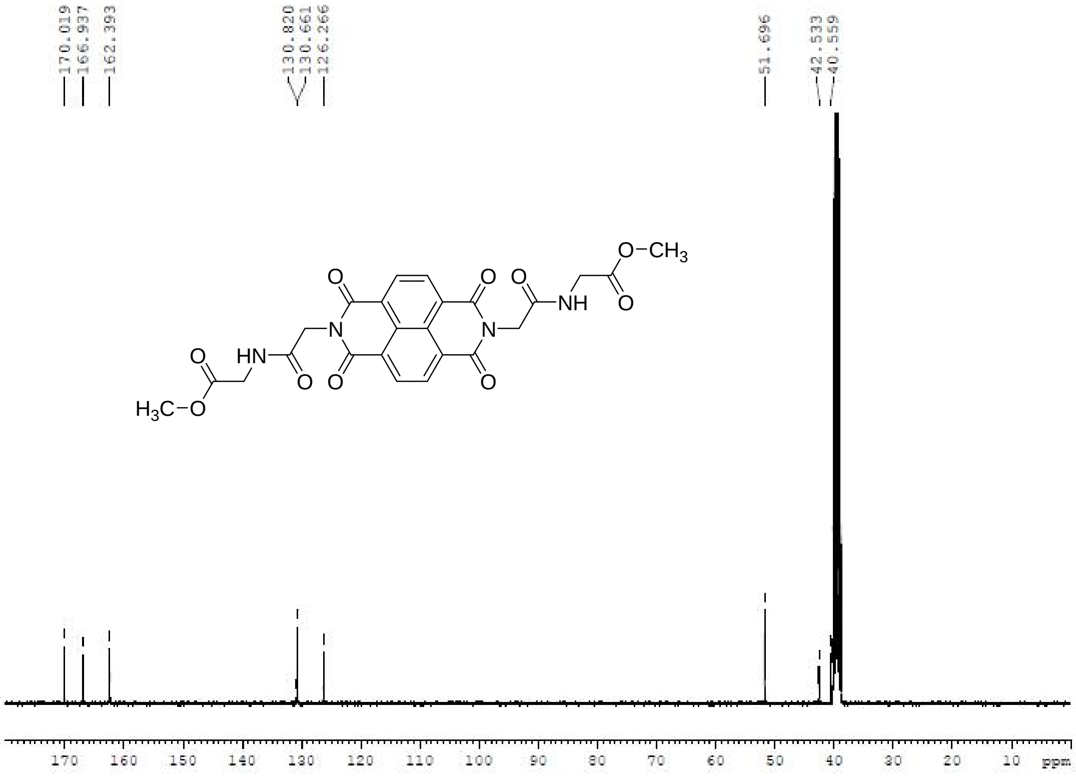

^{1}H NMR spectra (DMSO-*d6*, 400 MHz) of **4**

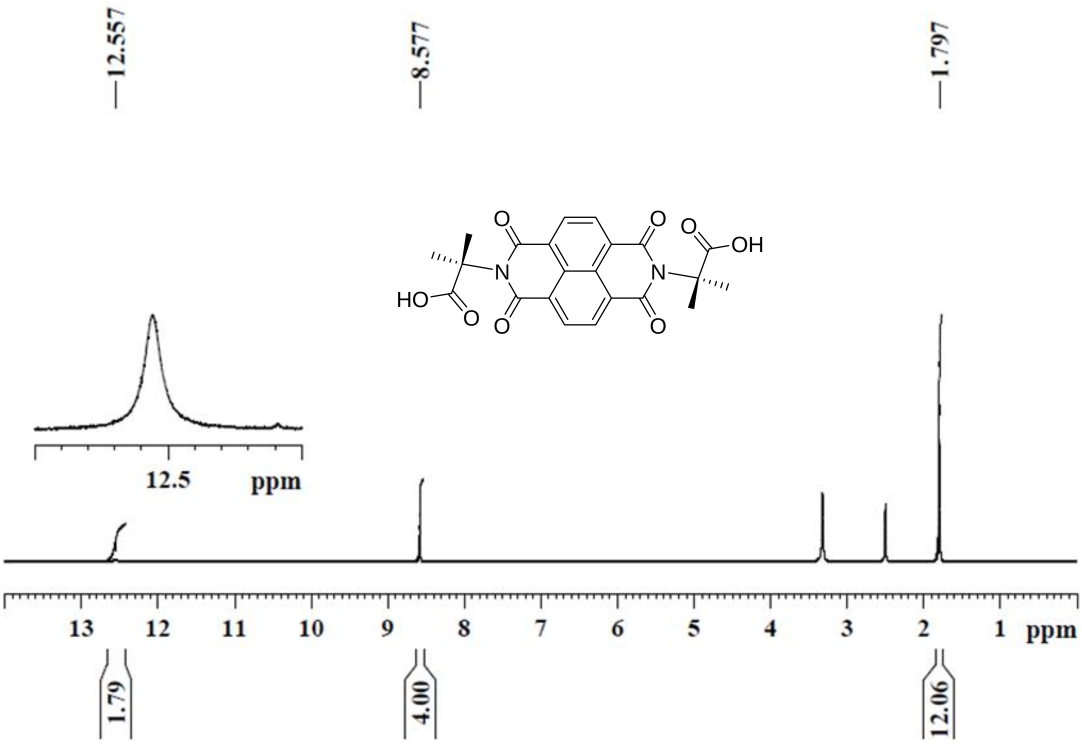

^{1}H NMR spectra (DMSO-*d6*, 400 MHz) of **5**

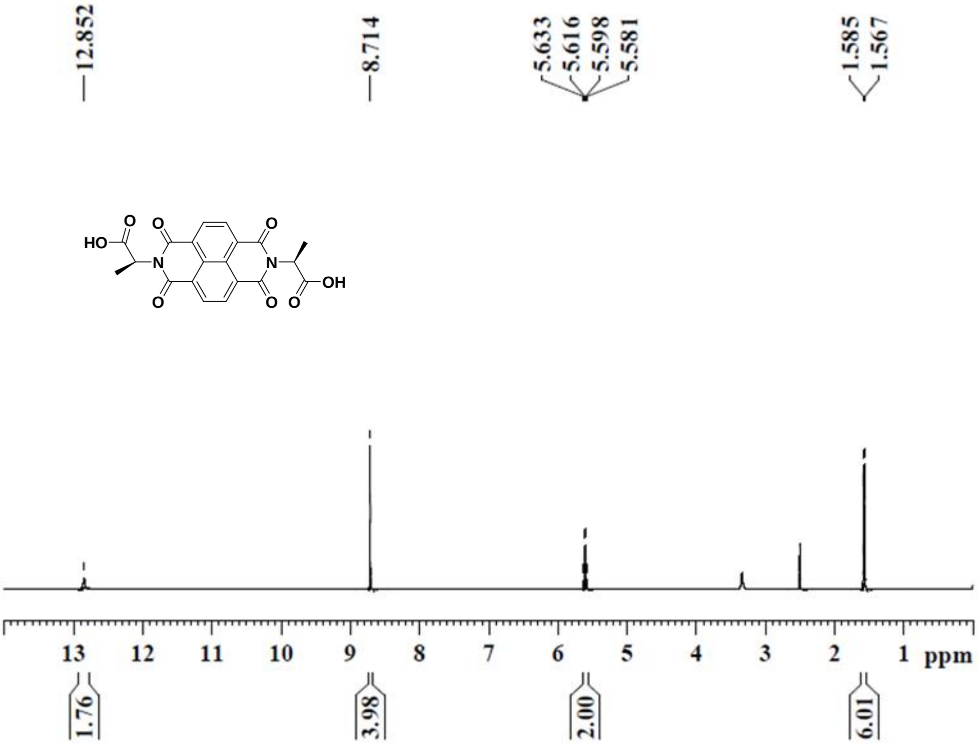

^{1}H NMR spectra (DMSO-*d6*, 400 MHz) of **6**

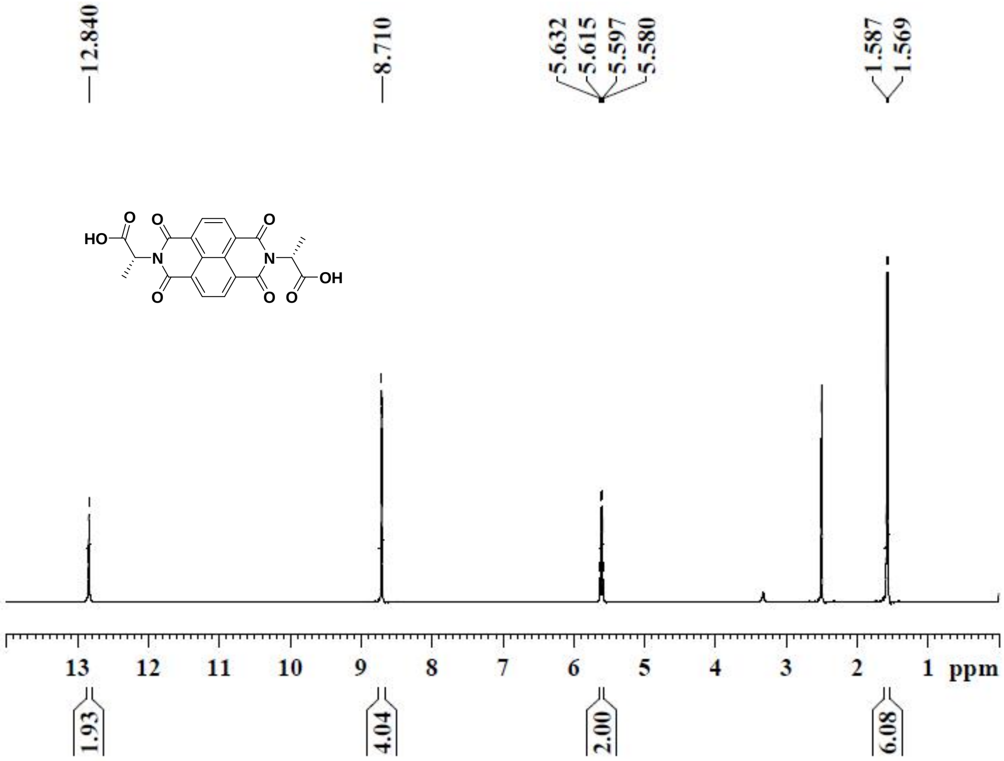

^{1}H NMR spectra (*$CDCl_3$*, 400 MHz) of **1**

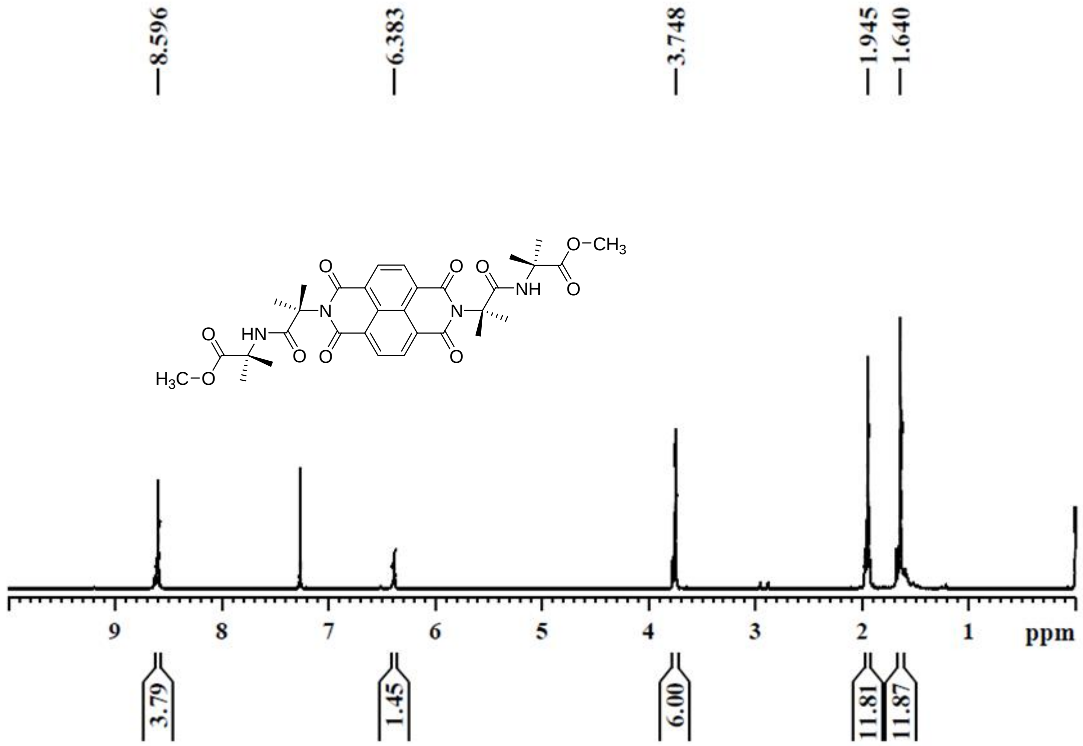

^{13}C NMR spectra (*$CDCl_3$*, 100 MHz) of **1**

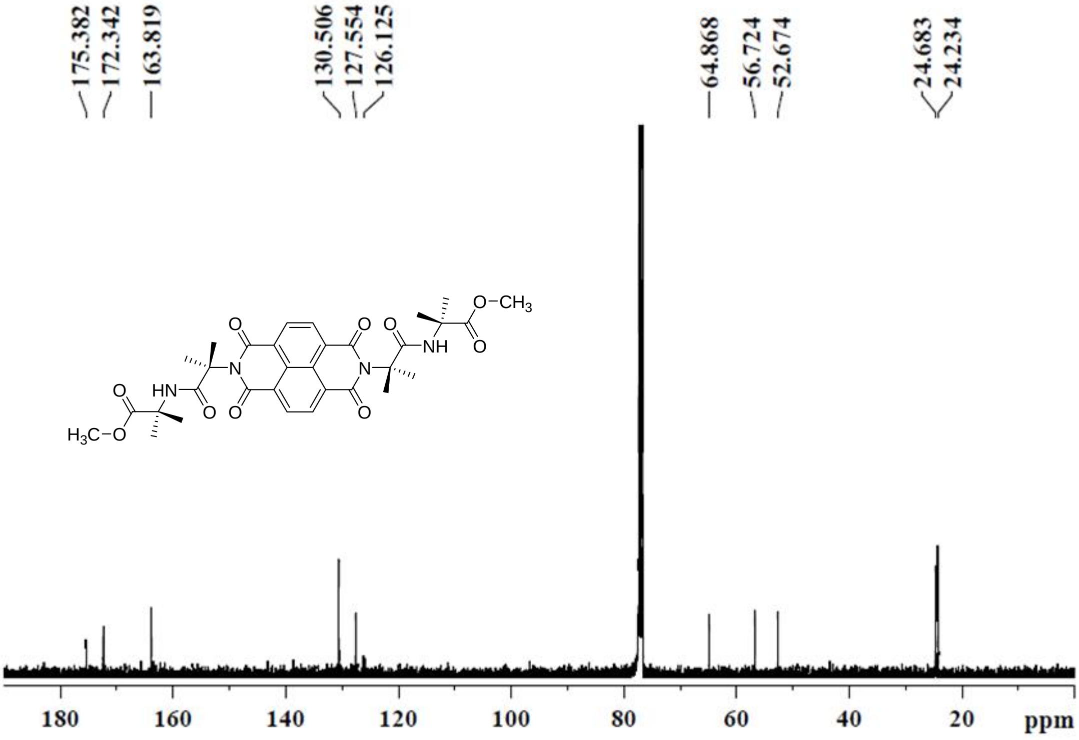

^{1}H NMR spectra (*DMSO-d$_6$*, 400 MHz) of **2**

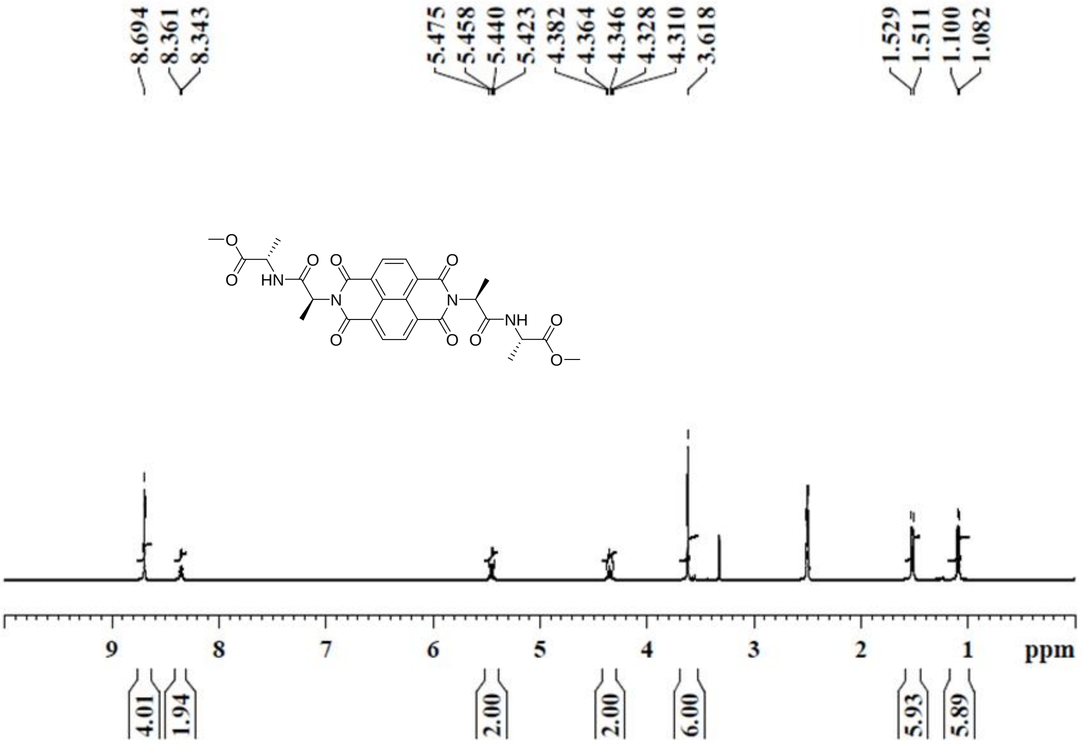

^{13}C NMR spectra (*DMSO-d$_6$*, 100 MHz) of **2**

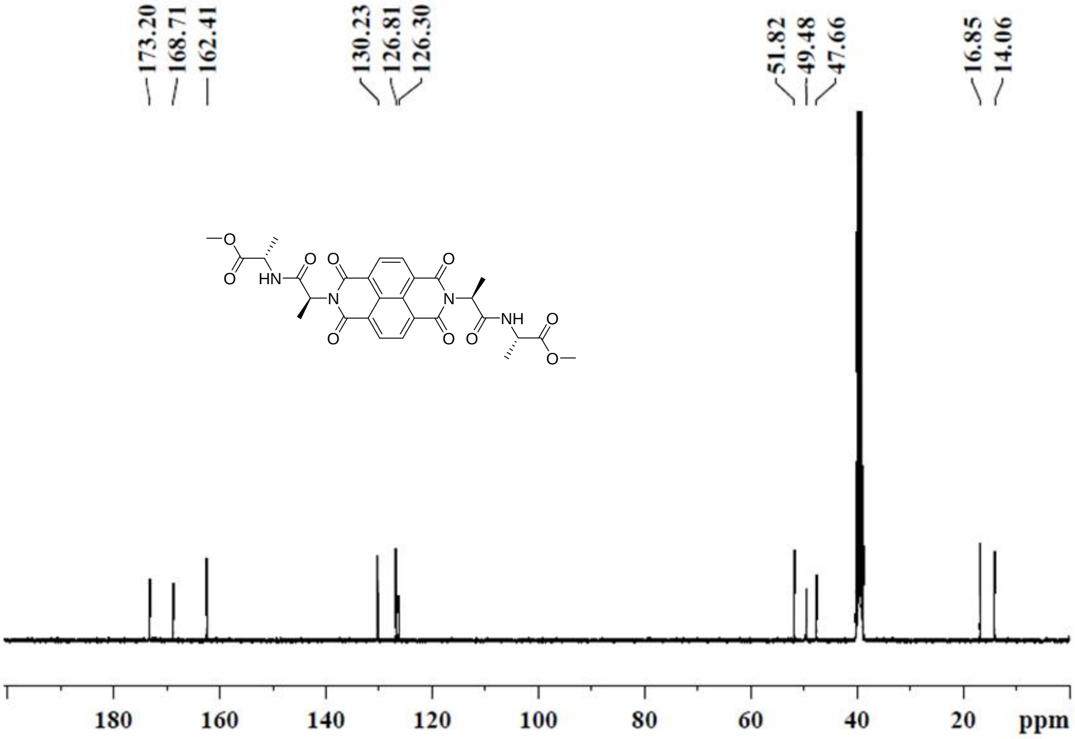

^{1}H NMR spectra (*DMSO-d_6*, 400 MHz) of **3**

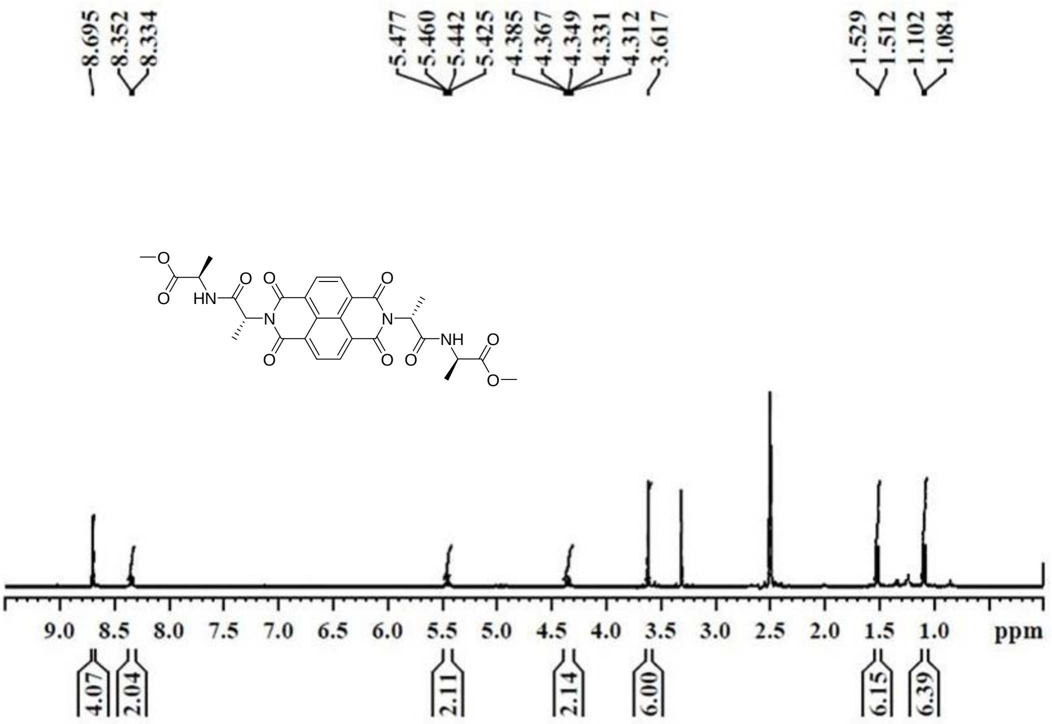

^{13}C NMR spectra (*DMSO-d_6*, 100 MHz) of **3**

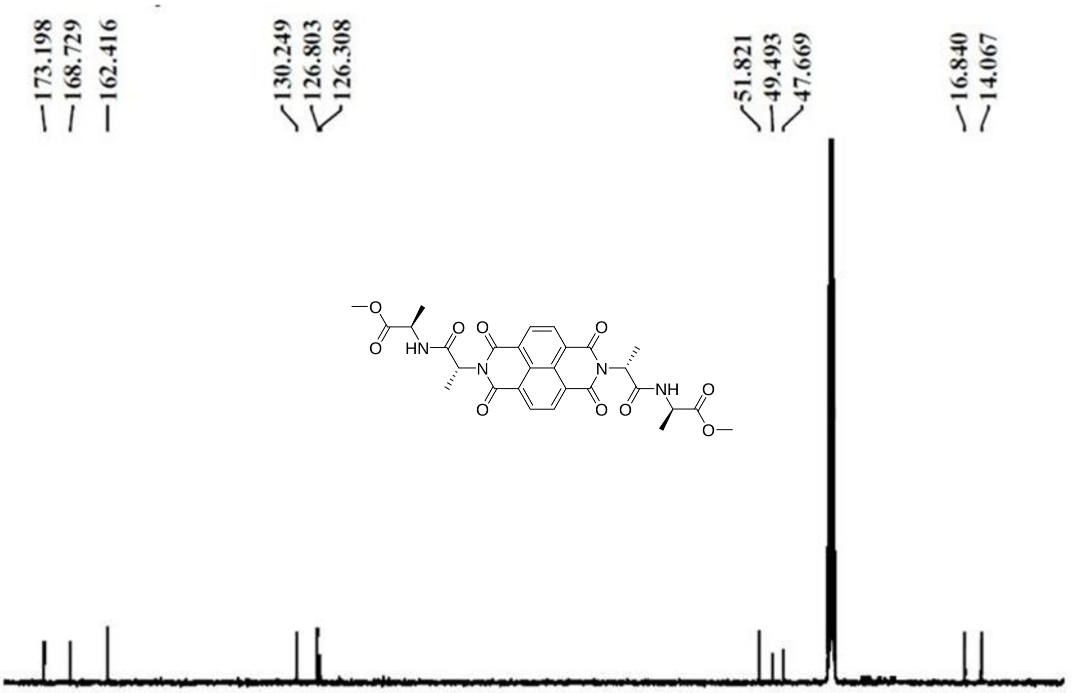

MALDI-TOF-MS of **LL**

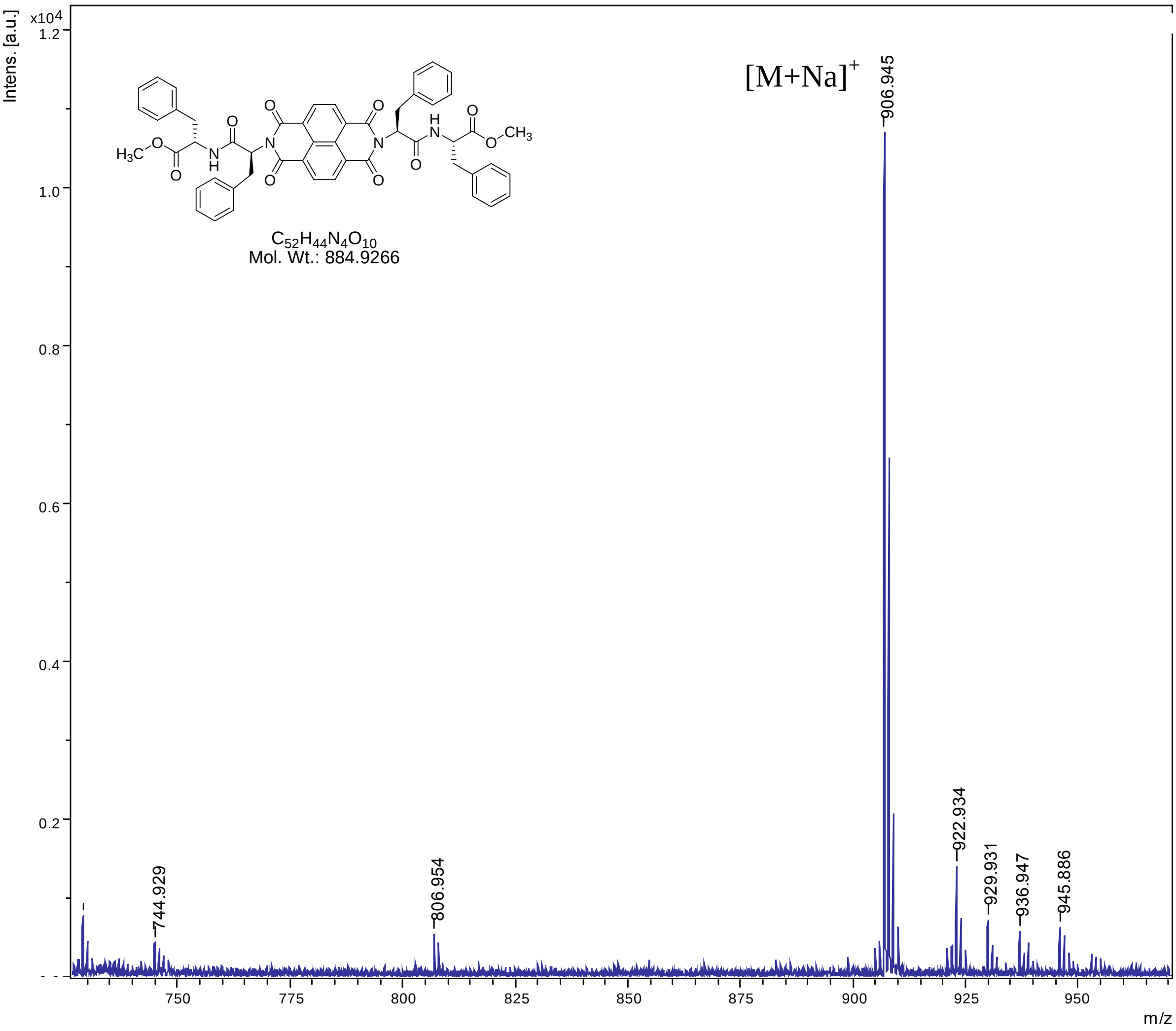

MALDI-TOF-MS of **DD**

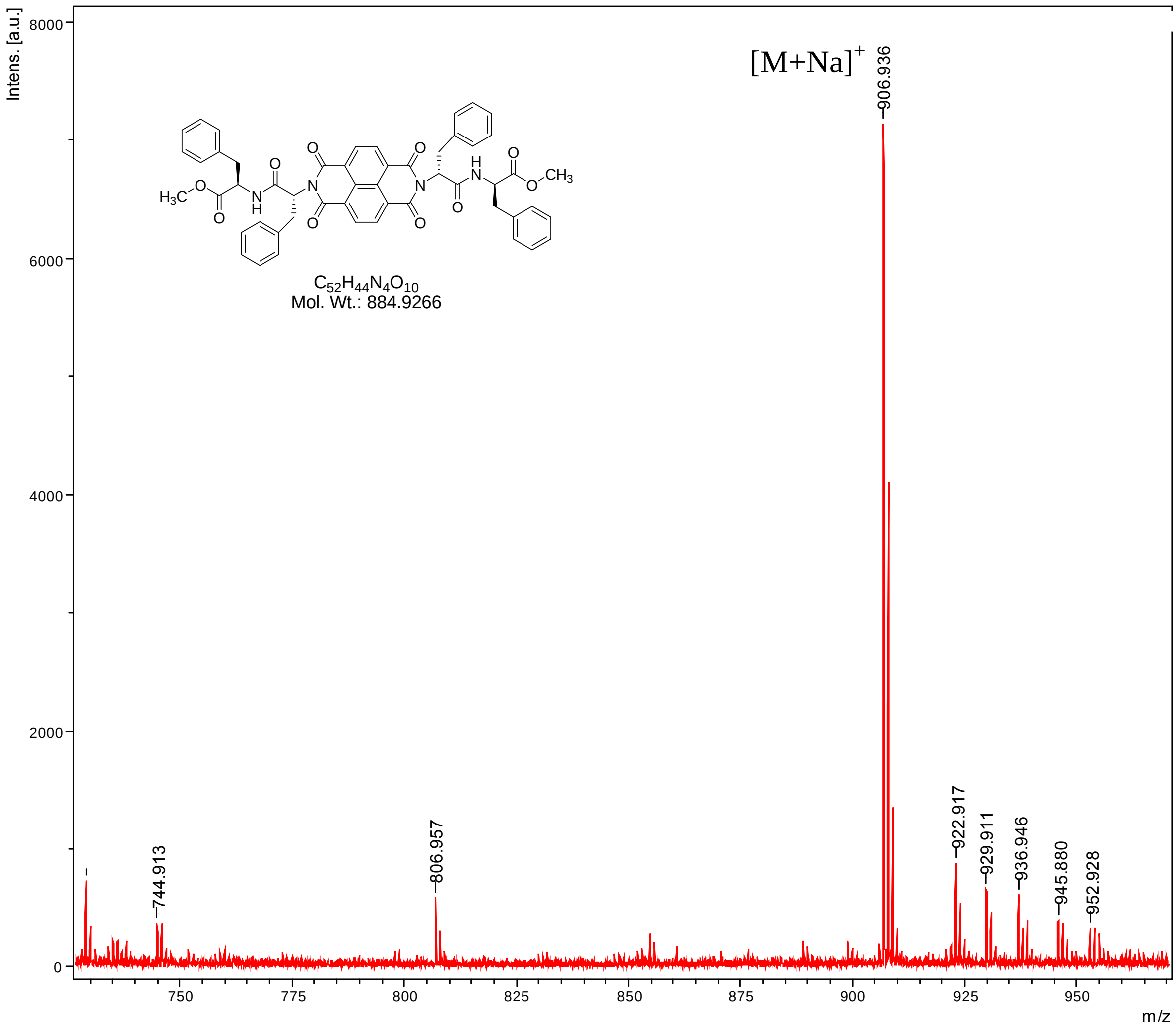

MALDI-TOF-MS of **LD**

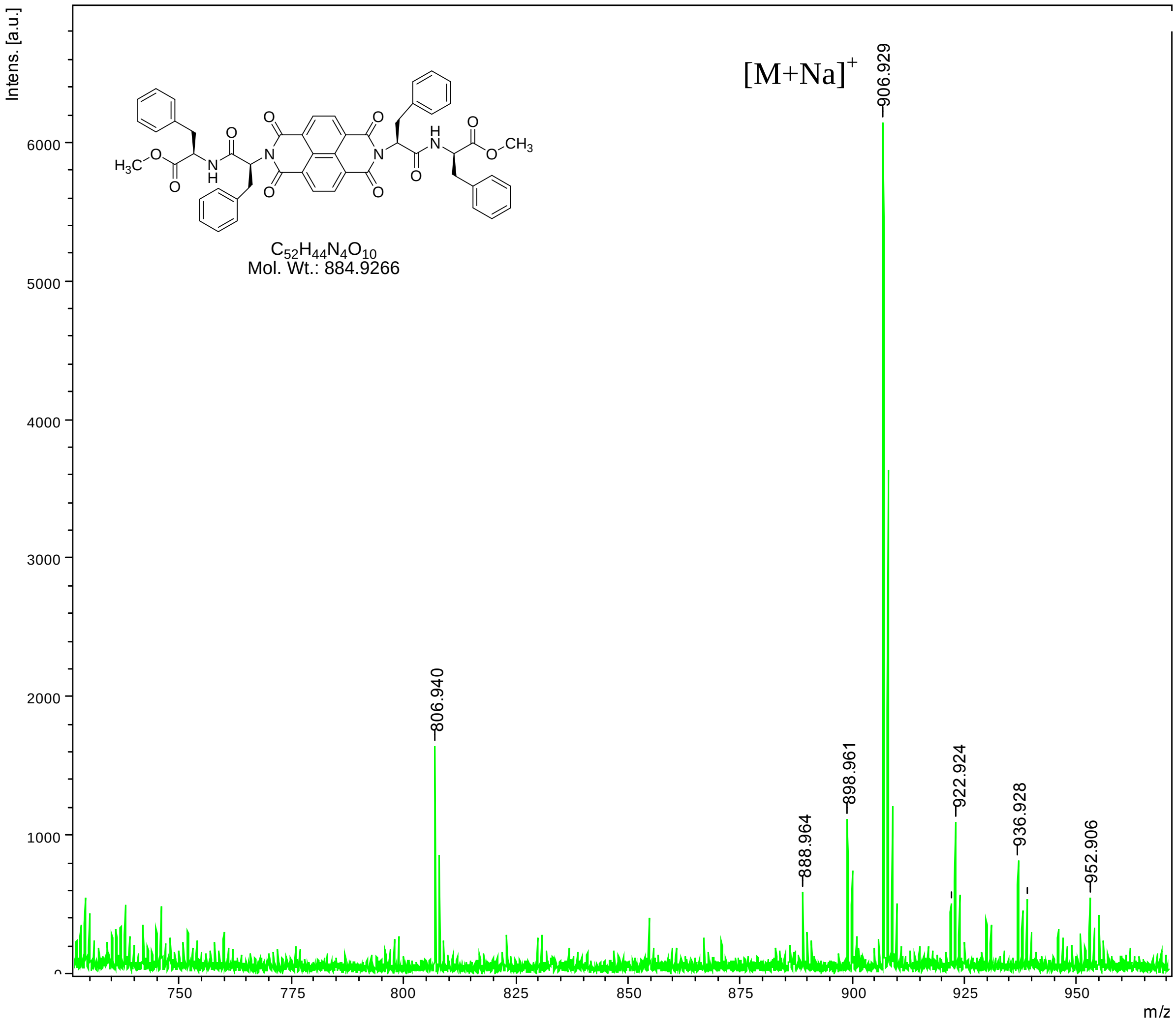

MALDI-TOF-MS of **DL**

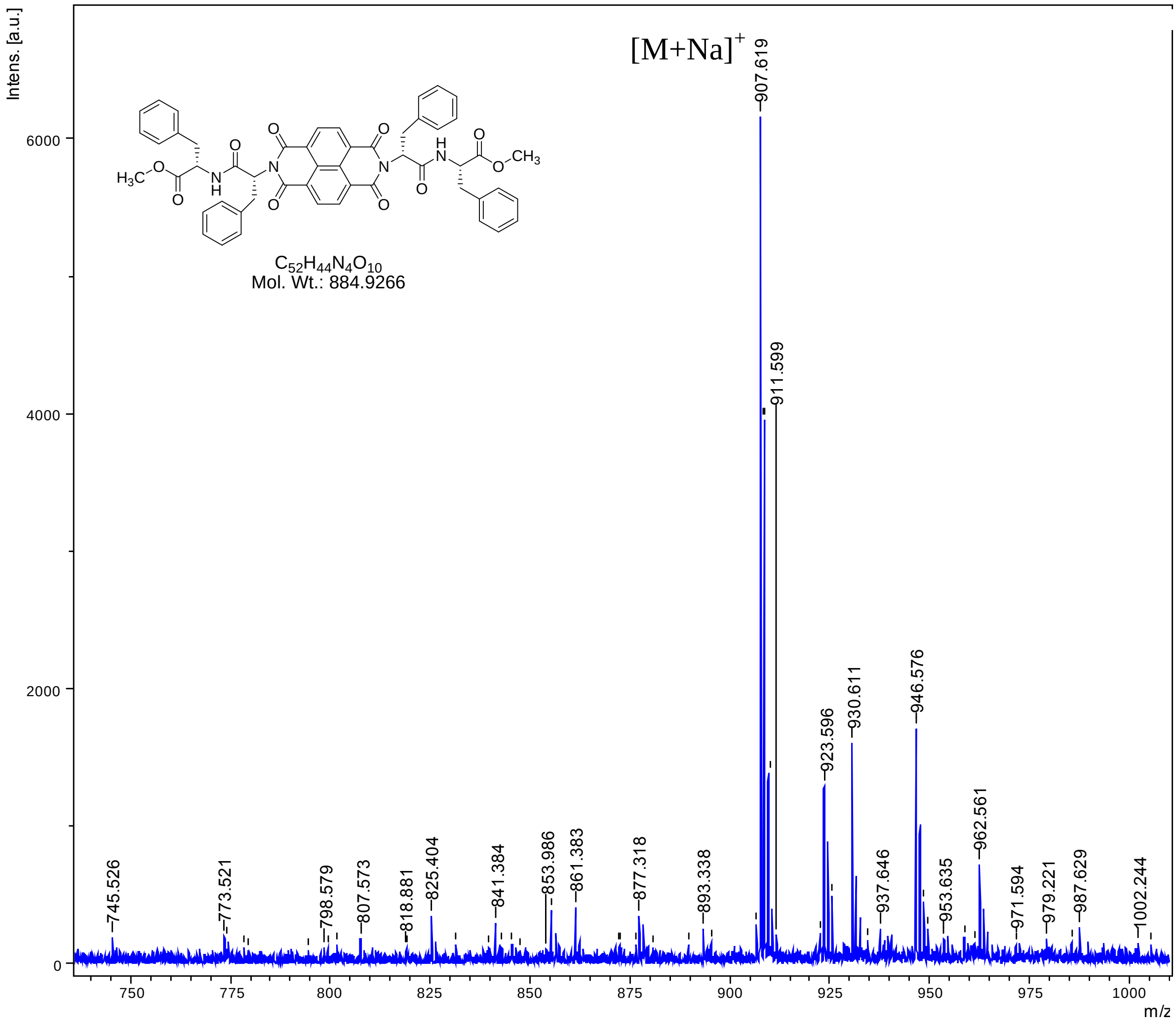

MALDI-TOF-MS of **AA**

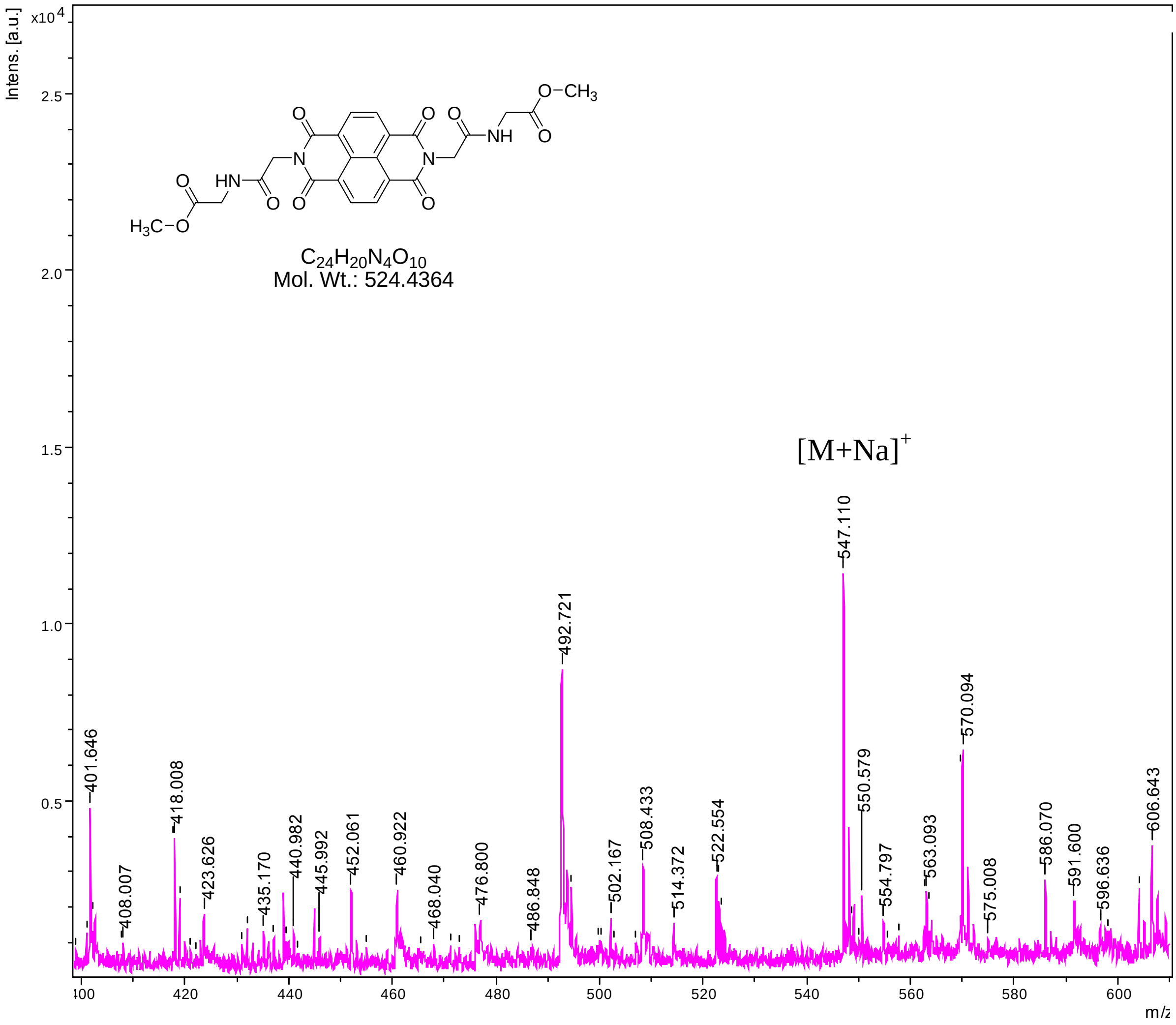

HRMS of **1**

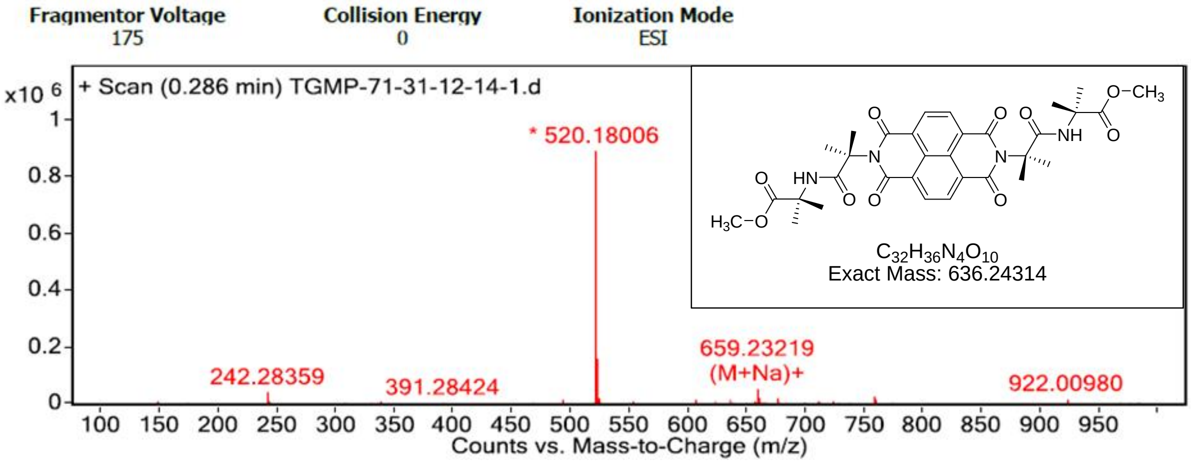

HRMS of **2**

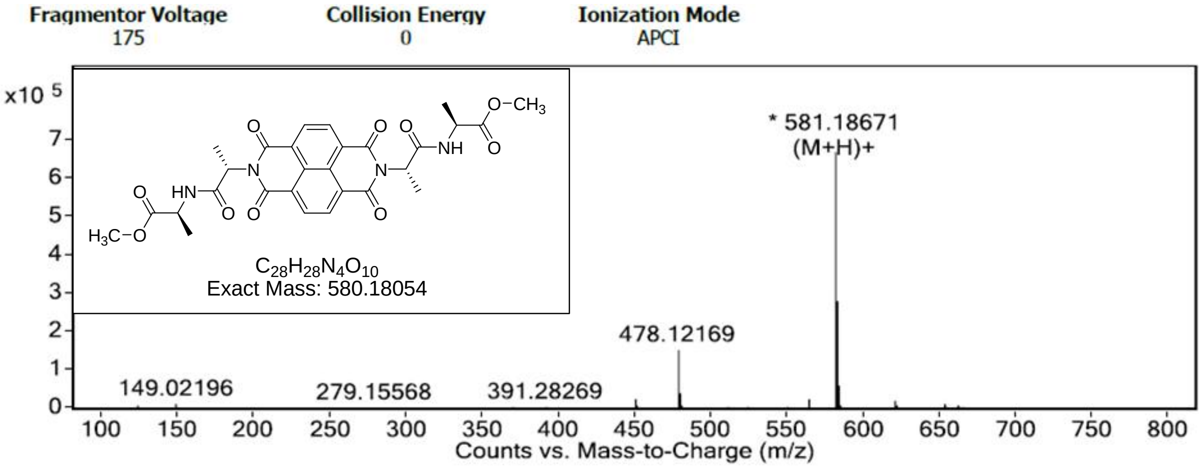

HRMS of **3**

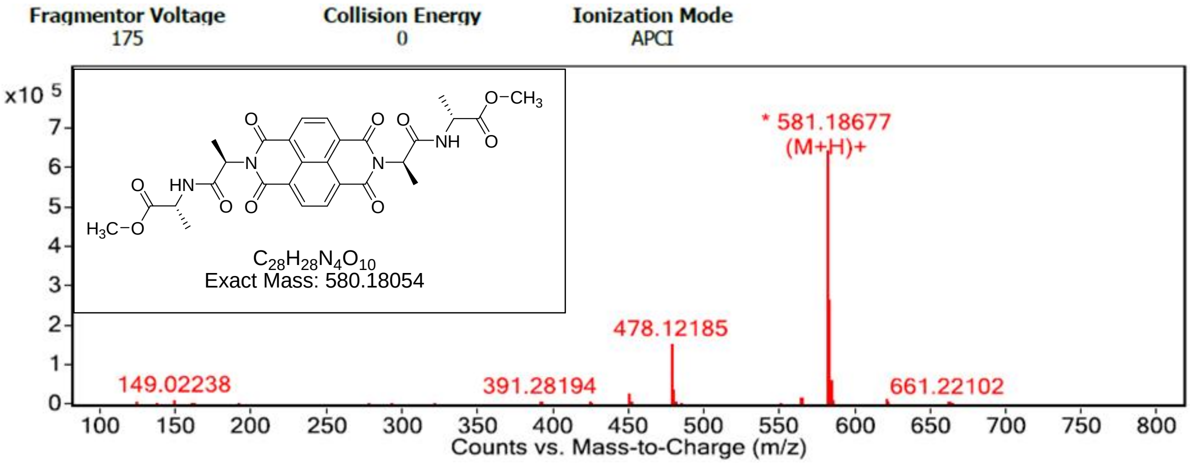

4.2.6 References

1. Lehn, J.-M., Supramolecular Chemistry, Concepts and Perspectives. *Wiley-VCH, Weinheim* **1995**.

2. Reinhoudt, D. N.; Crego-Calama, M., Synthesis beyond the molecule. *Science* **2002,** *295*, 2403-2407.

3. Schmuck, C., Molecules with helical structure: How to build a molecular spiral staircase. *Angew. Chem. Int. Ed.* **2003,** *42*, 2448-2452.

4. Borovkov, V. V.; Hembury, G. A.; Inoue, Y., Origin, Control, and Application of Supramolecular Chirogenesis in Bisporphyrin-Based Systems. *Acc. Chem. Res.* **2004,** *37*, 449-459.

5. Mateos-Timoneda, M. A.; Crego-Calama, M.; Reinhoudt, D. N., Supramolecular chirality of self-assembled systems in solution. *Chem. Soc. Rev.* **2004,** *33*, 363-372.

6. Palmans, A. R. A.; Meijer, E. W., Amplification of chirality in dynamic supramolecular aggregates. *Angew. Chem. Int. Ed.* **2007,** *46*, 8948-8968.

7. Hembury, G. A.; Borovkov, V. V.; Inoue, Y., Chirality-Sensing Supramolecular Systems. *Chem. Rev.* **2008,** *108*, 1-73.

8. Gottarelli, G.; Lena, S.; Masiero, S.; Pieraccini, S.; Spada, G. P., The use of circular dichroism spectroscopy for studying the chiral molecular self-assembly: an overview. *Chirality* **2008,** *20*, 471-485.

9. Ziegler, M.; Davis, A. V.; Johnson, D. W.; Raymond, K. N., Supramolecular chirality: A reporter of structural memory. *Angew. Chem. Int. Ed.* **2003,** *42*, 665-668.

10. de Jong, J. J. D.; Lucas, L. N.; Kellogg, R. M.; van Esch, J. H.; Feringa, B. L., Reversible Optical Transcription of Supramolecular Chirality into Molecular Chirality. *Science* **2004,** *304*, 278-281.

11. Anderson, T. W.; Sanders, J. K. M.; Pantos, G. D., The sergeants-and-soldiers effect: chiral amplification in naphthalenediimide nanotubes. *Org. Biomol. Chem.* **2010,** *8*, 4274-4280.

12. Ajayaghosh, A.; Varghese, R.; George, S. J.; Vijayakumar, C., Transcription and amplification of molecular chirality to oppositely biased supramolecular π helices. *Angew. Chem. Int. Ed.* **2006,** *45*, 1141-1144.

13. Green, M. M.; Park, J. W.; Sato, T.; Teramoto, A.; Lifson, S.; Selinger, R. L. B.; Selinger, J. V., The macromolecular route to chiral amplification. *Angew. Chem. Int. Ed.* **1999,** *38*, 3139-3154.

14. Green, M. M.; Reidy, M. P.; Johnson, R. D.; Darling, G.; O'Leary, D. J.; Willson, G., Macromolecular stereochemistry: the out-of-proportion influence of optically active comonomers on the conformational characteristics of polyisocyanates. The sergeants and soldiers experiment. *J. Am. Chem. Soc.* **1989,** *111*, 6452-6454.

15. Prins, L. J.; Timmerman, P.; Reinhoudt, D. N., Amplification of chirality: the "sergeants and soldiers" principle applied to dynamic hydrogen-bonded assemblies. *J. Am. Chem. Soc.* **2001,** *123*, 10153-10163.

16. Prins, L. J.; Thalacker, C.; Wurthner, F.; Timmerman, P.; Reinhoudt, D. N., Chiral exciton coupling of merocyanine dyes within a well defined hydrogen-bonded assembly. *Proc. Natl. Acad. Sci. U. S. A.* **2001,** *98*, 10042-10045.

17. Helmich, F.; Lee, C. C.; Schenning, A. P. H. J.; Meijer, E. W., Chiral Memory via Chiral Amplification and Selective Depolymerization of Porphyrin Aggregates. *J. Am. Chem. Soc.* **2010,** *132*, 16753-16755.

18. Smulders, M. M. J.; Stals, P. J. M.; Mes, T.; Paffen, T. F. E.; Schenning, A. P. H. J.; Palmans, A. R. A.; Meijer, E. W., Probing the Limits of the Majority-Rules Principle in a Dynamic Supramolecular Polymer. *J. Am. Chem. Soc.* **2010,** *132*, 620-626.

19. Helmich, F.; Smulders, M. M. J.; Lee, C. C.; Schenning, A. P. H. J.; Meijer, E. W., Effect of Stereogenic Centers on the Self-Sorting, Depolymerization, and Atropisomerization Kinetics of Porphyrin-Based Aggregates. *J. Am. Chem. Soc.* **2011,** *133*, 12238-12246.

20. Kauranen, M.; Verbiest, T.; Boutton, C.; Teerenstra, M. N.; Clays, K.; Schouten, A. J.; Nolte, R. J. M.; Persoons, A., Supramolecular second-order nonlinearity of polymers with orientationally correlated chromophores. *Science* **1995,** *270*, 966-969.

21. Yashima, E.; Maeda, K.; Nishimura, T., Detection and amplification of chirality by helical polymers. *Chem. - Eur. J.* **2004,** *10*, 42-51.

22. Zhang, J.; Albelda, M. T.; Liu, Y.; Canary, J. W., Chiral nanotechnology. *Chirality* **2005,** *17*, 404-420.

23. Aimi, J.; Oya, K.; Tsuda, A.; Aida, T., Chiroptical sensing of asymmetric hydrocarbons using a homochiral supramolecular box from a bismetalloporphyrin rotamer. *Angew. Chem. Int. Ed.* **2007,** *46*, 2031-2035.

24. Toyofuku, K.; Alam, M. A.; Tsuda, A.; Fujita, N.; Sakamoto, S.; Yamaguchi, K.; Aida, T., Amplified chiral transformation through helical assembly. *Angew. Chem. Int. Ed.* **2007,** *46*, 6476-6480.

25. Zhao, J.-S.; Ruan, Y.-B.; Zhou, R.; Jiang, Y.-B., Memory of chirality in J-type aggregates of an achiral perylene dianhydride dye created in a chiral asymmetric catalytic synthesis. *Chem. Sci.* **2011,** *2*, 937-944.

26. Green, M. M.; Cheon, K. S.; Yang, S. Y.; Park, J. W.; Swansburg, S.; Liu, W., Chiral studies across the spectrum of polymer science. *Acc. Chem. Res.* **2001,** *34*, 672-680.

27. Teramoto, A., Cooperative conformational transitions in linear macromolecules undergoing chiral perturbations. *Prog. Polym. Sci.* **2001,** *26*, 667-720.

28. van den Hout, K. P.; Martin-Rapun, R.; Vekemans, J. A. J. M.; Meijer, E. W., Tuning the stacking properties of C3-symmetrical molecules by modifying a dipeptide motif. *Chem. - Eur. J.* **2007,** *13*, 8111-8123.

29. Matmour, R.; De Cat, I.; George, S. J.; Adriaens, W.; Leclere, P.; Bomans, P. H. H.; Sommerdijk, N. A. J. M.; Gielen, J. C.; Christianen, P. C. M.; Heldens, J. T.; van Hest, J. C. M.; Loewik, D. W. P. M.; De Feyter, S.; Meijer, E. W.; Schenning, A. P. H. J., Oligo(p-phenylenevinylene)-Peptide Conjugates: Synthesis and Self-Assembly in Solution and at the Solid-Liquid Interface. *J. Am. Chem. Soc.* **2008,** *130*, 14576-14583.

30. Zheng, J.; Qiao, W. Q.; Wan, X. H.; Gao, J. P.; Wang, Z. Y., Near-Infrared Electrochromic and Chiroptical Switching Materials: Design, Synthesis, and Characterization of Chiral Organogels Containing Stacked Naphthalene Diimide Chromophores. *Chem. Mater.* **2008,** *20*, 6163-6168.

31. Soininen, A. J.; Kasemi, E.; Schluter, A. D.; Ikkala, O.; Ruokolainen, J.; Mezzenga, R., Self-Assembly and Induced Circular Dichroism in Dendritic Supramolecules with Cholesteric Pendant Groups. *J. Am. Chem. Soc.* **2010,** *132*, 10882-10890.

32. Wang, Q.; Chen, Y.; Ma, P.; Lu, J.; Zhang, X.; Jiang, J., Morphology and chirality controlled self-assembled nanostructures of porphyrin-pentapeptide conjugate: effect of the peptide secondary conformation. *J. Mater. Chem.* **2011,** *21*, 8057-8065.

33. Pandeeswar, M.; Avinash, M. B.; Govindaraju, T., Chiral transcription and retentive helical memory: probing peptide auxiliaries appended with naphthalenediimides for their one-dimensional molecular organization. *Chem. - Eur. J.* **2012,** *18*, 4818-4822.

34. Avinash, M. B.; Govindaraju, T., Engineering Molecular Organization of Naphthalenediimides: Large Nanosheets with Metallic Conductivity and Attoliter Containers. *Adv. Funct. Mater.* **2011,** *21*, 3875-3882.

35. Rosen, B. M.; Peterca, M.; Morimitsu, K.; Dulcey, A. E.; Leowanawat, P.; Resmerita, A.-M.; Imam, M. R.; Percec, V., Programming the supramolecular helical polymerization of dendritic dipeptides via the stereochemical information of the dipeptide. *J. Am. Chem. Soc.* **2011,** *133*, 5135-5151.

36. Jones, B. A.; Facchetti, A.; Wasielewski, M. R.; Marks, T. J., Tuning Orbital Energetics in Arylene Diimide Semiconductors. Materials Design for Ambient Stability of n-Type Charge Transport. *J. Am. Chem. Soc.* **2007,** *129*, 15259-15278.

37. Bhosale, S. V.; Jani, C. H.; Langford, S. J., Chemistry of naphthalene diimides. *Chem. Soc. Rev.* **2008,** *37*, 331-342.

38. Bhosale, R.; Misek, J.; Sakai, N.; Matile, S., Supramolecular n/p-heterojunction photosystems with oriented multicolored antiparallel redox gradients (OMARG-SHJs). *Chem. Soc. Rev.* **2010,** *39*, 138-149.

39. Sakai, N.; Mareda, J.; Vauthey, E.; Matile, S., Core-substituted naphthalenediimides. *Chem. Commun.* **2010,** *46*, 4225-4237.

40. Pantos, G. D.; Wietor, J.-L.; Sanders, J. K. M., Filling helical nanotubes with C60. *Angew. Chem. Int. Ed.* **2007,** *46*, 2238-2240.

41. Wietor, J.-L.; Pantos, G. D.; Sanders, J. K. M., Templated amplification of an unexpected receptor for C70. *Angew. Chem. Int. Ed.* **2008,** *47*, 2689-2692.

42. Shao, H.; Seifert, J.; Romano, N. C.; Gao, M.; Helmus, J. J.; Jaroniec, C. P.; Modarelli, D. A.; Parquette, J. R., Amphiphilic self-assembly of an n-type nanotube. *Angew. Chem. Int. Ed.* **2010,** *49*, 7688-7691.

43. Shao, H.; Parquette, J. R., A π-conjugated hydrogel based on an Fmoc-dipeptide naphthalene diimide semiconductor. *Chem. Commun.* **2010,** *46*, 4285-4287.

44. Au-Yeung, H. Y.; Cougnon, F. B. L.; Otto, S.; Pantos, G. D.; Sanders, J. K. M., Exploiting donor-acceptor interactions in aqueous dynamic combinatorial libraries: exploratory studies of simple systems. *Chem. Sci.* **2010,** *1*, 567-574.

45. Avinash, M. B.; Govindaraju, T., A bio-inspired design strategy: Organization of tryptophan-appended naphthalenediimide into well-defined architectures induced by molecular interactions. *Nanoscale* **2011,** *3*, 2536-2543.

46. Laquindanum, J. G.; Katz, H. E.; Dodabalapur, A.; Lovinger, A. J., n-Channel organic transistor materials based on naphthalene frameworks. *J. Am. Chem. Soc.* **1996,** *118*, 11331-11332.

47. Katz, H. E.; Johnson, J.; Lovinger, A. J.; Li, W., Naphthalenetetracarboxylic Diimide-Based n-Channel Transistor Semiconductors: Structural Variation and Thiol-Enhanced Gold Contacts. *J. Am. Chem. Soc.* **2000,** *122*, 7787-7792.

48. Sakai, N.; Bhosale, R.; Emery, D.; Mareda, J.; Matile, S., Supramolecular n/p-heterojunction photosystems with antiparallel redox gradients in electron- and hole-transporting pathways. *J. Am. Chem. Soc.* **2010,** *132*, 6923-6925.

49. Anthony, J. E.; Facchetti, A.; Heeney, M.; Marder, S. R.; Zhan, X., n-Type Organic Semiconductors in Organic Electronics. *Adv. Mater.* **2010,** *22*, 3876-3892.

50. Oh, J. H.; Suraru, S.-L.; Lee, W.-Y.; Koenemann, M.; Hoeffken, H. W.; Roeger, C.; Schmidt, R.; Chung, Y.; Chen, W.-C.; Wuerthner, F.; Bao, Z., High-performance air-stable n-type organic transistors based on core-chlorinated naphthalene tetracarboxylic diimides. *Adv. Funct. Mater.* **2010,** *20*, 2148-2156.

51. Ozser, M. E.; Uzun, D.; Elci, I.; Icil, H.; Demuth, M., Novel naphthalene diimides and a cyclophane thereof: synthesis, characterization, photophysical and electrochemical properties. *Photochem. Photobiol. Sci.* **2003,** *2*, 218-223.

52. Andric, G.; Boas, J. F.; Bond, A. M.; Fallon, G. D.; Ghiggino, K. P.; Hogan, C. F.; Hutchison, J. A.; Lee, M. A. P.; Langford, S. J.; Pilbrow, J. R.; Troup, G. J.; Woodward, C. P.,

Spectroscopy of naphthalene diimides and their anion radicals. *Aust. J. Chem.* **2004,** *57*, 1011-1019.

53. Gawronski, J.; Brzostowska, M.; Kacprzak, K.; Kolbon, H.; Skowronek, P., Chirality of aromatic bis-imides from their circular dichroism spectra. *Chirality* **2000,** *12*, 263-268.

54. Sakai, N.; Talukdar, P.; Matile, S., Use of the exciton chirality method in the investigation of ligand-gated synthetic ion channels. *Chirality* **2006,** *18*, 91-94.

55. Bulheller, B. M.; Pantos, G. D.; Sanders, J. K. M.; Hirst, J. D., Electronic structure and circular dichroism spectroscopy of naphthalenediimide nanotubes. *Phys. Chem. Chem. Phys.* **2009,** *11*, 6060-6065.

56. Messmore, B. W.; Sukerkar, P. A.; Stupp, S. I., Mirror Image Nanostructures. *J. Am. Chem. Soc.* **2005,** *127*, 7992-7993.

57. Tsai, W.-W.; Li, L.-s.; Cui, H.; Jiang, H.; Stupp, S. I., Self-assembly of amphiphiles with terthiophene and tripeptide segments into helical nanostructures. *Tetrahedron* **2008,** *64*, 8504-8514.

58. Palmer, L. C.; Stupp, S. I., Molecular Self-Assembly into One-Dimensional Nanostructures. *Acc. Chem. Res.* **2008,** *41*, 1674-1684.

59. Cui, H.; Muraoka, T.; Cheetham, A. G.; Stupp, S. I., Self-Assembly of Giant Peptide Nanobelts. *Nano Lett.* **2009,** *9*, 945-951.

60. Pashuck, E. T.; Stupp, S. I., Direct Observation of Morphological Transformation from Twisted Ribbons into Helical Ribbons. *J. Am. Chem. Soc.* **2010,** *132*, 8819-8821.

61. Hunter, C. A.; Lawson, K. R.; Perkins, J.; Urch, C. J., Aromatic interactions. *J. Chem. Soc., Perkin Trans. 2* **2001**, 651-669.

62. Gu, Y.; Kar, T.; Scheiner, S., Fundamental Properties of the CH···O Interaction: Is It a True Hydrogen Bond? *J. Am. Chem. Soc.* **1999,** *121*, 9411-9422.

63. Pantoş, G. D.; Pengo, P.; Sanders, J. K. M., Hydrogen-Bonded Helical Organic Nanotubes. *Angew. Chem. Int. Ed.* **2007,** *46*, 194-197.

64. Salonen, L. M.; Ellermann, M.; Diederich, F., Aromatic rings in chemical and biological recognition: energetics and structures. *Angew. Chem. Int. Ed.* **2011,** *50*, 4808-4842.

65. Riley, K. E.; Hobza, P., On the Importance and Origin of Aromatic Interactions in Chemistry and Biodisciplines. *Acc. Chem. Res.* **2013,** *46*, 927-936.

66. Avinash, M. B.; Govindaraju, T., Nanoarchitectonics of biomolecular assemblies for functional applications. *Nanoscale* **2014,** *6*, 13348-13369.

67. Ariga, K.; Kawakami, K.; Ebara, M.; Kotsuchibashi, Y.; Ji, Q.; Hill, J. P., Bioinspired nanoarchitectonics as emerging drug delivery systems. *New J. Chem.* **2014,** *38*, 5149-5163.

68. Ariga, K.; Ji, Q.; Nakanishi, W.; Hill, J. P.; Aono, M., Nanoarchitectonics: a new materials horizon for nanotechnology. *Mater. Horiz.* **2015,** *2*, 406-413.

69. Coropceanu, V.; Cornil, J.; Da Silva Filho, D. A.; Olivier, Y.; Silbey, R.; Bredas, J.-L., Charge Transport in Organic Semiconductors. *Chem. Rev.* **2007,** *107*, 926-952.

70. Mas-Torrent, M.; Rovira, C., Role of Molecular Order and Solid-State Structure in Organic Field-Effect Transistors. *Chem. Rev.* **2011,** *111*, 4833-4856.

71. Ariga, K.; Yamauchi, Y.; Rydzek, G.; Ji, Q.; Yonamine, Y.; Wu, K. C. W.; Hill, J. P., Layer-by-layer nanoarchitectonics: invention, innovation, and evolution. *Chem. Lett.* **2014,** *43*, 36-68.

72. Cheng, X.; Lowe, S. B.; Reece, P. J.; Gooding, J. J., Colloidal silicon quantum dots: from preparation to the modification of self-assembled monolayers (SAMs) for bio-applications. *Chem. Soc. Rev.* **2014,** *43*, 2680-2700.

73. Diao, Y.; Shaw, L.; Bao, Z.; Mannsfeld, S. C. B., Morphology control strategies for solution-processed organic semiconductor thin films. *Energy Environ. Sci.* **2014,** *7*, 2145-2159.

74. Pandeeswar, M.; Govindaraju, T., Green-fluorescent naphthalene diimide: conducting layered hierarchical 2D nanosheets and reversible probe for detection of aromatic solvents. *RSC Adv.* **2013,** *3*, 11459-11462.

75. Aida, T.; Meijer, E. W.; Stupp, S. I., Functional supramolecular polymers. *Science* **2012,** *335*, 813-817.

76. Sakakibara, K.; Hill, J. P.; Ariga, K., Thin-Film-Based Nanoarchitectures for Soft Matter: Controlled Assemblies into Two-Dimensional Worlds. *Small* **2011,** *7*, 1288-1308.

77. Ghosh, S.; Reches, M.; Gazit, E.; Verma, S., Bioinspired design of nanocages by self-assembling triskelion peptide elements. *Angew. Chem. Int. Ed.* **2007,** *46*, 2002-2004.

78. Jatsch, A.; Schillinger, E. K.; Schmid, S.; Baeuerle, P., Biomolecule assisted self-assembly of π-conjugated oligomers. *J. Mater. Chem.* **2010,** *20*, 3563-3578.

79. Ariga, K.; Kikuchi, J.-i.; Naito, M.; Koyama, E.; Yamada, N., Modulated Supramolecular Assemblies Composed of Tripeptide Derivatives: Formation of Micrometer-Scale Rods, Nanometer-Size Needles, and Regular Patterns with Molecular-Level Flatness from the Same Compound. *Langmuir* **2000,** *16*, 4929-4939.

80. Avinash, M. B.; Govindaraju, T., Amino acid derivatized arylenediimides: a versatile modular approach for functional molecular materials. *Adv. Mater.* **2012,** *24*, 3905-3922.

81. Avinash, M. B.; Samanta, P. K.; Sandeepa, K. V.; Pati, S. K.; Govindaraju, T., Molecular Architectonics of Stereochemically Constrained π-Complementary Functional Modules. *Eur. J. Org. Chem.* **2013,** *2013*, 5838-5847.

82. Govindaraju, T.; Avinash, M. B., Two-dimensional nanoarchitectonics: organic and hybrid materials. *Nanoscale* **2012,** *4*, 6102-6117.

83. Lewandowska, U.; Zajaczkowski, W.; Chen, L.; Bouilliere, F.; Wang, D.; Koynov, K.; Pisula, W.; Muellen, K.; Wennemers, H., Hierarchical supramolecular assembly of sterically demanding π-systems by conjugation with oligoprolines. *Angew. Chem. Int. Ed.* **2014,** *53*, 12537-12541.

84. Nalluri, S. K.; Berdugo, C.; Javid, N.; Frederix, P. W.; Ulijn, R. V., Biocatalytic self-assembly of supramolecular charge-transfer nanostructures based on n-type semiconductor-appended peptides. *Angew. Chem. Int. Ed.* **2014,** *53*, 5882-5887.

85. Peebles, C.; Piland, R.; Iverson, B. L., More than meets the eye: Conformational switching of a stacked dialkoxynaphthalene-naphthalenetetracarboxylic diimide (DAN-NDI) foldamer to an NDI-NDI fibril aggregate. *Chem. - Eur. J.* **2013,** *19*, 11598-11602.

86. Kumar, R. J.; MacDonald, J. M.; Singh, T. B.; Waddington, L. J.; Holmes, A. B., Hierarchical Self-Assembly of Semiconductor Functionalized Peptide α-Helices and Optoelectronic Properties. *J. Am. Chem. Soc.* **2011,** *133*, 8564-8573.

87. Dwivedi, A. K.; Pandeeswar, M.; Govindaraju, T., Assembly modulation of PDI derivative as a supramolecular fluorescence switching probe for detection of cationic surfactant and metal ions in aqueous media. *ACS Appl. Mater. Interfaces* **2014,** *6*, 21369-21379.

88. Pantos, G. D.; Pengo, P.; Sanders, J. K. M., Hydrogen-bonded helical organic nanotubes. *Angew. Chem. Int. Ed.* **2007,** *46*, 194-197.

89. Pandeeswar, M.; Govindaraju, T., Bioinspired Nanoarchitectonics of Naphthalene Diimide to Access 2D Sheets of Tunable Size, Shape, and Optoelectronic Properties. *J. Inorg. Organomet. Polym. Mater.* **2015,** *25*, 293-300.

90. Pandeeswar, M.; Khare, H.; Ramakumar, S.; Govindaraju, T., Crystallographic insight-guided nanoarchitectonics and conductivity modulation of an n-type organic semiconductor through peptide conjugation. *Chem. Commun.* **2015,** *51*, 8315-8318.

91. Nagaraj, R.; Balaram, P., Alamethicin, a transmembrane channel. *Acc. Chem. Res.* **1981,** *14*, 356-362.

92. Calvert, P., Materials science: silk and sequence. *Nature* **1998,** *393*, 309, 311.

93. Pandeeswar, M.; Khare, H.; Ramakumar, S.; Govindaraju, T., Biomimetic molecular organization of naphthalene diimide in the solid state: tunable (chiro-) optical, viscoelastic and nanoscale properties. *RSC Adv.* **2014,** *4*, 20154-20163.

94. Barth, A., Infrared spectroscopy of proteins. *Biochim. Biophys. Acta, Bioenerg.* **2007,** *1767*, 1073-1101.

95. Toniolo, C.; Palumbo, M., Solid-state infrared absorption spectra and chain arrangement in some synthetic homooligopeptides in the intermolecularly hydrogen-bonded pleated-sheet β-conformation. *Biopolymers* **1977,** *16*, 219-224.

96. Wu, Y.; Frasconi, M.; Gardner, D. M.; McGonigal, P. R.; Schneebeli, S. T.; Wasielewski, M. R.; Stoddart, J. F., Electron Delocalization in a Rigid Cofacial Naphthalene-1,8:4,5-bis(dicarboximide) Dimer. *Angew. Chem. Int. Ed.* **2014,** *53*, 9476-9481.

Chapter 5: Sugar Conjugated NDI Hierarchical Nanostructures as Templates for the Preparation of Ag Coated Nanotubes*

---

*Manuscript to be communicated.

5.1 Introduction

Chirality is one of the most ubiquitous property in biomolecules and occur at various hierarchical levels from small molecular building blocks (L-amino acids and D-sugars) to macromolecules (DNA double helix) to supramolecular (self-assembled proteins and polysaccharides) to macroscopic scales (seashells, horns, and plant tendrils).[1-6] It's intriguing, that chiral structural features play a pivotal role in diverse biological functions like structural stability, signal transduction and genetic information, replication, transcription, translation.[7] Moreover, many chiral biopolymers self-organized into hierarchical helical superstructures with inverse handedness. Collagen is one of the best exemple of this kind, wherein three left-handed helical polypeptide chains supercoiled together to make a right-handed triple helix.[8] Inspired by the biological chiral evolution and its unique functions, design and davelopement of hierarchical chiral nanoarchitectures have become an emerging but challenging interdisciplinary research area in biology, chemistry and materials science.[2,4,7,9-21] Owing to its fascinating chiral structural features, these architectures exhibit wide range of applications; in pharmacology as an enantioselective sensing,[19,22-27] separation[14] and catalysis,[28-30] understanding of Nature's mysterious selection of homochirality,[31] designing of biomimetics,[32] chiroptical switches,[17,20] chiral memory,[33-34] optical metamaterials[35] and nanomechanical devices,[2] templates for the helical organization of nanoparticles[15] and chirooptical,[36-38] nonlinear optics,[35,39] liquid crystal[40-41] and tissue engineering.[42-44] In particular, introduction of chirality into the organic conducting molecular systems known to display exceptional charge carrier mobilities, exciton diffusion characteristics and also lead to the observation of new phenomenon refer to electrical magneto-chiral anisotropy effect.[36,39,45-46] Therefore development of hierarchical, chiral nano-architectonics of organic semiconductor is currently receiving great interest in the area of multifunctional materials.[2,32,38,45] In the past decade, considerable efforts have been devoted to chiral transfer, induction and amplification in aromatic molecules, polymers, and π-conjugated small molecular systems by utilizing various noncovalent interactions, external stimuli and steric effects.[2,4,7,9-21,33,47-53] The majority of these approaches have produced chiral assemblies of π–electron-rich aromatic (hole transport, p-type) systems,[11-12,54-56] whereas n-type (electron transport) semiconductors have not been explored to their full potential. Moreover, the bioinspired hierarchical chiral superstructures with opposite helicity as that of molecular assembly are relatively uncommon owing to the very limited synthetic methodologies and non-availability of easy-to-adopt approaches.[57-60]

The basic biological building blocks amino acids,[61-70] sugars,[50,71-74] nucleobases[75] and phospholipids[76] have been considered as attractive auxiliaries for designing synthetic self-assembled helical nanostructures.[77-78] Apart from amino acids, sugars and their derivatives are most celebrated auxiliaries owing to inherent chiral effects and several hydrogen bonding interactions in the self-assembly processes.[50,71-74] These observations prompted us to design and develop sugar conjugated naphthalene diimides (NDIs) bolaamphiphile (**Glc-NDI**) (Figure 5.1). NDI and its derivatives are promising n-type organic semiconductors and exhibit a wide range of applications from biomedicine to materials science.[79-87] Herein, we report for the first time bioinspired synthetically unusual hierarchical helical self-organization of sugar conjugated n-type organic semiconductor NDI (**Glc-NDI)** and its concentration induced hydrogel formation via structural transformation from helical nanotapes to nanotubes. Furthermore, the silver mirror reaction on the **Glc-NDI** nanotubes afford uniformly silver coated nanotubes.

Glc-NDI bolaamphiphile was synthesized by two-step reaction via the condensation of β-alanine with 1,4,5,8-naphthalenetetracarboxylic dianhydride (NDA) followed by the coupling with glucosamine in good yield (60 %) (Figure 5.1). The formation of **Glc-NDI** was characterized by NMR spectroscopy and elemental analysis. **Glc-NDI** was found to be readily soluble in dimethyl sulfoxide (DMSO) at low concentrations, however at the high concentrations formation of the gel was observed in both DMSO and water respectively. To induce the self-assembly of **Glc-NDI** through hydrophobic effect, we chose to perform our spectroscopic and microscopy studies in aqueous solution (H_2O/DMSO).

5.2 Results and discussion

5.2.1 UV-vis absorption studies

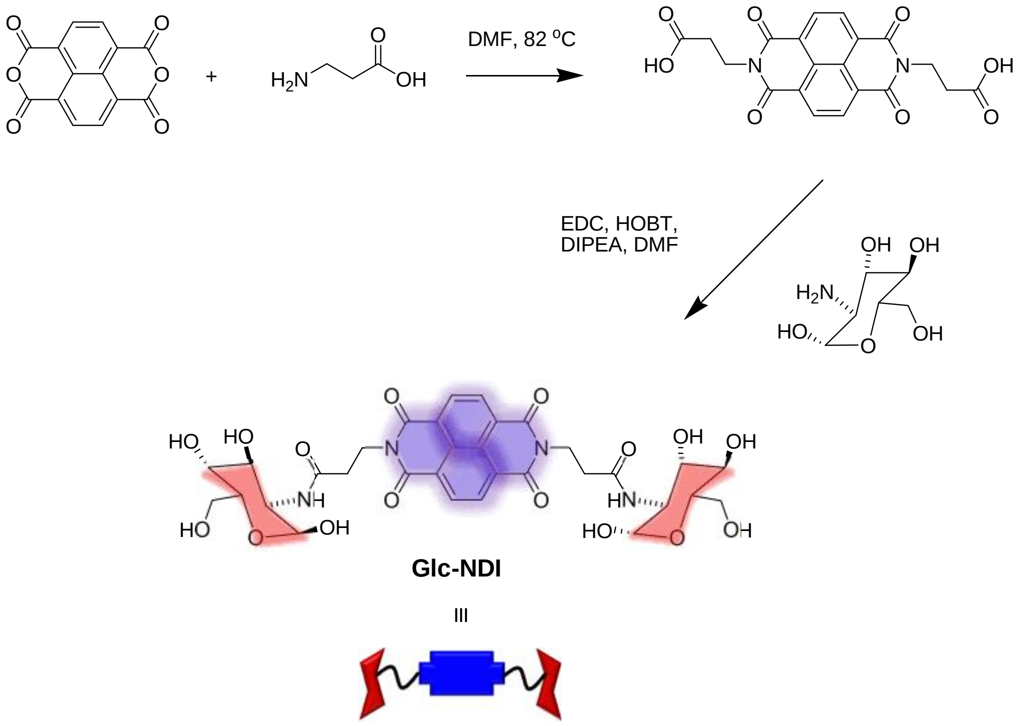

Figure 5.1 Synthesis of glucosamine conjugated NDI Derivative (**Glc-NDI**) and its schematic representation

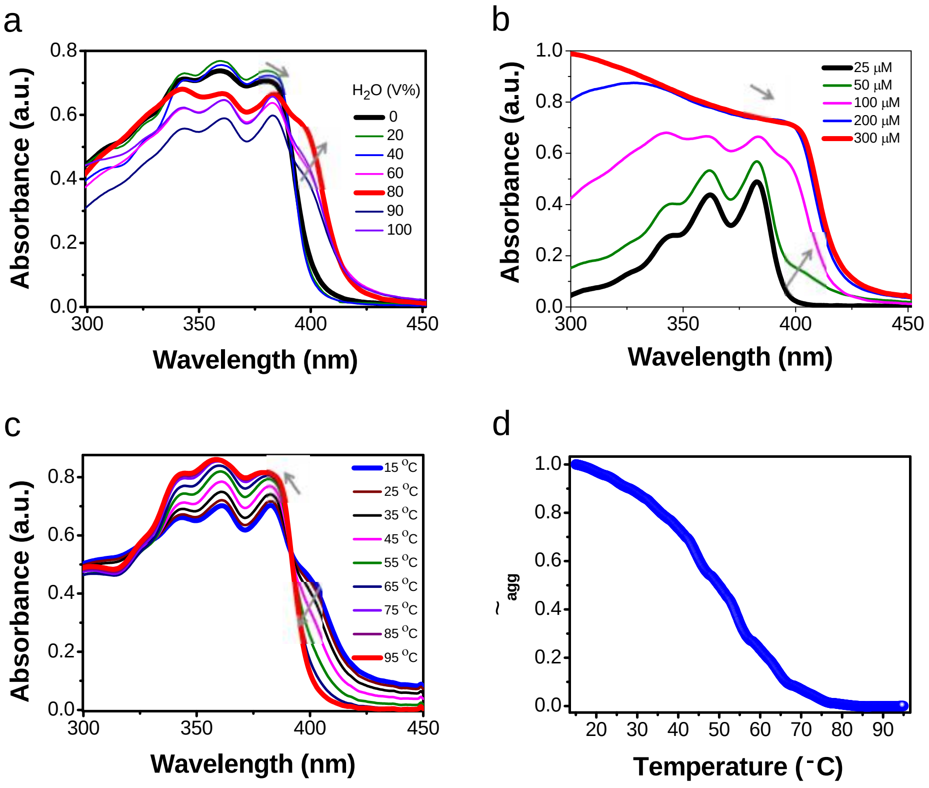

Figure 5.2 UV−vis absorption spectra of **Glc-NDI**, a) Solvent dependent studies. b) Concentration dependent studies. c) Temperature dependent studies. d) The plot of the change in the absorbance at 400 nm as a function of temperature.

The self-assembly behavior of **Glc-NDI** was explored through UV-vis absorption spectroscopy (Figure **5.2**). **Glc-NDI** in DMSO exhibited strong absorption bands in the region of 300–400 nm (band I) with λ_{max} at 380 nm, attributed to the characteristic π–π∗ transitions of NDI chromophore polarized along the z-axis (Figure **5.2**a). Interestingly, upon addition of water at different volume ratios the absorption spectra of **Glc-NDI** displayed significant hypochromicity along with red shift (~ 5 nm, 385 nm) and band broadening (Figure 5.2 a). In addition, a new broad band appeared in the long wavelength region (400 nm) which was absent in the spectra recorded in DMSO solution. These spectral features along with the new red shifted absorption band upon addition of water suggest the hydrophobic effect induced edge-to-face (J-type) exciton-coupled π−stacked NDI-NDI self-assembly of **Glc-NDI**. To evaluate the influence of concentration on the self-assembly of **Glc-NDI**, concentration dependent UV-vis absorption studies of **Glc-NDI** were performed in aqueous DMSO solution (H_2O/DMSO (90/10, v/v) (Figure **5.2** b). The absorption spectra of **Glc-NDI** at low concentration (25 μM) displayed sharp vibronic absorption bands in the range of 300–400 nm (band I) which is characteristic of the molecularly dissolved state. Further increase in concentration (50 μM to 300 μM) resulted in the significant changes in the spectra with loss of vibronic features, band broadening accompanied by the appearance of a new broad absorption band centered at around 400 nm. Furthermore, at high concentrations (8 mM) the aqueous solution of **Glc-NDI** turned into hydrogels gel upon ultrasonication for 15 min, suggesting the formation of extended self-assembly among **Glc-NDI** molecular units via strong intermolecular π–stacking and hydrogen bonding interactions. Further to know the thermal stability we carried out variable-temperature UV-visible absorption studies. With increasing temperature (15 ^{o}C to 95 ^{o}C), the band I absorption signals showed gradual hyperchromic shift with concomitant blue shift accompanied by the disappearance of the shoulder aggregation band. These absorption changes reiterate the reversible conversion of self-assembled structure to the monomeric **Glc-NDI**. From variable temperature UV-vis experiments, the value of α_{50}(T) (temperature at which α_{agg} = 0.5) for self-assembly of **Glc-NDI** in aqueous solution was estimated to be 50 ^{o}C as shown in Figure 5.2c.

5.2.2 Circular dichroism studies

In order to understand the effect of chirality of sugar (Glc) auxiliaries on the molecular assembly of the achiral NDI chromophore, we performed circular dichroism (CD) measurements of **Glc-NDI** in DMSO and aqueous solution (Figure 5.3). In agreement with the UV-vis absorption data, **Glc-NDI** displayed flat CD spectra in DMSO solution

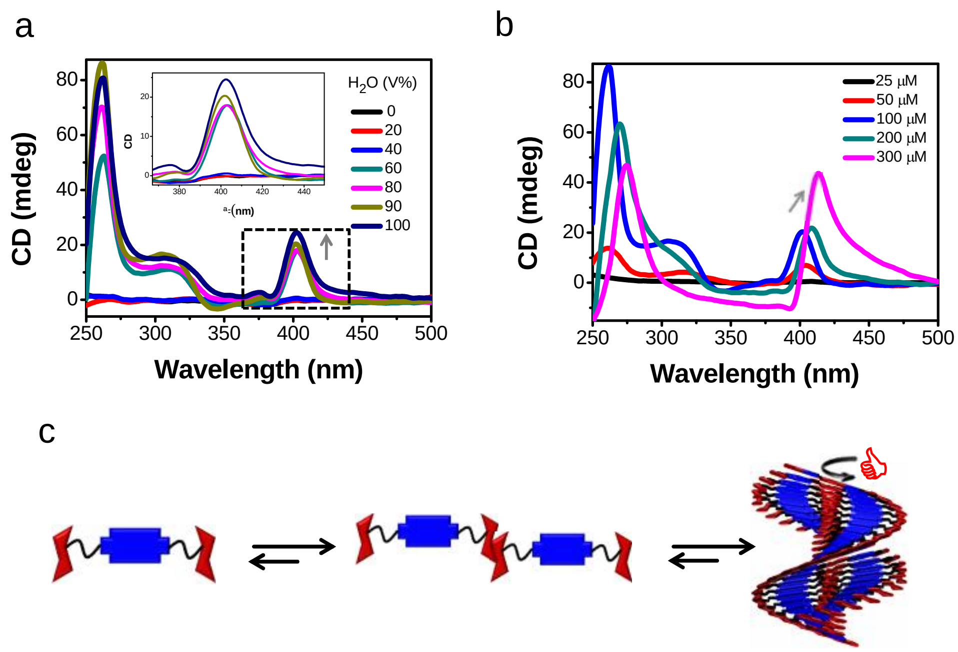

Figure 5.3 Circular dichroism (CD) spectra of **Glc-NDI**; a) solvent dependent studies ([**Glc-NDI**] = 100 μM). b) Concentration dependent studies in aqueous solution (H_2O/DMSO (90/10, v/v). c) Schematic representation of molecular organization of **Glc-NDI** from molecularly dissolved state (DMSO) to right hand chiral self-assembly (in aqueous solution). arrows indicating the spectral changes

due to molecularly dissolved state (Figure 5.3a). However, upon addition of water (≥ 40 V %) positive induced CD (ICD) signals were appeared in the NDI absorption region (250-400 nm) (Figure 5.3a). The positive ICD signal at λ_{max}=400 nm (NDI long axis π−π* electronic transitions), suggests right (*P*) - handed helical organization of **Glc-NDI** within a J-type stacked NDI chromophores aggregates (Figure 5.3c). The increase in water content showed enhancement in ICD signals suggesting the hydrophobic force induced NDI-NDI helical stacking interactions among the self-assembled **Glc-NDI** molecular aggregates. Furthermore, concentration-dependent CD studies of **Glc-NDI** in aqueous solution displayed a flat CD signal at low concentrations ((≤ 25 μM), however strong ICD signals at higher concentrations (≥ 50 μM) was observed, clearly suggesting self-assembly induced right handed helical organization of **Glc-NDI** molecules

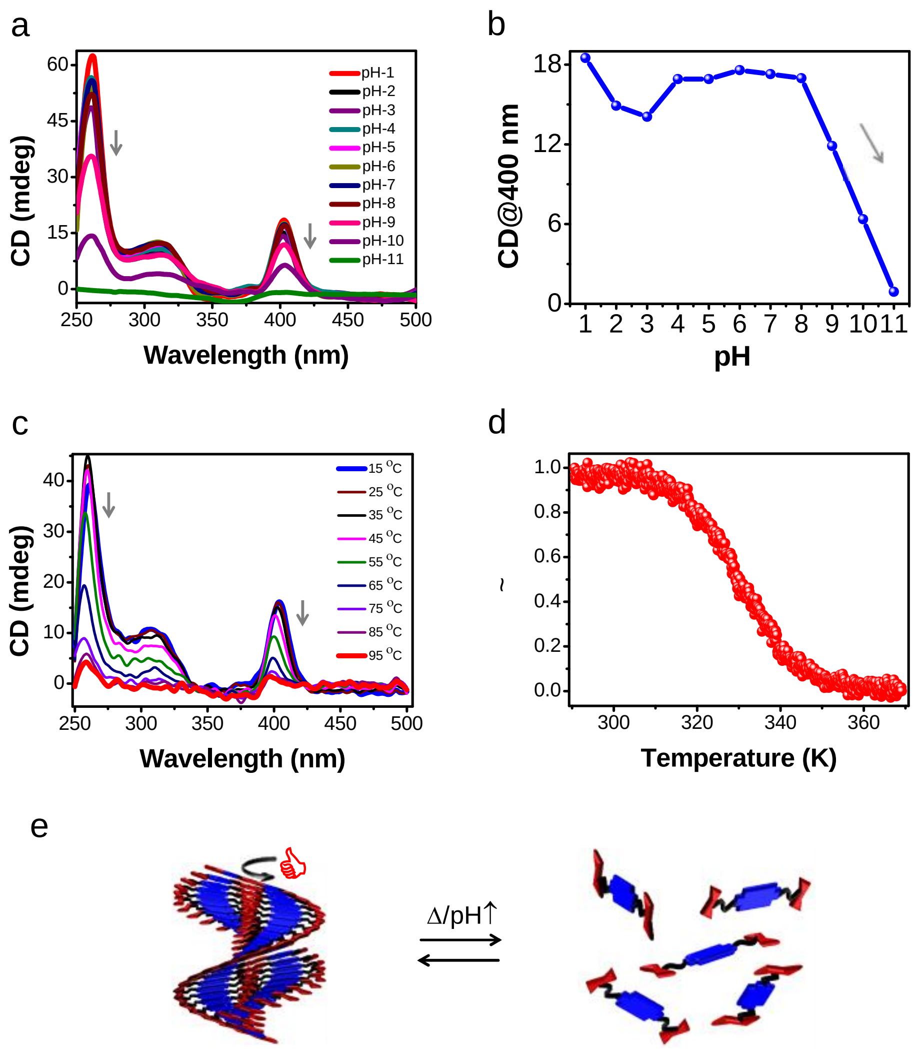

Figure 5.4 Circular dichroism (CD) spectra of **Glc-NDI** (100 μM); a) pH dependent studies. b) Plot of CD intensity at 400 nm as a function of pH. c) Temperature dependent studies in aqueous solution (H_2O/DMSO (90/10, v/v). d) Fraction of aggregates as a function of temperature. e) Schematic representation of stimuli responsive (pH and temperature (Δ)) disassembly of **Glc-NDI.** Arrows indicating the spectral changes.

(Figure 5.3b and c). To evaluate the role of intermolecular hydrogen bonding on the right-handed helical self-organization of **Glc-NDI** molecules, we carried out the pH-dependent CD studies (Figure 5.4a and b). As the pH values increase from 1 to 8, no significant changes in the ICD signals of **Glc-NDI** was observed. However further increase in pH from 8 to 11 resulted in the decrease ICD signal magnitude and almost vanished at the pH above 10 (Figure 5.4a and b). This can be attributed to the deprotenation of Glc under strong basic conditions lead to the disruption of self-assembly among **Glc-NDI** molecules. Unlike covalent bonding, noncovalent interactions are strongly dependent on temperature. To understand the thermal stability of **Glc-NDI** helical aggregates, variable-temperature (VT) CD studies were carried out (Figure 5.4c and d). As the temperature increases from 15 ºC to 95 ºC, the VTCD showed the gradual decreases in ICD NDI signals attributed to the thermal induced disassembly of **Glc-NDI** helical aggregates. The fraction of aggregates (α) monitored at 400 nm for the aqueous solution of **Glc-NDI** as a function of temperature exhibited sigmoidal transition (Figure 5.4d). For a 100 µM concentration of **Glc-NDI**, the melting temperature T_m defined as the temperature for which $\alpha = 0.5$ was found to be 329.15 K.

5.2.3 Morphological studies

In order to visualize the helical assembly of **Glc-NDI** in solution and hydrogels, field emission scanning electron microscopy (FESEM) studies was performed by drop casting the aqueous solutions and xerogels onto Si wafers followed by vacuum drying under room temperature (Figure 5.5). Surprisingly the dilute aqueous solution (50 μM) exhibited left-handed helical nanotapes, in contrast to right-handed chiral assembly observed in solution state (Figure 5.5a and Figure 5.3a). This remarkable difference in chirality is attributed to the ability of multiple intermolecular hydrogen bonding interactions among Glc units on both sides of **Glc-NDI** right handed helical molecular stacks which further self–organized to form left-handed supercoiled coil or superhelical nanotapes (Figure 5.5d). These left-handed helical nanotapes exhibited average diameters of 50 nm and pitch of 82 nm with an angle of 55º as shown in the Figure 5.5 a. Interestingly, similar hierarchical chiral superstructures are found in nature for example in collagen and very few synthetic supramolecular and polymeric systems.[8,57-60] Moreover, increase in concentration of **Glc-NDI** to 100 μM, the self-assembled left-handed

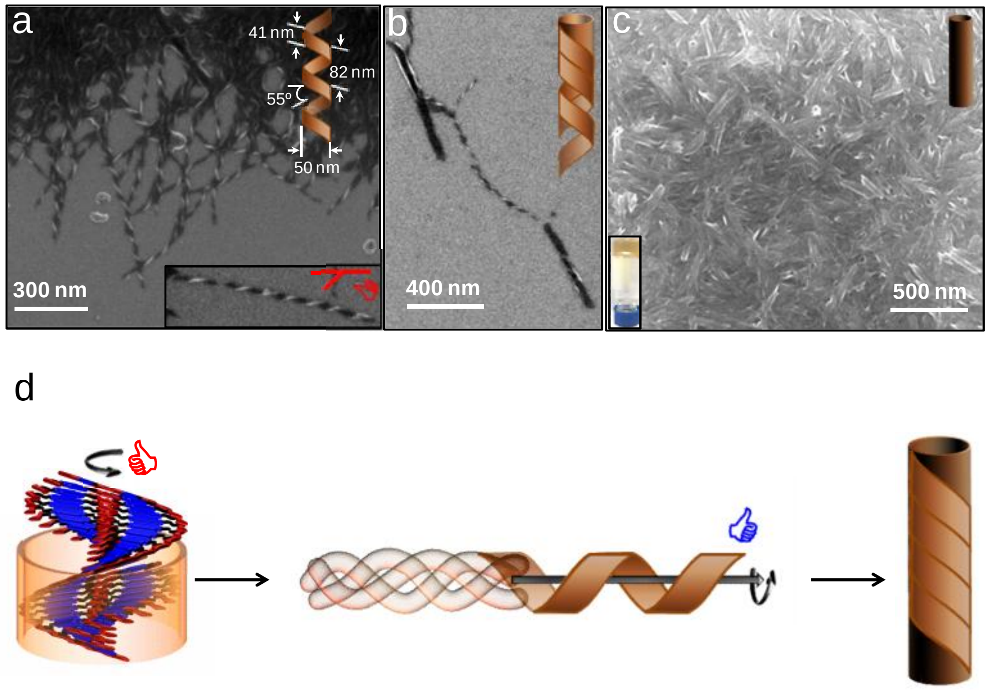

Figure 5.5 FESEM micrographs of **Glc-NDI**; a) From 100 μM aqueous solution (H_2O/DMSO (90/10, v/v) of **Glc-NDI,** show left-handed helical nanotapes; *inset*: Schematic representation of helical nanotapes and corresponding dimensions. b) Conversion of left-handed helical nanotapes to nanotube with schematic representation. c) Dense forest of nanotube morphology from xerogel, *inset:* Photograph of hydrogel, schematic representation of nanotube. d) Schematic representation of the hierarchical self-assembly of **Glc-NDI,** from right-handed chiral molecular stacks to left handed supercoiled helical nanotapes and nanotubes.

superstructures undergo further transformation to form self-organized nanotubes (Figure 5.5 b).[72] Consequently, the xerogels displayed a dense forest of nanotubes with average inner diameter of around 50-100 nm (Figure 5.5c). Furthermore, we exploited the Glc-functionality on nanotube surface for performing the silver mirror reaction within the **Glc-NDI** hydrogels (Figure 5.6a). Interestingly, the pale yellow colored hydrogel turned into red after addition of tollen's reagent indicating the reduction of silver ions to silver metal by Glc moieties of **Glc-NDI** (Figure 5.6a).[74,88] This was further evident from the FESEM micrographs of corresponding xerogels, which showed uniformly silver coated nanotubes (Figure 5.6b). The energy dispersive X-ray analysis (EDAX) chemical composition mapping graph on corresponding nanotubes indicated the presence of silver

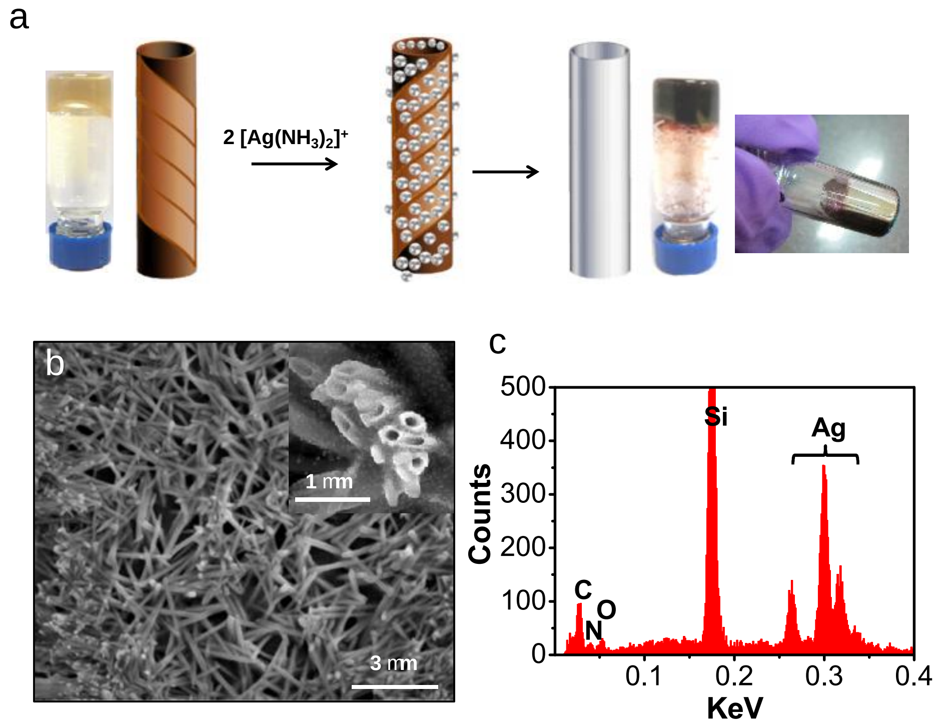

Figure 5.6 a) Schematic representation of formation of uniformly silver coated **Glc-NDI** nanotubes in presence of tollens solution, Photograph **Glc-NDI** hydrogel before, after addition of tollens reagent (a clear visible color change from pale yellow to red was observed) and after complete evaporation of solvent showing deposition of silver metal on the inner surface of the glass vial . b) FESEM micrographs of uniformly silver coated nanotubes; *inset*: magnified image. c) EDAX chemical composition mapping graph on the nanotubes shown in b.

metal (Ag) along with carbon (C), oxygen (O) and nitrogen (N) as shown in the Figure 5.6c.

5.3 Conclusion

In conclusion, a sugar functionalized NDI bolaamphiphile **Glc-NDI** was synthesized and investigated the transcription and expression of chirality on both supramolecular and nanoscale material levels. An unprecedented biological relevant, but synthetically challenging phenomenon of chirality control over the hierarchical self-organization was achieved (Figure 5.7). The circular dichroism experiments in aqueous solution showed the transcription of chiral information of glucosamine moiety of **Glc-NDI** to the achiral

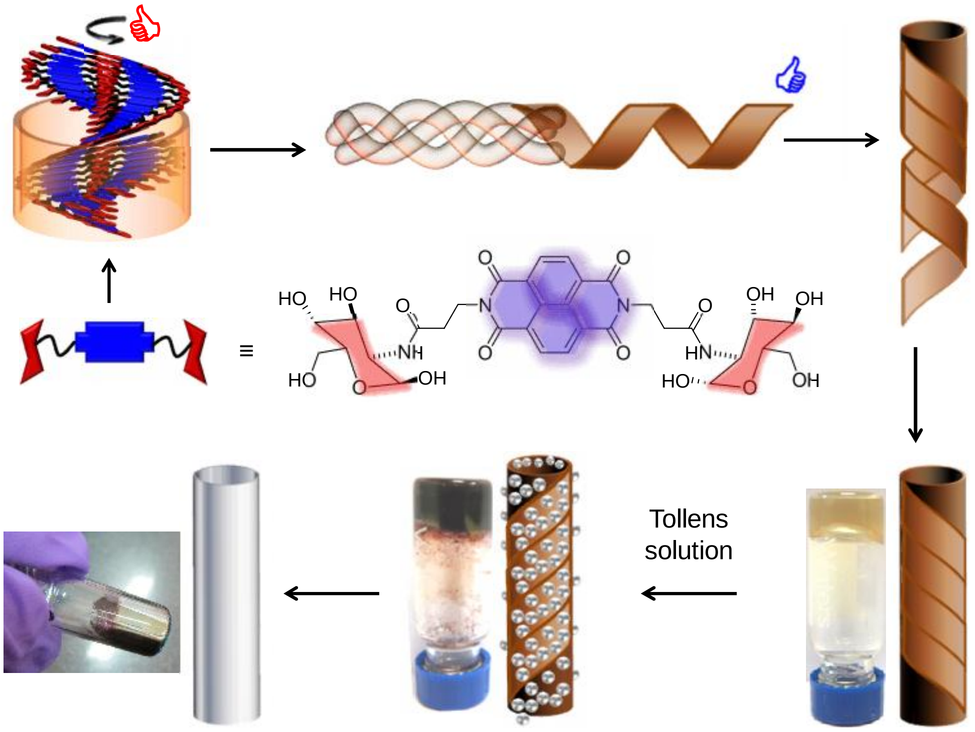

Figure 5.7 Schematic representation of overall proposed hierarchical self-assembly of **Glc-NDI** from right-handed chiral molecular stacks to left handed supercoiled helical nanotapes and nanotubes, template for the preparation of uniformly coated silver nanotube, photographs corresponding hydrogels.

NDI core and subsequently lead to right-handed helical self-assembly. Surprisingly, the microscopy studies revealed formation of helical nanotapes with opposite chirality (left-handed) in contrast to right-handed helical self-assembly formed in solution. This remarkable transformation revealed the various levels of hierarchical self-organization of right-handed molecular stacks subsequently yields supercoiled left-handed helical nanotape structures. Further, increase in concentration (8 mM) resulted in conversion of nanotapes to nanotubes accompanied by sol to gel transformation. Moreover, the nanotube surface-exposed glucosamine moiety is exploited to reduce silver ions to form uniform silver coated nanotubes. Therefore the new bolaamphiphile molecule **Glc-NDI** takes advantage of the biomolecular functionalities of n-type organic semiconductor (NDI), hierarchical self-assembly and reactivity to a specific metal ion. Thus, the study presented here showed exploitation of sugar functionality (Glc) is a promising way to designing hierarchical organic semiconductor chiral nanomaterials with possible applications in optoelectronics, biomaterials, chiral technology and reactive metallization templates.

5.4 Experimental section

5.4.1 Materials and methods

Materials. 1,4,5,8-Naphthalenetetracarboxylic dianhydride (NDA), was obtained from Sigma-Aldrich. Triethylamine, β–alanine, glucosamine, 1-ethyl-3-(3 dimethyllaminopropyl) carbodiimide hydrochloride and 1-hydroxybenzotriazole, N, N-diisopropylethylamine were purchased from Spectrochem Pvt. Ltd. (Mumbai, India). All other reagents and solvents were of reagent grade and used without further purification.

Absorption spectroscopy. UV–vis spectra were recorded on a Perkin Elmer Model Lambda 900 spectrophotometer by using quartz cuvette of 10 mm path length.

Circular dichroism (CD). CD measurements were carried out on a Jasco J-815 spectropolarimeter under nitrogen atmosphere by using quartz cuvette of 10 mm path length.

NMR spectroscopy. ^{1}H and ^{13}C NMR spectra were recorded on a Bruker AV-400 spectrometer with chemical shifts reported as ppm (in $CDCl_3$/DMSO-d_6 with tetramethylsilane as internal standard).

Field emission scanning electron microscopy (FESEM). FESEM images were acquired with a FEI Nova nanoSEM-600 equipped with a field-emission gun operating at 15 kV. The xerogels were prepared by transfer of hydrogels onto a Si (111) substrate and dried in air followed by vacuum drying at room temperature.

Gelation experiments. milliQ water was added to the solution of **Glc-NDI** in DMSO to make 8 mM, under ultrasonication (H_2O/ DMSO) = 90:10 (v/v)). After a few minutes the formation of hydrogels was observed. The gel formation is determined by tilting or inverting the sample vial upside down.

Silver mirror reaction. Tollens solution was prepared according to the reported procedure[74,88] $AgNO_3$ (0.17 g, 1.0 mmol) was dissolved in Milli-Q water (1.0 mL) and added to 12% NH_4OH until a brown precipitate appeared, followed by the disappearance of the precipitate. Freshly prepared Tollens solution (500 mL) was added to the **Glc-NDI** hydrogel and ultrasonicated for 5 min. After 1 h the pale yellow hydrogel converted into red colored hydrogel. Further, after a few days (3 days) complete evaporation of solvent resulted in the appearance of shiny silver metal deposition on the inner surface of the vial.

5.4.2 Synthesis of Jalanine appended naphthalenediimide.

1,4,5,8-Naphthalenetetracarboxylic dianhydride (0.5 g, 1.8 mmol) and β–alanine (0.33 g, 3.7 mmol) were suspended in 10 mL of DMF. To this suspension triethylamine (0.2 mL) was added and allowed to reflux for 12 h. After cooling to room temperature the reaction mixture was poured into 2N HCl (500 mL) and was stirred for 1 h. The precipitate was filtered, washed with excess of distilled water and dried in vacuum to obtain β-alanine appended naphthalenediimide in good yield (80%).

5.4.3 Synthesis of Glc-NDI.

β-Alanine appended naphthalenediimide (0.3 g, 0.7 mmol), 1-ethyl-3-(3 dimethyllaminopropyl) carbodiimide hydrochloride (220 mg, 1.1 mmol) and 1-hydroxybenzotriazole (230 mg, 1.1 mmol) were suspended in DMF (10 mL). After 15 min., glucosamine (0.26 g, 1.4 mmol) and N, N-diisopropylethylamine (440 mg, 3.4 mmol) were added to the reaction mixture and allowed to stir at room temperature for 12 h. The precipitate was filtered, washed with excess distilled water and dried in vacuum to obtain **Glc-NDI** in good yield (50%).

^{1}H NMR (*DMSO-d*$_6$, 400 MHz) δ_H 8.65 (4H, s), 7.8 (2H, d), 6.43 (2H, q), 4.90-4.80 (4H, m), 4.55-4.44 (4H, m), 4.26 (4H, br), 3.63-3.56 (8H, br), 3.46-3.06 (3H, br), 2.58-2.54 (5H, m); ^{13}C NMR (*DMSO-d*$_6$, 100 MHz) δ_C 169.8, 162.4, 130.3, 126.3, 126.2, 90.5, 72.0, 71.1, 70.4, 61.1, 54.2, 36.9, 33.0. Elemental analysis: found C, 52.47; H, 4.99; N, 7.62; calcd C, 52.46; H, 4.95; N, 7.65 for $C_{32}H_{36}N_4O_{16}$.

5.5 Appendix

- ^{1}H and ^{13}C NMR spectra of **Glc-NDI**

^{1}H NMR spectra (DMSO-*d6*, 400 MHz) of **Glc-NDI**

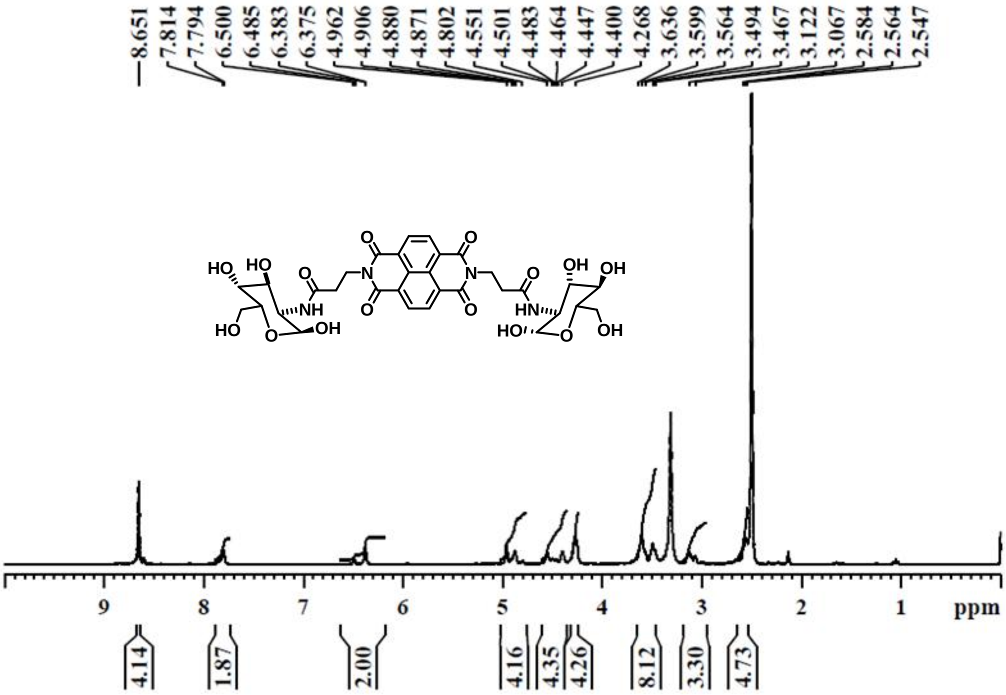

^{13}C NMR spectra (DMSO-*d6*, 100 MHz) of **Glc-NDI**

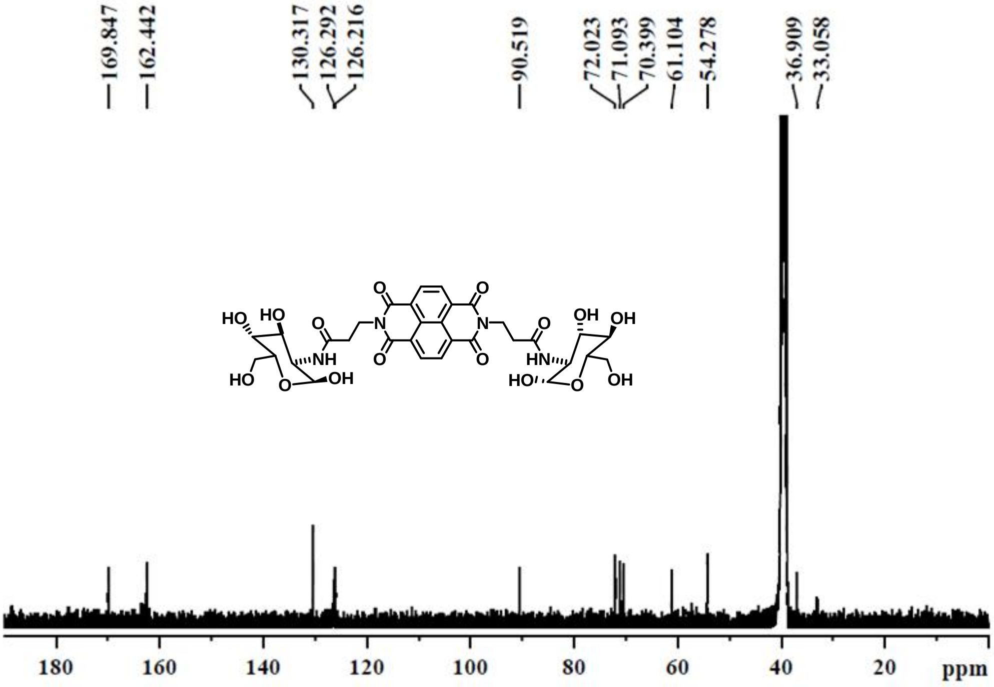

5.6 References

1. Watson, J. D.; Crick, F. H., Molecular structure of nucleic acids; a structure for deoxyribose nucleic acid. *Nature* **1953,** *171*, 737-738.
2. Wang, Y.; Xu, J.; Wang, Y.; Chen, H., Emerging chirality in nanoscience. *Chem. Soc. Rev.* **2013,** *42*, 2930-2962.
3. Hegstrom, R. A.; Kondepudi, D. K., The Handedness of the Universe. *Sci. Am.* **1990,** *262*, 108-115.
4. Liu, M.; Zhang, L.; Wang, T., Supramolecular Chirality in Self-Assembled Systems. *Chem. Rev.* **2015,** *115*, 7304-7397.
5. McLachlan, A. D., Structural implications of the myosin amino acid sequence. *Annu. Rev. Biophys. Bioeng.* **1984,** *13*, 167-189.
6. Cronin, J. R.; Pizzarello, S., Enantiomeric excesses in meteoritic amino acids. *Science* **1997,** *275*, 951-955.
7. Mateos-Timoneda, M. A.; Crego-Calama, M.; Reinhoudt, D. N., Supramolecular chirality of self-assembled systems in solution. *Chem. Soc. Rev.* **2004,** *33*, 363-372.
8. Eyre, D. R., Collagen: molecular diversity in the body's protein scaffold. *Science* **1980,** *207*, 1315-1322.
9. Wang, A. D.; Huang, J. B.; Yan, Y., Hierarchical molecular self-assemblies: construction and advantages. *Soft Matter* **2014,** *10*, 3362-3373.
10. Duan, P. F.; Cao, H.; Zhang, L.; Liu, M. H., Gelation induced supramolecular chirality: chirality transfer, amplification and application. *Soft Matter* **2014,** *10*, 5428-5448.
11. Jin, W.; Fukushima, T.; Niki, M.; Kosaka, A.; Ishii, N.; Aida, T., Self-assembled graphitic nanotubes with one-handed helical arrays of a chiral amphiphilic molecular graphene. *Proc. Natl. Acad. Sci. U. S. A.* **2005,** *102*, 10801-10806.
12. Torsi, L.; Farinola, G. M.; Marinelli, F.; Tanese, M. C.; Omar, O. H.; Valli, L.; Babudri, F.; Palmisano, F.; Zambonin, P. G.; Naso, F., A sensitivity-enhanced field-effect chiral sensor. *Nat. Mater.* **2008,** *7*, 412-417.
13. O'Leary, L. E. R.; Fallas, J. A.; Bakota, E. L.; Kang, M. K.; Hartgerink, J. D., Multi-hierarchical self-assembly of a collagen mimetic peptide from triple helix to nanofibre and hydrogel. *Nature Chem.* **2011,** *3*, 821-828.
14. Perez-Garcia, L.; Amabilino, D. B., Spontaneous resolution under supramolecular control. *Chem. Soc. Rev.* **2002,** *31*, 342-356.
15. Noguez, C.; Garzon, I. L., Optically active metal nanoparticles. *Chem. Soc. Rev.* **2009,** *38*, 757-771.
16. Lee, C. C.; Grenier, C.; Meijer, E. W.; Schenning, A. P., Preparation and characterization of helical self-assembled nanofibers. *Chem. Soc. Rev.* **2009,** *38*, 671-683.

17. Canary, J. W., Redox-triggered chiroptical molecular switches. *Chem. Soc. Rev.* **2009,** *38*, 747-756.

18. Amabilino, D. B., Chiral nanoscale systems: preparation, structure, properties and function. *Chem. Soc. Rev.* **2009,** *38*, 669-670.

19. Hembury, G. A.; Borovkov, V. V.; Inoue, Y., Chirality-sensing supramolecular systems. *Chem. Rev.* **2008,** *108*, 1-73.

20. Feringa, B. L.; van Delden, R. A.; Koumura, N.; Geertsema, E. M., Chiroptical Molecular Switches. *Chem. Rev.* **2000,** *100*, 1789-1816.

21. Cornelissen, J. J.; Rowan, A. E.; Nolte, R. J.; Sommerdijk, N. A., Chiral architectures from macromolecular building blocks. *Chem. Rev.* **2001,** *101*, 4039-4070.

22. Jo, H. H.; Lin, C. Y.; Anslyn, E. V., Rapid optical methods for enantiomeric excess analysis: from enantioselective indicator displacement assays to exciton-coupled circular dichroism. *Acc. Chem. Res.* **2014,** *47*, 2212-2221.

23. Rekharsky, M. V.; Yamamura, H.; Inoue, C.; Kawai, M.; Osaka, I.; Arakawa, R.; Shiba, K.; Sato, A.; Ko, Y. H.; Selvapalam, N.; Kim, K.; Inoue, Y., Chiral recognition in cucurbituril cavities. *J. Am. Chem. Soc.* **2006,** *128*, 14871-14880.

24. Miao, W.; Zhang, L.; Wang, X.; Qin, L.; Liu, M., Gelation-induced visible supramolecular chiral recognition by fluorescent metal complexes of quinolinol-glutamide. *Langmuir* **2013,** *29*, 5435-5442.

25. Li, X.; Tanasova, M.; Vasileiou, C.; Borhan, B., Fluorinated porphyrin tweezer: a powerful reporter of absolute configuration for erythro and threo diols, amino alcohols, and diamines. *J. Am. Chem. Soc.* **2008,** *130*, 1885-1893.

26. Biedermann, F.; Nau, W. M., Noncovalent chirality sensing ensembles for the detection and reaction monitoring of amino acids, peptides, proteins, and aromatic drugs. *Angew Chem Int Ed Engl* **2014,** *53*, 5694-5699.

27. Pu, L., Enantioselective Fluorescent Sensors: A Tale of BINOL. *Acc. Chem. Res.* **2012,** *45*, 150-163.

28. Shi, L.; Wang, X. W.; Sandoval, C. A.; Li, M. X.; Qi, Q. Y.; Li, Z. T.; Ding, K. L., Engineering a polymeric chiral catalyst by using hydrogen bonding and coordination interactions. *Angew. Chem., Int. Ed.* **2006,** *45*, 4108-4112.

29. Hatano, M.; Mizuno, T.; Izumiseki, A.; Usami, R.; Asai, T.; Akakura, M.; Ishihara, K., Enantioselective Diels-Alder Reactions with Anomalous endo/exo Selectivities Using Conformationally Flexible Chiral Supramolecular Catalysts. *Angew. Chem., Int. Ed.* **2011,** *50*, 12189-12192.

30. Jin, Q. X.; Zhang, L.; Cao, H.; Wang, T. Y.; Zhu, X. F.; Jiang, J.; Liu, M. H., Self-Assembly of Copper(II) Ion-Mediated Nanotube and Its Supramolecular Chiral Catalytic Behavior. *Langmuir* **2011,** *27*, 13847-13853.

31. Pandeeswar, M.; Avinash, M. B.; Govindaraju, T., Chiral Transcription and Retentive Helical Memory: Probing Peptide Auxiliaries Appended with Naphthalenediimides for Their One-Dimensional Molecular Organization. *Chem. Eur. J.* **2012,** *18*, 4818-4822.
32. Zou, W. J.; Yan, Y.; Fang, J.; Yang, Y.; Liang, J.; Deng, K.; Yao, J. L.; Wei, Z. X., Biomimetic Superhelical Conducting Microfibers with Homochirality for Enantioselective Sensing. *J. Am. Chem. Soc.* **2014,** *136*, 578-581.
33. Yashima, E.; Maeda, K.; Iida, H.; Furusho, Y.; Nagai, K., Helical Polymers: Synthesis, Structures, and Functions. *Chem. Rev.* **2009,** *109*, 6102-6211.
34. Zhang, W.; Jin, W.; Fukushima, T.; Ishii, N.; Aida, T., Dynamic or nondynamic? Helical trajectory in hexabenzocoronene nanotubes biased by a detachable chiral auxiliary. *J. Am. Chem. Soc.* **2013,** *135*, 114-117.
35. Verbiest, T.; Van Elshocht, S.; Kauranen, M.; Hellemans, L.; Snauwaert, J.; Nuckolls, C.; Katz, T. J.; Persoons, A., Strong enhancement of nonlinear optical properties through supramolecular chirality. *Science* **1998,** *282*, 913-915.
36. Zhang, Y. Q.; Chen, P. L.; Jiang, L.; Hu, W. P.; Liu, M. H., Controllable Fabrication of Supramolecular Nanocoils and Nanoribbons and Their Morphology-Dependent Photoswitching. *J. Am. Chem. Soc.* **2009,** *131*, 2756-2757.
37. Peeters, E.; Christiaans, M. P. T.; Janssen, R. A. J.; Schoo, H. F. M.; Dekkers, H. P. J. M.; Meijer, E. W., Circularly polarized electroluminescence from a polymer light-emitting diode. *J. Am. Chem. Soc.* **1997,** *119*, 9909-9910.
38. Watanabe, K.; Osaka, I.; Yorozuya, S.; Akagi, K., Helically π-Stacked Thiophene-Based Copolymers with Circularly Polarized Fluorescence: High Dissymmetry Factors Enhanced by Self-Ordering in Chiral Nematic Liquid Crystal Phase. *Chem. Mater.* **2012,** *24*, 1011-1024.
39. Yang, Y.; da Costa, R. C.; Fuchter, M. J.; Campbell, A. J., Circularly polarized light detection by a chiral organic semiconductor transistor. *Nat. Photonics* **2013,** *7*, 634-638.
40. Keith, C.; Reddy, R. A.; Hauser, A.; Baumeister, U.; Tschierske, C., Silicon-containing polyphilic bent-core molecules: The importance of nanosegregation for the development of chirality and polar order in liquid crystalline phases formed by achiral molecules. *J. Am. Chem. Soc.* **2006,** *128*, 3051-3066.
41. Zhang, C.; Diorio, N.; Lavrentovich, O. D.; Jakli, A., Helical nanofilaments of bent-core liquid crystals with a second twist. *Nat. Commun.* **2014,** *5*.
42. Liu, G. F.; Zhang, D.; Feng, C. L., Control of Three-Dimensional Cell Adhesion by the Chirality of Nanofibers in Hydrogels. *Angew. Chem., Int. Ed.* **2014,** *53*, 7789-7793.
43. Das, R. K.; Zouani, O. F.; Labrugere, C.; Oda, R.; Durrieu, M. C., Influence of Nanohelical Shape and Periodicity on Stem Cell Fate. *ACS Nano* **2013,** *7*, 3351-3361.
44. Lv, K.; Zhang, L.; Lu, W.; Liu, M., Control of supramolecular chirality of nanofibers and its effect on protein adhesion. *ACS Appl. Mater. Interfaces* **2014,** *6*, 18878-18884.

45. Feng, X. L.; Marcon, V.; Pisula, W.; Hansen, M. R.; Kirkpatrick, J.; Grozema, F.; Andrienko, D.; Kremer, K.; Mullen, K., Towards high charge-carrier mobilities by rational design of the shape and periphery of discotics. *Nat. Mater.* **2009,** *8*, 421-426.
46. Autschbach, J.; Nitsch-Velasquez, L.; Rudolph, M., Time-dependent density functional response theory for electronic chiroptical properties of chiral molecules. *Top. Curr. Chem.* **2011,** *298*, 1-98.
47. Rudick, J. G.; Percec, V., Induced helical backbone conformations of self-organizable dendronized polymers. *Acc. Chem. Res.* **2008,** *41*, 1641-1652.
48. Yashima, E.; Maeda, K.; Furusho, Y., Single- and double-stranded helical polymers: synthesis, structures, and functions. *Acc. Chem. Res.* **2008,** *41*, 1166-1180.
49. Yashima, E.; Maeda, K.; Furusho, Y., Single- and double-stranded helical polymers: Synthesis, structures, and functions. *Acc. Chem. Res.* **2008,** *41*, 1166-1180.
50. Fuhrhop, J. H.; Wang, T., Bolaamphiphiles. *Chem. Rev.* **2004,** *104*, 2901-2937.
51. Rowan, A. E.; Nolte, R. J. M., Helical molecular programming. *Angew. Chem. Int. Ed.* **1998,** *37*, 63-68.
52. Berl, V.; Huc, I.; Khoury, R. G.; Lehn, J.-M., Helical molecular programming: supramolecular double helices by dimerization of helical oligopyridine-dicarboxamide strands. *Chem. - Eur. J.* **2001,** *7*, 2810-2820.
53. Schmuck, C., Molecules with helical structure: How to build a molecular spiral staircase. *Angew. Chem. Int. Ed.* **2003,** *42*, 2448-2452.
54. Huang, Y. W.; Wei, Z. X., Self-assembly of chiral amphiphiles with pi-conjugated tectons. *Chin. Sci. Bull.* **2012,** *57*, 4246-4256.
55. Avarvari, N.; Wallis, J. D., Strategies towards chiral molecular conductors. *J. Mater. Chem.* **2009,** *19*, 4061-4076.
56. Leclere, P.; Surin, M.; Lazzaroni, R.; Kilbinger, A. F. M.; Henze, O.; Jonkheijm, P.; Biscarini, F.; Cavallini, M.; Feast, W. J.; Meijer, E. W.; Schenning, A. P. H. J., Surface-controlled self-assembly of chiral sexithiophenes. *J. Mater. Chem.* **2004,** *14*, 1959-1963.
57. Sommerdijk, N. A. J. M.; Buynsters, P. J. J. A.; Akdemir, H.; Geurts, D. G.; Pistorius, A. M. A.; Feiters, M. C.; Nolte, R. J. M.; Zwanenburg, B., Expression of supramolecular chirality in aggregates of chiral amide-containing surfactants. *Chem. - Eur. J.* **1998,** *4*, 127-136.
58. Danila, I.; Riobe, F.; Piron, F.; Puigmarti-Luis, J.; Wallis, J. D.; Linares, M.; Agren, H.; Beljonne, D.; Amabilino, D. B.; Avarvari, N., Hierarchical chiral expression from the nano- to mesoscale in synthetic supramolecular helical fibers of a nonamphiphilic C3-symmetrical pi-functional molecule. *J. Am. Chem. Soc.* **2011,** *133*, 8344-8353.
59. Elemans, J. A. A. W.; Rowan, A. E.; Nolte, R. J. M., Mastering molecular matter. Supramolecular architectures by hierarchical self-assembly. *J. Mater. Chem.* **2003,** *13*, 2661-2670.

60. Cornelissen, J.; Fischer, M.; Sommerdijk, N.; Nolte, R. J. M., Helical superstructures from charged Poly(styrene)-Poly(isocyanodipeptide) block copolymers. *Science* **1998,** *280*, 1427-1430.

61. Cui, H. G.; Cheetham, A. G.; Pashuck, E. T.; Stupp, S. I., Amino Acid Sequence in Constitutionally Isomeric Tetrapeptide Amphiphiles Dictates Architecture of One-Dimensional Nanostructures. *J. Am. Chem. Soc.* **2014,** *136*, 12461-12468.

62. Pandeeswar, M.; Avinash, M. B.; Govindaraju, T., Chiral Transcription and Retentive Helical Memory: Probing Peptide Auxiliaries Appended with Naphthalenediimides for Their One-Dimensional Molecular Organization. *Chem. - Eur. J.* **2012,** *18*, 4818-4822.

63. Dwivedi, A. K.; Pandeeswar, M.; Govindaraju, T., Assembly Modulation of PDI Derivative as a Supramolecular Fluorescence Switching Probe for Detection of Cationic Surfactant and Metal Ions in Aqueous Media. *ACS Appl. Mater. Interfaces* **2014,** *6*, 21369-21379.

64. Pandeeswar, M.; Khare, H.; Ramakumar, S.; Govindaraju, T., Crystallographic insight-guided nanoarchitectonics and conductivity modulation of an n-type organic semiconductor through peptide conjugation. *Chem. Commun.* **2015,** *51*, 8315-8318.

65. Pandeeswar, M.; Govindaraju, T., Bioinspired Nanoarchitectonics of Naphthalene Diimide to Access 2D Sheets of Tunable Size, Shape, and Optoelectronic Properties. *J. Inorg. Organomet. Polym.* **2015,** *25*, 293-300.

66. Pandeeswar, M.; Govindaraju, T., Green-fluorescent naphthalene diimide: conducting layered hierarchical 2D nanosheets and reversible probe for detection of aromatic solvents. *RSC Adv.* **2013,** *3*, 11459-11462.

67. Pandeeswar, M.; Khare, H.; Ramakumar, S.; Govindaraju, T., Biomimetic molecular organization of naphthalene diimide in the solid state: tunable (chiro-) optical, viscoelastic and nanoscale properties. *RSC Adv.* **2014,** *4*, 20154-20163.

68. Manchineella, S.; Prathyusha, V.; Priyakumar, U. D.; Govindaraju, T., Solvent-Induced Helical Assembly and Reversible Chiroptical Switching of Chiral Cyclic-Dipeptide-Functionalized Naphthalenediimides. *Chem. - Eur. J.* **2013,** *19*, 16615-16624.

69. Avinash, M. B.; Govindaraju, T., Extremely Slow Dynamics of an Abiotic Helical Assembly: Unusual Relevance to the Secondary Structure of Proteins. *J Phys Chem Lett* **2013,** *4*, 583-588.

70. Avinash, M. B.; Govindaraju, T., Amino Acid Derivatized Arylenediimides: A Versatile Modular Approach for Functional Molecular Materials. *Adv. Mater.* **2012,** *24*, 3905-3922.

71. Huang, Y. W.; Hu, J. C.; Kuang, W. F.; Wei, Z. X.; Faul, C. F. J., Modulating helicity through amphiphilicity-tuning supramolecular interactions for the controlled assembly of perylenes. *Chem. Commun.* **2011,** *47*, 5554-5556.

72. Shimizu, T.; Masuda, M.; Minamikawa, H., Supramolecular nanotube architectures based on amphiphilic molecules. *Chem. Rev.* **2005,** *105*, 1401-1443.

73. Hu, J. C.; Kuang, W. F.; Deng, K.; Zou, W. J.; Huang, Y. W.; Wei, Z. X.; Faul, C. F. J., Self-Assembled Sugar-Substituted Perylene Diimide Nanostructures with Homochirality and High Gas Sensitivity. *Adv. Funct. Mater.* **2012,** *22*, 4149-4158.
74. Komizo, K.; Ikedo, H.; Sato, S.; Takenaka, S., Metallization of Double-Stranded DNA Triggered by Bound Galactose-Modified Naphthalene Diimide. *Bioconjugate Chem.* **2014,** *25*, 1547-1555.
75. Narayanaswamy, N.; Suresh, G.; Priyakumar, U. D.; Govindaraju, T., Double zipper helical assembly of deoxyoligonucleotides: mutual templating and chiral imprinting to form hybrid DNA ensembles. *Chem. Commun.* **2015,** *51*, 5493-5496.
76. Nakashima, N.; Asakuma, S.; Kunitake, T., Optical microscopic study of helical superstructures of chiral bilayer membranes. *J. Am. Chem. Soc.* **1985,** *107*, 509-510.
77. Avinash, M. B.; Govindaraju, T., Nanoarchitectonics of biomolecular assemblies for functional applications. *Nanoscale* **2014,** *6*, 13348-13369.
78. Avinash, M. B.; Govindaraju, T., Nanoarchitectonics of biomolecular assemblies for functional applications. *Nanoscale* **2014,** *6*, 13348-13369.
79. Bhosale, S. V.; Jani, C. H.; Langford, S. J., Chemistry of naphthalene diimides. *Chem. Soc. Rev.* **2008,** *37*, 331-342.
80. Tumiatti, V.; Milelli, A.; Minarini, A.; Micco, M.; Gasperi Campani, A.; Roncuzzi, L.; Baiocchi, D.; Marinello, J.; Capranico, G.; Zini, M.; Stefanelli, C.; Melchiorre, C., Design, Synthesis, and Biological Evaluation of Substituted Naphthalene Imides and Diimides as Anticancer Agent. *J. Med. Chem.* **2009,** *52*, 7873-7877.
81. Takashima, Y.; Martinez, V. M.; Furukawa, S.; Kondo, M.; Shimomura, S.; Uehara, H.; Nakahama, M.; Sugimoto, K.; Kitagawa, S., Molecular decoding using luminescence from an entangled porous framework. *Nat. Commun.* **2011,** *2*, 1-8, 8 pp.
82. Bhosale, S. V.; Bhosale, S. V.; Bhargava, S. K., Recent progress of core-substituted naphthalenediimides: highlights from 2010. *Org. Biomol. Chem.* **2012,** *10*, 6455-6468.
83. Narayanaswamy, N.; Avinash, M. B.; Govindaraju, T., Exploring hydrogen bonding and weak aromatic interactions induced assembly of adenine and thymine functionalised naphthalenediimides. *New J. Chem.* **2013,** *37*, 1302.
84. Takai, A.; Yasuda, T.; Ishizuka, T.; Kojima, T.; Takeuchi, M., A Directly Linked Ferrocene-Naphthalenediimide Conjugate: Precise Control of Stacking Structures of π-Systems by Redox Stimuli. *Angew. Chem. Int. Ed.* **2013,** *52*, 9167-9171.
85. Avinash, M. B.; Govindaraju, T., Amino acid derivatized arylenediimides: a versatile modular approach for functional molecular materials. *Adv. Mater.* **2012,** *24*, 3905-3922.
86. Avinash, M. B.; Govindaraju, T., Engineering Molecular Organization of Naphthalenediimides: Large Nanosheets with Metallic Conductivity and Attoliter Containers. *Adv. Funct. Mater.* **2011,** *21*, 3875-3882.

87. Govindaraju, T.; Avinash, M. B., Two-dimensional nanoarchitectonics: organic and hybrid materials. *Nanoscale* **2012,** *4*, 6102-6117.

88. Fischler, M.; Simon, U.; Nir, H.; Eichen, Y.; Burley, G. A.; Gierlich, J.; Gramlich, P. M. E.; Carell, T., Formation of bimetallic Ag-Au nanowires by metallization of artificial DNA duplexes. *Small* **2007,** *3*, 1049-1055.

Chapter 6: Mutual Templating of Nucleobase Conjugated NDI and Oligonucleotide (dT_n) and their Application in Optoelectronics and Ultrasensitive Detection of Hg^{2+}*

---

*Manuscript to be communicated.

6.1 Introduction

Monitoring ultra-low concentration levels of toxic heavy metal ions in our ecosystem is essential due to widespread impact they have on human health and the environment.[1-3] Mercury (Hg) is one of the most predominant of all the heavy metals with both natural (volcanic and oceanic emissions) and anthropogenic (major industrial sources like coal and gold mining, fossil fuel combustion) source and exists in multiple forms such as elemental (Hg^0), inorganic salts (Hg^{2+}) and organometallic compounds (CH_3Hg and CH_3HgCH_3).[4] Alarmingly, very low concentrations of mercury in any form (neutral or ionic) can be readily absorbed by the human brain, heart, kidneys and lungs through tight binding to proteins and causes fatal diseases.[5-6] The contaminated natural water bodies, drinking water and food chain particularly consumption of fish are regarded as some of the major sources of mercury exposure to humans.[7] Despite high toxicity, mercury has been widely used as chemical additive and energy source in many industrial applications for decades including cosmetics, thermometers, batteries, agricultural chemicals and fluorescent lamps.

On account of increasing threat and adverse effects of mercury on human health and the environment, the use and manufacture of mercury-based products has been regulated by many developed countries. According to United States Environmental Protection Agency (EPA) report the maximum permissible level of Hg^{2+} in food and drinking water is ∼2 ppb (~10 nM).[5] Therefore, selective and sensitive detection of different forms of mercury at ultra-low concentration is of paramount importance to eliminate potential hazards, and protect and maintain good human health. There have been consistent efforts in developing ways to detect mercury using various spectroscopic,[8-19] electrochemical[20-21] and conductivity[22-25] based techniques. However, most of the techniques are limited by either sensitivity or selectivity or the ecological footprint of the sensor materials. Thus, high toxicity of mercury, even at ultra-low concentrations warrants the pressing need for developing new Ultrasensitive and selective detection methods to monitor different forms of mercury that is suitable for situations involving matters of public health.

Strong and specific thymine-mercury-thymine (T-Hg-T) interaction has been used as a promising approach for the selective detection of Hg^{2+}.[8,10,12,14,16-17,26-32] A wide variety of colorimetric and fluorometric sensors based on thymine rich DNA sequences functionalized gold nanoparticles,[14,26-29] fluorophores,[8,30] and in the form of hydrogels[12,31] and DNA-based machines[8,10,16,32] have been developed. However, many of these platforms suffer from sensitivity, selectivity, robustness or stability, time consuming, high cost and poor portability. Herein, we report a novel method for Ultrasensitive detection of mercury based on the mutually templated co-assembly of organic semiconductor (adenine conjugated naphthalenediimide, BNA) and complementary single strand (ss) DNA (deoxyribooligothymidine: dT_n, where n= 6, 10, 20) by means of changes in the chiroptical and electrical conductivity (Figure 6.1). Surprisingly, relatively long homo-dT_n (6> n) sequences have not been employed to achieve extended $[dT\text{-}Hg\text{-}dT]_n$ metallo-DNA duplex probably due to the lack of proper molecular design which stabilize such extended structures. In principle, a successful molecular design involving relatively longer dT_n would significantly enhance the sensitivity of detection in comparison to previous methods where mixed apatamers and ssDNA containing only few thymine units were used. We chose to develop a novel mutually templated noncovalent co-assembly strategy involving suitably designed small organic semiconductor (BNA) and dT_n (n= 6, 10, 20). These noncovalent co-assembly systems further serve as platform to detect mercury through the assembly and disassembly process to enable sensing of ultra-low

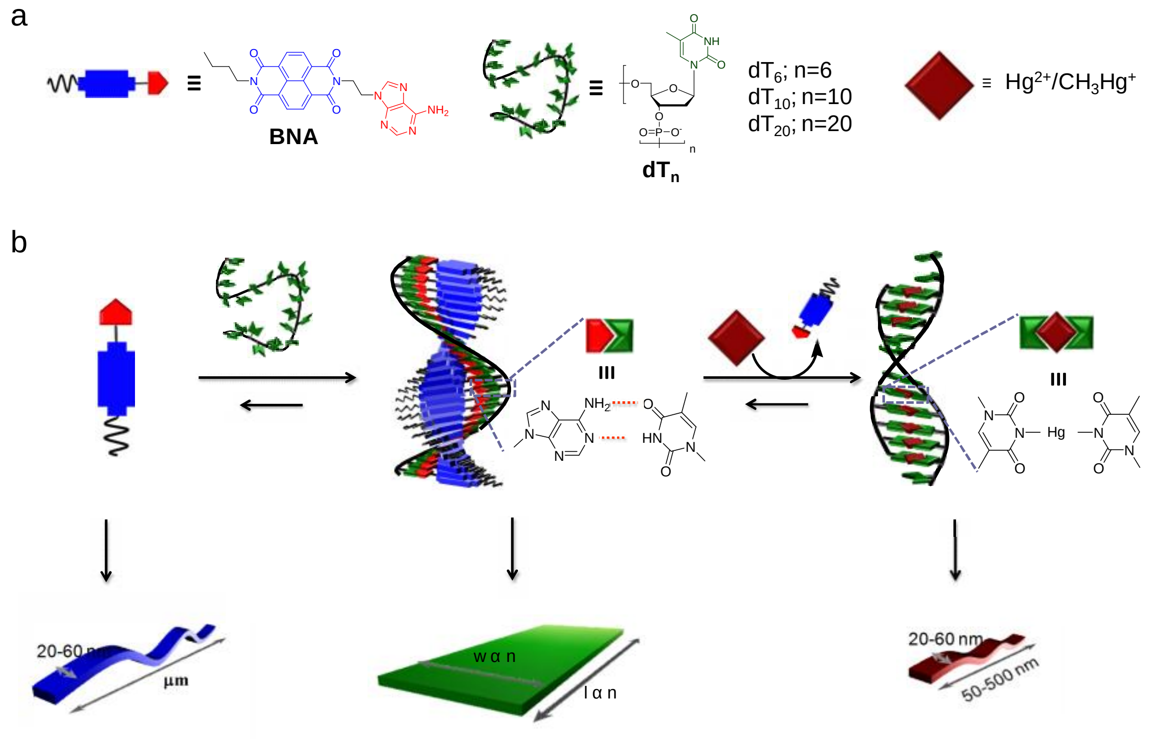

Figure 6.1 a) Molecular structures of BNA, dT_n and their pictorial representation with Hg^{2+}/CH_3Hg^+. b) Proposed molecular packing model for BNA_n-dT_n mutually templated co-assembly via complementary Watson-Crick (WC) A-T hydrogen bonding interactions and mercury mediated disassembly via formation of $[DT\text{-}Hg\text{-}DT]_n$ metallo-DNA duplex; Schematic representation of respective self-assembled structures and thier dimensions (l= length, w= width).

concentrations of the toxic mercury. The small molecular-template BNA strategically contain a butyl-group to support noncovalent hydrophobic interaction, the NDI core for aromatic π–π interaction and serve as electrically active moiety for electrical conductivity-based measurements, and adenine as a complementary nucleobase to interact with thymine units in dT_n through Watson-Crick (WC) hydrogen bonding which intern supported by the former two interactions, to aid the mutually templated co-assembly of BNA and dT_n (Figure 6.1a and b). In spite of the fact that DNA templated dyes, extended π–conjugated systems and polymers have been studied, the control over conductivity property and sensor applications has not yet been investigated.[33-41] Herein, we exploit the intrinsic property of dT_n towards the complementary base pairing with adenine containing

BNA for mutually templated chiral co-assembly and derived functional properties therein (Figure 6.1). Interestingly, the BNA alone self-assemble into 1D tapes, whereas the mutually templated co-assembly of BNA_n-dT_n forms 2D sheets with lateral dimensions of the sheets depends on dT_n length, signifying the tunable 2D morphology (Figure 6.1b). Such co-assembly behavior allows us to modulate the chirooptical, morphological and conductivity property of the BNA_n-dT_n co-assembly (Figure 6.1). Furthermore, through this strategy mutually templated BNA_n-dT_n co-assembly be used for achieving maximum thymine-mercury interaction in the form of metal supported $[dT\text{-}Hg\text{-}dT]_n$ homo-DNA duplex. The transformation of mutually templated BNA_n-dT_n co-assembly to $[T\text{-}Hg\text{-}T]_n$ metallo-DNA duplex give rise to distinct chiroptical, morphological and electrical conductivity properties which can be subsequently used as highly sensitive and selective Opto-electronic sensor system for mercury detection in solution and solid-state (Figure 6.1). Remarkably, the BNA_n-dT_n sensor system allows a ultra-low sensitivity of up to ≥ 0.1 nM for both organic (CH_3Hg) and inorganic (Hg^{2+}) mercury in water.

6.2 Results and discussion

6.2.1 Mutually templated co-assembly

N-butyl and adenine functionalized naphthalenediimide (BNA) was synthesized by two step reaction route (Figure 6.2). 1,4,5,8-Naphthalenetetracarboxylic dianhydride (NDA) was substituted with n-butylamine and 9-(2-aminoethyl)-9H-purin-6-amine as imide functionalities to obtain asymmetrically functionalised BNA in good yield. In BNA template molecules, adenine on one end is expected to make hydrogen bonding with the complementary thymines of dT_n through WC base pairing and the n-butyl chain on the other end provide hydrophobic van der Waal interactions to support the extended NDI-NDI π–stacking to form helical co-assembly of the type BNA_n-dT_n.[42]

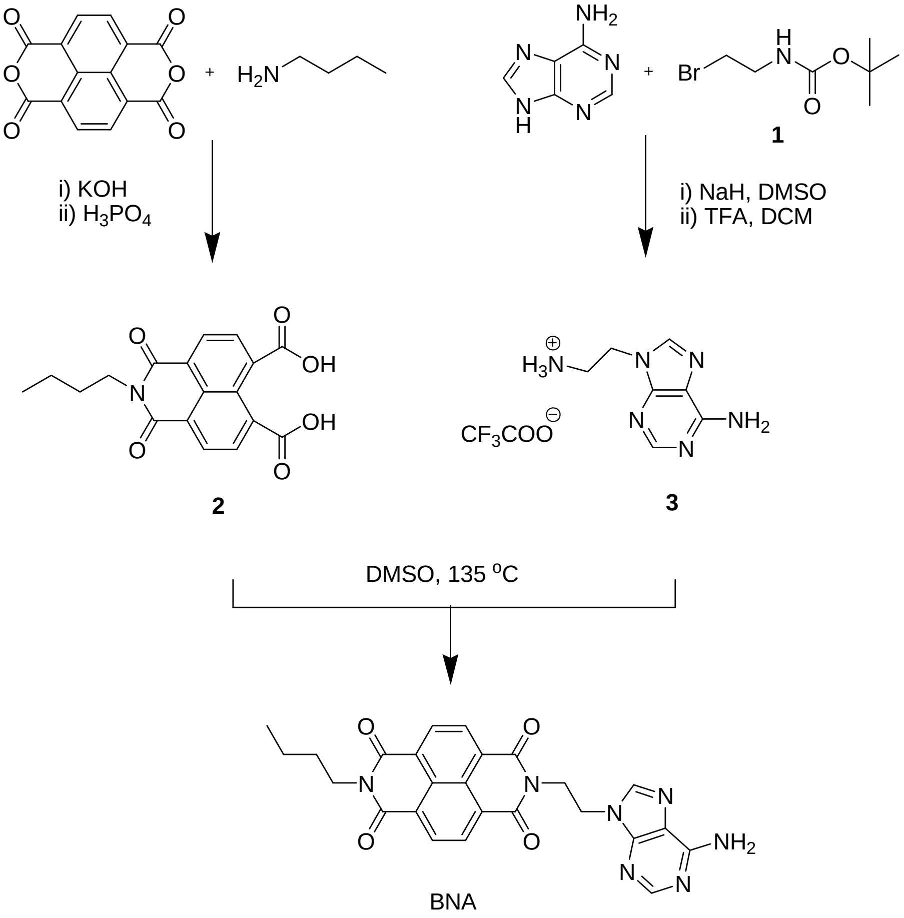

Figure 6.2 Syntheis of BNA

6.2.1.1 UV-vis absorption studies

The mutually templated co-assembly of BNA (100 μM) and dT_n (n= 6, 10 and 20) was investigated by photophysical measurements upon mixing in phosphate-buffered saline (PBS, 5% DMSO, v/v) at 294 K. The UV-vis absorption spectra of BNA displayed broad absorption bands at 300-420 nm (band-I) and 240-260 nm (band-II) corresponds to π–π* transitions polarized along long and short axis of stacked NDI chromophores respectively (Figure 6.3a). On the other hand, dT_{10} exhibited an intense broad absorption band at 263 nm. Interestingly, upon mixing BNA with dT_n (n= 6, 10 and 20) a significant hypochromic effect followed by the bathochromic shift in the band-I absorption maxima was observed suggesting edge-to-face (J-type) π–stacked NDI chromophores

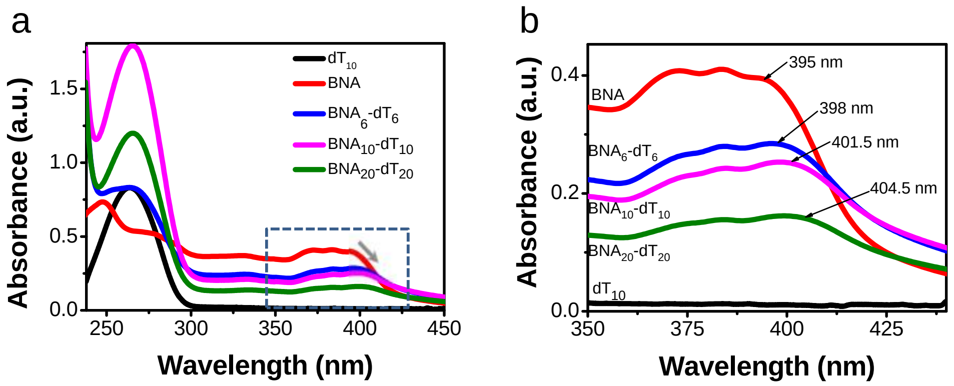

Figure 6.3 a) UV-vis absorption spectra of BNA_n-dT_n as a function of dT_n sequence length. b) The enlarged band (I) region of BNA_n-dT_n indicted as dotted box in a.

organization along the dT_n sequence (Figure 6.3a). The extent of bathochromic shift in the band-I absorption maxima was found to vary with the sequence length of dT_n ($\Delta\lambda_{max}$ ~ 3.0, 6.5, 9.5 nm for dT_6, dT_{10}, dT_{20} respectively) indicating the control over the degree of host-guest interactions among the co-assembly of BNA and dT_n (Figure 6.3b).

6.2.1.2 Circular dichroism (CD) studies

To understand the long-range molecular orientations within the BNA and dT_n co-assembly, we carried out the circular dichroism (CD) spectroscopic studies owing to its excellent and rapid assessment of induced chiral organization in a mutually templated co-assembly (Figure 6.4). BNA independently displayed flat CD signal in the absorption region of 250-400 nm signifying the absence of any preferential helical order in the self-assembly of BNA (Figure 6.4a). The complementary dT_{10} alone showed a bisignated CD cotton effect with a negative maximum at 250 nm and positive maximum at 276 nm. Remarkably, upon mixing BNA with dT_{10} at 1:1 ratio (where one BNA molecule per one thymine unit on dT_{10} template, i.e., BNA:T of dT_{10}) CD spectrum showed intense negative induced CD signal (ICD) at band-I (240-260 nm) and band-II (300-420 nm) absorption regions of NDI (Figure 6.4a). The observed ICD signal with negative

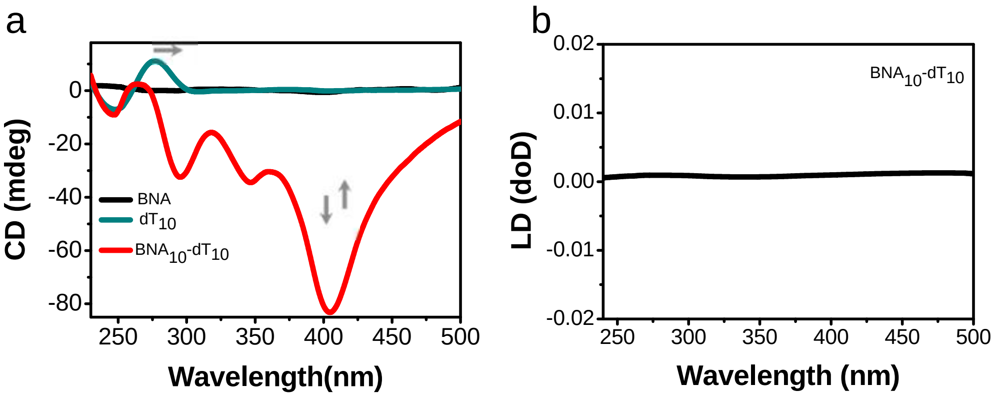

Figure 6.4 a) CD spectra of BNA (100 µM), dT_{10} (10 µM) and BNA_{10}-dT_{10} (1:1(BNA:T)) in 10 mM PBS containing 5% DMSO, at pH = 7 and 293 K. b) Linear dichroism (LD) spectra of BNA_{10}-$dT_{10,}$ the flat spectral feature indicates the absence of LD artifacts for the observed CD spectra in a.

maximum at 405 nm corresponding to π–stacked NDI chromophores, which revealed left handed (*M*-type) helical arrangement of BNA accompanied by edge-to-face stacking of transition dipoles along the NDI long axis upon co-assembly of BNA with dT_{10} (Figure 6.1).[43-44] Furthermore, the linear dichroism (LD) studies of BNA_{10}-dT_{10} showed a flat LD signal revealing the absence of any microscopic alignment artifacts for the observed CD (Figure 6.4b). Although we presume mutually adapted left handed helical assembly for dT_{10}, the overlap of NDI band I (250- 300 nm) absorption region with that of nucleobase absorption complicated the assignment at this stage. However, our subsequent studies discussed in following sections prove that assembly of BNA and dT_{10} is through mutually templating of each other to form left handed hybrid co-assembly structure.

The nucleobase preference and selectivity for the mutually templated chiral co-assembly of BNA and ssDNA (dB_n, B = A/T/G/C) was assessed by evaluating the interaction of BNA with four different dB_{10} (dA_{10}/T_{10}/G_{10}/C_{10}) (Figure 6.5a and b). The

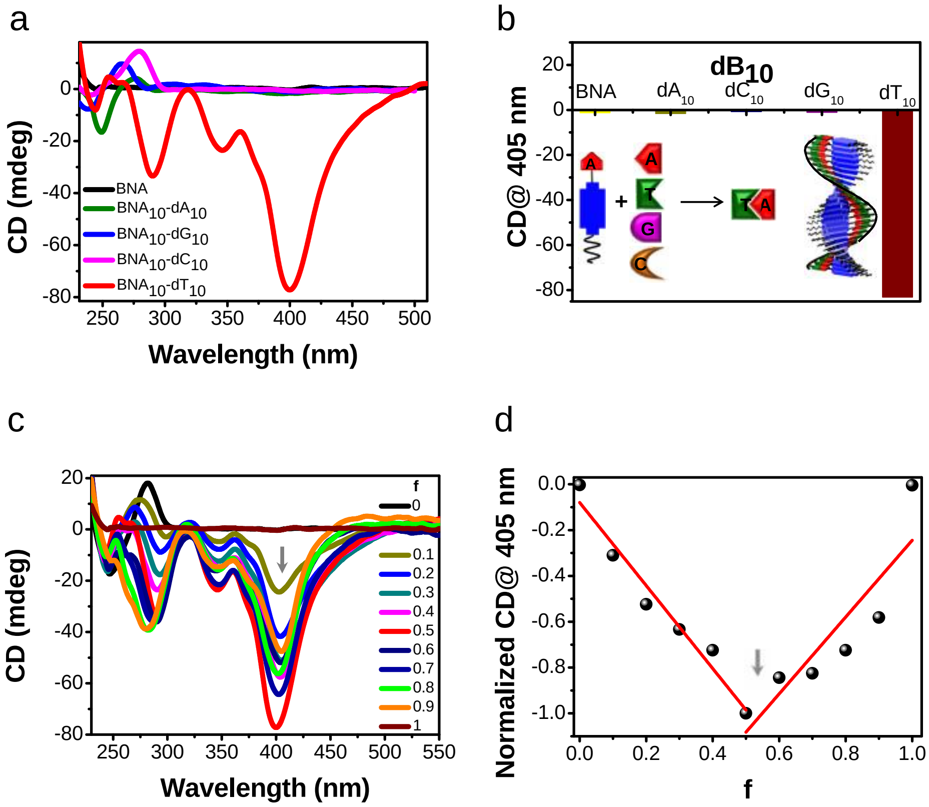

Figure 6.5 a) CD spectra of BNA in presence of various dB_n ([BNA]= 100 µM, [dB_n]= 10 µM) recorded in PBS containing 5% DMSO, at 293 K, indicating that the dT_{10} selective mutually templated co-assembly of BNA. b) The plot of CD intensity at 405 nm of BNA in presence of different oligonucleotides (dB_{10}) for the observed CD spectra in a. c) CD Job plot experiment after mixing different fractions of BNA to dT_{10}, where the total concentration [BNA]+[dT_{10}]= 110 µM kept constant and varied the fraction of BNA (f= [BNA]/110 µM) in BNA_{10}-dT_{10}. d) CD Job plot monitored at 405 nm as a function of fraction BNA.

CD data revealed that among all dB_n only complementary dT_{10} showed ICD in the 300-420 nm region, a conclusive evidence that WC base pairing (A=T) is one of the main driving force for the formation of BNA_{10}-dT_{10} helical co-assembly (Figure 6.5a and b). In order to determine the binding stoichiometry, CD Job-titration experiments were performed by keeping the total number of binding-sites constant, but varied the ratio of dT_{10} and BNA concentration ([BNA]+[dT_{10}]= 110 µM with a fraction of BNA in BNA_{10}-dT_{10} (f) = [BNA]/110 µM)] (Figure 6.5c). The job plot generated by monitoring the CD at 405 nm versus f showed an inflection point at f= 0.5 that correspond to thymine (dT_{10}): BNA ratio of 1:1 (Figure 6.5d). Therefore, Job plot data revealed that as many molecules of BNA bind to dT_{10} is equal to umber of thymine units in dT_{10} to form mutually templated BNA_{10}-dT_{10} co-assembly (Figure 6.5d).

After validating the mutually templated helical co-assembly of BNA and dT_{10}, we studied the influence of dT_n sequence length on the BNA_n-dT_n co-assembly by choosing variable lengths of dT_n. Upon mixing BNA and dT_n (n= 6, 10 and 20) in the stoichiometric (nucleobase) ratio 1:1, CD spectra showed similar ICD spectral features, but the intensity increased from dT_6 to dT_{20} suggesting higher the sequence length of dT_n better is the structural stability and integrity of BNA_n-dT_n co-assembly (Figure 6.6a). Subsequently, the thermal stability of BNA_n-dT_n co-assemblies were examined by variable-temperature CD (VT-CD) studies (Figure 6.6b). All the BNA_n-dT_n (n=6, 10 and 20) co-assemblies exhibited relatively high thermal stability as compared to that of regular (A_{10}-T_{10}) DNA duplex (melting temperature, T_m = 294.25 K)[34] suggesting the synchronized effect of WC base pairing, NDI-core aromatic π–π stacking and hydrophobic interactions of n-butyl chain in stabilising the BNA_n-dT_n helical co-assembly (Figure 6.6b). Moreover, the T_m values of BNA_n-dT_n were found to be strongly dependent on the sequence length of dT_n (T_m = 343.1, 346.5 and 353.1 K for co- assemblies with dT_6, dT_{10} and dT_{20} respectively). The observed dT_n sequence length dependent increase in T_m values of BNA_n-dT_n clearly indicates the formation extended, tightly bound co-assemblies without the loss of structural stability and integrity. The hydrogen bonding systems are known to strongly depend on the pH of the media and thus, we examined the impact of pH on the BNA_{10}-dT_{10} co-assembly at 293 K (Figure 6.6c and d). The pH of the BNA_{10}-dT_{10} solution was varied from strongly basic to acidic(pH = 11 to 1) and the ICD signal at 405 nm was monitored (Figure 6.6d). As the pH decreased from 11 to 1, the ICD

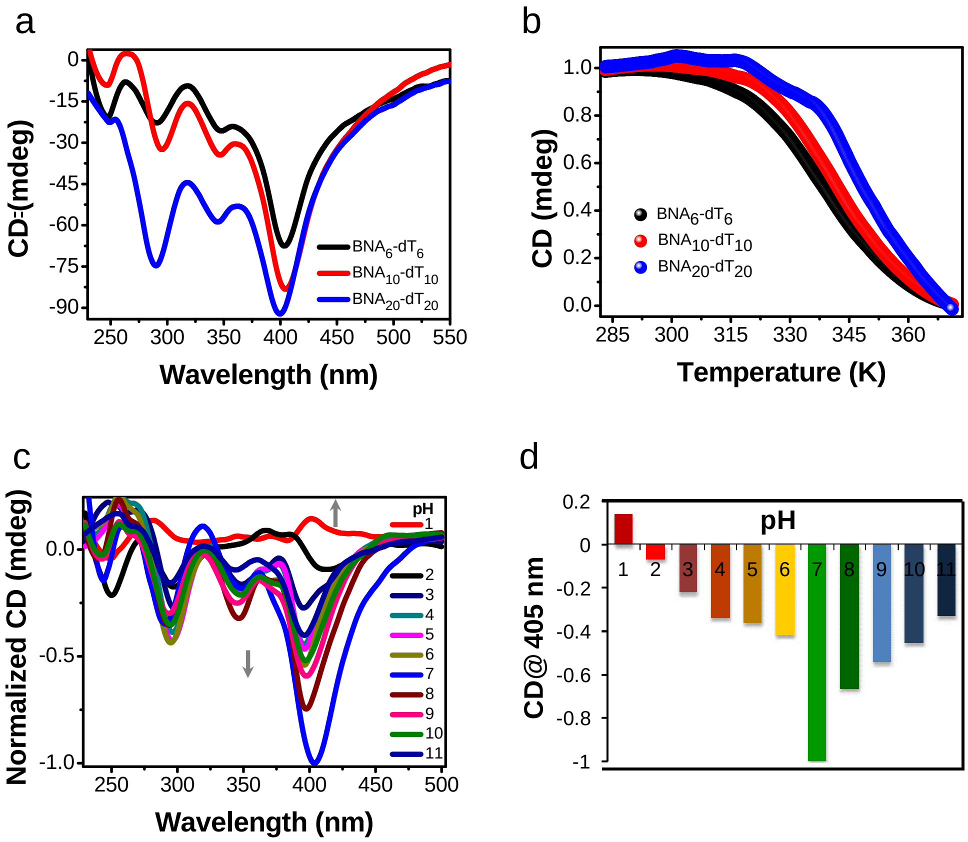

Figure 6.6 a) The dT_n sequence length dependent CD spectra of BNA_n-dT_n. b) Variable temperature CD (VT-CD) spectra of mutually templated co-assemblies of BNA_n-dT_n (n=6, 10 and 20) in 10 mM, PBS containing 5% DMSO, at pH 7. c) pH dependent CD spectra of BNA_{10}-dT_{10}. d) The plot of CD intensity at 405 nm of BNA as a function of in pH of the solution for the observed CD spectra in c.

maximum at 405 nm increases gradually to pH 7 and a further decrease in pH from 7 to 2 resulted in reduction in intensity of signal at 405 due to the protonation of an adenine moiety of BNA under acid conditions. Interestingly, this decrease is accompanied by the inversion of the cotton effect from the negative ICD (left handed helical organization) band to positive ICD (right handed helical organization) band at pH 1 (Figure 6.6c and d). This transformation is likely due to the protonation of an adenine moiety of BNA that trigger the chiral inversion through additional electrostatic interactions between the negatively charged phosphate groups on the dT_{10} backbone and positively charged adenine (AH^+) on BNA.[45]

6.2.1.3 ATR-IR studies

Furthermore, attenuated total reflection infrared (ATR-IR) spectra of BNA in aqueous D_2O solution showed N-H (adenine NH_2 BNA) symmetric stretching frequency at 3419 cm^{-1} and upon mixing with dT_{10} (BNA_{10}-dT_{10} co-assembly) this band shifted to a lower wave number (3366 cm^{-1}, broad) (Figure 6.7).[42] The significant change ($\Delta\nu \sim 53$ cm^{-1}) in the N-H symmetric stretching frequency suggest the existence of hydrogen bonding among the complementary base pairs (adenines from BNA and thymines of dT_{10}, (Figure 6.1b) which is one of the main driving forces for the formation of mutually templated helical co-assembly of BNA_{10}-dT_{10}.

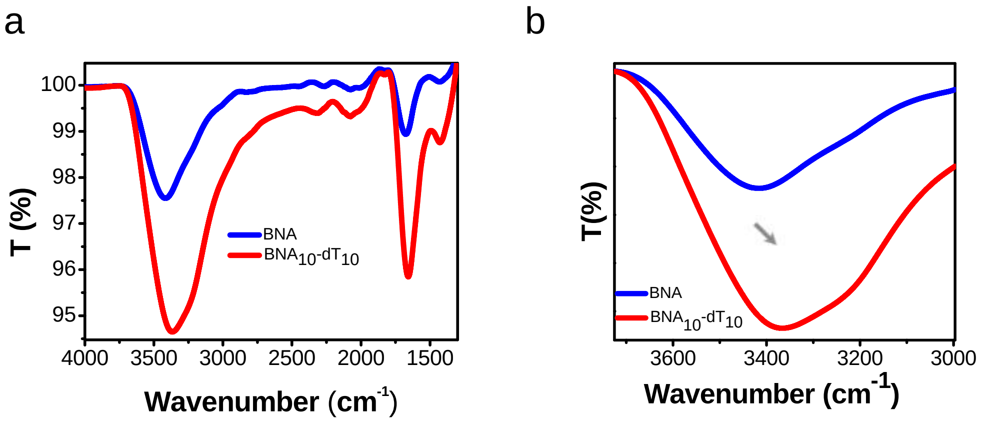

Figure 6.7 a) ATIR spectra of BNA and BNA_{10}-dT_{10}. b) The BNA adenine amine (NH) symmetric stretching frequency region (3600-3000 cm^{-1}) of BNA before and after addition of dT_{10}.

6.2.1.4 Morphological studies

To visualize the morphology of BNA_n-dT_n co-assembly, field emission scanning electron microscopy (FESEM) measurements were performed by drop-casting their solutions (PBS, pH=7.4) onto a silicon (111) surface followed by washing with milliQ water to

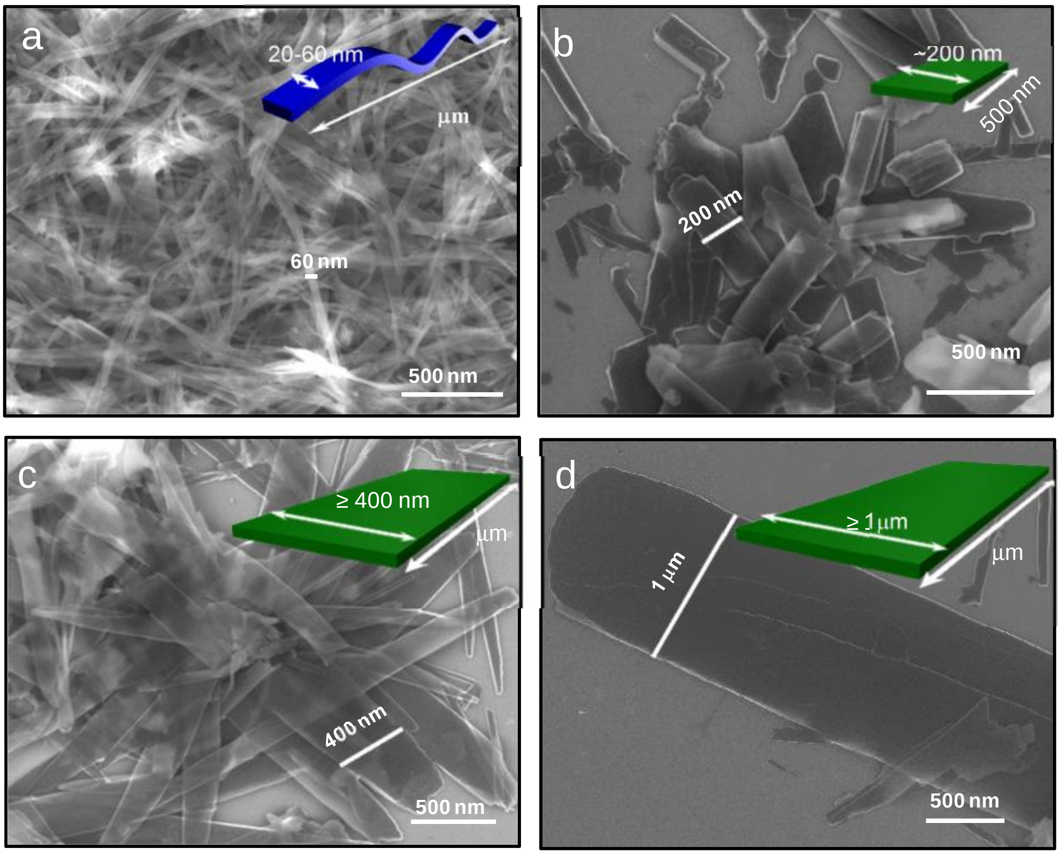

Figure 6.8 FESEM micrographs of BNA (a), BNA_6-dT_6 (b), BNA_{10}-dT_{10} (c) and BNA_{20}-dT_{20} (d); schematic representation of respective structures and their lateral dimensions.

remove excess salt and dried under high vacuum at room temperature (Figure 6.8). BNA alone displayed high aspect ratio self-assembled 1D tapes with micrometers in length and 20-60 nm width (Figure 6.8a). Under similar conditions, mutually templated BNA_n-dT_n (n = 6, 10, 20) co-assemblies showed 2D sheets with variable lateral dimensions dependent on dT_n sequence length, as shown in Figure 6.8b-d. The 2D sheets of BNA_6-dT_6 co-assembly showed average lateral dimensions of ~200 nm (width) and ~500 nm (length) (Figure 6.8b). While BNA_{10}-dT_{10} (Figure 6.8c, length: ~ 1.5 µm and width: ~400 nm) and BNA_{20}:dT_{20} (Figure 6.8d, length: ~1 mM and width: 3 µm) exhibited much larger lateral dimension.

6.2.1.5 DLS and PXRD studies

The above microscopic results were further supported by dynamic light scattering (DLS) data of BNA in the absence and presence of dT_n (Figure 6.9a). BNA alone showed aggregates of relatively small size distribution at around 164 nm. Under similar conditions, BNA_n-dT_n co-assemblies displayed size distribution with mean sizes at 396 nm, 531 nm and 615 nm corresponding to variable lengths of dT_n (n = 6, 10 and 20, respectively) (Figure 6.9a). Thus, significant change in the nanoscale morphology and DLS size distribution of BNA_n-dT_n co-assemblies, and perfect correlation with dT_n (n = 6, 10 and 20) length suggest robustness our methodology and it is possible to construct

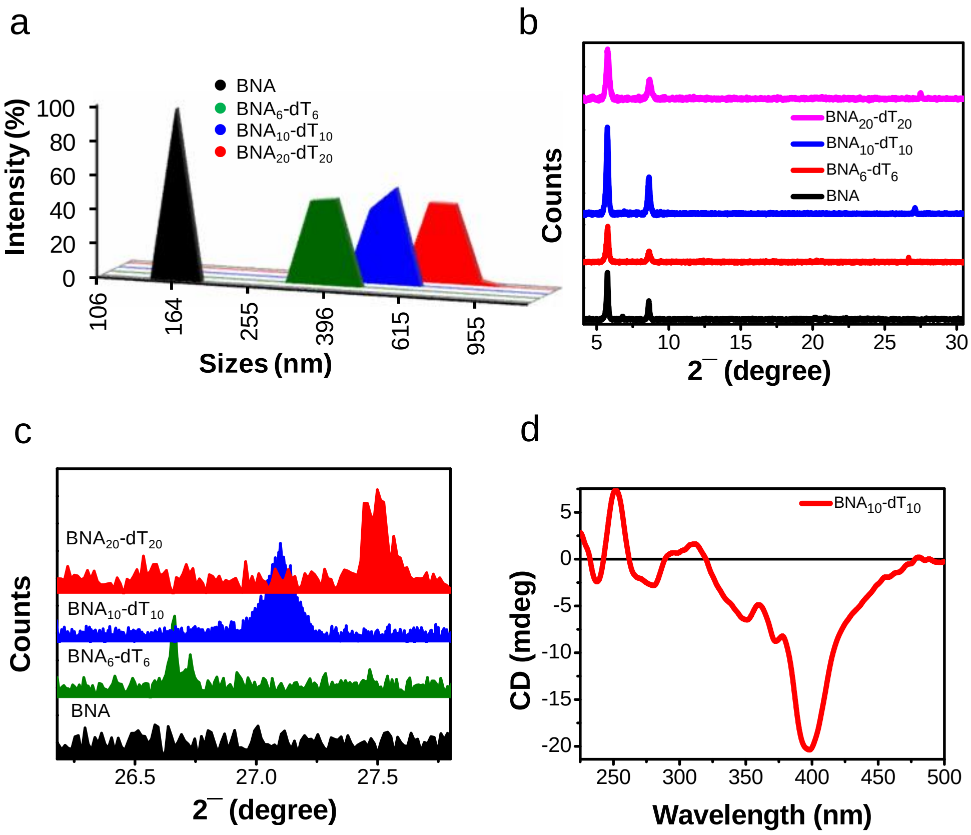

Figure 6.9 a) DLS spectra of BNA_n-dT_n. b) PXRD spectra of mutually templated co-assembly of BNA_n-dT_n (n= 6, 10 and 20). c) PXRD diffraction patterns at an aromatic π–stacking region (2θ= 26°-27°) of BNA_n-dT_n for the observed spectra in b. d) Thin film CD spectra of BNA_{10}-dT_{10} recorded on quartz substrate.

and control extended co-assemblies in solution as well as in the form of nanostructures just by varying the length of dT_n. Powder X-ray diffraction (PXRD) data of 1D and 2D nanostructures of BNA and BNA_n-dT_n, respectively displayed sharp diffraction signals suggesting the crystalline molecular organization within the nanostructures (Figure 6.9b). Interestingly, 2D sheets of BNA_n-dT_n co-assemblies exhibited new dT_n-length dependent diffraction signal in the region $2\theta = 26^o$- 28^o corresponding to aromatic NDI-NDI $\pi-\pi$ stacking distance. 2D sheets of BNA_6-dT_6 displayed diffraction signals at $2\theta=26.6^o$ which further upward shifted (or downward for d-spacing values) with increasing the length of dT_n to 27^o for BNA_{10}:dT_{10} and 27.5^o for BNA_{20}:dT_{20} (Figure 6.9c). Therefore, the gradual decrease in d-spacing values of NDI-NDI $\pi-\pi$ stacking with increase in dT_n sequence length clearly signify the formation of tighter packing of BNA molecules within the BNA_n-dT_n co-assembly due to increased cooperative binding of constituent partners supported by hydrophobic, aromatic $\pi-\pi$ stacking and hydrogen bonding interactions.

In majority of cases, the chiral molecular organization observed in solution is lost in their corresponding nanostructures. Therefore, to verify the chiral molecular packing within the 2D sheets of BNA_n-dT_n, we carried out thin film CD studies (Figure 6.9d). Interestingly, in agreement with the solution studies, thin film CD spectra showed intense negative ICD signal at both band-I (250-300 nm) and band-II (350-380 nm) absorption regions of the NDI chromophore with λ_{max} at 400 nm confirming the retention of chiral molecular packing within the 2D sheets.

6.2.1.6 Charge Transport Measurements

To understand the role of the dT_n and BNA based mutually templated co-assembly we further performed detailed transport measurements on self-assembled structures of BNA and BNA_n-dT_n (Figure 6.10). Bottom contact top gate FET structures were fabricated by introducing the BNA and BNA_n-dT_n structures from the solution phase on BCB dielectric

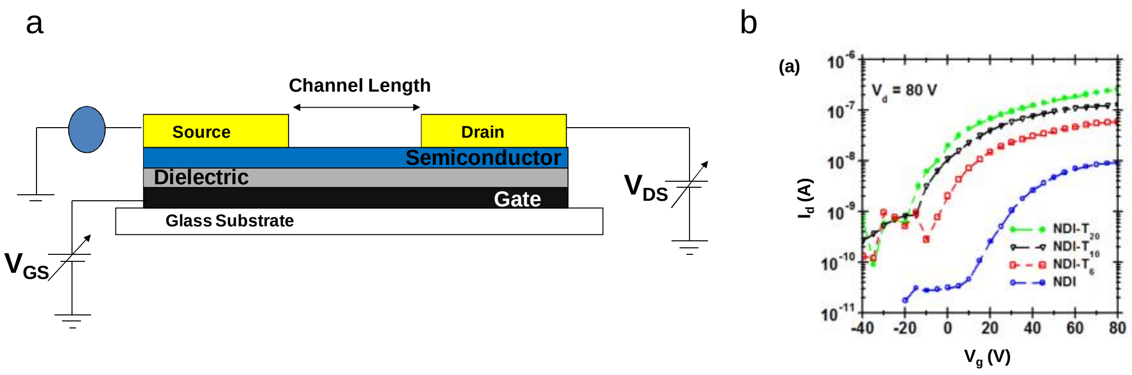

Figure 6.10 a) Bottom contact top gate FET structures. b) Typical transconductance plots for different self-assembled structures of BNA_n-dT_n.

layer followed by coating the Au source-drain electrode (Figure 6.10a). All the structures exhibited typical n-type transport with μ_{FET} in the range of 10^{-3} $cm^2V^{-1}s^{-1}$ (Figure 6.10b). The μ_{FET} increases by at least four times with the mutually templated dT_n and BNA co-assembly structures (Table 6.1). Additionally, it was also observed that μ_{FET} scales linearly with the length of the dT_n utilized for the assembly. It is evident from these observations that the transport variation is inherent to the assembly (Table 6.1). From a microscopic point of view, the dT_n and BNA mutually templated co-assembly structure demonstrated a higher degree of crystallinity with a decrease in the π-π stacking distance. In other words, dT_n and BNA mutually templated co-assembly results in a tighter packing with ordered lamellae which is expected to promote charge transport with more tolerance towards defects and disorder. Macroscopically, the molecular structure originating from BNA_n-dT_n results in a formation of 2D sheet like structure which is more tolerant to disorder compared to the 1-D tapes obtained from pristine BNA moiety. The role of morphology on the transport at the dielectric-semiconductor interface becomes evident upon comparing the doping level on the 1-D tapes and 2-D sheets. For a capacitance of $4nF/cm^2$ the doping level estimated for the tapes were obtained to be 10^9 for 1-D tapes of the pristine BNA moiety and 10^{11} for 2D sheets obtained with BNA_{20}-dT_{20}. Thus, a

Table 6.1 FET charecteristics

	μ_{max} (cm^{2}V^{-1}s^{-1}) X 10^{-3}	μ_{avg} (cm^{2}V^{-1}s^{-1}) X 10^{-3}	I_{on}/I_{off}
BNA	1.6	1.5	$> 10^3$
BNA+dT$_6$	3.5	2.7	$> 10^2$
BNA+dT$_{10}$	5.1	4.5	$> 10^2$
BNA+dT$_{20}$	6.7	6.0	$> 10^2$

combination of all these factors contributes to the better transport properties of the BNA$_n$-dT$_n$ mutual template co-assembly.

6.2.2 Hg^{2+} induced disassembly of BNA$_{10}$-dT$_{10}$

On successfully achieving the extended mutually templated co-assemblies of BNA$_n$-dT$_n$, we examined the selectivity and sensitivity of the co-assembly towards Hg^{2+} using thin film CD measurements (Figure 6.11). To assess the selectivity, perchlorate salts of Na$^+$, Mg^{2+}, K$^+$, Ca^{2+}, Co^{3+}, Ni^{2+}, Cu^{2+}, Hg^{2+} and Pb^{2+} were tested at their excess concentration (100 μM) in water. The ICD signals of BNA$_{10}$-dT$_{10}$ in the 250-420 nm region were unaffected by most of the metal ions tested except for Hg^{2+} (Figure 6.11a and c). Addition of Hg^{2+} to BNA$_{10}$-dT$_{10}$ helical co-assembly resulted in significant reduction in the intensity of ICD signals in the 250-300 nm (band II) and 350-420 nm (band I) regions of BNA that confirmed the potential of BNA$_{10}$-dT$_{10}$ as a selective chiroptical sensing platform for Hg^{2+} (Figure 6.11a). Furthermore, in presence of Hg^{2+} a huge red shift (~38 nm) in the CD signal of the nucleobase absorption region (from λ_{max}= 252 nm to 290 nm) was observed signifying the transformation of BNA$_{10}$-dT$_{10}$ helical co-assembly to[dT-Hg-dT]$_{10}$ metallo-DNA duplex (Figure 6.11a).[46] To estimate the sensitivity of detection ICD signal intensity of BNA$_{10}$:dT$_{10}$ at 405 nm was monitored upon adding increasing concentrations (0.1 nM to 50 μM) of perchlorate salt of Hg^{2+} (Figure 6.11b

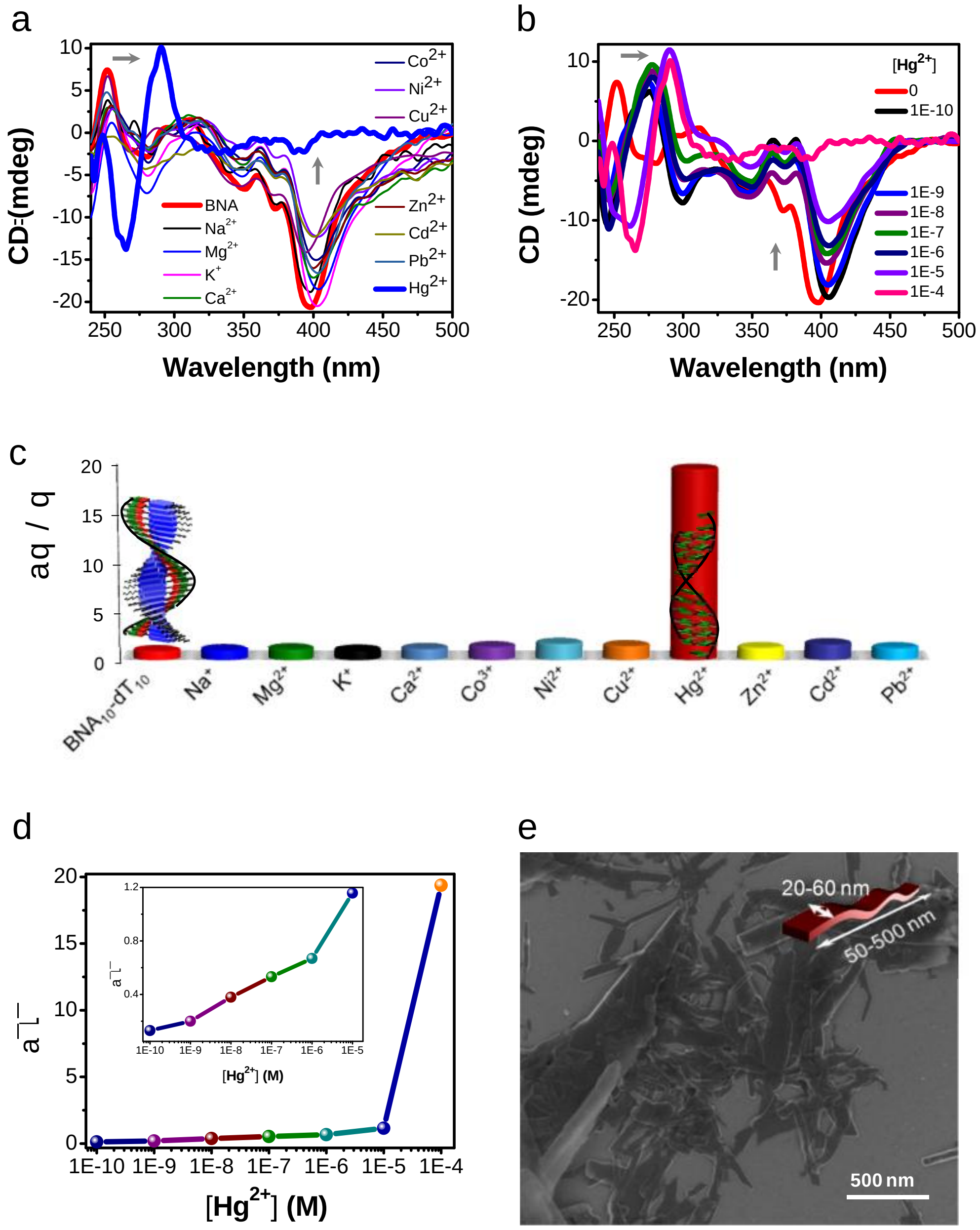

Figure 6.11 a) Thin film CD spectra of BNA$_{10}$-dT$_{10}$ in the presence of different metal ions ([M^{n+}]=100 µM). b) Thin film CD spectra of BNA$_{10}$-dT$_{10}$ upon adding various concentrations of Hg^{2+} (0.1 nM to 100 µM). c) Relative CD intensity of BNA$_{10}$-dT$_{10}$ thin film at 400 nm in presence of various metal ions (where [M^{n+}]= 100 µM, Δθ= CD$_0$- CD where CD$_0$ and CD are CD intensity at 400 nm before and after addition of metal ions respectively). d) Relative CD intensity of BNA$_{10}$-dT$_{10}$ thin film at 400 nm as a function of [Hg^{2+}] added. *Inset:* Enhanced selected spectral region (0.1 nM to 10 µM). d) FESEM micrograph of BNA$_{10}$-dT$_{10}$ +Hg^{2+}.

and d). The titration data revealed that Hg^{2+} concentrations of ≥ 0.1 nM can be easily detected by the significant change in the ICD signal intensity. Interestingly, the morphological study revealed that addition of Hg^{2+} transformed the 2D sheets of BNA_{10}-dT_{10} into fragments of 1D tapes possibly attributed to self-assembled structures of BNA alone and formation of $[dT\text{-}Hg\text{-}dT]_{10}$ metallo-DNA duplex (Figure 6.11e). Overall, property of reduction in the ICD signals of NDI in BNA_{10}-dT_{10} co-assembly and the corresponding transformation of 2D to 1D structural morphology in presence of Hg^{2+} can be effectively used to detect the toxic metal ion at sub-nanomolar concentrations.

6.2.2.1 Hg^{2+} sensing device characteristics

The ability to tune the transport property through the mutual templated co-assembly was further utilized in developing devices for sensing application. It has been discussed in the earlier section that Hg^{2+} has preferential selectivity towards dT_n. This property of dynamic assembly of BNA_n-dT_n and selectivity towards Hg^{2+} was tapped to design selective and ultra-sensitive sensor (Figure 6.12). The device structure involved fabrication of a two terminal device to monitor the I-V curves and estimating the conductivity (σ) of BNA_{10}-dT_{10} mutual template 2D structures. Typical, σ of ~ 10^{-6} S/cm and current density (J at 5 V) as high a 5×10^3 A/m^2 is obtained for the BNA_{10}-dT_{10} active layer (Figure 6.12a). For the sensing purpose, 20 μl solutions of different metallic salts (like Na^+, K^+, $CH_3Hg^+$and Hg^{2+}) were introduced onto the self-assembled active layer (L = 60 μm, W = 1 mm) from a 0.1 μM solution. Upon introduction of metal ions (like Na^+, K^+), one order increase in the current density magnitude was obtained (Figure 6.12a), however when different forms of mercury ions (CH_3Hg^+ or Hg^{2+}) were introduced a decrease in the current density was observed (Figure 6.12b). The observed increase in the J and σ in the case of devices with added Na^+ or K^+ ions can be attributed to the additional ionic conduction. Further evidence for ionic conduction also comes from the

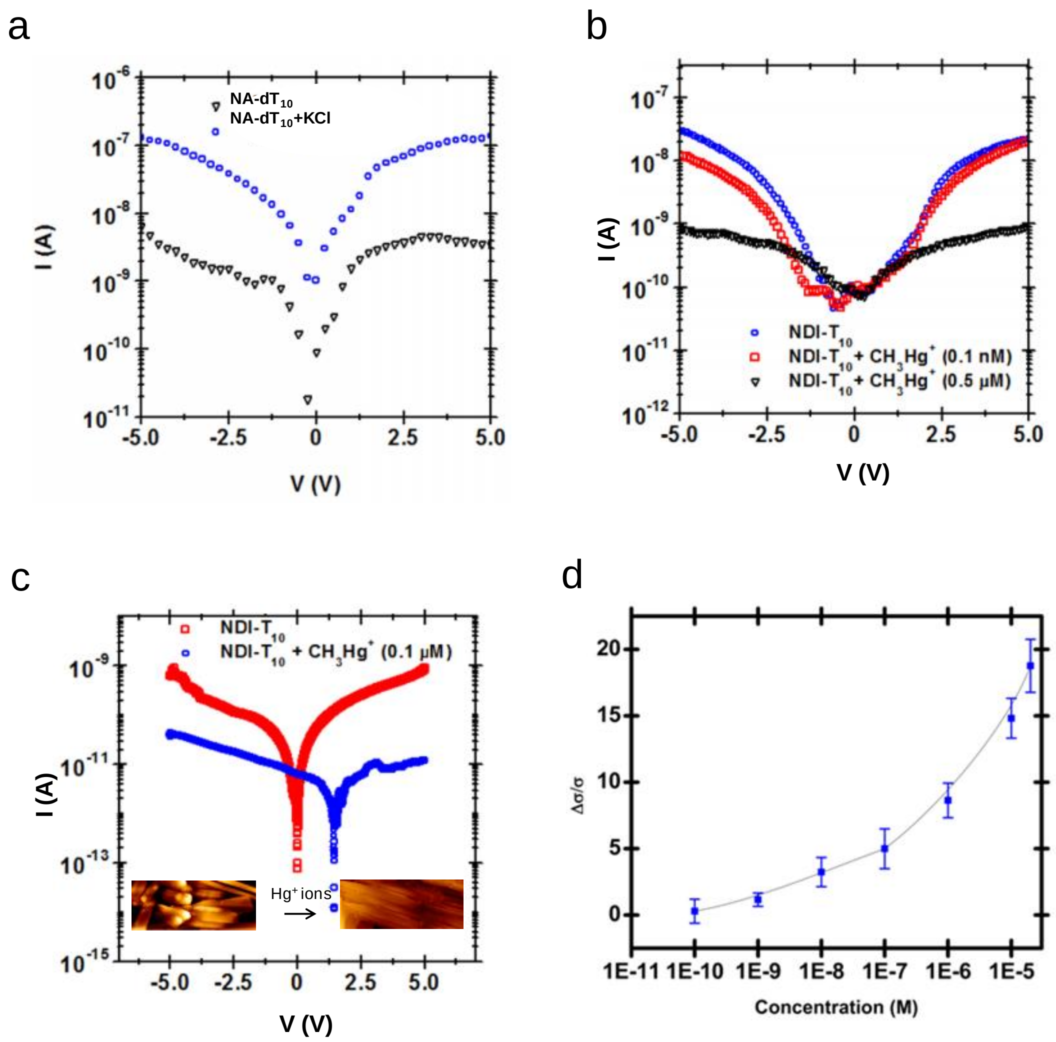

Figure 6.12 a) BNA_{10}-dT_{10} device response before and after addition of KCl. b) Conductometric sensing of CH_3Hg^+ ions. c) Conducting AFM measurements on the self-assembled structure confirming the variation in the assembly with the addition of CH_3Hg^+ ions. d) Probing the mechanism of self-assembly from the conductometric measurements obtained for different concentrations of CH_3Hg^+ ions.

fact that the J is restored to its original lower magnitude upon washing the device with water. In the case of devices where mercury ions were added to the BNA_{10}-dT_{10} active layer, the decrease in the J and σ can be related to the self-assembly dynamics. Mercury ions have preferential binding with the dT_{10} thereby, breaking the co-assembly of the BNA_{10}-dT_{10} to the lower conducting pristine BNA molecules. The extent of dissociation in the co-assembled nanostructure is proportional to the amount of the mercury ions added to the thin films. It should be noted that this variation in the conductivity upon the introduction of mercury ions in the assembly is retained for a concentration as low as 0.1 nM which sets the lower limit on the sensitivity of our conductometric based mercury sensing device (Figure 6.12b). To confirm that the observed variation in the conductivity and the current density is directly related to the self-assembly dynamics and not because of any spurious accumulation of ions or device degradation, we performed conducting-AFM measurement (CAFM) on a single sheet ((Figure 6.12c). CAFM measurements on the co-assembled NDI-DNA sheet exhibit a decrease in conductivity by an order of magnitude when 0.1 μM of mercury ions was added. We define the sensitivity of the device (χ) by the ratio of $\sigma_{before}/\sigma_{after}$. The variation of this parameter with the concentration of salt added can analytically confirm the mechanism of the self-assembly. As evident from the Figure 6.12d the net change in the conductivity as a function of CH_3Hg^+ concentration can be fitted with a nonsigmoidal decay indicating a cooperative behavior in the BNA_n-dT_n co-assembly.

Thus, it may be stated that the formation of mutually templated co-assembly of BNA and dT_{10} is supported by various noncovalent interactions such as WC base pairs (A=T, between BNA_n and dT_n), NDI-NDI aromatic $\pi-\pi$ stacking and hydrophobic interactions of n-butyl chains. Remarkably, stronger T-Hg-T interactions drives the disassembly of BNA_{10}-dT_{10} co-assembly and formation of $[dT\text{-}Hg\text{-}dT]_{10}$ metallo-DNA duplex and validate the promise of using this structural transformation for chiroptical and conductivity-based sensing platform for Hg^{2+} in water.

6.3 Conclusion

We developed a novel strategy based on mutually templated co-assembly (BNA_n-dT_n) of organic semiconductor and ssDNA for the selective, and ultrasensitive detection of mercury in water. Both chiroptical and conductivity-based measurements revealed sub-nanomolar sensitivity (0.1 nM or 0.02 ppb) towards mercury ions (inorganic and organometallic forms) in water, which is ten-folds of magnitude lower than the allowed United States Environmental Protection Agency (EPA) standard limit (10 nM, 2 ppb) in drinking water. The transition from mutually templated co-assembly of BNA_{10}-dT_{10} to $[dT\text{-}Hg\text{-}dT]_{10}$ metallo-DNA duplex formation in presence of mercury offers a selective and ultrasensitive sensor platform for mercury detection. Furthermore, BNA_n-dT_n (n = 6, 10 and 20) co-assembly exhibited structural stability, integrity and properties linearly dependent on the sequence length of dT_n. Thus, extended and stronger BNA_n-dT_n co-assemblies can be prepared with longer dT_n for enhancing the sensitivity of the systems towards the detection of mercury. This work also highlights the concept of templated DNA nanotechnology and its potential applications.

6.4 Experimental section

Materials and methods. Deoxyoligonucleotides/ssDNA (dB_n/oligos: dA_{10}, dT_{10}, dG_{10}, dC_{10}, dT_6, and dT_{20}), phosphate buffered saline (PBS), 1,4,5,8-naphthalenetetracarboxylic dianhydride (NDA), n-butylamine, thyminyl-1-acetic acid, 2- bromo-ethylamine hydrogen bromide were purchased from Sigma–Aldrich. Di-tert-butyl dicarbonate, bromo-methyl acetate, and adenine were obtained from Spectrochem Pvt. Ltd. Mumbai (India). All reagents were used as received unless otherwise mentioned.

Sequence information of ssDNA (dB_n, B = A/T/G/C) used in this study.

dT_6: 5’-TTTTTT-3’

dA_{10}: 5’-AAAAAAAAAA-3’

dT_{10}: 5’-TTTTTTTTTT-3’

dG_{10}: 5’-GGGGGGGGGG-3’

dC_{10}: 5’-CCCCCCCCCC-3’

dT_{20}: 5’-TTTTTTTTTTTTTTTTTTTT-3’

Sample preparation for UV-vis and CD measurements. dB_n (dA_{10}, dT_{10}, dG_{10}, dC_{10}, dT_6, and dT_{20}) stock solutions were prepared by dissolving the oligos in double deionized water in the order of 10^{-4} M. The mutually templated co-assembly (BNA_n-dT_n) of oligos were prepared by adding the BNA (from 4 mM stock solution in DMSO) into PBS-buffer solution (10 mM, pH = 7, 5% DMSO) and solution was subjected to annealing by heating the sample to 85 ºC for 15 min followed by cooling it to room temperature for 7 h, stored in refrigerator for 4 h.

Absorption spectroscopy. UV–vis spectra were recorded on a Perkin Elmer Model Lambda 900 spectrophotometer. All the samples were analyzed in quartz cuvette of 10 mm path length. Blank sample containing PBS buffer solution (10 mM, pH = 7, 5% DMSO) was recorded and subtracted from the collected data.

Circular dichroism (CD). CD measurements were carried out on a Jasco J-815 spectrometer under nitrogen atmosphere. Solution state CD was recorded in quartz cuvette of 10 mm path length with the speed of 200 nm/min and the spectra represent an average of three scans. Temperature dependent measurements were performed by employing Peltier-type temperature controller (CDF-4265/15) in the range of 283 K to 371K with a ramp rate of 1 K/min. All CD raw data were subtracted from the blank sample CD containing PBS buffer (10 mM, pH = 7, 5% DMSO). Thin film CD spectra were recorded on quartz substrate by drop casting the respective solutions onto a quartz substrate and dried in air followed by vacuum drying at room temperature. Before drop casting the samples, the quartz substrates were cleaned by immersing them in three different solvents (first isopropyl alcohol, second double distilled water and finally acetone) under ultrasonication for 20 minutes and dried by blowing a stream of nitrogen gas. Metal ion screening studies were performed by drop casting the 100 μM aqueous perchlorate salts of alkali and transition metal ions (Na^+, Mg^{2+}, K^+, Ca^{2+}, Co^{3+}, Ni^{2+}, Cu^{2+}, Zn^{2+}, Cd^{2+}, Hg^{2+} and Pb^{2+}) on top of preformed BNA_{10}-dT_{10} thin film containing quartz substrate and allowed to dry in air followed by vacuum drying at room temperature. The $\Delta\theta$ was defined as, $\Delta\theta = CD_0 - CD$ where CD_0 and CD are CD intensity at 400 nm before and after addition of metal ions respectively and θ is CD intensity at 400 nm after addition of metal ions.

NMR spectroscopy. ^1H and ^{13}C NMR spectra were recorded on a Bruker AV-400 spectrometer with chemical shifts reported as ppm (in $CDCl_3$/DMSO-d_6 with tetramethylsilane as internal standard).

Field emission scanning electron microscopy (FESEM). FESEM images were acquired with a FEI Nova nanoSEM-600 equipped with a field-emission gun operating at 15 kV. The samples were prepared by drop casting solutions on to the silicon (111) surface and dried in air followed by washing with excess amount of milli Q water (to remove salt on assembled structures) and vacuum dried at room temperature. Before sample preparation the silicon surface was cleaned by immersing them in three different solvents (first isopropyl alcohol, next double distilled water and finally acetone) under ultrasonication for 20 minutes and dried by blowing a stream of nitrogen gas.

ATIR spectroscopy. ATIR spectra were recorded on Perkin Elmer spectrophotometer. The highly dried powder samples were placed on diamond crystal and spectra were recorded from 4000 cm^{-1} to 400 cm^{-1} at ambient conditions.

Powder X-ray diffraction (PXRD). PXRD patterns were recorded with a Rigaku-99 (Miniflex) diffractometer using Cu Kα radiation (λ=1.5406 Å). The samples were prepared by drop casting the aqueous solutions onto a quartz substrate and allowed to dry in air followed by vacuum drying at room temperature. The diffraction peaks were indexed by DICVOL program. Before all measurements the quartz substrate were cleaned as mentioned above.

Dynamic light scattering (DLS). DLS measurements were performed on a NanoZS (Malvern UK) employing a 532 nm laser at a back scattering angle of 173°.

Synthesis of tert-butyl-2-bromoethylcarbamate (1).

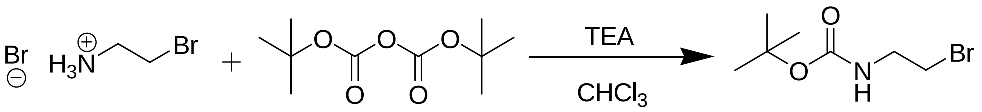

1

To a stirred solution of 2-bromo-ethylamine hydrogen bromide (2 g, 9.85 mmol) in chloroform, triethyl amine (1.75 mL, 9.85 mmol) was added at 0 °C. After 10 min. Di-*tert*-butyl dicarbonate in chloroform ($CHCl_3$) solution was added dropwise to the above solution and the reaction was allowed to stir for 6 h. After completion of the reaction, solvent was evaporated under vacuo. The compound was extracted with DCM (100 mL), organic layer was washed with water (200 mL and dried over anhydrous sodium sulfate. The crude product was purified using column chromatography on silica gel using ethyl acetate (EtOAc)/petroleum ether (15/85) as an eluent to afford colorless liquid of **1** in good yield (93%). ^{1}H-NMR (400 MHz, *CDCl$_3$*) δ_{ppm} 4.87 (1H, br), 3.46 (2H, t), 3.39 (2H, t), 1.38 (9H, s),. ^{13}C-NMR (100 MHz, *CDCl$_3$*) δ_{ppm} 155.2, 79.0, 41.3, 31.8, 27.3. MALDI-TOF-MS: found 223.40 $[M]^+$, calcd. 223.02 for $C_7H_{14}BrNO_2$.

Synthesis of Boc-protected adeninyl-9-ethylamine (2).

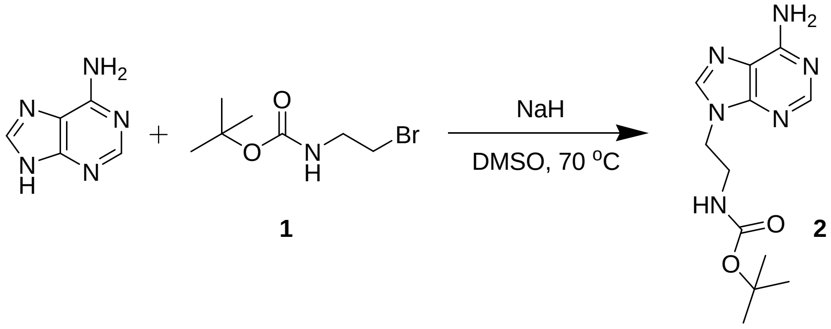

Adenine (1 g, 7.40 mmol) and sodium hydride (0.59 g, 14.8 mmol) were dissolved in DMF solution at 0 ºC and stirred for 30 min. To this mixture, *tert*-butyl-2-bromoethylcarbamate (**1**) (1.65 g, 7.40 mmol) was added. The reaction mixture was heated up to 65 ºC and allowed to stir for 24 h. The reaction progress was monitored with TLC. After completion of the reaction, solution was dissolved in 0.5 N HCl at 0 ºC, solvent was evaporated under vacuo. The crude product was purified by column chromatography on silica gel using MeOH/$CHCl_3$ (2/98) as an eluent to afford white solid of **2** in moderate yield (30%). ^{1}H-NMR (400 MHz, *CDCl$_3$*) δ_{ppm} 8.34 (1H, s), 7.76 (1H, s), 5.61 (2H, br), 5.03 (1H, s), 4.35 (2H, d), 3.57 (2H, q), 1.40 (9H, s).^{13}C-NMR (100 MHz, *CDCl$_3$*) δ_{ppm} 155.0, 152.9, 150.1, 140.9, 119.7, 79.9, 43.7, 40.4, 28.2. MALDI-TOF-MS: found 278.54 $[M]^+$, calcd. 278.14 for $C_{12}H_{18}N_6O_2$.

Synthesis of Boc-deprotected adeninyl-9-ethylamine (3).

Compound **2** was dissolved in dichloromethane (CH_2Cl_2) and then trifluoroacetic acid (TFA) was added and allowed to stir for 6 h. The completion of the reaction was confirmed by TLC and solvent was evaporated under vacuo. The compound was washed with toluene to remove trace amount TFA. The resultant product **3** was used for the next

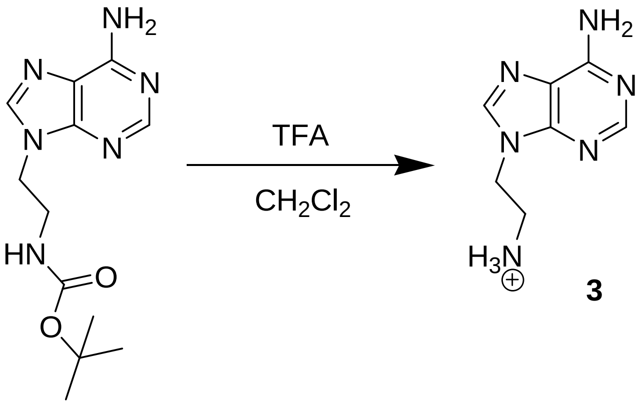

reaction without any further purification.

Synthesis of butylimido dicarboxylic acid intermediate (4).

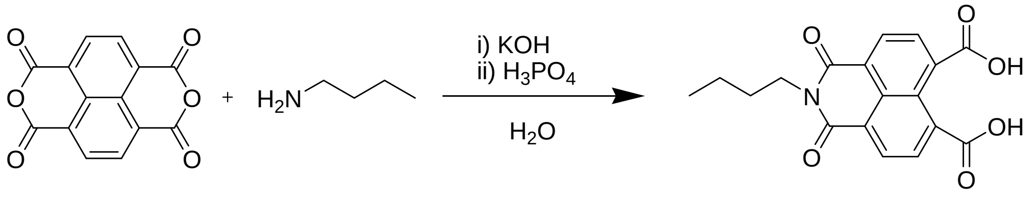

4

To the stirred solution of 1,4,5,8-naphthalenetetracarboxylicdianhydride (NDA) (1 g, 3.72 mmol) in water, KOH (0.9 g, 17.15 mmol) was added. The pH of the dark brown solution was adjusted to 6.3 by dropwise addition of dilute phosphoric acid (H_3PO_4). After 5-10 min. of vigorous stirring n-butyl amine was added fallowed by re-adjusting the pH of the solution to 6.3 with dilute H_3PO_4. The reaction mixture was heated up to 110 ºC and allowed to stir for 20 h. The reaction mixture was cooled to room temperature. The fine precipitate was removed by filtration. The resulting clear filtrate was acidified to pH 4 with acetic acid under vigorously stirred condition for 1 h. A light yellow color cream precipitate was collected by filtration under suction and washed with 10% dilute acetic acid, excess of distilled water fallowed drying at 45° C overnight to give brown colored powder **4** in good yield (60%).^{1}H-NMR (*DMSO-d6*, 400 MHz) δ_H 0.93(3H, t) , 1.37 (2H, t), 1.63 (2H, m), 4.04 (2H, t), 8.19 (2H, d), 8.55 (2H, d), 13.55 (2H, br); HRMS: found

342.0956 $[M+H]^+$, calcd. 341.0899 for $C_{18}H_{15}NO_6$.

Synthesis of BNA. To the stirred solution of **3** in DMSO, DIPEA was added and allowed to stir for 15 min. Compound **4** was added to the reaction mixture and allowed to stir another 20 h at 135° C in a sealed top vial. After cooling to room temperature, reaction mixture was transferred to 100 mL chloroform, the resulting precipitate was collected by filtration and washed with excess of $CHCl_3$, MeOH and diethyl ether before being dried in vacuum at 60 ºC

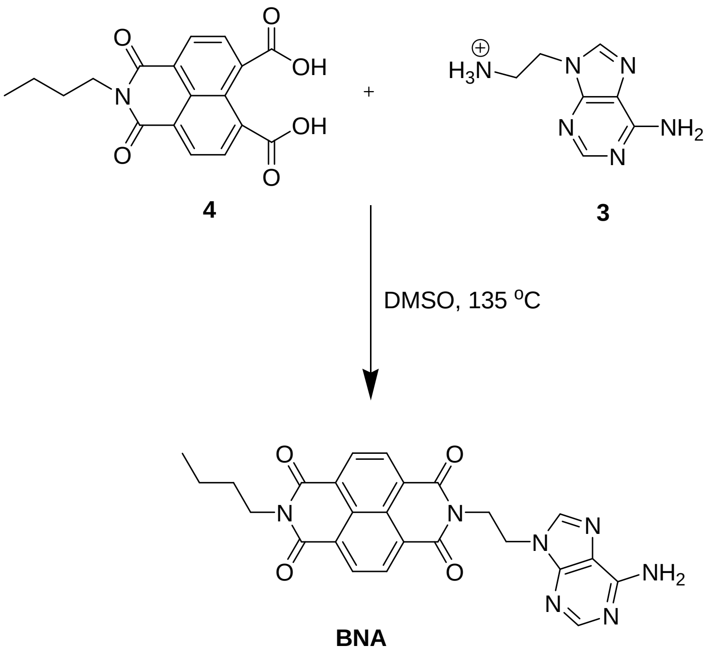

overnight to offer brown color solid BNA in good yield (40%). ^{1}H NMR (*DMSO-d6*, 400 MHz) δ_H, 8.61 (2H, d), 8.52 (2H, d), 8.14 (1H, s), 7.47 (1H, s), 7.05 (1H, s), 4.53 (2H, t), 4.48 (2H, t), 4.05 (2H, t), 1.64 (2H, m), 1.38 (2H, m), 0.959 (3H, s); ^{13}C NMR (*DMSO-d6+TFA*, 400 MHz) δ_C , 162.6, 162.4, 149.6, 148.8, 144.4, 144.2, 130.3, 130.2, 126.4, 126.0, 125.7,117.8, 42.2, 29.4, 19.6, 13.3; Elem. Anal. found C, 62.10; H, 4.40; N, 20.25; calcd. C, 62.11; H, 4.38; N, 20.28; O, 13.24 for $C_{25}H_{21}N_7O_4$.

6.5 Appendix

- ^{1}H-NMR and ^{13}C NMR spectra of **1**
- ^{1}H-NMR spectra of **4**
- ^{1}H-NMR and ^{13}C NMR spectra of BNA

^{1}H-NMR spectra (*CDCl$_3$*, 400 MHz, 298 K) of **1**

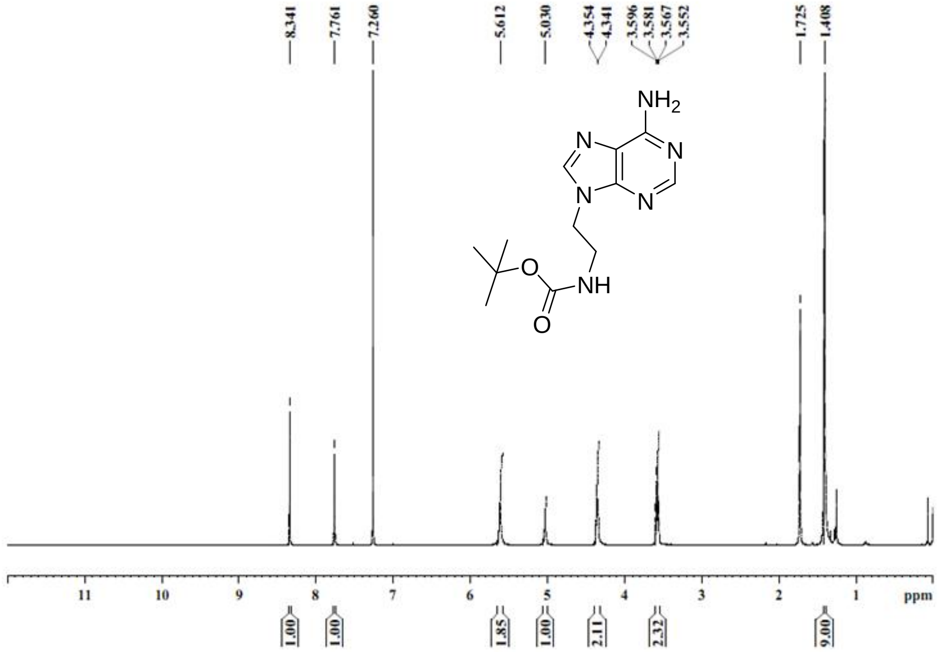

^{13}C NMR spectra (*$CDCl_3$*, 100 MHz, 298 K) of **1**

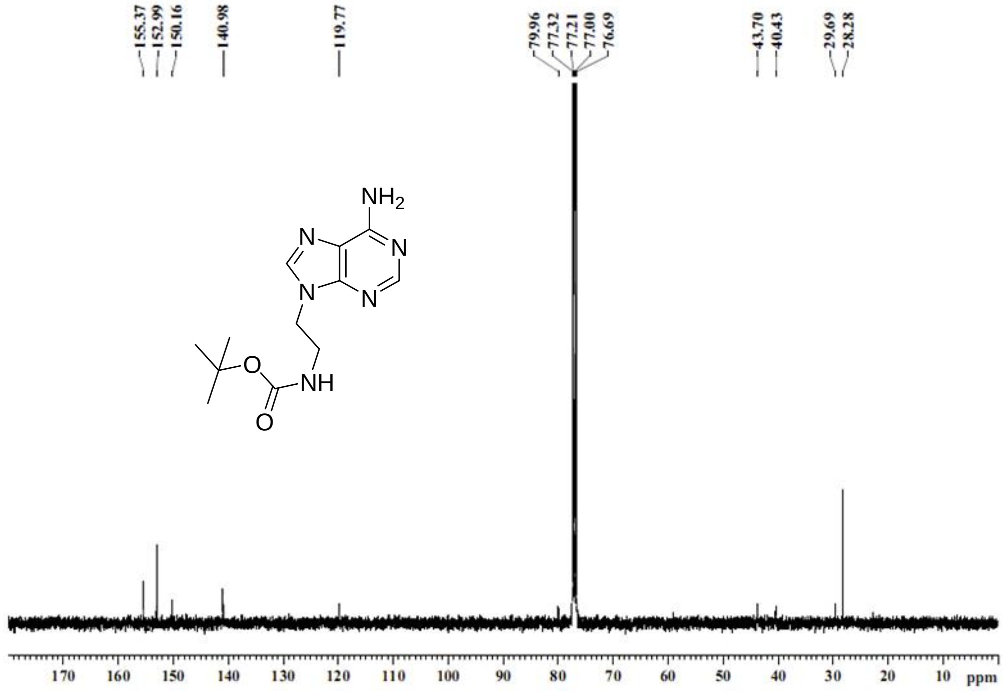

^{1}H-NMR spectra (*$CDCl_3$*, 400 MHz, 298 K) of **4**

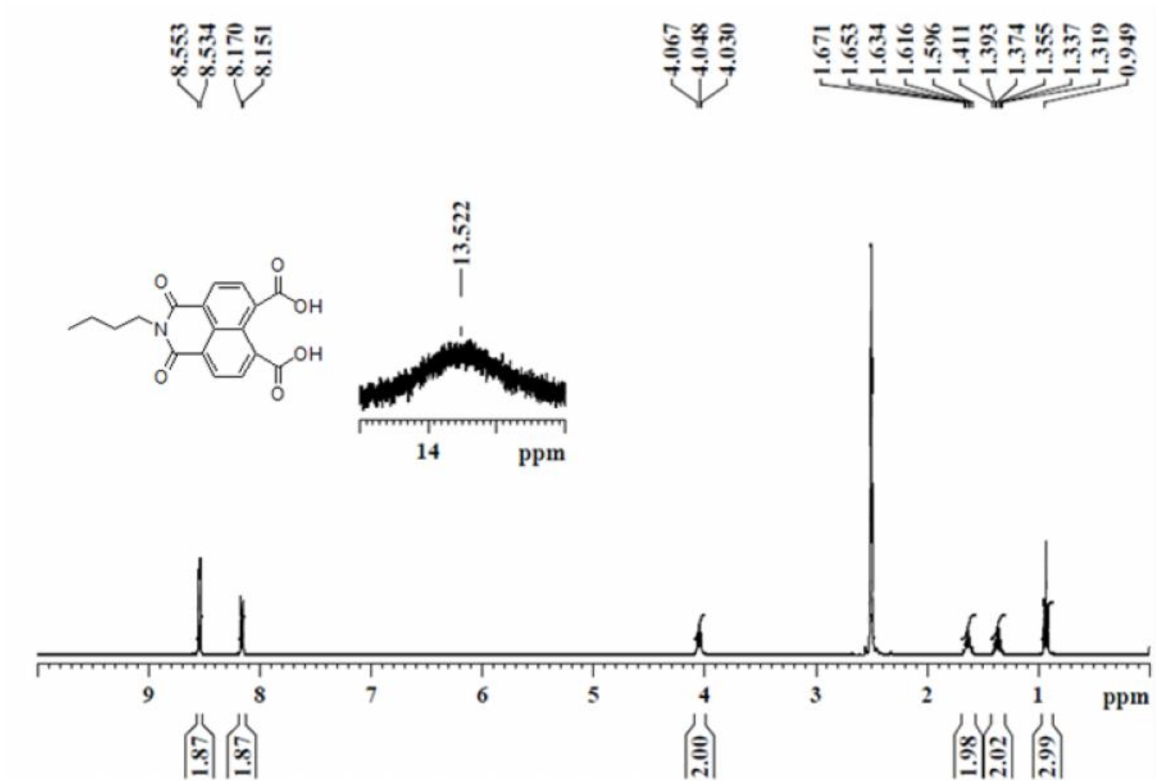

^{1}H-NMR spectra (DMSO-*d6*, 400 MHz, 298 K) of BNA

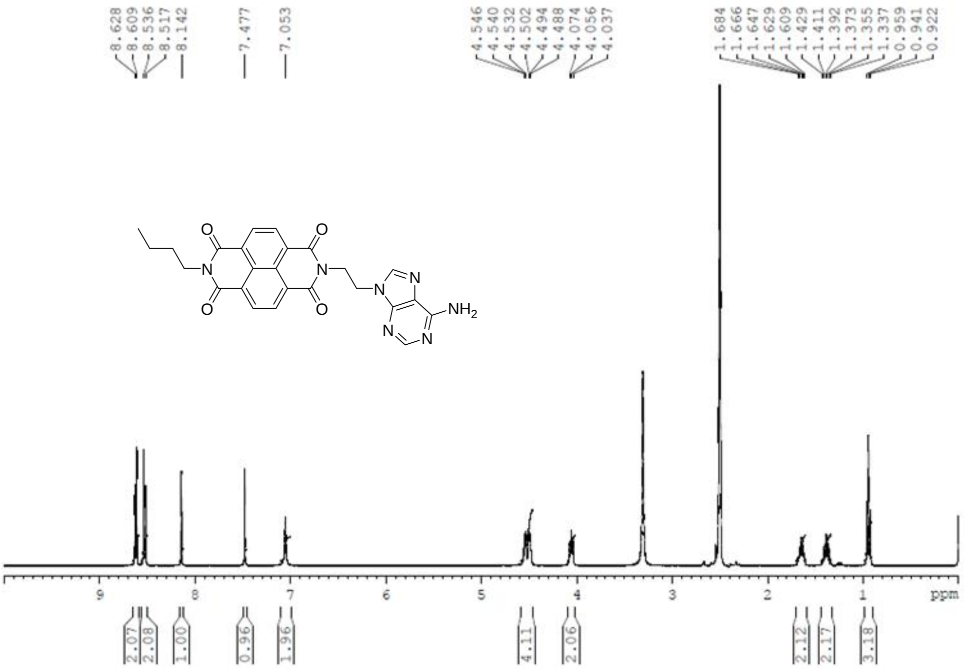

^{13}C-NMR spectra (DMSO-*d6*+TFA, 100 MHz, 298 K) of BNA

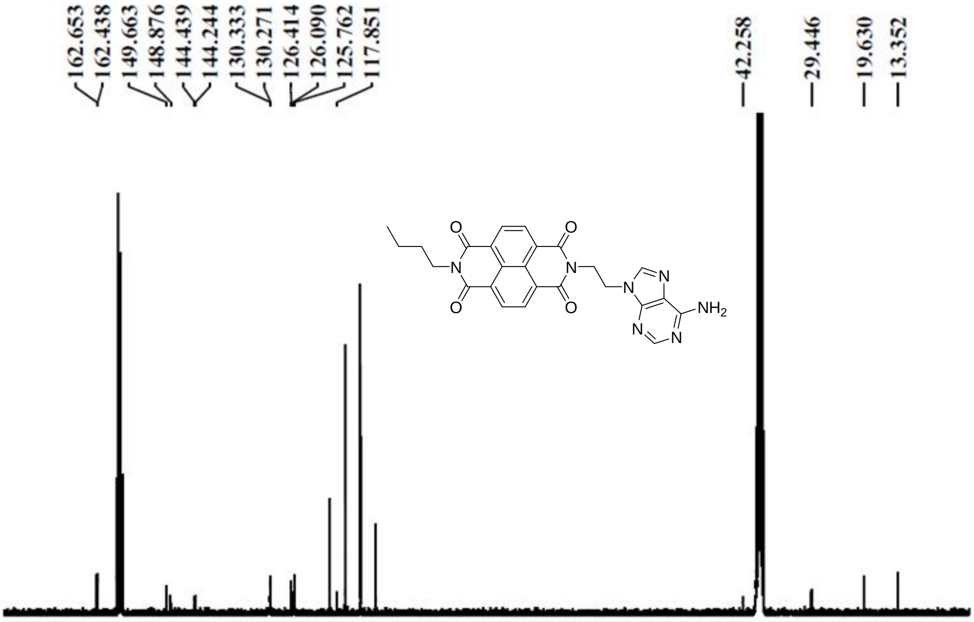

6.6 References

1. Lamborg, C. H.; Hammerschmidt, C. R.; Bowman, K. L.; Swarr, G. J.; Munson, K. M.; Ohnemus, D. C.; Lam, P. J.; Heimburger, L.-E.; Rijkenberg, M. J. A.; Saito, M. A., A global ocean inventory of anthropogenic mercury based on water column measurements. *Nature* **2014,** *512*, 65-68.
2. Kim, H. N.; Ren, W. X.; Kim, J. S.; Yoon, J., Fluorescent and colorimetric sensors for detection of lead, cadmium, and mercury ions. *Chem. Soc. Rev.* **2012,** *41*, 3210-3244.
3. Nicholson, J. K.; Kendall, M. D.; Osborn, D., Cadmium and mercury nephrotoxicity. *Nature* **1983,** *304*, 633-635.
4. UNEP, Global Mercury Assessment 2013: Sources, Emissions, Releases and Environmental Transport *UNEP Chemicals Branch,Geneva* **2013**, Switzerland.
5. Nolan, E. M.; Lippard, S. J., Tools and tactics for the optical detection of mercuric ion. *Chem. Rev.* **2008,** *108*, 3443-3480.
6. Jensen, S.; Jernelov, A., Biological methylation of mercury in aquatic organisms. *Nature* **1969,** *223*, 753-754.
7. Renzoni, A.; Zino, F.; Franchi, E., Mercury levels along the food chain and risk for exposed populations. *Environ. Res.* **1998,** *77*, 68-72.
8. Ono, A.; Togashi, H., Highly selective oligonucleotide-based sensor for mercury(II) in aqueous solutions. *Angew. Chem. Int. Ed.* **2004,** *43*, 4300-4302.
9. Kim, I. B.; Bunz, U. H., Modulating the sensory response of a conjugated polymer by proteins: an agglutination assay for mercury ions in water. *J. Am. Chem. Soc.* **2006,** *128*, 2818-2819.
10. Liu, J.; Lu, Y., Rational design of "turn-on" allosteric DNAzyme catalytic beacons for aqueous mercury ions with ultrahigh sensitivity and selectivity. *Angew. Chem. Int. Ed.* **2007,** *46*, 7587-7590.
11. Wegner, S. V.; Okesli, A.; Chen, P.; He, C., Design of an emission ratiometric biosensor from MerR family proteins: a sensitive and selective sensor for Hg2+. *J. Am. Chem. Soc.* **2007,** *129*, 3474-3475.
12. Dave, N.; Chan, M. Y.; Huang, P. J.; Smith, B. D.; Liu, J., Regenerable DNA-functionalized hydrogels for ultrasensitive, instrument-free mercury(II) detection and removal in water. *J. Am. Chem. Soc.* **2010,** *132*, 12668-12673.
13. Loe-Mie, F.; Marchand, G.; Berthier, J.; Sarrut, N.; Pucheault, M.; Blanchard-Desce, M.; Vinet, F.; Vaultier, M., Towards an efficient microsystem for the real-time detection and quantification of mercury in water based on a specifically designed fluorogenic binary task-specific ionic liquid. *Angew. Chem. Int. Ed.* **2010,** *49*, 424-427.
14. Ye, B. C.; Yin, B. C., Highly sensitive detection of mercury(II) ions by fluorescence polarization enhanced by gold nanoparticles. *Angew. Chem. Int. Ed.* **2008,** *47*, 8386-8389.

15. Han, D.; Lim, S. Y.; Kim, B. J.; Piao, L.; Chung, T. D., Mercury(ii) detection by SERS based on a single gold microshell. *Chem. Commun.* **2010,** *46*, 5587-5589.

16. Wen, S.; Zeng, T.; Liu, L.; Zhao, K.; Zhao, Y.; Liu, X.; Wu, H. C., Highly sensitive and selective DNA-based detection of mercury(II) with alpha-hemolysin nanopore. *J. Am. Chem. Soc.* **2011,** *133*, 18312-18317.

17. Xue, X.; Wang, F.; Liu, X., One-step, room temperature, colorimetric detection of mercury (Hg2+) using DNA/nanoparticle conjugates. *J. Am. Chem. Soc.* **2008,** *130*, 3244-3245.

18. Zheng, P.; Li, M.; Jurevic, R.; Cushing, S. K.; Liu, Y.; Wu, N., A gold nanohole array based surface-enhanced Raman scattering biosensor for detection of silver(i) and mercury(ii) in human saliva. *Nanoscale* **2015,** *7*, 11005-11012.

19. Du, J.; Jiang, L.; Shao, Q.; Liu, X.; Marks, R. S.; Ma, J.; Chen, X., Colorimetric detection of mercury ions based on plasmonic nanoparticles. *Small* **2013,** *9*, 1467-1481.

20. Mor-Piperberg, G.; Tel-Vered, R.; Elbaz, J.; Willner, I., Nanoengineered electrically contacted enzymes on DNA scaffolds: functional assemblies for the selective analysis of Hg2+ ions. *J. Am. Chem. Soc.* **2010,** *132*, 6878-6879.

21. Zeng, T.; Li, T.; Li, Y.; Liu, L.; Wang, X.; Liu, Q.; Zhao, Y.; Wu, H. C., DNA-based detection of mercury(II) ions through characteristic current signals in nanopores with high sensitivity and selectivity. *Nanoscale* **2014,** *6*, 8579-8584.

22. Lin, Z. H.; Zhu, G.; Zhou, Y. S.; Yang, Y.; Bai, P.; Chen, J.; Wang, Z. L., A self-powered triboelectric nanosensor for mercury ion detection. *Angew. Chem. Int. Ed.* **2013,** *52*, 5065-5069.

23. Zhang, T.; Cheng, Z.; Wang, Y.; Li, Z.; Wang, C.; Li, Y.; Fang, Y., Self-assembled 1-octadecanethiol monolayers on graphene for mercury detection. *Nano Lett.* **2010,** *10*, 4738-4741.

24. Cho, E. S.; Kim, J.; Tejerina, B.; Hermans, T. M.; Jiang, H.; Nakanishi, H.; Yu, M.; Patashinski, A. Z.; Glotzer, S. C.; Stellacci, F.; Grzybowski, B. A., Ultrasensitive detection of toxic cations through changes in the tunnelling current across films of striped nanoparticles. *Nat. Mater.* **2012,** *11*, 978-985.

25. Knopfmacher, O.; Hammock, M. L.; Appleton, A. L.; Schwartz, G.; Mei, J.; Lei, T.; Pei, J.; Bao, Z., Highly stable organic polymer field-effect transistor sensor for selective detection in the marine environment. *Nat. Commun.* **2014,** *5*, 2954.

26. Huang, C. C.; Yang, Z.; Lee, K. H.; Chang, H. T., Synthesis of highly fluorescent gold nanoparticles for sensing mercury(II). *Angew. Chem. Int. Ed.* **2007,** *46*, 6824-6828.

27. Lee, J. S.; Han, M. S.; Mirkin, C. A., Colorimetric detection of mercuric ion (Hg2+) in aqueous media using DNA-functionalized gold nanoparticles. *Angew. Chem. Int. Ed.* **2007,** *46*, 4093-4096.

28. Li, D.; Wieckowska, A.; Willner, I., Optical analysis of Hg2+ ions by oligonucleotide-gold-nanoparticle hybrids and DNA-based machines. *Angew. Chem. Int. Ed.* **2008,** *47*, 3927-3931.

29. Zhu, Y.; Xu, L.; Ma, W.; Xu, Z.; Kuang, H.; Wang, L.; Xu, C., A one-step homogeneous plasmonic circular dichroism detection of aqueous mercury ions using nucleic acid functionalized gold nanorods. *Chem. Commun.* **2012,** *48*, 11889-11891.

30. Zhang, L.; Li, T.; Li, B.; Li, J.; Wang, E., Carbon nanotube-DNA hybrid fluorescent sensor for sensitive and selective detection of mercury(II) ion. *Chem. Commun.* **2010,** *46*, 1476-1478.

31. Helwa, Y.; Dave, N.; Froidevaux, R.; Samadi, A.; Liu, J., Aptamer-functionalized hydrogel microparticles for fast visual detection of mercury(II) and adenosine. *ACS Appl. Mater. Interfaces* **2012,** *4*, 2228-2233.

32. Xu, H.; Zhu, X.; Ye, H.; Yu, L.; Liu, X.; Chen, G., A simple "molecular beacon"-based fluorescent sensing strategy for sensitive and selective detection of mercury (II). *Chem. Commun.* **2011,** *47*, 12158-12160.

33. Houlton, A.; Pike, A. R.; Angel Galindo, M.; Horrocks, B. R., DNA-based routes to semiconducting nanomaterials. *Chem. Commun.* **2009**, 1797-1806.

34. Narayanaswamy, N.; Suresh, G.; Priyakumar, U. D.; Govindaraju, T., Double zipper helical assembly of deoxyoligonucleotides: mutual templating and chiral imprinting to form hybrid DNA ensembles. *Chem. Commun.* **2015,** *51*, 5493-5496.

35. Ruiz-Carretero, A.; Janssen, P. G.; Kaeser, A.; Schenning, A. P., DNA-templated assembly of dyes and extended pi-conjugated systems. *Chem. Commun.* **2011,** *47*, 4340-4347.

36. Hannah, K. C.; Armitage, B. A., DNA-templated assembly of helical cyanine dye aggregates: a supramolecular chain polymerization. *Acc. Chem. Res.* **2004,** *37*, 845-853.

37. de la Escosura, A.; Janssen, P. G.; Schenning, A. P.; Nolte, R. J.; Cornelissen, J. J., Encapsulation of DNA-templated chromophore assemblies within virus protein nanotubes. *Angew. Chem. Int. Ed.* **2010,** *49*, 5335-5338.

38. Varghese, R.; Wagenknecht, H. A., DNA as a supramolecular framework for the helical arrangements of chromophores: towards photoactive DNA-based nanomaterials. *Chem. Commun.* **2009**, 2615-2624.

39. Teo, Y. N.; Kool, E. T., DNA-multichromophore systems. *Chem. Rev.* **2012,** *112*, 4221-4245.

40. Bandy, T. J.; Brewer, A.; Burns, J. R.; Marth, G.; Nguyen, T.; Stulz, E., DNA as supramolecular scaffold for functional molecules: progress in DNA nanotechnology. *Chem. Soc. Rev.* **2011,** *40*, 138-148.

41. Malinovskii, V. L.; Wenger, D.; Haner, R., Nucleic acid-guided assembly of aromatic chromophores. *Chem. Soc. Rev.* **2010,** *39*, 410-422.

42. Iwaura, R.; Iizawa, T.; Minamikawa, H.; Ohnishi-Kameyama, M.; Shimizu, T., Diverse morphologies of self-assemblies from homoditopic 1,18-nucleotide-appended

bolaamphiphiles: effects of nucleobases and complementary oligonucleotides. *Small* **2010,** *6*, 1131-1139.

43. Nakamura, M.; Okaue, T.; Takada, T.; Yamana, K., DNA-templated assembly of naphthalenediimide arrays. *Chem. Eur. J.* **2012,** *18*, 196-201.

44. Iwaura, R.; Ohnishi-Kameyama, M.; Iizawa, T., Construction of helical J-aggregates self-assembled from a thymidylic acid appended anthracene dye and DNA as a template. *Chem. Eur. J.* **2009,** *15*, 3729-3735.

45. Puppels, G. J.; Otto, C.; Greve, J.; Robert-Nicoud, M.; Arndt-Jovin, D. J.; Jovin, T. M., Raman Microspectroscopic Study of Low-pH-Induced Changes in DNA Structure of Polytene Chromosomes. *Biochemistry* **1994,** *33*, 3386-3395.

46. Oh, B. N.; Park, S.; Ren, J.; Jang, Y. J.; Kim, S. K.; Kim, J., Label-free emission assay of mercuric ions using DNA duplexes of poly(dT). *Dalton Trans.* **2011,** *40*, 6494-6499.